F. Borghese · P. Denti · R. Saija

Scattering from Model Nonspherical Particles

Theory and Applications to Environmental Physics

Second Edition

Springer

Scattering from Model Nonspherical Particles

Physics of Earth and Space Environments

The series *Physics of Earth and Space Environments* is devoted to monograph texts dealing with all aspects of atmospheric, hydrospheric and space science research and advanced teaching. The presentations will be both qualitative as well as quantitative, with strong emphasis on the underlying (geo)physical sciences.
Of particular interest are

- contributions which relate fundamental research in the aforementioned fields to present and developing environmental issues viewed broadly
- concise accounts of newly emerging important topics that are embedded in a broader framework in order to provide quick but readable access of new material to a larger audience

The books forming this collection will be of importance for graduate students and active researchers alike.

F. Borghese P. Denti R. Saija

Scattering from Model Nonspherical Particles

Theory and Applications to Environmental Physics

Second Edition

With 144 Figures

Springer

Professor Dr. Ferdinando Borghese
Professor Dr. Paolo Denti
Dr. Rosalba Saija

Università di Messina
Dipartimento di Fisica della Materia e Tecnologie
Fisiche Avanzate
Salita Sperone 31
98166 Messina
Italy
e-mail: ferdinando.borghese@unime.it
paolo.denti@unime.it
rosalba.saija@unime.it

Library of Congress Control Number: 2006931920

ISSN 1610-1677
ISBN-10 3-540-37413-2 Springer Berlin Heidelberg New York
ISBN-13 978-3-540-37413-8 Springer Berlin Heidelberg New York
ISBN 3-540-44014-3 1st Edition Springer Berlin Heidelberg New York

Springer is a part of Springer Science+Business Media
springer.com

Typesetting: by the authors and techbooks using a Springer LaTeX macro package
Cover design: Erich Kirchner, Heidelberg

Printed on acid-free paper SPIN: 11810209 54/techbooks 5 4 3 2 1 0

To my wife…for reasons that are quite evident
to whomever knew her
Nando

Preface to the Second Edition

Since the publication of the first edition of this book, we have become deeply involved in astrophysics research, particularly the study of the interstellar medium. Modeling scattering particles as layered spheres or as aggregates of spherical scatterers, expanding the electromagnetic field in a series of vector multipole fields, and resorting to the T-matrix approach for averaging over the orientations of a dispersion of nonspherical particles are effective tools for studying scattering theory, which we described and extensively applied in the first edition of this book. In fact, these tools also proved to be adequate for studying cosmic dust, even when they must be applied to a new range of current problems. We refer, for example, to the description of mechanical interaction of electromagnetic radiation with cosmic dust grains, which is believed to be of paramount importance in determining the dynamics of the grains. Since this book is conceived as a summary of our work, the desire to encompass all new topics led us to revise both its content and its structure. Of course, beyond the changes that we outline below, all chapters were carefully revised.

Marginal changes and additions were made in Chap. 1, while Chap. 2 has been substantially revised to cover the light of general polarization and, in particular, with the description of the state of polarization of electromagnetic waves of general form. In this chapter we reserved ample space for the representation of the kinematics of the scattering processes both in the plane of scattering and in the meridional planes. We also discuss a generalization of the Stokes parameters that is suitable to describe the state of polarization of waves of general form.

Chapter 3 presents novel material, dealing with the conservation theorems for combined systems of fields and particles, and with their consequences. Thus, this chapter deals not only with the widely known Poynting theorem, but also with the conservation of linear momentum, which is responsible for the radiation pressure and with the conservation of angular momentum, which may be responsible for the (at least partial) alignment of the cosmic dust grains, and the consequent linear polarization of starlight. The explicit expressions for the radiation force $\boldsymbol{F}_{\mathrm{rad}}$, the radiation torque $\boldsymbol{\Gamma}_{\mathrm{rad}}$ and the emission force $\boldsymbol{F}_{\mathrm{e}}$ are presented.

Chapter 4 has been significantly revised. We introduce the appropriate multipole expansion for waves of general wavevector (both real and complex) and of general state of polarization. Formulas for the orientational averages have also been reported for particles with cylindrical symmetry. Radiation forces and torque dealt with in Chap. 3 are expressed here in terms of the transition matrix.

Chapter 5, which deals with the calculation of the transition matrix of aggregates of spherical scatterers, now includes the case of metal spheres that can sustain the propagation of longitudinal waves.

Chapter 6, dealing with scattering from particles in the vicinity of a plane interface, is almost unchanged. Nevertheless, we added new material relating to total internal reflection and scattering of evanescent waves, which is presently considered a good method to study the properties of biological particles, and is also relevant for near-field spectroscopy.

Chapter 7 has been greatly enlarged to include a number of new applications, such as the scattering by aggregates of large spheres, and by aggregates of metal spheres sustaining longitudinal waves. We also include applications regarding the radiation force and torque on aggregates of spherical scatterers as well as regarding the force due to the emission of radiation.

The only addition to Chap. 8 relates to the scattering of evanescent waves both from single spheres and from aggregated spheres.

No changes have been made in Chap. 9, while Chap. 10 now contains a few new sections on the effect of radiation pressure and radiation torque on cosmic dust grains. We also added a study of the morphology of the dust grains and of the distribution and polarization of the electromagnetic field in the interior of aggregated dust grains. The subject of these new sections was inspired by the wide interest of the astrophysicist community in the dynamics of the interstellar medium and in astrochemistry.

We renew our thanks to Dr. Orazio I. Sindoni, Dr. Maria Antonia Iatì, Prof. Santi Aiello and Dr. Cesare Cecchi-Pestellini, who we also mentioned in the first edition and who were partners in the research we report in this book. We also gratefully acknowledge the efforts of Dr. Arianna Giusto.

We want to express our sincere thanks to Prof. David Williams, University College London, whose understanding of all aspects of the astrophysical research has been the inspiration behind our astrophysics working, and Prof. Flavio Scappini, Istituto per i Materiali Nanostrutturati del Consiglio Nazionale delle Ricerche, Bologna, whose knowledge of astrochemistry was invaluable when facing certain aspects of the chemical effects of the radiation.

We are grateful to several colleagues for fruitful discussions that helped us in revising the book. In particular, our sincere thanks go to Prof. Nikolai Voshchinnikov, Sobolev Astronomical Institute, St. Petersburg, Russia, who gave us good advice on the didactical aspects of the book.

Last, but not least, we want to thank Springer, to whose publishing policy we owe the printing of this enlarged edition.

Messina, Italy
March 2006

Ferdinando Borghese
Paolo Denti
Rosalba Saija

Preface to the First Edition

The Mie theory is known to be the first approach to the electromagnetic scattering from homogeneous spheres endowed with all the accuracy of the Maxwell electromagnetic theory. It applies to spheres of arbitrary radius and refractive index and marks, therefore, noticeable progress over the approximate approach of Rayleigh, which applies to particles much smaller than the wavelength. As a consequence, after the publication of the Mie theory in 1908, several scattering objects, even when their shape was known to be nonspherical, were described in terms of equivalent spherical scatterers. It soon became evident, however, that the morphological details of the actual particles were often too important to be neglected, especially in some wavelength ranges. On the other hand, setting aside some particular cases in which the predictions of the Mie theory were acceptable, no viable alternative for the description of scattering from particles of arbitrary shape was at hand. This situation lasted, with no substantial changes, until about 25 years ago, when the exact solution to the problem of dependent scattering from aggregates of spheres was devised. This solution is a real improvement over the Mie theory because several processes that occur, e.g., in the atmospheric aerosols and in the interstellar medium, can be interpreted in terms of clustering of otherwise spherical scatterers. Moreover, nonspherical particles may be so distributed (both in size and orientation) as to smooth out the individual scattering properties. In this case, aggregates of spherical scatterers may be designed to approximate the real objects through a wise choice of the geometry and of the refractive indices of their components.

In the last 20 years, we have been active in the study of the scattering properties of aggregates of spheres, to whose theory we and our coworkers made some significant contributions that are, however, badly scattered throughout the literature. For this reason, we resolved to collect in this book these contributions organized within a coherent formalism, namely, the formalism of the multipole expansions in the framework of the transition matrix approach. The theory is supplemented by several results of calculations performed by ourselves and by our coworkers, whose inclusion is meant to yield information on the possible practical applications of the theory to systems of interest. In order to achieve uniformity of representation, the calculations were renewed and the results replotted. Therefore, this book should not be understood as a treatise on scattering, although the general theory is described in some detail, but rather as a digest of the experience we have gained through our work in the field. The general topic of the comparison of our results with the experimental data or with the results yielded by other theoretical methods and approaches is pursued, but we do not pretend to be exhaustive because both the theoretical and the experimental study of scattering from actual nonspherical particles is a fast-moving field. Anyway, references to the relevant papers and books are given for all the cases of interest.

We start by summarizing in Chap. 1 the general theory of the spherical vector multipole fields, which are a basic tool for the development of the whole electromagnetic theory.

In Chap. 2 we recall the essentials of the theory of electromagnetic scattering and of the propagation of electromagnetic waves through dispersions of particles of arbitrary shape. The whole chapter is meant to establish a notation and to stress the need for introducing averages over the orientation of the particles in order to get predictions that are comparable to the observational data.

In Chap. 3 we expand the electromagnetic field in terms of spherical vector multipole fields and relate the expansion of the incident to that of the scattered field through the introduction of the transition matrix. The transformation properties of latter operator under rotation of the coordinate frame are exploited to show how orientational averages over an ensemble of particles can be performed. Explicit formulas for the averages of quantities of practical interest are given for a few instances of orientational distribution functions in which the averaging can be performed analytically.

In Chap. 4, after recalling the essentials of the Mie theory for homogeneous spheres and its extensions to layered and radially nonhomogeneous spheres, we introduce the equations that solve the problem for an aggregate of spherical scatterers of arbitrary geometry. The theory for homogeneous spheres containing one or more spherical inclusions is also expounded. In the last section of this chapter, we summarize the essentials of the discrete dipole approximation and of the finite difference time domain method. This summary is meant to help the reader to appreciate the advantages of the transition matrix approach and to better understand our considerations when comparing our results with those of other researchers in the field.

In Chap. 5 the topic of the scattering of particles in the presence both of a metallic and a dielectric plane interface is discussed. Even in this case the problem of the orientational average over the particles is dealt with in some detail.

The applications of the theory are described in Chap. 6, where the scattering properties of single and aggregated spheres and of spheres containing inclusions are considered, and in Chap. 7, where single and aggregated spheres and hemispheres in the presence of a plane interface are dealt with.

Finally, in Chaps. 8 and 9 we discuss how the theory can be applied in two specific contexts, the study of atmospheric ice crystals and of the interstellar dust grains, respectively.

We conclude this book with a short Appendix meant to review the mathematics implied in the calculations we presented. Actually, this appendix is rather cursory as we constantly resorted to mathematical tools that are quite standard in electromagnetics and in the theory of angular momentum. Our choice allowed us to use the mathematics that is reported in the existing literature instead of proving and reporting the needed significant relations. Anyway, in our opinion, the content of the mathematical appendix should be sufficient to give useful hints to whomever wants to face the problem of electromagnetic scattering through the transition matrix approach.

Before closing, we want to acknowledge the effort of our colleagues Dr. Orazio I. Sindoni, Prof. Giuditta Toscano, Dr. Enrico Fucile, Dr. Maria Antonia Iatì, Prof. Santi Aiello, and Dr. Cesare Cecchi-Pestellini who in time collaborated to the research on which this book is based. Finally, we want to express our sincere thanks to Prof. Michael I. Mishchenko for a critical reading of the manuscript and for several helpful suggestions and to Prof. Rodolfo Guzzi, whose advice and encouragement greatly helped us in writing this book.

Messina, Italy
July 2002

Ferdinando Borghese
Paolo Denti
Rosalba Saija

Contents

1 Multipole Fields

1.1 Introduction

The propagation of an electromagnetic wave through an assembly of particles embedded within a homogeneous matrix is known to depend, to a large extent, both on the distribution and on the specific features of the particles themselves. The simplest case is that of a plane wave that impinges on a particle. As a result of the field-particle interaction, the incident wave undergoes *extinction*, i.e., a detector along the path of the wave records a smaller intensity than would be recorded in the absence of the particle. Extinction itself, however, is the result of two concurrent processes: the particle, on one hand, *absorbs* and, on the other hand, *scatters* the impinging radiation. The absorption process implies the transformation of the electromagnetic energy into some other form, in general heat. This can be accounted for by attributing to the particle a complex index of refraction whose choice falls into the realm of the solid state physics and will not be further discussed here. In turn, the scattering process can be roughly described by stating that the incident field excites the particle to emit a wave that at a large distance looks like a more or less spherical outgoing wave superposed to the original incident field. The whole process is uniquely determined by the boundary conditions that the components of the field must satisfy across the surface of the particle and at infinity. The form of the equations that stem from the boundary conditions, however, may turn out to be unmanageably complicated depending on the shape of the particle, so it is not surprising that, until recently, the scattering has been exactly calculated only for particles of simple shape.

The case in which the plane wave propagates through a medium containing several particles is even more complex. The field that excites the scattering from each particle does not coincide with the primary incident wave but is rather the superposition of the latter with the field that has previously been scattered by all other particles in the dispersion. Therefore, describing the propagation through such a medium requires taking into account the *multiple scattering processes* that occur among all the particles present. This, in turn, implies knowing the position as well as the orientation of all the particles in the dispersion.

A great simplification is achieved by assuming the particles to be spherical and homogeneous; in this case the scattered field does not depend on the orientation of the particles and can be described by the so-called Mie theory. It is not surprising, however, that Mie theory calculations are often of little use for the interpretation of the experimental data, because the particles that form the most common inhomogeneous media, e.g., an aerosol, are far from spherical. Furthermore, the particles can undergo aggregation processes that yield complex nonspherical scatterers. Therefore, in order to get useful information on the propagation through an inhomogeneous medium, one needs to resort to *computationally suitable models* both for the particles and for their dispersions.

In choosing a suitable model, we are guided by the remark that in several cases either nonspherical scatterers turn out to be aggregations of spherical monomers [1], or the distribution of the particles, both in size and in shape, may be such as to smooth out the specific scattering features that depend on the details of their shape. As a result, it is reasonable that the dispersion as a whole has a memory, at most, of the quantity of scattering material within the individual particles and of their overall shape. Therefore, we choose a *cluster of spherical scatterers* as a model to approximate the properties of the actual particles in the dispersion. The most striking advantage of this model is that no limitation of principle needs to be imposed on the radii and on the refractive indices of the component spheres. Furthermore, once the model for a given particle is set up, no further approximation is necessary.

The mathematical technique that is used to calculate the scattering of electromagnetic waves from a cluster of spheres is based on the expansion of the electromagnetic field in terms of a complete set of *multipole fields* [2] and on the introduction of a *transition matrix* [3] that transforms the expansion of the incident field into that of the scattered field. The transformation properties of the multipole fields under rotation of the coordinate axes can then be extensively used to assess the dependence of the scattered field and of other quantities of interest on the orientation of the scattering particle with respect to the incident field.

According to the considerations above, this chapter is devoted to summarizing the properties of the multipole fields with a particular emphasis on their transformation properties. A number of formulas will be established that will be useful both for setting up the theory and for establishing the relation among the scattering properties of the particles and the macroscopic observable quantities.

1.2 Field Equations

The behavior of the electromagnetic field is governed by the Maxwell equations that we write here in Gaussian units [4]

$$\nabla \times \bar{\boldsymbol{E}} = -\frac{1}{c}\frac{\partial \bar{\boldsymbol{B}}}{\partial t} \;, \tag{1.1a}$$

$$\nabla \times \bar{\boldsymbol{H}} = \frac{1}{c}\frac{\partial \bar{\boldsymbol{D}}}{\partial t} + \frac{4\pi}{c}\bar{\boldsymbol{\jmath}} \;, \tag{1.1b}$$

$$\nabla \cdot \bar{\boldsymbol{D}} = 4\pi\bar{\rho} \;, \tag{1.1c}$$

$$\nabla \cdot \bar{\boldsymbol{B}} = 0 \;. \tag{1.1d}$$

Equations (1.1a–d) must be supplemented by the constitutive equations that relate to each other $\bar{\boldsymbol{E}}$, $\bar{\boldsymbol{D}}$, $\bar{\boldsymbol{B}}$, and $\bar{\boldsymbol{H}}$ within a given medium. Here, we are concerned with *linear media* whose electromagnetic properties are described by the constitutive equations

$$\bar{\boldsymbol{D}} = \epsilon\bar{\boldsymbol{E}} \;, \qquad \bar{\boldsymbol{B}} = \mu\bar{\boldsymbol{H}} \;, \qquad \bar{\boldsymbol{\jmath}} = \sigma\bar{\boldsymbol{E}} \;,$$

where ϵ, μ, and σ are (Cartesian) tensors whose components may be space-dependent but, on account of the assumed linearity of the medium, are independent of the field strength. Hereafter, we will deal with nonmagnetic, isotropic media so that we take $\mu = 1$, whereas ϵ and σ will reduce to scalars that are space-dependent as far as the medium of interest is nonhomogeneous. With a few exceptions, this book deals with homogeneous media, however. Therefore, unless the nonhomogeneity is explicitly stated, ϵ, μ and σ are to be considered as space-independent scalars.

The linearity of the field equations and of the constitutive equations makes them applicable to each of the monochromatic components of the time Fourier transform of the fields $\bar{\boldsymbol{E}}$ and $\bar{\boldsymbol{B}}$ as well as of the sources $\bar{\rho}$ and $\bar{\boldsymbol{\jmath}}$. Accordingly, we assume, without loss of generality, that all the quantities of interest depend on time trough the factor $\exp(-\mathrm{i}\omega t)$ and, since all the fields must be real, we write e.g.

$$\bar{\boldsymbol{E}}(\boldsymbol{r}, t) = \mathrm{Re}\big[\boldsymbol{E}(\boldsymbol{r})\exp(-\mathrm{i}\omega t)\big] \;, \tag{1.2}$$

where the space-dependent part of the field $\boldsymbol{E}(\boldsymbol{r})$ may be complex. In practice, we work with the complex quantities and, only at the end of algebraic manipulations, take the real part of results.

For monochromatic fields, since μ has been assumed to be a constant scalar, (1.1a) and (1.1b) become

$$\nabla \times \boldsymbol{E} = \mathrm{i}k_{\mathrm{v}}\boldsymbol{B} \;, \tag{1.3a}$$

$$\nabla \times \boldsymbol{B} = -\mathrm{i}k_{\mathrm{v}}n^2\boldsymbol{E} \;, \tag{1.3b}$$

where we define the magnitude of the propagation vector in vacuo k_{v} and the complex refractive index n as

$$k_{\mathrm{v}} = \frac{\omega}{c} \;, \qquad n^2 = \mu\left(\epsilon + \frac{4\pi\mathrm{i}\sigma}{\omega}\right) \;.$$

Note that the positive sign in front of the imaginary part of n^2 stems from our choice of the time dependence of the fields through the factor $\exp(-\mathrm{i}\omega t)$.

This choice is opposite to that assumed, e.g., by van de Hulst [5] that leads to a negative sign in front of the imaginary part of n^2. We also remark that both ϵ and σ may be frequency dependent, so that the value of n in (1.3b) must be that appropriate to the frequency concerned.

From (1.3b) and the assumed homogeneity of the medium, it follows that

$$\nabla \cdot \boldsymbol{E} = 0 \, , \tag{1.4}$$

and, with the help of the identity

$$\mathrm{curl}\,\mathrm{curl} = \mathrm{grad}\,\mathrm{div} - \nabla^2 \, , \tag{1.5}$$

it is an easy matter to see that the electric and the magnetic field should satisfy the pair of (decoupled) vector Helmholtz equations

$$(\nabla^2 + n^2 k_\mathrm{v}^2)\boldsymbol{E} = 0 \, , \qquad (\nabla^2 + n^2 k_\mathrm{v}^2)\boldsymbol{B} = 0 \, . \tag{1.6}$$

Of course, across any surface that separates two (homogeneous) media of different refractive indexes, say n_1 and n_2, the solutions to (1.6) should satisfy the boundary conditions

$$\hat{\boldsymbol{n}} \times (\boldsymbol{E}_2 - \boldsymbol{E}_1) = 0 \, , \quad \hat{\boldsymbol{n}} \times (\boldsymbol{B}_2 - \boldsymbol{B}_1) = 0 \, ,$$

where $\hat{\boldsymbol{n}}$ is the unit normal to the separation surface. Note that the second equation above holds true for media of finite conductivity [6].

1.3 Vector Helmholtz Equation

Before proceeding further, a word of caution is necessary on the vector nature of (1.6). In fact, the operator ∇^2 is defined as

$$\nabla^2 \equiv \mathrm{div}\,\mathrm{grad}$$

and should therefore be applied to scalar functions only. Nevertheless, using (1.5), it is an easy matter to see that, provided rectangular coordinates are used, $\nabla^2\boldsymbol{E}$ can be consistently defined as a vector whose rectangular components are $\nabla^2 E_x$, $\nabla^2 E_y$, and $\nabla^2 E_z$. This definition grants separation of the vector Helmholtz equation into three scalar equations, each of which involves only one rectangular component of the field. As an example, each of the rectangular components of the polarized plane wave

$$\boldsymbol{E} = E_0 \hat{\boldsymbol{e}} \exp(\mathrm{i}\boldsymbol{k} \cdot \boldsymbol{r}) \, ,$$

where $\hat{\boldsymbol{e}}$ is a constant vector and $\boldsymbol{k} = k\hat{\boldsymbol{k}}$, with $k = nk_\mathrm{v}$, satisfies the Helmholtz equation, provided that

$$\boldsymbol{k} \cdot \hat{\boldsymbol{e}} = 0 \, ,$$

as required by (1.4).

Using rectangular coordinates is undoubtedly the best choice when one is concerned with the solution of the Helmholtz equations that should satisfy the boundary conditions across a plane surface. Nevertheless, when the boundary conditions need to be imposed across a differently shaped surface, for instance across a spherical surface, the choice of a more appropriate system of coordinates is in order. In fact, the vector Helmholtz equation separates in several systems of orthogonal curvilinear coordinates, but each of the resulting scalar equations always involves more than one component of the field. Since this kind of separation can hardly be considered as a simplification, it is advisable to search for a complete set of elementary vector solutions to (1.6), in terms of which each field vector could be conveniently expanded.

1.4 Transformation Properties of Vector Fields

The distinctive features of the vector fields stem from the transformation properties of their components under rotation of the coordinate system. Since the Helmholtz operator $\Omega_k = \nabla^2 + k^2$ is invariant under rotations, a detailed investigation of the transformation properties of the vector fields will help us determining the most convenient choice for the vector solutions to the Helmholtz equation.

1.4.1 Cartesian Vectors

We consider a rectangular coordinate system $Ox_1x_2x_3$ that a rotation around the origin through a vector angle $\boldsymbol{\omega} = \omega\hat{\boldsymbol{n}}$ transforms into the system $Ox_1'x_2'x_3'$. These systems will be referred to as Σ and Σ', respectively. As usual, the amplitude ω is counted as positive in a counterclockwise sense with respect to the unit vector $\hat{\boldsymbol{n}}$ along the axis of rotation. The transformation of Σ into Σ' is uniquely defined by the real orthogonal matrix $\mathrm{R}(\boldsymbol{\omega})$ that transforms the coordinates in Σ of any arbitrarily chosen point P into those that the *same point* has in Σ'. The transformation rule reads

$$x_i' = \sum_j R_{ij} x_j , \quad \text{or, matrixwise,} \quad \boldsymbol{r}' = \mathrm{R}(\boldsymbol{\omega})\boldsymbol{r} ,$$

where $\boldsymbol{r}$ and $\boldsymbol{r}'$ must be understood as two different representations of the coordinates of the same point P. Then, a *vector* is defined as a set of three quantities v_1, v_2, and v_3, that are its components in Σ, whose transformation rule under rotation of the coordinate system is identical to that of the coordinates of a point. Thus

$$v_i' = \sum_j R_{ij} v_j , \quad \text{or} \quad \boldsymbol{v}' = \mathrm{R}(\boldsymbol{\omega})\boldsymbol{v} ,$$

where v_1', v_2', and v_3' are to be understood as the components of the same vector $\boldsymbol{v}$ in Σ'. It may be worth stressing that the real orthogonal matrix R has an inverse R^{-1}, so that

$$\boldsymbol{r} = \mathrm{R}^{-1}(\boldsymbol{\omega})\boldsymbol{r}' \ . \tag{1.7}$$

When $\boldsymbol{v}$ is space dependent, both $\boldsymbol{v}$ and its argument transform alike under rotation of the coordinate system. Accordingly we write

$$\boldsymbol{v}'(\boldsymbol{r}') = \mathrm{R}(\boldsymbol{\omega})\boldsymbol{v}(\boldsymbol{r}) \ ,$$

or, on account of (1.7),

$$\boldsymbol{v}'(\boldsymbol{r}') = \mathrm{R}(\boldsymbol{\omega})\boldsymbol{v}(\mathrm{R}^{-1}(\boldsymbol{\omega})\boldsymbol{r}') \ .$$

Now, since $\boldsymbol{r}'$ denotes the vector coordinate of any point, the prime can be dropped, and the preceding equation is accordingly rewritten as

$$\boldsymbol{v}'(\boldsymbol{r}) = \mathrm{R}(\boldsymbol{\omega})\boldsymbol{v}(\mathrm{R}^{-1}(\boldsymbol{\omega})\boldsymbol{r}) \ . \tag{1.8}$$

Then, we associate to the transformation effected by the matrix R the operator $\mathrm{O_R} \equiv \mathrm{O}_{\boldsymbol{\omega}}$ defined by the equation

$$\mathrm{O}_{\boldsymbol{\omega}}\boldsymbol{v}(\boldsymbol{r}) = \boldsymbol{v}'(\boldsymbol{r}) \ ,$$

and, accordingly, rewrite (1.8) in the form

$$\mathrm{O}_{\boldsymbol{\omega}}\boldsymbol{v}(\boldsymbol{r}) = \mathrm{R}(\boldsymbol{\omega})\boldsymbol{v}(\mathrm{R}^{-1}(\boldsymbol{\omega})\boldsymbol{r}) \ , \tag{1.9}$$

which yields the general transformation rule of a vector field under rotation of the coordinate axes [7].

1.4.2 Spin of a Vector Field

We now apply (1.9) to investigate the transformation of the components of any vector field. To this end it suffices to consider only infinitesimal rotations $\mathrm{d}\boldsymbol{\omega}$ that are effected by the matrix $\mathrm{R}(\mathrm{d}\boldsymbol{\omega})$ with associated operator $\mathrm{O}_{\mathrm{d}\boldsymbol{\omega}}$. It is an easy matter to see that, for general direction of $\mathrm{d}\boldsymbol{\omega}$, the transformation of $\boldsymbol{r}$ reads [8]

$$\mathrm{R}(\mathrm{d}\boldsymbol{\omega})\boldsymbol{r} = \boldsymbol{r}' = \boldsymbol{r} - \mathrm{d}\boldsymbol{\omega} \times \boldsymbol{r} \ . \tag{1.10}$$

In particular, for rotations around the z axis $\mathrm{d}\boldsymbol{\omega} = \mathrm{d}\omega\,\hat{\boldsymbol{e}}_z$, and (1.10) becomes

$$\boldsymbol{r}' = \boldsymbol{r} - \mathrm{d}\omega\,\hat{\boldsymbol{e}}_z \times \boldsymbol{r} \ ,$$

which is equivalent to the scalar equations

$$\begin{aligned} x' &= x + y\,\mathrm{d}\omega \ , \\ y' &= y - x\,\mathrm{d}\omega \ , \\ z' &= z \ , \end{aligned}$$

with inverses

$$\begin{aligned} x &= x' - y'\,\mathrm{d}\omega \ , \\ y &= y' + x'\,\mathrm{d}\omega \ , \\ z &= z' \ . \end{aligned}$$

As a consequence, the components of any vector field $\boldsymbol{v}(\boldsymbol{r})$ transform according to the equations

$$\begin{aligned} v'_x(x,y,z) &= v_x(x - \mathrm{d}\omega\, y, y + \mathrm{d}\omega\, x, z) + \mathrm{d}\omega\, v_y(x - \mathrm{d}\omega\, y, y + \mathrm{d}\omega\, x, z) \ , \\ v'_y(x,y,z) &= v_y(x - \mathrm{d}\omega\, y, y + \mathrm{d}\omega\, x, z) - \mathrm{d}\omega\, v_x(x - \mathrm{d}\omega\, y, y + \mathrm{d}\omega\, x, z) \ , \\ v'_z(x,y,z) &= v_z(x - \mathrm{d}\omega\, y, y + \mathrm{d}\omega\, x, z) \ . \end{aligned}$$

Series expansion to first order in $\mathrm{d}\omega$ then yields

$$\begin{aligned} v'_x(x,y,z) &= v_x(x,y,z) - \mathrm{d}\omega \left(y\frac{\partial}{\partial x} - x\frac{\partial}{\partial y} \right) v_x(x,y,z) + \mathrm{d}\omega\, v_y(x,y,z) \ , \\ v'_y(x,y,z) &= v_y(x,y,z) - \mathrm{d}\omega \left(y\frac{\partial}{\partial x} - x\frac{\partial}{\partial y} \right) v_y(x,y,z) - \mathrm{d}\omega\, v_x(x,y,z) \ , \\ v'_z(x,y,z) &= v_z(x,y,z) - \mathrm{d}\omega \left(y\frac{\partial}{\partial x} - x\frac{\partial}{\partial y} \right) v_z(x,y,z) \ , \end{aligned}$$

i.e., in operator form

$$\mathrm{O}_{\mathrm{d}\boldsymbol{\omega}}\boldsymbol{v}(x,y,z) = (\mathbf{1} - \mathrm{i}\mathrm{d}\boldsymbol{\omega}\,\mathrm{J}_z)\boldsymbol{v}(x,y,z) \ , \tag{1.11}$$

where

$$\mathrm{J}_z = \mathrm{L}_z + \mathrm{s}_z \ ,$$

with

$$\mathrm{L}_z = -\mathrm{i}\left(y\frac{\partial}{\partial x} - x\frac{\partial}{\partial y} \right)\mathbf{1} \quad \text{and} \quad \mathrm{s}_z = \begin{pmatrix} 0 & -\mathrm{i} & 0 \\ \mathrm{i} & 0 & 0 \\ 0 & 0 & 0 \end{pmatrix} \ .$$

Equation (1.11) shows that the vector fields transform according to a rule that is different from that appropriate for scalar fields. In fact, for rotations around the z axis, the generator of the transformations of a scalar field is known to be L_z, the z component of the orbital angular momentum operator. According to (1.11), the generator of the transformation of a vector field turns out to be J_z, which is the sum of L_z and of a new angular momentum operator s_z that is represented by a 3×3 matrix and has therefore the quantum number

$s = 1$. In other words any vector field, by its very nature, has an intrinsic *spin* of 1. As a check, we can effect two further infinitesimal rotations around the x and the y axis and find that

$$\mathrm{s}_x = \begin{pmatrix} 0 & 0 & 0 \\ 0 & 0 & -\mathrm{i} \\ 0 & \mathrm{i} & 0 \end{pmatrix} , \quad \mathrm{s}_y = \begin{pmatrix} 0 & 0 & \mathrm{i} \\ 0 & 0 & 0 \\ -\mathrm{i} & 0 & 0 \end{pmatrix} .$$

It is then an easy matter to see that the matrices s_x, s_y, and s_z satisfy the commutation rule

$$\left[\mathrm{s}_x, \mathrm{s}_y\right] = \mathrm{i}\mathrm{s}_z ,$$

and cyclical permutations, which are the defining relations of the angular momentum operators.

1.5 Eigenvectors of the Angular Momentum

The results in Sect. 1.4 suggest that, from the point of view of the transformation properties, the most suitable set of vector basis functions for the expansion of any vector field, and in particular of the electromagnetic field, is composed of the simultaneous vector eigenfunctions of J^2 and J_z. In order to build these eigenfunctions, it is convenient to start from their transformation properties that will now be investigated in some detail. In the course of our study we will also establish a number of formulas that will prove useful for later applications.

1.5.1 Representations of the Rotation Operators

In the preceding section we associated to the transformation of coordinates defined by the matrix $\mathrm{R}(\boldsymbol{\omega})$ the operator $\mathrm{O}_{\boldsymbol{\omega}}$ that transforms the vector fields according to (1.9). For finite rotations, the form of $\mathrm{O}_{\boldsymbol{\omega}}$ is [8]

$$\mathrm{O}_{\boldsymbol{\omega}} = \exp(-\mathrm{i}\boldsymbol{\omega} \cdot \mathrm{J}) ,$$

which can be easily checked by expanding $\mathrm{O}_{\boldsymbol{\omega}}$ to first order in $\boldsymbol{\omega}$ and letting $\boldsymbol{\omega} \to \mathrm{d}\boldsymbol{\omega}$. Note that the hermiticity of J grants the unitarity of $\mathrm{O}_{\boldsymbol{\omega}}$ that characterizes any rotation operator. In principle, $\mathrm{O}_{\boldsymbol{\omega}}$ can be represented on any orthonormal basis, but the most convenient choice proves to be the set of the eigenvectors $|j, m\rangle$, i.e., the solutions of the simultaneous eigenvalue equations

$$\mathrm{J}^2|j\,m\rangle = j(j+1)|j\,m\rangle ,$$
$$\mathrm{J}_z|j\,m\rangle = m|j\,m\rangle ,$$

with $j \geq 0$ and $-j \leq m \leq j$. Operating on the eigenvectors $|j\,m\rangle$, $\mathrm{O}_{\boldsymbol{\omega}}$ yields a linear combination of them with the same j but different m, i.e.,

$$\mathrm{O}_{\boldsymbol{\omega}}|j\,m\rangle = \sum_{m'} |j\,m'\rangle \mathcal{D}^{(j)}_{m'm}(\boldsymbol{\omega}) \ ,$$

where we define

$$\mathcal{D}^{(j)}_{m'm}(\boldsymbol{\omega}) = \langle j\,m'|\mathrm{O}_{\boldsymbol{\omega}}|j\,m\rangle \ .$$

The coefficients $\mathcal{D}^{(j)}_{m'm}$ are the elements of the matrices $\mathrm{D}^{(j)}$ that form a representation of order $2j+1$ of the three-dimensional rotation operators on the basis of the eigenvectors $|j\,m\rangle$. Their explicit form is customarily given in terms of the Euler rotations that are described below (see also Fig. 1.1) and, according to commonly accepted conventions, are considered as positive when effected counterclockwise.

First, the rotation through an angle α around the z axis of Σ transforms the axes $Oxyz$ into the axes $Ox'y'z'$. The operator associated to this rotation is

$$\mathrm{O}_\alpha = \exp(-\mathrm{i}\alpha \mathrm{J}_z) \ .$$

Second, the rotation through an angle β around the y' axis transforms the axes $Ox'y'z'$ into $Ox''y''z''$. The associated operator is

$$\mathrm{O}_\beta = \exp(-\mathrm{i}\beta \mathrm{J}_{y'}) \ .$$

Third, the rotation through an angle γ around the z'' axis transforms the axes $Ox''y''z''$ into the axes $Ox'''y'''z'''$. The associated operator is

$$\mathrm{O}_\gamma = \exp(-\mathrm{i}\gamma \mathrm{J}_{z''}) \ .$$

It may be worth noticing that the preceding definition of the Euler angles is such that, in Σ, the polar angles ϑ and φ of the z'' axis around which the rotation γ is effected coincide with β and α, respectively.

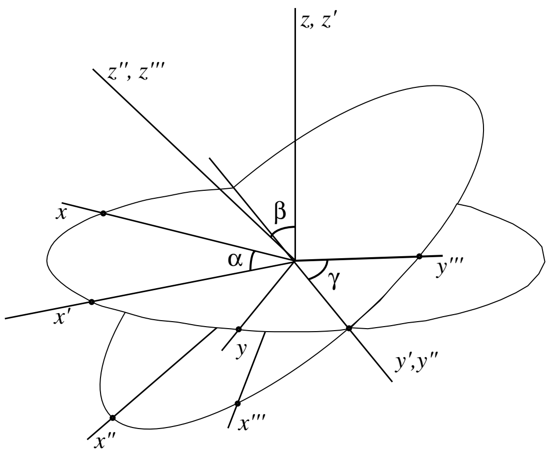

Fig. 1.1. The Eulerian angles

Hereafter, we denote with the symbol O_Θ the operator associated to the rotation defined by the Eulerian angles α, β and γ. We thus write

$$\mathrm{O}_\Theta = \exp(-\mathrm{i}\gamma \mathrm{J}_{z''}) \exp(-\mathrm{i}\beta \mathrm{J}_{y'}) \exp(-\mathrm{i}\alpha \mathrm{J}_z) \,, \tag{1.12}$$

whose representation on the basis of the $|j\,m\rangle$ vectors yield the required $\mathrm{D}^{(j)}$ matrices. We remark, however, that the form of O_Θ in (1.12) is not suitable for finding its representation because the three Eulerian rotations are effected around axes belonging to different reference frames. Nevertheless, it can be shown that an alternative form of O_Θ is [7]

$$\mathrm{O}_\Theta = \exp(-\mathrm{i}\alpha \mathrm{J}_z) \exp(-\mathrm{i}\beta \mathrm{J}_y) \exp(-\mathrm{i}\gamma \mathrm{J}_z) \,, \tag{1.13}$$

i.e., the Eulerian rotations can be effected around the axes of Σ, provided that their order is reversed. Using (1.13) it is an easy matter to show that the matrix elements of O_Θ are

$$\begin{aligned} \mathcal{D}^{(j)}_{m'm}(\alpha,\beta,\gamma) &= \langle j\,m'|\exp(-\mathrm{i}\alpha \mathrm{J}_z) \exp(-\mathrm{i}\beta \mathrm{J}_y) \exp(-\mathrm{i}\gamma \mathrm{J}_z)|j\,m\rangle \\ &= \exp(-\mathrm{i}m'\alpha)\, d^{(j)}_{m'm}(\beta) \exp(-\mathrm{i}m\gamma) \,, \end{aligned}$$

where we use the notation

$$d^{(j)}_{m'm}(\beta) = \langle j\,m'|\exp(-\mathrm{i}\beta \mathrm{J}_y)|j\,m\rangle$$

for the matrix elements of O_β. The explicit expression of the matrix elements $d^{(j)}_{m'm}(\beta)$ has been found by Wigner and turns out to be [7]

$$\begin{aligned} d^{(j)}_{m'm}(\beta) &= (-)^{m'-m}\left[(j+m)!(j-m)!(j+m')!(j-m')!\right]^{1/2} \\ &\times \sum_\kappa (-)^\kappa \frac{(\cos\beta/2)^{2j+m-m'-2\kappa}(\sin\beta/2)^{m'-m+2\kappa}}{(j-m'-\kappa)!(j+m-\kappa)!(\kappa+m'-m)!\kappa!} \,, \end{aligned}$$

which holds true for $m' \geq m$ only, however. For $m' < m$ we resort to the properties

$$d^{(j)}_{m'm}(\beta) = d^{(j)}_{mm'}(-\beta) = (-)^{m-m'} d^{(j)}_{mm'}(\beta) \,,$$

which stem from the unitarity of $\mathrm{d}^{(j)}$. Close examination of the expression of $d^{(j)}_{m'm}$ yields the relations

$$d^{(j)}_{m'm}(\beta) = d^{(j)}_{-m\,,-m'}(\beta) = (-)^{m'-m} d^{(j)}_{-m'\,,-m}(\beta) \,,$$

which, when inserted into the definition of $\mathrm{D}^{(j)}$ imply

$$\mathcal{D}^{(j)}_{m'm}(-\gamma,-\beta,-\alpha) = \mathcal{D}^{(j)*}_{mm'}(\alpha,\beta,\gamma) = (-)^{m-m'} \mathcal{D}^{(j)}_{-m\,,-m'}(\alpha,\beta,\gamma) \,.$$

Since the matrices $\mathrm{D}^{(j)}$ transform a set of $2j+1$ orthonormal vectors into a new set of $2j+1$ rotated orthonormal vectors, their elements $\mathcal{D}^{(j)}_{m'm}$ must satisfy the customary orthonormality conditions

$$\sum_m \mathcal{D}^{(j)*}_{m'm}(\alpha,\beta,\gamma)\mathcal{D}^{(j)}_{m''m}(\alpha,\beta,\gamma) = \delta_{m'm''} \ ,$$
$$\sum_m \mathcal{D}^{(j)*}_{mm'}(\alpha,\beta,\gamma)\mathcal{D}^{(j)}_{mm''}(\alpha,\beta,\gamma) = \delta_{m'm''} \ .$$

It can also be proved that the elements $\mathcal{D}^{(j)}_{m'm}$ satisfy the integral relation

$$\int \mathcal{D}^{(j_1)*}_{\mu_1 m_1}(\alpha,\beta,\gamma)\,\mathcal{D}^{(j_2)}_{\mu_2 m_2}(\alpha,\beta,\gamma)\,\mathrm{d}\Theta = \frac{8\pi^2}{2j_1+1}\delta_{\mu_1\mu_2}\delta_{m_1m_2}\delta_{j_1j_2} \ , \tag{1.14}$$

where

$$\mathrm{d}\Theta = \mathrm{d}\alpha\,\sin\beta\,\mathrm{d}\beta\,\mathrm{d}\gamma \ ,$$

with

$$0 \le \alpha \le 2\pi \ , \quad 0 \le \beta \le \pi \ , \quad 0 \le \gamma \le 2\pi \ .$$

Equation (1.14) thus states the orthogonality of the rotation matrix elements on the surface of the unit sphere.

The transformation law of the eigenvectors of the angular momentum allows us to define uniquely the so called *irreducible spherical tensors* as follows:

> An irreducible spherical tensor of rank j is a set of $2j+1$ quantities that under rotation of the coordinate axes transform according to $\mathrm{D}^{(j)}$.

The $2j+1$ quantities that form an irreducible spherical tensor of rank j are its *spherical components*, and each one of them may be a Cartesian tensor of any rank. For instance, a set of three *vectors* that under rotation of the coordinate system transform among themselves according to $\mathrm{D}^{(1)}$ form an irreducible spherical tensor of rank 1. We shall see later that each of the three eigenvectors of the spin of a vector field is a Cartesian vector with complex components, but the whole set transforms under rotation according to $\mathrm{D}^{(1)}$, so that they are also the components of an irreducible spherical tensor of rank 1. In any case, since the transformation of the vector fields is governed by the angular momentum $\mathrm{J} = \mathrm{L} + \mathrm{s}$, it is convenient to consider in some detail the eigenstates of L and those of s.

1.5.2 Spherical Harmonics

The spherical harmonics, i.e., the simultaneous eigenfunctions of L^2 and L_z, are defined by the simultaneous eigenvalue equations

$$\mathrm{L}^2 Y_{lm}(\hat{\boldsymbol{r}}) = l(l+1)Y_{lm}(\hat{\boldsymbol{r}}) \ ,$$
$$\mathrm{L}_z Y_{lm}(\hat{\boldsymbol{r}}) = mY_{lm}(\hat{\boldsymbol{r}}) \ ,$$

with $l \ge 0$ and $-l \le m \le l$, and their explicit form is [4]

$$Y_{lm}(\hat{\boldsymbol{r}}) \equiv Y_{lm}(\vartheta,\varphi) = \sqrt{\frac{2l+1}{4\pi}\frac{(l-m)!}{(l+m)!}}\,P_{lm}(\cos\vartheta)\,\mathrm{e}^{\mathrm{i}m\varphi}\ . \tag{1.15}$$

In (1.15) the quantities P_{lm} are the associated Legendre functions of the first kind

$$P_{lm}(z) = \frac{(-)^m}{2^l l!}\,(1-z^2)^{m/2}\,\frac{\mathrm{d}^{l+m}}{\mathrm{d}z^{l+m}}(z^2-1)^l\,, \tag{1.16}$$

with

$$P_{l,-m}(z) = (-)^m\frac{(l-m)!}{(l+m)!}P_{lm}(z)\ ,$$

whose argument z may be either real or complex. The spherical harmonics form a complete orthonormal set on the surface of the unit sphere

$$\int Y^*_{lm}\,Y_{l'm'}\,\mathrm{d}\Omega = \delta_{ll'}\delta_{mm'}\ ,$$

and, under rotation of the coordinate system, transform according to $\mathrm{D}^{(l)}$

$$\mathrm{O}_\Theta Y_{lm}(\vartheta,\varphi) = \sum_{m'} Y_{lm'}(\vartheta,\varphi)\mathcal{D}^{(l)}_{m'm}(\alpha,\beta,\gamma)\ . \tag{1.17}$$

The spherical harmonics with a given l are thus the components of an irreducible spherical tensor of rank l. For real argument they satisfy the complex conjugation equation

$$Y^*_{lm} = (-)^m\,Y_{l\,,-m}\ ,$$

and their parity is defined by the equation

$$Y_{lm}(\hat{\boldsymbol{r}}) = (-)^l\,Y_{lm}(-\hat{\boldsymbol{r}})\ .$$

In case $\boldsymbol{r}$ is parallel or antiparallel to the z axis the spherical harmonics take on the simple form

$$Y_{lm}(0,\varphi) = \delta_{m0}\left(\frac{2l+1}{4\pi}\right)^{1/2}\ ,\quad Y_{lm}(\pi,\varphi) = (-)^l Y_{lm}(0,\varphi)\ , \tag{1.18}$$

respectively, that will prove useful in several instances. We will find useful also the relation

$$\frac{4\pi}{2l+1}\sum_m Y^*_{lm}(\vartheta_1,\varphi_1)Y_{lm}(\vartheta_2,\varphi_2) = P_l(\cos\omega)\ , \tag{1.19}$$

where P_l is a Legendre polynomial of degree l and ω is the angle between the directions defined by the polar angles (ϑ_1,φ_1) and (ϑ_2,φ_2). Equation (1.19) is customarily referred to as the *addition theorem for the spherical harmonics.*

1.5.3 Spin Eigenvectors

The simultaneous eigenvectors of s^2 and s_z belonging to $s = 1$ are less known but no less important than the spherical harmonics. They are, in fact, essential for a correct description of the transformation properties of the vector fields. According to the results in Sect. 1.4.2, they should be three-dimensional vectors and should satisfy the eigenvalue equations

$$\begin{aligned} \mathrm{s}^2 \boldsymbol{v} &= s(s+1)\boldsymbol{v} \;, \qquad \text{with } s = 1 \;, \\ \mathrm{s}_z \boldsymbol{v} &= \mu \boldsymbol{v} \;, \qquad \text{with } \mu = 0, \pm 1 \;. \end{aligned}$$

With the help of the explicit form of s_x, s_y and s_z given in Sect. 1.4.2, it is an easy matter to see that the spin eigenvectors should be proportional to linear combinations of the unit vectors that characterize the rectangular axes. It can be checked that the required eigenvectors are

$$\boldsymbol{\xi}_{\pm 1} = \mp \tfrac{1}{\sqrt{2}}(\hat{\boldsymbol{e}}_x \pm \mathrm{i}\hat{\boldsymbol{e}}_y) \;, \qquad \boldsymbol{\xi}_0 = \hat{\boldsymbol{e}}_z \;. \tag{1.20}$$

For our purposes it may be useful to stress that these eigenvectors, under rotation of the coordinate system, transform according to $\mathrm{D}^{(1)}$ and are therefore the components of an irreducible spherical tensor of rank 1.

The vectors $\boldsymbol{\xi}_\mu$ satisfy the conjugation condition

$$\boldsymbol{\xi}_\mu^* = (-)^\mu \boldsymbol{\xi}_{-\mu} \;,$$

and the orthonormality relation

$$\boldsymbol{\xi}_\mu \cdot \boldsymbol{\xi}_{\mu'}^* = (-)^{\mu'} \boldsymbol{\xi}_\mu \cdot \boldsymbol{\xi}_{-\mu'} = \delta_{\mu\mu'} \;.$$

They form the so-called (covariant) spherical basis and are suitable for representing any three-dimensional vector. In fact, besides the usual representation on the cartesian basis, i.e. on the unit vectors of the rectangular coordinate axes, any three-dimensional vector can be represented as

$$\boldsymbol{B} = \sum_\mu (-)^\mu B_\mu \boldsymbol{\xi}_{-\mu} \;, \tag{1.21}$$

where

$$B_\mu = \boldsymbol{\xi}_\mu \cdot \boldsymbol{B} \tag{1.22}$$

defines the *spherical components* of $\boldsymbol{B}$. Then, the dot product of any pair of vectors in terms of their spherical components can be written as

$$\boldsymbol{A} \cdot \boldsymbol{B} = \sum_\mu (-)^\mu A_\mu B_{-\mu} \;. \tag{1.23}$$

The usefulness of this representation stems from the fact that the spherical components of any Cartesian vector are the components of an irreducible spherical tensor of rank 1.

In any case, it may be useful to give the explicit expression of the cartesian components of a three-dimensional vector $\boldsymbol{A}$ in terms of its spherical components,

$$A_x = \frac{1}{\sqrt{2}}(A_{-1} - A_1), \quad A_y = \frac{\mathrm{i}}{\sqrt{2}}(A_{-1} + A_1), \quad A_z = A_0 \,.$$

Also useful is the expression of any unit vector $\hat{\boldsymbol{v}}$, and in particular of the unit vector $\hat{\boldsymbol{r}}$, in terms of its spherical components

$$\hat{\boldsymbol{v}} = \sum_{\mu} (-)^{\mu} \sqrt{\frac{4\pi}{3}} Y_{1\mu}(\vartheta_v, \varphi_v) \boldsymbol{\xi}_{-\mu} \,, \tag{1.24}$$

where ϑ_v and φ_v denote the polar angles of $\hat{\boldsymbol{v}}$.

Finally, we give the cross product of two vectors in terms of their spherical components [9]. To this end, with the help of the definition (1.20) we find

$$\boldsymbol{\xi}_{\mu} \times \boldsymbol{\xi}_{\mu'} = \mathrm{i}S(\mu - \mu')\boldsymbol{\xi}_{\mu+\mu'} \,,$$

where $S(\mu - \mu')$ is the sign of $\mu - \mu'$ and is zero when $\mu = \mu'$. Accordingly we have

$$\boldsymbol{A} \times \boldsymbol{B} = \mathrm{i} \sum_{\mu\mu'} (-)^{\mu+\mu'} A_{-\mu} B_{-\mu'} S(\mu - \mu') \boldsymbol{\xi}_{\mu+\mu'} = \begin{vmatrix} \boldsymbol{\xi}_1 & \boldsymbol{\xi}_0 & \boldsymbol{\xi}_{-1} \\ A_1 & A_0 & A_{-1} \\ B_1 & B_0 & B_{-1} \end{vmatrix} \,. \tag{1.25}$$

1.6 Spherical Tensors on the Unit Sphere

The angular momentum eigenvectors that were determined in the preceding section are a good basis for the description of any vector field. In fact, since the transformation properties of the latter are governed by the total angular momentum $\mathrm{J} = \mathrm{L} + \mathrm{s}$, we can resort to the general theory of the coupling of angular momenta to combine the eigenvectors of L and those of s to yield the eigenvectors of J. The resulting eigenvectors will transform according to $\mathrm{D}^{(j)}$ and thus according to a rule that decrees their identification with the components of an irreducible spherical tensor of rank j.

1.6.1 Coupling of Angular Momenta

Let us consider two angular momentum operators, J_1 and J_2, whose respective eigenvectors we denote as $|j_1, m_1\rangle$ and $|j_2, m_2\rangle$. Since the vector spaces spanned by these two sets are linearly independent, the vector sum of the operators J_1 and J_2 is the operator

$$\mathrm{J} = \mathrm{J}_1 + \mathrm{J}_2 \,,$$

which is easily verified to be itself an angular momentum. Our present task is therefore to build the eigenvectors of J out of the sets of eigenvectors $|j_1, m_1\rangle$ and $|j_2, m_2\rangle$.

We remark that the set of the direct product vectors $|j_1, m_1\rangle|j_2, m_2\rangle$ are not eigenvectors of the square of the total angular momentum J^2 but are eigenvectors of J_z. It suffices to state that the set of the product eigenvectors form a complete set that spans the space of the eigenvectors of J. As a consequence, the simultaneous eigenvectors of J^2 and J_z can be built as linear combinations of the product vectors. In fact, we can write

$$|j, m\rangle = \sum_{m_1 m_2} C(j_1, j_2, j; m_1, m_2, m)|j_1, m_1\rangle|j_2, m_2\rangle \ , \tag{1.26}$$

where the C's are the so-called Clebsch–Gordan coefficients. The latter can be understood as the elements of the unitary matrix that transforms the set of the $(2j_1 + 1)(2j_2 + 1)$ product vectors into the set of the simultaneous eigenvectors of J^2 and J_z. The explicit expression of the Clebsch–Gordan coefficients can be determined in the framework of group theory and turns out to be [7]

$$\begin{aligned} C(j_1, j_2, j; m_1, m_2, m) &= \delta_{m, m_1+m_2} \\ &\times \left[(2j+1) \frac{(j_1 + j_2 - j)!(j + j_1 - j_2)!(j + j_2 - j_1)!}{(j_1 + j_2 + j + 1)!} \right. \\ &\left. \times \, (j_1 + m_1)!(j_1 - m_1)!(j_2 + m_2)!(j_2 - m_2)!(j + m)!(j - m)! \right]^{1/2} \\ &\times \sum_\nu \frac{(-)^\nu}{\nu!} \Big[(j_1 + j_2 - j - \nu)!(j_1 - m_1 - \nu)!(j_2 + m_2 - \nu)! \\ &\times (j - j_2 + m_1 + \nu)!(j - j_1 - m_2 + \nu)! \Big]^{-1} \ . \end{aligned} \tag{1.27}$$

The Clebsch–Gordan coefficients possess symmetry properties that relate to each other the coefficients that differ for the order of the quantum numbers j_1, j_2, and j or for the sign of the projection quantum numbers. These relations, which can be inferred from the explicit expression (1.27), are

$$\begin{aligned} &C(j_1, j_2, j; m_1, m_2, m) \\ &\quad = (-)^{j_1+j_2-j} C(j_1, j_2, j; -m_1, -m_2, -m) \\ &\quad = (-)^{j_1+j_2-j} C(j_2, j_1, j; m_2, m_1, m) \\ &\quad = (-)^{j_1-m_1} \left(\frac{2j+1}{2j_2+1} \right)^{1/2} C(j_1, j, j_2; m_1, -m, -m_2) \ . \end{aligned}$$

The preceding relations are the fundamental ones and can help in finding the further relations

$$
\begin{aligned}
&C(j_1, j_2, j; m_1, m_2, m) \\
&\qquad = (-)^{j_2+m_2} \left(\frac{2j+1}{2j_1+1}\right)^{1/2} C(j, j_2, j_1; -m, m_2, -m_1) \\
&\qquad = (-)^{j_1-m_1} \left(\frac{2j+1}{2j_2+1}\right)^{1/2} C(j, j_1, j_2; m, -m_1, m_2) \\
&\qquad = (-)^{j_2+m_2} \left(\frac{2j+1}{2j_1+1}\right)^{1/2} C(j_2, j, j_1; -m_2, m, m_1) \,,
\end{aligned}
$$

which complete the set of the symmetry properties.

We remark that, because of the factor δ_{m,m_1+m_2} in (1.27), the double sum in (1.26) is actually a single sum. Accordingly, we also denote the Clebsch–Gordan coefficients as $C(j_1, j_2, j; m_1, m_2)$ and, since $m_2 = m - m_1$, we rewrite the coupling equation as

$$
|j, m\rangle = \sum_{m_1} C(j_1, j_2, j; m_1, m - m_1)|j_1, m_1\rangle|j_2, m - m_1\rangle \,. \tag{1.28}
$$

The Clebsch–Gordan coefficients vanish unless their arguments satisfy the so called triangular relation

$$
|j_1 - j_2| \le j \le j_1 + j_2 \,,
$$

which is denoted for short as $\Delta(j_1, j_2, j)$. Furthermore, the unitarity of the matrix of the C-coefficients imply that they should satisfy the orthogonality relations

$$
\sum_{m_1} C(j_1, j_2, j; m_1, m - m_1) C(j_1, j_2, j'; m_1, m - m_1) = \delta_{jj'} \,, \tag{1.29a}
$$

$$
\sum_{j} C(j_1, j_2, j; m_1, m - m_1) C(j_1, j_2, j; m_1', m' - m_1') = \delta_{m_1 m_1'} \delta_{mm'} \,. \tag{1.29b}
$$

Equation (1.29b) can be used to show that the inverse to (1.28) reads

$$
|j_1, m_1\rangle|j_2, m - m_1\rangle = \sum_{j} C(j_1, j_2, j; m_1, m - m_1)|j, m\rangle. \tag{1.30}
$$

1.6.2 Clebsch–Gordan Series

The coupling of the angular momentum applies not only to the eigenvectors $|j, m\rangle$ but also to the elements of the $\mathrm{D}^{(j)}$-matrices. In fact, under rotation of the coordinate system, equation (1.30) becomes

$$
\begin{aligned}
&\sum_{\mu_1} \sum_{\mu_2} \mathcal{D}^{(j_1)}_{\mu_1 m_1} \mathcal{D}^{(j_2)}_{\mu_2 m_2} |j_1, \mu_1\rangle|j_2, \mu_2\rangle \\
&\qquad\qquad = \sum_{j} \sum_{\mu} C(j_1, j_2, j; m_1, m_2) \mathcal{D}^{(j)}_{\mu, m_1+m_2} |j, \mu\rangle \,,
\end{aligned}
$$

where all the D-matrix elements should have the same argument. By using in place of $|j,\mu\rangle$ its expression given by (1.28) we get

$$\sum_{\mu_1}\sum_{\mu_2}\mathcal{D}^{(j_1)}_{\mu_1 m_1}\mathcal{D}^{(j_2)}_{\mu_2 m_2}|j_1,\mu_1\rangle|j_2,\mu_2\rangle$$
$$=\sum_{j}\sum_{\mu\mu_1'} Cj_1,j_2,j;m_1,m_2)C(j_1,j_2,j;\mu_1',\mu-\mu_1')$$
$$\times\,\mathcal{D}^{(j)}_{\mu,\,m_1+m_2}|j_1,\mu_1'\rangle|j_2,\mu-\mu_1'\rangle\ .$$

The sum over μ can be replaced by a sum over $\mu_2'=\mu-\mu_1'$, and the prime on the resulting sum index can be dropped. Doing this and comparing the coefficients of $|j_1,\mu_1\rangle|j_2,\mu_2\rangle$ in both sides leads to the result

$$\mathcal{D}^{(j_1)}_{\mu_1 m_1}\mathcal{D}^{(j_2)}_{\mu_2 m_2}=\sum_j C(j_1,j_2,j;m_1,m_2)C(j_1,j_2,j;\mu_1,\mu_2)\mathcal{D}^{(j)}_{\mu_1+\mu_2,\,m_1+m_2}\ , \tag{1.31}$$

where the sum index j must satisfy the triangular relation $\Delta(j_1j_2j)$. A similar procedure can be used to prove the inverse coupling law

$$\mathcal{D}^{(j)}_{\mu m}=\sum_{\mu_1}\sum_{m_1}C(j_1,j_2,j;\mu_1,\mu-\mu_1)C(j_1,j_2,j;m_1,m-m_1)$$
$$\times\mathcal{D}^{(j_1)}_{\mu_1\,m_1}\mathcal{D}^{(j_2)}_{\mu-\mu_1,\,m-m_1}\ ,$$

which can be used for calculating any $\mathrm{D}^{(j)}$ matrix by coupling D-matrices of lower rank.

As an immediate application of the Clebsch-Gordan series (1.31) we are able to give the integral of the product of three rotation matrix elements. In fact, with the help of (1.14) we get

$$\int\mathcal{D}^{(j_3)*}_{\mu_3 m_3}\mathcal{D}^{(j_2)}_{\mu_2 m_2}\mathcal{D}^{(j_1)}_{\mu_1 m_1}\,\mathrm{d}\Theta=\delta_{\mu_1+\mu_2,\mu_3}\delta_{m_1+m_2,m_3}$$
$$\times\frac{8\pi^2}{2j_3+1}C(j_1,j_2,j_3;\mu_1,\mu_2)C(j_1,j_2,j_3;m_1,m_2)\ . \tag{1.32}$$

As a last item, we prove the so-called Gaunt formula for the integral of the product of three spherical harmonics. We start from the addition theorem for the spherical harmonics (1.19) that, with the help of the relation

$$Y_{l0}(\omega,0)=\left(\frac{2l+1}{4\pi}\right)^{1/2}P_l(\cos\omega)\ ,$$

that stems from (1.15), can be rewritten as

$$Y_{l0}(\omega,0)=\left(\frac{4\pi}{2l+1}\right)^{1/2}\sum_m Y^*_{lm}(\vartheta_1,\varphi_1)Y_{lm}(\vartheta_2,\varphi_2)\ . \tag{1.33}$$

Transforming $Y_{lm}(\vartheta_2, \varphi_2)$ by means of (1.17) in which the rotation is chosen so that the polar angles of the z'' axis are ϑ_1 and φ_1, one gets

$$Y_{l0}(\omega, 0) = \sum_m Y_{lm}(\vartheta_2, \varphi_2) \mathcal{D}^{(l)}_{m0}(\varphi_1, \vartheta_1, 0) \ .$$

Comparison of the latter equation with (1.33) leads to the conclusion that

$$\mathcal{D}^{(l)}_{m0}(\alpha, \beta, 0) = \left(\frac{4\pi}{2l+1} \right)^{1/2} Y^*_{lm}(\beta, \alpha) \ . \tag{1.34}$$

We now write (1.31) with $j_1 = L$, $j_2 = l$ and $m_1 = m_2 = 0$ and make use of (1.34) with the result

$$\begin{aligned} Y_{LM}(\vartheta, \varphi) Y_{lm}(\vartheta, \varphi) = \sum_\lambda & \left[\frac{(2L+1)(2l+1)}{4\pi(2\lambda+1)} \right]^{1/2} \\ & \times C(L, l, \lambda; M, m) C(L, l, \lambda; 0, 0) Y_{\lambda,\, M+m}(\vartheta, \varphi) \ . \end{aligned} \tag{1.35}$$

Multiplication of (1.35) by $Y^*_{l'm'}$ and integration over the full solid angle, on account of the orthogonality of the spherical harmonics, yields the result

$$\begin{aligned} & \int Y_{LM} Y_{lm} Y^*_{l'm'} \, \mathrm{d}\Omega = I(LM, l, l'm') \\ & = \left[\frac{(2L+1)(2l+1)}{4\pi(2l'+1)} \right]^{1/2} C(L, l, l'; M, m' - M) C(L, l, l'; 0, 0) \ , \end{aligned} \tag{1.36}$$

which is the required Gaunt integral. It is worth noticing that the symmetry properties of the Clebsch–Gordan coefficients decree the vanishing of the Gaunt integrals unless

$$|L - l| \le l' \le L + l \ , \quad \text{and} \quad L + l + l' = \text{even integer,}$$

so that $C(L, l, l'; 0, 0) \neq 0$. The Gaunt integrals will be used in Sect. 1.8 to demonstrate an addition theorem for the multipole fields.

1.6.3 Irreducible Spherical Tensors

We are now able to build the simultaneous eigenvectors of the total angular momentum of a vector field by coupling the eigenfunctions of L^2 and L_z with those of s^2 and s_z. The required eigenvectors turn out to be

$$\boldsymbol{T}_{jlm}(\hat{\boldsymbol{r}}) = \sum_\mu C(1, l, j; -\mu, m+\mu) \, Y_{l,m+\mu}(\hat{\boldsymbol{r}}) \, \boldsymbol{\xi}_{-\mu} \ , \tag{1.37}$$

and each of them is clearly a vector even though they are the components of an irreducible spherical tensor of rank j. We will find useful the inverse to (1.37) that reads

$$Y_{lm}\boldsymbol{\xi}_{-\mu} = \sum_j C(1,l,j;-\mu,m)\boldsymbol{T}_{jl,m-\mu}\ . \tag{1.38}$$

Each of the vectors $\boldsymbol{T}_{jlm}$ satisfies the simultaneous eigenvalue equations

$$\begin{aligned}
\mathrm{J}^2\,\boldsymbol{T}_{jlm} &= j(j+1)\boldsymbol{T}_{jlm}\ ,\\
\mathrm{J}_z\,\boldsymbol{T}_{jlm} &= m\boldsymbol{T}_{jlm}\ ,\\
\mathrm{L}^2\,\boldsymbol{T}_{jlm} &= l(l+1)\boldsymbol{T}_{jlm}\ ,\\
\mathrm{s}^2\,\boldsymbol{T}_{jlm} &= 2\boldsymbol{T}_{jlm}\ .
\end{aligned}$$

Their parity is given by the equation

$$\boldsymbol{T}_{jlm}(-\hat{\boldsymbol{r}}) = (-)^l\boldsymbol{T}_{jlm}(\hat{\boldsymbol{r}})\ ,$$

and the conjugation relation reads

$$\boldsymbol{T}^*_{jlm} = (-)^{1+l-j+m}\boldsymbol{T}_{jl,-m}\ .$$

The triangular relation $\Delta(1lj)$ implies that for any value of j there exist three mutually independent vectors $\boldsymbol{T}$ with $l=j, j\pm 1$ and that j cannot take the value 0. Furthermore, from their very definition it follows that, under rotation of the coordinate system, the $\boldsymbol{T}_{jlm}$ transform according to the equation

$$\mathrm{O}_\Theta\boldsymbol{T}_{jlm}(\hat{\boldsymbol{r}}) = \sum_{m'}\boldsymbol{T}_{jlm'}(\hat{\boldsymbol{r}})\mathcal{D}^{(j)}_{m'm}(\Theta)\ ,$$

were we used Θ as a shorthand for the eulerian angles that define the coordinate rotation that transforms $\boldsymbol{r}$ into $\boldsymbol{r}'$. The latter equation confirms our previous statement that the $2j+1$ *vectors* $\boldsymbol{T}_{jlm}$ are the components of an irreducible spherical tensor of rank j and parity $(-)^l$. The $\boldsymbol{T}_{jlm}$ have the property

$$\int \boldsymbol{T}^*_{j'l'm'}\cdot\boldsymbol{T}_{jlm}\,\mathrm{d}\Omega = \delta_{jj'}\delta_{ll'}\delta_{mm'}\ ,$$

so that they form a complete orthonormal set on the surface of the unit sphere. Since

$$\boldsymbol{r}\cdot\boldsymbol{T}_{llm} = 0\ , \tag{1.39}$$

this vector is tangent to the surface of the unit sphere, whereas the vectors $\boldsymbol{T}_{l,l\pm1,m}$ are, in general, neither tangent nor orthogonal to such a surface. Finally, by recalling the identity

$$\nabla = \hat{\boldsymbol{r}}\frac{\partial}{\partial r} - \frac{\mathrm{i}}{r}\hat{\boldsymbol{r}}\times\mathrm{L}\ , \tag{1.40}$$

it is an easy matter to show that

$$\nabla\cdot\boldsymbol{T}_{llm} = 0\ . \tag{1.41}$$

Hereafter, we will often need the Clebsch-Gordan coefficients of the form $C(1,l,\bar{l};\mu,\bar{m}-\mu)$ with $l=\bar{l}, \bar{l}\pm 1$ that appear in the expression of the irreducible spherical tensors. Since these coefficients can be given in closed form, we report them in Table 1.1.

Table 1.1. Clebsch-Gordan coefficients $C(1,l,\bar{l};\mu,\bar{m}-\mu)$ [9]

	$\mu=-1$	$\mu=0$	$\mu=1$
$l=\bar{l}-1$	$\sqrt{\frac{(\bar{l}-1-\bar{m})(\bar{l}-\bar{m})}{2\bar{l}(2\bar{l}-1)}}$	$\sqrt{\frac{(\bar{l}-\bar{m})(\bar{l}+\bar{m})}{\bar{l}(2\bar{l}-1)}}$	$\sqrt{\frac{(\bar{l}-1+\bar{m})(\bar{l}+\bar{m})}{2\bar{l}(2\bar{l}-1)}}$
$l=\bar{l}$	$-\sqrt{\frac{(\bar{l}-\bar{m})(\bar{l}+1+\bar{m})}{2\bar{l}(\bar{l}+1)}}$	$-\frac{\bar{m}}{\sqrt{\bar{l}(\bar{l}+1)}}$	$\sqrt{\frac{(\bar{l}+\bar{m})(\bar{l}+1-\bar{m})}{2\bar{l}(\bar{l}+1)}}$
$l=\bar{l}+1$	$\sqrt{\frac{(\bar{l}+2+\bar{m})(\bar{l}+1+\bar{m})}{2(\bar{l}+1)(2\bar{l}+3)}}$	$-\sqrt{\frac{(\bar{l}+1-\bar{m})(\bar{l}+1+\bar{m})}{(\bar{l}+1)(2\bar{l}+3)}}$	$\sqrt{\frac{(\bar{l}+1-\bar{m})(\bar{l}+2-\bar{m})}{2(\bar{l}+1)(2\bar{l}+3)}}$

1.6.4 Vector Solutions to the Helmholtz Equation

The considerations in the preceding sections led us to write the vector solutions to the Helmholtz equation for a homogeneous medium as the product of an irreducible spherical tensor of rank j by a function that depends on r only. Accordingly, we write

$$\boldsymbol{A}_{jlm}(\boldsymbol{r}) = R(r)\boldsymbol{T}_{jlm}(\hat{\boldsymbol{r}}) \ ,$$

where the functions $R(r)$ should be appropriately chosen. On account of the identity

$$\nabla^2 \equiv \frac{\mathrm{d}^2}{\mathrm{d}r^2} + \frac{2}{r}\frac{\mathrm{d}}{\mathrm{d}r} - \frac{\mathrm{L}^2}{r^2} \ ,$$

and of the fact that the vectors $\boldsymbol{T}_{jlm}$ are eigenfunctions of L^2 with eigenvalue $l(l+1)$, it is an easy matter to see that the vector functions $\boldsymbol{A}_{jlm}$ satisfy the Helmholtz equation provided that the radial function satisfy the equation

$$\frac{1}{r^2}\frac{\mathrm{d}}{\mathrm{d}r}\left(r^2\frac{\mathrm{d}R}{\mathrm{d}r}\right) + \left[k^2 - \frac{l(l+1)}{r^2}\right]R = 0 \ ,$$

which is immediately identified with the spherical Bessel equation of order l. Hereafter, the radial function will be denoted as $f_l(kr)$ with the understanding that it should be a spherical Bessel function or a spherical Hankel function of the first kind according to whether the required solution must be regular at the origin or must satisfy the radiation condition at infinity. The vector functions $\boldsymbol{A}_{jlm}$ will be referred to as vector Helmholtz harmonics (VHH).

For the sake of convenience we report here the fundamental properties of the spherical Bessel and Hankel functions [10]

$$f_{l+1}(kr) + f_{l-1}(kr) = \frac{2l+1}{kr}\, f_l(kr) \ , \tag{1.42a}$$

$$f_l'(kr) = \frac{1}{2l+1}[l f_{l-1}(kr) - (l+1)f_{l+1}(kr)] \ , \tag{1.42b}$$

$$\left(\frac{\partial}{\partial r} - \frac{l}{r}\right) f_l(kr) = k\left[f_l'(kr) - \frac{l}{kr}f_l(kr)\right] = -k f_{l+1}(kr) \ , \tag{1.42c}$$

$$\left(\frac{\partial}{\partial r} + \frac{l+1}{r}\right) f_l(kr) = k\left[f_l'(kr) + \frac{l+1}{kr}f_l(kr)\right] = k f_{l-1}(kr) \ , \tag{1.42d}$$

which are needed for further developments. We will also need the limiting expressions of the Bessel and Hankel functions as well as of their derivatives. For $kr \to 0$ we have

$$j_l(kr) \approx \frac{(kr)^l}{(2l+1)!!} \,,$$

$$h_l(kr) \approx \frac{(2l-1)!!}{(kr)^{l+1}} \,,$$

whereas for $kr \to \infty$

$$j_l(kr) \sim \frac{1}{kr} \sin(kr - l\pi/2) \,, \tag{1.43a}$$

$$h_l(kr) \sim (-\mathrm{i})^{l+1} \frac{\mathrm{e}^{\mathrm{i}kr}}{kr} \,, \tag{1.43b}$$

and

$$j_l'(kr) \sim \frac{1}{kr} \sin(kr - (l-1)\pi/2) \tag{1.44a}$$

$$h_l' \sim (-\mathrm{i})^l \frac{\mathrm{e}^{\mathrm{i}kr}}{kr} \tag{1.44b}$$

The Wronskian

$$W[j_l(kr), h_l(kr)] = \mathrm{i}/(kr)^2$$

will also be useful for algebraic manipulations.

1.6.5 Divergence and Curl of the Vector Helmholtz Harmonics

The vector Helmholtz harmonics form a complete orthonormal set that is suitable as a basis for the expansion of the electromagnetic field. To perform these expansions, we will often need the explicit expression for the divergence and curl of these functions that stem from the so-called gradient formula whose demonstration has been reported, e.g., by Rose [7]:

$$\begin{aligned}
\nabla f_l(kr) Y_{lm}(\hat{\boldsymbol{r}}) &= -\sqrt{\frac{l+1}{2l+1}} \left(\frac{\partial}{\partial r} - \frac{l}{r} \right) f_l(kr) \boldsymbol{T}_{l,l+1,m}(\hat{\boldsymbol{r}}) \\
&\quad + \sqrt{\frac{l}{2l+1}} \left(\frac{\partial}{\partial r} + \frac{l+1}{r} \right) f_l(kr) \boldsymbol{T}_{l,l-1,m}(\hat{\boldsymbol{r}}) \\
&= \sqrt{\frac{l+1}{2l+1}} k f_{l+1}(kr) \boldsymbol{T}_{l,l+1,m}(\hat{\boldsymbol{r}}) \\
&\quad + \sqrt{\frac{l}{2l+1}} k f_{l-1}(kr) \boldsymbol{T}_{l,l-1,m}(\hat{\boldsymbol{r}}) \,.
\end{aligned}$$

The expressions for the curl are [11]

$$\begin{aligned}
\nabla \times f_{l+1}(kr)\boldsymbol{T}_{l,l+1,m}(\hat{\boldsymbol{r}}) =& -\mathrm{i}\left(\frac{\partial}{\partial r}+\frac{l+2}{r}\right) f_{l+1}(kr)\sqrt{\frac{l}{2l+1}}\boldsymbol{T}_{llm}(\hat{\boldsymbol{r}}) \\
=& -\mathrm{i}k f_l(kr)\sqrt{\frac{l}{2l+1}}\boldsymbol{T}_{llm}(\hat{\boldsymbol{r}}) \,, \qquad (1.45\mathrm{a}) \\
\nabla \times f_l(kr)\boldsymbol{T}_{llm}(\hat{\boldsymbol{r}}) =& -\mathrm{i}\left(\frac{\partial}{\partial r}-\frac{l}{r}\right) f_l(kr)\sqrt{\frac{l}{2l+1}}\boldsymbol{T}_{l,l+1,m}(\hat{\boldsymbol{r}}) \\
& -\mathrm{i}\left(\frac{\partial}{\partial r}+\frac{l+1}{r}\right) f_l(kr)\sqrt{\frac{l+1}{2l+1}}\boldsymbol{T}_{l,l-1,m}(\hat{\boldsymbol{r}}) \\
=& \mathrm{i}k\left[\sqrt{\frac{l}{2l+1}}f_{l+1}(kr)\boldsymbol{T}_{l,l+1,m}(\hat{\boldsymbol{r}})\right. \\
& \left. -\sqrt{\frac{l+1}{2l+1}}f_{l-1}(kr)\boldsymbol{T}_{l,l-1,m}(\hat{\boldsymbol{r}})\right] \,, \qquad (1.45\mathrm{b}) \\
\nabla \times f_{l-1}(kr)\boldsymbol{T}_{l,l-1,m}(\hat{\boldsymbol{r}}) =& -\mathrm{i}\left(\frac{\partial}{\partial r}-\frac{l-1}{r}\right) f_{l-1}(kr)\sqrt{\frac{l+1}{2l+1}}\boldsymbol{T}_{llm}(\hat{\boldsymbol{r}}) \\
=& \mathrm{i}k f_l(kr)\sqrt{\frac{l+1}{2l+1}}\boldsymbol{T}_{llm}(\hat{\boldsymbol{r}}) \,, \qquad (1.45\mathrm{c})
\end{aligned}$$

and the formulas for the divergence turn out to be

$$\begin{aligned}
\nabla \cdot f_{l+1}(kr)\boldsymbol{T}_{l,l+1,m}(\hat{\boldsymbol{r}}) =& -\sqrt{\frac{l+1}{2l+1}}\left(\frac{\partial}{\partial r}+\frac{l+2}{r}\right) f_{l+1}(kr)Y_{lm}(\hat{\boldsymbol{r}}) \\
=& -\sqrt{\frac{l+1}{2l+1}}k f_l(kr)Y_{lm}(\hat{\boldsymbol{r}}) \,, \qquad (1.46\mathrm{a}) \\
\nabla \cdot f_l(kr)\boldsymbol{T}_{llm}(\hat{\boldsymbol{r}}) =& 0 \,, \qquad (1.46\mathrm{b}) \\
\nabla \cdot f_{l-1}(kr)\boldsymbol{T}_{l,l-1,m}(\hat{\boldsymbol{r}}) =& \sqrt{\frac{l}{2l+1}}\left(\frac{\partial}{\partial r}-\frac{l-1}{r}\right) f_{l-1}(kr)Y_{lm}(\hat{\boldsymbol{r}}) \\
=& -\sqrt{\frac{l}{2l+1}}k f_l(kr)Y_{lm}(\hat{\boldsymbol{r}}) \,. \qquad (1.46\mathrm{c})
\end{aligned}$$

Note that, because of (1.39) and (1.41), (1.46b) hold true for any choice of the radial function.

1.7 Multipole Fields

Although the VHH solve the problem of expanding the electromagnetic field, there are cases in which their direct use is not advisable. We refer to the fact that the VHH do not form a set of vector functions that are orthogonal or tangential to the surface of the unit sphere. Moreover, the VHH are neither solenoidal nor irrotational, a property that would be desirable because the most general vector field is a superposition of an irrotational field and of a solenoidal field [12]. In particular, in a homogeneous medium both $\boldsymbol{E}$ and $\boldsymbol{B}$ are solenoidal and so they can be expanded in terms of solenoidal vector functions only. These considerations call for the determination of alternative forms for the solutions of the vector Helmholtz equation that are either solenoidal or irrotational. Of course, since the VHH form a complete set, the alternative solutions, once determined, can be related to the VHH.

1.7.1 Hansen's Vectors

We start by remarking that there should exist three mutually independent vector solutions to the Helmholtz equation because, in three-dimensional space, any vector can always be expressed as a linear combination of three mutually independent vectors. Now, let ψ be a scalar solution to the Helmholtz equation and $\boldsymbol{e}$ a constant vector, not necessarily of unit magnitude. Then it is an easy matter to verify that the vector functions $\boldsymbol{e}\psi$ and $\nabla\psi$ actually satisfy the Helmholtz equation. We further remark that if $\boldsymbol{A}$ is a vector solution to the Helmholtz equation then $\nabla \times \boldsymbol{A}$ is also a solution. Accordingly, we can write three mutually independent vector solutions to (1.6) as [6]

$$\boldsymbol{L} = \nabla\psi \ , \quad \boldsymbol{M} = \nabla \times \boldsymbol{e}\psi \ , \quad \boldsymbol{N} = \frac{1}{k}\nabla \times \boldsymbol{M} \ , \tag{1.47}$$

where the factor $1/k$ in the definition of $\boldsymbol{N}$ has been introduced so that

$$\frac{1}{k}\nabla \times \boldsymbol{N} = \boldsymbol{M} \ . \tag{1.48}$$

Equations (1.47) define the so-called Hansen's vectors [13] that are easily verified to be actually linearly independent even though they do not form an orthonormal set because, for general choice of $\boldsymbol{e}$ we have

$$\boldsymbol{L} \cdot \boldsymbol{M} = \boldsymbol{M} \cdot \boldsymbol{N} = 0 \ , \ \text{but } \boldsymbol{L} \cdot \boldsymbol{N} \neq 0 \ .$$

From the definition in (1.47) it also turns out that

$$\nabla \cdot \boldsymbol{M} = \nabla \cdot \boldsymbol{N} = 0 \ , \qquad \nabla \times \boldsymbol{L} = 0 \ , \tag{1.49}$$

so that Hansen's vectors are either solenoidal or irrotational as required. As a consequence, any solenoidal solution to the Helmholtz equation can be projected into the subspace spanned by $\boldsymbol{M}$ and $\boldsymbol{N}$, whereas any irrotational solution can be expressed in terms of $\boldsymbol{L}$ only.

The definition (1.47) of the Hansen's vectors is appropriate when the boundary conditions must be imposed across a plane surface; in this case, in fact, choosing $\boldsymbol{e}$ parallel to the surface greatly simplifies the algebraic manipulations. Nevertheless, in many optical problems one has to impose the boundary conditions across spherical surfaces, and this task is hardly manageable in terms of the vectors $\boldsymbol{M}$ and $\boldsymbol{N}$ defined in (1.47). The definition (1.47) is not unique, however, so that we can resort to the following alternative definition of Hansen's vectors.

Let ψ be a scalar solution to the Helmholtz equation and let O be a vector operator that, when applied to any space-dependent scalar function, yields a vector function $\boldsymbol{A}$. Then, by operating with O on the scalar Helmholtz equation we get

$$\mathrm{O}(\nabla^2 + k^2)\psi = (\nabla^2 + k^2)\mathrm{O}\psi + [\mathrm{O}, \nabla^2]\psi = 0 \; .$$

Therefore, if O commutes with ∇^2, any vector function of the form $\boldsymbol{A} = \mathrm{O}\psi$ is a solution to the Helmholtz equation. Now, the operator $\Omega_k = \nabla^2 + k^2$ is invariant under translations as well as under rotations of the coordinate system. This implies that Ω_k commutes with the operators of the linear momentum $\mathrm{p} = -\mathrm{i}\nabla$ and of the angular momentum $\mathrm{L} = -\mathrm{i}\boldsymbol{r} \times \nabla$. Furthermore, it is easily verified that Ω_k also commutes with the operator $\nabla \times \mathrm{L}$. As a consequence, from any scalar solution ψ we get the three linearly independent vector solutions

$$\mathrm{p}\psi \; , \quad \mathrm{L}\psi \; , \quad \nabla \times \mathrm{L}\psi \; ,$$

which will be particularly useful when

$$\psi = \psi_{lm}(\boldsymbol{r}) = [l(l+1)]^{-1/2} f_l(kr)\, Y_{lm}(\hat{\boldsymbol{r}}) \; ,$$

i.e., when ψ is an eigenfunction of the angular momentum. Of course, the factor $[l(l+1)]^{-1/2}$ in the definition of ψ has been inserted for convenience in further manipulations.

1.7.2 Vector Spherical Harmonics

We are now able to write the following useful form of Hansen's vectors. With the help of (1.40) we find

$$\boldsymbol{L}_{lm} = \frac{1}{k}\nabla\psi_{lm} = [l(l+1)]^{-1/2} f_l'(kr) Y_{lm}\hat{\boldsymbol{r}} - \frac{\mathrm{i}}{kr} f_l(kr)\hat{\boldsymbol{r}} \times \boldsymbol{X}_{lm} \; , \tag{1.50a}$$

$$\boldsymbol{M}_{lm} = \mathrm{L}\psi_{lm} = f_l(kr)\boldsymbol{X}_{lm} \; , \tag{1.50b}$$

$$\begin{aligned}\boldsymbol{N}_{lm} = \frac{1}{k}\nabla \times \mathrm{L}\psi_{lm} &= \frac{\mathrm{i}}{kr}[l(l+1)]^{1/2} f_l(kr) Y_{lm}\hat{\boldsymbol{r}} \\ &\quad + \frac{1}{kr}[kr\, f_l(kr)]'\hat{\boldsymbol{r}} \times \boldsymbol{X}_{lm} \; ,\end{aligned} \tag{1.50c}$$

where the prime denotes differentiation with respect to the argument. In (1.50) we define the vector functions

$$\boldsymbol{X}_{lm} = [l(l+1)]^{-1/2}\mathrm{L}Y_{lm} \tag{1.51}$$

that are customarily called *vector spherical harmonics* [4], and the factor $1/k$ has been included in the definition of $\boldsymbol{N}$ to ensure the validity of (1.48) whereas in the definition of $\boldsymbol{L}$ it has been included for normalization purposes. It may be useful to note that, in terms of spherical components, (1.51) reads

$$\begin{aligned}\boldsymbol{X}_{lm} =& [l(l+1)]^{-1/2}\sum_{\mu}(-)^{\mu}\mathrm{L}_{\mu}Y_{lm}\boldsymbol{\xi}_{-\mu} \\ =& -\sum_{\mu}C(1,l,l;-\mu,m+\mu)Y_{l,m+\mu}\boldsymbol{\xi}_{-\mu} = -\boldsymbol{T}_{llm}\;,\end{aligned} \tag{1.52}$$

and thus, according to (1.37), the $\boldsymbol{X}_{lm}$ are irreducible spherical tensors of rank l.

The advantage of the definition (1.50) stems from the fact that the vector spherical harmonics $\hat{\boldsymbol{r}}Y_{lm}$, $\boldsymbol{X}_{lm}$, and $\hat{\boldsymbol{r}}\times\boldsymbol{X}_{lm}$ constitute an orthonormal set of eigenfunctions of the angular momentum with the orthogonality properties

$$\int \boldsymbol{X}^*_{l'm'}\cdot\boldsymbol{X}_{lm}\,\mathrm{d}\Omega = \int \hat{\boldsymbol{r}}\times\boldsymbol{X}^*_{l'm'}\cdot\hat{\boldsymbol{r}}\times\boldsymbol{X}_{lm}\,\mathrm{d}\Omega = \delta_{ll'}\delta_{mm'}\;, \tag{1.53}$$

$$\int \boldsymbol{X}^*_{l'm'}\cdot\hat{\boldsymbol{r}}\times\boldsymbol{X}_{lm}\,\mathrm{d}\Omega = \int \boldsymbol{X}^*_{l'm'}\cdot\hat{\boldsymbol{r}}Y_{lm}\,\mathrm{d}\Omega = \int \hat{\boldsymbol{r}}\times\boldsymbol{X}^*_{l'm'}\cdot\hat{\boldsymbol{r}}Y_{lm}\,\mathrm{d}\Omega = 0\;. \tag{1.54}$$

Moreover, the harmonic $\hat{\boldsymbol{r}}Y_{lm}$ is clearly orthogonal to the surface of the unit sphere, whereas the harmonics $\boldsymbol{X}_{lm}$ and $\hat{\boldsymbol{r}}\times\boldsymbol{X}_{lm}$ are tangent so that

$$\hat{\boldsymbol{r}}\cdot\boldsymbol{X}_{lm} = \hat{\boldsymbol{r}}\cdot\hat{\boldsymbol{r}}\times\boldsymbol{X}_{lm} = 0\;.$$

We also remark that $\boldsymbol{L}_{lm}$, $\boldsymbol{M}_{lm}$ and $\boldsymbol{N}_{lm}$ satisfy (1.49).

For later developments, it is convenient to define the *transverse vector harmonics* [14]

$$\boldsymbol{Z}^{(1)}_{lm}(\hat{\boldsymbol{r}}) = \boldsymbol{X}_{lm}(\hat{\boldsymbol{r}})\;, \quad \boldsymbol{Z}^{(2)}_{lm}(\hat{\boldsymbol{r}}) = \boldsymbol{X}_{lm}(\hat{\boldsymbol{r}})\times\hat{\boldsymbol{r}}\;, \tag{1.55}$$

which will be extensively used to expand any transverse field. In fact, they are mutually orthogonal in the usual vector sense

$$\boldsymbol{Z}^{(1)}_{lm}(\hat{\boldsymbol{r}})\cdot\boldsymbol{Z}^{(2)}_{lm}(\hat{\boldsymbol{r}}) = 0\;,$$

and orthogonal to their argument

$$\boldsymbol{Z}^{(1)}_{lm}(\hat{\boldsymbol{r}})\cdot\hat{\boldsymbol{r}} = \boldsymbol{Z}^{(2)}_{lm}(\hat{\boldsymbol{r}})\cdot\hat{\boldsymbol{r}} = 0\;.$$

It is worth stressing that the definitions (1.55) imply that the transverse harmonics are irreducible spherical tensors of rank l so that, under rotation of the coordinate system, they transform according to $\mathrm{D}^{(l)}$. In fact, in the next section we will show that $\boldsymbol{Z}^{(1)}_{lm}$ is proportional to an irreducible sperical tensor of rank l whereas $\boldsymbol{Z}^{(2)}_{lm}$ turns out to be a linear combination of two irreducible spherical tensors of rank l.

1.7.3 Spherical Multipole Fields

We are now able to give the general expression of the vector functions that we are going to use. To this end we give the following definition:

> The *multipole fields* are the solutions to the Maxwell equations that are eigenvectors of L^2 and L_z as well as of the parity.

According to this definition both the Hansen's vectors and the VHHs are a complete set of multipole fields. Using the former or the latter is a matter of convenience for the algebraic manipulations. Anyway, we will show presently that Hansen's vectors can be written as linear combinations of the appropriate VHHs. In fact, we note that, according to (1.50b) the vector function $\boldsymbol{M}_{lm}$ is solenoidal and that according to (1.46b) $f_l \boldsymbol{T}_{llm}$ too is solenoidal. Actually, from (1.52)

$$\boldsymbol{M}_{lm} = f_l \boldsymbol{X}_{lm} = -f_l \boldsymbol{T}_{llm} \, . \tag{1.56}$$

Then, according to (1.47) and (1.45b) we find

$$\boldsymbol{N}_{lm} = \mathrm{i}\left[\sqrt{\frac{l+1}{2l+1}} f_{l-1}(kr)\boldsymbol{T}_{l,l-1,m} - \sqrt{\frac{l}{2l+1}} f_{l+1}(kr)\boldsymbol{T}_{l,l+1,m}\right] \, , \tag{1.57}$$

which is easily verified through (1.46a) and (1.46c) to have vanishing divergence. With the help of (1.45a) and (1.45c), we find that

$$\boldsymbol{L}_{lm} = \left[\sqrt{\frac{l}{2l+1}} f_{l-1}(kr)\boldsymbol{T}_{l,l-1,m} + \sqrt{\frac{l+1}{2l+1}} f_{l+1}(kr)\boldsymbol{T}_{l,l+1,m}\right] \, , \tag{1.58}$$

which is easily verified to have vanishing curl. Moreover, both (1.57) and (1.58) are linear combinations of $\boldsymbol{T}_{l,l+1,m}$ and $\boldsymbol{T}_{l,l-1,m}$ and thus their parity is opposite to that of $\boldsymbol{M}_{lm}$.

Hereafter, we need to distinguish the multipole fields that are regular at the origin from those that satisfy the radiation condition at infinity. Accordingly, we will use in place of $\boldsymbol{M}_{lm}$ and $\boldsymbol{N}_{lm}$, the notation

$$\boldsymbol{J}^{(1)}_{lm} = j_l(kr)\boldsymbol{X}_{lm}(\hat{\boldsymbol{r}}) \, , \quad \boldsymbol{J}^{(2)}_{lm} = \frac{1}{k}\nabla \times \boldsymbol{J}^{(1)}_{lm} \, , \tag{1.59}$$

respectively, when their radial function is a spherical Bessel function $j_l(kr)$. We will use the notation

$$\boldsymbol{H}^{(1)}_{lm} = h_l(kr)\boldsymbol{X}_{lm}(\hat{\boldsymbol{r}}) \, , \quad \boldsymbol{H}^{(2)}_{lm} = \frac{1}{k}\nabla \times \boldsymbol{H}^{(1)}_{lm} \, , \tag{1.60}$$

for the case in which the radial function of the multipole fields is a spherical Hankel function of the first kind $h_l(kr)$. The superscript $p = 1, 2$ that has been attached to $\boldsymbol{J}$ and $\boldsymbol{H}$ is an index that distinguishes the magnetic multipole fields $\boldsymbol{M}$, $(p = 1)$, from the electric ones $\boldsymbol{N}$, $(p = 2)$.

The equations [2]

$$\hat{\boldsymbol{r}} Y_{lm}(\hat{\boldsymbol{r}}) = \sqrt{\frac{l}{2l+1}} \boldsymbol{T}_{l,\,l-1,\,m}(\hat{\boldsymbol{r}}) - \sqrt{\frac{l+1}{2l+1}} \boldsymbol{T}_{l,\,l+1,\,m}(\hat{\boldsymbol{r}}) \,, \tag{1.61a}$$

$$-\mathrm{i}\hat{\boldsymbol{r}} \times \boldsymbol{X}_{lm}(\hat{\boldsymbol{r}}) = \sqrt{\frac{l+1}{2l+1}} \boldsymbol{T}_{l,\,l-1,\,m}(\hat{\boldsymbol{r}}) + \sqrt{\frac{l}{2l+1}} \boldsymbol{T}_{l,\,l+1,\,m}(\hat{\boldsymbol{r}}) \,, \tag{1.61b}$$

relate the vector spherical harmonics to the irreducible spherical tensors. Moreover, one may find useful the equations

$$\boldsymbol{H}_{lm}^{(1)} = h_l \boldsymbol{Z}_{lm}^{(1)} \,, \quad \boldsymbol{H}_{lm}^{(2)} = \frac{\mathrm{i}}{kr}[l(l+1)]^{1/2} h_l Y_{lm} \hat{\boldsymbol{r}} - \frac{1}{kr}\left[kr h_l\right]' \boldsymbol{Z}_{lm}^{(2)} \,, \tag{1.62}$$

which give the explicit expression of the $\boldsymbol{H}$-multipole fields in terms of transverse vector harmonics. Of course, similar equations hold also for the $\boldsymbol{J}$-multipole fields.

Also useful proves to be the explicit expression of the transverse harmonics for argument parallel or antiparallel to the z axis. In fact, since the general expression of the transverse harmonics is given by (1.52) and (1.61b) with the help of (1.18) we get

$$\boldsymbol{Z}_{lm}^{(p)}(\hat{\boldsymbol{e}}_z) = -(m\delta_{p1} + \mathrm{i}\delta_{p2})\delta_{m,\pm 1}\sqrt{\frac{2l+1}{8\pi}} \boldsymbol{\xi}_m \,, \tag{1.63a}$$

$$\boldsymbol{Z}_{lm}^{(p)}(-\hat{\boldsymbol{e}}_z) = (-)^{l+p-1} \boldsymbol{Z}_{lm}^{(p)}(\hat{\boldsymbol{e}}_z) \,. \tag{1.63b}$$

1.8 Addition Theorem for Multipole Fields

We will now use the translational invariance of Helmholtz equation to establish an addition theorem that relates the VHHs referred to two systems of spherical coordinates that differ for a translation of their origins. To achieve our task we will at first consider the case of the scalar harmonics [15] and will then extend our findings to the case of the vector harmonics.

1.8.1 Nozawa's Theorem

Let us consider two frames of reference, say Σ and Σ', in which we define two systems of rectangular coordinates whose axes are mutually parallel and whose origins differ by a translation. A point P has vector position $\boldsymbol{r}$ in Σ and $\boldsymbol{r}'$ in Σ', so that we can write $\boldsymbol{r} = \boldsymbol{r}' + \boldsymbol{R}$, where $\boldsymbol{R}$ is the vector position of the origin of Σ' with respect to Σ. Then, for a scalar plane wave the identity holds

$$\exp(\mathrm{i}\boldsymbol{k} \cdot \boldsymbol{r}) = \exp(\mathrm{i}\boldsymbol{k} \cdot \boldsymbol{R}) \exp(\mathrm{i}\boldsymbol{k} \cdot \boldsymbol{r}') \,.$$

We use the Bauer formula to expand each of the exponentials that appear in both sides of this equation with the result

$$4\pi \sum_{l''m''} \mathrm{i}^{l''} j_{l''}(kr) Y_{l''m''}(\hat{\boldsymbol{r}}) Y^*_{l''m''}(\hat{\boldsymbol{k}})$$
$$= 4\pi \sum_{l'm'} \mathrm{i}^{l'} j_{l'}(kr') Y_{l'm'}(\hat{\boldsymbol{r}}') Y^*_{l'm'}(\hat{\boldsymbol{k}}) 4\pi \sum_{LM} \mathrm{i}^{L} j_L(kR) Y^*_{LM}(\hat{\boldsymbol{R}}) Y_{LM}(\hat{\boldsymbol{k}}) \, .$$

Multiplication of both sides by $Y_{lm}(\hat{\boldsymbol{k}})$ and integration over the solid angle leads to the equation

$$j_l(kr) Y_{lm}(\hat{\boldsymbol{r}}) = \sum_{l'm'} j_{l'}(kr') Y_{l'm'}(\hat{\boldsymbol{r}}')$$
$$\times \, 4\pi \sum_{LM} \mathrm{i}^{l'-l+L} j_L(kR) Y^*_{LM}(\hat{\boldsymbol{R}}) \int Y_{lm} Y_{LM} Y^*_{l'm'} \, \mathrm{d}\Omega_{\boldsymbol{k}} \, ,$$

which can be rewritten as

$$j_l(kr) Y_{lm}(\hat{\boldsymbol{r}}) = \sum_{l'm'} j_{l'}(kr') Y_{l'm'}(\hat{\boldsymbol{r}}') G_{l'm'lm}(\boldsymbol{R}, k) \, ,$$

where we define

$$G_{l'm'lm}(\boldsymbol{R}, k) = 4\pi \sum_{L} \mathrm{i}^{l'-l+L} I(lm, L, l'm') j_L(kR) Y^*_{L,m'-m}(\hat{\boldsymbol{R}}) \, ,$$

and the I are Gaunt integrals (1.36).

Using the Neuman expansion of the function [10]

$$\frac{\mathrm{e}^{\mathrm{i}k|\boldsymbol{r}'+\boldsymbol{R}|}}{\mathrm{i}k|\boldsymbol{r}'+\boldsymbol{R}|},$$

it is possible to show that an analogous formula holds for the function $h_l(kr) Y_{lm}(\hat{\boldsymbol{r}})$, i.e., for the case in which the radial function is a Hankel function of the first kind. Ultimately we can write

$$f_l(kr) Y_{lm}(\hat{\boldsymbol{r}}) = \sum_{l'm'} g_{l'}(kr') Y_{l'm'}(\hat{\boldsymbol{r}}') G_{l'm'lm}(\boldsymbol{R}, k) \, , \tag{1.64}$$

with

$$G_{l'm'lm}(\boldsymbol{R}, k) = 4\pi \sum_{L} \mathrm{i}^{l'-l+L} I(lm, L, l'm') \psi_L(kR) Y^*_{L,\,m'-m}(\hat{\boldsymbol{R}}) \, , \tag{1.65}$$

where, when $f_l = j_l$, $\psi_l = j_l$ and $g_l = j_l$; when $f_l = h_l$ then

$$\begin{array}{lll} \psi_l = h_l \, , & g_l = j_l \, , & \text{for } r' < R \, , \\ \psi_l = j_l \, , & g_l = h_l \, , & \text{for } r' > R \, . \end{array}$$

Equations (1.64) and (1.65) express Nozawa's addition theorem for scalar Helmholtz harmonics.

1.8.2 Addition Theorem for the Vector Helmholtz Harmonics

Let us consider the VHH

$$\boldsymbol{A}_{jlm}(\boldsymbol{r}) = f_l(kr)\boldsymbol{T}_{jlm}(\hat{\boldsymbol{r}}) \ ,$$

which is centered at the origin, and let us express this function in terms of vector Helmholtz harmonics centered at a point of vector coordinate $\boldsymbol{R}$ [16]. To this end we recall that the definition of $\boldsymbol{A}_{jlm}$ is

$$\boldsymbol{A}_{jlm}(\boldsymbol{r}) = \sum_{\mu} C(1, l, j; -\mu, m+\mu) f_l(kr) Y_{l,\,m+\mu}(\hat{\boldsymbol{r}})\boldsymbol{\xi}_{-\mu} \ ,$$

so that Nozawa's theorem applies to each of the terms $f_l(kr)Y_{l\,m+\mu}(\hat{\boldsymbol{r}})$, whereas the spherical basis vectors $\boldsymbol{\xi}_{-\mu}$ are left unchanged by the translation. Therefore we get

$$\begin{aligned}\boldsymbol{A}_{jlm}(\boldsymbol{r}) = &\sum_{\mu} C(1, l, j; -\mu, m+\mu) \sum_{l'm''} G_{l'm''l,m+\mu}(\boldsymbol{R}, k) \\ &\times \sum_{j'} C(1, l', j'; -\mu, m'')\, g_{l'}(kr')\boldsymbol{T}_{j'l',m''-\mu}(\hat{\boldsymbol{r}}') \ ,\end{aligned} \tag{1.66}$$

in which we used the inverse coupling relation (1.38). Then, the replacement $m' = m'' - \mu$ and the definition

$$\begin{aligned}\mathcal{G}_{j'l'm'jlm} = &\sum_{\mu} C(1, l', j'; -\mu, m'+\mu) \\ &\times G_{l',m'+\mu,l,m+\mu}(\boldsymbol{R}, k) C(1, l, j; -\mu, m+\mu) \ ,\end{aligned}$$

yield the equation

$$\boldsymbol{A}_{jlm}(\boldsymbol{r}) = \sum_{j'l'm'} g_{l'}(kr')\boldsymbol{T}_{j'l'm'}(\hat{\boldsymbol{r}}')\mathcal{G}_{j'l'm'jlm} \ ,$$

which is the required addition theorem [16].

1.8.3 Application to Hansen's Vectors

In view of (1.56) and (1.57), theorem (1.66) can be applied to each of the VHHs that appear in the definitions of $\boldsymbol{M}_{lm}$ and $\boldsymbol{N}_{lm}$. Accordingly we get, for instance,

$$\begin{aligned}\boldsymbol{M}_{lm}(\boldsymbol{r}) = -\sum_{l'm'} \big[&g_{l'}(kr')\boldsymbol{T}_{l'l'm'}(\hat{\boldsymbol{r}}')\mathcal{G}_{l'l'm'llm} \\ &+ g_{l'-1}(kr')\boldsymbol{T}_{l',l'-1,m'}(\hat{\boldsymbol{r}}')\mathcal{G}_{l',l'-1,m'llm} \\ &+ g_{l'+1}(kr')\boldsymbol{T}_{l',l'+1,m'}(\hat{\boldsymbol{r}}')\mathcal{G}_{l',l'+1,m'llm} \big] \ .\end{aligned} \tag{1.67}$$

Since $\boldsymbol{M}_{lm}$ and $\boldsymbol{N}_{lm}$ are solenoidal, the preceding equation yields the relation

$$\sqrt{l'+1}\mathcal{G}_{l',l'+1,m'llm} + \sqrt{l'}\mathcal{G}_{l',l'-1,m'llm} = 0 \;, \tag{1.68}$$

that can also by proved by direct use of the properties of the Clebsch–Gordan coefficients. On account of (1.68), we can rewrite (1.69) as

$$\boldsymbol{M}_{lm}(\boldsymbol{r}) = \sum_{l'm'} \left[\bar{\boldsymbol{M}}_{l'm'}(\boldsymbol{r}')A(l'm',lm) + \bar{\boldsymbol{N}}_{l'm'}(\boldsymbol{r}')B(l'm',lm) \right] \;, \tag{1.69}$$

where we define

$$A(l'm',lm) = \mathcal{G}_{l'l'm'llm} \;, \quad B(l'm',lm) = \mathrm{i}\sqrt{\frac{2l'+1}{l'+1}}\mathcal{G}_{l',l'-1,m'llm} \;,$$

and $\bar{\boldsymbol{M}}_{l'm'}$ and $\bar{\boldsymbol{N}}_{l'm'}$ are identical to $\boldsymbol{M}_{l'm'}$ and $\boldsymbol{N}_{l'm'}$, respectively, except for the substitution of g_l in place of f_l. On account of (1.47) and (1.48), we take the curl of (1.69) and get

$$\boldsymbol{N}_{lm}(\boldsymbol{r}) = \sum_{l'm'} \left[\bar{\boldsymbol{N}}_{l'm'}(\boldsymbol{r}')A(l'm',lm) + \bar{\boldsymbol{M}}_{l'm'}(\boldsymbol{r}')B(l'm',lm) \right] \;. \tag{1.70}$$

Hereafter, when the addition theorem is applied to the multipole fields $\boldsymbol{H}_{lm}^{(p)}$ and $\boldsymbol{J}_{lm}^{(p)}$ we will use the notation

$$\boldsymbol{H}_{lm}^{(p)}(\boldsymbol{r},k) = \sum_{p'l'm'} \boldsymbol{J}_{l'm'}^{(p')}(\boldsymbol{r}',k)\mathcal{H}_{l'm'lm}^{(p'p)}(\boldsymbol{R},k), \quad \text{for } \; r' < R \;, \tag{1.71a}$$

$$\boldsymbol{H}_{lm}^{(p)}(\boldsymbol{r},k) = \sum_{p'l'm'} \boldsymbol{H}_{l'm'}^{(p')}(\boldsymbol{r}',k)\mathcal{J}_{l'm'lm}^{(p'p)}(\boldsymbol{R},k), \quad \text{for } \; r' > R \;, \tag{1.71b}$$

and

$$\boldsymbol{J}_{lm}^{(p)}(\boldsymbol{r},k) = \sum_{p'l'm'} \boldsymbol{J}_{l'm'}^{(p')}(\boldsymbol{r}',k)\mathcal{J}_{l'm'lm}^{(p'p)}(\boldsymbol{R},k) \;, \tag{1.72}$$

respectively. Comparison with equations (1.69) and (1.70) leads to the conclusion that the quantities $\mathcal{H}_{lml'm'}^{(1\,1)}$ and $\mathcal{H}_{lml'm'}^{(1\,2)}$ are identical to $A(l'm',lm)$ and $B(l'm',lm)$, respectively, with $\psi_l = h_l$, whereas in the quantities $\mathcal{J}_{lml'm'}^{(1\,1)}$ and $\mathcal{J}_{lml'm'}^{(1\,2)}$ we have $\psi_l = j_l$. Moreover,

$$\mathcal{H}_{l'm'lm}^{(1\,1)} = \mathcal{H}_{l'm'lm}^{(2\,2)} \;, \qquad \mathcal{H}_{l'm'lm}^{(pp')} = \mathcal{H}_{l'm'lm}^{(p'p)} \;,$$

$$\mathcal{J}_{l'm'lm}^{(1\,1)} = \mathcal{J}_{l'm'lm}^{(2\,2)} \;, \qquad \mathcal{J}_{l'm'lm}^{(pp')} = \mathcal{J}_{l'm'lm}^{(p'p)} \;.$$

The explicit expression of the elements of matrices H and J is

$$\begin{aligned}\mathcal{H}^{(p'p)}_{l'm'lm}(\boldsymbol{R},k) =&(1-\delta_{R,0})\left[\delta_{pp'}+\mathrm{i}\sqrt{\frac{2l'+1}{l'+1}}\,(1-\delta_{pp'})\right]\\&\times\sum_{\mu}C(1,l'-1+\delta_{pp'},l';-\mu,m'+\mu)\\&\times G_{l'-1+\delta_{pp'},m'+\mu,l,m+\mu}(\boldsymbol{R},k)C(1,l,l;-\mu,m+\mu)\ ,\end{aligned}\tag{1.73a}$$

$$\begin{aligned}\mathcal{J}^{(p'p)}_{l'm'lm}(\boldsymbol{R},k) =&\left[\delta_{pp'}+\mathrm{i}\sqrt{\frac{2l'+1}{l'+1}}(1-\delta_{pp'})\right]\\&\times\sum_{\mu}C(1,l'-1+\delta_{pp'},l';-\mu,m'+\mu)\\&\times G_{l'-1+\delta_{pp'},m'+\mu,l,m+\mu}(\boldsymbol{R},k)C(1,l,l;-\mu,m+\mu)\ ,\end{aligned}\tag{1.73b}$$

where G is still given by (1.65). In particular, when $\boldsymbol{R}=\pm a\,\hat{\boldsymbol{e}}_z$, i.e., when the translation takes place along the z axis, the matrices H and J become diagonal in m. Indeed, the spherical harmonics that occur in G are those given by (1.18) so that

$$G_{lml'm'}=G_{ll';m}\delta_{mm'}\ ,$$

and, as a consequence,

$$\mathcal{H}^{(pp')}_{lml'm'}=\mathcal{H}^{(pp')}_{ll';m}\delta_{mm'}\ ,\quad \mathcal{J}^{(pp')}_{lml'm'}=\mathcal{J}^{(pp')}_{ll';m}\delta_{mm'}\ .\tag{1.74}$$

In case we have to translate multipole fields from an origin O_α at $\boldsymbol{R}_\alpha$ to another origin $O_{\alpha'}$ at $\boldsymbol{R}_{\alpha'}$ the transfer vector is $\boldsymbol{R}_{\alpha\alpha'}=\boldsymbol{R}_{\alpha'}-\boldsymbol{R}_\alpha$, and we can alternatively use the notation

$$\mathcal{H}^{(p'p)}_{\alpha'l'm'\alpha lm}=\mathcal{H}^{(p'p)}_{l'm'lm}(\boldsymbol{R}_{\alpha\alpha'},k)\ ,\quad \mathcal{J}^{(p'p)}_{\alpha'l'm'\alpha lm}=\mathcal{J}^{(p'p)}_{l'm'lm}(\boldsymbol{R}_{\alpha\alpha'},k)\ .\tag{1.75}$$

The addition theorem we discussed so far helps to clarify the meaning of the customary classification of the multipole fields into magnetic and electric. In fact, this classification is deceiving because (1.71) and (1.72) show that a multipole field that is purely magnetic or electric with respect to a given origin becomes a superposition of both magnetic and electric multipole fields with respect to a different origin. In other words, the classification of the multipole fields is meaningful only when the frame of reference is specified. The preceding consideration should be borne in mind when discussing, e.g., the optical resonances of nonspherical particles.

2 Propagation Through an Assembly of Nonspherical Scatterers

In this chapter, we study the propagation of electromagnetic waves through a nonhomogeneous medium composed of a dispersion of nonspherical particles within an otherwise homogeneous isotropic matrix. Our purpose is to relate the scattering features of the individual particles to the macroscopic optical properties of the medium as a whole. In particular we will consider how the propagation depends on the polarization of the field and derive a number of relations and develop a notation that will prove useful later. All the relations we will deal with can be established in general terms under conditions that are met by several media of interest, such as atmospheric aerosols and the interstellar medium.

2.1 Scattering Amplitude

In Sect. 1.1 we stated that, when a wave impinges on a particle, the latter emits a field that, at a large distance, looks like an outgoing spherical wave. In order to give a more detailed description of this process, let us assume that the particle is embedded into a homogeneous, isotropic indefinite medium of (real) refractive index n and that the incident field is the plane wave

$$\boldsymbol{E}_{\mathrm{I}} = E_0 \hat{\boldsymbol{e}}_{\mathrm{I}} \exp(\mathrm{i}\boldsymbol{k}_{\mathrm{I}} \cdot \boldsymbol{r}) \ , \tag{2.1}$$

of (unit) polarization vector $\hat{\boldsymbol{e}}_{\mathrm{I}}$ and propagation vector $\boldsymbol{k}_{\mathrm{I}} = k\hat{\boldsymbol{k}}_{\mathrm{I}}$, with $k = nk_{\mathrm{v}}$. The scattering process depends both on the geometry and on the physical features of the particle, but the form of the scattered wave at a large distance from the particle can be established on general grounds. Let us recall that, since the scattered field $\boldsymbol{E}_{\mathrm{S}}$ satisfies the vector Helmholtz equation (1.7), each of its rectangular components should be a solution of the scalar Helmholtz equation. Therefore, denoting with ψ any of the rectangular components of $\boldsymbol{E}_{\mathrm{S}}$, we can write

$$(\nabla^2 + k^2)\psi(\boldsymbol{r}, k) = 0 \ . \tag{2.2}$$

The solutions to (2.2) that describe an actual scattering process must satisfy appropriate boundary conditions at the surface of the particle and should depend both on the direction of the incident wavevector $\hat{\boldsymbol{k}}_{\mathrm{I}}$ and on the direction of observation $\hat{\boldsymbol{k}}_\mathrm{S} = \hat{\boldsymbol{r}}$. By choosing the frame of reference so that the origin lies within the particle, the solution $\psi(\boldsymbol{r}, k)$ can be expanded in a series of spherical harmonics in the form

$$\psi(\boldsymbol{r}, k) = \sum_{lm} C_{lm}(\hat{\boldsymbol{k}}_\mathrm{I}) Y_{lm}(\hat{\boldsymbol{r}}) R_l(r, k)/r \; . \tag{2.3}$$

Substitution of expansion (2.3) into equation (2.2) leads to the equation for the radial functions

$$\frac{\mathrm{d}^2 R_l}{\mathrm{d}r^2} + \left[k^2 - \frac{l(l+1)}{r^2}\right] R_l = 0 \; ,$$

whereas the amplitudes C_{lm}, which depend on $\hat{\boldsymbol{k}}_\mathrm{I}$, are determined by the boundary conditions at the surface of the particle. Therefore, for small values of r, $\psi(\boldsymbol{r}, k)$ has, in general, a complicated form that depends both on the geometry and on the physical features of the particle. Nevertheless, when we go to consider the radial equation in the *far zone*, i.e., for large values of r, we get

$$\frac{\mathrm{d}^2 R_l}{\mathrm{d}r^2} + k^2 R_l = 0 \; , \tag{2.4}$$

whose solutions are clearly independent of l. Since the scattered field should satisfy the *radiation condition*, i.e., it should include only outgoing waves at infinity [6, 17], the only acceptable solution to (2.4) is

$$R_l = E_0 \exp(\mathrm{i}kr) \; ,$$

for all values of l, so that the asymptotic form of $\psi(\boldsymbol{r}, k)$ results

$$\psi(\boldsymbol{r}, k) = E_0 f(\hat{\boldsymbol{k}}_\mathrm{S}, \hat{\boldsymbol{k}}_\mathrm{I}) \frac{\mathrm{e}^{\mathrm{i}kr}}{r} \; ,$$

where we define

$$f(\hat{\boldsymbol{k}}_\mathrm{S}, \hat{\boldsymbol{k}}_\mathrm{I}) = \sum_{lm} C_{lm}(\hat{\boldsymbol{k}}_\mathrm{I}) Y_{lm}(\hat{\boldsymbol{r}}) \; ,$$

with $\hat{\boldsymbol{k}}_\mathrm{S} = \hat{\boldsymbol{r}}$. Since $\psi(\boldsymbol{r}, k)$ is any of the rectangular components of $\boldsymbol{E}_\mathrm{S}$, the whole vector should have the asymptotic form

$$\boldsymbol{E}_\mathrm{S} = E_0 \frac{\mathrm{e}^{\mathrm{i}kr}}{r} \boldsymbol{f}(\hat{\boldsymbol{k}}_\mathrm{S}, \hat{\boldsymbol{k}}_\mathrm{I}) \tag{2.5}$$

that defines the so-called *normalized scattering amplitude* $\boldsymbol{f}(\hat{\boldsymbol{k}}_\mathrm{S}, \hat{\boldsymbol{k}}_\mathrm{I})$, whose vector nature gives a correct description of the state of polarization of the scattered wave. For particles of general shape the scattering amplitude depends both on the direction of propagation of the incident wave, $\hat{\boldsymbol{k}}_\mathrm{I}$, and on the direction of observation, $\hat{\boldsymbol{k}}_\mathrm{S}$, whereas, for spherical particles, it depends on the angle of scattering, i. e. on the angle between $\hat{\boldsymbol{k}}_\mathrm{I}$ and $\hat{\boldsymbol{k}}_\mathrm{S}$, only. It is also worth noticing that, for nonspherical particles, the scattering amplitude depends on the orientation of the particle itself with respect to the incident field. Moreover, the condition $\nabla \cdot \boldsymbol{E}_{\mathrm{S}} = 0$ yields

$$\nabla \cdot \boldsymbol{E}_{\mathrm{S}} = E_0 \left(\nabla \frac{\mathrm{e}^{ikr}}{r} \right) \cdot \boldsymbol{f} + E_0 \frac{\mathrm{e}^{ikr}}{r} \nabla \cdot \boldsymbol{f} = 0 \, .$$

The latter equation, on account that we expand $\boldsymbol{E}_{\mathrm{S}}$ in terms of Hansen's vectors, and with the help of (1.50b), (1.50c), (1.55), (1.43b), and (1.44b) gives

$$\hat{\boldsymbol{k}}_{\mathrm{S}} \cdot \boldsymbol{f} = 0 \, , \tag{2.6}$$

whence

$$\nabla \cdot \boldsymbol{f} = 0 \, .$$

Equation (2.6) shows that in the far zone the scattered field is transverse to the direction of observation, so that, when necessary, the scattered wave can be approximated by a locally plane wave.

2.2 Cross Sections

The scattering amplitude encompasses all the observable features of the scattering process, as it is related to the flux of the electromagnetic energy that the particle scatters within the unit solid angle around the direction of observation $\hat{\boldsymbol{k}}_{\mathrm{S}}$.

The flux of the electromagnetic energy that impinges on the particle is given by the time averaged Poynting vector of the incident field (see Sect. 3.1.4)

$$\langle \boldsymbol{S}_{\mathrm{I}} \rangle = \frac{c}{8\pi} \mathrm{Re}(\boldsymbol{E}_{\mathrm{I}} \times \boldsymbol{B}_{\mathrm{I}}^*) = \frac{nc}{8\pi} |E_0|^2 \hat{\boldsymbol{k}}_{\mathrm{I}} \, .$$

In turn, the flux of the scattered energy in the direction $\hat{\boldsymbol{k}}_{\mathrm{S}}$ in the far zone is

$$\langle \boldsymbol{S}_{\mathrm{S}} \rangle = \frac{c}{8\pi} \mathrm{Re}(\boldsymbol{E}_{\mathrm{S}} \times \boldsymbol{B}_{\mathrm{S}}^*) = \frac{nc}{8\pi} |\boldsymbol{E}_{\mathrm{S}}|^2 \hat{\boldsymbol{k}}_{\mathrm{S}} \, .$$

We can then define the *differential scattering cross section* as

$$\frac{\mathrm{d}\sigma_{\mathrm{S}}}{\mathrm{d}\Omega} = \lim_{r \to \infty} \frac{r^2 |\langle \boldsymbol{S}_{\mathrm{S}} |\rangle}{|\langle \boldsymbol{S}_{\mathrm{I}} \rangle|} = |\boldsymbol{f}(\hat{\boldsymbol{k}}_{\mathrm{S}}, \hat{\boldsymbol{k}}_{\mathrm{I}})|^2 \, , \tag{2.7}$$

i.e., as the ratio of the energy scattered by the particle into the unit solid angle around $\hat{\boldsymbol{k}}_{\mathrm{S}}$ to the incident energy. Therefore, the ratio of all the energy scattered by the particle to the incident energy is

$$\sigma_{\mathrm{S}} = \int \frac{\mathrm{d}\sigma_{\mathrm{S}}}{\mathrm{d}\Omega} \, \mathrm{d}\Omega = \int |\boldsymbol{f}(\hat{\boldsymbol{k}}_{\mathrm{S}} = \hat{\boldsymbol{r}}, \hat{\boldsymbol{k}}_{\mathrm{I}})|^2 \, \mathrm{d}\Omega \, , \tag{2.8}$$

where the quantity σ_{S} has the dimension of an area and is called the *scattering cross section*. This result could have been obtained by integrating the flux of the real part of the Poynting vector on any surface that includes the particle. Of course, the dependence of $\boldsymbol{f}$ on the orientation of the particle, implies that the cross section itself depends on this orientation.

We can also define the *absorption cross section* σ_{A} by considering the total flux of electromagnetic energy that *enter* the particle according to the equation

$$\sigma_{\mathrm{A}} = -\frac{1}{|\boldsymbol{S}_{\mathrm{I}}|}\frac{c}{8\pi}\int \mathrm{Re}(\boldsymbol{E}\times\boldsymbol{B}^*)\cdot\hat{\boldsymbol{n}}\,\mathrm{d}S\ , \tag{2.9}$$

where $\hat{\boldsymbol{n}}$ is the unit outward normal to the surface of the particle. The same result is obtained by calculating the flux that enter any surface that includes the particle. The definition in (2.9) implies the vanishing of σ_{A} when the refractive index of the particle is real. Let us, indeed, use the Gauss theorem to transform (2.9) into

$$\sigma_{\mathrm{A}} = -\frac{1}{|\boldsymbol{S}_{\mathrm{I}}|}\frac{c}{8\pi}\int \mathrm{Re}\big[\nabla\cdot(\boldsymbol{E}\times\boldsymbol{B}^*)\big]\,\mathrm{d}V\ .$$

This equation can be further transformed with the help of the vector identity

$$\nabla\cdot(\boldsymbol{E}\times\boldsymbol{B}^*) = \boldsymbol{B}^*\cdot\nabla\times\boldsymbol{E} - \boldsymbol{E}\cdot\nabla\times\boldsymbol{B}^*\ .$$

Substituting in place of $\nabla\times\boldsymbol{B}^*$ and $\nabla\times\boldsymbol{E}$ their respective expressions given by (1.3) we get

$$\sigma_{\mathrm{A}} = \frac{1}{|\boldsymbol{S}_I|}\frac{c}{8\pi}\int \mathrm{Re}\big(\mathrm{i}k_{\mathrm{v}}n_0^{*2}|\boldsymbol{E}|^2 - \mathrm{i}k_{\mathrm{v}}|\boldsymbol{B}|^2\big)\,\mathrm{d}V\ ,$$

where n_0 denotes the refractive index of the particle. Clearly, the second term is purely imaginary and gives no contribution to the integral. The first term, in turn, has a nonvanishing real part only when n_0 has a nonvanishing imaginary part. This proves our earlier statement that complex refractive indexes take into account the absorption properties of the particles.

The sum of the scattering and of the absorption cross sections gives the total cross sections that in optical studies is customarily called *extinction cross section*,

$$\sigma_{\mathrm{T}} = \sigma_{\mathrm{S}} + \sigma_{\mathrm{A}}\ .$$

Finally, it is worth stressing that none of the cross sections defined above coincides with the geometrical cross section of the particle. Actually, σ_{S} and σ_{A} are the areas that would block from the incident beam as much energy as the particle removes by scattering and absorption, respectively. σ_{T} is thus the area that blocks the energy that would be removed by the combined effect of scattering and absorption. Therefore, it is often convenient to characterize a scattering particle through *efficiencies* that are defined by the ratios

$$Q_{\mathrm{T}} = \frac{\sigma_{\mathrm{T}}}{G}, \quad Q_{\mathrm{S}} = \frac{\sigma_{\mathrm{S}}}{G}, \quad Q_{\mathrm{A}} = \frac{\sigma_{\mathrm{A}}}{G} , \tag{2.10}$$

where G is the geometrical cross section of the particle in a plane orthogonal to the direction of incidence. Another quantity that characterizes the optical properties of a particle is the *albedo* that is defined as

$$\varpi = \sigma_{\mathrm{S}}/\sigma_{\mathrm{T}} = Q_{\mathrm{S}}/Q_{\mathrm{T}} .$$

The albedo, when considered in terms of photons impinging on a particle, gives the probability that a photon be scattered rather than absorbed [5].

2.3 Optical Theorem

In the preceding section the scattering amplitude has been directly related to the scattering cross section only. Nevertheless, it is also directly related to the extinction cross section through the *optical theorem* that we are now going to derive. In our derivation, that as far as possible follows the arguments of van de Hulst [5], we assume that the scattering particle is embedded in a medium with a real refractive index, n. Nevertheless, when the medium is absorptive, i.e., when its refractive index has a nonvanishing imaginary part, the theorem can be reformulated along the lines indicated by Bohren and Gilra [18].

2.3.1 Nonabsorbing Host Medium

We assume, with no loss of generality, that the scattering particle lies at the origin of the frame of reference and that the incident wave is linearly polarized and propagating along the z axis. With these assumptions the incident field reads

$$\boldsymbol{E}_{\mathrm{I}} = E_0 \hat{\boldsymbol{e}}_{\mathrm{I}} \mathrm{e}^{\mathrm{i}kz} , \tag{2.11}$$

with $k = nk_{\mathrm{v}}$. We now consider the field scattered in the forward direction, i.e. for $\hat{\boldsymbol{k}}_{\mathrm{S}} = \hat{\boldsymbol{k}}_{\mathrm{I}}$. In this case we denote the scattering amplitude as $\boldsymbol{f}(0)$ for short and, according to (2.5), we write the scattered field in the form

$$\boldsymbol{E}_{\mathrm{S}} = E_0 \frac{\mathrm{e}^{\mathrm{i}kr}}{r} \boldsymbol{f}(0) . \tag{2.12}$$

Then, by dot multiplying (2.11) and (2.12) by $\hat{\boldsymbol{e}}_{\mathrm{I}}$ we get the equations

$$\boldsymbol{E}_{\mathrm{I}} \cdot \hat{\boldsymbol{e}}_{\mathrm{I}} = E_0 \mathrm{e}^{\mathrm{i}kz} ,$$

$$\boldsymbol{E}_{\mathrm{S}} \cdot \hat{\boldsymbol{e}}_{\mathrm{I}} = E_0 \frac{\mathrm{e}^{\mathrm{i}kr}}{r} \boldsymbol{f}(0) \cdot \hat{\boldsymbol{e}}_{\mathrm{I}} ,$$

that can be combined into

$$\boldsymbol{E}_{\mathrm{S}} \cdot \hat{\boldsymbol{e}}_{\mathrm{I}} = \frac{\mathrm{e}^{\mathrm{i}k(r-z)}}{r} \boldsymbol{f}(0) \cdot \hat{\boldsymbol{e}}_{\mathrm{I}} (\boldsymbol{E}_{\mathrm{I}} \cdot \hat{\boldsymbol{e}}_{\mathrm{I}}) \; .$$

We now remark that, in the forward direction, at a distance z from the scattering particle, an optical instrument records the combined intensity of the incident and the scattered wave. The plane of the receiving lens, whose diameter is d, has the equation $z = \text{cost}$ so that, for $z \gg d$, we can write

$$r = (z^2 + x^2 + y^2)^{1/2} \approx z + \frac{x^2 + y^2}{2z} \; ,$$

and the total field on the lens is

$$\boldsymbol{E}_{\mathrm{S}} \cdot \hat{\boldsymbol{e}}_{\mathrm{I}} + \boldsymbol{E}_{\mathrm{I}} \cdot \hat{\boldsymbol{e}}_{\mathrm{I}} = \left[1 + \frac{\mathrm{e}^{\mathrm{i}k(x^2+y^2)/2z}}{z} \boldsymbol{f}(0) \cdot \hat{\boldsymbol{e}}_{\mathrm{I}} \right] (\boldsymbol{E}_{\mathrm{I}} \cdot \hat{\boldsymbol{e}}_{\mathrm{I}}) \; .$$

The corresponding intensity is

$$|\boldsymbol{E}_{\mathrm{S}} \cdot \hat{\boldsymbol{e}}_{\mathrm{I}} + \boldsymbol{E}_{\mathrm{I}} \cdot \hat{\boldsymbol{e}}_{\mathrm{I}}|^2 = \left\{ 1 + \frac{2}{z} \operatorname{Re} \left[\mathrm{e}^{\mathrm{i}k(x^2+y^2)/2z} \boldsymbol{f}(0) \cdot \hat{\boldsymbol{e}}_{\mathrm{I}} \right] \right\} |\boldsymbol{E}_{\mathrm{I}} \cdot \hat{\boldsymbol{e}}_{\mathrm{I}}|^2 \; ,$$

which has been obtained by neglecting the term $|\boldsymbol{f}(0) \cdot \hat{\boldsymbol{e}}_{\mathrm{I}}|^2/z^2$ that is actually negligible for large z. The total energy recorded by the instrument is given by integrating the preceding expression on the surface of the front lens, i.e., letting x, $y \leq d/2$. Close examination of the integrand shows, however, that when $\sqrt{z\lambda} \ll d \ll z$, as in the present case, the integration limits can be extended from $-\infty$ to ∞ without appreciably affecting the result. Now,

$$\int_{-\infty}^{\infty} \mathrm{d}x \int_{-\infty}^{\infty} \mathrm{e}^{\mathrm{i}k(x^2+y^2)/2z} \, \mathrm{d}y = \frac{2\pi \mathrm{i} z}{k} \; ,$$

so that, according to Sect. 2.2, the energy recorded by the instrument is

$$W = \left\{ A - \frac{4\pi}{k} \operatorname{Im} \big[\boldsymbol{f}(0) \cdot \hat{\boldsymbol{e}}_{\mathrm{I}} \big] \right\} I_0 \; ,$$

where

$$I_0 = \frac{nc}{8\pi} |\boldsymbol{E}_{\mathrm{I}} \cdot \hat{\boldsymbol{e}}_{\mathrm{I}}|^2 = \frac{nc}{8\pi} I_{\mathrm{I}} \; .$$

This equation shows that, due to the interference of the incident and the scattered wave, the front lens of the receiving instrument has seemingly an area smaller than A and is therefore able to collect a smaller quantity of energy than in the absence of the particle. Actually, since I_0 is the intensity of the incident wave, the term AI_0 is the energy that the instrument would collect in the absence of the particle. The second term

$$I_{\mathrm{T}} = \frac{4\pi}{k} \operatorname{Im} \big[\boldsymbol{f}(0) \cdot \hat{\boldsymbol{e}}_{\mathrm{I}} \big] I_0$$

measures the energy that is lacking because of the presence of the particle. The lacking energy should be equal to the energy that the particle removes from the incident beam by absorption and scattering, so that, according to the argument at the end of Sect. 2.2, the coefficient of I_0 must coincide with the extinction cross section. We are thus led to the relation

$$\sigma_{\mathrm{T}} = \frac{4\pi}{k} \,\mathrm{Im}[\boldsymbol{f}(\hat{\boldsymbol{k}}_{\mathrm{S}} = \hat{\boldsymbol{k}}_{\mathrm{I}}, \hat{\boldsymbol{k}}_{\mathrm{I}}) \cdot \hat{\boldsymbol{e}}_{\mathrm{I}}] \tag{2.13}$$

that is just the expression of the *optical theorem*.

2.3.2 Absorbing Host Medium

In the preceding section we derived the optical theorem for a particle embedded into a homogeneous isotropic medium through a procedure that holds true only when the host medium has a real refractive index. When the host medium is absorptive, i.e. its refractive index has a nonvanishing imaginary part, our derivation must be reconsidered. In fact, a wave propagating in an absorbing medium undergoes attenuation so that the amplitude of the incident field depends on the position of the scattering particle. Moreover, the amplitude of the scattered field turns out to depend on the position of the detecting instrument. In spite of these difficulties, the extinction cross section of a particle embedded in an absorbing medium can still be defined without ambiguity through a generalization of the optical theorem. Nevertheless, the scattering and absorption cross sections cannot be defined without ambiguity and, as a consequence, it is no longer possible to state that the extinction cross section is the sum of the scattering and of the absorption cross section.

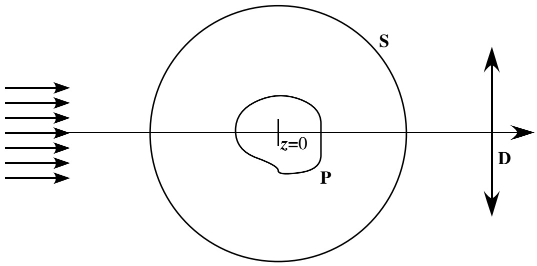

Fig. 2.1. Geometry for the optical theorem in an absorbing host medium

Let us thus assume, without loss of generality, that the incident plane wave propagate along the z axis and that the origin $z = 0$ lies within the particle. The front lens of the detecting instrument is located at $z = z_1$ and the plane wave is emitted by a plane (orthogonal to the z axis) located at $z = z_0$ on the negative side of the z axis. Accordingly, the incident plane wave has to travel a distance $z_1 - z_0$ before reaching the front lens of the detector. At this stage our derivation proceeds exactly as in the preceding subsection, with the *proviso* that the propagation constant k is now complex. As a result, when calculating the total energy detected by the instrument we get

$$W = \left\{A - 4\pi \,\mathrm{Im}\left[\boldsymbol{f}(0) \cdot \hat{\boldsymbol{e}}_{\mathrm{I}}/k\right]\right\} I_0 \ ,$$

where

$$I_0 = \frac{c n_{\mathrm{r}}}{8\pi} |\boldsymbol{E}_{\mathrm{I}} \cdot \hat{\boldsymbol{e}}_{\mathrm{I}}|^2$$

with $n_{\mathrm{r}} = \mathrm{Re}(n)$. Now, the expansion of the factor $|\boldsymbol{E}_{\mathrm{I}} \cdot \hat{\boldsymbol{e}}_{\mathrm{I}}|^2$ gives

$$|\boldsymbol{E}_{\mathrm{I}} \cdot \hat{\boldsymbol{e}}_{\mathrm{I}}|^2 = |E_0|^2 \exp\left[-2k_{\mathrm{i}}(z_1 - z_0)\right] = I_{\mathrm{I}} \exp\left[-2k_{\mathrm{i}}(z_1 - z_0)\right] \ ,$$

where k_{i} is the imaginary part of the propagation constant and I_{I} is the intensity of the incident plane wave at $z = z_1$. Now, by definition, the extinction cross section is the ratio of the energy recorded by the detector to the incident energy, i.e. the energy that would be recorded in the absence of the particle. Thus we get

$$\sigma_{\mathrm{T}} = 4\pi \,\mathrm{Im}\left[\boldsymbol{f}(\hat{\boldsymbol{k}}_{\mathrm{S}} = \hat{\boldsymbol{k}}_{\mathrm{I}}, \hat{\boldsymbol{k}}_{\mathrm{I}}) \cdot \hat{\boldsymbol{e}}_{\mathrm{I}}/k\right] \tag{2.14}$$

that is independent of the position both of the particle and of the detector [19]. Equation (2.14) is identical to the one obtained by Bohren and Gilra [18] for spherical particles through an extension of Mie theory and differs very little from the usual expression of the optical theorem.

If we attempt to define in a similar way the scattering cross section we have to consider the flux of the scattered Poynting vector across any surface that includes the particle, for instance the sphere S in Fig. 2.14. Then, it is an easy matter to see that the result would depend on the radius of S. For this reason it has been proposed that the only surface suitable for the purpose would be the surface of the particle itself. This suggestion is unsatisfactory from a conceptual viewpoint and leads to unsurmountable problems when the particle itself is composed by more than one piece, i.e. when the surface of the particle is not connected. Similar results are reached for the absorption cross section. In any case, when a particle is embedded in an absorbing medium there is no possibility of defining in an unambiguous way the scattering and absorption cross sections.

2.4 Scattering by an Ensemble of Particles

We are now able to relate the scattering properties of the single particles with the macroscopic optical properties of a dispersion of them. To this end, we need to assume both that each particle scatters independently of the other particles present and that it is quite unlikely that a beam would be scattered more than once. Actually, these conditions amount to requiring that the field that illuminates each particle be the original incident field. In practice, we can speak of independent scattering when the particles are well separated, e.g. when their mutual distance is more or less twice their size for the particles bigger than the wavelength [20]. Of course, when the number density of the dispersion is low, the particles surely scatter independently. We can also say that only single scattering processes need to be considered when the *optical thickness* $\tau \ll 0.1$, where $\exp(-\tau)$ is the attenuation undergone by the intensity in traversing the dispersion [5, 21]. Hereafter, we will term a dispersion possessing the features mentioned above as a *tenuous dispersion.*

If the positions of the particles are randomly distributed, the waves scattered by each one of them into any given direction, with the exception of the forward direction, interfere with random phase difference. As a consequence, the field scattered by the whole dispersion does not depend on the phases of the single waves, and we have to sum their intensities [22]. Using the index ν to label the quantities that refer to the νth particle we can write

$$I_\mathrm{S} = \sum_\nu I_{\mathrm{S}\nu} \ ,$$

and the scattering cross sections too turn out to be additive [22], i.e.,

$$\sigma_\mathrm{S} = \sum_\nu \sigma_{\mathrm{S}\nu} \ . \tag{2.15}$$

On the other hand, if forward scattering is considered, it should be borne in mind that any shift of the position of the particles does not alter the phase of the scattered wave. As a consequence, in the forward direction we need to sum the fields and not the intensities. Therefore we write

$$\boldsymbol{E}_\mathrm{S} = \sum_\nu \boldsymbol{E}_{\mathrm{S}\nu} \ .$$

The optical theorem then decrees that the extinction cross sections are additive

$$\sigma_\mathrm{T} = \sum_\nu \sigma_{\mathrm{T}\nu} \ . \tag{2.16}$$

Equations (2.15) and (2.16) state that, although for quite different physical reasons, the extinction and the scattering cross sections are additive, provided the dispersion is tenuous in the sense discussed above. From this constatation the additivity of the absorption cross sections follows at once. Therefore, even for these cross sections we can write

$$\sigma_\mathrm{A} = \sum_\nu \sigma_{\mathrm{A}\nu} \ .$$

2.5 Refractive Index of a Dispersion of Particles

We now show that the propagation of a plane wave through a dispersion of particles can be characterized by a macroscopic *refractive index* that is the analogous of the refractive index of homogeneous media. We consider first the case of a monodispersion, this term being used here in a restricted sense to indicate a dispersion of particles with identical morphology and orientation with respect to the incident field. This restriction, which will be removed later, allows us to use the same scattering amplitude to describe the field scattered by each particle. It is necessary, however, that the dispersion be tenuous, in the sense discussed in the preceding section. We assume that all the particles be included within a layer limited by a pair of parallel planes a distance l apart and orthogonal to the z axis, N denotes the number density of the particles, so that the volume element $\mathrm{d}V$ includes $N\,\mathrm{d}V$ scatterers (see Fig. 2.2). The plane wave

$$\boldsymbol{E}_{\mathrm{I}} = E_0 \hat{\boldsymbol{e}}_{\mathrm{I}} \mathrm{e}^{\mathrm{i}kz}$$

that propagates through the layer undergoes scattering by the particles so that a detector located on the z axis, say at z_0, at a large distance from the layer, records the superposition of the original plane wave and of the waves scattered by the particles. The waves coming from particles included within the volume of intersection of the layer and of the aperture cone of the observation instrument sum coherently. Provided that this cone is narrow enough, the only waves that will be recorded are those scattered in the forward direction. Now, at z_0 the field scattered by a particle that is located at $\boldsymbol{R}$ is

$$\boldsymbol{E}_{\mathrm{S}} = E_0 \frac{\mathrm{e}^{\mathrm{i}kR}}{R} \mathrm{e}^{\mathrm{i}kz} \boldsymbol{f}(0) \ ,$$

where

$$R = \left[x^2 + y^2 + (z_0 - z)^2\right]^{1/2}$$

and the phase factor $\mathrm{e}^{\mathrm{i}kz}$ accounts for the position of the particle within the layer. The total field scattered by the whole dispersion is therefore

$$\boldsymbol{E}_{\mathrm{S}} = N E_0 \int_V \frac{\mathrm{e}^{\mathrm{i}kR}}{R} \mathrm{e}^{\mathrm{i}kz} \boldsymbol{f}(0)\,\mathrm{d}V \ , \tag{2.17}$$

where V is the volume that contains the scatterers that take part in the process. The correctness of (2.17), which contains an integration over the volume instead of a sum over the particles, is granted as long as even for our tenuous dispersion the volume of integration contains a large number of scatterers. Since z_0 is large and, however, very much larger than the values of z within the layer, the distance R can be expanded as

$$R \approx (z_0 - z) + (x^2 + y^2)/2(z_0 - z) \ ,$$

in analogy to the procedure in Sect. 2.3. Accordingly, (2.17) becomes

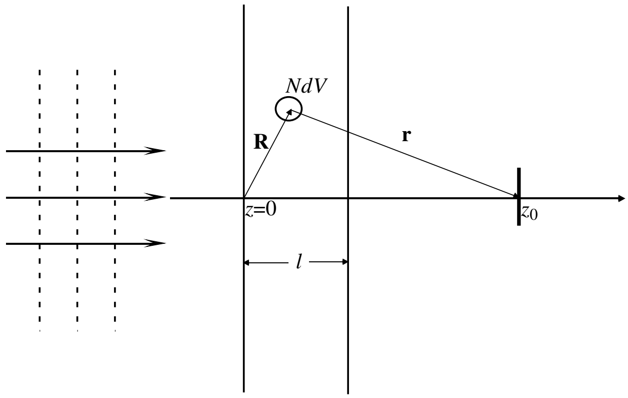

Fig. 2.2. Propagation through a layer of particles

$$\boldsymbol{E}_{\mathrm{S}} = N E_0 \mathrm{e}^{\mathrm{i}kz_0} \int_0^l \mathrm{d}z \int_{-\infty}^{\infty} \mathrm{d}x \int_{-\infty}^{\infty} \mathrm{d}y \frac{\exp[\mathrm{i}k(x^2+y^2)/2(z_0-z)]}{(z_0-z)} \boldsymbol{f}(0) \ .$$

The integrals are of the kind that we already considered in Sect. 2.3, so that the final result is

$$\boldsymbol{E}_{\mathrm{S}} = N E_0 \mathrm{e}^{\mathrm{i}kz_0} \frac{2\pi \mathrm{i} l}{k} \boldsymbol{f}(0) \ .$$

Ultimately, the total field recorded by the instrument at z_0 is

$$\boldsymbol{E}_{\mathrm{T}} = E_0 \mathrm{e}^{\mathrm{i}kz_0} \left[\hat{\boldsymbol{e}}_{\mathrm{I}} + \frac{2\pi \mathrm{i} N l}{k} \boldsymbol{f}(0) \right] \ . \tag{2.18}$$

The preceding result can be interpreted by substituting for the actual medium of refractive index n containing the dispersion a plane parallel plate of homogeneous material with (complex) refractive index $\bar{n}n$ and thickness l. Classical optics states that within the plate the incident plane wave becomes

$$\boldsymbol{E}_{\mathrm{I}} = E_0 \hat{\boldsymbol{e}}_{\mathrm{I}} \mathrm{e}^{\mathrm{i}\bar{n}kz} \ ,$$

so that, after crossing the thickness l, it is attenuated to the ratio

$$|\boldsymbol{E}_{\mathrm{I}} \cdot \hat{\boldsymbol{e}}_{\mathrm{I}}| / E_0 = \mathrm{e}^{\mathrm{i}kl(\bar{n}-1)} \approx 1 + \mathrm{i}kl(\bar{n}-1) \ ,$$

where the last expression is valid provided $|\bar{n}-1| \ll 1$. Now, by dot multiplying (2.18) by $\hat{\boldsymbol{e}}_{\mathrm{I}}$ we get

$$\boldsymbol{E}_{\mathrm{T}} \cdot \hat{\boldsymbol{e}}_{\mathrm{I}} = E_0 \mathrm{e}^{\mathrm{i}kz_0} \left[1 + \frac{2\pi \mathrm{i} N l}{k} \boldsymbol{f}(0) \cdot \hat{\boldsymbol{e}}_{\mathrm{I}} \right] \tag{2.19}$$

that, when compared with the preceding expression, leads to the conclusion that to a layer of scatterers can be attributed a formal refractive index

$$\bar{n} = 1 + \frac{2\pi}{k^2} N f(0) \;, \tag{2.20}$$

where $f(0) = \boldsymbol{f}(\hat{\boldsymbol{k}}_{\mathrm{I}}, \hat{\boldsymbol{k}}_{\mathrm{I}}) \cdot \hat{\boldsymbol{e}}_{\mathrm{I}}$ is the component of the forward scattering amplitude in the direction of polarization of the incident field. Equation (2.20) thus relates the scattering properties of the particles with the macroscopic optical properties of a monodispersion of them.

Little modifications make (2.20) applicable to the case of a dispersion that includes more that one kind of particles. In fact, even when the dispersion includes particles with a different morphology and/or orientation with respect to the incident field, the effect of each kind can be considered separately and the results added. This possibility stems from our assumption that the dispersion be tenuous so that the multiple scattering processes can be neglected, and there is no interaction among particles either of the same or of a different kind. Accordingly, denoting with the index ν the quantities that refer to particles of the ν-th kind, (2.20) can be rewritten as

$$\bar{n} = 1 + \frac{2\pi}{k^2} \sum_{\nu} N_{\nu} f_{\nu}(0) \;. \tag{2.21}$$

Of course, the preceding equation should be considered only a definition, because nothing has been said on the procedure to actually perform the sum over the particles of the various kinds. This problem will be addressed in the next chapters.

2.6 Description of Polarization

In the preceding sections the vector nature of the electromagnetic field has been taken into full account. Nevertheless, the polarization of the field needs to be described into some detail, because it is related to the the quantities that can actually be measured by optical instruments. To do this we define a *reference plane*, characterized by its unit normal $\hat{\boldsymbol{n}}$, through the direction of propagation $\hat{\boldsymbol{k}}$. We also define a unit vector $\hat{\boldsymbol{p}}$ lying in the reference plane such that

$$\hat{\boldsymbol{p}} \times \hat{\boldsymbol{n}} = \hat{\boldsymbol{k}} \;.$$

In other words the triplet $\hat{\boldsymbol{p}}$, $\hat{\boldsymbol{n}}$ and $\hat{\boldsymbol{k}}$ form a right-handed basis for the analysis of the field. In fact, the choice of this basis permits to take full advantage of the transversality of the field with respect to the direction of propagation, as the only (possibly) nonvanishing components of the field are those along $\hat{\boldsymbol{n}}$ and along $\hat{\boldsymbol{p}}$. We will now specialize our study of the polarization to the case of the incident plane wave and to that of the scattered field in the far zone.

2.6.1 Incident Plane Wave

Let us consider the field

$$\boldsymbol{E} = E_0 \hat{\boldsymbol{e}} \exp(\mathrm{i}\boldsymbol{k} \cdot \boldsymbol{r}) \;, \tag{2.22}$$

with

$$\hat{\boldsymbol{e}} \cdot \boldsymbol{k} = 0 \;.$$

For real $\hat{\boldsymbol{e}}$ (2.22) represents a linearly polarized plane wave. In particular, when $\hat{\boldsymbol{e}} = \hat{\boldsymbol{p}}$ the field is parallel to the plane of reference, and we say that the wave is l-polarized whereas, when $\hat{\boldsymbol{e}} = \hat{\boldsymbol{n}}$ the field is orthogonal to the plane of reference, and we say that the wave is r-polarized (or, from the German senkrecht, s-polarized). The nomenclature above follows the one introduced by van de Hulst [5] that uses the final letters of the words parallel and perpendicular, respectively. Actually, an appropriate linear combination of two waves, such as those in (2.22), is able to describe a plane wave for whatever state of polarization. Let us thus consider three mutually orthogonal real unit vectors, $\hat{\boldsymbol{l}}_1$, $\hat{\boldsymbol{l}}_2$, and $\hat{\boldsymbol{k}}$, so oriented that

$$\hat{\boldsymbol{l}}_1 \times \hat{\boldsymbol{l}}_2 = \hat{\boldsymbol{k}} \;,$$

and the plane wave

$$\boldsymbol{E} = \sum_\eta E_{0\eta} \hat{\boldsymbol{l}}_\eta \exp(\mathrm{i}\boldsymbol{k} \cdot \boldsymbol{r}) \;. \tag{2.23}$$

Putting $\phi = \boldsymbol{k} \cdot \boldsymbol{r}$, $E_{0\eta} = a_\eta e^{\mathrm{i}\alpha_\eta}$ with real a_η and α_η and $a_\eta \geq 0$, (2.23) can be rewritten as

$$\boldsymbol{E} = \sum_\eta a_\eta \hat{\boldsymbol{l}}_\eta \exp[\mathrm{i}(\alpha_\eta + \phi)] \;. \tag{2.24}$$

A look to (2.24) will convince the reader that, according to whether $a_1 = 0$ or $a_2 = 0$, the field is linearly polarized along $\boldsymbol{l}_2$ or along $\boldsymbol{l}_1$, respectively. When $a_1 = a_2$ and $|\alpha_2 - \alpha_1| = \pi/2$ the field is circularly polarized. More precisely, it is left-circularly polarized, with positive helicity, when $\alpha_2 - \alpha_1 = +\pi/2$, whereas it is right-circularly polarized, with negative helicity, when $\alpha_2 - \alpha_1 = -\pi/2$.

It may be useful to define the three vectors $\hat{\boldsymbol{c}}_1$, $\hat{\boldsymbol{c}}_2$, and $\hat{\boldsymbol{k}}$, where

$$\hat{\boldsymbol{c}}_1 = \tfrac{1}{\sqrt{2}}\big(\hat{\boldsymbol{l}}_1 + \mathrm{i}\hat{\boldsymbol{l}}_2\big) \quad \text{and} \quad \hat{\boldsymbol{c}}_2 = \tfrac{1}{\sqrt{2}}\big(\hat{\boldsymbol{l}}_1 - \mathrm{i}\hat{\boldsymbol{l}}_2\big) \tag{2.25}$$

describe left-polarized and right-polarized waves, respectively. As a consequence, we have

$$\hat{\boldsymbol{l}}_1 = \tfrac{1}{\sqrt{2}}\big(\hat{\boldsymbol{c}}_1 + \hat{\boldsymbol{c}}_2\big) \;, \quad \hat{\boldsymbol{l}}_2 = -\tfrac{\mathrm{i}}{\sqrt{2}}\big(\hat{\boldsymbol{c}}_1 - \hat{\boldsymbol{c}}_2\big) \;, \tag{2.26}$$

which recall that any linearly-polarized state can be obtained by superposing a left- and a right-circularly polarized state. With the exception of the simple cases discussed above, (2.23) represents an elliptically polarized wave. Therefore, it may be useful to use, in place of the basis vectors $\hat{\boldsymbol{l}}_1$, $\hat{\boldsymbol{l}}_2$, and $\hat{\boldsymbol{k}}$, the vectors $\hat{\boldsymbol{e}}_1$, $\hat{\boldsymbol{e}}_2$, and $\hat{\boldsymbol{k}}$ with real $\hat{\boldsymbol{e}}_1$ and $\hat{\boldsymbol{e}}_2$, and $\hat{\boldsymbol{e}}_1$ lying along the major axis of the polarization ellipse. Using this basis we can rewrite (2.24) as

$$\boldsymbol{E} = \sum_\eta \bar{a}_\eta \hat{\boldsymbol{e}}_\eta \exp[\mathrm{i}(\bar{\alpha}_\eta + \phi)] \; , \tag{2.27}$$

with

$$\bar{a}_1 = a_0 \cos\beta \; , \quad \bar{a}_2 = \pm a_0 \sin\beta \; ,$$

$$\bar{\alpha}_1 = \alpha \; , \quad \bar{\alpha}_2 = \alpha \pm \pi/2 \; ,$$

where the upper or the lower sign apply according to whether $\beta > 0$ or $\beta < 0$, respectively. By defining $\hat{\boldsymbol{e}}_1 \cdot \hat{\boldsymbol{l}}_1 = \cos\chi$, (2.27) yields

$$\begin{aligned} \boldsymbol{E} = &\big[(\bar{a}_1 \cos\chi\, \mathrm{e}^{\mathrm{i}\bar{\alpha}_1} - \bar{a}_2 \sin\chi\, \mathrm{e}^{\mathrm{i}\bar{\alpha}_2})\hat{\boldsymbol{l}}_1 \\ &+ (\bar{a}_1 \sin\chi\, e^{\mathrm{i}\bar{\alpha}_1} + \bar{a}_2 \cos\chi\, e^{\mathrm{i}\bar{\alpha}_2})\hat{\boldsymbol{l}}_2\big] \exp(\mathrm{i}\phi) \; . \end{aligned}$$

At this stage, we recall that what is actually observable is the real part of the field, so that we write

$$\mathrm{Re}(\boldsymbol{E}) = a_0 \big(\hat{\boldsymbol{e}}_1 \cos\beta \cos\phi - \hat{\boldsymbol{e}}_2 \sin\beta \sin\phi\big)$$

and the ellipticity, i.e., the ratio of the minor to the major axis of the ellipse described by the field, is given by $\tan\beta$, whose sign is positive or negative according to whether the wave is left- or right-polarized.

Ultimately, the preceding considerations make it clear that (2.23) can be rewritten with respect to any basis, in particular with respect the basis $\hat{\boldsymbol{c}}_1$, $\hat{\boldsymbol{c}}_2$, $\hat{\boldsymbol{k}}$ when convenient. Hereafter, we will refer with the notation $\hat{\boldsymbol{u}}_1$, $\hat{\boldsymbol{u}}_2$, $\hat{\boldsymbol{k}}$, to any of the bases described above with $\hat{\boldsymbol{u}}_\eta$ either real or complex according to the choice, so that

$$\boldsymbol{E}_\mathrm{I} = \sum_\eta \boldsymbol{E}_{\mathrm{I}\eta} = \sum_\eta E_{0\eta} \hat{\boldsymbol{u}}_{\mathrm{I}\eta} \mathrm{e}^{\mathrm{i}\boldsymbol{k}\cdot\boldsymbol{r}} . \tag{2.28}$$

Thus, the quantities $E_{0\eta}$ are the amplitudes of the incident plane wave in the chosen basis. Of course, $E_{0\eta}$ can be trasformed from the circular basis to the linear one and viceversa with the help of (2.25) and (2.26).

In conclusion

- The expression of the fields in terms of $E_{0\eta}$ will be hereafter referred to as *representation on basis-polarized components.*
- When the field is already polarized along one of the basis vectors, the only nonvanishing component will be simply denoted as E_0.

2.6.2 Scattered Wave and Scattering Amplitude Matrix

In Sect. 2.1 it has been stressed that the scattered field in the far zone is transverse to the direction of observation. As a consequence, by chosing a plane of reference through $\hat{\boldsymbol{k}}_\mathrm{S}$ the state of polarization of the scattered wave can be analyzed by projecting $\boldsymbol{E}_\mathrm{S}$ onto the unit vectors $\hat{\boldsymbol{u}}_{\mathrm{S}\eta}$. Here, the vectors

$\hat{\boldsymbol{u}}_\eta$ bear the index S to recall that they are those appropriate to the scattered field. Since the latter depends on the polarization of the incident wave, we attach to the scattering amplitude the index η which recalls that the incident wave is polarized along $\hat{\boldsymbol{u}}_{\mathrm{I}\eta}$, and write

$$\boldsymbol{E}_{\mathrm{S}} = \sum_\eta \boldsymbol{E}_{\mathrm{S}\eta} = \frac{\mathrm{e}^{\mathrm{i}kr}}{r} \sum_\eta E_{0\eta} \boldsymbol{f}_\eta(\hat{\boldsymbol{k}}_{\mathrm{S}}, \hat{\boldsymbol{k}}_{\mathrm{I}}) \ .$$

It is worth noticing that the plane of reference for the scattered field is, in general, different from that of the incident field. In terms of the components of $\boldsymbol{E}_{\mathrm{S}}$ along $\hat{\boldsymbol{u}}_{\mathrm{S}\eta'}$ we can then write

$$\boldsymbol{E}_{\mathrm{S}} = \sum_{\eta'\eta} E_{\mathrm{S}\eta'\eta} \hat{\boldsymbol{u}}_{\mathrm{S}\eta'} = \frac{\mathrm{e}^{\mathrm{i}kr}}{r} \sum_{\eta'\eta} E_{0\eta} f_{\eta'\eta} \hat{\boldsymbol{u}}_{\mathrm{S}\eta'} \ ,$$

where we define the components of the scattering amplitude as

$$f_{\eta'\eta} = \boldsymbol{f}_\eta \cdot \hat{\boldsymbol{u}}^*_{\mathrm{S}\eta'} \ . \tag{2.29}$$

We dot multiplied by $\hat{\boldsymbol{u}}^*_{\mathrm{S}\eta'}$ to allow for the choice of a circular polarization basis. Finally, it is important to realize that, in general, the components of the scattering amplitude are complex and nonvanishing for both values of η'. Therefore, in analogy with the incident plane wave, we can write

$$f_{\eta'\eta} = a_{\eta'\eta} \mathrm{e}^{\mathrm{i}\alpha_{\eta'\eta}}$$

to stress that the components of the scattered wave may have a different phase. In fact, even when the incident wave is linearly polarized, α_1 may differ from α_2 and, as a consequence, the scattered wave may be elliptically polarized. The quantities $f_{\eta'\eta}$ form a 2×2 matrix that is customarily termed the *scattering amplitude matrix.*

Provided the medium into which the scattering particle is embedded is homogeneous, nonabsorbing and isotropic, the elements $f_{\eta'\eta}$ have the property

$$f_{\eta\eta'}(-\hat{\boldsymbol{k}}_{\mathrm{I}}, -\hat{\boldsymbol{k}}_{\mathrm{S}}) = (-)^{\eta'-\eta} f_{\eta'\eta}(\hat{\boldsymbol{k}}_{\mathrm{S}}, \hat{\boldsymbol{k}}_{\mathrm{I}}) \ . \tag{2.30}$$

This property establishes the so-called *reciprocity theorem*, whose demonstration has been originally given by Saxon [23].

2.6.3 Polarization of Light and Refractive Index of a Dispersion

As an application of the formalism developed so far we will now study how the refractive index of a dispersion of particles that is defined by (2.20) and its extension (2.21) depend on the polarization of the incident wave. In fact, since $\hat{\boldsymbol{k}}_{\mathrm{I}}$ and $\hat{\boldsymbol{k}}_{\mathrm{S}}$ coincide, we chose a single plane of reference through their common direction. Then, by chosing in (2.19) $\hat{\boldsymbol{e}}_{\mathrm{I}} = \hat{\boldsymbol{u}}_\eta$, it is an easy matter to see that the refractive index turns out to be a 2×2 matrix with complex elements [22]. Actually, these elements take on the form

$$\mathcal{N}_{\eta\eta'} = \delta_{\eta\eta'} + \frac{2\pi}{k^2} N f_{\eta\eta'}(0) \; , \tag{2.31}$$

which holds true whether the chosen basis is linear or circular. The diagonal elements of (2.31) give the complex refractive index for the two states of polarization of the incident wave, whereas the off-diagonal elements give information on the change of the plane of polarization. More precisely, the real part of the diagonal elements

$$\mathrm{Re}(\mathcal{N}_{\eta\eta}) = 1 + \frac{2\pi}{k^2} N \mathrm{Re}[f_{\eta\eta}(0)]$$

takes account that the phase velocity, i.e., the wavelength of a wave may depend on the polarization. This phenomenon is known as *birefringence*. The imaginary part of the diagonal elements

$$\mathrm{Im}(\mathcal{N}_{\eta\eta}) = \frac{2\pi}{k^2} N \mathrm{Im}[f_{\eta\eta}(0)]$$

takes account of the *dichroism*, i.e., of the polarization-dependent absorption by the medium. In particular, it is an easy matter to realize that the absorption coefficient for the propagation through the dispersion of a plane wave polarized along $\hat{\boldsymbol{u}}_\eta$ is

$$\gamma_\eta = 2k \mathrm{Im}(\mathcal{N}_{\eta\eta}) \; ,$$

i.e., by the optical theorem

$$\gamma_\eta = N \sigma_{\mathrm{T}\eta} \; ,$$

where we attached the subscript η to the cross section to recall that, in general, it depends on the polarization of the incident wave.

2.7 Kinematics of a Scattering Process

The planes of reference of the incident and of the scattered field may have no specific relation to each other. Nevertheless, when describing the kinematics of a process of scattering, it is convenient to choose a single plane of reference, *the plane of scattering*, defined by the wavevectors of the incident and of the scattered wave. We can, alternatively, fix a reference frame in the laboratory and choose as planes of reference two possibly different *meridional planes* defined by the z axis and the wavevector of the incident and of the scattered wave, respectively. These alternatives will now be discussed categorically.

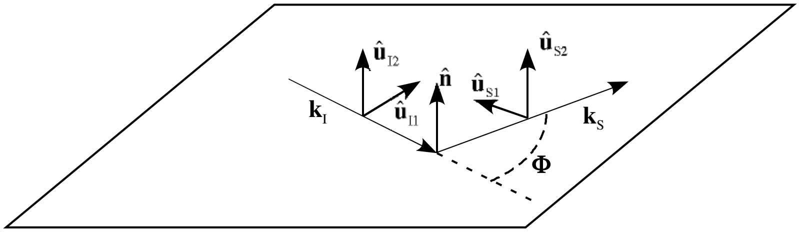

Fig. 2.3. The scattering plane. The pairs of basis vectors $\hat{\boldsymbol{u}}_{\mathrm{I}\eta}$ and $\hat{\boldsymbol{u}}_{\mathrm{S}\eta}$ for the description of the state of polarization are shown

2.7.1 Plane of Scattering

The kinematics of the scattering process is uniquely determined by the unit vectors $\hat{\boldsymbol{k}}_{\mathrm{I}}$ and $\hat{\boldsymbol{k}}_{\mathrm{S}}$ that define the directions of propagation of the incident and of the scattered wave, respectively. By introducing a system of rectangular coordinates, say Σ, with the particle at the origin and axes characterized by the unit vectors $\hat{\boldsymbol{e}}_x$, $\hat{\boldsymbol{e}}_y$, and $\hat{\boldsymbol{e}}_z$, the unit vectors $\hat{\boldsymbol{k}}_{\mathrm{I}}$ and $\hat{\boldsymbol{k}}_{\mathrm{S}}$ can be defined by the polar angles $\vartheta_{\mathrm{I}}, \varphi_{\mathrm{I}}$, and $\vartheta_{\mathrm{S}}, \varphi_{\mathrm{S}}$, respectively, i.e., by the direction cosines

$$\begin{aligned}\hat{\boldsymbol{k}}_{\mathrm{I}} &\equiv (\alpha_{\mathrm{I}} = \sin\vartheta_{\mathrm{I}}\cos\varphi_{\mathrm{I}},\ \beta_{\mathrm{I}} = \sin\vartheta_{\mathrm{I}}\sin\varphi_{\mathrm{I}},\ \gamma_{\mathrm{I}} = \cos\vartheta_{\mathrm{I}})\ ,\\ \hat{\boldsymbol{k}}_{\mathrm{S}} &\equiv (\alpha_{\mathrm{S}} = \sin\vartheta_{\mathrm{S}}\cos\varphi_{\mathrm{S}},\ \beta_{\mathrm{S}} = \sin\vartheta_{\mathrm{S}}\sin\varphi_{\mathrm{S}},\ \gamma_{\mathrm{S}} = \cos\vartheta_{\mathrm{S}})\ ,\end{aligned} \tag{2.32}$$

and the *scattering angle*, i.e., the angle Φ between $\hat{\boldsymbol{k}}_{\mathrm{I}}$ and $\hat{\boldsymbol{k}}_{\mathrm{S}}$ is given by

$$\begin{aligned}\cos\Phi &= \hat{\boldsymbol{k}}_{\mathrm{I}}\cdot\hat{\boldsymbol{k}}_{\mathrm{S}} = \alpha_{\mathrm{I}}\alpha_{\mathrm{S}} + \beta_{\mathrm{I}}\beta_{\mathrm{S}} + \gamma_{\mathrm{I}}\gamma_{\mathrm{S}}\\ &= \cos\vartheta_{\mathrm{I}}\cos\vartheta_{\mathrm{S}} + \sin\vartheta_{\mathrm{I}}\sin\vartheta_{\mathrm{S}}\cos(\varphi_{\mathrm{S}} - \varphi_{\mathrm{I}})\ .\end{aligned}$$

The plane defined by $\hat{\boldsymbol{k}}_{\mathrm{I}}$ and $\hat{\boldsymbol{k}}_{\mathrm{S}}$ (see Fig. 2.3) is the scattering plane, whose equation is

$$\hat{\boldsymbol{n}}\cdot\boldsymbol{r} = 0\ , \tag{2.33}$$

where the unit normal $\hat{\boldsymbol{n}}$ is defined by

$$\hat{\boldsymbol{n}} = \hat{\boldsymbol{k}}_{\mathrm{I}}\times\hat{\boldsymbol{k}}_{\mathrm{S}}/\sin\Phi\ .$$

In view of its definition the plane of scattering yields a good frame of reference for the description of the polarization both of the incident and of the scattered field in the far zone. Both fields are, indeed, transverse to the respective propagation vectors, and can therefore be decomposed into their components parallel and perpendicular to the plane of scattering. To this end we define two pairs of real unit vectors $\hat{\boldsymbol{u}}_{\mathrm{I}\eta}$ and $\hat{\boldsymbol{u}}_{\mathrm{S}\eta}$ ($\eta = 1, 2$) so oriented that

$$\hat{\boldsymbol{u}}_{\mathrm{I}1}\times\hat{\boldsymbol{u}}_{\mathrm{I}2} = \hat{\boldsymbol{k}}_{\mathrm{I}}\ ,\quad \hat{\boldsymbol{u}}_{\mathrm{S}1}\times\hat{\boldsymbol{u}}_{\mathrm{S}2} = \hat{\boldsymbol{k}}_{\mathrm{S}}\ ,$$

with $\hat{\boldsymbol{u}}_{\mathrm{I}1}\equiv\hat{\boldsymbol{p}}_{\mathrm{I}}$ and $\hat{\boldsymbol{u}}_{\mathrm{S}1}\equiv\hat{\boldsymbol{p}}_{\mathrm{S}}$ lying in the plane of scattering, and $\hat{\boldsymbol{u}}_{\mathrm{I}2}\equiv\hat{\boldsymbol{u}}_{\mathrm{S}2}\equiv\hat{\boldsymbol{n}}$.

The above definition of the plane of scattering holds true for any value of Φ except for forward scattering, $\Phi = 0°$, and backscattering, $\Phi = 180°$. In these cases, any plane through the common direction of $\hat{\boldsymbol{k}}_{\mathrm{I}}$ and $\hat{\boldsymbol{k}}_{\mathrm{S}}$ can be chosen as the plane of scattering. However, once one such plane has been chosen, a single pair of unit vectors, e.g. $\hat{\boldsymbol{u}}_{\mathrm{I}\eta}$, can be used to analyze the polarization both of the incident and of the scattered field.

2.7.2 The Meridional Plane

The discussion in the preceding sections has shown that the plane of scattering gives a complete description of the kinematics of the scattering process. Nevertheless, not always such a description is the most useful. In fact, the scattering process is often observed by keeping mutually independent the reference planes of the incident and of the scattered wave.

We associate to the cartesian system of axes Σ of Sect. 2.7.1 a system of polar coordinates, ϑ, φ. Then, both the direction of incidence, $\hat{\boldsymbol{k}}_{\mathrm{I}}$, and of scattering, $\hat{\boldsymbol{k}}_{\mathrm{S}}$, can be characterized by the polar angles ϑ_{I}, φ_{I} and ϑ_{S}, φ_{S}, respectively, or by the direction cosines given by (2.32). As the incident field is orthogonal to $\hat{\boldsymbol{k}}_{\mathrm{I}}$ it is convenient to take its components with respect to the couple of unit vectors $\hat{\boldsymbol{\vartheta}}_{\mathrm{I}}$ and $\hat{\boldsymbol{\varphi}}_{\mathrm{I}}$ along the meridians and the parallels of the polar coordinate system. Analogously, we take the components of the scattered field with respect to the unit vectors $\hat{\boldsymbol{\vartheta}}_{\mathrm{S}}$ and $\hat{\boldsymbol{\varphi}}_{\mathrm{S}}$. We will refer to this representation as the *representation in the meridional plane.* Thus, we have for the incident field the alternative description in terms of the triplet $\hat{\boldsymbol{u}}_{\mathrm{I}1} = \hat{\boldsymbol{\vartheta}}_{\mathrm{I}}$, $\hat{\boldsymbol{u}}_{\mathrm{I}2} = \hat{\boldsymbol{\varphi}}_{\mathrm{I}}$ and $\hat{\boldsymbol{k}}_{\mathrm{I}} = \hat{\boldsymbol{\vartheta}}_{\mathrm{I}} \times \hat{\boldsymbol{\varphi}}_{\mathrm{I}}$. An analogous description holds for the scattered field. Triplets of this kind are also known as *polar basis vectors.*

The trasformation of the representation of the electric field of the incident wave from the meridional plane to the plane of scattering can be performed as follows:

$$\begin{aligned} E_{\mathrm{I}p} =& E_{\mathrm{I}\vartheta} s_{11} + E_{\mathrm{I}\varphi} s_{21} \ , \\ E_{\mathrm{I}n} =& E_{\mathrm{I}\vartheta} s_{12} + E_{\mathrm{I}\varphi} s_{22} \ , \end{aligned}$$

with inverse transformation

$$\begin{aligned} E_{\mathrm{I}\vartheta} =& E_{\mathrm{I}p} s_{11} + E_{\mathrm{I}n} s_{12} \ , \\ E_{\mathrm{I}\varphi} =& E_{\mathrm{I}p} s_{21} + E_{\mathrm{I}n} s_{22} \ , \end{aligned}$$

where we define

$$\begin{aligned} s_{11} &= \hat{\boldsymbol{\vartheta}}_{\mathrm{I}} \cdot \hat{\boldsymbol{p}}_{\mathrm{I}}, \qquad & s_{12} &= \hat{\boldsymbol{\vartheta}}_{\mathrm{I}} \cdot \hat{\boldsymbol{n}}, \\ s_{21} &= \hat{\boldsymbol{\varphi}}_{\mathrm{I}} \cdot \hat{\boldsymbol{p}}_{\mathrm{I}}, \qquad & s_{22} &= \hat{\boldsymbol{\varphi}}_{\mathrm{I}} \cdot \hat{\boldsymbol{n}} \ . \end{aligned} \tag{2.34}$$

By denoting with γ the angle between $\hat{\boldsymbol{\vartheta}}$ and $\hat{\boldsymbol{p}}$ we have

$$\tan\gamma = s_{21}/s_{11},$$

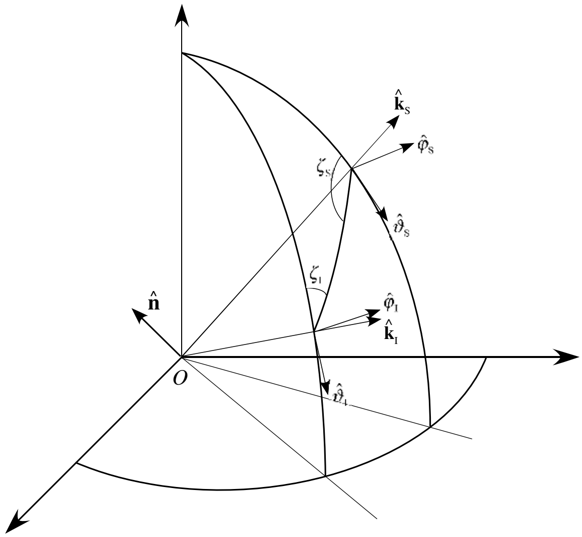

Fig. 2.4. Sketch of the unit vectors for the description of the polarization of the incident and scattered field with respect to the meridional planes. The plane of scattering is individuated by the origin O, $\hat{\boldsymbol{k}}_{\mathrm{I}}$, and $\hat{\boldsymbol{k}}_{\mathrm{S}}$; $\hat{\boldsymbol{n}}$ is the normal to the plane of scattering

and

$$\begin{aligned} s_{11} &= s_{22} = \cos\gamma, \\ s_{21} &= \cos(\gamma - \pi/2), \\ s_{12} &= -s_{21} = \cos(\gamma + \pi/2) \ . \end{aligned}$$

The relations above are a particular case of the relations that are necessary to transform the representation of the field and related quantities when the plane of reference is rotated through an angle γ around $\hat{\boldsymbol{k}}$. If the original plane is characterized by the pair $\hat{\boldsymbol{p}}$, $\hat{\boldsymbol{n}}$, and the new plane by $\hat{\boldsymbol{p}}'$, $\hat{\boldsymbol{n}}'$, we have

$$\begin{aligned} \cos\gamma &= s_{11} = \hat{\boldsymbol{p}} \cdot \hat{\boldsymbol{p}}', \\ \sin\gamma &= s_{21} = -s_{12} = \hat{\boldsymbol{n}} \cdot \hat{\boldsymbol{p}}' \ , \end{aligned}$$

so that

$$\begin{aligned} E_{p'} =& E_p s_{11} + E_n s_{21} \ , \\ E_{n'} =& E_p s_{12} + E_n s_{22} \ . \end{aligned}$$

In particular, we will need the angles that the plane of scattering forms with the meridional planes of $\hat{\boldsymbol{k}}_{\mathrm{I}}$ and $\hat{\boldsymbol{k}}_{\mathrm{S}}$. Denoting these angles with ζ_{I} and ζ_{S}, respectively, a little geometry yields

$$\cos\zeta_{\mathrm{I}} = \frac{\cos\vartheta_{\mathrm{S}} - \cos\vartheta_{\mathrm{I}}\cos\Phi}{\sin\vartheta_{\mathrm{I}}\sin\Phi} ,$$
$$\cos\zeta_{\mathrm{S}} = \frac{\cos\vartheta_{\mathrm{I}} - \cos\vartheta_{\mathrm{S}}\cos\Phi}{\sin\vartheta_{\mathrm{S}}\sin\Phi} . \tag{2.35}$$

2.8 Stokes Parameters

In Sect. 2.6.1 we showed that the most general monochromatic plane wave is fully characterized by the amplitudes a_1 and a_2 and by the phase difference $\delta = \alpha_2 - \alpha_1$. The discussion of Sect. 2.6.2 stressed that similar quantities also characterize the scattered wave. The measurement of these quantities cannot, however, be performed directly, as optical measurements allow for the determination of *intensities*. Nevertheless, there exist physical procedures to measure a set of parameters, the so-called *Stokes parameters*, that have the dimension of intensities and yield the maximum information on the state of any optical wave. Since there is no unanimity either in the notation or in the definition of these parameters we stick to the choice of Mishchenko, Hovenier, and Travis [21].

If a linear basis is used, the Stokes parameters are defined by the equations

$$I = |E_1|^2 + |E_2|^2 = a_1^2 + a_2^2 , \tag{2.36a}$$
$$Q = |E_1|^2 - |E_2|^2 = a_1^2 - a_2^2 , \tag{2.36b}$$
$$U = -2\mathrm{Re}(E_1 E_2^*) = -2a_1 a_2 \cos\delta , \tag{2.36c}$$
$$V = 2\mathrm{Im}(E_1 E_2^*) = -2a_1 a_2 \sin\delta , \tag{2.36d}$$

from which it is an easy matter to get the relevant quantities

$$a_1^2 = \tfrac{1}{2}(I + Q) , \tag{2.37a}$$
$$a_2^2 = \tfrac{1}{2}(I - Q) , \tag{2.37b}$$
$$\tan\delta = V/U . \tag{2.37c}$$

Sometimes it may be convenient to use, instead of I and Q, the modified parameters

$$I_1 = |\hat{\boldsymbol{u}}_1 \cdot \boldsymbol{E}|^2 = a_1^2 ,$$
$$I_2 = |\hat{\boldsymbol{u}}_2 \cdot \boldsymbol{E}|^2 = a_2^2 ,$$

that give the intensity of the component parallel and perpendicular to the plane of reference and are related to I and Q by (2.37a) and (2.37b). Note that we can also write

$$
\begin{aligned}
&I = a_0^2 \;, \quad Q = a_0^2 \cos 2\beta \cos 2\chi \;, \\
&I_1 = \tfrac{1}{2} a_0^2 (1 + \cos 2\beta \cos 2\chi) \;, \\
&I_2 = \tfrac{1}{2} a_0^2 (1 - \cos 2\beta \cos 2\chi) \;, \\
&U = -a_0^2 \cos 2\beta \sin 2\chi, \quad V = -a_0^2 \sin 2\beta \;,
\end{aligned}
$$

so that the geometry of any monochromatic optical wave is fully defined.

When using the circular basis is preferable, the Stokes parameters can still be calculated through (2.36), provided a_η and δ are those appropriate for the $\hat{\boldsymbol{c}}_\eta$ basis. A more usual definition to which we do not stick, however, scrambles the newly defined parameters in such a way that

$$
I_c = I \;, V_c = Q \;, Q_c = U \;, U_c = V \;.
$$

We stress that whatever representation is chosen the Stokes parameters depend on the choice of the plane of reference. However, they can be easily transformed under rotation of the plane of reference around $\hat{\boldsymbol{k}}$ using the considerations we made at the end of Sect. 2.7.2. The resulting transformation for the Stokes parameters in the linear basis turns out to be

$$
\begin{pmatrix} I' \\ Q' \\ U' \\ V' \end{pmatrix} = \mathbf{L}(\gamma) \begin{pmatrix} I \\ Q \\ U \\ V \end{pmatrix} \;,
$$

where the primed quantities refer to the rotated plane of reference and

$$
\mathbf{L}(\gamma) = \begin{pmatrix} 1 & 0 & 0 & 0 \\ 0 & \cos 2\gamma & -\sin 2\gamma & 0 \\ 0 & \sin 2\gamma & \cos 2\gamma & 0 \\ 0 & 0 & 0 & 1 \end{pmatrix} \;. \tag{2.38}
$$

Whatever the basis, the Stokes parameters of a monochromatic wave satisfy the relation

$$
I^2 = Q^2 + U^2 + V^2 \;,
$$

so that for a single wave they are never independent. It should be borne in mind, however, that actual optical beams, even when monochromatic to a high degree, still contain a large number of frequencies, i.e., they are quasi-monochromatic. As a result, the Stokes parameters of an actual optical beam are, in fact, an average over wavepackets within which the polarization may change fairly fast in an unpredictable manner. Actually, an optical beam can be interpreted as the propagation of an assembly of photons, whose polarization and time of arrival on the detecting instrument are predictable only within the laws of quantum statistics. Anyway, measured Stokes parameters of actual optical beams do not satisfy the relation reported above, but in general

$$I^2 \geq Q^2 + U^2 + V^2 \; . \tag{2.39}$$

A beam for which the equality sign holds is said to be fully polarized because the equality implies that all the component waves have the same value of χ and β. In the opposite case in which $Q = U = V = 0$, the beam is completely incoherent: it is natural light. According to these considerations it is useful to define the degree of polarization of an optical beam as

$$P = (Q^2 + U^2 + V^2)^{1/2}/I \; . \tag{2.40}$$

We can give a complete characterization of any beam with Stokes parameters I, Q, U, and V by considering separately its unpolarized (natural) part and its (possibly) polarized part. In practice,

$$I = I_\mathrm{N} + I_\mathrm{P} \; , \tag{2.41}$$

where I_N is the intensity of the unpolarized part and I_P the intensity of the fully polarized part. The Stokes parameters of the unpolarized part are

$$I_\mathrm{N} = I - \sqrt{Q^2 + U^2 + V^2}, \quad Q_\mathrm{N} = 0, \quad U_\mathrm{N} = 0, \quad V_\mathrm{N} = 0 \; ,$$

whereas those of the fully polarized part are

$$I_\mathrm{P} = \sqrt{Q^2 + U^2 + V^2}, \quad Q_\mathrm{P} = Q, \quad U_\mathrm{P} = U, \quad V_\mathrm{P} = V \; .$$

We can also take into account the parts of the polarized beam parallel and perpendicular to the plane of reference through the modified Stokes parameters I_P1 and I_P2.

2.8.1 Phase Matrix, Scattering Matrix and Extinction Matrix

As the components of the scattered field are related to those of the incident field by the scattering amplitude matrix, it is possible to define a matrix that transforms the Stokes parameters of the incident field into those of the scattered field. To this end we define the Stokes vector $\underline{\mathcal{I}}$ as the one-column vector whose components are the Stokes parameters either of the incident or of the scattered wave. Thus,

$$\underline{\mathcal{I}}_\mathrm{S} = \frac{1}{r^2} \underline{\mathcal{M}} \, \underline{\mathcal{I}}_\mathrm{I} \; ,$$

where the subscripts I and S refer to the incident and to the scattered wave, respectively, and $\underline{\mathcal{M}}$ is the so-called *Müller transformation matrix*. Actually, the term Müller matrix applies to any 4×4 matrix that effect the transformation of the Stokes parameters of an optical beam by any instrument. From a more theoretical point of view we define two kinds of transformation matrix, the *phase matrix* $\underline{\mathcal{Z}}$ and the *scattering matrix* $\underline{\mathcal{F}}$. These two matrices transform the Stokes parameters when referred to the meridional planes and to the scatterig plane, respectively. The elements of $\underline{\mathcal{F}}$ are formally identical to those of the phase matrix which are given by

$$\begin{aligned}
Z_{11} &= \tfrac{1}{2}\left(|f_{11}|^2 + |f_{12}|^2 + |f_{21}|^2 + |f_{22}|^2\right) ,\\
Z_{12} &= \tfrac{1}{2}\left(|f_{11}|^2 - |f_{12}|^2 + |f_{21}|^2 - |f_{22}|^2\right) ,\\
Z_{13} &= -\mathrm{Re}\left(f_{11}f_{12}^* + f_{22}f_{21}^*\right) ,\\
Z_{14} &= -\mathrm{Im}\left(f_{11}f_{12}^* - f_{22}f_{21}^*\right) ,\\
Z_{21} &= \tfrac{1}{2}\left(|f_{11}|^2 + |f_{12}|^2 - |f_{21}|^2 - |f_{22}|^2\right) ,\\
Z_{22} &= \tfrac{1}{2}\left(|f_{11}|^2 - |f_{12}|^2 - |f_{21}|^2 + |f_{22}|^2\right) ,\\
Z_{23} &= -\mathrm{Re}\left(f_{11}f_{12}^* - f_{22}f_{21}^*\right) ,\\
Z_{24} &= -\mathrm{Im}\left(f_{11}f_{12}^* + f_{22}f_{21}^*\right) ,\\
Z_{31} &= -\mathrm{Re}\left(f_{11}f_{21}^* + f_{22}f_{12}^*\right) ,\\
Z_{32} &= -\mathrm{Re}\left(f_{11}f_{21}^* - f_{22}f_{12}^*\right) ,\\
Z_{33} &= \mathrm{Re}\left(f_{11}f_{22}^* + f_{12}f_{21}^*\right) ,\\
Z_{34} &= \mathrm{Im}\left(f_{11}f_{22}^* + f_{21}f_{12}^*\right) ,\\
Z_{41} &= -\mathrm{Im}\left(f_{21}f_{11}^* + f_{22}f_{12}^*\right) ,\\
Z_{42} &= -\mathrm{Im}\left(f_{21}f_{11}^* - f_{22}f_{12}^*\right) ,\\
Z_{43} &= \mathrm{Im}\left(f_{22}f_{11}^* - f_{12}f_{21}^*\right) ,\\
Z_{44} &= \mathrm{Re}\left(f_{22}f_{11}^* - f_{12}f_{21}^*\right) .
\end{aligned} \tag{2.42}$$

Let us insist that the equality of the elements of $\underline{\mathcal{F}}$ with those of $\underline{\mathcal{Z}}$ is purely formal because these matrices transform the Stokes parameters that are referred to different planes of reference. Actually $\underline{\mathcal{F}}$ and $\underline{\mathcal{Z}}$ can easily be tranformed into each other through the equation

$$\underline{\mathcal{Z}} = \mathrm{L}(-\zeta_{\mathrm{S}})\underline{\mathcal{F}}\mathrm{L}(\pi - \zeta_{\mathrm{I}}) , \tag{2.43}$$

where the transformation matrix L is given by (2.38) and its arguments are given by (2.35).

It has been shown by Hovenier and van der Mee [24–26] that the elements of the scattering matrix must satisfy a number of relations that may help the observer to check the consistency of the recorded data. In turn, van de Hulst [5] studied the structure of $\underline{\mathcal{F}}$ for dispersions of particles of various geometries and in various space distributions. Bottiger [27] has discussed how, once the plane of scattering has been chosen, the scattering matrix gives information on the shape of the particles.

In Sects. 2.2 and 2.3 we stated that the differential scattering cross section and the extinction cross section of a nonspherical particle depend on the orientation of the latter with respect to the incident field. This statement implies that the cross sections depend on the polarization of the incident field. In fact, by recalling the definition of the differential scattering cross Sect. 2.7, on account of (2.28), (2.29), (2.36), and (2.42), we have

$$\frac{\mathrm{d}\sigma_{\mathrm{S}}}{\mathrm{d}\Omega} = \frac{1}{I_{\mathrm{I}}}\left(Z_{11}I_{\mathrm{I}} + Z_{12}Q_{\mathrm{I}} + Z_{13}U_{\mathrm{I}} + Z_{14}V_{\mathrm{I}}\right) , \tag{2.44}$$

and by (2.8) we obtain σ_{S}. A similar expression for the extinction cross section requires introducing the so-called extinction matrix $\underline{\mathcal{K}}$ with elements

$$
\begin{aligned}
&K_{jj} = c_{\mathrm{T}}\mathrm{Im}\big(f_{11} + f_{22}\big)\,, \quad (j = 1, \ldots, 4)\,,\\
&K_{12} = K_{21} = c_{\mathrm{T}}\mathrm{Im}\big(f_{11} - f_{22}\big)\,,\\
&K_{13} = K_{31} = -c_{\mathrm{T}}\mathrm{Im}\big(f_{12} + f_{21}\big)\,,\\
&K_{14} = K_{41} = c_{\mathrm{T}}\mathrm{Re}\big(f_{21} - f_{12}\big)\,,\\
&K_{23} = -K_{32} = c_{\mathrm{T}}\mathrm{Im}\big(f_{21} - f_{12}\big)\,,\\
&K_{24} = -K_{42} = -c_{\mathrm{T}}\mathrm{Re}\big(f_{12} + f_{21}\big)\,,\\
&K_{34} = -K_{43} = c_{\mathrm{T}}\mathrm{Re}\big(f_{22} - f_{11}\big)\,,
\end{aligned}
\tag{2.45}
$$

where $c_{\mathrm{T}} = 2\pi/k$ and the elements $f_{\eta'\eta}$ are calculated for $\hat{\boldsymbol{k}}_{\mathrm{S}} = \hat{\boldsymbol{k}}_{\mathrm{I}}$, i.e. for forward scattering. Then, according to (2.13), the extinction cross section results

$$\sigma_{\mathrm{T}} = \frac{1}{I_{\mathrm{I}}}\big(K_{11}I_{\mathrm{I}} + K_{12}Q_{\mathrm{I}} + K_{13}U_{\mathrm{I}} + K_{14}V_{\mathrm{I}}\big)\,. \tag{2.46}$$

2.9 Polarization of Waves of General Form

In the preceding sections we dealt essentially with monochromatic homogeneous plane waves or with scattered waves in the far field zone. The distinctive feature of both these kind of waves is that at any point in space the plane in which the field varies as a function of time is orthogonal to the direction of $\hat{\boldsymbol{k}}_{\mathrm{I}}$ or $\hat{\boldsymbol{k}}_{\mathrm{S}}$, which coincide with the direction of propagation of the incident and of the scattered electromagnetic energy, respectively. This is in not true for waves, even for monochromatic waves, of general form, such as the scattered waves in the near zone or the nonhomogeneous plane waves. Actually, the direction of propagation of the electromagnetic energy is given by the real part of the complex Poynting vector $\boldsymbol{S}$ and we will show that, in general, the plane in which the field of a wave of general form varies as a function of time, is not orthogonal to the direction of propagation. The polarization of waves of general form, therefore, deserves a closer examination, as for such waves the usual description in terms of the Stokes parameters does not apply.

We start from the representation of the field given in (1.2) and recall that its time-independent part $\boldsymbol{E}$ is, in general, complex. Therefore, according to Born and Wolf [28], we define a pair of real vectors $\boldsymbol{p}(\boldsymbol{r})$ and $\boldsymbol{q}(\boldsymbol{r})$ such that

$$\boldsymbol{E}(\boldsymbol{r}) = \boldsymbol{p}(\boldsymbol{r}) + \mathrm{i}\boldsymbol{q}(\boldsymbol{r}),$$

and write

$$\bar{\boldsymbol{E}}(\boldsymbol{r}, t) = \mathrm{Re}\Big\{\big[\boldsymbol{p}(\boldsymbol{r}) + \mathrm{i}\boldsymbol{q}(\boldsymbol{r})\big]\exp(-\mathrm{i}\omega t)\Big\}. \tag{2.47}$$

At any given point, say $\boldsymbol{r}_0$, the vectors $\boldsymbol{p}$ and $\boldsymbol{q}$ define a plane on which $\bar{\boldsymbol{E}}$ varies as a function of time. We first remark that, since $\bar{\boldsymbol{E}}(\boldsymbol{r}_0, t)$ is periodic, its tip should describe a closed curve on this plane. In order to show that this curve is an ellipse, let us define a pair of real vectors $\boldsymbol{a}$ and $\boldsymbol{b}$ such that

$$\boldsymbol{p} + \mathrm{i}\boldsymbol{q} = \big(\boldsymbol{a} + \mathrm{i}\boldsymbol{b}\big)\exp(\mathrm{i}\gamma),$$

where γ is a real phase, that can be chosen so that $\boldsymbol{a}$ and $\boldsymbol{b}$ are mutually orthogonal. In fact, since

$$\begin{aligned}\boldsymbol{a} &= \boldsymbol{p}\cos\gamma + \boldsymbol{q}\sin\gamma,\\ \boldsymbol{b} &= -\boldsymbol{p}\sin\gamma + \boldsymbol{q}\cos\gamma,\end{aligned}$$

the requirement of mutual orthogonality of $\boldsymbol{a}$ and $\boldsymbol{b}$,

$$\big(\boldsymbol{p}\cos\gamma + \boldsymbol{q}\sin\gamma\big)\cdot\big(-\boldsymbol{p}\sin\gamma + \boldsymbol{q}\cos\gamma\big) = 0,$$

yields

$$\tan 2\gamma = \frac{2\boldsymbol{p}\cdot\boldsymbol{q}}{\boldsymbol{p}^2 - \boldsymbol{q}^2}.$$

As a result we can write

$$\bar{\boldsymbol{E}}(\boldsymbol{r}_0, t) = \mathrm{Re}\big\{[\boldsymbol{a}(\boldsymbol{r}_0) + \mathrm{i}\boldsymbol{b}(\boldsymbol{r}_0)]\exp[-\mathrm{i}(\omega t - \gamma)]\big\}$$

and, by chosing a rectangular system of axes with origin at $\boldsymbol{r}_0$ and the x and y axes along $\boldsymbol{a}$ and $\boldsymbol{b}$, respectively, we have

$$\begin{aligned}\bar{E}_x(\boldsymbol{r}_0, t) &= a\cos(\omega t - \gamma),\\ \bar{E}_y(\boldsymbol{r}_0, t) &= b\sin(\omega t - \gamma),\end{aligned}$$

i.e.

$$\frac{\bar{E}_x^2}{a^2} + \frac{\bar{E}_y^2}{b^2} = 1.$$

This shows that any monochromatic electromagnetic wave is, in general, elliptically polarized. Of course, according to the physical conditions, the ellipse may degenerate into a circle or into a straight line. In the latter case the *area of the polarization ellipse*, whose physical dimension is that of a field intensity,

$$A = \pi ab$$

vanishes. Now, since $\boldsymbol{E}$, and of course also its complex conjugate $\boldsymbol{E}^*$, lie in the plane of the polarization ellipse, the real vector

$$\boldsymbol{V} = \mathrm{i}\boldsymbol{E}\times\boldsymbol{E}^* = \mathrm{i}(\boldsymbol{a} + \mathrm{i}\boldsymbol{b})\times(\boldsymbol{a} - \mathrm{i}\boldsymbol{b}) = 2\boldsymbol{a}\times\boldsymbol{b} \tag{2.48}$$

individuates the normal to this plane [29, 30], and, according to definition (2.48), the electric field rotates counterclockwise with respect to $\boldsymbol{V}$. In turn, the magnitude of $\boldsymbol{V}$, in view of the orthogonality of $\boldsymbol{a}$ and $\boldsymbol{b}$, is

$$|\boldsymbol{V}| = 2ab = \frac{2}{\pi}A$$

and, therefore, vanishes for linear polarization. In general, when $\boldsymbol{V} \neq 0$ we have

$$\boldsymbol{V}\times\boldsymbol{S} \neq 0,$$

i.e. $\boldsymbol{V}$ is not parallel to the direction of propagation of the wave and thus the plane of the polarization ellipse is not orthogonal to the direction of propagation. Anyway, $\boldsymbol{V}$ gives information on the sense of rotation of the field with respect to the direction of $\boldsymbol{S}$. In fact, it is reasonable to assume that this information is given by the sign of the quantity

$$V_{\mathrm{s}} = \boldsymbol{V} \cdot \boldsymbol{S}/|\boldsymbol{S}| ,$$

i.e. by the projection of $\boldsymbol{V}$ in the direction of $\boldsymbol{S}$. Of course, $\boldsymbol{V}$ and $\boldsymbol{S}$ can never become mutually orthogonal. Actually, it is an easy matter to see that $V_{\mathrm{s}} = 0$ only when $\boldsymbol{V} = 0$, i.e. for linear polarization.

2.9.1 Spectral Density Tensor

The considerations in the preceding section imply that for an electromagnetic monochromatic wave of general form the state of polarization cannot be described through the customary Stokes parameters because the field, as a function of time varies in a plane that is not orthogonal to the direction of propagation. Note, that the vectors $\boldsymbol{a}$ and $\boldsymbol{b}$ depend on $\boldsymbol{r}$, so that the state of polarization changes from point to point: only in the case of a homogeneous plane wave, the direction of the Poynting vector is constant from point to point. Then, for homogeneous plane waves, we can define a propagation vector (of the same constant direction of $\boldsymbol{S}$), to which the field, as time varies, is orthogonal and the customary Stokes parameters give a full description of the state of polarization. The Stokes parameters make sense also in the case of a spherical wave, because, as we remarked in Sect. 2.9, the direction of propagation is along the radius vector from the source, and the field is constantly orthogonal to this direction [31]. Although plane and spherical waves are the most commonly dealt with, the considerations in the preceding section are not of a pure academic interest. In fact, according to Sect. 2.1 the field scattered by an irregularly shaped particle in the near zone has just a general form and thus requires a general approach to the description of its polarization.

It is well known that all the information on the state of the field is given by the coherency dyad

$$\boldsymbol{\rho} = \boldsymbol{E}(\boldsymbol{r}) \otimes \boldsymbol{E}^{*}(\boldsymbol{r}),$$

where $\otimes$ denotes dyadic product. The representation of $\boldsymbol{\rho}$ in rectangular coordinates is known as the spectral density tensor

$$\mathrm{S_{d3}} = \begin{pmatrix} E_x E_x^* & E_x E_y^* & E_x E_z^* \\ E_y E_x^* & E_y E_y^* & E_y E_z^* \\ E_z E_x^* & E_z E_y^* & E_z E_z^* \end{pmatrix} .$$

Actually, the elements of $\mathrm{S_{d3}}$ encompass full information on the state of polarization of the field. For instance, let us consider the pseudovector associated to $\mathrm{S_{d3}}$, whose components are

$$F_i = \sum_{jk} \varepsilon_{ijk} \left(\mathrm{S}_{\mathrm{d}3}\right)_{jk},$$

where ε_{ijk} is the totally antisymmetric Ricci tensor. It is an easy matter to see that $\boldsymbol{F} = \boldsymbol{E} \times \boldsymbol{E}^* = -\mathrm{i}\boldsymbol{V}$.

In the case of a homogeneous plane wave we take advantage of the transformation properties of $\mathrm{S}_{\mathrm{d}3}$ to rotate the rectangular axes so that, e.g., the z' axis is parallel to the direction of propagation. As a consequence only the components of the field along the x' and y' axes are nonvanishing and we can recover the customary description of the polarization in terms of the Stokes parameters. Of course, from the alternative representation of $\boldsymbol{\rho}$ with respect to the meridional plane, we can recover the Stokes parameters for a spherical wave.

2.9.2 Spectral Density Stokes Parameters

Although the Stokes parameters have been already dealt with in the preceding sections, it may be useful to resume the technique by which they are introduced in the framework of the spectral density tensor. In fact, the same technique can be used to introduce generalized parameters that are appropriate for the case of waves of general form.

Let us consider a homogeneous plane wave whose spectral density tensor has been transformed to a frame of reference with the z' axis in the direction of propagation. Denoting with a prime the rotated quantities, the tensor $\mathrm{S}'_{\mathrm{d}3}$ has only vanishing elements in the third row and third column. It is then convenient to rewrite

$$\mathrm{S}'_{\mathrm{d}2} = \begin{pmatrix} E'_x E'^*_x & E'_x E'^*_y \\ E'_y E'^*_x & E'_y E'^*_y \end{pmatrix}, \tag{2.49}$$

so that the cartesian representation of $\mathrm{S}'_{\mathrm{d}3}$ appears as an actually two dimensional matrix. Now, it is well known that the most general 2×2 matrix can be expanded in terms of the two-dimensional unit matrix $\mathbf{1}_2$ and of the three Pauli spin matrices $\boldsymbol{\sigma}_i$ $(i = 1, 2, 3)$: these matrices are, indeed, the generators of the Special Unitary Group SU(2). The expansion leads to the result

$$\mathrm{S}'_{\mathrm{d}2} = \frac{1}{2} \begin{pmatrix} \mathcal{I} + \mathcal{Q} & -\mathcal{U} + \mathrm{i}\mathcal{V} \\ -\mathcal{U} - \mathrm{i}\mathcal{V} & \mathcal{I} - \mathcal{Q} \end{pmatrix}, \tag{2.50}$$

where

$$\begin{aligned}
\mathcal{I} &= E'_x E'^*_x + E'_y E'^*_y, \\
\mathcal{Q} &= E'_x E'^*_x - E'_y E'^*_y, \\
\mathcal{U} &= -\left(E'_x E'^*_y + E'_y E'^*_x\right), \\
\mathcal{V} &= -\mathrm{i}\left(E'_x E'^*_y - E'_y E'^*_x\right)
\end{aligned}$$

are the *spectral density Stokes parameters* [4, 28]. The preceding definitions can be cast into a more familiar form by remarking that, although the z' axis should lie along the direction of propagation, the direction of the x' and y' axes, except for the mutual orthogonality, is arbitrary. Therefore by chosing the $z'x'$ plane as a plane of reference one gets

$$\begin{aligned}
\mathcal{I} &= E'_l E'^*_l + E'_r E'^*_r\,,\\
\mathcal{Q} &= E'_l E'^*_l - E'_r E'^*_r\,,\\
\mathcal{U} &= -\big(E'_l E'^*_r + E'_r E'^*_l\big),\\
\mathcal{V} &= -\mathrm{i}\big(E'_l E'^*_r - E'_r E'^*_l\big)\,.
\end{aligned}$$

Since the determinant of $\mathrm{S}'_{\mathrm{d}2}$, [see (2.49)], vanishes, the relation holds

$$\mathcal{Q}^2 + \mathcal{U}^2 + \mathcal{V}^2 = \mathcal{I}^2, \tag{2.51}$$

i.e., we recover the result that a purely monochromatic plane wave is fully polarized. Nevertheless, we already stressed that the optical beams that occur in practice, even when monochromatic to a high degree, are always wavepackets that include many frequencies in a narrow band centered on the nominal frequency ω_0. In this respect, let us stress that $\boldsymbol{E}$ depends on frequency so that also the spectral density Stokes parameters are frequency dependent. In fact, a wavepacket is characterized by a spectral tensor of the form

$$\mathrm{S}(\omega_0, \Delta\omega) = \int_{\omega_0-\Delta\omega/2}^{\omega_0+\Delta\omega/2} \mathrm{S}_{\mathrm{d}2}(\omega)\,\mathrm{d}\omega.$$

The corresponding Stokes parameters I, Q, U, V, instead of (2.51), satisfy the relation (2.39) so that one can define the degree of polarization of the packet according to (2.40).

Let us now go to see what is the analogous of the above quantities for a wave of general form. The most general 3×3 matrix can be expanded in terms of the unit matrix $\mathbf{1}_3$ and of the eight Gell-Mann matrices $\boldsymbol{\lambda}_i$ $(i = 1,\ldots,8)$ that are the generators of the group SU(3) [32]. Then, the expansion of the spectral density tensor reads

$$\begin{aligned}
\mathrm{S}_{\mathrm{d}3} &= \frac{1}{3}\Lambda_0\mathbf{1}_3 + \frac{1}{2}\sum_{i=1}^{8}\Lambda_i\boldsymbol{\lambda}_i\\
&= \begin{pmatrix}
\frac{1}{3}\Lambda_0 + \frac{1}{2}\Lambda_3 + \frac{1}{2\sqrt{3}}\Lambda_8 & -\frac{1}{2}\Lambda_1 + \mathrm{i}\frac{1}{2}\Lambda_2 & -\frac{1}{2}\Lambda_4 - \mathrm{i}\frac{1}{2}\Lambda_5\\
-\frac{1}{2}\Lambda_1 - \mathrm{i}\frac{1}{2}\Lambda_2 & \frac{1}{3}\Lambda_0 - \frac{1}{2}\Lambda_3 + \frac{1}{2\sqrt{3}}\Lambda_8 & \frac{1}{2}\Lambda_6 - \mathrm{i}\frac{1}{2}\Lambda_7\\
-\frac{1}{2}\Lambda_4 + \mathrm{i}\frac{1}{2}\Lambda_5 & \frac{1}{2}\Lambda_6 + \mathrm{i}\frac{1}{2}\Lambda_7 & \frac{1}{3}\Lambda_0 - \frac{1}{\sqrt{3}}\Lambda_8
\end{pmatrix}.
\end{aligned}$$

The expansion coefficients Λ_i, $(i = 0,\ldots,8)$ can be taken as the analogous of the spectral density Stokes parameters for a monochromatic wave of general form. In fact, for the case of a plane wave that propagates along the z axis, $\mathrm{S}_{\mathrm{d}3}$ reduces to the form (2.50). Furthermore, the trace of both $\mathrm{S}_{\mathrm{d}3}$ and $\mathrm{S}_{\mathrm{d}2}$, give the intensity of the wave. Therefore, one can assume that the degree of polarization of a quasimonochromatic wavepacket of general form is given by

$$P^2 = \frac{1}{3} \frac{\sum_{i=1}^{8} \Lambda_i^2}{\Lambda_0^2}, \tag{2.52}$$

as suggested originally by Samson [33] and by Barakat [34, 35]. The explicit expression of the parameters Λ_i as a function of the cartesian components of the field is

$$\begin{aligned}
\Lambda_0 &= E_x E_x^* + E_y E_y^* + E_z E_z^*, \\
\Lambda_1 &= -\left(E_x E_y^* + E_y E_x^*\right), \\
\Lambda_2 &= -\mathrm{i}\left(E_x E_y^* - E_y E_x^*\right), \\
\Lambda_3 &= E_x E_x^* - E_y E_y^*, \\
\Lambda_4 &= -\left(E_z E_x^* + E_x E_z^*\right), \\
\Lambda_5 &= -\mathrm{i}\left(E_z E_x^* - E_x E_z^*\right), \\
\Lambda_6 &= E_z E_y^* + E_y E_z^*, \\
\Lambda_7 &= \mathrm{i}\left(E_y E_z^* - E_z E_y^*\right), \\
\Lambda_8 &= \tfrac{1}{\sqrt{3}}\left(E_x E_x^* + E_y E_y^* - 2E_z E_z^*\right).
\end{aligned}$$

As an example of the information that can be gained from the knowlwdge of the generalized Stokes parameters, consider that the vector $\boldsymbol{V}$, that gives information on the polarization ellipse, turns out to be

$$\boldsymbol{V} = (\Lambda_7 \hat{\mathbf{e}}_x - \Lambda_5 \hat{\mathbf{e}}_y - \Lambda_2 \hat{\mathbf{e}}_z).$$

Furthermore, Setälä et al. [36] exploited the generalized Stokes parameters, and in particular Eq. (2.52), to describe the degree of polarization of the light emitted by a heated surface in the near zone. We ourselves used the vector $\boldsymbol{V}$ to study the polarization of the field inside model interstellar dust grains [37, 38].

3 Radiation Force, Radiation Torque and Thermal Emission

Besides scattering and absorption, that occur as a result of the interaction of the radiation field with particles, the interaction also yields mechanical and thermal effects that may be important in determining the behavior of the particles. This Chapter is just devoted to a discussion of these effects.

3.1 Conservation Laws

The interaction of electromagnetic radiation with particles is governed by conservation laws. Strictly speaking, one can state that the conservation of energy, of linear momentum and of angular momentum holds true in the interaction of the electromagnetic field with a system of currents and charges contained within a volume V bounded by a surface S. Nevertheless, matter is ultimately composed by (possibly moving) charges so that, on a macroscopic scale, the conservation laws hold true for the combined system of field and particles, even when the latter bear no net charge.

In this chapter we stick to the notation introduced in Sect. 1.2; thus, the quantities with overbar are real functions of $\boldsymbol{r}$ and t. We also stress, that the conservation laws we are going to discuss hold true provided the dielectric properties of the macroscopic media involved are linear.

Throughout this chapter, since we assume that the medium in which the particles are embedded is the vacuum, we need to consider the fields $\bar{\boldsymbol{E}}$ and $\bar{\boldsymbol{B}}$ only.

3.1.1 Poynting Theorem

The conservation of energy is stated by the Poynting theorem which, in integral form, reads

$$\int_V \bar{\boldsymbol{\jmath}} \cdot \bar{\boldsymbol{E}} \, \mathrm{d}V = -\int_V \left(\frac{\partial w}{\partial t} + \nabla \cdot \boldsymbol{S} \right) \mathrm{d}V \, . \tag{3.1}$$

In (3.1), $\bar{\boldsymbol{\jmath}}$ is the current density associated with the motion of the charges within volume V,

$$w = \frac{1}{8\pi} \left(\bar{\boldsymbol{E}}^2 + \bar{\boldsymbol{B}}^2 \right)$$

is the energy density of the field, and

$$\boldsymbol{S} = \frac{c}{4\pi}\left(\bar{\boldsymbol{E}} \times \bar{\boldsymbol{B}}\right) \tag{3.2}$$

is the Poynting vector that represents the flux of the energy associated to the electromagnetic field.

The integral on the left hand side of (3.1) is the work done by the field on the system of charges and currents that ultimately form the particles. As a result of this work, the total energy of the particles, both thermal and mechanical, changes at a rate $\mathrm{d}E_{\mathrm{mech}}/\mathrm{d}t$. Thus, provided no particle flows across surface S that bounds volume V, we can write

$$\frac{\mathrm{d}E_{\mathrm{mech}}}{\mathrm{d}t} = \int_V \bar{\boldsymbol{\jmath}} \cdot \bar{\boldsymbol{E}}\, \mathrm{d}V \,.$$

Consequently, by defining the total field energy within V as

$$E_{\mathrm{field}} = \int_V w\, \mathrm{d}V \,,$$

and using Gauss theorem to transform the second term on the right of (3.1) into a surface integral, the Poynting theorem can be cast into the form

$$\frac{\mathrm{d}E}{\mathrm{d}t} = \frac{\mathrm{d}}{\mathrm{d}t}\left(E_{\mathrm{mech}} + E_{\mathrm{field}}\right) = -\oint_{\mathrm{S}} \hat{\boldsymbol{n}} \cdot \boldsymbol{S}\, \mathrm{d}S \,, \tag{3.3}$$

where $\hat{\boldsymbol{n}}$ is the unit outward normal to the surface S. Equation (3.3) states the conservation of energy for the combined system of fields and particles.

3.1.2 Conservation of Linear Momentum

The radiation field, besides its energy, is endowed of linear momentum, whose conservation in the interaction of the field with a particle, implies a force exerted on the latter. Actually, the force that an electromagnetic field exerts on a distribution of charges and currents is given by

$$\boldsymbol{F} = \int_V \left(\bar{\rho}\bar{\boldsymbol{E}} + \frac{1}{c}\bar{\boldsymbol{\jmath}} \times \bar{\boldsymbol{B}}\right) \mathrm{d}V \,, \tag{3.4}$$

so that we can write

$$\boldsymbol{F} = \frac{\mathrm{d}\boldsymbol{P}_{\mathrm{mech}}}{\mathrm{d}t} \,,$$

where $\boldsymbol{P}_{\mathrm{mech}}$ is the mechanical momentum of the charges. We do not go through the details that are fully expounded, e.g., by Jackson [4]; we simply recall that, by eliminating in (3.4) $\bar{\rho}$ and $\bar{\boldsymbol{\jmath}}$ by means of the Maxwell equations, one gets

$$\frac{\mathrm{d}}{\mathrm{d}t}\left(\boldsymbol{P}_{\mathrm{mech}} + \boldsymbol{P}_{\mathrm{field}}\right) = \int_V \nabla \cdot \mathsf{T}_{\mathrm{M}}\, \mathrm{d}V \,. \tag{3.5}$$

In (3.5) we define the linear momentum of the field as

$$\boldsymbol{P}_{\text{field}} = \int_V \boldsymbol{g}\, \mathrm{d}V \ ,$$

where

$$\boldsymbol{g} = \frac{1}{4\pi c}\left(\bar{\boldsymbol{E}} \times \bar{\boldsymbol{B}}\right)$$

is the momentum density. In turn, T_{M} is the Maxwell stress tensor that we write here in dyadic notation as

$$\mathsf{T}_{\mathrm{M}} = \frac{1}{4\pi}\left[\bar{\boldsymbol{E}} \otimes \bar{\boldsymbol{E}} + \bar{\boldsymbol{B}} \otimes \bar{\boldsymbol{B}} - \tfrac{1}{2}\left(\bar{\boldsymbol{E}} \cdot \bar{\boldsymbol{E}} + \bar{\boldsymbol{B}} \cdot \bar{\boldsymbol{B}}\right)\mathsf{I}\right] , \tag{3.6}$$

where $\otimes$ denotes dyadic product and I is the unit dyadic. Then, (3.5) can be cast into the form

$$\frac{\mathrm{d}}{\mathrm{d}t}\left(\boldsymbol{P}_{\text{mech}} + \boldsymbol{P}_{\text{field}}\right) = \oint_S \hat{\boldsymbol{n}} \cdot \mathsf{T}_{\mathrm{M}}\, \mathrm{d}S \ . \tag{3.7}$$

The conservation of the linear momentum stated by this equation for the combined system of field and particles plays a fundamental role in determining the dynamical behavior and the distribution of the aerosol particles and of the grains of the interstellar medium.

3.1.3 Conservation of Angular Momentum

The conservation of angular momentum for the combined system of radiation field and particles has recently found useful applications both in the manipulation of small particles under controlled laboratory conditions and in understanding the behavior of the grains of the interstellar medium, e.g., their partial alignment. In order to state this conservation law, we need to choose a frame of reference with respect to whose origin the angular momentum, both of particles and field, is evaluated. Then, using the definition of the angular momentum and the conservation law (3.7) one easily gets

$$\frac{\mathrm{d}}{\mathrm{d}t}\left(\boldsymbol{L}_{\text{mech}} + \boldsymbol{L}_{\text{field}}\right) = -\oint_{\mathrm{S}} \hat{\boldsymbol{n}} \cdot \mathbf{M}\, \mathrm{d}S \ , \tag{3.8}$$

where $\boldsymbol{L}_{\text{mech}}$ is the mechanical angular momentum of the particles,

$$\boldsymbol{L}_{\text{field}} = \int_V \boldsymbol{r} \times \boldsymbol{g}\, \mathrm{d}V$$

is the angular momentum of the field, and

$$\mathbf{M} = \mathsf{T}_{\mathrm{M}} \times \boldsymbol{r} \ .$$

The right hand side of (3.8) represents the flux of angular momentum that enters the surface S.

3.1.4 Monochromatic Fields

The conservation laws that we discussed so far hold true for general form of the electromagnetic field. In particular, they hold true for each of the monochromatic components of the Fourier transform of the field, provided the values of the dielectric function and of the magnetic permeability of the macroscopic media involved are those appropriate to the frequency under consideration. Nevertheless, no observation device is able to follow the time variations of the field at optical and infrared frequencies: at most, optical instruments are able to record time averages over several periods of the radiation. Therefore, in order to link the theory to the experiment, we rewrite the conservation laws in terms of time averages.

Since the physical fields must be real, we use for their monochromatic components the notation established in (1.2). In practice

$$\mathrm{Re}\big[\boldsymbol{E}(\boldsymbol{r})\exp(-\mathrm{i}\omega t)\big] = \tfrac{1}{2}\big[\boldsymbol{E}(\boldsymbol{r})\exp(-\mathrm{i}\omega t) + \boldsymbol{E}^*(\boldsymbol{r})\exp(\mathrm{i}\omega t)\big] ,$$

whose time average $\langle\bar{\boldsymbol{E}}(\boldsymbol{r},t)\rangle$ vanish, of course. Nevertheless, when one has to deal with dot or cross products such as

$$\bar{\boldsymbol{E}}\cdot\bar{\boldsymbol{\jmath}} = \tfrac{1}{4}\big[\boldsymbol{E}(\boldsymbol{r})\mathrm{e}^{-\mathrm{i}\omega t} + \boldsymbol{E}^*(\boldsymbol{r})\mathrm{e}^{\mathrm{i}\omega t}\big]\cdot\big[\boldsymbol{j}(\boldsymbol{r})\mathrm{e}^{-\mathrm{i}\omega t} + \boldsymbol{j}^*(\boldsymbol{r})\mathrm{e}^{\mathrm{i}\omega t}\big]$$

the time average is

$$\langle\bar{\boldsymbol{E}}\cdot\bar{\boldsymbol{\jmath}}\rangle = \tfrac{1}{2}\mathrm{Re}\big(\boldsymbol{E}\cdot\boldsymbol{j}^*\big) .$$

Hence the convention follows that the time average of dot or cross products of field quantities is given by half the real part of the product of one of the quantities with the complex conjugate of the other.

The first consequence of the above considerations is the vanishing, for monochromatic fields, of the time averages

$$\langle\frac{\mathrm{d}E_{\mathrm{field}}}{\mathrm{d}t}\rangle, \qquad \langle\frac{\mathrm{d}\boldsymbol{P}_{\mathrm{field}}}{\mathrm{d}t}\rangle, \qquad \langle\frac{\mathrm{d}\boldsymbol{L}_{\mathrm{field}}}{\mathrm{d}t}\rangle .$$

The time average of the Maxwell stress tensor (3.6) results

$$\langle\mathsf{T}_{\mathrm{M}}\rangle = \frac{1}{8\pi}\mathrm{Re}\big[\boldsymbol{E}\otimes\boldsymbol{E}^* + \boldsymbol{B}\otimes\boldsymbol{B}^* - \tfrac{1}{2}\big(\boldsymbol{E}\cdot\boldsymbol{E}^* + \boldsymbol{B}^*\cdot\boldsymbol{B}^*\big)\mathsf{I}\big] , \tag{3.9}$$

and the time average of the Poynting vector (3.2) is

$$\langle\boldsymbol{S}\rangle = \frac{c}{8\pi}\mathrm{Re}\big(\boldsymbol{E}\times\boldsymbol{B}^*\big) .$$

Therefore, as far as time averages are concerned, the Poynting theorem (3.3) reads

$$\langle\frac{\mathrm{d}E_{\mathrm{mech}}}{\mathrm{d}t}\rangle = -\oint\hat{\boldsymbol{n}}\cdot\langle\boldsymbol{S}\rangle\,\mathrm{d}S .$$

In turn, the conservation of linear momentum (3.7) reads

$$\langle \frac{\mathrm{d}\boldsymbol{P}_{\mathrm{mech}}}{\mathrm{d}t} \rangle = \boldsymbol{F}_{\mathrm{Rad}} = \oint \hat{\boldsymbol{n}} \cdot \langle \mathsf{T}_{\mathrm{M}} \rangle \, \mathrm{d}S \,, \tag{3.10}$$

and the conservation of angular momentum (3.8)

$$\langle \frac{\mathrm{d}\boldsymbol{L}_{\mathrm{mech}}}{\mathrm{d}t} \rangle = \boldsymbol{\Gamma}_{\mathrm{Rad}} = -\oint \hat{\boldsymbol{n}} \cdot \langle \mathsf{T}_{\mathrm{M}} \rangle \times \boldsymbol{r} \, \mathrm{d}S \,. \tag{3.11}$$

3.2 Radiation Force and Radiation Torque

When a radiation field interacts with a particle, the conservation of the linear momentum decrees that the latter experiences the so called *radiation force*, and, as a result of the conservation of angular momentum during the interaction, the particle experiences also a torque, the *radiation torque* [39]. In this section we deal with the case in which the radiation field is a monochromatic plane wave, so that (3.10) and (3.11) apply. In principle, any surface surrounding the particle can be chosen as the integration surface; indeed, since both $\boldsymbol{F}_{\mathrm{Rad}}$ and $\boldsymbol{\Gamma}_{\mathrm{Rad}}$ stem from conservation theorems, none of them can depend on the choice of S although the integrands in (3.10) and (3.11) may be dependent on $\boldsymbol{r}$. Nevertheless, the calculations are greatly simplified by chosing S to be a sphere with center within the particle and a radius large enough that its surface is entirely in far field zone. At the end of the algebraic manipulations we can possibly take the limit for $r \to \infty$.

3.2.1 Radiation Force

Let us first consider the radiation force in some detail. Due to our choice of the integration surface, we can rewrite (3.10) as

$$\boldsymbol{F}_{\mathrm{Rad}} = r^2 \int_{\Omega} \hat{\boldsymbol{r}} \cdot \langle \mathsf{T}_{\mathrm{M}} \rangle \, \mathrm{d}\Omega \,, \tag{3.12}$$

where the fields that enter the definition of the Maxwell stress tensor are the superposition of the incident and of the scattered field. We assume that the incident field be the plane polarized wave (2.1), whereas the scattered field can be taken in the far zone form (2.5). In order to perform the surface integration it is convenient to follow the suggestion of Saxon [23] and to express the incident field in the far zone as a superposition of incoming and outgoing spherical waves

$$\boldsymbol{E}_{\mathrm{I}} = E_0 \hat{\boldsymbol{e}}_{\mathrm{I}} \frac{2\pi \mathrm{i}}{k} \left[\delta(\hat{\boldsymbol{k}}_{\mathrm{I}} + \hat{\boldsymbol{r}}) \frac{\mathrm{e}^{-ikr}}{r} - \delta(\hat{\boldsymbol{k}}_{\mathrm{I}} - \hat{\boldsymbol{r}}) \frac{\mathrm{e}^{ikr}}{r} \right] \,. \tag{3.13}$$

In fact, a straightforward but lenghty calculation with help of (3.13) shows that the first two terms in (3.9) give no contribution to the integral in (3.12). Since $\mathsf{I} \cdot \hat{\boldsymbol{r}} = \hat{\boldsymbol{r}}$, we have

$$\boldsymbol{F}_{\mathrm{Rad}} = -\frac{1}{4} r^2 \frac{1}{4\pi} \mathrm{Re} \int_{\Omega} \left[|\boldsymbol{E}_{\mathrm{I}} + \boldsymbol{E}_{\mathrm{S}}|^2 + |\boldsymbol{B}_{\mathrm{I}} + \boldsymbol{B}_{\mathrm{S}}|^2 \right] \hat{\boldsymbol{r}} \, \mathrm{d}\Omega \, .$$

Now, the terms in square brackets in the integrand give

$$|\boldsymbol{E}_{\mathrm{I}}+\boldsymbol{E}_{\mathrm{S}}|^2+|\boldsymbol{B}_{\mathrm{I}}+\boldsymbol{B}_{\mathrm{S}}|^2 = |\boldsymbol{E}_{\mathrm{I}}|^2+|\boldsymbol{E}_{\mathrm{S}}|^2+2\boldsymbol{E}_{\mathrm{I}}\cdot\boldsymbol{E}_{\mathrm{S}}^*+|\boldsymbol{B}_{\mathrm{I}}|^2+|\boldsymbol{B}_{\mathrm{S}}|^2+2\boldsymbol{B}_{\mathrm{I}}\cdot\boldsymbol{B}_{\mathrm{S}}^* \, .$$

The terms $|\boldsymbol{E}_{\mathrm{I}}|^2$ and $|\boldsymbol{B}_{\mathrm{I}}|^2$ turn out to be constants independent of r and, therefore, give no contribution to the integral. The remaining terms, according to (2.5) and (3.13), give

$$\boldsymbol{F}_{\mathrm{Rad}} = \frac{2\pi}{k} \hat{\boldsymbol{k}}_{\mathrm{I}} \mathrm{Im} \left[\boldsymbol{f}(\hat{\boldsymbol{k}}_{\mathrm{S}} = \hat{\boldsymbol{k}}_{\mathrm{I}}, \hat{\boldsymbol{k}}_{\mathrm{I}}) \cdot \hat{\boldsymbol{e}}_{\mathrm{I}} \right] \frac{I_{\mathrm{I}}}{4\pi} - \frac{1}{2} \frac{I_{\mathrm{I}}}{4\pi} \int_{\Omega} |\boldsymbol{f}(\hat{\boldsymbol{k}}_{\mathrm{S}} = \hat{\boldsymbol{r}}, \hat{\boldsymbol{k}}_{\mathrm{I}})|^2 \hat{\boldsymbol{r}} \, \mathrm{d}\Omega \, ,$$

where $I_{\mathrm{I}} = |E_0|^2$ is the *intensity of the field* $\boldsymbol{E}_{\mathrm{I}}$. Thus, on account of the optical theorem (2.13) and of the definition of the differential scattering cross Sect. 2.7, we have

$$\boldsymbol{F}_{\mathrm{Rad}} = \frac{I_0}{c} \left(\hat{\boldsymbol{k}}_{\mathrm{I}} \sigma_{\mathrm{T}} - \int_{\Omega} \frac{\mathrm{d}\sigma_{\mathrm{S}}}{\mathrm{d}\Omega} \hat{\boldsymbol{r}} \, \mathrm{d}\Omega \right) , \tag{3.14}$$

where

$$I_0 = \frac{c}{8\pi} I_{\mathrm{I}} \tag{3.15}$$

is the magnitude of the time averaged flux of the Poynting vector, i.e. the *intensity of the incident plane wave.* Equation (3.14) relates the radiation force to the optical properties of the particles and shows that, for nonspherical particles, the direction of $\boldsymbol{F}_{\mathrm{Rad}}$ does not coincide with the direction of the incident wave. Furthermore, the radiation force depends on the polarization as is easily seen with the help of (2.44) and (2.46) which express the cross sections in terms of the phase matrix and of the extinction matrix.

Now, we take the components of $\boldsymbol{F}_{\mathrm{Rad}}$ with respect to the triplet $\hat{\boldsymbol{v}}_\zeta$, where $\hat{\boldsymbol{v}}_1 = \hat{\boldsymbol{u}}_{\mathrm{I}1}$ and $\hat{\boldsymbol{v}}_2 = \hat{\boldsymbol{u}}_{\mathrm{I}2}$ are the vectors of the linear basis on the meridional plane of $\hat{\boldsymbol{v}}_3 = \hat{\boldsymbol{k}}_{\mathrm{I}}$. It is an easy matter to see that the result is

$$F_\zeta = \boldsymbol{F}_{\mathrm{Rad}} \cdot \hat{\boldsymbol{v}}_\zeta = \frac{I_0}{c} \left(\sigma_{\mathrm{T}} \delta_{\zeta 3} - g_\zeta \sigma_{\mathrm{S}} \right) , \tag{3.16}$$

where we define the asymmetry parameters

$$g_\zeta = \frac{1}{\sigma_{\mathrm{S}}} \int_{\Omega} \frac{\mathrm{d}\sigma_{\mathrm{S}}}{\mathrm{d}\Omega} \hat{\boldsymbol{k}}_{\mathrm{S}} \cdot \hat{\boldsymbol{v}}_\zeta \, \mathrm{d}\Omega \, . \tag{3.17}$$

Since $\hat{\boldsymbol{k}}_{\mathrm{S}} \cdot \hat{\boldsymbol{v}}_3 = \cos \Phi$, where Φ is the angle of scattering, g_3 is easily recognized as the customary asymmetry parameter and F_3 is identified with the customary definition of the radiation pressure. The results (3.16) and (3.17) for $\zeta = 3$ have also been derived by van de Hulst through a reasoning based just on the conservation of the linear momentum. The two further components of $\boldsymbol{F}_{\mathrm{Rad}}$ define the transverse components of the radiation force whose importance for the dynamics of the interstellar dust has been recognized in the last few years [40]. Anyway, when dealing with the radiation pressure it is convenient to define the *radiation pressure cross section*

$$\sigma_{\mathrm{pr}} = \sigma_{\mathrm{T}} - \sigma_{\mathrm{S}} g_3$$

and the corresponding *efficiency*

$$Q_{\mathrm{pr}} = \sigma_{\mathrm{pr}} / G \ .$$

3.2.2 Radiation Torque

We now go to consider the radiation torque. As the consideration of torques requires a well established origin, we choose a frame of reference with origin within the particle concerned. Since the dynamics of a particle is determined by its center of mass and by its principal axes of inertia, chosing this particular set of axes as a frame of reference would greatly simplify the study of the dynamics. However, as far as the electromagnetic part of our study is concerned any set of axes with origin within the particle will do. The integration surface can then be chosen as in the preceding subsection and we can write

$$\boldsymbol{\Gamma}_{\mathrm{Rad}} = -r^3 \int_{\Omega} \hat{\boldsymbol{r}} \cdot \langle \mathsf{T}_{\mathrm{M}} \rangle \times \hat{\boldsymbol{r}} \, \mathrm{d}\Omega \ , \tag{3.18}$$

where, since $\hat{\boldsymbol{r}} \cdot \mathsf{I} \times \hat{\boldsymbol{r}} \equiv 0$, the last two terms in (3.9) give no contribution to (3.18). The remaining terms are, as usual, the superposition of the incident and of the scattered field, so that

$$\begin{aligned} \boldsymbol{\Gamma}_{\mathrm{Rad}} = -\frac{r^3}{8\pi} \mathrm{Re} \int \Big[& \hat{\boldsymbol{r}} \cdot \left(\boldsymbol{E}_{\mathrm{I}} + \boldsymbol{E}_{\mathrm{S}} \right) \left(\boldsymbol{E}_{\mathrm{I}}^* + \boldsymbol{E}_{\mathrm{S}}^* \right) \times \hat{\boldsymbol{r}} \\ & + \hat{\boldsymbol{r}} \cdot \left(\boldsymbol{B}_{\mathrm{I}} + \boldsymbol{B}_{\mathrm{S}} \right) \left(\boldsymbol{B}_{\mathrm{I}}^* + \boldsymbol{B}_{\mathrm{S}}^* \right) \times \hat{\boldsymbol{r}} \Big] \, \mathrm{d}\Omega \ . \end{aligned} \tag{3.19}$$

At this stage the reader is warned that the far field expression of the scattered fields in terms of the scattering amplitude cannot be used. Actually, according to (2.6) the scattering amplitude is orthogonal to the radial unit vector $\hat{\boldsymbol{r}}$, so that one would get a vanishing result. For a correct calculation of the radiation torque one has to retain the radial terms of the fields, that for the case of the radiation force have beeen neglected because they vanish faster than $1/r$. We will show in the next chapter how the relevant terms can be taken into account in order to get the correct nonvanishing result.

3.3 Thermal Emission

In Sect. 2.2 it has been shown that when the refractive index of a particle has a nonvanishing imaginary part, an absorption process occurs. The absorbed energy is converted into heat thus increasing the temperature of the particle that, just because of the heating, reemits radiation with a spectral distribution given by the black body distribution function at the temperature of emission. Of course, thermal equilibrium is soon reached and the temperature of equilibrium can be determined using the condition that the absorbed power and the emitted power are equal, i.e.

$$\int_0^\infty \frac{c}{\omega^2}\sigma_{\mathrm{A}}(\omega) I_\omega \,\mathrm{d}\omega = \int_0^\infty \frac{c}{\omega^2}\sigma_{\mathrm{A}}(\omega) I_{\mathrm{b}}(\omega, T_{\mathrm{e}}) \,\mathrm{d}\omega$$

where I_ω is the intensity of the incident field at (circular) frequency ω, T_{e} is the temperature of equilibrium and

$$I_{\mathrm{b}}(\omega, T) = \hbar\omega^3 \left[4\pi^3 c^2 \big(\exp(\hbar\omega/k_{\mathrm{B}}T) - 1\big)\right]^{-1}$$

is Planck blackbody energy distribution. Note that the blackbody spectrum is completely unpolarized, whereas the emitted radiation may be polarized. From the point of view of the Stokes vector formalism this implies that the blackbody radiation is described by a four elements one column vector $\underline{\mathcal{I}}_{\mathrm{b}}$ whose first element is equal to $I_{\mathrm{b}}(\omega, T)$, all other elements being zero; the emitted radiation, in turn, is described by a four components column vector $\underline{\mathcal{K}}_{\mathrm{e}}$ with elements $K_{\mathrm{e}j}$ $(j = 1, \ldots 4)$, whose first element is so defined that $K_{\mathrm{e}1}(\hat{\boldsymbol{r}}, \omega, T)/r^2$ gives the electromagnetic power emitted per unit solid angle around the direction of observation $\hat{\boldsymbol{r}}$ at the frequency ω.

Strictly speaking, the calculation of the elements $K_{\mathrm{e}j}$ would require using the fluctuation-dissipation theorem. Nevertheless for our purposes we can use the following intuitive argument. Let us consider a particle in thermal equilibrium with the radiation field of a blackbody. The particle scatters as well as re-emits radiation that can be recorded by an optical instrument, sensitive to the polarization, whose front lens, of area ΔS is seen by the particle to span a solid angle $\Delta\Omega$. If we recall that there is no interference between the blackbody radiation and the radiation scattered and re-emitted by the particle, we conclude that the Stokes vector of the signal recorded by the instrument $\underline{\mathcal{I}}_{\mathrm{R}}$ turns out to be

$$\begin{aligned}\underline{\mathcal{I}}_{\mathrm{R}} =& \underline{\mathcal{I}}_{\mathrm{b}}(\omega, T)\,\Delta S\,\Delta\Omega \\ &+ \underline{\mathcal{K}}_{\mathrm{e}}(\hat{\boldsymbol{r}}, \omega, T)\Delta\Omega - \underline{\mathcal{K}}(\hat{\boldsymbol{r}}, \omega)\underline{\mathcal{I}}_{\mathrm{b}}(\omega, T)\,\Delta\Omega + \Delta\Omega \int \mathrm{d}\hat{\boldsymbol{r}}'\,\underline{\mathcal{Z}}(\hat{\boldsymbol{r}}, \hat{\boldsymbol{r}}', \omega)\underline{\mathcal{I}}_{\mathrm{b}}(T, \omega)\ ,\end{aligned}$$

where $\underline{\mathcal{K}}(\hat{\boldsymbol{r}}, \omega)$ is the extinction matrix of the particle and $\underline{\mathcal{Z}}(\hat{\boldsymbol{r}}, \hat{\boldsymbol{r}}', \omega)$ is its phase matrix; $\hat{\boldsymbol{r}} = \hat{\boldsymbol{k}}_{\mathrm{S}}$ and $\hat{\boldsymbol{r}}' = \hat{\boldsymbol{k}}_{\mathrm{I}}$ are the direction of observation and of incidence, respectively. Since the presence of the particle does not alter the distribution of radiation, we can equate the blackbody Stokes vector with the signal received by the instrument with the result

$$K_{\mathrm{e}j}(\hat{\boldsymbol{r}}, \omega, T) = I_{\mathrm{b}}(\omega, T) K_{j1}(\hat{\boldsymbol{r}}, \omega) - I_{\mathrm{b}}(\omega, T) \int \mathrm{d}\hat{\boldsymbol{r}}'\, Z_{j1}(\hat{\boldsymbol{r}}, \hat{\boldsymbol{r}}', \omega)\ . \qquad (3.20)$$

Note that the preceding equation has been written at a general temperature and not at the temperature of equilibrium T_e. In fact, the thermal emission occurs at any temperature $T > 0$ and in this respect we could say that the thermal emission is a feature of any particle.

As the emitted radiation is endowed of a linear momentum, as a result of the emission process the particle should experience a force, the *emission force* $\boldsymbol{F}_\mathrm{e}$, whose expression

$$\boldsymbol{F}_\mathrm{e} = -\frac{1}{c}\int_0^\infty \mathrm{d}\omega \int \mathrm{d}\hat{\boldsymbol{r}}\,\hat{\boldsymbol{r}}\,K_{\mathrm{e}1}\ , \tag{3.21}$$

can be inferred from (3.14), with the help of (2.44) and (2.46). Of course, since the emitted radiation is also endowed of angular momentum, the particle should experience a small contribution to the radiation torque, which we do not consider here, however.

We end this section by showing that the emission force is bound to vanish for particles with a real refractive index, i.e. in the absence of absorption. In fact, according to (3.21), the emission force depends on the element $K_{\mathrm{e}1}$ of the emission Stokes vector. Using (3.20) we have

$$\frac{K_{\mathrm{e}1}(\hat{\boldsymbol{k}}_\mathrm{S})}{I_\mathrm{b}} = K_{11}(\hat{\boldsymbol{k}}_\mathrm{S}) - \int \mathrm{d}\hat{\boldsymbol{k}}_\mathrm{I} Z_{11}(\hat{\boldsymbol{k}}_\mathrm{S}, \hat{\boldsymbol{k}}_\mathrm{I})\ , \tag{3.22}$$

where the arguments T and ω have been omitted for the sake of simplicity. Now, from the reciprocity theorem (2.30) we get

$$K_{11}(\hat{\boldsymbol{k}}_\mathrm{I}) = K_{11}(-\hat{\boldsymbol{k}}_\mathrm{I}), \quad \text{and} \quad Z_{11}(\hat{\boldsymbol{k}}_\mathrm{S}, \hat{\boldsymbol{k}}_\mathrm{I}) = Z_{11}(-\hat{\boldsymbol{k}}_\mathrm{I}, -\hat{\boldsymbol{k}}_\mathrm{S})\ .$$

Then, by recalling the definition of the scattering and extinction cross sections in terms of extinction and phase matrices [see (2.44) and (2.46), respectively], we easily see that (3.22) becomes

$$\frac{K_{\mathrm{e}1}(\hat{\boldsymbol{k}}_\mathrm{S})}{I_\mathrm{b}} = \sigma_\mathrm{T}(-\hat{\boldsymbol{k}}_\mathrm{S}) - \sigma_\mathrm{S}(-\hat{\boldsymbol{k}}_\mathrm{S}) = \sigma_A(-\hat{\boldsymbol{k}}_\mathrm{S})\ . \tag{3.23}$$

In Sect. 2.2, however, the absorption cross section has been proved to vanish for real refractive index, so that $K_{\mathrm{e}1} = 0$ for nonabsorbing particles. This result, when substituted into (3.21), decrees the vanishing of the thermal emission force for particles with real refractive index.

4 Multipole Expansions and Transition Matrix

The theory in Chaps. 2 and 3 yields a number of useful relations but gives no prescription for calculating the quantities of interest. In this chapter we use the theory of the multipole fields to establish equations that are suitable for actual calculations. In fact, by expanding both the incident and the scattered field in a series of spherical vector multipole fields, one is lead to introduce the *transition matrix* that proved to be one of the most fruitful concepts in the theory of scattering. Beyond encompassing all the information on the morphology and on the orientation of the scattering particle with respect to the incident field, the transition matrix has well-defined transformation properties under rotation of the coordinate frame. These properties will be shown to be the key tool for the description of the propagation of light through an assembly of nonspherical particles.

4.1 Multipole Expansions of Plane Waves

Our starting point is the expansion of the incident and of the scattered field. Let us consider an electromagnetic plane wave whose planes of equal phase and of equal amplitude are mutually parallel to each other: a plane wave of this kind is said to be *homogeneous*. The condition for homogeneity is fulfilled either when the propagation vector $\boldsymbol{k}$ is real or when the real and the imaginary part of the propagation vector are collinear. In the next subsections we consider first the case of a real propagation vector, then the case of a complex propagation vector. Actually, unless we state otherwise, the medium through which the incident and the scattered field propagate is assumed to be homogeneous with real refractive index n.

4.1.1 Plane Waves with Real Propagation Vector

The electric and magnetic field vectors of the wave we are going to consider are

$$\boldsymbol{E} = E_0 \hat{\boldsymbol{e}} \exp(\mathrm{i}\boldsymbol{k}\cdot\boldsymbol{r}) \ , \tag{4.1a}$$

$$\mathrm{i}\boldsymbol{B} = \mathrm{i}nE_0(\hat{\boldsymbol{k}}\times\hat{\boldsymbol{e}}) \exp(\mathrm{i}\boldsymbol{k}\cdot\boldsymbol{r}) \ , \tag{4.1b}$$

where $\boldsymbol{k} = nk_{\mathrm{v}}\hat{\boldsymbol{k}}$. We assume that the multipole expansion of the fields (4.1) can be written as

$$\boldsymbol{E} = E_0 \sum_{plm} \boldsymbol{J}_{lm}^{(p)}(\boldsymbol{r}, k) W_{lm}^{(p)}(\hat{\boldsymbol{e}}, \hat{\boldsymbol{k}}) \,, \tag{4.2a}$$

$$\mathrm{i}\boldsymbol{B} = nE_0 \sum_{plm} \boldsymbol{J}_{lm}^{(p)}(\boldsymbol{r}, k) W_{lm}^{(p')}(\hat{\boldsymbol{e}}, \hat{\boldsymbol{k}}) \text{ with } p' \neq p \,, \tag{4.2b}$$

where we used $\boldsymbol{J}$-multipole fields to ensure the finiteness at the origin, and the *multipole amplitudes* $W_{lm}^{(p)}(\hat{\boldsymbol{e}}, \hat{\boldsymbol{k}})$ will be determined presently. To this end, we dot multiply (4.2a) and (4.2b) by $\boldsymbol{X}_{lm}^{*}(\hat{\boldsymbol{r}})$ and integrate over the solid angle. The orthogonality relations of the vector spherical harmonics (1.53) and (1.54), with the help of (1.55) and the analogous of (1.62) for the $\boldsymbol{J}$-fields, yield

$$E_0 W_{lm}^{(1)} j_l(kr) = \int \boldsymbol{E} \cdot \boldsymbol{X}_{lm}^{*} \mathrm{d}\Omega \,,$$

$$nE_0 W_{lm}^{(2)} j_l(kr) = \mathrm{i} \int \boldsymbol{B} \cdot \boldsymbol{X}_{lm}^{*} \mathrm{d}\Omega \,.$$

Substitution in place of the fields of their expressions given by (4.1) leads to

$$W_{lm}^{(1)} j_l(kr) = \int \exp(\mathrm{i}\boldsymbol{k} \cdot \boldsymbol{r}) \hat{\boldsymbol{e}} \cdot \boldsymbol{X}_{lm}^{*} \mathrm{d}\Omega \,, \tag{4.3a}$$

$$W_{lm}^{(2)} j_l(kr) = \mathrm{i} \int \exp(\mathrm{i}\boldsymbol{k} \cdot \boldsymbol{r}) (\hat{\boldsymbol{k}} \times \hat{\boldsymbol{e}}) \cdot \boldsymbol{X}_{lm}^{*} \mathrm{d}\Omega \,. \tag{4.3b}$$

The integrals in (4.3) can be evaluated by recalling that, according to the definition (1.52),

$$\hat{\boldsymbol{e}} \cdot \boldsymbol{X}_{lm}^{*}(\hat{\boldsymbol{r}}) = [l(l+1)]^{-1/2} \hat{\boldsymbol{e}} \cdot [\mathrm{L} Y_{lm}(\hat{\boldsymbol{r}})]^{*} = [l(l+1)]^{-1/2} [\hat{\boldsymbol{e}}^{*} \cdot \mathrm{L} Y_{lm}(\hat{\boldsymbol{r}})]^{*} \,.$$

Now, in terms of spherical components,

$$\hat{\boldsymbol{e}}^{*} \cdot \mathrm{L} = \sum_{\mu} (-)^{\mu} \hat{e}_{\mu}^{*} \mathrm{L}_{-\mu} \,,$$

where, of course,

$$\mathrm{L}_0 = \mathrm{L}_z \,, \quad \mathrm{L}_{\pm 1} = \mp \tfrac{1}{\sqrt{2}} \mathrm{L}_{\pm} = \mp \tfrac{1}{\sqrt{2}} (\mathrm{L}_x \pm \mathrm{i} \mathrm{L}_y) \,.$$

Therefore, letting $\mathrm{L}_{\pm}$ and L_z operate on Y_{lm} we get [8]

$$\begin{aligned}\hat{\boldsymbol{e}} \cdot \boldsymbol{X}_{lm}^{*}(\hat{\boldsymbol{r}}) = [l(l+1)]^{-1/2} \big\{ & \hat{e}_z C_z Y_{lm}(\hat{\boldsymbol{r}}) \\ & + \tfrac{1}{2} [-\hat{e}_1 C_{-} Y_{l,\, m-1}(\hat{\boldsymbol{r}}) + \hat{e}_{-1} C_{+} Y_{l,\, m+1}(\hat{\boldsymbol{r}})] \big\}^{*},\end{aligned}$$

where

$$C_z = m \; , \qquad C_\pm = [l(l+1) - m(m \pm 1)]^{1/2} \; .$$

A quite analogous result is obtained for $(\hat{\boldsymbol{k}} \times \hat{\boldsymbol{e}}) \cdot \boldsymbol{X}^*_{lm}(\hat{\boldsymbol{r}})$. At this stage we substitute in place of the exponentials in (4.3) the Bauer expansion

$$\exp(\mathrm{i}\boldsymbol{k} \cdot \boldsymbol{r}) = 4\pi \sum_{lm} \mathrm{i}^l j_l(kr) Y^*_{lm}(\hat{\boldsymbol{k}}) Y_{lm}(\hat{\boldsymbol{r}})$$

and perform the integration. The orthogonality properties of the spherical harmonics then yield the result

$$W^{(1)}_{lm}(\hat{\boldsymbol{e}}, \hat{\boldsymbol{k}}) = 4\pi \mathrm{i}^l \hat{\boldsymbol{e}} \cdot \boldsymbol{X}^*_{lm}(\hat{\boldsymbol{k}}) \; ,$$
$$W^{(2)}_{lm}(\hat{\boldsymbol{e}}, \hat{\boldsymbol{k}}) = 4\pi \mathrm{i}^{l+1} (\hat{\boldsymbol{k}} \times \hat{\boldsymbol{e}}) \cdot \boldsymbol{X}^*_{lm}(\hat{\boldsymbol{k}}) \; ,$$

which, in terms of the transverse vector harmonics (1.56), can be put in the more compact form [14]

$$W^{(p)}_{lm}(\hat{\boldsymbol{e}}, \hat{\boldsymbol{k}}) = 4\pi \mathrm{i}^{p+l-1} \hat{\boldsymbol{e}} \cdot \boldsymbol{Z}^{(p)*}_{lm}(\hat{\boldsymbol{k}}) \; . \tag{4.4}$$

The polarization vector $\hat{\boldsymbol{e}}$ in (4.4) is quite general and may be either real (linear polarization) or complex (elliptical polarization). Actually, (4.4) is independent of the introduction of a basis for the description of the polarization. However, if a polarization basis, say $\hat{\boldsymbol{u}}_\eta$, has been chosen, (4.4) can be rewritten in the form

$$W^{(p)}_{lm}(\hat{\boldsymbol{e}}, \hat{\boldsymbol{k}}) = \frac{1}{E_0} \sum_\eta E_{0\eta} W^{(p)}_{lm}(\hat{\boldsymbol{u}}_\eta, \hat{\boldsymbol{k}}) \; , \tag{4.5}$$

where

$$E_{0\eta} = E_0 \hat{\boldsymbol{e}} \cdot \hat{\boldsymbol{u}}^*_\eta \tag{4.6}$$

and thus

$$E_0 \hat{\boldsymbol{e}} = E_{01} \hat{\boldsymbol{u}}_1 + E_{02} \hat{\boldsymbol{u}}_2 \; .$$

Therefore, (4.2a) can be rewritten as

$$\boldsymbol{E} = \sum_\eta E_{0\eta} \sum_{plm} \boldsymbol{J}^{(p)}_{lm}(\boldsymbol{r}, k) W^{(p)}_{lm}(\hat{\boldsymbol{u}}_\eta, \hat{\boldsymbol{k}}) \; . \tag{4.7}$$

The amplitudes $W^{(p)}_{lm}(\hat{\boldsymbol{u}}_\eta, \hat{\boldsymbol{k}})$ satisfy either the sum rule [41, 42]

$$\sum_m W^{(p)*}_{lm}(\hat{\boldsymbol{u}}_\eta, \hat{\boldsymbol{k}}) W^{(p')}_{lm}(\hat{\boldsymbol{u}}_{\eta'}, \hat{\boldsymbol{k}}) = 2\pi(2l+1) \left[\delta_{\eta\eta'} \delta_{pp'} + \mathrm{i}(-)^\eta (1 - \delta_{\eta\eta'})(1 - \delta_{pp'}) \right] \; , \tag{4.8}$$

or

$$\sum_m W^{(p)*}_{lm}(\hat{\boldsymbol{u}}_\eta, \hat{\boldsymbol{k}}) W^{(p')}_{lm}(\hat{\boldsymbol{u}}_{\eta'}, \hat{\boldsymbol{k}}) = 2\pi(2l+1) \delta_{\eta\eta'} \left[\delta_{pp'} + (-)^{\eta+1} (1 - \delta_{pp'}) \right] \; , \tag{4.9}$$

according to whether $\hat{\boldsymbol{u}}_\eta$ is a linear basis or a circular basis, respectively. It is worth remarking that (4.9), unlike (4.8), implies the vanishing of the sum for $\eta' \neq \eta$.

With the help of (1.63a), a particularly simple and useful form can be given to the amplitudes $W_{lm}^{(p)}$ by choosing a reference frame with the z axis parallel to $\hat{\boldsymbol{k}}$. The result is

$$W_{lm}^{(p)}(\hat{\boldsymbol{u}}_\eta, \hat{\boldsymbol{k}} = \hat{\boldsymbol{e}}_z) = \left(\mathrm{i}^{l-\eta+1}\sqrt{\pi}\sqrt{2l+1}\right)\delta_{m,\pm1}\left[1 - 2(1-\delta_{\eta p})\delta_{m,-1}\right] \quad (4.10)$$

when $\hat{\boldsymbol{u}}_\eta$ is a linear basis, and

$$W_{lm}^{(p)}(\hat{\boldsymbol{u}}_\eta, \hat{\boldsymbol{k}} = \hat{\boldsymbol{e}}_z) = \left(\mathrm{i}^{l}\sqrt{2\pi}\sqrt{2l+1}\right)\delta_{-m,(-)^\eta}\left[\delta_{1\eta} - \delta_{2\eta}(-)^p\right] \quad (4.11)$$

when $\hat{\boldsymbol{u}}_\eta$ is a circular basis.

4.1.2 Plane Waves with Complex Propagation Vector

We now go to determine the multipole expansion of a vector plane wave with complex propagation vector. This includes the case of the homogeneous plane waves with collinear real and imaginary part of the propagation vector, as well as *inhomogeneous plane waves* [4] whose propagation vector has a real and an imaginary part that are not collinear and thus has equiphase and equiamplitude planes that are not mutually parallel [43]. We stress that the wavevector may be complex not only because the medium is absorptive but also because it may be convenient to assume a complex propagation vector in order to perform particular expansions. One such expansion will be used in Chap. 6.

When performing the multipole expansion of a plane wave with complex propagation vector it should be borne in mind that the orthogonality of the vector spherical harmonics in the form (1.53) holds true for real argument only. For complex $\hat{\boldsymbol{k}}$ we have

$$(-)^{m+1}\int \boldsymbol{X}_{lm}(\hat{\boldsymbol{k}}) \cdot \boldsymbol{X}_{l,-m}(\hat{\boldsymbol{k}})\mathrm{d}\Omega_{\hat{\boldsymbol{k}}} = \delta_{ll'}\delta_{mm'} \; .$$

Note that for real argument $\boldsymbol{X}_{lm}^* = (-)^{m+1}\boldsymbol{X}_{l,-m}$. With this *proviso*, the procedure described in the preceding section can be applied to the expansion of a plane wave with complex propagation vector with the result

$$\hat{\boldsymbol{e}}\exp(\mathrm{i}\boldsymbol{k}\cdot\boldsymbol{r}) = 4\pi\sum_{plm}\mathrm{i}^{p+l+1}(-)^{m+1}\left[\boldsymbol{Z}_{l,-m}^{(p)}(\hat{\boldsymbol{k}})\cdot\hat{\boldsymbol{e}}\right]\boldsymbol{J}_{lm}^{(p)}(\boldsymbol{r},k) \; ,$$

so that

$$W_{lm}^{(p)}(\hat{\boldsymbol{e}}, \hat{\boldsymbol{k}}) = 4\pi\mathrm{i}^{p+l-1}(-)^{m+1}\hat{\boldsymbol{e}}\cdot\boldsymbol{Z}_{l,-m}^{(p)}(\hat{\boldsymbol{k}}) \; . \quad (4.12)$$

4.2 Multipole Expansion of the Scattered Field

In analogy to the incident field

$$\boldsymbol{E}_{\mathrm{I}} = E_0 \sum_{plm} \boldsymbol{J}_{lm}^{(p)}(\boldsymbol{r}, k) W_{lm}^{(p)}(\hat{\boldsymbol{e}}_{\mathrm{I}}, \hat{\boldsymbol{k}}_{\mathrm{I}}) , \tag{4.13}$$

we expand the scattered field as

$$\boldsymbol{E}_S = E_0 \sum_{plm} \boldsymbol{H}_{lm}^{(p)}(\boldsymbol{r}, k) A_{lm}^{(p)}(\hat{\boldsymbol{e}}_{\mathrm{I}}, \hat{\boldsymbol{k}}_{\mathrm{I}}) , \tag{4.14}$$

where we use $\boldsymbol{H}$-multipole fields because $\boldsymbol{E}_{\mathrm{S}}$ should satisfy the radiation condition at infinity [44], and the *amplitudes* $A_{lm}^{(p)}$, which are determined by the boundary conditions across the surface of the particle, bear the temporary arguments $\hat{\boldsymbol{e}}_{\mathrm{I}}$ and $\hat{\boldsymbol{k}}_{\mathrm{I}}$ to stress that, in general, they depend on the orientation of the (nonspherical) scattering particle with respect to the incident field. We can also write

$$\boldsymbol{E}_S = \sum_{\eta} E_{0\eta} \sum_{plm} \boldsymbol{H}_{lm}^{(p)}(\boldsymbol{r}, k) A_{lm}^{(p)}(\hat{\boldsymbol{u}}_{\mathrm{I}\eta}, \hat{\boldsymbol{k}}_{\mathrm{I}}) , \tag{4.15}$$

so that, in analogy with (4.5), and with the help of (4.6),

$$A_{lm}^{(p)}(\hat{\boldsymbol{e}}_{\mathrm{I}}, \hat{\boldsymbol{k}}_{\mathrm{I}}) = \frac{1}{E_0} \sum_{\eta} E_{0\eta} A_{lm}^{(p)}(\hat{\boldsymbol{u}}_{\mathrm{I}\eta}, \hat{\boldsymbol{k}}_{\mathrm{I}}) . \tag{4.16}$$

The multipole expansion of the normalized scattering amplitude is easily obtained by taking the limit of the $\boldsymbol{H}$-multipole fields for $r \to \infty$. Indeed, with the help of (1.43b), (1.44b), and (1.62) we get

$$\boldsymbol{H}_{lm}^{(p)}(\boldsymbol{r}, k) = (-\mathrm{i})^{l+p} \frac{\mathrm{e}^{\mathrm{i}kr}}{kr} \boldsymbol{Z}_{lm}^{(p)}(\hat{\boldsymbol{k}}_S) .$$

Therefore, the asymptotic form of the scattered field is

$$\boldsymbol{E}_{\mathrm{S}} = \frac{E_0}{k} \frac{e^{\mathrm{i}kr}}{r} \sum_{plm} (-\mathrm{i})^{l+p} \boldsymbol{Z}_{lm}^{(p)}(\hat{\boldsymbol{k}}_{\mathrm{S}}) A_{lm}^{(p)}(\hat{\boldsymbol{e}}_{\mathrm{I}}, \hat{\boldsymbol{k}}_{\mathrm{I}}) ,$$

and comparison with (2.5) yields

$$\boldsymbol{f}(\hat{\boldsymbol{k}}_{\mathrm{S}}, \hat{\boldsymbol{k}}_{\mathrm{I}}; \hat{\boldsymbol{e}}_{\mathrm{I}}) = \frac{1}{k} \sum_{plm} (-\mathrm{i})^{l+p} \boldsymbol{Z}_{lm}^{(p)}(\hat{\boldsymbol{k}}_{\mathrm{S}}) A_{lm}^{(p)}(\hat{\boldsymbol{e}}_{\mathrm{I}}, \hat{\boldsymbol{k}}_{\mathrm{I}}) , \tag{4.17}$$

which is the required expression. Note that we added to $\boldsymbol{f}$ the temporary argument $\hat{\boldsymbol{e}}_{\mathrm{I}}$ to emphasize the dependence on the polarization of the incident field. In terms of the amplitudes $A_{\eta lm}^{(p)}$ (4.17) reads

$$\boldsymbol{f}_\eta(\hat{\boldsymbol{k}}_\mathrm{S},\hat{\boldsymbol{k}}_\mathrm{I}) = \frac{1}{k}\sum_{plm}(-\mathrm{i})^{l+p}\boldsymbol{Z}_{lm}^{(p)}(\hat{\boldsymbol{k}}_\mathrm{S})A_{lm}^{(p)}(\hat{\boldsymbol{u}}_{\mathrm{I}\eta},\hat{\boldsymbol{k}}_\mathrm{I}) \;, \tag{4.18}$$

where the temporary argument $\hat{\boldsymbol{e}}_\mathrm{I}$ has been substituted by the label η that recalls the polarization of the incident field. On account of (2.29), the normalized scattering amplitude matrix elements on the basis $\hat{\boldsymbol{u}}_{\mathrm{S}\eta'}$ of the scattered field are then obtained by dot multiplying (4.18) by $\hat{\boldsymbol{u}}^*_{\mathrm{S}\eta'}$ with the result

$$f_{\eta'\eta} = -\frac{\mathrm{i}}{4\pi k}\sum_{plm}W_{lm}^{(p)*}(\hat{\boldsymbol{u}}_{\mathrm{S}\eta'},\hat{\boldsymbol{k}}_\mathrm{S})A_{lm}^{(p)}(\hat{\boldsymbol{u}}_{\mathrm{I}\eta},\hat{\boldsymbol{k}}_\mathrm{I}) \;, \tag{4.19}$$

where the definition (4.4) has been used.

4.2.1 Amplitudes of the Multipole Fields and Cross Sections

At this stage we are able to give explicit expressions for the extinction and for the scattering cross section of a particle in terms of the amplitudes of the fields. Since the extinction cross section is related to the forward scattering amplitude through the optical theorem (2.13), we get

$$\begin{aligned}\sigma_\mathrm{T} =& \frac{4\pi}{k}\mathrm{Im}\big[\boldsymbol{f}(\hat{\boldsymbol{k}}_\mathrm{S}=\hat{\boldsymbol{k}}_\mathrm{I},\hat{\boldsymbol{k}}_\mathrm{I};\hat{\boldsymbol{e}}_\mathrm{I})\cdot\hat{\boldsymbol{e}}_\mathrm{I}\big]\\ =& -\frac{1}{k^2}\mathrm{Re}\Big[\sum_{plm}W_{lm}^{(p)*}(\hat{\boldsymbol{e}}_\mathrm{I},\hat{\boldsymbol{k}}_\mathrm{I})A_{lm}^{(p)}(\hat{\boldsymbol{e}}_\mathrm{I},\hat{\boldsymbol{k}}_\mathrm{I})\Big] \;. \end{aligned} \tag{4.20}$$

In turn, using the definitions (2.8), (4.17) and (1.55), and the orthogonalities (1.53) and (1.54) we obtain

$$\sigma_\mathrm{S} = \int|\boldsymbol{f}(\hat{\boldsymbol{k}}_\mathrm{S}=\hat{\boldsymbol{r}},\hat{\boldsymbol{k}}_\mathrm{I};\hat{\boldsymbol{e}}_\mathrm{I})|^2\mathrm{d}\Omega = \frac{1}{k^2}\sum_{plm}A_{lm}^{(p)*}(\hat{\boldsymbol{e}}_\mathrm{I},\hat{\boldsymbol{k}}_\mathrm{I})A_{lm}^{(p)}(\hat{\boldsymbol{e}}_\mathrm{I},\hat{\boldsymbol{k}}_\mathrm{I}) \;. \tag{4.21}$$

The cross sections can also be written in terms of the basis-polarized amplitudes. Let us introduce once for all the following abridged notation:

$$\begin{gathered}A_{\eta lm}^{(p)} = A_{lm}^{(p)}(\hat{\boldsymbol{u}}_{\mathrm{I}\eta},\hat{\boldsymbol{k}}_\mathrm{I}) \;,\\ W_{\mathrm{I}\eta lm}^{(p)} = W_{lm}^{(p)}(\hat{\boldsymbol{u}}_{\mathrm{I}\eta},\hat{\boldsymbol{k}}_\mathrm{I}), \quad \text{and} \quad W_{\mathrm{S}\eta lm}^{(p)} = W_{lm}^{(p)}(\hat{\boldsymbol{u}}_{\mathrm{S}\eta},\hat{\boldsymbol{k}}_\mathrm{S}) \;.\end{gathered} \tag{4.22}$$

Then, using (4.15) we get

$$\begin{aligned}\sigma_\mathrm{T} = \frac{4\pi}{I_\mathrm{I}k}\sum_{\eta\eta'}\mathrm{Im}\big(I_{\eta\eta'}f_{\eta\eta'}\big) &= -\frac{1}{I_\mathrm{I}}\frac{1}{k^2}\sum_{\eta\eta'}\mathrm{Re}\Big(I_{\mathrm{I}\eta\eta'}\sum_{plm}W_{\mathrm{I}\eta lm}^{(p)*}A_{\eta' lm}^{(p)}\Big)\\ &= \frac{1}{I_\mathrm{I}}\sum_{\eta\eta'}\mathrm{Re}\big(I_{\mathrm{I}\eta\eta'}\check{\sigma}_{\mathrm{T}\eta\eta'}\big)\end{aligned} \tag{4.23}$$

and

$$\sigma_{\mathrm{S}} = \frac{1}{I_{\mathrm{I}}} \frac{1}{k^2} \sum_{\eta\eta'} \mathrm{Re}\Big(I_{\mathrm{I}\eta\eta'} \sum_{plm} A^{(p)*}_{\eta lm} A^{(p)}_{\eta' lm} \Big) = \frac{1}{I_{\mathrm{I}}} \sum_{\eta\eta'} \mathrm{Re}\left(I_{\mathrm{I}\eta\eta'} \check{\sigma}_{\mathrm{S}\eta\eta'} \right) \,, \qquad (4.24)$$

where

$$I_{\mathrm{I}} = |E_0|^2, \qquad I_{\mathrm{I}\eta\eta'} = E^*_{0\eta} E_{0\eta'} \,. \qquad (4.25)$$

Equations (4.23) and (4.24) also define the cross sections $\sigma_{\mathrm{T}\eta} = \mathrm{Re}\big(\check{\sigma}_{\mathrm{T}\eta\eta}\big)$ and $\sigma_{\mathrm{S}\eta} = \check{\sigma}_{\mathrm{S}\eta\eta}$ for the case in which the incident field is polarized along $\hat{\boldsymbol{u}}_{\mathrm{I}\eta}$.

We will also need the expression of the differential scattering cross section. On account of the definition (2.8), using (4.17) and the position (4.15), it is an easy matter to see that

$$\frac{\mathrm{d}\sigma_{\mathrm{S}}}{\mathrm{d}\Omega} = \frac{1}{k^2} \frac{1}{I_{\mathrm{I}}} \sum_{\eta\eta'} \mathrm{Re}\left(I_{\mathrm{I}\eta\eta'} \boldsymbol{f}^*_{\eta} \cdot \boldsymbol{f}_{\eta'} \right) = \frac{1}{I_{\mathrm{I}}} \sum_{\eta\eta'} \mathrm{Re}\left(I_{\mathrm{I}\eta\eta'} \frac{\mathrm{d}\check{\sigma}_{\mathrm{S}\eta\eta'}}{\mathrm{d}\Omega} \right) \,, \qquad (4.26)$$

where

$$\frac{\mathrm{d}\check{\sigma}_{\mathrm{S}\eta\eta'}}{\mathrm{d}\Omega} = \frac{1}{k^2} \sum_{\bar{\eta}} f^*_{\bar{\eta}\eta} f_{\bar{\eta}\eta'} \,,$$

and, according to (4.22),

$$f_{\eta\eta'} = -\frac{\mathrm{i}}{4\pi k} \sum_{plm} W^{(p)*}_{\mathrm{S}\eta lm} A^{(p)}_{\eta' lm} \,.$$

In (4.24) and (4.26) the sums over polarization indexes are performed over the real parts only, on account that σ_{S} and $\mathrm{d}\sigma_{\mathrm{S}}/\mathrm{d}\Omega$ are on the whole real quantities.

Let us insist that the preceding equations hold true provided the incident plane wave is fully polarized. In case the wave is only partially polarized we can proceed as already explained in Sect. 2.8, i.e., by subdividing the incident intensity into a natural part and a fully polarized part. The result, either for extinction or for scattering cross section, is

$$\sigma = \frac{\sigma_1 + \sigma_2}{2} \frac{I_{\mathrm{IN}}}{I_{\mathrm{I}}} + \frac{1}{I_{\mathrm{I}}} \mathrm{Re}\Big(\sum_{\eta\eta'} \check{\sigma}_{\eta\eta'} I_{\mathrm{IP}\eta\eta'} \Big) \,.$$

In particular,

$$\sigma = \frac{\sigma_1 + \sigma_2}{2}$$

for natural incident light.

In any case, it can be shown that the results (4.23) and (4.24) coincide with the ones we reported in terms of the extinction matrix $\underline{\mathcal{K}}$ in (2.46) and in terms of the phase matrix $\underline{\mathcal{Z}}$ by integration over $\hat{\boldsymbol{k}}_{\mathrm{S}}$ of (2.44), respectively.

4.3 Transition Matrix

From a formal point of view, the scattering process can be described by a linear operator S defined by the equation

$$\boldsymbol{E}_{\mathrm{S}} = \mathrm{S}\boldsymbol{E}_{\mathrm{I}} \, .$$

Operator S, known as the *transition operator*, can be introduced due to the linearity of all the equations that describe the field, including those that express the boundary conditions across the surface of the scattering particle. In turn, the representation of the operator S on the basis of the spherical multipole fields is known as the *transition matrix* and is defined by the equation [3]

$$A_{lm}^{(p)}(\hat{\boldsymbol{e}}_{\mathrm{I}}, \hat{\boldsymbol{k}}_{\mathrm{I}}) = \sum_{p'l'm'} \mathcal{S}_{lml'm'}^{(pp')} W_{l'm'}^{(p')}(\hat{\boldsymbol{e}}_{\mathrm{I}}, \hat{\boldsymbol{k}}_{\mathrm{I}}) \, , \tag{4.27}$$

which relates the multipole amplitudes of the incident field to those of the scattered field. The quantities $\mathcal{S}_{lml'm'}^{(pp')}$, which are the elements of the transition matrix, take into account the morphology of the particle as well as the boundary conditions, but are independent of the state of polarization of the incident field. Therefore, (4.27) holds true whatever the polarization. For instance, the equation

$$A_{\eta lm}^{(p)} = \sum_{p'l'm'} \mathcal{S}_{lml'm'}^{(pp')} W_{\mathrm{I}\eta l'm'}^{(p')} \, , \tag{4.28}$$

relates the basis-polarized amplitudes of the incident and of the scattered field. Then, substituting (4.28) into (4.19) we get

$$f_{\eta'\eta} = -\frac{\mathrm{i}}{4\pi k} \sum_{plm} \sum_{p'l'm'} W_{\mathrm{S}\eta'lm}^{(p)*} \mathcal{S}_{lml'm'}^{(pp')} W_{\mathrm{I}\eta l'm'}^{(p')} \, . \tag{4.29}$$

Equation (4.29), that gives the explicit relation between the scattering amplitude and the transition matrix, is perhaps the most important equation of the theory of scattering. In fact, the observable quantities such as the cross sections of the particles are given in terms of the scattering amplitude matrix elements, whereas the transition matrix elements can be calculated once a suitable model for the scattering particles has been chosen. Indeed, assuming the transition matrix elements are known, we have

$$\check{\sigma}_{\mathrm{T}\eta\eta'} = -\frac{1}{k^2} \sum_{plm} \sum_{p'l'm'} W_{\mathrm{I}\eta lm}^{(p)*} \mathcal{S}_{lml'm'}^{(pp')} W_{\mathrm{I}\eta' l'm'}^{(p')} \tag{4.30}$$

and

$$\check{\sigma}_{\mathrm{S}\eta\eta'} = \frac{1}{k^2} \sum_{plm} \sum_{p'l'm'} \sum_{p''l''m''} \mathcal{S}_{lml'm'}^{(pp')*} W_{\mathrm{I}\eta l'm'}^{(p')*} \mathcal{S}_{lml''m''}^{(pp'')} W_{\mathrm{I}\eta' l''m''}^{(p'')} \, ,$$

which give the explicit relations between the transition matrix and the optical properties of the particle.

On account of (4.29) one should expect that the transition matrix has some symmetry properties that stem from the reciprocity theorem. In fact, with the help of (2.30) one gets

$$\mathcal{S}^{(p'p)}_{l'm'lm} = (-)^{m+m'} \mathcal{S}^{(pp')}_{l,-m;l',-m'} , \tag{4.31}$$

This symmetry property does not depend on the morphology of the particle, but the transition matrix has also symmetry properties that depend on the symmetry of the particle itself. As a representative example let us consider a scatterer with cylindrical symmetry: in fact, assuming the symmetry axis as the z axis, the transition matrix elements have the property [3]

$$\mathcal{S}^{(pp')}_{lml'm'} = \mathcal{S}^{(pp')}_{ll';m} \delta_{mm'} . \tag{4.32}$$

In particular, when the scatterer has spherical symmetry, (4.31) and (4.32) decree the complete diagonality of the transition matrix and the independence of m of its elements, i.e.,

$$\mathcal{S}^{(pp')}_{lml'm'} = \mathcal{S}^{(p)}_{l} \delta_{pp'} \delta_{ll'} \delta_{mm'} . \tag{4.33}$$

4.3.1 Transformation Properties of the Transition Matrix

The elements of the transition matrix depend on the frame of reference with respect to which the scattering process is described. This dependence will now be determined explicitly with the help of the transformation properties of the multipole fields under rotation [45]. To this end we recall that the transition matrix does not depend on the polarization so that, without loss of generality, we assume that the impinging radiation is polarized along $\hat{\boldsymbol{u}}_{\mathrm{I}\eta}$.

We choose into the laboratory a frame of reference, say Σ, and associate to the scattering particle a local frame of reference, say $\bar{\Sigma}$, whose orientation with respect to Σ is individuated by the Eulerian angles $\Theta \equiv (\alpha, \beta, \gamma)$ that describe the transformation of Σ into $\bar{\Sigma}$. As the same scattering process can be described in both frames of reference, we denote with an overbar all the quantities referred to $\bar{\Sigma}$ and, according to their definitions, they are considered as dependent on variables all referred to $\bar{\Sigma}$.

In the laboratory frame the polarized plane wave (4.13) impinges onto the particle and is transformed into the scattered wave (4.14). Of course, the relation among the amplitudes of the incident field and those of the scattered field are given by (4.28). The same scattering process, when described in the local reference frame $\bar{\Sigma}$, implies the expressions

$$\boldsymbol{E}_{\mathrm{I}\eta} = E_0 \sum_{plm} \bar{\boldsymbol{J}}^{(p)}_{lm} \bar{W}^{(p)}_{\mathrm{I}\eta lm} \tag{4.34}$$

for the incident field, and

$$\boldsymbol{E}_{\mathrm{S}\eta} = E_0 \sum_{plm} \bar{\boldsymbol{H}}^{(p)}_{lm} \bar{A}^{(p)}_{\eta lm} \tag{4.35}$$

for the scattered field. In $\bar{\Sigma}$ the relation among the amplitudes of the incident field and those of the scattered field is given by the analog of (4.28)

$$\bar{A}^{(p)}_{\eta lm} = \sum_{p'l'm'} \bar{\mathcal{S}}^{(pp')}_{lml'm'} \bar{W}^{(p')}_{\mathrm{I}\eta l'm'} \; . \tag{4.36}$$

The spherical multipole fields transform under rotation according to $\mathrm{D}^{(l)}$ [2, 7], so that the equations hold

$$\boldsymbol{J}^{(p)}_{lm} = \sum_{\mu} \bar{\boldsymbol{J}}^{(p)}_{l\mu} \mathcal{D}^{(l)}_{\mu m}(\Theta) \tag{4.37}$$

and

$$\bar{\boldsymbol{H}}^{(p)}_{l\mu} = \sum_{m} \boldsymbol{H}^{(p)}_{lm} \left[\mathrm{D}^{(l)}(\Theta)\right]^{-1}_{m\mu} \; . \tag{4.38}$$

Then, we substitute (4.37) into (4.13), (4.38) into (4.35) and compare the resulting equations with (4.34) and (4.14), respectively. Since the field strength cannot depend on the choice of the frame of reference, on account of the mutual independence of the spherical multipole fields, the equalities hold

$$\bar{W}^{(p)}_{\mathrm{I}\eta l\mu} = \sum_{m} \mathcal{D}^{(l)}_{\mu m}(\Theta) W^{(p)}_{\mathrm{I}\eta lm} \; , \tag{4.39}$$

which gives the transformation rule for the amplitudes of the incident field, and

$$A^{(p)}_{\eta lm} = \sum_{\mu} \left[\mathrm{D}^{(l)}(\Theta)\right]^{-1}_{m\mu} \bar{A}^{(p)}_{\eta l\mu} = \sum_{\mu} \mathcal{D}^{(l)*}_{\mu m}(\Theta) \bar{A}^{(p)}_{\eta l\mu} \; , \tag{4.40}$$

which gives the transformation rule for the amplitudes of the scattered field under rotation. At this stage, substitution in (4.40) of $\bar{A}$ as given by (4.36) and successive substitution into the resulting equation of (4.39) in place of $\bar{W}^{(p)}_{\mathrm{I}\eta l\mu}$ yields the result

$$A^{(p)}_{\eta lm} = \sum_{\mu\mu'} \sum_{p'l'm'} \mathcal{D}^{(l)*}_{\mu m}(\Theta) \bar{\mathcal{S}}^{(pp')}_{l\mu l'\mu'} \mathcal{D}^{(l')}_{\mu' m'}(\Theta) W^{(p')}_{\mathrm{I}\eta l'm'} \; . \tag{4.41}$$

Comparison of (4.41) and (4.28) then leads to

$$\mathcal{S}^{(pp')}_{lml'm'} = \sum_{\mu\mu'} \mathcal{D}^{(l)*}_{\mu m}(\Theta) \bar{\mathcal{S}}^{(pp')}_{l\mu l'\mu'} \mathcal{D}^{(l')}_{\mu' m'}(\Theta) \; , \tag{4.42}$$

which establishes the transformation rule of the transition matrix elements under rotation of the coordinate frame [46]. Note that transformation rules analogous to (4.37) and (4.38) hold true for the transverse harmonics $\boldsymbol{Z}^{(p)}_{lm}$ because, according to Sect. 1.7.2, they are irreducible spherical tensors of rank l.

4.4 Refractive Index of a Polydispersion of Particles

The results in Sect. 4.3.1 make us able to extend the definition of the refractive index of a dispersion to the case in which the component particles have the same morphology but are not all oriented alike [45]. As far as we know, using the transformation properties of the transition matrix for performing sums over the orientation of the particles has been proposed by Varadan [47], who also devised a specific formula for the description of light propagation through a dispersion of randomly oriented ellipsoids [48]. Nevertheless, a general study of Khlebtzov [49] proved the occurrence of some drawbacks in Varadan's approach and results, so that the first correct procedure turns out to be the one that we are going to describe [45]. We stress however, that the problem of the orientational average of all the quantities of interest in electromagnetic scattering has been successfully faced later in the framework of the Stokes parameters formalism [50–53].

Let us assign to each particle a local frame of reference, say $\bar{\Sigma}_\nu$ for the ν-th particle, whose axes are so chosen that, when two particles are brought into coincidence, their respective local frames of reference also coincide. The Eulerian angles that individuate the orientation of $\bar{\Sigma}_\nu$ with respect to Σ, to which the whole dispersion is referred, will be collectively indicated by the symbol Θ_ν. Now, letting N_ν be the number density of the particles whose orientation is Θ_ν, the refractive index of the dispersion reads

$$\mathcal{N}_{\eta\eta'} = \delta_{\eta\eta'} + \frac{2\pi}{k^2} \sum_\nu N_\nu f_{\nu,\eta\eta'}(\hat{\boldsymbol{k}}_\mathrm{I}, \hat{\boldsymbol{k}}_\mathrm{I}) \; , \tag{4.43}$$

where $f_{\nu,\eta\eta'}(\hat{\boldsymbol{k}}_\mathrm{I}, \hat{\boldsymbol{k}}_\mathrm{I})$ is the forward-scattering amplitude of the νth particle. Equation (4.43) seems to imply the need for calculating the scattering amplitudes of all the particles that differ in their orientation with respect to Σ before the sum can be performed. Nevertheless, if we substitute into (4.19) for the scattering amplitude the expression for the amplitudes of the scattered field given by (4.41), we get

$$\begin{aligned} f_{\nu,\eta\eta'}(\boldsymbol{k}_\mathrm{S}, \boldsymbol{k}_\mathrm{I}) = -\frac{\mathrm{i}}{4\pi k} \sum_{plm} \sum_{p'l'm'} \sum_{\mu\mu'} & W^{(p)*}_{\mathrm{S}\eta lm} \\ & \times \mathcal{D}^{(l)*}_{\mu m}(\Theta_\nu) \bar{\mathcal{S}}^{(pp')}_{l\mu l'\mu'} \mathcal{D}^{(l')}_{\mu' m'}(\Theta_\nu) W^{(p')}_{\mathrm{I}\eta' l' m'} \; . \end{aligned} \tag{4.44}$$

It is important to note that in the preceding equation the amplitudes W are given in the laboratory frame Σ, whereas the elements of the transition matrix are given in the local frame $\bar{\Sigma}_\nu$ and are, therefore, independent of the particle index ν.

At this stage it is reasonable to assume that, although we consider a tenuous dispersion, the number of the particles is still so large that the orientations can be considered as distributed with continuity. Therefore, the sum over ν can be substituted by an integral so that

$$\mathcal{N}_{\eta\eta'} = \delta_{\eta\eta'} - \frac{\mathrm{i}}{2k^3} \sum_{plm} \sum_{p'l'm'} \sum_{\mu\mu'} \int N(\Theta) W^{(p)*}_{\mathrm{I}\eta lm} \times \mathcal{D}^{(l)*}_{\mu m}(\Theta) \bar{\mathcal{S}}^{(pp')}_{l\mu l'\mu'} \mathcal{D}^{(l')}_{\mu' m'}(\Theta) W^{(p')}_{\mathrm{I}\eta' l' m'} \, \mathrm{d}\Theta \;, \tag{4.45}$$

where $N(\Theta)$ is the number density of the particles with orientation Θ. Ultimately, the integral to be performed has the form

$$\mathcal{I} = \int N(\Theta) \mathcal{D}^{(l)*}_{\mu m}(\Theta) \mathcal{D}^{(l')}_{\mu' m'}(\Theta) \, \mathrm{d}\Theta \;,$$

and in several cases can be performed analytically.

4.5 Orientational Averages

The need to perform orientational averages does not arise only when calculating the refractive index of a dispersion. Several quantities of actual interest must be calculated through averages over the orientation of the particles concerned [46]. Therefore, we give explicit formulas for calculating the orientational averages of the most important of them. To this end, let us put $N(\Theta) = N_0 P(\Theta)$, where N_0 is the number density of the particles. Then the orientational average of any quantity of interest, say Q, in a scattering problem reads

$$\langle Q \rangle = \int P(\Theta) Q(\Theta) \, \mathrm{d}\Theta \;.$$

Such an average can be performed with the help of (4.42) provided Q is expressed in terms of the transition matrix S and of the amplitudes W.

The elements of the Müller transformation matrix of a particle can be expressed in terms of the quantities

$$\mathcal{F}_{\eta\eta'\eta''\eta'''} = f^*_{\eta\eta'}(\hat{\boldsymbol{k}}_{\mathrm{S}}, \hat{\boldsymbol{k}}_{\mathrm{I}}) f_{\eta''\eta'''}(\hat{\boldsymbol{k}}_{\mathrm{S}}, \hat{\boldsymbol{k}}_{\mathrm{I}}) \;,$$

from which the co-polarized and the cross-polarized components of the scattered intensity can be obtained by putting $\eta'' = \eta$ and $\eta''' = \eta'$. In fact,

$$I_{\mathrm{S}\eta\eta'}(\hat{\boldsymbol{k}}_{\mathrm{S}}, \hat{\boldsymbol{k}}_{\mathrm{I}}) = |\boldsymbol{E}_{\mathrm{S}\,\eta'} \cdot \hat{\boldsymbol{u}}^*_{\mathrm{S}\,\eta}|^2 = \frac{I_{\mathrm{I}}}{r^2} |f_{\eta\eta'}(\hat{\boldsymbol{k}}_{\mathrm{S}}, \hat{\boldsymbol{k}}_{\mathrm{I}})|^2 \;, \tag{4.46}$$

where $I_{\mathrm{I}} = I_{\mathrm{I}\eta'\eta'}$, is the intensity for the case in which the incident wave is polarized along $\hat{\boldsymbol{u}}_{\mathrm{I}\eta'}$ and we consider the component of the scattered field polarized along $\hat{\boldsymbol{u}}_{\mathrm{S}\eta}$. As a result of the transformation properties of S matrix elements [see (4.42)] and on account of (4.29), the quantities to be integrated to get the required averages are actually products of up to four D matrix elements multiplied by the weight function $P(\Theta)$. Of course, the products of D matrix elements can be simplified by a wise use of the Clebsch–Gordan series [see (1.31)]. It is important to note that, when performing averages of

Table 4.1. Orientational weight functions

	$u(\alpha)$	$v(\beta)$	$w(\gamma)$
1	$1/2\pi$	$1/2$	$1/2\pi$
2	$1/2\pi$	$v(\beta)$	$1/2\pi$
3	$1/2\pi$	$\delta(\beta)/\sin\beta$	$1/2\pi$
4	$1/2\pi$	$\delta(\beta)/\sin\beta$	$\delta(\gamma)$
5	$1/2\pi$	$\delta(\beta-\pi/2)/\sin\beta$	$1/2\pi$

the Müller matrix elements and, in particular, of the intensity, it is necessary that the size of the whole dispersion be small in comparison with the distance of observation.

Hereafter, our attention will focus on a few cases of physical interest for which the averages can be performed analytically and thus explicit formulas can be given [46]. The appropriate weight functions have been factorized as

$$P(\Theta) = u(\alpha)v(\beta)w(\gamma)$$

and are listed in Table 3.1.

In Case 1 the particles are randomly oriented and the average is easily performed with the the help of the orthogonality properties (1.14) of the rotation matrix elements $\mathcal{D}^{(l)}_{\mu m}(\Theta)$. The result is

$$\langle f_{\eta'\eta}(\hat{\mathbf{k}}_{\mathrm{I}}, \hat{\mathbf{k}}_{\mathrm{I}})\rangle = c_{\mathrm{A}} \sum_{pp'} \sum_{l} \sum_{m\mu} \frac{1}{2l+1} W^{(p)*}_{\mathrm{I}\,\eta' lm} \bar{\mathcal{S}}^{(pp')}_{l\mu l\mu} W^{(p')}_{\mathrm{I}\,\eta lm}\,, \tag{4.47a}$$

$$\langle \check{\sigma}_{\mathrm{S}\eta'\eta}\rangle = c_{\mathrm{S}} \sum_{plm} \sum_{p'p''} \sum_{l'} \sum_{m'\mu} \frac{1}{2l'+1} \bar{\mathcal{S}}^{(pp')*}_{lml'\mu} W^{(p')*}_{\mathrm{I}\eta' l'm'} \bar{\mathcal{S}}^{(pp'')}_{lml'\mu} W^{(p'')}_{\mathrm{I}\eta l'm'}\,, \tag{4.47b}$$

$$\langle \mathcal{F}_{\eta\eta'\eta''\eta'''}\rangle = c_{\mathrm{I}} \sum_{L} \sum_{\mu\mu'} \frac{1}{2L+1} F^{*}_{\eta\eta' L\mu\mu'} F_{\eta''\eta''' L\mu\mu'}\,, \tag{4.47c}$$

where

$$c_{\mathrm{A}} = -\mathrm{i}/(4\pi k)\,, \quad c_{\mathrm{S}} = 1/k^2\,, \quad c_{\mathrm{I}} = 1/(4\pi k)^2\,.$$

In (4.47c) we define

$$\begin{aligned} F_{\eta'\eta L\mu\mu'} = &\sum_{pp'} \sum_{ll'} \sum_{mm'} \sum_{\bar{m}\bar{m}'} (-)^{m'-\bar{m}'} C(l,l',L;m,-m') C(l,l',L;\bar{m},-\bar{m}') \\ &\times W^{(p)*}_{\mathrm{S}\eta' lm} \bar{\mathcal{S}}^{(pp')}_{l\bar{m}l'\bar{m}'} W^{(p')}_{\mathrm{I}\eta l'm'} \delta_{\mu,m-m'} \delta_{\mu',\bar{m}-\bar{m}'}\,, \end{aligned} \tag{4.48}$$

where, as usual, the C's are Clebsch–Gordan coefficients [7]. Of course (4.47a) and (4.47b) can be simplified with the help of the sum rules (4.8), in case of the linear polarization basis, or (4.9), in case of the circular polarization basis.

In Case 2 the $\bar{z}$ axis of the local reference frame may form an angle β with the z axis of the laboratory frame with probability $v(\beta)$, whereas the particle is randomly oriented around the $\bar{z}$ axis which, in turn, may have any value of α for a given β. This kind of distribution is particularly significant when the $\bar{z}$ axis is chosen to be the highest-symmetry axis of the particle: the set of the orientations that can be assumed by the particle can be visualized by thinking of a spinning symmetrical top precessing around the vertical with its axis at an angle β with probability $v(\beta)$. The averages are

$$\langle f_{\eta'\eta}(\hat{\boldsymbol{k}}_{\mathrm{I}}, \hat{\boldsymbol{k}}_{\mathrm{I}}) \rangle = c_{\mathrm{A}} \sum_L F_{\eta'\eta L00} \mathcal{I}_L \,, \tag{4.49a}$$

$$\begin{aligned} \langle \check{\sigma}_{\mathrm{S}\eta'\eta} \rangle &= c_{\mathrm{S}} \sum_{plm} \sum_{p'p''} \sum_{l'l''} \sum_{m'\mu} \sum_L \bar{\mathcal{S}}^{(pp')*}_{lml'\mu} W^{(p')*}_{\mathrm{I}\eta' l'm'} \bar{\mathcal{S}}^{(pp'')}_{lml''\mu} W^{(p'')}_{\mathrm{I}\eta l''m'} \\ &\times (-)^{m'-\mu} C(l', l'', L; m', -m') C(l', l'', L; \mu, -\mu) \mathcal{I}_L \,, \end{aligned} \tag{4.49b}$$

$$\begin{aligned} \langle \mathcal{F}_{\eta\eta'\eta''\eta'''} \rangle &= c_{\mathrm{I}} \sum_{LL'} \sum_{\lambda} \sum_{\mu\mu'} F^*_{\eta\eta' L\mu\mu'} F_{\eta''\eta''' L'\mu\mu'} (-)^{\mu-\mu'} \\ &\times C(L, L', \lambda; \mu, -\mu) C(L, L', \lambda; \mu' - \mu') \mathcal{I}_\lambda \,, \end{aligned} \tag{4.49c}$$

where

$$\mathcal{I}_l = \int_0^\pi v(\beta) P_l(\cos\beta) \, \sin\beta \, d\beta \tag{4.50}$$

in which $P_l(\cos\beta)$ is the Legendre polynomial of degree l. In a sense, the preceding equations are the fundamental ones as regards orientational averages. In fact, by choosing $v(\beta) = 1/2$, (4.50) yields $\mathcal{I}_l = \delta_{l0}$ and one gets back the case of randomly oriented particles. Case 3 too can be obtained by choosing in (4.50) $v(\beta) = \delta(\beta)/\sin\beta$, which yields $\mathcal{I}_l = 1$ for any l. In fact, this choice implies that the $\bar{z}$ axis is parallel to the z axis but the particle is otherwise randomly oriented. Even in this case the set of the orientations can be visualized by thinking of a symmetrical top spinning with its axis vertical. In the next section we will show that this case occurs when prolate particles are oriented by the effect of a strong electrostatic field [42].

Case 4 differs from Case 3 only because the angle γ is held fixed. Nevertheless, a moment's thought will convince the reader that, according to the definition of the Eulerian angles, the actual orientational distribution does not differ from the one considered in Case 3. As a consequence, the formulas for these two cases are equivalent in spite of their formal differences. Since using either formulas is a matter of convenience in actual calculations, we report below the explicit formulas for Case 4. We have

$$\langle f_{\eta'\eta}(\hat{\boldsymbol{k}}_{\mathrm{I}}, \hat{\boldsymbol{k}}_{\mathrm{I}})\rangle = c_{\mathrm{A}} \sum_{pl} \sum_{p'l'} \sum_{m} W^{(p)*}_{\mathrm{I}\eta' lm} \bar{\mathcal{S}}^{(pp')}_{lml'm} W^{(p')}_{\mathrm{I}\eta l'm} , \tag{4.51a}$$

$$\langle \bar{\sigma}_{\mathrm{S}\eta'\eta}\rangle = c_{\mathrm{S}} \sum_{plm} \sum_{p'l'} \sum_{p''l''} \sum_{m'} \bar{\mathcal{S}}^{(pp')*}_{lml'm'} W^{(p')*}_{\mathrm{I}\eta' l'm'} \bar{\mathcal{S}}^{(pp'')}_{lml''m'} W^{(p'')}_{\mathrm{I}\eta l''m'} , \tag{4.51b}$$

$$\langle \mathcal{F}_{\eta\eta'\eta''\eta'''}\rangle = c_{\mathrm{I}} \sum_{mm'} \sum_{m''m'''} T^{*}_{\eta\eta' mm'} T_{\eta''\eta''' m''m'''} \delta_{m-m'-m''+m''',0} \tag{4.51c}$$

with

$$T_{\eta\eta' mm'} = \sum_{pl} \sum_{p'l'} W^{(p)*}_{\mathrm{S}\eta lm} \bar{\mathcal{S}}^{(pp')}_{lml'm'} W^{(p')}_{\mathrm{I}\eta' l'm'} .$$

It may be useful to remark that in (4.51c) the Kronecker delta comes from the integral

$$\mathcal{I}_\mu = \int_0^{2\pi} u(\alpha) \mathrm{e}^{\mathrm{i}\alpha\mu} \,\mathrm{d}\alpha .$$

In fact, when $u(\alpha) = 1/2\pi$, i.e., when angle α is randomly distributed, we get $\mathcal{I}_\mu = \delta_{\mu 0}$. When $u(\alpha) = \delta(\alpha)$, i.e., when angle α is fixed, we have $\mathcal{I}_\mu = 1$ and, consequently,

$$\langle \mathcal{F}_{\eta\eta'\eta''\eta'''}\rangle = \mathcal{F}_{\eta\eta'\eta''\eta'''} . \tag{4.52}$$

The latter is an obvious result that is due to the fact that no average over angle α has actually been performed.

A case somewhat complementary to Case 4 occurs when a strong electrostatic field acts on oblate particles, the effect being that the $\bar{z}$ axis lies in the xy plane of the laboratory frame where it can have any orientation [42]. At the same time the particle may have any angle γ around $\bar{z}$. This configuration, indicated as Case 5 in Table 4.1, is obtained by choosing $v(\beta) = \delta(\beta - \pi/2)/\sin\beta$ and thus getting $\mathcal{I}_l = P_l(0)$ from (4.50). In this case we can think of a symmetrical top spinning with its axis held horizontal.

When the scatterer has cylindrical symmetry around the $\bar{z}$ axis of $\bar{\Sigma}$, (4.32) implies that, according to (4.49) and (4.51), averaging is useless in Cases 3 and 4 because the scatterer is unaffected by any rotation around the cylindrical-symmetry axis.

Property (4.32) for the particles with cylindrical symmetry around the $\bar{z}$ axis can be used even in the other cases in Table 4.1 to simplify the formulas reported above. In fact, for Case 1 we have

$$\langle f_{\eta'\eta}(\hat{\boldsymbol{k}}_{\mathrm{I}}, \hat{\boldsymbol{k}}_{\mathrm{I}})\rangle = c_{\mathrm{A}} \sum_{pp'} \sum_{l} \sum_{m\mu} \frac{1}{2l+1} W^{(p)*}_{\mathrm{I}\eta' lm} \bar{\mathcal{S}}^{(pp')}_{ll;\mu} W^{(p')}_{\mathrm{I}\eta lm} , \tag{4.53a}$$

$$\langle \check{\sigma}_{\mathrm{S}\eta'\eta}\rangle = c_{\mathrm{S}} \sum_{pl} \sum_{p'p''} \sum_{l'} \sum_{m'\mu} \frac{1}{2l'+1} \bar{\mathcal{S}}^{(pp')*}_{ll';\mu} W^{(p')*}_{\mathrm{I}\eta' l'm'} \bar{\mathcal{S}}^{(pp'')}_{ll';\mu} W^{(p'')}_{\mathrm{I}\eta l'm'} , \tag{4.53b}$$

$$\langle \mathcal{F}_{\eta\eta'\eta''\eta'''}\rangle = c_{\mathrm{I}} \sum_{L} \sum_{\mu} \frac{1}{2L+1} F'^{*}_{\eta\eta' L\mu} F'_{\eta''\eta''' L\mu} , \tag{4.53c}$$

whereas for Case 2 we get

$$\begin{aligned}
\langle f_{\eta'\eta}(\hat{\boldsymbol{k}}_{\mathrm{I}},\hat{\boldsymbol{k}}_{\mathrm{I}})\rangle =& c_{\mathrm{A}}\sum_{L} F'_{\eta'\eta L0}\mathcal{I}_L \ , && (4.54\mathrm{a})\\
\langle \check{\sigma}_{\mathrm{S}\eta'\eta}\rangle =& c_{\mathrm{S}}\sum_{pl}\sum_{p'p''}\sum_{l'l''}\sum_{m'\mu}\sum_{L} \bar{\mathcal{S}}^{(pp')*}_{ll';\mu} W^{(p')*}_{\mathrm{I}\eta' l'm'} \bar{\mathcal{S}}^{(pp'')}_{ll'';\mu} W^{(p'')}_{\mathrm{I}\eta l''m'} \\
& \times(-)^{m'-\mu} C(l',l'',L;m',-m')C(l',l'',L;\mu,-\mu)\mathcal{I}_L \ , && (4.54\mathrm{b})\\
\langle \mathcal{F}_{\eta\eta'\eta''\eta'''}\rangle =& c_{\mathrm{I}}\sum_{LL'}\sum_{\lambda}\sum_{\mu} F'^{*}_{\eta\eta' L\mu} F'_{\eta''\eta''' L'\mu}(-)^{\mu} \\
& \times C(L,L',\lambda;\mu-\mu)C(L,L',\lambda;0,0)\mathcal{I}_\lambda \ . && (4.54\mathrm{c})
\end{aligned}$$

In (4.53c), (4.54a), and (4.54c) we define

$$\begin{aligned}
F'_{\eta'\eta L\mu} = & \sum_{pp'}\sum_{ll'}\sum_{mm'}\sum_{\bar{m}}(-)^{m'-\bar{m}} C(l,l',L;m,-m') \\
& \times C(l,l',L;\bar{m},-\bar{m}) W^{(p)*}_{\mathrm{S}\eta' lm} \bar{\mathcal{S}}^{(pp')}_{ll';\bar{m}} W^{(p')}_{\mathrm{I}\eta l'm'} \delta_{\mu,m-m'} \ .
\end{aligned} \tag{4.55}$$

The mutual relations among the cases discussed above show that the orientational averaging procedure that we presented in this section is endowed with internal coherence, even in limiting cases. We will return to the subject when discussing the results of specific applications of the theory. Here, we simply state that the procedures described so far can also be applied to the calculations of averages of the efficiencies and of the albedo. In fact, according to their customary definitions,

$$\langle Q_{\mathrm{T}}\rangle = \frac{\langle \sigma_{\mathrm{T}}\rangle}{\langle G\rangle}, \quad \langle Q_{\mathrm{S}}\rangle = \frac{\langle \sigma_{\mathrm{S}}\rangle}{\langle G\rangle}, \quad \langle Q_{\mathrm{A}}\rangle = \frac{\langle \sigma_{\mathrm{A}}\rangle}{\langle G\rangle},$$

and

$$\langle \varpi\rangle = \frac{\langle \sigma_{\mathrm{S}}\rangle}{\langle \sigma_{\mathrm{T}}\rangle} \ .$$

4.6 Effect of an Electrostatic Field

A typical case in which the orientational distribution of a dispersion of particles is nonrandom occurs when the ensemble is subject to the effect of an electrostatic field. In fact, in thermal equilibrium and in the absence of any applied field, the particles of a dispersion are randomly distributed both in space and orientation. Therefore, the dispersion on the whole is isotropic and cannot show either birefringence or linear dichroism. Of course, when an electrostatic field is applied the distribution becomes nonrandom, and the optical properties of the dispersion are bound to change [42]. To give a quantitative content to this intuitive statement, we assume that the particles of interest are uncharged so that an electrostatic field has no effect on their space distribution. We further assume that the particles are identical to each other and that the whole dispersion is in thermal equilibrium at the temperature T. When an electrostatic field is applied the orientational distribution function $P(\Theta)$ can be assumed to be [54]

$$P(\Theta) = \frac{\exp[-U(\Theta)/k_B T]}{Z} ,$$

where $U(\Theta)$ is the interaction energy that, as explicitly indicated, depends on the orientation of the particles, k_B is the Boltzmann constant and

$$Z = \int \exp[-U(\Theta)/k_B T] \, \mathrm{d}\Theta .$$

In general, by indicating with x_1, x_2, and x_3 the rectangular coordinates in the laboratory reference frame Σ, the interaction energy $U(\Theta)$ can be written as [4]

$$U(\Theta) = -\tfrac{1}{2} \sum_{ij} \alpha_{ij} E_i E_j ,$$

where α_{ij} are the components of the polarizability tensor of the particle. By choosing the x_3 axis of Σ to be parallel to the electrostatic field, the interaction energy simplifies into

$$U(\Theta) = -\tfrac{1}{2} \alpha_{33} E^2 .$$

We now attach to the particle a local frame of reference $\bar{\Sigma}$ whose coordinates are transformed into those of Σ by the matrix R. Then we can write

$$\alpha_{ij} = \sum_{lk} R_{li} R_{kj} \bar{\alpha}_{lk} ,$$

where,

$$\bar{\alpha}_{lk} = \bar{\alpha}_k \delta_{lk} ,$$

provided the axes of $\bar{\Sigma}$ are the principal axes of the polarizability tensor.

Hereafter, we restrict our study to the case in which

$$\bar{\alpha}_1 = \bar{\alpha}_2 = \alpha_\perp, \qquad \bar{\alpha}_3 = \alpha_\parallel , \tag{4.56}$$

which is typical not only of axially symmetric particles but also of particles with an appropriate symmetry group. In terms of the Eulerian angles, the relation between α_{33} and the $\bar{\alpha}_{ij}$ is [7]

$$\alpha_{33} = \sum_k R_{k3}^2 \bar{\alpha}_k = \bar{\alpha}_1 \sin^2\beta \cos^2\gamma + \bar{\alpha}_2 \sin^2\beta \sin^2\gamma$$
$$+ \bar{\alpha}_3 \cos^2\beta = \alpha_\perp + (\alpha_\parallel - \alpha_\perp) \cos^2\beta .$$

Therefore, by defining

$$u = (\alpha_{\|} - \alpha_{\perp})E^2/2k_B T \tag{4.57}$$

and

$$I_0 = \int_0^{\pi} \exp(u \cos^2 \beta) \sin \beta \, \mathrm{d}\beta \; ,$$

the orientational distribution function results

$$P(\Theta) = \frac{1}{4\pi^2} v(\beta) = \frac{1}{4\pi^2 I_0} \exp(u \cos^2 \beta) \; . \tag{4.58}$$

The latter equation shows that for axially symmetric particles $P(\Theta)$ is a function of β only. Furthermore, according to (4.57) and (4.58), the effect of the electrostatic field will be the more considerable the more $\alpha_{\|}$ and $\alpha_{\perp}$ are different.

At this stage the orientational average of the forward scattering amplitude can be performed through (4.54a), or (4.49a), and (4.50).

4.6.1 Polarizability of a Particle of Arbitrary Shape

The usefulness of the results of the preceding section depends on the knowledge of the polarizability of the particles of interest. The literature reports a few expressions for the polarizability of objects of simple shape, e.g., the Clausius–Mossotti and the Lorentz–Lorenz formulas for spheres [4], and the expression devised by Clark Jones for ellipsoids and disks [55]. On the other hand, the polarizability has been widely used in the framework of the Rayleigh scattering approximation (RSA) that assumes that the scattered field from a small sphere is well approximated by the field of the dipole moment that is induced by the incident electromagnetic wave [5]. The relation between the incident field and the induced dipole is, indeed, given through the polarizability although the latter, at least in principle, is a static and not a dynamic quantity.

The preceding considerations will presently be extended by working out a general relation between the polarizability tensor and the transition matrix of a particle of arbitrary shape [42]. We start by recalling that, in the long-wavelength limit, the field that is scattered by a particle is well approximated by the field of the electric dipole that is induced by the incident wave and can, therefore, be written as [4]

$$\begin{aligned} \boldsymbol{E}_{\mathrm{S}} &\approx \frac{\exp(\mathrm{i}kr)}{r} k^2 (\hat{\boldsymbol{k}}_{\mathrm{S}} \times \boldsymbol{p}) \times \hat{\boldsymbol{k}}_{\mathrm{S}} \\ &= \frac{\exp(\mathrm{i}kr)}{r} k^2 [\boldsymbol{p} - (\boldsymbol{p} \cdot \hat{\boldsymbol{k}}_{\mathrm{S}}) \hat{\boldsymbol{k}}_{\mathrm{S}}] \; , \end{aligned} \tag{4.59}$$

where $\boldsymbol{p}$ is the induced electric dipole moment. Here and hereafter we use the symbol $\approx$ to denote the approximate equalities that become rigorous as

$k \to 0$. Thus, if k is sufficiently small, (2.5) and (4.59) become comparable and yield the equality

$$E_0 \boldsymbol{f} \approx k^2 [\boldsymbol{p} - (\boldsymbol{p} \cdot \hat{\boldsymbol{k}}_{\mathrm{S}}) \hat{\boldsymbol{k}}_{\mathrm{S}}] \tag{4.60}$$

that relates the dynamic and the static features of the scattering particle. At this stage, we substitute into (4.60) the expression of $\boldsymbol{f}$ given by (4.17), dot multiply both sides of the resulting equation by the transverse harmonics $\boldsymbol{Z}_{lm}^{(p)*}(\hat{\boldsymbol{k}}_{\mathrm{S}})$ and integrate over the solid angle. We get

$$\begin{aligned} E_0 A_{lm}^{(1)} &= \mathrm{i}^{l+1} k E_0 \int \boldsymbol{f} \cdot \boldsymbol{Z}_{lm}^{(1)*}(\hat{\boldsymbol{k}}_{\mathrm{S}}) \, \mathrm{d}\Omega_{\mathrm{S}} \\ &\approx \mathrm{i}^{l+1} k^3 \boldsymbol{p} \cdot \int \boldsymbol{Z}_{lm}^{(1)*}(\hat{\boldsymbol{k}}_{\mathrm{S}}) \, \mathrm{d}\Omega_{\mathrm{S}} = 0 \end{aligned} \tag{4.61}$$

and

$$E_0 A_{lm}^{(2)} = -\mathrm{i}^l k E_0 \int \boldsymbol{f} \cdot \boldsymbol{Z}_{lm}^{(2)*}(\hat{\boldsymbol{k}}_{\mathrm{S}}) \, \mathrm{d}\Omega_{\mathrm{S}} \approx -\mathrm{i}^l k^3 \boldsymbol{p} \cdot \int \boldsymbol{Z}_{lm}^{(2)*}(\hat{\boldsymbol{k}}_{\mathrm{S}}) \, \mathrm{d}\Omega_{\mathrm{S}} \ . \tag{4.62}$$

The integral in (4.62) can be evaluated with the help of (1.24), (1.52), (1.25), and Table 1.1. The result is

$$E_0 A_{lm}^{(2)} \approx k^3 \sqrt{\frac{8\pi}{3}} \, (-)^m p_{-m} \delta_{l1} \ . \tag{4.63}$$

Clearly, (4.61) and (4.63) establish an extension of the RSA to particles of arbitrary shape as they give the amplitudes of the scattered field in terms of the induced dipole moment.

To relate the amplitudes $A_{1m}^{(2)}$ to the polarizability of the particle, we write the relation between the spherical components of the incident field and those of the induced dipole as

$$p_m = \sum_{m'} \alpha_{mm'} E_{m'} \ .$$

Since the origin of the frame of reference has been chosen within the scattering particle, the incident plane wave reduces to its amplitude and we can write

$$p_m = \sum_{m'} \alpha_{mm'} \hat{e}_{m'} E_0 \ ,$$

where $\hat{e}_{m'}$ denotes the spherical components of the polarization vector of the incident wave. With the help of the identity

$$\hat{e}_m = \hat{\boldsymbol{e}} \cdot \boldsymbol{\xi}_m = [(\hat{\boldsymbol{k}}_{\mathrm{I}} \times \hat{\boldsymbol{e}}) \times \hat{\boldsymbol{k}}_{\mathrm{I}}] \cdot \boldsymbol{\xi}_m = (\hat{\boldsymbol{k}}_{\mathrm{I}} \times \hat{\boldsymbol{e}}) \cdot (\hat{\boldsymbol{k}}_{\mathrm{I}} \times \boldsymbol{\xi}_m) \ ,$$

and of (1.24), (1.25), (1.52), (1.55), (4.4) a straightforward calculation gives the final result

$$A^{(2)}_{1m} \approx -\mathrm{i}k^3 \frac{8\pi}{3} \sum_{m'} (-)^{m+m'} \alpha_{-m,\,-m'} (\hat{\boldsymbol{k}}_\mathrm{I} \times \hat{\boldsymbol{e}}) \cdot \boldsymbol{X}^*_{1m'}(\hat{\boldsymbol{k}}_\mathrm{I})$$
$$= \frac{2}{3} ik^3 \sum_{m'} (-)^{m+m'} \alpha_{-m,\,-m'} W^{(2)}_{1m'}(\hat{\boldsymbol{e}}, \hat{\boldsymbol{k}}_\mathrm{I}) \,. \tag{4.64}$$

The preceding equation is the required relation between the polarizability of a particle of arbitrary shape and the electric dipole amplitudes of the scattered field. By substituting $A^{(2)}_{1m}$ as given by (4.28) into (4.64), one gets the required relation between the components of the polarizability of a particle of arbitrary shape and the elements of its transition matrix in the form

$$\alpha_{-m,\,-m'} = -\frac{3}{2} \mathrm{i} (-)^{m+m'} \lim_{k \to 0} \frac{1}{k^3} \mathcal{S}^{(2\,2)}_{1m1m'} \,. \tag{4.65}$$

We stress that it is just the limit for $k \to 0$ that transforms the approximate equality (4.64) into the rigorous equation (4.65).

By choosing the axes of the reference frame so as to diagonalize the Cartesian representation of the polarization tensor the corresponding spherical representation takes on the form [7]

$$\bar{\alpha}_{mm'} = \frac{1}{2} \begin{pmatrix} \bar{\alpha}_1 + \bar{\alpha}_2 & 0 & \bar{\alpha}_2 - \bar{\alpha}_1 \\ 0 & 2\bar{\alpha}_3 & 0 \\ \bar{\alpha}_2 - \bar{\alpha}_1 & 0 & \bar{\alpha}_1 + \bar{\alpha}_2 \end{pmatrix} \tag{4.66}$$

so that (4.65) simplifies into

$$\bar{\alpha}_{-m,-m} = -\frac{3}{2} \mathrm{i} \lim_{k \to 0} \frac{1}{k^3} \bar{\mathcal{S}}^{(2\,2)}_{1m1m} \tag{4.67}$$

for all the particles such that $\bar{\alpha}_1 = \bar{\alpha}_2$. The preceding equation applies, in particular, to axially symmetric particles, provided their high-symmetry axis coincides with the $\bar{z}$ axis. In this case one also has $\bar{\alpha}_{-1,-1} = \bar{\alpha}_{11}$ and, since these latter quantities characterize the polarizability in the plane that is orthogonal to the cylindrical axis, we can put

$$\bar{\alpha}_{-1,-1} = \bar{\alpha}_{11} = \alpha_\perp \,, \quad \bar{\alpha}_0 = \alpha_\parallel \,. \tag{4.68}$$

A look to (4.66) shows that $\alpha_\parallel$ and $\alpha_\perp$ as defined above coincide with the corresponding quantities in (4.56).

In the next chapter we will show that, for small spheres, (4.65) reduces to the well known form that is used in the Rayleigh approximation.

4.7 Effect of the Diffusive Motion

The orientational distribution functions that we have considered so far are, in a sense, static as none of them allows for the motion of the particles. Nevertheless, in some cases the diffusion motion may affect the intensity of the field scattered by the whole dispersion. When this happens we have to deal with a dynamic light-scattering process and for its description we have to consider both the electromagnetic and the statistical behavior of the dispersion, including the motion of the particles concerned. The electromagnetic and the statistical aspects of dynamic light scattering are connected by the Wiener–Kinchin theorem that relates the electromagnetic scattering properties and the diffusive motion of the particles. More precisely, the Wiener–Kinchin theorem [56] relates the intensity of the light scattered by a dispersion of particles to the ensemble average of the time autocorrelation function of the field scattered by the individual objects. As a consequence, a reliable interpretation of the observed spectra requires a good description of the scattering properties of the particles involved and a reliable estimate of the dynamical distribution function, both in space and orientation, of the particles themselves. In this section we focus on the averages of the dynamic distribution function by the methods described earlier in this chapter. The calculation of the scattering properties of the particles is deferred to Chap. 7.

Let a polarized plane wave of wavevector $\boldsymbol{k}_{\mathrm{I}}$ and (circular) frequency ω_0 propagating in vacuo ($n = 1$) be scattered by an assembly of particles. We refer the scattering process to some plane chosen once for all as the plane of reference, so that the polarization both of the incident and the scattered field can be analyzed, e.g., as we did in Sect. 2.7.1 with respect to the plane of scattering. Accordingly, we denote with

$$\bar{E}_{\mathrm{S}\eta\eta'} = \bar{\boldsymbol{E}}_{\mathrm{S}\eta'} \cdot \hat{\boldsymbol{u}}^*_{\mathrm{S}\eta}$$

the component polarized along $\hat{\boldsymbol{u}}_{\mathrm{S}\eta}$ of the field $\bar{\boldsymbol{E}}_{\mathrm{S}\eta'}$ scattered by the whole assembly when the incident field is polarized along $\hat{\boldsymbol{u}}_{\mathrm{I}\eta'}$. The spectral scattered intensity is then

$$I_{\mathrm{S}\eta\eta'}(\boldsymbol{r},\omega) = \lim_{T\to\infty} \frac{1}{T} \bar{E}^*_{\mathrm{S}\eta\eta'}(\boldsymbol{r},\omega;T)\bar{E}_{\mathrm{S}\eta\eta'}(\boldsymbol{r},\omega;T) \ ,$$

where

$$\bar{E}_{\mathrm{S}\eta\eta'}(\boldsymbol{r},\omega;T) = \int_{-\infty}^{\infty} \bar{E}_{\mathrm{S}\eta\eta'}(\boldsymbol{r},t;T) \exp(\mathrm{i}\omega t)\mathrm{d}t$$

with

$$\bar{E}_{\mathrm{S}\eta\eta'}(\boldsymbol{r},t;T) = \begin{cases} \bar{E}_{\mathrm{S}\eta\eta'}(\boldsymbol{r},t) & \text{when } |t| < T \\ 0 & \text{when } |t| > T \end{cases} .$$

Provided the number density of the dispersion is low enough, the scattered field can be given as the superposition of the fields scattered by the individual particles. For a particle at the origin, we write

$$E_{\mathrm{S}\eta\eta'}(\boldsymbol{r},\omega) = E_0 \frac{\exp(\mathrm{i}kr)}{r} f_{\eta\eta'}(\hat{\boldsymbol{k}}_{\mathrm{S}}, \hat{\boldsymbol{k}}_{\mathrm{I}}, \omega, \Theta) \ ,$$

where $f_{\eta\eta'}$ bears the additional arguments ω and Θ to recall that the scattering amplitude depends also on the frequency of the incident wave and on the orientation of the scattering particle. At this stage, the Wiener–Kinchin theorem relates the scattered intensity and the scattering amplitude in the form

$$I_{\mathrm{S}\eta\eta'}(\boldsymbol{r},\omega) = \frac{N|E_0|^2}{r^2} \int \langle f^*_{\eta\eta'}(\hat{\boldsymbol{k}}_{\mathrm{S}}, \hat{\boldsymbol{k}}_{\mathrm{I}}, \omega, \Theta_0) f_{\eta\eta'}(\hat{\boldsymbol{k}}_{\mathrm{S}}, \hat{\boldsymbol{k}}_{\mathrm{I}}, \omega, \Theta)\rangle \\ \times F(\boldsymbol{k}_{\mathrm{I}} - \boldsymbol{k}_{\mathrm{S}}, \tau) \exp[\mathrm{i}(\omega - \omega_0)\tau] \mathrm{d}\tau \;, \tag{4.69}$$

where N is the number of the particles, $\Theta_0 = \Theta(0)$ is the initial orientation, $\Theta = \Theta(\tau)$ is the orientation at time τ, and $\langle \ldots \rangle$ denotes the average over the orientations on the customary assumption of no correlation existing between the position and orientation of the particles. In turn, $F(\boldsymbol{k}_{\mathrm{I}} - \boldsymbol{k}_{\mathrm{S}}, \tau)$ is the dynamic structure factor of the dispersion that can be defined as

$$F(\boldsymbol{K},\tau) = \frac{1}{N} \int \mathrm{d}\boldsymbol{r}' \int \mathrm{d}\boldsymbol{R} \exp(\mathrm{i}\boldsymbol{K}\cdot\boldsymbol{R}) \langle n(\boldsymbol{r}'+\boldsymbol{R},\tau) n(\boldsymbol{r}',0)\rangle \;,$$

where

$$n(\boldsymbol{r},t) = \sum_{i=1}^{N} \delta\big(\boldsymbol{r} - \boldsymbol{R}_i(t)\big)$$

is the number density of a dispersion of identical particles with instantaneous vector position $\boldsymbol{R}_i(t)$.

Equation (4.69) is the most general relation among the quantities of interest in an actual experiment of dynamic light scattering, viz., the spectral intensity and the time-dependent autocorrelation function of the scattered field. Equation (4.69) differs from that reported, e.g. by Reichl [56], because the latter author assumes the particles to be so small that their electromagnetic response can be described by their polarizability tensor. On the contrary, we describe the scattering properties of the particles through their scattering amplitude matrix so that we have no need to assume that the particles concerned are small with respect to the wavelength. Anyway, in order to give a reliable description of the orientational distribution function of the particles, we assume that they are axially symmetric. In fact, such a kind of particles has the dynamical features of a symmetrical top so that the appropriate weight function has the form [57]

$$P(\Theta,\tau;\Theta_0) = \sum_{LKM} \frac{2L+1}{(8\pi^2)^2} \mathcal{D}^{(L)}_{KM}(\Theta_0) \mathcal{D}^{(L)*}_{KM}(\Theta) \exp(-\nu_{LK}\tau) \;,$$

with

$$\nu_{LK} = D_\perp L(L+1) + (D_\parallel - D_\perp)K^2 \;,$$

where $D_\perp$ and $D_\parallel$ are the rotational diffusion coefficients. As a result, the orientational average

$$\langle f^*_{\eta\eta'}(\Theta_0) f_{\eta\eta'}(\Theta)\rangle = \int \mathrm{d}\Theta_0\, \mathrm{d}\Theta\, f^*_{\eta\eta'}(\Theta_0) f_{\eta\eta'}(\Theta) P(\Theta,\tau;\Theta_0) \;,$$

can be performed analytically because it implies the well known integrals (1.32). Therefore, the final result is [58]

$$\langle f^*_{\eta\eta'}(\Theta_0) f_{\eta\eta'}(\Theta)\rangle = \frac{1}{16\pi^2 k^2} \sum_L R_{\eta\eta'\,L} \exp\left[-D_\perp L(L+1)\tau\right] , \qquad (4.70)$$

with

$$R_{\eta\eta'\,L} = (2L+1) \sum_M |F_{\eta\eta'\,LM}|^2 , \qquad (4.71)$$

where

$$\begin{aligned} F_{\eta\eta'\,LM} = & \sum_{plm} \sum_{p'l'm'} \sum_{\mu} \frac{1}{2l+1} C(L,l,l';0,\mu,\mu) \\ & \times C(L,l,l';M,m,m') W^{(p)*}_{\mathrm{S}\eta lm} \bar{\mathcal{S}}^{(pp')}_{ll';\mu} W^{(p')}_{\mathrm{I}\eta' l'm'} . \end{aligned} \qquad (4.72)$$

It may be worth recalling that the configurational average in (4.70), when multiplied by the dynamical structure factor, is just the time-dependent autocorrelation function that is the quantity which is actually measured in photon correlation experiments. We also note that, according to (4.69) the spectral intensity turns out to have an exponential-like behavior as required by statistical physics. More precisely, each of the exponentials has its own amplitude that can be calculated from the knowledge of the transition matrix of the particles. Note that the amplitude of each exponential depends on the polarization and on the angle of scattering, as is evident from the expression of $F_{\eta\eta' LM}$ above. To this angular dependence, one should superpose the contribution from the dynamic structure factor that is customarily assumed to have the form

$$F(\boldsymbol{k}_\mathrm{I} - \boldsymbol{k}_\mathrm{S}, \tau) \propto \exp(-q^2 D\tau) ,$$

with

$$q = |\boldsymbol{k}_\mathrm{I} - \boldsymbol{k}_\mathrm{S}| \approx 2k \sin(\Phi/2) ,$$

where Φ is the angle of scattering and D is the translational diffusion coefficient.

We can thus conclude that the averaging procedures that we have described in this chapter are also suitable for dealing with cases in which the motion of the particles need to be taken into account.

4.8 Radiation Force on Nonspherical Particles

In Sect. 3.2.1 it has been shown that, as a result of the conservation of linear momentum, the interaction of radiation with particles implies that the latter experience a force. In the present section we discuss in some detail how this force can be dealt with in the framework of the transition matrix approach for particles of arbitrary shape. We also deal with the problem of averaging over the orientation of the particles taking advantage of the theory developed in the preceding sections [59]. Nevertheless, we stress that averaging on the response of individual particles to the electromagnetic field may easily become meaningless, since we do not always have a collective dynamical behavior that is relevant for the study at hand.

Let us consider the radiation force produced by a monochromatic plane wave. According to (3.16) we need the asymmetry parameters (3.17) that require the scattering cross section σ_{S}, which is given by (4.21), and the differential scattering cross section $\mathrm{d}\sigma_{\mathrm{S}}/\mathrm{d}\Omega$ which is given in terms of the scattering amplitude by (4.26). Another required ingredient is the dot product $\hat{\boldsymbol{k}}_{\mathrm{S}} \cdot \hat{\boldsymbol{v}}_{\zeta}$ which, by exploiting (1.23) and (1.24), can be expressed in terms of spherical components as

$$\hat{\boldsymbol{k}}_{\mathrm{S}} \cdot \hat{\boldsymbol{v}}_{\zeta} = \frac{4\pi}{3} \sum_{\mu} Y_{1\mu}(\hat{\boldsymbol{k}}_{\mathrm{S}}) Y^*_{1\mu}(\hat{\boldsymbol{v}}_{\zeta}) \ .$$

The differential scattering cross section of the particle, with the help of (4.26) and (4.29) turns out to be

$$\frac{\mathrm{d}\sigma_{\mathrm{S}}}{\mathrm{d}\Omega} = \frac{1}{I_{\mathrm{I}}} c_{\mathrm{I}} \sum_{\eta\eta'} \mathrm{Re}\Big(I_{\mathrm{I}\eta\eta'} \sum_{\bar{\eta}} \sum_{plm} \sum_{p'l'm'} W^{(p)}_{\mathrm{S}\bar{\eta}lm} W^{(p')*}_{\mathrm{S}\bar{\eta}l'm'} A^{(p)*}_{\eta lm} A^{(p')}_{\eta' l'm'} \Big) \ ,$$

where $c_{\mathrm{I}} = 1/(4\pi k)^2$. Therefore, we need

$$K^{(pp')}_{\mu;lml'm'} = \sum_{\bar{\eta}} \int Y_{1\mu}(\hat{\boldsymbol{k}}_{\mathrm{S}}) W^{(p)}_{\mathrm{S}\bar{\eta}lm} W^{(p')*}_{\mathrm{S}\bar{\eta}l'm'} \, \mathrm{d}\Omega_{\mathrm{S}} \ ,$$

which can be calculated by expanding all the functions in terms of functions in the frame of reference with $\hat{\boldsymbol{k}}_{\mathrm{S}} = \hat{\boldsymbol{e}}_z$. With the help of (4.39) and (1.17) we get

$$K^{(pp')}_{\mu;lml'm'} = \sum_{\bar{\eta}\bar{\mu}} \sum_{\bar{m}\bar{m}'} W^{(p)}_{\mathrm{Z}\bar{\eta}l\bar{m}} W^{(p')*}_{\mathrm{Z}\bar{\eta}l'\bar{m}'} Y_{\mathrm{Z}1\bar{\mu}} \frac{1}{2\pi} \int \mathcal{D}^{(1)}_{\bar{\mu}\mu} \mathcal{D}^{(l)*}_{\bar{m}m} \mathcal{D}^{(l')}_{\bar{m}'m'} \, \mathrm{d}\Theta \ ,$$

where the integral is now performed over the full range of the Eulerian angles, the factor $1/2\pi$ compensating for the integration over γ, and we introduced the notation

$$W^{(p)}_{\mathrm{Z}\bar{\eta}lm} = W^{(p)}_{lm}(\hat{\boldsymbol{u}}_{\mathrm{S}\bar{\eta}}, \hat{\boldsymbol{k}}_{\mathrm{S}} = \hat{\boldsymbol{e}}_z) \quad \text{and} \quad Y_{\mathrm{Z}1\bar{\mu}} = Y_{1\bar{\mu}}(\hat{\boldsymbol{e}}_z) = \sqrt{\frac{3}{4\pi}} \delta_{\bar{\mu}0} \ .$$

The integration is easily performed with the help of (1.32) with the result

$$\begin{aligned} K^{(pp')}_{\mu lml'm'} = & \sum_{\bar{\eta}} \sum_{\bar{m}'} W^{(p)}_{\mathrm{Z}\bar{\eta}l\bar{m}'} W^{(p')*}_{\mathrm{Z}\bar{\eta}l'\bar{m}'} \sqrt{\frac{3}{4\pi}} \\ & \times \frac{4\pi}{2l+1} C(1,l',l;0,\bar{m}',\bar{m}') C(1,l',l;\mu,m',m) \ . \end{aligned}$$

Further algebraic manipulations are more easily performed, without loss of generality, by operating in the circular polarization basis. In fact, on account of (4.11), we get

$$K^{(pp')}_{\mu;lml'm'} = \sqrt{\frac{3}{4\pi}} C(1, l', l; \mu, m', m) \mathrm{i}^{p'-p} O^{(pp')}_{ll'} \ ,$$

where

$$\begin{aligned}
O^{(pp')}_{ll} &= -\frac{1}{\sqrt{l(l+1)}}(1-\delta_{pp'}) \ , \\
O^{(pp')}_{l,l-1} &= \sqrt{\frac{(l-1)(l+1)}{l(2l+1)}}\delta_{pp'} \ , \\
O^{(pp')}_{l,l+1} &= -\sqrt{\frac{l(l+2)}{(l+1)(2l+1)}}\delta_{pp'} \ .
\end{aligned}$$

4.8.1 Orientational Averages of Asymmetry Parameters

The results obtained in the preceding section stem from the implicit assumption that the orientation of the particle with respect to the incident field is known. As this is rather unlikely to happen when the radiation field interacts with a dispersion of particles we need to consider orientational averages.

Let us refer a dispersion of particles with the same morphology to a frame of reference Σ fixed in the laboratory and, according to Sect. 4.5, let us associate to each particle a local frame of reference, say $\bar{\Sigma}_\nu$ for the ν-th particle. Of course, the whole theory in the preceding section can be expressed in the local frame of the ν-th particle by giving the amplitudes $\bar{A}^{(p)}_{\eta lm}$ in terms of the transition matrix calculated in the frame $\bar{\Sigma}_\nu$. Then, we can write

$$\sigma_{\mathrm{S}} g_\zeta = \frac{c_{\mathrm{I}}}{I_{\mathrm{I}}} \sum_{\eta\eta'} \mathrm{Re}\Bigg(I_{\mathrm{I}\eta\eta'} \sum_{plm} \sum_{p'l'm'} \sum_{\bar{p}\bar{l}\bar{m}} \sum_{\bar{p}'\bar{l}'\bar{m}'} \bar{\mathcal{S}}^{(p\bar{p})*}_{lm\bar{l}\bar{m}} \bar{\mathcal{S}}^{(p'\bar{p}')*}_{l'm'\bar{l}'\bar{m}'} \times \bar{W}^{(\bar{p})*}_{\mathrm{I}\eta\bar{l}\bar{m}} \bar{W}^{(\bar{p}')}_{\mathrm{I}\eta'\bar{l}'\bar{m}'} \frac{4\pi}{3} \sum_{\mu} \bar{Y}^*_{1\mu}(\hat{\boldsymbol{v}}_\zeta) K^{(pp')}_{\mu lml'm'} \Bigg) \ ,$$

where the quantities calculated in $\bar{\Sigma}_\nu$ are indicated by an overbar. Note that K bears not an overbar because it does not depend on the orientation of the particle. We can exploit (4.39) and (1.17) to transform the amplitudes $\bar{W}^{(p)}_{\mathrm{I}\eta lm}$ and the spherical harmonic $\bar{Y}^*_{1\mu}(\hat{\boldsymbol{v}}_\zeta)$ into the laboratory frame. Once this has been done we see that the only quantity that depends on the orientation of the particle is

$$\mathcal{D}^{(1\bar{l}'\bar{l})}_{\mu\mu'\bar{m}'\bar{\mu}'\bar{m}\bar{\mu}}(\Theta) = \mathcal{D}^{(1)}_{\mu\mu'} \mathcal{D}^{(\bar{l}')}_{\bar{m}'\bar{\mu}'} \mathcal{D}^{(\bar{l})*}_{\bar{m}\bar{\mu}}$$

that is thus the only quantity that needs to be averaged. Therefore, for a dispersion of N_0 particles we must calculate

$$\left\langle \mathcal{D}^{(1\bar{l}'\bar{l})}_{\mu\mu'\bar{m}'\bar{\mu}'\bar{m}\bar{\mu}}(\Theta) \right\rangle = \int P(\Theta)\mathcal{D}^{(1)}_{\mu\mu'}\mathcal{D}^{(\bar{l}')}_{\bar{m}'\bar{\mu}'}\mathcal{D}^{(\bar{l})*}_{\bar{m}\bar{\mu}}\,\mathrm{d}\Theta \; ,$$

where $P(\Theta)$ is the probability density that a particle have orientation Θ. Hereafter we focus on the physically significant cases of random orientation (Case 1 in Table 4.1) and orientation with the $\bar{z}$ axis of the local frame parallel to the z axis of Σ (Case 3 in Table 4.1) to which we will refer as axial average.

In case of *random* orientation we get at once

$$\left\langle \mathcal{D}^{(1\bar{l}'\bar{l})}_{\mu\mu'\bar{m}'\bar{\mu}'\bar{m}\bar{\mu}}(\Theta) \right\rangle = \frac{1}{2\bar{l}+1} C(1,\bar{l}',\bar{l};\mu,\bar{m}',\bar{m})C(1,\bar{l}',\bar{l};\mu',\bar{\mu}',\bar{\mu}) \; ,$$

so that

$$\begin{aligned}\langle \sigma_{\mathrm{S}} g_\zeta \rangle = \frac{c_{\mathrm{I}}}{I_{\mathrm{I}}} \sum_{\eta\eta'} \mathrm{Re}\Big(I_{\mathrm{I}\eta\eta'} \sum_{plm} \sum_{p'l'm'} \sum_{\bar{p}\bar{l}\bar{m}} \sum_{\bar{p}'\bar{l}'\bar{m}'} \bar{\mathcal{S}}^{(p\bar{p})}_{lm\bar{l}\bar{m}} \bar{\mathcal{S}}^{(p'\bar{p}')*}_{l'm'\bar{l}'\bar{m}'} \\ \times \sum_{\mu} K^{(pp')}_{\mu;rlml'm'} \frac{1}{2\bar{l}+1} \sum_{\mu'} \sum_{\bar{\mu}\bar{\mu}'} C(1,\bar{l}'\bar{l};\mu,\bar{m}',\bar{m}) \\ \times C(1,\bar{l}',\bar{l};\mu',\bar{\mu}',\bar{\mu}) W^{(\bar{p})*}_{\mathrm{I}\eta\bar{l}\bar{\mu}} W^{(\bar{p}')}_{\mathrm{I}\eta'\bar{l}'\bar{\mu}'} Y^*_{1\mu'}(\hat{\boldsymbol{v}}_\zeta) \Big) \; . \end{aligned} \tag{4.73}$$

Needless to say that the above equations can be simplified in case of particles with cylindrical symmetry.

We are then able to show that in case of random orientation, the transverse components of the radiation force are bound to vanish. In fact, since a dispersion of randomly oriented particles has an overall spherical symmetry the direction of the incident field has no importance. Therefore we choose $\hat{\boldsymbol{k}}_{\mathrm{I}}$ parallel to the z axis and note that, according to their definition, the amplitudes $W^{(p)}_{\mathrm{I}\eta lm}$ do not vanish for $m = \pm 1$ only. As a consequence $\mu' = 0$ and since

$$\sqrt{\frac{4\pi}{3}} Y^*_{10}(\hat{\boldsymbol{v}}_\zeta) = \delta_{\zeta 3} \; ,$$

the averages $\langle g_1 \rangle$ and $\langle g_2 \rangle$ are boud to vanish, whereas $\langle g_3 \rangle$, i.e. the customary asymmetry parameter, is in general nonzero. It is important to notice that this result, that is reported e.g. by van de Hulst, is actually independent of the elements of the transition matrix, i.e. on the morphology of the particles.

In case of *axial* average we get

$$\left\langle \mathcal{D}^{(1\bar{l}'\bar{l})}_{\mu\mu'\bar{m}'\bar{\mu}'\bar{m}\bar{\mu}}(\Theta) \right\rangle = \delta_{\mu\mu'}\delta_{\bar{m}'\bar{\mu}'}\delta_{\bar{m}\bar{\mu}}\delta_{\bar{m}-\bar{m}'-\mu,0} \; ,$$

so that

$$\begin{aligned}\langle \sigma_{\mathrm{S}} g_\zeta \rangle = \frac{c_{\mathrm{I}}}{I_{\mathrm{I}}} \sum_{\eta\eta'} \mathrm{Re}\Big(I_{\mathrm{I}\eta\eta'} \frac{4\pi}{3} \sum_{plm} \sum_{p'l'm'} \sum_{\bar{p}\bar{l}} \sum_{\bar{p}'\bar{l}'} \sum_{\mu\bar{\mu}} Y^*_{1\mu}(\hat{\boldsymbol{v}}_\zeta) \\ \times K^{(pp')}_{\mu;lml'm'} \bar{\mathcal{S}}^{(p\bar{p})}_{lm\bar{l}\bar{\mu}} \bar{\mathcal{S}}^{(p'\bar{p}')*}_{l'm'\bar{l}',\bar{\mu}-\mu} W^{(\bar{p})*}_{\mathrm{I}\eta\bar{l}\bar{\mu}} W^{(\bar{p}')}_{\mathrm{I}\eta'\bar{l}',\bar{\mu}-\mu} \Big) \; . \end{aligned} \tag{4.74}$$

Now, the customary definition of the averaged asymmetry parameters is

$$\langle g_\zeta \rangle = \frac{\langle \sigma_{\mathrm{S}} g_\zeta \rangle}{\langle \sigma_{\mathrm{S}} \rangle} \ ,$$

where $\langle \sigma_{\mathrm{S}} g_\zeta \rangle$ is just given by (4.73) or (4.74) and $\langle \sigma_{\mathrm{S}} \rangle$ is the corresponding average of the scattering cross section. Actually, analogous definitions were assumed for the average of the efficiencies $\langle Q_{\mathrm{T}} \rangle$, $\langle Q_{\mathrm{S}} \rangle$, and $\langle Q_{\mathrm{A}} \rangle$, and of the albedo $\langle \varpi \rangle$. Ultimately, (4.73) and (4.74), according to (3.16), also yield $\langle F_\zeta \rangle$.

4.9 Radiation Torque on Nonspherical Particles

In Sect. 3.2.2 it has been shown that, as a result of the law of conservation of the angular momentum, the interaction of the radiation with particles produces a torque acting on the latter. The influence of the radiation torque on the dynamics of the cosmic dust grains has been discussed by Purcell [60] and computationally dealt with in the framework of the discrete dipole approximation by Draine and Weingartner [61]. As a result, the radiation torque has been recognized as a non-negligible cause of the partial alignment of the cosmic dust grains. As far as we know, Marston and Crichton [62] were the first researchers who, by exploiting the multipole expansion of the fields, presented a detailed calculation of the radiation torque applied by a circularly polarized plane wave to a homogeneous sphere. More recently, de Abajo [63, 64] extended the multipole approach to the calculation of the radiation torque on nonspherical particles, but he did not report the development of the theory except the final formula. Actually, the literature includes only a few papers that deal with the radiation torque, so that the subject cannot be considered as a well-known one. Moreover, a cursory look to the paper of Marston and Crickton will convince the reader that the algebraic manipulations that are required for the development of the theory are rather long and delicate, even in the comparatively simple case of a spherical scatterer. Therefore, on one hand we will report the procedure developed by ourselves in Ref. [65] where we exploit the multipole expansion both of the incident and of the scattered field, although the length and complication of the algebraic manipulations forces us to describe the fundamental steps only. On the other hand, in a rather unusual manner for this book, we will compare our resulting formulas with those reported in Refs. [62–64].

We start by observing that, according to (3.19), the calculation of the radiation torque requires the knowledge both of the incident and of the scattered field and that the integral can be calculated on the surface of a sphere of large radius. Nevertheless, we already warned the reader that the scattered field cannot be expressed through the scattering amplitude lest to get a vanishing result. Therefore, the scattered field must be calculated exactly and then, when considering its large distance limit, we must retain all the terms that give contributions of order $1/r^3$ to the integral in (3.19). Accordingly, since the incident and the scattered field are expanded into the series of vector multipole fields (4.13) and (4.14), respectively, we search for the limiting expression of the $\boldsymbol{H}$- and $\boldsymbol{J}$-multipole fields. With the help of (1.62), (1.43b), and (1.44b) we get for the $\boldsymbol{H}$-multipole fields

$$\boldsymbol{H}_{lm}^{(1)} \to (-\mathrm{i})^{l+1} \frac{\mathrm{e}^{\mathrm{i}kr}}{kr} \boldsymbol{Z}_{lm}^{(1)} , \tag{4.75a}$$

$$\boldsymbol{H}_{lm}^{(2)} \to \frac{(-\mathrm{i})^l}{k^2 r^2} \sqrt{l(l+1)} \mathrm{e}^{\mathrm{i}kr} Y_{lm} \hat{\boldsymbol{r}} - \frac{(-\mathrm{i})^{l+1}}{k^2 r^2} \mathrm{e}^{\mathrm{i}kr} \boldsymbol{Z}_{lm}^{(2)} - \frac{(-\mathrm{i})^l}{kr} \mathrm{e}^{\mathrm{i}kr} \boldsymbol{Z}_{lm}^{(2)} , \tag{4.75b}$$

whereas, using (1.43a), and (1.44a) we get for the $\boldsymbol{J}$-multipole fields

$$\boldsymbol{J}_{lm}^{(1)} \to \frac{1}{kr} \sin(kr - l\pi/2) \boldsymbol{Z}_{lm}^{(1)} , \tag{4.76a}$$

$$\begin{aligned} \boldsymbol{J}_{lm}^{(2)} \to & \frac{\mathrm{i}}{k^2 r^2} \sqrt{l(l+1)} \sin(kr - l\pi/2) Y_{lm} \hat{\boldsymbol{r}} - \frac{1}{k^2 r^2} \sin(kr - l\pi/2) \boldsymbol{Z}_{lm}^{(2)} \\ & - \frac{1}{kr} \sin[kr - (l-1)\pi/2] \boldsymbol{Z}_{lm}^{(2)} . \end{aligned} \tag{4.76b}$$

Now, the $\boldsymbol{H}$- and $\boldsymbol{J}$-fields enter the integrand in (3.19) through the dot products

$$\begin{aligned} \hat{\boldsymbol{r}} \cdot \boldsymbol{H}_{lm}^{(2)} &= \sqrt{l(l+1)} (-\mathrm{i})^l \frac{\mathrm{e}^{\mathrm{i}kr}}{k^2 r^2} Y_{lm} = c_{\mathrm{r}2l} Y_{lm} , \\ \hat{\boldsymbol{r}} \cdot \boldsymbol{J}_{lm}^{(2)} &= \mathrm{i} \sqrt{l(l+1)} \frac{\sin(kr - l\pi/2)}{k^2 r^2} Y_{lm} = c_{\mathrm{r}1l} Y_{lm} , \end{aligned}$$

which can be calculated with the help of (1.23) and (1.24), and through the cross products

$$\boldsymbol{H}_{\bar{l}\bar{m}}^{(\bar{p})*} \times \hat{\boldsymbol{r}} = \mathrm{i}^{\bar{l}+\bar{p}} \frac{\mathrm{e}^{-\mathrm{i}kr}}{kr} \boldsymbol{Z}_{\bar{l}\bar{m}}^{(\bar{p})*} \times \hat{\boldsymbol{r}} = c_{\mathrm{t}2\bar{l}}^{(\bar{p})} \boldsymbol{Z}_{\bar{l}\bar{m}}^{(\bar{p})*} \times \hat{\boldsymbol{r}} , \tag{4.77a}$$

$$\boldsymbol{J}_{\bar{l}\bar{m}}^{(\bar{p})*} \times \hat{\boldsymbol{r}} = \frac{\sin[kr - (\bar{l} + \bar{p} - 1)\pi/2]}{kr} \boldsymbol{Z}_{\bar{l}\bar{m}}^{(\bar{p})*} \times \hat{\boldsymbol{r}} = c_{\mathrm{t}1\bar{l}}^{(\bar{p})} \boldsymbol{Z}_{\bar{l}\bar{m}}^{(\bar{p})*} \times \hat{\boldsymbol{r}} , \tag{4.77b}$$

which can be calculated by exploiting (1.24) and (1.25). Strictly speaking (4.77a) and (4.77b) should include a further term that would come from (4.75b) and (4.76b), respectively. However, this term vanishes at infinity to an order higher than the order we have to retain and has, therefore, been neglected.

Let us now define the vector $\check{\boldsymbol{\Gamma}}$ such that

$$\boldsymbol{\Gamma}_{\mathrm{Rad}} = \mathrm{Re}(\check{\boldsymbol{\Gamma}})$$

and in terms of whose spherical components the cartesian components of $\boldsymbol{\Gamma}_{\mathrm{Rad}}$, according to Sect. 1.5.3, read

$$
\begin{aligned}
\mathit{\Gamma}_{\mathrm{Rad}\,x} =& \mathrm{Re}\Big[\frac{1}{\sqrt{2}}\big(\check{\mathit{\Gamma}}_{-1} - \check{\mathit{\Gamma}}_{1}\big)\Big] \,, \\
\mathit{\Gamma}_{\mathrm{Rad}\,y} =& \mathrm{Re}\Big[\frac{\mathrm{i}}{\sqrt{2}}\big(\check{\mathit{\Gamma}}_{-1} + \check{\mathit{\Gamma}}_{1}\big)\Big] \,, \\
\mathit{\Gamma}_{\mathrm{Rad}\,z} =& \mathrm{Re}\big(\check{\mathit{\Gamma}}_{0}\big) \,,
\end{aligned}
\tag{4.78}
$$

where

$$
\check{\mathit{\Gamma}}_{\mu} = \sum_{\eta\bar{\eta}} I_{\mathrm{I}\bar{\eta}\eta} \check{\mathit{\Gamma}}_{\mu;\bar{\eta}\eta} \,, \tag{4.79}
$$

using a notation analogous to that of Sect. 4.2.1. In the following, on account that all the fields are given in terms of vector spherical harmonics, we found convenient to focus just on the spherical components $\check{\mathit{\Gamma}}_{\mu}$, i.e., actually, on $\check{\mathit{\Gamma}}_{\mu;\bar{\eta}\eta}$. Accordingly, we note that the integrand in (3.19) gets contributions that can be written as

$$
K^{(p\bar{p})}_{\mu;\alpha\bar{\alpha}lm\bar{l}\bar{m}} = \delta_{p2}\, d_{\alpha lm}\, v^{(\bar{p})}_{\mu;\bar{\alpha}\bar{l}\bar{m}} \,, \tag{4.80}
$$

where

$$
d_{1lm} = \hat{\boldsymbol{r}} \cdot \boldsymbol{J}^{(2)}_{lm}, \quad d_{2lm} = \hat{\boldsymbol{r}} \cdot \boldsymbol{H}^{(2)}_{lm} \,,
$$

$$
v^{(\bar{p})}_{\mu;1\bar{l}\bar{m}} = (\boldsymbol{J}^{(\bar{p})*}_{\bar{l}\bar{m}} \times \hat{\boldsymbol{r}})_{\mu}, \quad v^{(\bar{p})}_{\mu;2\bar{l}\bar{m}} = (\boldsymbol{H}^{(\bar{p})*}_{\bar{l}\bar{m}} \times \hat{\boldsymbol{r}})_{\mu} \,.
$$

The subscripts α and $\bar{\alpha}$ in (4.80) denote terms coming from the incident field (α, $\bar{\alpha} = 1$) or from the scattered field (α, $\bar{\alpha} = 2$). We thus get

$$
\begin{aligned}
K^{(21)}_{1;\alpha\bar{\alpha}lm\bar{l}\bar{m}} =& \mathrm{i} c_{\mathrm{r}\alpha l} c^{(1)}_{\mathrm{t}\bar{\alpha}\bar{l}} Y_{lm} \sqrt{\frac{4\pi}{3}} \big[Y_{10} C(1,\bar{l},\bar{l};1,\bar{m}-1) Y^{*}_{\bar{l},\bar{m}-1} \\
&- Y_{11} C(1,\bar{l},\bar{l};0,\bar{m}) Y^{*}_{\bar{l}\bar{m}}\big] \,, \\
K^{(21)}_{0;\alpha\bar{\alpha}lm\bar{l}\bar{m}} =& \mathrm{i} c_{\mathrm{r}\alpha l} c^{(1)}_{\mathrm{t}\bar{\alpha}\bar{l}} Y_{lm} \sqrt{\frac{4\pi}{3}} \big[Y_{1,-1} C(1,\bar{l},\bar{l};1,\bar{m}-1) Y^{*}_{\bar{l},\bar{m}-1} \\
&- Y_{11} C(1,\bar{l},\bar{l};-1,\bar{m}+1) Y^{*}_{\bar{l}\bar{m}+1}\big] \,, \\
K^{(21)}_{-1;\alpha\bar{\alpha}lm\bar{l}\bar{m}} =& \mathrm{i} c_{\mathrm{r}\alpha l} c^{(1)}_{\mathrm{t}\bar{\alpha}\bar{l}} Y_{lm} \sqrt{\frac{4\pi}{3}} \big[Y_{1,-1} C(1,\bar{l},\bar{l};0,\bar{m}) Y^{*}_{\bar{l},\bar{m}} \\
&- Y_{10} C(1,\bar{l},\bar{l};-1,\bar{m}+1) Y^{*}_{\bar{l},\bar{m}+1}\big] \,,
\end{aligned}
$$

$$
K^{(22)}_{\mu;\alpha\bar{\alpha}lm\bar{l}\bar{m}} = c_{\mathrm{r}\alpha l} c^{(2)}_{\mathrm{t}\bar{\alpha}\bar{l}} Y_{lm} C(1,\bar{l},\bar{l};\mu,\bar{m}-\mu) Y^{*}_{\bar{l},\bar{m}-\mu} \,.
$$

When these contributions, according to (3.19), are integrated we get

$$
\begin{aligned}
I^{(21)}_{1;\alpha\bar{\alpha}lm\bar{l}\bar{m}} =& \left[\mathrm{i} c_{\mathrm{r}\alpha l} c^{(1)}_{\mathrm{t}\bar{\alpha}\bar{l}} \sqrt{\frac{2l+1}{2\bar{l}+1}} C(1,l,\bar{l};0,0) \right] \\
&\times \big[C(1,\bar{l},\bar{l};1,\bar{m}-1) C(1,l,\bar{l};0,m,\bar{m}-1) \\
&\quad - C(1,\bar{l},\bar{l};0,\bar{m}) C(1,l,\bar{l};1,m,\bar{m}) \big] \delta_{m,\bar{m}-1} \ , \\
I^{(21)}_{0;\alpha\bar{\alpha}lm\bar{l}\bar{m}} =& \left[\mathrm{i} c_{\mathrm{r}\alpha l} c^{(1)}_{\mathrm{t}\bar{\alpha}\bar{l}} \sqrt{\frac{2l+1}{2\bar{l}+1}} C(1,l,\bar{l};0,0) \right] \\
&\times \big[C(1,\bar{l},\bar{l};1,\bar{m}-1) C(1,l,\bar{l};-1,m,\bar{m}-1) \\
&\quad - C(1,\bar{l},\bar{l};-1,\bar{m}+1) C(1,l,\bar{l};1,m,\bar{m}+1) \big] \delta_{m,\bar{m}} \ ,
\end{aligned}
$$

$$
\begin{aligned}
I^{(21)}_{-1;\alpha\bar{\alpha}lm\bar{l}\bar{m}} =& \left[\mathrm{i} c_{\mathrm{r}\alpha l} c^{(1)}_{\mathrm{t}\bar{\alpha}\bar{l}} \sqrt{\frac{2l+1}{2\bar{l}+1}} C(1,l,\bar{l};0,0) \right] \\
&\times \big[C(1,\bar{l},\bar{l};0,\bar{m}) C(1,l,\bar{l};-1,m,\bar{m}) \\
&\quad - C(1,\bar{l},\bar{l};-1,\bar{m}+1) C(1,l,\bar{l};0,m,\bar{m}+1) \big] \delta_{m,\bar{m}+1} \ ,
\end{aligned}
$$

and

$$
I^{(22)}_{\mu;\alpha\bar{\alpha}lm\bar{l}\bar{m}} = c_{\mathrm{r}\alpha l} c^{(2)}_{\mathrm{t}\bar{\alpha}\bar{l}} C(1,l,\bar{l};\mu,\bar{m}-\mu) \delta_{l\bar{l}} \delta_{m,\bar{m}-\mu} \ . \tag{4.81}
$$

Finally, collecting all the terms one obtains

$$
\begin{aligned}
\check{\Gamma}_{\mu;\bar{\eta}\eta} =& - \frac{r^3}{8\pi} \\
&\times \sum_{\alpha\bar{\alpha}} \left[\sum_{\bar{p}} \sum_{\bar{p}' \neq \bar{p}} \sum_{lm} \sum_{\bar{l}\bar{m}} I^{(2\bar{p})}_{\mu\alpha\bar{\alpha}lm\bar{l}\bar{m}} \left(a^{(2)}_{\alpha\eta lm} a^{(\bar{p})*}_{\bar{\alpha}\bar{\eta}\bar{l}\bar{m}} + a^{(1)}_{\alpha\eta lm} a^{(\bar{p}')*}_{\bar{\alpha}\bar{\eta}\bar{l}\bar{m}} \right) \right] \ ,
\end{aligned} \tag{4.82}
$$

where

$$
a^{(p)}_{1\eta lm} = W^{(p)}_{\mathrm{I}\eta lm}, \quad \text{and} \quad a^{(p)}_{2\eta lm} = A^{(p)}_{\eta lm} \ .
$$

At this stage a number of remarks are in order. Equation (4.82) could be used for a brute force calculation of the spherical components of the radiation torque, but we can obtain a more efficient formula through a detailed inspection of the terms present. In fact, (4.82) is built as a sum of contributions with different α, $\bar{\alpha}$, and $\bar{p}$ or $\bar{p}'$. The same is true for $\boldsymbol{\Gamma}_{\mathrm{Rad}}$ on account of (4.78) and (4.79). A careful analysis and rather long manipulations then lead to the following conclusions that refer just to the contributions to $\boldsymbol{\Gamma}_{\mathrm{Rad}}$ for each η and $\bar{\eta}$.

- The contributions with $\alpha = \bar{\alpha} = 1$ are just vanishing both for $\bar{p} = 2$ or $\bar{p} = 1$ and for $\bar{p}' = 1$ or $\bar{p}' = 2$. This result, that is identical to the one of Marston and Crickton, comes from the fact that these terms describe the flux of the momentum of the Maxwell stress tensor trough a closed surface in the absence of any scatterer.
- The contribution with $\alpha = \bar{\alpha} = 2$ vanishes both for $\bar{p} = 1$ and for $\bar{p}' = 2$.

- The contributions for $\alpha \neq \bar{\alpha}$ depend on r, i.e. on the radius of the spherical surface of integration. Nevertheless, those with $\bar{p} = 1$ are identical but of opposite sign and cancel each other; on the other hand, the sum of those with $\bar{p} = 2$ turns out to be independent of r. Analogous considerations hold true for the contributions with $\bar{p}' = 2$ and $\bar{p}' = 1$, respectively. This result is a consequence of the fact that, according to (3.18), the torque cannot depend on the choice of the surface of integration.

Now, separating in (4.82) the sum over $\alpha \neq \bar{\alpha}$ from the one over $\alpha = \bar{\alpha}$, we can write

$$\check{\Gamma}_{\mu;\bar{\eta}\eta} = \check{\Gamma}^{(\mathrm{ext})}_{\mu;\bar{\eta}\eta} - \check{\Gamma}^{(\mathrm{sca})}_{\mu;\bar{\eta}\eta} \ . \tag{4.83}$$

In (4.83)

$$\check{\Gamma}^{(\mathrm{ext})}_{\mu;\bar{\eta}\eta} = c_\Gamma \sum_{plm} s_{\mu;lm} W^{(p)}_{\mathrm{I}\eta l,m-\mu} A^{(p)*}_{\bar{\eta}lm} \ , \tag{4.84}$$

whereas the quantities $\check{\Gamma}^{(\mathrm{sca})}_{\mu;\eta\bar{\eta}}$ are identical to the $\check{\Gamma}^{(\mathrm{ext})}_{\mu;\eta\bar{\eta}}$ above, except for the substitution of $A^{(p)}_{\eta lm}$ in place of $W^{(p)}_{\mathrm{I}\eta lm}$ and for the change of the sign. In (4.84) we define $c_\Gamma = 1/8\pi k^3$ and

$$s_{-1;lm} = -\sqrt{\frac{(l-m)(l+1+m)}{2}} \ , \tag{4.85a}$$

$$s_{0;lm} = -m \ , \tag{4.85b}$$

$$s_{1;lm} = \sqrt{\frac{(l+m)(l+1-m)}{2}} \ . \tag{4.85c}$$

At this stage we remark that the results yielded by our formula are identical to those of Marston and Crichton when we deal with a sphere. In fact, let us write (4.84) in a compact form as

$$\check{\Gamma}^{(\mathrm{ext})}_{\mu;\bar{\eta}\eta} = c_\Gamma \sum_{plm} V^{(p)}_{\mu;\eta lm} A^{(p)*}_{\bar{\eta}lm} \ ,$$

where $V^{(p)}_{\mu;\eta lm} = s_{\mu;lm} W^{(p)}_{\mathrm{I}\eta l,m-\mu}$. Considering the vector $\boldsymbol{V}^{(p)}_{\eta lm}$ with spherical components $V^{(p)}_{\mu;\eta lm}$, we find for a circular polarization basis

$$\boldsymbol{V}^{(p)}_{\eta lm} \cdot \hat{\boldsymbol{k}}_{\mathrm{I}} = \sum_\mu (-)^\mu V^{(p)}_{-\mu;\eta lm} \hat{k}_{\mathrm{I}\mu} = (-)^\eta W^{(p)}_{\mathrm{I}\eta lm} \ .$$

Note that this equation does not hold true in a linear polarization basis. In practice, obtaining this result requires long manipulations for general direction of $\hat{\boldsymbol{k}}_{\mathrm{I}}$ but it is immediately obtained in the case $\hat{\boldsymbol{k}}_{\mathrm{I}} = \hat{\boldsymbol{e}}_z$. As a consequence,

$$\check{\boldsymbol{\Gamma}}^{(\mathrm{ext})}_{\bar{\eta}\eta} \cdot \hat{\boldsymbol{k}}_{\mathrm{I}} = \frac{(-)^{\eta-1}}{8\pi k} \frac{-1}{k^2} \sum_{plm} A^{(p)*}_{\bar{\eta}lm} W^{(p)}_{\mathrm{I}\eta lm} = \frac{(-)^{\eta-1}}{8\pi k} \check{\sigma}^*_{\mathrm{T}\eta\bar{\eta}} \ . \tag{4.86}$$

On the contrary,

$$\check{\boldsymbol{\Gamma}}^{(\mathrm{sca})}_{\bar{\eta}\eta} \cdot \hat{\boldsymbol{k}}_{\mathrm{I}} \neq \frac{(-)^{\eta-1}}{8\pi k} \check{\sigma}^{*}_{\mathrm{S}\eta\bar{\eta}} \tag{4.87}$$

unless the scatterer is axially symmetric and $\hat{\boldsymbol{k}}_{\mathrm{I}}$ is parallel to its axis. Of course, (4.87) becomes a true equality for whatever direction of incidence when the scatterer is a sphere. This result is related to the property (4.32) of the transition matrix and to the remark that

- When the scatterer is axially symmetric and $\hat{\boldsymbol{k}}_{\mathrm{I}}$ is parallel to its axis the contribution for $\alpha = 2$, $\bar{\alpha} = 1$ with $\bar{p} = 2$ and that for $\alpha = 1$, $\bar{\alpha} = 2$ with $\bar{p} = 1$ are equal; the same is also true for $\alpha = 2$, $\bar{\alpha} = 1$ with $\bar{p}' = 1$ and for $\alpha = 1$, $\bar{\alpha} = 2$ with $\bar{p}' = 2$.

On account that in the case above, using a circular polarization basis, one finds $\sigma_{\mathrm{T}1} = \sigma_{\mathrm{T}2}$, $\sigma_{\mathrm{S}1} = \sigma_{\mathrm{S}2}$, and $\check{\sigma}_{\mathrm{T}\eta\bar{\eta}} = \check{\sigma}_{\mathrm{S}\eta\bar{\eta}} = 0$ for $\eta \neq \bar{\eta}$, the result is

$$\boldsymbol{\Gamma}_{\mathrm{Rad}} \cdot \hat{\boldsymbol{k}}_{\mathrm{I}} = \frac{1}{8\pi k} \big(I_{\mathrm{I}11} - I_{\mathrm{I}22}\big) \sigma_{\mathrm{A}} \ , \tag{4.88}$$

whereas there is no component of the torque perpendicular to the axis, for obvious symmetry reasons. Thus, a plane wave propagating along the axis can apply a torque to the axially symmetric particle only when the latter is absorbing and the wave is elliptically polarized. This is just the result that Marston and Crickton obtained for a spherical scatterer. As regards the result of de Abajo (equation (11) of Ref. [63] and equation (4) of Ref. [64]) , a factor $\delta_{ll'}$ is missing because of a misprint. In fact, (4.84) differs from the equations by de Abajo because in the latter the amplitudes $A^{(p)*}_{\bar{\eta}lm}$ and $W^{(p)}_{\mathrm{I}\eta l',m-\mu}$, in our notation, bear the different indexes l and l', and one has to sum both over l and l'. According to (4.81) and to our previous analysis of the contributions to $\boldsymbol{\Gamma}_{\mathrm{Rad}}$, such a double sum is incorrect.

4.9.1 Axial Average of Radiation Torque

The radiatiation torque depends on the orientation of the particle with respect to the incident field, i.e. with respect to the direction of incidence and to the polarization. Nevertheless, it is not to be expected that a dispersion of particles shows a collective response to the torque exerted by the incident field: from a dynamical point of view each particle has its own response. However, since the rotation of a particle around a principal axis of inertia through its center of mass is a stable one [66], it may be interesting to consider the average of the radiation torque applied to a particle in a complete rotation. In other words it is meaningful calculating the *axial average* of the radiation torque. Let us assume that the particle rotates around the local $\bar{z}$ axis which remains always parallel to the z axis of the laboratory frame. This kind of average has been already performed for $\boldsymbol{F}_{\mathrm{Rad}}$. The spherical components of the radiation torque transform under rotation as a first rank tensor, i.e. according to $\mathrm{D}^{(1)}$, and this property must be borne in mind when transforming $\boldsymbol{\Gamma}_{\mathrm{Rad}}$ from the local frame of reference $\bar{\Sigma}$ to the laboratory frame Σ. Therefore,

$$\check{\Gamma}_{\mu';\bar{\eta}\eta} = \sum_{\mu} \check{\bar{\Gamma}}_{\mu;\bar{\eta}\eta} \mathcal{D}^{(1)}_{\mu\mu'} , \tag{4.89}$$

where

$$\check{\bar{\Gamma}}_{\mu;\bar{\eta}\eta} = \check{\bar{\Gamma}}^{(\mathrm{ext})}_{\mu;\bar{\eta}\eta} - \check{\bar{\Gamma}}^{(\mathrm{sca})}_{\mu;\bar{\eta}\eta} .$$

According to (4.84),

$$\begin{aligned} \check{\bar{\Gamma}}^{(\mathrm{ext})}_{\mu;\bar{\eta}\eta} &= c_{\Gamma} \sum_{plm} s_{\mu;lm} \bar{W}^{(p)}_{\mathrm{I}\eta l,m-\mu} \bar{A}^{(p)*}_{\bar{\eta}lm} , \\ \check{\bar{\Gamma}}^{(\mathrm{sca})}_{\mu;\bar{\eta}\eta} &= -c_{\Gamma} \sum_{plm} s_{\mu;lm} \bar{A}^{(p)}_{\eta l,m-\mu} \bar{A}^{(p)*}_{\bar{\eta}lm} . \end{aligned} \tag{4.90}$$

Now, by (4.36) and (4.39), we get

$$\bar{A}^{(p)}_{\eta lm} = \sum_{p'l'm'} \sum_{\bar{m}'} \bar{\mathcal{S}}^{(pp')}_{lml'm'} \mathcal{D}^{(l')}_{m'\bar{m}'} W^{(p')}_{\mathrm{I}\eta l'\bar{m}'} , \tag{4.91}$$

Substitution into (4.90) according to (4.39) and to (4.91), leads us to the conclusion that the axial average of (4.89) requires calculating the integrals

$$\int \mathcal{D}^{(1)}_{\mu\mu'} \mathcal{D}^{(l)}_{m-\mu,\bar{m}} \mathcal{D}^{(l')*}_{m'\bar{m}'} P(\Theta)\,\mathrm{d}\Theta = \delta_{\mu\mu'} \delta_{m-\mu,\bar{m}} \delta_{m'\bar{m}'} \delta_{mm'}$$

and

$$\int \mathcal{D}^{(1)}_{\mu\mu'} \mathcal{D}^{(l')}_{m'\bar{m}'} \mathcal{D}^{(l'')*}_{m''\bar{m}''} P(\Theta)\,\mathrm{d}\Theta = \delta_{\mu\mu'} \delta_{m'\bar{m}'} \delta_{m''\bar{m}''} \delta_{\mu+m',m''} ,$$

where

$$P(\Theta) = \frac{1}{2\pi} \frac{\delta(\beta)}{\sin\beta} \delta\gamma ,$$

as we are dealing with Case 4 in Table 4.1. Ultimately,

$$\begin{aligned} \langle \check{\Gamma}^{(\mathrm{ext})}_{\mu;\bar{\eta}\eta} \rangle &= c_{\Gamma} \sum_{plm} s_{\mu;lm} \sum_{\bar{p}\bar{l}} W^{(p)}_{\mathrm{I}\eta l,m-\mu} \bar{\mathcal{S}}^{(p\bar{p})*}_{\bar{l}\bar{m}\bar{l}\bar{m}} W^{(\bar{p})*}_{\mathrm{I}\bar{\eta}\bar{l}\bar{m}} , \\ \langle \check{\Gamma}^{(\mathrm{sca})}_{\mu;\bar{\eta}\eta} \rangle &= c_{\Gamma} \sum_{plm} s_{\mu;lm} \sum_{\bar{p}\bar{p}'} \sum_{\bar{l}\bar{l}'} \sum_{m'} \bar{\mathcal{S}}^{(p\bar{p})}_{lm\bar{l},m'-\mu} W^{(\bar{p})}_{\mathrm{I}\eta\bar{l},m'-\mu} \bar{\mathcal{S}}^{(p\bar{p}')*}_{lm\bar{l}'m'} W^{(\bar{p}')*}_{\mathrm{I}\bar{\eta}\bar{l}m} , \end{aligned}$$

where again $c_{\Gamma} = 1/8\pi k^3$ and $s_{\mu;lm}$ are given by (4.85).

4.10 Thermal Emission Force on Nonspherical Particles

In Sect. 3.3 it has been shown that any heated particle should emit radiation and that, as a consequence of the emission, it experiences a force that is akin to the radiation pressure. In order to calculate the thermal emission force on a particle of general shape let us rewrite (3.21) as

$$\boldsymbol{F}_{\mathrm{e}} = \frac{1}{c}\int \mathrm{d}\omega \tilde{\boldsymbol{K}} I_{\mathrm{b}} \ ,$$

where we define

$$\tilde{\boldsymbol{K}} = -\int \mathrm{d}\hat{\boldsymbol{r}}\, \hat{\boldsymbol{r}} K_{11} + \int \mathrm{d}\hat{\boldsymbol{r}}\, \hat{\boldsymbol{r}} \int \mathrm{d}\hat{\boldsymbol{r}}'\, Z_{11} = \tilde{\boldsymbol{K}}^{(\mathrm{ext})} - \tilde{\boldsymbol{K}}^{(\mathrm{sca})} \ .$$

We now calculate the components of the thermal emission force by projecting $\boldsymbol{F}_{\mathrm{e}}$ on an orthonormal triplet $\hat{\boldsymbol{e}}_j$, so that

$$\boldsymbol{F}_{\mathrm{e}} = \sum_j F_{\mathrm{e}j} \hat{\boldsymbol{e}}_j = \frac{1}{c}\sum_j \int \mathrm{d}\omega \big[\hat{\boldsymbol{e}}_j \cdot \big(\tilde{\boldsymbol{K}}^{(\mathrm{ext})} - \tilde{\boldsymbol{K}}^{(\mathrm{sca})}\big) I_{\mathrm{b}}\big] \hat{\boldsymbol{e}}_j , \tag{4.92}$$

with

$$\hat{\boldsymbol{e}}_j \cdot \tilde{\boldsymbol{K}}^{(\mathrm{ext})} = -\hat{\boldsymbol{e}}_j \cdot \int \mathrm{d}\hat{\boldsymbol{r}}\, \hat{\boldsymbol{r}} K_{11} \ .$$

and

$$\hat{\boldsymbol{e}}_j \cdot \tilde{\boldsymbol{K}}^{(\mathrm{sca})} = -\hat{\boldsymbol{e}}_j \cdot \int \mathrm{d}\hat{\boldsymbol{r}}\, \hat{\boldsymbol{r}} \int \mathrm{d}\hat{\boldsymbol{r}}'\, Z_{11} \ .$$

The dot product $\hat{\boldsymbol{e}}_j \cdot \hat{\boldsymbol{r}}$ can be expressed in terms of spherical components by exploiting (1.23) and (1.24), whereas Z_{11} and K_{11}, according to their definition (2.42) and (2.45), respectively, can be expressed in terms of the elements of the scattering amplitude matrix (4.29). The results are

$$\begin{aligned}\hat{\boldsymbol{e}}_j \cdot \tilde{\boldsymbol{K}}^{(\mathrm{ext})} =& \frac{1}{2k^2}\mathrm{Re}\Bigg(\sum_\mu \sqrt{\frac{4\pi}{3}} Y^*_{1\mu}(\vartheta_j, \varphi_j) \\ &\times \sum_{plm}\sum_{p'l'm'}\sum_{\eta} \mathcal{S}^{(pp')*}_{lml'm'} \sqrt{\frac{4\pi}{3}} \int \mathrm{d}\Omega Y_{1\mu}(\vartheta,\varphi) W^{(p)}_{\mathrm{S}\eta lm} W^{(p')*}_{\mathrm{S}\eta l'm'}\Bigg)\end{aligned}$$

and

$$\begin{aligned}\hat{\boldsymbol{e}}_j \cdot \tilde{\boldsymbol{K}}^{(\mathrm{sca})} =& -\frac{1}{32\pi^2 k^2}\sum_\mu \sqrt{\frac{4\pi}{3}} Y^*_{1\mu}(\vartheta_j,\varphi_j) \\ &\times \sum_{plm}\sum_{\bar{p}\bar{l}\bar{m}}\sum_{p'l'm'}\sum_{\bar{p}'\bar{l}'\bar{m}'}\sum_{\eta\eta'} \mathcal{S}^{(p\bar{p})*}_{lm\bar{l}\bar{m}} \mathcal{S}^{(p'\bar{p}')}_{l'm'\bar{l}'\bar{m}'} \\ &\times \sqrt{\frac{4\pi}{3}} \int \mathrm{d}\Omega\, Y_{1\mu}(\vartheta,\varphi) W^{(p)}_{\mathrm{S}\eta lm} W^{(p')*}_{\mathrm{S}\eta l'm'} \\ &\times \int \mathrm{d}\Omega'\, W^{(\bar{p})*}_{\mathrm{I}\eta'\bar{l}\bar{m}} W^{(\bar{p}')}_{\mathrm{I}\eta'\bar{l}'\bar{m}'} \ .\end{aligned}$$

The integrals involved in the preceding equations can be calculated as we did in Sect. 4.8, i.e. by expanding the integrands in terms of functions in the frame of reference with $\hat{\boldsymbol{k}}_{\mathrm{I}} = \hat{\boldsymbol{e}}_z$ or $\hat{\boldsymbol{k}}_{\mathrm{S}} = \hat{\boldsymbol{e}}_z$, according to the need. We get

$$\begin{aligned}\hat{\boldsymbol{e}}_j \cdot \tilde{\boldsymbol{K}}^{(\mathrm{ext})} =& \frac{4\pi^2}{k^2}\mathrm{Re}\Bigg(\sum_{\mu}\sqrt{\frac{4\pi}{3}}Y^*_{1\mu}(\vartheta_j,\varphi_j)\sum_{plm}\sum_{p'l'm'}\mathcal{S}^{(pp')*}_{lml'm'}\\ &\times\sqrt{\frac{2l'+1}{2l+1}}C(1,l',l;\mu,m',m)O^{(pp')}_{ll'}\Bigg)\,,\end{aligned} \tag{4.93}$$

and

$$\begin{aligned}\hat{\boldsymbol{e}}_j \cdot \tilde{\boldsymbol{K}}^{(\mathrm{sca})} =& -\frac{4\pi^2}{k^2}\sum_{\mu}\sqrt{\frac{4\pi}{3}}Y^*_{1\mu}(\vartheta_j,\varphi_j)\sum_{plm}\sum_{p'l'm'}\sum_{\bar{p}\bar{l}\bar{m}}\mathcal{S}^{(p\bar{p})*}_{lm\bar{l}\bar{m}}\mathcal{S}^{(p'\bar{p})}_{l'm'\bar{l}\bar{m}}\\ &\times\sqrt{\frac{2l'+1}{2l+1}}C(1,l',l;\mu,m',m)O^{(pp')}_{ll'}\,,\end{aligned} \tag{4.94}$$

where

$$O^{(pp')}_{ll'} = \left[(-)^{p+p'}C(1,l',l;0,-1,-1) + C(1,l',l;0,1,1)\right]\mathrm{i}^{l-l'}\,.$$

According to Table 1.1, $O^{(pp')}_{ll'} = 0$ for $l' < l-1$ and for $l' > l+1$, and

$$\begin{aligned}O^{(pp')}_{l,l-1} =& 2\mathrm{i}\sqrt{\frac{(l-1)(l+1)}{l(2l-1)}}\,\delta_{pp'}\,,\\ O^{(pp')}_{ll} =& -\frac{2}{\sqrt{l(l+1)}}(1-\delta_{pp'})\,,\\ O^{(pp')}_{l,l+1} =& 2\mathrm{i}\sqrt{\frac{l(l+2)}{(l+1)(2l+3)}}\,\delta_{pp'}\,.\end{aligned}$$

Results (4.93) and (4.94), when substituted into (4.92), allow us to evaluate $\boldsymbol{F}_{\mathrm{e}}$.

At this stage a number of remarks are in order. First, the orientation of the triplet $\hat{\boldsymbol{e}}_j$ is quite arbitrary: for instance, it can be chosen to be the triplet that characterizes the axes of the laboratory frame or the triplet of the local frame attached to the emitting particle. In the latter case, we can perform orientational averages over a dispersion of identical particles. In particular, the random average of the emission force turns out to vanish, because

$$\langle \hat{\boldsymbol{e}}_j \cdot \tilde{\boldsymbol{K}} \rangle = 0\,.$$

Actually, according to (4.94) and (4.93), averaging over the orientations implies $\bar{Y}^*_{1\mu}(\bar{\vartheta}_j,\bar{\varphi}_j)$ only and, in the case of random average one has

$$\frac{1}{8\pi^2} \sum_{\mu'} Y^*_{1\mu'}(\vartheta_j, \varphi_j) \int \mathcal{D}^{(1)}_{\mu\mu'} \, \mathrm{d}\Theta = 0 \; .$$

Moreover, it can be shown that, still assuming random average,

$$\langle K_{\mathrm{e}1} \rangle / I_{\mathrm{b}} = \langle \sigma_{\mathrm{T}} \rangle - \langle \sigma_{\mathrm{S}} \rangle = \langle \sigma_{\mathrm{A}} \rangle$$

which vanishes for nonabsorbing particles. This is an expected result because in the averaging process all the quantities in (3.23) lose their dependence on $\hat{\boldsymbol{k}}_{\mathrm{S}}$, as the reader may easily guess. Finally, let us remark that, without performing any integration except for the one over $\mathrm{d}\Omega$ in the expression for $\hat{\boldsymbol{e}}_j \cdot \tilde{\boldsymbol{K}}^{(\mathrm{sca})}$, putting $\hat{\boldsymbol{r}}' = \hat{\boldsymbol{e}}_j$ yields the longitudinal component of the radiation force, i.e. the radiation pressure.

In conclusion, the procedure described so far shows an internal consistency, as the radiation pressure stems as a byproduct of the calculation of the thermal emission force. Nevertheless, we stress that the vanishing of the random average $\langle \boldsymbol{F}_{\mathrm{e}} \rangle$ is likely to have little significance in several cases, e.g., for the interpretation of the behavior of the grains of the interstellar medium. Finally, we warn the reader that the formulas that we reported thus far for the radiation force, the radiation torque and the thermal emission force, were set up on the assumption that the medium in which the particles are embedded is the vacuum. When this is not the case, there is no effect on the electromagnetic part of the calculation, provided the correct refractive index of the embedding medium is considered. However, when one is interested in realistic calculations of the dynamics of a dispersion of particles, the mechanical effect of the external medium should be taken into account [61].

5 Transition Matrix of Single and Aggregated Spheres

In Chap. 4 we dealt with the relations between the transition matrix of individual particles and the macroscopic optical properties of a dispersion of them. Since the knowledge of the transition matrix of the particles concerned has turned out to be of paramount importance for the interpretation of the observational data, this chapter is devoted to the description of the procedure for calculating the transition matrix of single and aggregated spheres. Limiting our effort to such kinds of scatterers is less restrictive than one may think because, as we outlined in Sect. 1.1, the parameters that individuate the morphology of an aggregate can be chosen so as to fit the properties of a large class of actual particles.

Our approach to the scattering problem and to the calculation of the transition matrix is based on the expansion of the field into a series of spherical multipole fields and on the imposition of the boundary conditions across the surface of the particles. First, we consider homogeneous and radially nonhomogeneous spheres, and, in the latter case, we show the relation with the case of layered spheres. Next, we consider the scatterers composed by aggregated spheres and those composed by a sphere containing either a single eccentric inclusion or more spherical inclusions (often referred to as internal aggregation). Except for the case of single spheres, either homogeneous or concentrically layered, that are isotropic, all other scatterers that we consider in this chapter are anisotropic to a more or less large extent. We will also discuss the onset of optical resonances because these features of the extinction spectrum proved to be of help in studying the morphology of the scattering particles.

In the last section we will report a brief survey of a few other methods that are commonly used to calculate the field scattered by nonspherical particles. In fact, we feel that this survey will be useful for a better understanding of our conclusions when we compare our results with those of other researchers in the field.

5.1 Homogeneous Spheres

The complete solution to the problem of scattering from homogeneous spheres of arbitrary size and refractive index was given by Mie as early as 1908 [67].

For this reason it is customarily referred to as the Mie theory. No generality is lost by assuming that the center of the sphere, of radius ρ and (possibly complex) refractive index n_0, coincides with the origin of the coordinate frame. The incident electric field is assumed to be that of a plane polarized wave, whose multipole expansion is given by (4.13). In turn, the electric field of the scattered wave has, at any point outside the sphere, the multipole expansion (4.14). Finally, since the field within the sphere must be regular at the origin, its expansion can be taken in the form

$$\boldsymbol{E}_{\mathrm{T}\eta} = E_0 \sum_{plm} \boldsymbol{J}_{lm}^{(p)}(\boldsymbol{r}, k_0) C_{\eta lm}^{(p)} , \tag{5.1}$$

with $k_0 = n_0 k_{\mathrm{v}}$. The magnetic field, that is also needed for imposing the boundary conditions, is given by the equation

$$\mathrm{i}\boldsymbol{B} = \frac{1}{k_{\mathrm{v}}} \nabla \times \boldsymbol{E} , \tag{5.2}$$

both within and outside the sphere. In fact, the amplitudes of the field within the sphere as well as those of the field in the external region, where there is the superposition of the incident and of the scattered fields, must satisfy the appropriate boundary conditions across the surface of the sphere.

We assume that the material of the sphere and that of the surrounding medium are nonmagnetic, so that the boundary conditions reduce to the requirement of continuity of the tangential components both of the electric and of the magnetic field. These conditions are often stated by taking the components of the fields along the unit vectors $\hat{\boldsymbol{\vartheta}}$ and $\hat{\boldsymbol{\varphi}}$ of a spherical coordinate system with origin at the center of the sphere [5, 21]; in other words, the field is represented with reference to the meridional plane. In our approach, we prefer a more general procedure. In fact, on account that the transverse harmonics form a complete orthonormal set tangent to the surface of the unit sphere, we equate the dot products of the internal and of the external fields by the transverse harmonics $\boldsymbol{Z}_{lm}^{(p)*}$ and integrate the resulting equations over the solid angle. Accordingly, we write the equalities

$$\int (\boldsymbol{E}_{\mathrm{I}\eta} + \boldsymbol{E}_{\mathrm{S}\eta}) \cdot \boldsymbol{Z}_{lm}^{(p)*} \,\mathrm{d}\Omega = \int \boldsymbol{E}_{\mathrm{T}\eta} \cdot \boldsymbol{Z}_{lm}^{(p)*} \,\mathrm{d}\Omega , \tag{5.3a}$$

$$\int (\boldsymbol{B}_{\mathrm{I}\eta} + \boldsymbol{B}_{\mathrm{S}\eta}) \cdot \boldsymbol{Z}_{lm}^{(p)*} \,\mathrm{d}\Omega = \int \boldsymbol{B}_{\mathrm{T}\eta} \cdot \boldsymbol{Z}_{lm}^{(p)*} \,\mathrm{d}\Omega , \tag{5.3b}$$

that, due to the orthogonality of the multipole fields, yield a system of equations among which the the amplitudes of the internal field can be easily eliminated. In practice, by substituting into (5.3) the expansions for the fields and performing the integrations we get, for each l and m, the four equations

$$h_l(x)A^{(1)}_{\eta lm} + j_l(x)W^{(1)}_{\mathrm{I}\eta lm} = j_l(x_0)C^{(1)}_{\eta lm} \,, \tag{5.4a}$$

$$\frac{1}{x}\left\{\left[xh_l(x)\right]' A^{(2)}_{\eta lm} + \left[xj_l(x)\right]' W^{(2)}_{\mathrm{I}\eta lm}\right\} = \frac{1}{x_0}\left[x_0 j_l(x_0)\right]' C^{(2)}_{\eta lm} \,, \tag{5.4b}$$

$$\frac{n}{x}\left\{\left[xh_l(x)\right]' A^{(1)}_{\eta lm} + \left[xj_l(x)\right]' W^{(1)}_{\mathrm{I}\eta lm}\right\} = \frac{n_0}{x_0}\left[x_0 j_l(x_0)\right]' C^{(1)}_{\eta lm} \,, \tag{5.4c}$$

$$n\left[h_l(x)A^{(2)}_{\eta lm} + j_l(x)W^{(2)}_{\mathrm{I}\eta lm}\right] = n_0 j_l(x_0)C^{(2)}_{\eta lm} \,, \tag{5.4d}$$

where the prime denotes differentiation with respect to the argument and we put $x = k\rho$, $x_0 = k_0\rho$. Then, by eliminating the amplitudes of the internal field $C^{(p)}_{\eta lm}$ among (5.4) and solving the resulting equations for the amplitudes $A^{(p)}_{\eta lm}$, we get

$$A^{(1)}_{\eta lm} = -\frac{n_0 u_l'(x_0)u_l(x) - nu_l(x_0)u_l'(x)}{n_0 u_l'(x_0)w_l(x) - nu_l(x_0)w_l'(x)} W^{(1)}_{\mathrm{I}\eta lm} = -R^{(1)}_l W^{(1)}_{\mathrm{I}\eta lm} \,, \tag{5.5a}$$

$$A^{(2)}_{\eta lm} = -\frac{nu_l'(x_0)u_l(x) - n_0 u_l(x_0)u_l'(x)}{nu_l'(x_0)w_l(x) - n_0 u_l(x_0)w_l'(x)} W^{(2)}_{\mathrm{I}\eta lm} = -R^{(2)}_l W^{(2)}_{\mathrm{I}\eta lm} \,, \tag{5.5b}$$

where $u_l(x) = xj_l(x)$ and $w_l(x) = xh_l(x)$ are Riccati–Bessel and Riccati–Hankel functions [10], respectively. The quantities $R^{(1)}_l$ and $R^{(2)}_l$ coincide with the well known Mie scattering coefficients, b_l and a_l, respectively, for a homogeneous sphere of refractive index n_0 embedded into a medium of refractive index n [5]. Equations (5.5) can be written in more compact form as

$$A^{(p)}_{\eta lm} = -R^{(p)}_l W^{(p)}_{\mathrm{I}\eta lm} \,, \tag{5.6}$$

where

$$R^{(p)}_l = \frac{(1+\bar{n}\delta_{p1})u_l'(x_0)u_l(x) - (1+\bar{n}\delta_{p2})u_l(x_0)u_l'(x)}{(1+\bar{n}\delta_{p1})u_l'(x_0)w_l(x) - (1+\bar{n}\delta_{p2})u_l(x_0)w_l'(x)} \tag{5.7}$$

with $\bar{n} = (n_0/n) - 1$. Equation (5.6) shows that the quantities $-R^{(p)}_l$ can also be interpreted as the elements of the transition matrix for a homogeneous sphere. In fact, according to (4.28), (4.33), and (5.6)

$$\mathcal{S}^{(p)}_l = -R^{(p)}_l \,. \tag{5.8}$$

Moreover, although according to (4.29) and (5.6) the scattering amplitude has the form

$$f_{\eta\eta'} = \frac{\mathrm{i}}{4\pi k}\sum_{plm} W^{(p)*}_{\mathrm{S}\eta lm} R^{(p)}_l W^{(p)}_{\mathrm{I}\eta' lm} \,, \tag{5.9}$$

it is actually diagonal in η on account of the reciprocity theorem (2.30). It should be borne in mind, however, that the diagonal elements $f_{\eta\eta}$ are complex numbers with a different phase, so that the scattered wave turns out to be elliptically polarized even when the incident wave is linearly polarized.

To get an accurate representation of the scattered field, the sum in (5.9) must be extended to a sufficiently high value of l, say l_{M}. In other words, the convergence of the calculation must always be checked. A detailed discussion of this point has been given, e.g. by Stratton [6], who shows that, to get a fair convergence for a sphere of *size parameter* x, it is necessary to include into (5.9) terms up to $l_{\mathrm{M}} > x$. In practice, when $x \leq 0.1$ one needs to consider the $l = 1$ or, at most, the terms up $l = 2$ only and, for smaller values of x, one can expand the elements of the transition matrix in powers of x thus obtaining the well known RSA (see Sect. 4.6.1) [5]. It should be borne in mind, however, that the elements of the transition matrix as well as the convergence of the scattered field depends not only on the *size parameter* but also on the refractive index n_0 (that is contained in x_0). Therefore, as long as the refractive indexes are frequency independent, the response of a spherical scatterer does not depend separately on ρ and λ, but rather on their ratio. This is the principle of *optical scaling* that allows the experimentalists to test the reliability of the theoretical predictions using microwave devices and large scale scatterers [68]. We will return on this point in Chap. 7, just when discussing the comparison of theoretical predictions with the experimental data.

We conclude this section by showing that (4.65) for the polarizability of a particle of arbitrary shape reduces to the well known Lorentz–Lorenz form when the particle at hand is a small homogeneous sphere of radius ρ and refractive index n_0. Due to spherical symmetry, the transition matrix elements are independent of m so that from (5.8) we get

$$\alpha = \frac{3}{2}\mathrm{i} \lim_{k \to 0} \frac{1}{k^3} R_1^{(2)} \tag{5.10}$$

and thus the polarizability reduces to a scalar. It is then an easy matter to see that, by expanding $R_1^{(2)}$ in terms of the size parameter, one gets by (5.10) the Lorentz–Lorenz formula [5], which, for a homogeneous sphere, gives α in terms of the refractive index.

5.1.1 Homogeneous Spheres Sustaining Longitudinal Waves

Mie theory is endowed of all the accuracy of Maxwell electromagnetic theory. Nevertheless, it is based on the assumption that the material of the scattering sphere can sustain the propagation of transverse waves only. This assumption, quite natural at the time Mie theory was formulated, came into question when Ferrell [69] and Ferrel and Stern [70] were able to show that thin metal foils may sustain the propagation of longitudinal polarization waves when the frequency of the exciting field exceeds the plasma frequency. Of course, the occurrence of logitudinal waves implies a revision of the boundary conditions that must be satisfied by the electromagnetic field [71]. Melnyk and Harrison [72] formulated the theory of the excitation of plasma waves in metals and were able to establish the correct boundary conditions for the electromagnetic field across the surface between a nondispersive nonabsorbing dielectric medium, tipically the vacuum, and a semiinfinite metallic nonmagnetic material. The key remark of Melnyk and Harrison is that, when a plane wave impinges on the surface at nonnormal incidence, inhomogeneous plane waves may arise and propagate within the metal. Eventually, Ruppin [73] extended Mie theory to the case of small metal spheres whose material sustains the propagation of longitudinal waves. The conclusions of Ruppin are that, when the frequency of the incident plane wave exceeds the plasma frequency, the optical properties of the scattering sphere may be noticeably affected whereas, at lower frequencies, they are practically indistinguishable from those predicted by the classical Mie theory.

The theory that we are going to expound is essentially that of Ruppin transcribed into the notation we use in this book. Accordingly, we consider a homogeneous sphere of radius ρ centered at the origin of the coordinate frame. The external field is, as usual, the superposition of an incident polarized plane wave, whose multipole expansion is given by (4.13), and the scattered field whose expansion is given by (4.14). The expansion of the field within the sphere requires some further comment, however. When longitudinal waves can propagate the equation $\nabla \cdot \boldsymbol{E} = 0$ is no longer valid so that the waves are not transverse. As a result, the usual divergenceless multipole fields $\boldsymbol{J}_{lm}^{(p)}$ are not sufficient for the expansion but must be supplemented by the longitudinal multipole fields

$$\boldsymbol{J}_{\mathrm{L}lm}(\boldsymbol{r}, k_{\mathrm{L}}) = \frac{1}{k_{\mathrm{L}}}[l(l+1)]^{-1/2} \nabla j_l(k_{\mathrm{L}} r) Y_{lm}(\hat{\boldsymbol{r}}) \ ,$$

where $k_{\mathrm{L}} = n_{\mathrm{L}} k_{\mathrm{v}}$ is the propagation constant of the longitudinal waves and n_{L} is the corresponding refractive index. The refractive index appropriate to the propagation of the transverse waves will be denoted with n_0 as in the preceding section. Actually, the longitudinal multipole fields $\boldsymbol{J}_{\mathrm{L}lm}$ coincide with the Hansen's vectors $\boldsymbol{L}_{lm}$ with an everywhere regular radial function. Accordingly the internal electric field can be written as a superposition of the customary transverse field with expansion given by (5.1) and of a longitudinal field with expansion

$$\boldsymbol{E}_{\mathrm{L}\eta} = E_0 \sum_{lm} \boldsymbol{J}_{\mathrm{L}lm}(\boldsymbol{r}, k_{\mathrm{L}}) C_{\mathrm{L}\eta lm} \ . \tag{5.11}$$

Note that, since expansion (5.11) includes curl-free multipole fields only, there is no magnetic field associated to the longitudinal waves. Therefore, the expansion of the total magnetic field is not affected by the occurrence of longitudinal waves, as it is necessary in any non magnetic material. Of course, besides the customary boundary conditions (continuity of the tangential components of the electric and magnetic field) a further condition must be satisfied, i.e., the normal component of the electric displacement must be continuous. On account that the vector harmonics $\hat{\boldsymbol{r}} Y_{lm}$ form with the transverse harmonics $\boldsymbol{Z}_{lm}^{(p)}$ a complete ortonormal set, we use the same technique of the preceding section and write the boundary conditions as

$$\int (\boldsymbol{E}_{\mathrm{I}\eta} + \boldsymbol{E}_{\mathrm{S}\eta}) \cdot \boldsymbol{Z}_{lm}^{(p)*}\, \mathrm{d}\Omega = \int (\boldsymbol{E}_{\mathrm{T}\eta} + \boldsymbol{E}_{\mathrm{L}\eta}) \cdot \boldsymbol{Z}_{lm}^{(p)*}\, \mathrm{d}\Omega \,,$$
$$\int (\boldsymbol{B}_{\mathrm{I}\eta} + \boldsymbol{B}_{\mathrm{S}\eta}) \cdot \boldsymbol{Z}_{lm}^{(p)*}\, \mathrm{d}\Omega = \int \boldsymbol{B}_{\mathrm{T}\eta} \cdot \boldsymbol{Z}_{lm}^{(p)*}\, \mathrm{d}\Omega \,,$$
$$\int (\boldsymbol{E}_{\mathrm{I}\eta} + \boldsymbol{E}_{\mathrm{S}\eta}) \cdot \hat{\boldsymbol{r}} Y_{lm}^{*}\, \mathrm{d}\Omega = \int (\boldsymbol{E}_{\mathrm{T}\eta} + \boldsymbol{E}_{\mathrm{L}\eta}) \cdot \hat{\boldsymbol{r}} Y_{lm}^{*}\, \mathrm{d}\Omega \,.$$

Substitution of the appropriate expansions then yields for each l and m the equations

$$h_l(x) A_{\eta lm}^{(1)} + j_l(x) W_{\mathrm{I}\eta lm}^{(1)} = j_l(x_0) C_{\eta lm}^{(1)} \,, \tag{5.12a}$$

$$\frac{1}{x}\left\{ \left[x h_l(x)\right]' A_{\eta lm}^{(2)} + \left[x j_l(x)\right]' W_{\mathrm{I}\eta lm}^{(2)} \right\} = \frac{1}{x_0}\left[x_0 j_l(x_0)\right]' C_{\eta lm}^{(2)} - \frac{\mathrm{i}}{x_\mathrm{L}} j_l(x_\mathrm{L}) C_{\mathrm{L}\eta lm} \,, \tag{5.12b}$$

$$\frac{n}{x}\left\{ \left[x h_l(x)\right]' A_{\eta lm}^{(1)} + \left[x j_l(x)\right]' W_{\mathrm{I}\eta lm}^{(1)} \right\} = \frac{n_0}{x_0}\left[x_0 j_l(x_0)\right]' C_{\eta lm}^{(1)} \,, \tag{5.12c}$$

$$n\left[h_l(x) A_{\eta lm}^{(2)} + j_l W_{\mathrm{I}\eta lm}^{(2)}\right] = n_0 j_l(x_0) C_{\eta lm}^{(2)} \,, \tag{5.12d}$$

$$\frac{\mathrm{i}\sqrt{l(l+1)}}{x} j_l(x) W_{\mathrm{I}\eta lm}^{(2)} + \frac{\mathrm{i}\sqrt{l(l+1)}}{x} h_l(x) A_{\eta lm}^{(2)} = \frac{1}{\sqrt{l(l+1)}} j_l'(x_\mathrm{L}) C_{\mathrm{L}\eta lm} \,, \tag{5.12e}$$

where $x_\mathrm{L} = k_\mathrm{L}\rho$ and the definitions of other symbols are as given in Sec. 5.1. Eliminating the amplitudes of the internal field, both transverse and longitudinal, we get for $A_{\eta lm}^{(1)}$ the same expression (5.5a) of Sect. 5.1, whereas the expression for $A_{\eta lm}^{(2)}$ turns out to be

$$A_{\eta lm}^{(2)} = -\frac{j_l'(x_\mathrm{L})\left[n u_l'(x_0) u_l(x) - n_0 u_l(x_0) u_l'(x)\right]/k_\mathrm{v} + j_l(x) d_l}{j_l'(x_\mathrm{L})\left[n u_l'(x_0) w_l(x) - n_0 u_l(x_0) w_l'(x)\right]/k_\mathrm{v} + h_l(x) d_l} W_{\mathrm{I}\eta lm}^{(2)} = -R_l^{(2)} W_{\mathrm{I}\eta lm}^{(2)} \,, \tag{5.13}$$

with

$$d_l = (n_0^2 - n^2)\frac{l(l+1)}{k_\mathrm{L}} j_l(x_0) j_l(x_\mathrm{L}) \,.$$

Even in this case the transition matrix is given by (5.6) as the spherical symmetry implies the independence of m of the elements of S.

5.2 Radially Nonhomogeneous Spheres

The Mie theory has been extended by Wyatt [74] to radially nonhomogeneous spheres, viz., to spheres of radius ρ whose refractive index, $n_0 = n_0(r)$, is a regular function of the distance from the center. The external medium is again assumed to be homogeneous and nonabsorbing so that both the incident and the scattered field still have the multipole expansions (4.13) and (4.14), respectively. On the contrary, the expansion of the field within the sphere requires some further consideration, because, when the refractive index is space-dependent, the electric and the magnetic field do not satisfy the Helmholtz equation but rather the system

$$\nabla \times \nabla \times \boldsymbol{E} - n_0^2 k_{\mathrm{v}}^2 \boldsymbol{E} = 0 , \tag{5.14a}$$

$$\nabla \times \nabla \times \boldsymbol{B} - n_0^2 k_{\mathrm{v}}^2 \boldsymbol{B} = -\mathrm{i} k_{\mathrm{v}} \nabla n_0^2 \times \boldsymbol{E} , \tag{5.14b}$$

that is coupled because of the assumed nonhomogeneity of the medium. Due to the spherical symmetry of the scatterer, however, the internal field can still be expanded in a series of vector spherical harmonics, whereas the inhomogeneity of the refractive index suggests that a single radial function is not sufficient for the description of the field. Therefore, we assume that the electric and the magnetic field can be expanded in the form

$$\boldsymbol{E}_{\mathrm{T}\eta} = E_0 \sum_{lm} \left[C^{(1)}_{\eta lm} \Phi_l(r) \boldsymbol{X}_{lm}(\hat{\boldsymbol{r}}) + C^{(2)}_{\eta lm} \frac{1}{n_0^2} \frac{1}{k_{\mathrm{v}}} \nabla \times \Psi_l(r) \boldsymbol{X}_{lm}(\hat{\boldsymbol{r}}) \right] , \tag{5.15a}$$

$$\mathrm{i}\boldsymbol{B}_{\mathrm{T}\eta} = E_0 \sum_{lm} \left[C^{(1)}_{\eta lm} \frac{1}{k_{\mathrm{v}}} \nabla \times \Phi_l(r) \boldsymbol{X}_{lm}(\hat{\boldsymbol{r}}) + C^{(2)}_{\eta lm} \Psi_l(r) \boldsymbol{X}_{lm}(\hat{\boldsymbol{r}}) \right] , \tag{5.15b}$$

where the radial functions $\Phi_l(r)$ and $\Psi_l(r)$ must satisfy appropriate equations. The expansions (5.15) are suggested by the fact that, for whatever choice of the radial functions $\nabla \cdot \boldsymbol{B} = 0$ and, as it is easily verified, $\nabla \cdot n_0^2 \boldsymbol{E} = 0$ for any radial dependence of the refractive index. We now substitute the expansions (5.15) into (1.3b) with the result

$$\begin{aligned} \sum_{lm} \Bigg[C^{(1)}_{\eta lm} \nabla \times \Phi_l(r) \boldsymbol{X}_{lm}(\hat{\boldsymbol{r}}) &+ C^{(2)}_{\eta lm} \frac{1}{n_0^2} \frac{1}{k_{\mathrm{v}}} \nabla \times \nabla \times \Psi_l(r) \boldsymbol{X}_{lm}(\hat{\boldsymbol{r}}) \\ &+ C^{(2)}_{\eta lm} \left(\frac{\mathrm{d}}{\mathrm{d}r} \frac{1}{n_0^2} \right) \frac{1}{k_{\mathrm{v}}} \hat{\boldsymbol{r}} \times \nabla \times \Psi_l(r) \boldsymbol{X}_{lm}(\hat{\boldsymbol{r}}) \Bigg] \\ = \sum_{lm} \left[C^{(1)}_{\eta lm} \nabla \times \Phi_l(r) \boldsymbol{X}_{lm}(\hat{\boldsymbol{r}}) \right. &+ \left. k_{\mathrm{v}} C^{(2)}_{\eta lm} \Psi_l(r) \boldsymbol{X}_{lm}(\hat{\boldsymbol{r}}) \right] , \end{aligned}$$

from which, due to the independence of the vector spherical harmonics, it follows

$$\begin{aligned} \frac{1}{n_0^2} \frac{1}{k_{\mathrm{v}}} \nabla \times \nabla \times \Psi_l(r) \boldsymbol{X}_{lm}(\hat{\boldsymbol{r}}) &- \frac{2}{n_0^3} \frac{\mathrm{d}n_0}{\mathrm{d}r} \frac{1}{k_{\mathrm{v}}} \hat{\boldsymbol{r}} \times \nabla \times \Psi_l(r) \boldsymbol{X}_{lm}(\hat{\boldsymbol{r}}) \\ &= k_{\mathrm{v}} \Psi_l(r) \boldsymbol{X}_{lm}(\hat{\boldsymbol{r}}) . \end{aligned}$$

Now, according to (1.46b), $\nabla \cdot \Psi_l(r)\boldsymbol{X}_{lm}(\hat{\boldsymbol{r}}) = 0$, for whatever choice of the radial function. Therefore, with the help of the identity (1.5) we get

$$-\nabla^2 \Psi_l(r)\boldsymbol{X}_{lm}(\hat{\boldsymbol{r}}) + \frac{2}{n_0}\frac{\mathrm{d}n_0}{\mathrm{d}r}\frac{1}{r}\frac{\mathrm{d}}{\mathrm{d}r}\big[r\Psi_l(r)\big]\boldsymbol{X}_{lm}(\hat{\boldsymbol{r}}) - k_\mathrm{v}^2 n_0^2 \Psi_l(r)\boldsymbol{X}_{lm}(\hat{\boldsymbol{r}}) = 0 \,.$$

Since the vector spherical harmonics are eigenvectors of the angular momentum, we conclude that the radial function $\Psi_l(r)$ should be a solution, regular at $r = 0$, of the equation

$$\left[\frac{\mathrm{d}^2}{\mathrm{d}r^2} - \frac{l(l+1)}{r^2} + k_\mathrm{v}^2 n_0^2 - \frac{2}{n_0}\frac{\mathrm{d}n_0}{\mathrm{d}r}\frac{\mathrm{d}}{\mathrm{d}r}\right]\big[r\Psi_l(r)\big] = 0 \,. \tag{5.16}$$

Analogously, by substituting the expansions (5.15) into (1.3b), we find that the radial function $\Phi_l(r)$ must be a solution, regular at $r = 0$, of the equation

$$\left[\frac{\mathrm{d}^2}{\mathrm{d}r^2} - \frac{l(l+1)}{r^2} + k_\mathrm{v}^2 n_0^2\right]\big[r\Phi_l(r)\big] = 0 \,. \tag{5.17}$$

It may be useful to stress that the radial equations (5.16) and (5.17) can also be obtained by substituting the expansions (5.15) into (5.14) instead than into the Maxwell equations (1.3). Anyway, by introducing the variable $\xi = kr$ and the functions

$$G_l^{(1)} = \xi\Phi_l \,, \quad G_l^{(2)} = \xi\Psi_l \,,$$

equations (5.16) and (5.17) can be rewritten in more compact form as

$$\frac{\mathrm{d}^2 G_l^{(p)}}{\mathrm{d}\xi^2} - \frac{2}{n_0}\frac{\mathrm{d}n_0}{\mathrm{d}\xi}\frac{\mathrm{d}G_l^{(2)}}{\mathrm{d}\xi}\delta_{p2} + \left[\left(\frac{n_0}{n}\right)^2 - \frac{l(l+1)}{\xi^2}\right] G_l^{(p)} = 0 \,, \tag{5.18}$$

that can be integrated numerically. Needless to say that, if n_0 becomes a constant, (5.17) becomes identical to (5.16), and one can choose the normalization so that $\Phi_l = \Psi_l = j_l(n_0 k_\mathrm{v} r)$.

We are now able to impose the boundary conditions by the same procedure that we used for homogeneous spheres. The result is

$$A_{\eta lm}^{(p)} = -R_l^{(p)} W_{\mathrm{I}\eta lm}^{(p)} \,,$$

where [75]

$$R_l^{(p)} = \frac{G_l^{(p)\prime}(x)u_l(x) - (1+\bar{n}\delta_{p2})^2 G_l^{(p)}(x)u_l'(x)}{G_l^{(p)\prime}(x)w_l(x) - (1+\bar{n}\delta_{p2})^2 G_l^{(p)}(x)w_l'(x)} \tag{5.19}$$

with $x = k\rho$. We stress again that, due to the spherical symmetry, the transition matrix is diagonal and its elements are independent of m.

An interesting application of the theory expounded so far is the calculation of the field scattered by spheres with a soft surface [76, 77], i.e., by spherical scatterers for which the transition from the material of the sphere to that of the surrounding medium is not sharp but occurs with a continuous variation both of the refractive index and of its radial derivative. Accordingly, we assume that in the interval $r_- \leq r \leq r_+$ the refractive index varies from n_- to n_+. By defining the quantities

$$\Delta = n_+^2 - n_-^2 \, , \qquad s = \frac{r - r_-}{r_+ - r_-} \, ,$$

we can assume that, in the layer between r_- and r_+, the refractive index varies according to the formula

$$n_0^2(r) = n_-^2 + (3s^2 - 2s^3)\Delta \, . \tag{5.20}$$

The preceding law of variation ensures the continuity both of n_0^2 and of its radial derivative and can therefore be inserted into (5.18) for calculating the radial functions. The same technique can be used to describe the scattering from spheres composed of several concentric layers. To this end it suffices to interpose between any pair of contiguous layers a thin transition layer within which the refractive index varies according to (5.20). Our experience proved that, provided the transition layer is thin enough, the scattering properties of the spheres are not altered within numerical accuracy [76].

Finally, we note that (5.10) for the polarizability of a small sphere applies also to radially nonhomogeneous spheres provided that $R_1^{(2)}$ is given by (5.19).

5.3 Resonances

When the extinction cross section of spheres is plotted versus the size parameter, more or less sharp peaks may occur, and we say that the scattering process has undergone resonances. The origin of this phenomenon for homogeneous spheres is easily understood on the ground of the theory in Sect. 5.1, provided the spheres cannot sustain the propagation of longitudinal waves. Equations (5.5), in fact, show that, when either

$$n_0 u_l'(x_0) w_l(x) - n u_l(x_0) w_l'(x) = 0 \, , \tag{5.21a}$$

or

$$n u_l'(x_0) w_l(x) - n_0 u_l(x_0) w_l'(x) = 0 \, , \tag{5.21b}$$

the amplitude of the scattered wave may become large even for small amplitude of the incident wave. In other words, spheres of radius ρ satisfying either of (5.21) support (almost) self-sustaining scattering modes even when the strength of the incident field is vanishingly small. Equations (5.21) can be satisfied by complex values of x_0 and, since the radius ρ is real, the wavevector must be complex thus yielding a damping of the field. Provided the imaginary part of x_0 is small, the damping itself will be small, and a resonance peak of finite height and width could occur. The interested reader can find the details of the analysis referred to above in the books of van de Hulst [5] and of Newton [22].

An alternative fruitful formulation of the theory of resonances both of homogeneous and radially nonhomogeneous spheres has been given by Johnson [78]. The starting point of this formulation is the remark that (5.16) becomes identical to the radial Schrödinger equation for a spherically symmetric system whose potential is

$$v_l(r) = \begin{cases} k_{\mathrm{v}}^2[n^2 - n_0^2(r)] + l(l+1)/r^2 \ , & \text{for } 0 \le r \le \rho \\ l(l+1)/r^2 \ , & \text{for } \rho \le r \le \infty \end{cases} \ . \tag{5.22}$$

The eigenvalue is $E = k_{\mathrm{v}}^2$ and, as usual, is determined by the condition of continuity of the radial function and of its radial derivative. The connection with the theory of the resonances stems from the remark that the potential function (5.22) may have a well in the vicinity of the surface of the particle for some ranges of k_{v}^2. In this respect, it should be borne in mind that the potential function itself is a function of the eigenvalue. Any eigenvalue that is located in the range between the top and the bottom of the well then belongs to a state in which the field can tunnel out of the potential well. This is just a resonance state in the same sense in which this term is used in quantum mechanics. Therefore, in Johnson's theory a resonance is to be interpreted as due to the shape of the potential. At this stage, using techniques that are well known in quantum mechanics, Johnson is able to give formulas for the width of the resonance for all the cases of interest for the refractive index of the sphere. In spite of its applicability to spherically symmetric scatterers only, Johnson's approach is, in our opinion, the method of choice for the interpretation of the observed resonances.

In case a homogeneous sphere can sustain the propagation of longitudinal waves, the theory of the resonances should be based on the vanishing of the denominator of (5.13). An analysis of this kind of resonances has been made by Ruppin [73] in whose paper the interested reader can find the details as well as a number of interesting results.

5.4 Aggregates of Spheres

The scatterers considered so far (homogeneous and radially nonhomogeneous spheres), on account of the ease of computation of their optical properties, have been widely used to attempt the interpretation of the observational data. These attempts have often been unsuccessful, however, because the particles that are most commonly met in actual observations are nonspherical to a more or less large extent and, even when their orientations are randomly distributed, there is not an unique spherical scatterer which can represent the average particle of the dispersion. In fact, according to the results of Sect. 4.5, the behavior of S in its general form cannot be assimilated by any averaging to that given by (4.33) for a spherical particle. In other words, the effects that stem from the lack of sphericity may be attenuated but never fully cancelled by the averaging procedure. The correctness of this statement will be proved in Chap. 7 through the discussion of actual calculations.

Several attempts have been made to devise model nonspherical particles whose optical properties could be calculated as exactly as possible, i.e., without resorting to any approximation. The first real progress was marked by Bruning and Lo [79] who devised a technique to calculate the optical properties of linear chains of identical spherical scatterers. The properties of this model were investigated by Peterson and Ström [80] for general geometry of the aggregation, whereas, as far as we know, the first application of the cluster model to the description of real particles is due to Gérardy and Ausloos [81]. Here we present the procedure devised for the calculation of the transition matrix of a group of N not necessarily equal spheres whose mutual distances are so small that they must be dealt with as one object [82]. The geometry of such kind of scatterer is arbitrary to a large extent, so that aggregates can be built to model particles of various shapes, in the sense of Sect. 1.1. The emphasis is on the transition matrix on account of the usefulness of the latter for performing orientational averages. The surrounding medium is assumed to be a homogeneous dielectric so that the incident field still has the form of a polarized plane wave whose multipole expansion is given by (4.13).

We number the spheres by an index α and indicate with $\boldsymbol{R}_\alpha$ the vector position of the center of the αth sphere of radius ρ_α and refractive index n_α (see Fig. 5.1). The following theory refers to aggregates of spheres that, if isolated, could be described by Mie Theory. This assumption is hardly necessary, however. To deal with metal spheres sustaining longitudinal waves or with radially nonhomogeneous spheres the theory requires only minor modifications that will be expounded later. We write the field scattered by the whole aggregate as the superposition of the fields scattered by each of the spheres in the form

$$\boldsymbol{E}_{\mathrm{S}\eta} = E_0 \sum_{\alpha} \sum_{plm} \boldsymbol{H}^{(p)}_{lm}(\boldsymbol{r}_\alpha, k) \mathcal{A}^{(p)}_{\eta\alpha lm} , \tag{5.23}$$

where the amplitudes $\mathcal{A}^{(p)}_{\eta\alpha lm}$ should be calculated so that $\boldsymbol{E}_{\mathrm{S}\eta}$ satisfy the appropriate boundary conditions at the surface of each of the spheres. The radiation condition at infinity is automatically satisfied by the field (5.23), because the expansion includes $\boldsymbol{H}$-multipole fields only. The field within each sphere is in turn taken in the form

$$\boldsymbol{E}_{\mathrm{T}\eta\alpha} = E_0 \sum_{plm} \boldsymbol{J}^{(p)}_{lm}(\boldsymbol{r}_\alpha, k_\alpha) \mathcal{C}^{(p)}_{\eta\alpha lm} , \tag{5.24}$$

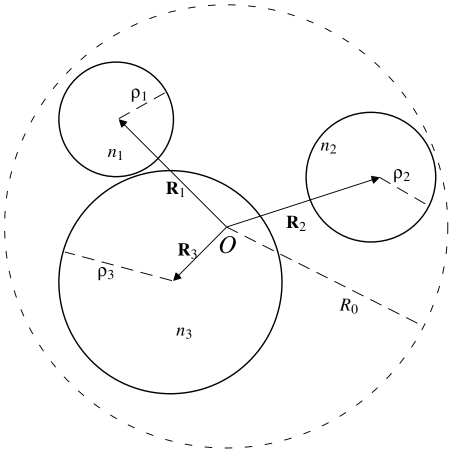

Fig. 5.1. Geometry for a cluster of three spheres. The dashed sphere separates the near-field from the far-field region

with $k_\alpha = n_\alpha k_\mathrm{v}$, so that it is regular everywhere within the sphere. The magnetic field is given by (5.2).

We now remark that the scattered field is given by a linear combination of multipole fields that have different origins, whereas the incident field is given by a combination of multipole fields centered at the origin of the coordinates. Since the boundary conditions must be imposed at the surface of each of the spheres, e.g. of the αth sphere, we resort to the addition theorem of Sect. 1.8 to rewrite the whole field in terms of multipole fields centered at $\boldsymbol{R}_\alpha$. In fact, with the help of this theorem the scattered field at the surface of the αth sphere turns out to be

$$\boldsymbol{E}_{\mathrm{S}\eta} = E_0 \sum_{plm} \left[\boldsymbol{H}_{lm}^{(p)}(\boldsymbol{r}_\alpha, k)\mathcal{A}_{\eta\alpha lm}^{(p)} + \sum_{\alpha'} \sum_{p'l'm'} \boldsymbol{J}_{lm}^{(p)}(\boldsymbol{r}_\alpha, k)\mathcal{H}_{\alpha lm\alpha' l'm'}^{(pp')}\mathcal{A}_{\eta\alpha' l'm'}^{(p')} \right] ,$$

where the quantities $\mathcal{H}$ are given by (1.73a) in the notation (1.75). Analogously, the incident field at the surface of the αth sphere is

$$\boldsymbol{E}_{\mathrm{I}\eta} = E_0 \sum_{plm} \sum_{p'l'm'} \boldsymbol{J}_{lm}^{(p)}(\boldsymbol{r}_\alpha, k)\mathcal{J}_{\alpha lm0l'm'}^{(pp')} W_{\mathrm{I}\eta l'm'}^{(p')} , \tag{5.25}$$

where $\boldsymbol{R}_0 = 0$ is the vector position of the origin, and the quantities $\mathcal{J}$ are defined in (1.73b) with the notation (1.75). At this stage, it is an easy matter to impose the boundary conditions by the same technique that we used for homogeneous spheres. Accordingly, we get for each α four equations among which the elimination of the amplitudes of the internal field is trivial. Once this elimination is effected, we remain with the system of linear nonhomogeneous equations

$$\sum_{\alpha'}\sum_{p'l'm'} \mathcal{M}^{(pp')}_{\alpha lm\alpha' l'm'} \mathcal{A}^{(p')}_{\eta\alpha' l'm'} = -\mathcal{W}^{(p)}_{\mathrm{I}\eta\alpha lm} , \tag{5.26}$$

where we define

$$\mathcal{W}^{(p)}_{\mathrm{I}\eta\alpha lm} = \sum_{p'l'm'} \mathcal{J}^{(pp')}_{\alpha lm0l'm'} W^{(p')}_{\mathrm{I}\eta l'm'} , \tag{5.27}$$

and

$$\mathcal{M}^{(pp')}_{\alpha lm\alpha' l'm'} = \left(R^{(p)}_{\alpha l}\right)^{-1} \delta_{\alpha\alpha'}\delta_{pp'}\delta_{ll'}\delta_{mm'} + \mathcal{H}^{(pp')}_{\alpha lm\alpha' l'm'} . \tag{5.28}$$

We notice that the quantities $R^{(p)}_{\alpha l}$ are the Mie coefficients for the scattering from the αth sphere. These quantities are the only ones that must be modified in case the spheres in the cluster either can sustain longitudinal waves or are radially nonhomogeneous. In the first case $R^{(1)}_l$ is still given by (5.5a) but $R^{(2)}_l$ must be given by (5.13). In the second case $R^{(p)}_l$ must be redefined by (5.19). In any case the index α should be inserted where appropriate. In turn the matrix H describes the multiple scattering processes that, in view of the small mutual distance, occur with noticeable strength among the spheres of the aggregate. The occurrence of these processes is a manifestation of the coupling between spheres. As a consequence, the amplitudes of the scattered field cannot be calculated one at a time, as is instead the case for isolated spheres, but must be calculated by solving the system (5.26). We remark that the elements $\mathcal{H}^{(pp')}_{\alpha lm\alpha' l'm'}$ of the transfer matrix couple multipole fields both of the same and of different parity with origin on different spheres. This is an immediate consequence of the addition theorem for the VHHs.

We now consider the formal solution to system (5.26)

$$\mathcal{A}^{(p)}_{\eta\alpha lm} = -\sum_{p'l'm'} \left[\mathrm{M}^{-1}\right]^{(pp')}_{\alpha lm\alpha' l'm'} \mathcal{W}^{(p')}_{\mathrm{I}\eta\alpha' l'm'} . \tag{5.29}$$

This equation may lead to the conclusion that matrix M^{-1} be the transition matrix of the aggregate. This conclusion is wrong because, according to (4.28), the transition matrix relates the multipole amplitudes of the incident field to those of the field scattered by the whole object. On the contrary, (5.29) relates the amplitudes of the incident field to those of the fields scattered by each sphere in the aggregate. In order to define the transition matrix for the whole aggregate it is necessary to express the scattered field in terms of multipole fields with the same origin. Actually, with the help of the addition theorem for the VHH, the scattered field can be cast into the form

$$\begin{aligned}\boldsymbol{E}_{\mathrm{S}\eta} = E_0 \sum_{plm}\sum_{\alpha'}\sum_{p'l'm'} &\boldsymbol{H}^{(p)}_{lm}(\boldsymbol{r},k)\mathcal{J}^{(pp')}_{0lm\alpha' l'm'}\mathcal{A}^{(p')}_{\eta\alpha' l'm'} \\ &= E_0 \sum_{plm} \boldsymbol{H}^{(p)}_{lm}(\boldsymbol{r},k) A^{(p)}_{\eta lm} ,\end{aligned}$$

which is valid at a large distance from the aggregate or, at least, outside the smallest sphere with center at O that includes the whole aggregate. The preceding equation shows that the field scattered by the whole cluster can be expanded as a series of vector multipole fields with a single origin (monocentered expansion) provided that the amplitudes are

$$A_{\eta lm}^{(p)} = \sum_{\alpha'} \sum_{p'l'm'} \mathcal{J}_{0lm\alpha'l'm'}^{(pp')} \mathcal{A}_{\eta\alpha'l'm'}^{(p')} \, . \tag{5.30}$$

Substituting for the amplitudes $\mathcal{A}$ their expression (5.29) one is led to define the transition matrix of the aggregate as

$$\mathcal{S}_{lml'm'}^{(pp')} = -\sum_{\alpha\alpha'} \sum_{qLM} \sum_{q'L'M'} \mathcal{J}_{0lm\alpha LM}^{(pq)} \left[\mathrm{M}^{-1}\right]_{\alpha LM\alpha'L'M'}^{(qq')} \mathcal{J}_{\alpha'L'M'0l'm'}^{(q'p')} \, . \tag{5.31}$$

The transition matrix defined in the preceding equation has the correct transformation properties under rotation, although it is not diagonal as a consequence of the lack of spherical symmetry of the aggregate as a whole.

The principle of electromagnetic scaling holds true also for aggregates. In fact, the elements (5.31) depend only on n, n_α, x_α and on the adimensional parameters $x_{\alpha\beta} = kR_{\alpha\beta}$ [see (1.73)]. As a result, provided all the refractive indices (i.e., those of the component spheres, n_α, and that of the external medium, n) are independent of wavelength, the scattered field turns out to depend on the parameters mentioned above, but it is independent of the absolute size of the aggregate.

5.4.1 T-scheme, E-scheme and Convergence of Calculations

Calculating the transition matrix of a cluster requires the inversion of matrix M whose order is, in principle, infinite. Naturally, the system (5.26) must be truncated to some finite order by including into the multipole expansions of the fields all the terms up to the multipole order l_I chosen so as to ensure the numerical stability of the results. l_I is the maximum value which l can take in expansions (5.23)–(5.25), so that it depends, in general, on the sphere index α. In fact, according to their scattering power, the spherical components may give considerably different contribution to the scattering of the cluster as a whole. The refinement of assigning a specific l_I for each sphere is unnecessary, however, when the scattering powers of the individual spheres are similar and one deals with compact structures. Anyway, to streamline our argument, we will assign henceforth only one value to l_I to be applied to all the spheres composing the cluster. For a cluster of N spheres this implies inverting a matrix of order $d = 2Nl_\mathrm{I}(l_\mathrm{I} + 2)$ that may grow rather big. Actually, the inversion of matrix M is a $O(d^3)$ process that accounts for a large share of all the calculations one is confronted with to solve this kind of scattering problem. Once matrix M^{-1} has been obtained, one has still to insert its elements into (5.31) to get the transition matrix of the aggregate. In this respect, we remark that the translation matrix J need not be a square matrix. In fact, according to (5.31), the *internal* indices L, M and L', M' are actually summed up so that $L, L' \leq l_{\mathrm{I}}$. In turn, the *external* indices l, m and l', m' are summed up in (4.14) and in (5.27) to get the field scattered by the whole cluster. Clearly, there is no reason to perform these sums for $l, l' \leq l_{\mathrm{I}}$. We could rather choose a different upper limit, say l_{E}, and sum over $l, l' \leq l_{\mathrm{E}}$. In order to reduce the computational effort required by the inversion of M, l_{I} must be kept as low as possible, whereas it has a substantially lower cost to be generous in the choice of l_{E} taking $l_{\mathrm{E}} \geq l_{\mathrm{I}}$ in order to have a better description of the scattered field.

A case in which the geometry reduces the computational effort is that of a linear cluster. Provided the centers of the spheres are chosen to lie on the $\bar{z}$ axis, matrix M turns out to be diagonal with respect to m and m' because this property pertains to matrix H according to (1.74). As a result, the inversion of M factorizes into the inversion of the matrices M_m that one obtains for each value of m. The order of M_m is $d_m = 2N(l_{\mathrm{I}} - |m| + 1 - \delta_{m0})$ and the whole inversion process speeds up dramatically. In Appendix A.4 the interested reader will find useful hints for exploiting the cylindrical symmetry of a linear cluster whatever in case the cylindrical axis is orthogonal to the $\bar{z}$ axis.

As regards the choice of l_{I}, it should also be borne in mind that n, n_α, x_α, and $x_{\alpha\beta}$ all contribute in determining the rate of convergence. Therefore, no general criterion of convergence can be given and the actual convergence should be checked for any specific application.

When we substitute (5.31) into (4.29), the resulting expression for elements of the scattering amplitude matrix $f_{\eta\eta'}$ turns out to contain the quantities

$$\sum_{p'l'm'} \mathcal{J}^{(pp')}_{\alpha lm0l'm'} W^{(p')}_{\mathrm{I}\eta l'm'} \quad \text{and} \quad \sum_{plm} W^{(p)*}_{\mathrm{S}\eta lm} \mathcal{J}^{(pp')}_{0lm\alpha'l'm'} \, .$$

Now, on account that

$$\exp(\mathrm{i}\boldsymbol{k}_{\mathrm{I}} \cdot \boldsymbol{r}) = \exp(\mathrm{i}\boldsymbol{k}_{\mathrm{I}} \cdot \boldsymbol{R}_\alpha) \exp(\mathrm{i}\boldsymbol{k}_{\mathrm{I}} \cdot \boldsymbol{r}_\alpha) \, ,$$

by expanding $\hat{\boldsymbol{u}}_{\mathrm{I}\eta} \exp(\mathrm{i}\boldsymbol{k}_{\mathrm{I}} \cdot \boldsymbol{r})$ and $\hat{\boldsymbol{u}}_{\mathrm{I}\eta} \exp(\mathrm{i}\boldsymbol{k}_{\mathrm{I}} \cdot \boldsymbol{r}_\alpha)$ we get

$$\mathcal{W}^{(p)}_{\mathrm{I}\eta\alpha lm} = \exp(\mathrm{i}\boldsymbol{k}_{\mathrm{I}} \cdot \boldsymbol{R}_\alpha) W^{(p)}_{\mathrm{I}\eta lm} \, . \tag{5.32}$$

Comparison of last equation with (5.25) then yields

$$\sum_{p'l'm'} \mathcal{J}^{(pp')}_{\alpha lm0l'm'} W^{(p')}_{\mathrm{I}\eta l'm'} = \exp(\mathrm{i}\boldsymbol{k}_{\mathrm{I}} \cdot \boldsymbol{R}_\alpha) W^{(p)}_{\mathrm{I}\eta lm} \, . \tag{5.33}$$

Substitution in (5.33) of $\hat{\boldsymbol{u}}_{\mathrm{S}\eta}$ in place of $\hat{\boldsymbol{u}}_{\mathrm{I}\eta}$ and $\boldsymbol{k}_{\mathrm{S}}$ in place of $\boldsymbol{k}_{\mathrm{I}}$ and complex conjugation then yields

$$\sum_{p'l'm'} \mathcal{J}^{(pp')*}_{\alpha lm0l'm'} W^{(p')*}_{\mathrm{S}\eta l'm'} = \exp(-\mathrm{i}\boldsymbol{k}_\mathrm{S} \cdot \boldsymbol{R}_\alpha) W^{(p)*}_{\mathrm{S}\eta lm} .$$

Provided the refractive index n is real, the definition of J in Sect. 1.8 implies

$$\mathcal{J}^{(pp')*}_{\alpha lm0l'm'} = \mathcal{J}^{(p'p)}_{0l'm'\alpha lm} , \tag{5.34}$$

so that

$$\sum_{plm} W^{(p)*}_{\mathrm{S}\eta lm} \mathcal{J}^{(pp')}_{0lm\alpha' l'm'} = W^{(p')*}_{\mathrm{S}\eta l'm'} \exp(-\mathrm{i}\boldsymbol{k}_\mathrm{S} \cdot \boldsymbol{R}_{\alpha'}) . \tag{5.35}$$

Using (5.34) to get $f_{\eta\eta'}$ slightly reduces the amount of calculation. Using (5.33) and (5.35) is somewhat more advantageous but at a cost: their use prevents, indeed, obtaining the transition matrix as defined by (5.31). As a result, we cannot use the averaging procedures of Chap. 4. In fact, the true transition matrix cannot be reminiscent of information either on the excitation (through the factors $\exp(\mathrm{i}\boldsymbol{k}_\mathrm{I} \cdot \boldsymbol{R}_\alpha)$) or on observation (through the factors $\exp(-\mathrm{i}\boldsymbol{k}_\mathrm{S} \cdot \boldsymbol{R}_{\alpha'})$). Therefore, use of (5.33) and (5.35) is appropriate only when orientational averages are not required.

Hereafter we will refer to calculations in which we use only the transfer matrix J to get the transition matrix S as *T-scheme calculations*, whereas the calculations performed using either (5.33) or both (5.33) and (5.35) will be referred to as *scattering calculations by the E-scheme*. Unlike the approximate scheme devised by Xu [83] to get the expression of the scattered field in the far zone, the E-scheme is exact as it implies no further approximation beyond the customary truncation of the multipole expansions. The formulas for the E-scheme have been recently discussed by Stout, Auger and Lafait [84] in the framework of their thorough study of the formal properties of the scattering matrix of aggregates of spheres. On our part, we tested the reliability of this scheme through extensive use in comparing our theoretical predictions [85] with the experimental data of Schuerman and Wang from well characterized clusters in fixed orientation [86,87]. Finally, if different l_E and l_I are not used or when a value of l_E cannot be defined for the problem at hand, e.g. in the case of spherical scatterers, we will everywhere indicate the convergence value as l_M.

On account of the preceding considerations on convergence, one is led to conclude that, to get fairly convergent results, say to three or four decimal places, the computational effort may grow rather heavy. Nevertheless, there are several cases in which pursuing such an accuracy is pointless: in fact, as we outlined in Sect. 1.1, when one deals with a dispersion of particles, the distribution may be such that the scattering features of the single objects are smoothed out. When this is the case, achieving an accuracy lower than the one that is mathematically possible may be sufficient to all practical effects. Actually, one can save a safe control of the degree of convergence by starting the calculations with a comparatively low value of l_M and then increasing this value until necessary to achieve the required accuracy. In Chap. 7 we will return to this point by discussing the convergence in two specific applications.

5.5 Spheres Containing Spherical Inclusions

An interesting case that is often met in practice is that of a homogeneous sphere containing one or more spherical inclusions. Clearly, in case there exist a single centered inclusion the problem reduces to that of a layered sphere.

The procedure we are going to describe [88, 89] is similar to that devised by Fikioris and Uzunoglu [90]. These authors, however, limited themselves to approximate calculations appropriate for the case of a small inclusion whose refractive index differs little from that of the host sphere. A different approach has been used by Skaropoulos, Ioannidou, and Chrissoulidis [91] and by Ioannidou, and Chrissoulidis [92], but the final equations are essentially similar to those we are going to present and give identical results.

We partition the space into three regions (Fig. 5.2): the external region that is filled by a homogeneous nondispersive medium of refractive index n; the interstitial region, of radius ρ_0, filled by a homogeneous, possibly absorptive, medium of refractive index n_0; and the region within the inclusions, each of radius ρ_α, whose material has a refractive index n_α that may be radially nonhomogeneous and thus depend on r_α. The propagation constants in the regions defined above are

$$k = nk_{\rm v} \ , \quad k_0 = n_0 k_{\rm v} \ , \quad k_\alpha = n_\alpha k_{\rm v} \ ,$$

respectively. The field in the external region is, as usual, the superposition of the incident field and of the field scattered by the whole object. The respective multipole expansions are given by (4.13) and (4.14). In turn, the field

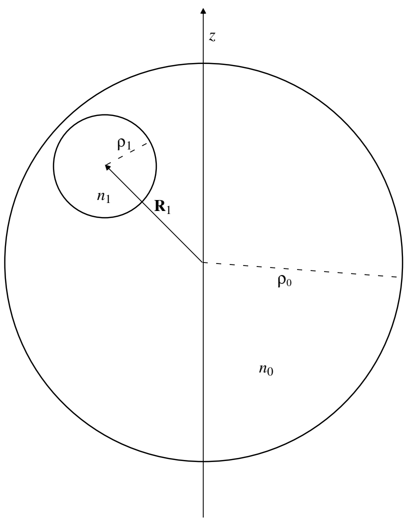

Fig. 5.2. Geometry for a sphere containing inclusions. Only one inclusion is shown for the sake of clarity

within the inclusions can be expanded in the form of (5.24) provided that they are homogeneous, whereas, when they are radially nonhomogeneous, the appropriate expansion is that in (5.15) as it reads for the αth sphere. Finally, we assume that the field in the interstitial region is the superposition of the field that would exist in the absence of any inclusion and of the field scattered by the inclusions themselves. Accordingly, within the interstitial region we expand the field in the form

$$\boldsymbol{E}_{\mathrm{T}\eta 0} = E_0 \sum_{plm} \left[\sum_{\alpha} \boldsymbol{H}_{lm}^{(p)}(\boldsymbol{r}_\alpha, k_0) \mathcal{P}_{\eta\alpha lm}^{(p)} + \boldsymbol{J}_{lm}^{(p)}(\boldsymbol{r}_0, k_0) \mathcal{P}_{\eta 0 lm}^{(p)} \right] . \tag{5.36}$$

The calculation of the multipole amplitudes of the field scattered by the whole object is performed in two steps. First, we impose the boundary conditions to the internal field and to the interstitial field across the surface of each one of the inclusions. This procedure leads us to eliminating the amplitudes of the field internal to each of the inclusions and to determine the amplitudes of the interstitial field. Second, we impose the boundary conditions to the interstitial field and to the external field across the surface of the host sphere to get the amplitudes of the scattered field. Of course, both steps require using the addition theorem for multipole fields in order to get the expansions in terms of multipole fields centered at the appropriate origin. Anyway, as a result of the first step, we get a system of linear nonhomogeneous equations that we write in matrix form as

$$\begin{vmatrix} (\mathrm{R})^{-1} + \mathrm{H} & \mathrm{J}_{\leftarrow 0} \\ \mathrm{R}_W \mathrm{J}_{0\leftarrow} & (\mathrm{R}_0)^{-1} \end{vmatrix} \begin{vmatrix} \mathrm{P} \\ \mathrm{P}_0 \end{vmatrix} = \begin{vmatrix} 0 \\ \mathrm{W} \end{vmatrix} , \tag{5.37}$$

or, more compactly

$$\mathcal{M}\mathcal{P} = \mathcal{W} .$$

To solve the system (5.37) we have to invert the matrix $\mathcal{M}$, but the actual calculation of the P's, on account of the particular form of the vector $\mathcal{W}$, that contains a subvector of zeros, involves only the rightmost columns of the inverted matrix. So, if we write $\mathcal{M}^{-1}$ in the partitioned form

$$\mathcal{M}^{-1} = \begin{vmatrix} \mathrm{Z}_1 & \mathrm{Z}_{10} \\ \mathrm{Z}_{01} & \mathrm{Z}_0 \end{vmatrix} ,$$

where all the submatrices are of the same order as the corresponding ones appearing in $\mathcal{M}$, and define the rectangular submatrix

$$\mathcal{Z} = \begin{vmatrix} \mathrm{Z}_{10} \\ \mathrm{Z}_0 \end{vmatrix} ,$$

the P's are given by the equation

$$\mathcal{P} = \mathcal{Z}\,\mathrm{W} .$$

Once the amplitudes P have been calculated, we proceed to the second step which yields

$$\mathrm{A} = \mathcal{T}\mathcal{P} = \mathrm{SW} , \tag{5.38}$$

where $\mathcal{T}$ is the rectangular matrix

$$\mathcal{T} = \left| \mathrm{M_W J_{0\leftarrow}} \quad \mathrm{M_0} \right| .$$

In the preceding equations, matrix R characterizes the inclusions and its matrix elements are given by the equation

$$\mathcal{R}^{(pp')}_{\alpha lm\alpha' l'm'} = \delta_{pp'}\delta_{ll'}\delta_{mm'}\,\delta_{\alpha\alpha'} R^{(p)}_{\alpha l} ,$$

where, in the case of homogeneous inclusions, the quantities $R^{(p)}_{\alpha\, l}$ are identical to those defined in Sect. 5.4 for aggregated spheres. We stress again that they are the only quantities that must be modified when the inclusions are radially nonhomogeneous, in which case, set aside the index α, they are given by (5.19), and as the inclusions are embedded into the interstitial medium, in calculating $R^{(p)}_{\alpha l}$ we must use $\bar{n}_\alpha = (n_\alpha/n_0) - 1$.

Matrix $\mathrm{R_0}$ characterizes the external sphere and its elements are given by

$$\mathcal{R}^{(pp')}_{0\,lml'm'} = \delta_{pp'}\delta_{ll'}\delta_{mm'}\, R^{(p)}_{0l}$$

with

$$R^{(p)}_{0l} = \mathrm{i}[(1+\bar{n}_0\delta_{p1})u_l(k_0\rho_0)w'_l(k\rho_0) - (1+\bar{n}_0\delta_{p2})u'_l(k_0\rho_0)w_l(k\rho_0)]^{-1} .$$

In turn, matrix H describes the multiple scattering processes that occur among the inclusions, whereas the matrices $\mathrm{J_{\leftarrow 0}}$ and $\mathrm{J_{0\leftarrow}}$ describe multiple scattering processes that occur among the inclusions and the external sphere. The matrix elements of H, $\mathrm{J_{\leftarrow 0}}$, and $\mathrm{J_{0\leftarrow}}$ are $\mathcal{H}^{(pp')}_{\alpha lm\alpha' l'm'}$, $\mathcal{J}^{(pp')}_{\alpha lm0l'm'}$, and $\mathcal{J}^{(pp')}_{0lm\alpha' l'm'}$, respectively. They are just the ones that we already used in Sect. 5.4 for aggregated spheres, with n_0 substituted for n, however.

Matrix $\mathrm{M_0}$ is diagonal and its elements are given by the equation

$$\mathcal{M}^{(pp')}_{0lml'm'} = \delta_{pp'}\delta_{ll'}\delta_{mm'}\, M^{(p)}_{0l} ,$$

where

$$M^{(p)}_{0l} = \mathrm{i}[(1+\bar{n}_0\delta_{p1})u_l(k_0\rho_0)u'_l(k\rho_0) - (1+\bar{n}_0\delta_{p2})u'_l(k_0\rho_0)u_l(k\rho_0)] .$$

Finally, the elements of the matrices $\mathrm{R_W}$ and $\mathrm{M_W}$ are

$$\mathcal{R}^{(pp')}_{\mathrm{W}lml'm'} = \delta_{pp'}\delta_{ll'}\delta_{mm'}\, R^{(p)}_{\mathrm{W}l}$$

and

$$\mathcal{M}^{(pp')}_{\mathrm{W}lml'm'} = \delta_{pp'}\delta_{ll'}\delta_{mm'}\, M^{(p)}_{\mathrm{W}l} ,$$

where

$$R_{\mathrm{W}l}^{(p)} = -\mathrm{i}[(1+\bar{n}_0\delta_{p1})w_l(k_0\rho_0)w_l'(k\rho_0) - (1+\bar{n}_0\delta_{p2})w_l'(k_0\rho_0)w_l(k\rho_0)]$$

and

$$M_{\mathrm{W}l}^{(p)} = \mathrm{i}[(1+\bar{n}_0\delta_{p1})w_l(k_0\rho_0)u_l'(k\rho_0) - (1+\bar{n}_0\delta_{p2})w_l'(k_0\rho_0)u_l(k\rho_0)] \; .$$

Note that, in defining $R_{0l}^{(p)}$, $M_{0l}^{(p)}$, $R_{\mathrm{W}l}^{(p)}$, and $M_{\mathrm{W}l}^{(p)}$, we use $\bar{n}_0 = (n/n_0) - 1$. The preceding equations solve the problem at hand. In particular, (5.38) gives the definition of the transition matrix S and allows us to perform, when necessary, orientational averages.

When the host sphere contains a single eccentric inclusion, (5.37) and (5.38) can be formally solved to get the transition matrix. In fact, (5.37) does not contain H, that appears only when more than one inclusion is present, so that

$$\mathrm{S} = \left(\mathrm{M}_0 - \mathrm{M}_W \mathrm{J}_{0\leftarrow 1}\mathrm{R}_1\mathrm{J}_{1\leftarrow 0}\right)\left(\mathrm{R}_0^{-1} - \mathrm{R}_W \mathrm{J}_{0\leftarrow 1}\mathrm{R}_1\mathrm{J}_{1\leftarrow 0}\right)^{-1} . \tag{5.39}$$

It may be useful to also consider the case in which there exist a single spherical inclusion concentric to the host sphere. In this case, both the matrices $\mathrm{J}_{\leftarrow 0}$ and $\mathrm{J}_{0\leftarrow}$ in (5.37) tend to $\mathbf{1}$ whereas the matrix H is not present. As a consequence, the system for the amplitudes P and P_0 becomes

$$\begin{vmatrix} (\mathrm{R})^{-1} & \mathbf{1} \\ \mathrm{R}_W & (\mathrm{R}_0)^{-1} \end{vmatrix} \begin{vmatrix} \mathrm{P} \\ \mathrm{P}_0 \end{vmatrix} = \begin{vmatrix} 0 \\ \mathrm{W} \end{vmatrix} , \tag{5.40}$$

Equation (5.40) is easily identified with the system reported by Kerker [75] for the solution of the problem of the layered sphere.

Considerations on convergence can be made along the lines of Sect. 5.4.1. Although one could introduce l_{E} and different values for l_{I}, here we consider a single l_{M} only. Once a convenient value of l_{M} is determined so as to ensure the convergence of the scattered field, the order of the matrix $\mathcal{M}$ to be inverted is $d = 2(N+1)l_{\mathrm{M}}(l_{\mathrm{M}}+2)$ for a sphere with N inclusions. Furthermore, when the inclusions form a linear chain lying on the diameter of the host sphere, i.e., when the scatterer as a whole has axial symmetry, the transition matrix turns out to be diagonal in m and matrix $\mathcal{M}$ factorizes into submatrices $\mathcal{M}_m$ of order $d_m = 2(N+1)(l_{\mathrm{M}} - |m| + 1 - \delta_{m0})$.

The two-step procedure that was used to calculate the scattered field is a direct matching procedure. In fact, it directly uses the boundary conditions to match the multipole expansions of the field across the surfaces of the inclusions and of the host sphere. This procedure is similar to the one used by Fikioris and Uzunoglu [90]. However, we mentioned above that the scattered field has been calculated by Skaropoulos, Ioannidou, and Chrissoulidis [91] and by Ioannidou and Chrissoulidis [92] through a one-step indirect matching procedure. These authors, indeed, use multipole expansions to describe the field within each region and match them across the surfaces present by resorting to Green's second vector identity. As a result, they obtain a single matrix equation whose solution yields all the expansion coefficients, including those of the scattered field. This procedure is quite correct but requires the inversion of a bigger matrix than that implied in our two-step procedure. In fact, the one-step procedure in [91] and [92] implies the inversion of a matrix of order $d' = 2(N+2)l_{\mathrm{M}}(l_{\mathrm{M}}+2) > d$. Even the one-step procedure yields factorization of the matrix to be inverted into matrices of order $d'_m = 2(N+2)(l_{\mathrm{M}} - |m| + 1 - \delta_{m0}) > d_m$, when the inclusions form a linear chain along the diameter of the host sphere. Since matrix inversion is an $O(N^3)$ process, the increase in computational effort is noticeable and is not compensated by the further calculations required by (5.38) to get the scattered field in the two-step procedure. In any case, we can safely state that the variety of contributions either in $\mathcal{M}$ and $\mathcal{T}$ or in the matrix of the two-step procedure prevents establishing any rule of thumb for determining l_{M}.

5.6 Finite Elements Methods

In the preceding sections we discussed a set of prescriptions for calculating the field scattered by some kinds of nonspherical model particles. Of course, the transition matrix approach on which our formulas are based is only one of the methods that were devised to study the scattering properties of nonspherical particles. Moreover, when one is interested in effects that depend on the precise shape of the particles concerned, using more sophisticated methods is in order. In this respect, we recall that the transition matrix method was derived by Waterman [3] starting from the integral equation formulation of electromagnetic scattering from particles. This formulation, also called extended boundary conditions method, relies on integrals over the volume or, more often, over the surface of the particle. Provided these integrals can be performed with a sufficient accuracy, the extended boundary conditions method accounts very well for the actual shape of the particle. We do not enter into the details that are fully discussed by Waterman in his original paper. A survey of all the methods that have been developed to deal with scattering from particles of general shape has been given by Mishchenko and Travis [93]. Here, we report a brief description of two of the so-called finite elements methods, which are in common use for studying electromagnetic scattering from particles of complicated shape. Our description does not pretend to be exhaustive and is meant to help the reader to better understand both the similarities and the differences of our results in comparison with those of other researchers.

5.6.1 Discrete Dipole Approximation

The discrete dipole approximation (DDA), that is also called the coupled dipole method, is a finite elements method originally devised by Purcell and Pennypacker [94] and later improved by Draine and Flatau [95]. The DDA simulates the actual particle by an array of N polarizable points, each characterized by its own polarizability tensor whose elements may be complex. The medium among the dipoles is always the vacuum. The dipole moment acquired by the point at $\boldsymbol{r}_j$ with polarizability $\boldsymbol{\alpha}_j$ is

$$\boldsymbol{P}_j = \boldsymbol{\alpha}_j \boldsymbol{E}_j$$

where $\boldsymbol{E}_j$ is the total electric field at $\boldsymbol{r}_j$. In fact, the field $\boldsymbol{E}_j$ is the superposition of the incident wave field and of the fields due to all dipoles other than the jth. Therefore, we can write

$$\boldsymbol{P}_j = \boldsymbol{\alpha}_j \left(\boldsymbol{E}_{\mathrm{I}j} - \sum_{k \neq j} \mathrm{A}_{jk} \boldsymbol{P}_k \right) ,$$

where $\boldsymbol{E}_{\mathrm{I}j}$ is the incident field at $\boldsymbol{r}_j$ and $-\mathrm{A}_{jk}\boldsymbol{P}_k$ is the contribution to the field at $\boldsymbol{r}_j$ of the dipole at $\boldsymbol{r}_k$. Matrices A_{jk}, $j \neq k$, that couple to each other all the dipoles present, are given by

$$\begin{aligned}\mathrm{A}_{jk}\boldsymbol{P}_k = &\frac{\exp(\mathrm{i}k_{\mathrm{v}}r_{jk})}{r_{jk}^3} \Bigg\{ k_{\mathrm{v}}^2 \boldsymbol{r}_{jk} \times (\boldsymbol{r}_{jk} \times \boldsymbol{P}_k) \\ &+ \frac{1 - \mathrm{i}k_{\mathrm{v}}r_{jk}}{r_{jk}^2} \left[r_{jk}^2 \boldsymbol{P}_k - 3\boldsymbol{r}_{jk}(\boldsymbol{r}_{jk} \cdot \boldsymbol{P}_k) \right] \Bigg\} ,\end{aligned}$$

with $\boldsymbol{r}_{jk} = \boldsymbol{r}_j - \boldsymbol{r}_k$. Draine found it convenient to also define the matrices

$$\mathrm{A}_{jj} = \boldsymbol{\alpha}_j^{-1} ,$$

so that the dipole moments are the solution of the system of linear nonhomogeneous equations

$$\sum_{k=1}^{N} \mathrm{A}_{jk} \boldsymbol{P}_k = \boldsymbol{E}_{\mathrm{I}j} .$$

The scattered field, once the $\boldsymbol{P}_k$ are known, can be calculated through the well known formulas reported, e.g. by Jackson [4].

In itself, the DDA is a powerful method that allows one to approximate particles of any shape by an appropriate choice of the array on which the point dipoles are located. The possible lack of homogeneity of the particles is not a problem because the polarizabilities need not be identical to each other. The absorption by the particle is accounted for by the imaginary part of the polarizability tensor. The serious problem with the DDA comes instead from the number of the dipoles that are needed to approximate adequately the particle concerned. In fact, since A_{jk} are 3×3 matrices and the dipole moments are three-dimensional vectors, the system to be solved is of order $3N$, and N itself may be of order 10^4–10^5 to approximate particles of not too complex shape. These problems have been faced by locating the dipoles on a regular cubic array, with lattice spacing d, so as to take advantage of numerical techniques based on the fast Fourier transform and on the conjugate gradient method in order to reduce the computational effort. However, the problem remains of choosing the polarizability tensor of each of the N points, the most obvious choice being the well known Lorentz–Lorenz formula [5]

$$\alpha_j^{(0)} = \frac{3d^3}{4\pi}\left(\frac{n_j^2 - 1}{n_j + 2}\right) ,$$

where n_j is the refractive index at the position of the jth point. Nevertheless, Draine [96] has shown that, since the scattered field must satisfy the optical theorem, the polarizability should include a radiative reaction correction of order $(k_\mathrm{v} d)^3$ so that

$$\boldsymbol{\alpha}_j = \frac{\alpha^{(\mathrm{nr})}}{1 - (2/3)\mathrm{i}(\alpha^{(\mathrm{nr})}/d^3)(k_\mathrm{v} d)^3}\mathbf{1} ,$$

where $\alpha^{(\mathrm{nr})}$ denotes the polarizability with no radiative correction included. In his earlier work Draine chose

$$\alpha_j^{(\mathrm{nr})} = \alpha_j^{(0)} ,$$

thus assuming a Lorentz–Lorenz polarizability including the radiative correction. This subject was further investigated by Draine and Goodman [97] by a thorough study of the propagation of a plane wave through a cubic array of point dipoles. Their main result can be summarized by stating that the array can sustain the propagation of a plane wave provided the polarizability satisfies a well defined dispersion relation that holds true for any value of $k_\mathrm{v} d$. Of course, if the lattice is meant to mimic the dielectric behavior of a continuous medium, as is the case with the DDA, one can consider the series expansion of dispersion relation in the long wavelength limit. As a result, to zero order one recovers the Lorentz–Lorenz formula and to first order the equation that includes the radiative correction.

Once a reliable choice of the polarizability has been made, the next problem with the DDA is to assess its range of validity. To this end the predictions of the DDA for homogeneous spheres have been compared with the analytic Mie theory solutions. The scattering from tetrahedra, for which no analytic solution is known, has instead been compared with the results of FDTD (see Sect. 5.6.2 below). The conclusions that stem from all these comparisons suggest that, provided the number of the dipoles N is sufficiently big to ensure good fitting of the shape of the particle, the interdipole distance must satisfy the condition

$$|n_0|k_{\mathrm{v}}d \leq 1$$

where n_0 is the refractive index of the particle. In particular, the scattered field is described with best accuracy when $|n_0 - 1| \leq 1$. In practice, when the refractive index is large, using the DDA requires great care in checking the reliability of the results.

The above considerations might convince the reader that the DDA should be the method of choice when dealing with scattering by irregularly shaped particles. Nevertheless, unlike the transition matrix approach, the DDA does not imply any simple relation between the particle orientation and the scattered field. Therefore, when orientational averages, such as those discussed in Chap. 4, are needed, it is necessary to calculate anew the scattered field for each of a sufficiently large number of orientations of the particle. Nevertheless, we call the attention of the reader on a paper by Mackowski [98] in which the author succeeds in extracting the transition matrix from the results of a DDA calculation. Although we did not experienced ourselves the procedure devised by Mackowski in actual calculations, in our opinion it should be borne in mind in case one is interested in the orientational averages of the scattering properties of highly irregularly shaped particles.

5.6.2 Finite Difference Time Domain Method

Most of the methods that are in common use for calculating the scattered field from particles seek for solutions of the Maxwell equations in the frequency domain. From a mathematical point of view, Maxwell equations in the frequency domain are elliptic, so that the imposition of the boundary conditions is essential for finding solutions that describe actual wave propagation. On the contrary, the finite difference time domain method (FDTD) is a finite-elements method based on the numerical integration of the Maxwell equations in the time domain [99]. This means that the solution to the problem of scattering is dealt with as an initial value problem and the incident field need not be a monochromatic wave. In principle, boundary conditions are not necessary because in the time domain the Maxwell equations are hyperbolic [100].

The region of space containing the scattering particle is discretized by defining a regular array of cells whose vertices, commonly referred to as the nodes, are individuated by three integers such that the vector position of node $(i,\ j,\ k)$ is

$$\boldsymbol{r}_{ijk} = i\Delta x\,\hat{\boldsymbol{e}}_x + j\Delta y\,\hat{\boldsymbol{e}}_y + k\Delta z\,\hat{\boldsymbol{e}}_z\ .$$

The particle is then characterized by assigning the value of the refractive index (or of the dielectric function) at each node within the volume occupied by the particle itself. This procedure, which is similar to the one used in the DDA, does not require the particle to be homogeneous or to have a regular shape. Each space- and time-dependent variable, such as the components of the fields, is discretized as

$$F(\boldsymbol{r},t) \rightarrow F_{\mathrm{d}}(i,j,k;n) = F(i\Delta x, j\Delta y, k\Delta z; n\Delta t) \ ,$$

and this procedure is used to write the discretized version of the Maxwell curl equations to be integrated numerically.

The actual situation is more complicated than stated above. First, in order to ensure the stability of the numerical integration of the Mawxell equations the space and time increments must satisfy the condition [101]

$$c\Delta t \leq \left[1/(\Delta x)^2 + 1/(\Delta y)^2 + 1/(\Delta z)^2\right]^{-1/2}$$

that sets a lower limit to the number of nodes that are necessary to get reliable results.

Second, any scattering process occurs in infinite space, whereas, for evident computational reasons, the integration of the discretized Maxwell equations must be performed within a finite region. It is therefore necessary to introduce appropriate boundary conditions across the surface which limits the region of integration to prevent unphysical reflections of the field that would otherwise modify, even severely, the near field [101–103].

Third, the integration procedure must preserve the continuity of the appropriate components of the fields when going from node to node. To this end a cubic cell is considered around each node with vertices at $(i\pm\frac{1}{2},\ j\pm\frac{1}{2},\ k\pm\frac{1}{2})$. Then, the components of the field are selected so that the electric field is calculated at the center of the edges of the cell, whereas the magnetic field is calculated at the center of the faces of the cell [99]. This choice ensures that in going from cell to cell the orthogonal components of the magnetic field and the tangential components of the electric field are continuous. It is only at this stage that one can proceed to the integration of the discretized Maxwell equations. In practice, given the field at $t = 0$, one is confronted with the numerical integration of a system of six coupled finite-difference equations for the space-time propagation of the field. Six schemes of integrations have been devised, each of which is applicable to one of the six rules that are used to approximate the derivatives of the field components. Once a scheme is selected, one gets the field within the whole region of integration as a function of time.

Of course, the field calculated as outlined above is the near field, whereas to calculate the quantities of interest, such as the cross sections, one needs the far field. This task is faced by means of Green's second vector identity that ensures the matching of the near and the far field through an integration on any suitable surface containing the particle [104, 105].

Finally, let us recall that, since the incident field is, in general, nonmonochromatic, the far field also is nonmonochromatic. Therefore, in order to get the frequency response of the particle one has to resort to a discrete Fourier transform, so that the results of the FDTD method can be compared with those of more conventional methods that yield the field in the frequency domain. The results of such comparisons prove that the FDTD method achieves an extremely good precision in the calculation of the fields [106]. Nevertheless, the FDTD requires a computational effort even heavier than required by the DDA method.

6 Scattering from Particles on a Plane Surface

In this chapter, we study the scattering of electromagnetic waves from particles near to or deposited on the plane surface that separates two homogeneous media of different optical properties. The plane surface will be termed *the interface*, whereas we will call *accessible half-space* the one in which the particles and the detecting instrumentation are located. The medium that fills the accessible half-space is assumed to be nonabsorptive and to have, therefore, a *real* refractive index.

The presence of the interface has, in general, a striking effect on the scattering pattern from the particles. Indeed, unlike the case of particles in free space, the exciting field does not coincide with the incident plane wave and the observed field does not coincide with the field scattered by the particle. The field that illuminates the particles is partly or totally reflected by the interface and the reflected field contributes both to the exciting and to the observed field. Moreover, the field scattered by the particles is reflected by the interface and thus contributes to the exciting field. In other words there are multiple scattering processes between the particles and the interface. As a result, the field in the accessible half-space includes the incident field $\boldsymbol{E}_{\mathrm{I}}$, the reflected field $\boldsymbol{E}_{\mathrm{R}}$, the scattered field $\boldsymbol{E}_{\mathrm{S}}$ and, finally, the field $\boldsymbol{E}_{\mathrm{SR}}$ that after scattering by the particles is reflected by the surface. Therefore, a detecting instrument in the far zone within the accessible half-space records, in general, the superposition of $\boldsymbol{E}_{\mathrm{S}}$ and $\boldsymbol{E}_{\mathrm{SR}}$, whereas the reflected field will be recorded in the direction of reflection only.

The mathematical difficulties that are met in calculating the scattering pattern are due to the need that the field in the accessible half-space satisfy the boundary conditions both across the (closed) surface of the particles and across the (infinite) interface. In other words, even by assuming that we are able to impose the boundary conditions across the surface of the particle, the problem still remains of imposing the boundary conditions across the interface. In this respect, we remark that the particles may be in contact with the interface, so that the boundary conditions must be imposed to the near field, that, as remarked in Sect. 2.1, has a complicated space dependence. Moreover, the form of the boundary conditions across the interface depends on whether the medium that fills the nonaccessible half-space is a dielectric or a metal. For this reason we will deal separately with the case of a metallic surface [107] and with that of a dielectric substrate [108–110]. Nevertheless, in both cases, it is possible to define the transition matrix for particles in the presence of the interface. Of course, this amounts to the possibility of performing averages over the orientation of the particles with a reduced computational effort.

As the last item, we show how the same formalism that is used to deal with the scattering of plane waves by particles near to an interface can be applied also to scattering of evanescent waves generated by total internal reflection at the surface of a dielectric medium.

6.1 Incident and Reflected Fields

The reflection of a plane wave on a plane surface can be dealt with in general terms, i.e., without specifying whether the medium that fills the nonaccessible half-space is a dielectric or a metal. This information can, indeed, be supplied at the end of the algebraic manipulations. Let us thus assume that the interface is the plane $z = 0$ of a Cartesian frame of reference and that the half-space $z < 0$, which we take as the accessible half-space, is filled by a homogeneous medium of (real) refractive index n'. The half-space $z > 0$ is assumed to be filled by a homogeneous medium with (possibly complex) refractive index n''. The plane wave field

$$\boldsymbol{E}_{\mathrm{I}} = E_0 \hat{\boldsymbol{e}}_{\mathrm{I}} \exp(\mathrm{i}\boldsymbol{k}_{\mathrm{I}} \cdot \boldsymbol{r}) ,$$

which propagates within the accessible half-space, is reflected by the interface into the plane wave

$$\boldsymbol{E}_{\mathrm{R}} = E_0' \hat{\boldsymbol{e}}_{\mathrm{R}} \exp(\mathrm{i}\boldsymbol{k}_{\mathrm{R}} \cdot \boldsymbol{r}) ,$$

where $\boldsymbol{k}_{\mathrm{I}} = k'\hat{\boldsymbol{k}}_{\mathrm{I}}$ and $\boldsymbol{k}_{\mathrm{R}} = k'\hat{\boldsymbol{k}}_{\mathrm{R}}$ are the propagation vectors of the incident and of the reflected wave, respectively, $k' = n'k_{\mathrm{v}}$ and $\hat{\boldsymbol{e}}_{\mathrm{I}}$ and $\hat{\boldsymbol{e}}_{\mathrm{R}}$ are the respective unit polarization vectors. The polarization is analyzed with respect to the two pairs of unit vectors $\hat{\boldsymbol{u}}_{\mathrm{I}\eta}$ and $\hat{\boldsymbol{u}}_{\mathrm{R}\eta}$ that are parallel ($\eta = 1$) and perpendicular ($\eta = 2$) to the plane of incidence that, as usual, is defined as the plane that contains $\boldsymbol{k}_{\mathrm{I}}$, $\boldsymbol{k}_{\mathrm{R}}$ and the z axis. Our choice of the orientation is defined by the equations

$$\hat{\boldsymbol{u}}_{\mathrm{I}1} \times \hat{\boldsymbol{u}}_{\mathrm{I}2} = \hat{\boldsymbol{k}}_{\mathrm{I}} , \qquad \hat{\boldsymbol{u}}_{\mathrm{R}1} \times \hat{\boldsymbol{u}}_{\mathrm{R}2} = \hat{\boldsymbol{k}}_{\mathrm{R}} ,$$

with $\hat{\boldsymbol{u}}_{\mathrm{I}2} \equiv \hat{\boldsymbol{u}}_{\mathrm{R}2}$. In terms of the projections on the polarization basis, the incident and the reflected field can be written

$$\boldsymbol{E}_{\mathrm{I}} = E_0 \sum_{\eta} (\hat{\boldsymbol{e}}_{\mathrm{I}} \cdot \hat{\boldsymbol{u}}_{\mathrm{I}\eta}) \hat{\boldsymbol{u}}_{\mathrm{I}\eta} \exp(\mathrm{i}\boldsymbol{k}_{\mathrm{I}} \cdot \boldsymbol{r}) ,$$

and

$$\boldsymbol{E}_{\mathrm{R}} = E_0' \sum_{\eta} (\hat{\boldsymbol{e}}_{\mathrm{R}} \cdot \hat{\boldsymbol{u}}_{\mathrm{R}\eta}) \hat{\boldsymbol{u}}_{\mathrm{R}\eta} \exp(\mathrm{i}\boldsymbol{k}_{\mathrm{R}} \cdot \boldsymbol{r}) \; .$$

In the preceding equations the incident field $\boldsymbol{E}_{\mathrm{I}}$ and the reflected field $\boldsymbol{E}_{\mathrm{R}}$ are decomposed into their components parallel and orthogonal to the plane of incidence and can be referred to each other by means of the Fresnel coefficients F_η for the reflection of a plane wave with polarization along $\hat{\boldsymbol{u}}_\eta$. The reflection condition is imposed as usual [4] and yields the equation

$$E_0' (\hat{\boldsymbol{e}}_{\mathrm{R}} \cdot \hat{\boldsymbol{u}}_{\mathrm{R}\eta}) = E_0 F_\eta(\vartheta_{\mathrm{I}}) (\hat{\boldsymbol{e}}_{\mathrm{I}} \cdot \hat{\boldsymbol{u}}_{\mathrm{I}\eta}) \; , \tag{6.1}$$

where the Fresnel coefficients are defined as

$$F_1(\vartheta_{\mathrm{I}}) = \frac{\bar{n}^2 \cos\vartheta_{\mathrm{I}} - \beta}{\bar{n}^2 \cos\vartheta_{\mathrm{I}} + \beta} \; , \quad F_2(\vartheta_{\mathrm{I}}) = \frac{\cos\vartheta_{\mathrm{I}} - \beta}{\cos\vartheta_{\mathrm{I}} + \beta} \; , \tag{6.2}$$

in which ϑ_{I} is the angle between $\hat{\boldsymbol{k}}_{\mathrm{I}}$ and the z axis, $\bar{n} = n''/n'$, and

$$\beta = \left[(\bar{n}^2 - 1) + \cos^2\vartheta_{\mathrm{I}} \right]^{1/2} \; .$$

Using (6.1), the reflected wave can be rewritten as

$$\boldsymbol{E}_{\mathrm{R}} = E_0 \sum_{\eta} F_\eta(\vartheta_{\mathrm{I}}) (\hat{\boldsymbol{e}}_{\mathrm{I}} \cdot \hat{\boldsymbol{u}}_{\mathrm{I}\eta}) \hat{\boldsymbol{u}}_{\mathrm{R}\eta} \exp(\mathrm{i}\boldsymbol{k}_{\mathrm{R}} \cdot \boldsymbol{r}) \; .$$

We expand both the incident and the reflected field in terms of spherical vector multipole fields along the lines of Sect. 4.1. The result is

$$\begin{aligned} \boldsymbol{E}_{\mathrm{I}} &= \sum_{\eta} E_{0\eta} \sum_{plm} \boldsymbol{J}_{lm}^{(p)}(\boldsymbol{r}, k') W_{\mathrm{I}\eta lm}^{(p)} \; , \\ \boldsymbol{E}_{\mathrm{R}} &= \sum_{\eta} E_{0\eta} F_\eta(\vartheta_{\mathrm{I}}) \sum_{plm} \boldsymbol{J}_{lm}^{(p)}(\boldsymbol{r}, k') W_{\mathrm{R}\eta lm}^{(p)} \; , \end{aligned}$$

where we used (4.6) and

$$W_{\mathrm{R}\eta lm}^{(p)} = W_{lm}^{(p)}(\hat{\boldsymbol{u}}_{\mathrm{R}\eta}, \hat{\boldsymbol{k}}_{\mathrm{R}}) \tag{6.3}$$

has been added to the positions (4.22). In turn, the amplitudes $W_{lm}^{(p)}(\hat{\boldsymbol{e}}, \hat{\boldsymbol{k}})$ are given by (4.4). Because of the reflection condition, the amplitudes $W_{\mathrm{I}\eta lm}^{(p)}$ and $W_{\mathrm{R}\eta lm}^{(p)}$ cannot be mutually independent. Indeed, if ϑ_{I} and φ_{I} are the polar angles of $\hat{\boldsymbol{k}}_{\mathrm{I}}$, the polar angles of $\hat{\boldsymbol{u}}_{\mathrm{I}1}$ and $\hat{\boldsymbol{u}}_{\mathrm{I}2}$ are

$$\vartheta_{\mathrm{I}1} = \vartheta_{\mathrm{I}} + \frac{\pi}{2}, \quad \varphi_{\mathrm{I}1} = \varphi_{\mathrm{I}} \; , \quad \text{and} \quad \vartheta_{\mathrm{I}2} = \frac{\pi}{2}, \quad \varphi_{\mathrm{I}2} = \varphi_{\mathrm{I}} + \frac{\pi}{2} \; ,$$

respectively. In turn, the polar angles of $\hat{\boldsymbol{k}}_{\mathrm{R}}$ turn out to be

$$\vartheta_{\mathrm{R}} = \pi - \vartheta_{\mathrm{I}}, \quad \varphi_{\mathrm{R}} = \varphi_{\mathrm{I}} \; ,$$

and the polar angles of $\hat{\boldsymbol{u}}_{\mathrm{R}1}$ and $\hat{\boldsymbol{u}}_{\mathrm{R}2}$ are

$$\vartheta_{\mathrm{R}1} = \vartheta_{\mathrm{I}} + \frac{\pi}{2}, \quad \varphi_{\mathrm{R}1} = \varphi_{\mathrm{I}} + \pi \ , \quad \text{and} \quad \vartheta_{\mathrm{R}2} = \frac{\pi}{2}, \quad \varphi_{\mathrm{R}2} = \varphi_{\mathrm{I}} + \frac{\pi}{2} \ ,$$

respectively. According to (4.4) and to (6.3) and using the rule [111],

$$P_{lm}(-x) = (-)^{l+m} P_{lm}(x) \ ,$$

we get

$$W^{(p)}_{\mathrm{R}\eta lm} = (-)^{\eta+p+l+m} W^{(p)}_{\mathrm{I}\eta lm} \ , \tag{6.4}$$

so that the amplitudes of the reflected field never need to be explicitly considered.

In practice, for further developments, it is convenient to define the exciting field as the superposition

$$\boldsymbol{E}_{\mathrm{E}} = \boldsymbol{E}_{\mathrm{I}} + \boldsymbol{E}_{\mathrm{R}} \ . \tag{6.5}$$

The multipole expansion of $\boldsymbol{E}_{\mathrm{E}}$, in case the field is polarized along $\hat{\boldsymbol{u}}_{\mathrm{I}\eta}$, can be written as

$$\boldsymbol{E}_{\mathrm{E}\eta} = E_0 \sum_{plm} \boldsymbol{J}^{(p)}_{lm}(\boldsymbol{r}, k') W^{(p)}_{\mathrm{E}\eta lm} \tag{6.6}$$

with

$$W^{(p)}_{\mathrm{E}\eta lm} = [1 + F_\eta(\vartheta_{\mathrm{I}})(-)^{\eta+p+l+m}] W^{(p)}_{\mathrm{I}\eta lm} \ . \tag{6.7}$$

6.2 Perfectly Reflecting Surface

A well-polished metallic surface is a good approximation of a perfectly reflecting surface. Owing to the high conductivity of the metal, the tangential component of the electric field vanishes on the surface. This is, indeed, the actual boundary condition for perfect reflection. In this case the problem of scattering can be solved by resorting to *image theory*, according to which the field scattered into the accessible half-space by a particle in the presence of the reflecting surface coincides with the field scattered by the compound object that includes the particle and its image (hereafter referred to as the *effective scatterer*), provided the *exciting field* is the superposition of the actual incident field and of the field that comes from the image source. Since the latter field coincides with field reflected by the surface, the exciting field is the superposition (6.5) with multipole expansion given by (6.6) whose amplitude is obtained by substituting into (6.7) the limiting values of the Fresnel coefficients

$$F_\eta(\vartheta_{\mathrm{I}}) = (-)^{\eta-1} \ ,$$

which are appropriate for the case of a perfectly reflecting surface, i.e., for $n'' \to \infty$. Therefore, the resulting amplitudes are

$$W_{\mathrm{E}\eta lm}^{(p)} = [1 - (-)^{p+l+m}] W_{\mathrm{I}\eta lm}^{(p)} . \tag{6.8}$$

Of course, image theory reduces the complexity of the original problem provided one is able to solve the problem of scattering by the effective scatterer that must be considered as a single particle. Therefore, in no case can the scattered field be considered as the superposition of the fields that the actual particle and its image scatter independently. The process of scattering must be considered as a dependent scattering problem. Assuming, for instance, that the actual particle is a sphere, the problem becomes that of scattering by an aggregate of two identical spheres. This problem can be solved by the techniques expounded in Chap. 5. In case the actual object were itself an aggregate of spheres, the problem to be solved would be that for a cluster including twice the spheres as the original aggregate.

When the interface is perfectly reflecting, a further problem can be solved, namely, that of a hemisphere with its flat face on the surface. The effective scatterer is, in fact, a sphere whose scattering properties can be calculated through the well known Mie theory. The fact that the exciting field is not a simple plane wave but the superposition defined in (6.5) adds no further difficulty. Of course, nothing prevents the actual hemisphere from being radially nonhomogeneous, or from containing spherical inclusions or hemispherical inclusions whose flat face lies on the reflecting surface. The effective scatterer is, indeed, a sphere radially nonhomogeneous or containing one or more spherical inclusions (see Fig. 6.1).

With this in mind, we expand the field scattered by the effective scatterer in a series of $\boldsymbol{H}$-multipole fields, so that the radiation condition at infinity is fulfilled. The required expansion is

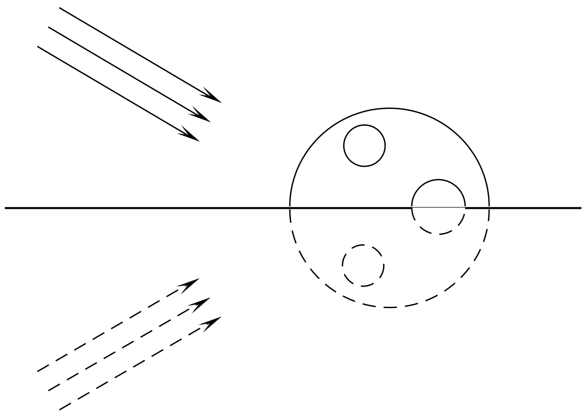

Fig. 6.1. Effective scatterer for the case of a hemisphere containing a hemispheric inclusion and a spherical eccentric inclusion. The images are characterized by *dashed lines*

$$\boldsymbol{E}_{\mathrm{S}\eta} = E_0 \sum_{plm} \boldsymbol{H}^{(p)}_{lm}(\boldsymbol{r}, k') A^{(p)}_{\eta lm} \, ,$$

and, according to our earlier remark, is valid only within the accessible half-space. In the spirit of the transition matrix approach, the amplitudes of the scattered field are related to those of the exciting field by the equation

$$A^{(p)}_{\eta lm} = \sum_{p'l'm'} \mathcal{S}^{(pp')}_{lml'm'} W^{(p')}_{\mathrm{E}\eta l'm'} \, ,$$

where the transition matrix is that of the effective scatterer.

The scattered intensity is given by the matrix

$$I_{\eta\eta'} = \left| \frac{E_0}{r} f_{\eta\eta'} \right|^2 . \tag{6.9}$$

Here and throughout this chapter we use $I_{\eta\eta'}$ in place of $I_{\mathrm{S}\eta\eta'}$ (see (4.46)) because the scattering amplitude in (6.9) never has the same meaning that it has in (4.46). For instance, in the present section $f_{\eta\eta'}$ is that of the effective scatterer. The effective scatterer, in turn, is excited not only by the usual incident wave but also by the reflected wave. In fact, the elements $f_{\eta\eta'}$ are related to the elements of the transition matrix through the equation

$$f_{\eta\eta'} = -\frac{\mathrm{i}}{4\pi k'} \sum_{plm} \sum_{p'l'm'} W^{(p)*}_{\mathrm{S}\eta lm} \, \mathcal{S}^{(pp')}_{lml'm'} \, W^{(p')}_{\mathrm{E}\eta' l'm'} \, . \tag{6.10}$$

It may be worth noticing that the direction of observation need not lie in the plane of incidence and that (6.10), except for the presence of the amplitudes of the exciting field in place of those of the incident field, is identical to (4.29) for particles in free space. We also notice that the convergence considerations that we made in Sect. 5.4.1 still apply, provided the number of the spheres that we consider be that appropriate for the effective scatterer.

6.2.1 Orientational Averages

If one has to calculate the scattering pattern from a single particle in the vicinity of the reflecting surface, (6.10) is quite efficient as its form shows that, once the transition matrix is known, the scattered intensity can be calculated without undue computational effort for any $\hat{\boldsymbol{k}}_{\mathrm{I}}$ and $\hat{\boldsymbol{k}}_{\mathrm{S}}$ and for whatever choice of the polarization both of the incident and the scattered field.

When one is interested in the pattern of the scattered radiation from an assembly of identical scatterers in front of the surface, the distribution of their orientations must be taken into account. This can be done, as explained in Sect. 4.3, by associating to each particle a local system of axes chosen so that, when two particles are brought into coincidence, their respective local axes coincide. Then, the components of the scattering amplitude of the νth particle of orientation Θ_ν are given by

$$f_{\nu,\eta\eta'} = -\frac{\mathrm{i}}{4\pi n' k} \sum_{plm} \sum_{p'l'm'} \sum_{\mu\mu'} W^{(p)*}_{\mathrm{S}\eta lm}\, \mathcal{D}^{(l)*}_{\mu m}(\Theta_\nu)\, \bar{\mathcal{S}}^{(pp')}_{l\mu l'\mu'}\, \mathcal{D}^{(l')}_{\mu' m'}(\Theta_\nu)\, W^{(p')}_{\mathrm{E}\eta' l' m'} \,, \tag{6.11}$$

where $\Theta_\nu \equiv (\alpha_\nu, \beta_\nu, \gamma_\nu)$ is a shorthand for the three Euler angles that characterize the orientation of the local frame of the νth particle with respect to the laboratory frame. Again we stress that (6.11) is identical to (4.44) except for the substitution of the amplitudes of the exciting field in place of those of the incident field. In fact, even in the presence of the interface, both $W^{(p)*}_{\mathrm{S}\eta\, lm}$ and $W^{(p')}_{\mathrm{E}\eta' l' m'}$ in (6.11) need to be calculated in the laboratory frame, whereas the elements of the transition matrix $\bar{\mathcal{S}}^{(pp')}_{l\mu l'\mu'}$ are calculated in the local frame and are thus independent of the orientation of the scatterer. Ultimately, (6.11) shows that, even when dealing with an assembly of identical scatterers in the presence of a perfectly reflecting surface, we need to calculate the transition matrix only once.

We have now all the ingredients that are necessary to calculate the scattered intensity from an assembly of identical particles in the vicinity of the interface. It is to be stressed, however, that the applicability of the method of the images requires that we consider a monolayer of particles that are so arranged that all the effective scatterers are identical to each other and that the orientations of any two of them differ for a rotation around an axis that is perpendicular to the surface. A moment's thought and a look to Fig. 6.2 will convince the reader of the need for this restriction on the orientation of the actual particles in spite of their identity. With this in mind, we can write the total scattered intensity as

$$\begin{aligned} \bar{I}_{\eta\eta'} &= \left(\sum_{\nu} E^*_{\nu,\,\eta\eta'} \right) \left(\sum_{\nu'} E_{\nu',\,\eta\eta'} \right) \\ &= N \langle |E_{\eta\eta'}(\boldsymbol{R}, \Theta)|^2 \rangle + (N^2 - N) \langle E^*_{\eta\eta'}(\boldsymbol{R}, \Theta) E_{\eta\eta'}(\boldsymbol{R}', \Theta') \rangle , \end{aligned}$$

where ν and ν' are, as usual, particle indexes, N is the number of the particles on the reflecting surface, $E_{\eta\eta'}(\boldsymbol{R}, \Theta)$ is the scattered field from a particle at the position $\boldsymbol{R}$ with orientation Θ, and the brackets denote the ensemble average over both the position and the orientation of the particles. The first term on the right-hand side, the so-called self term, contributes to the scattered intensity for any direction of observation. Even the second term, that is a two-body term, may become important for nonrandom distributions of the scatterers. On the contrary, when they are randomly distributed upon the surface, it does contribute in the direction of reflection only [54]. Ultimately, as long as we deal just with monolayers of randomly distributed scatterers, we will disregard the two-body term so that $\bar{I}_{\eta\eta'}$ reduces to

$$\bar{I}_{\eta\eta'} = N\langle I_{\eta\eta'}\rangle = N\int I_{\eta\eta'}(\boldsymbol{R},\Theta)P(\boldsymbol{R},\Theta)\,\mathrm{d}\boldsymbol{R}\,\mathrm{d}\Theta\ ,$$

where $P(\boldsymbol{R},\Theta)$ is the probability that a particle has position within $\boldsymbol{R}$ and $\boldsymbol{R}+\mathrm{d}\boldsymbol{R}$ and orientation within Θ and $\Theta+\mathrm{d}\Theta$. Since we assume that there is no correlation between the position and the orientation of the scatterers, P can be factorized as $P(\boldsymbol{R},\Theta) = P_{\boldsymbol{R}}(\boldsymbol{R})P_{\Theta}(\Theta)$. Furthermore, the distance of observation is assumed, as usual, to be very large with respect to the size of the reflecting surface, so that we can put $\boldsymbol{R}=0$ and write

$$\begin{aligned}\langle I_{\eta\eta'}\rangle &= \int I_{\eta\eta'}(\boldsymbol{R},\Theta)P_{\boldsymbol{R}}(\boldsymbol{R})P_{\Theta}(\Theta)\,\mathrm{d}\boldsymbol{R}\,\mathrm{d}\Theta \\ &\approx \int P_{\boldsymbol{R}}(\boldsymbol{R})\,\mathrm{d}\boldsymbol{R}\int I_{\eta\eta'}(0,\Theta)P_{\Theta}(\Theta)\,\mathrm{d}\Theta = \int I_{\eta\eta'}(0,\Theta)P_{\Theta}(\Theta)\,\mathrm{d}\Theta\end{aligned}$$

on account that

$$\int P_{\boldsymbol{R}}(\boldsymbol{R})\,\mathrm{d}\boldsymbol{R} = 1\ .$$

We stated above that the orientation of any two particles may differ only by a rotation around an axis that is orthogonal to the surface. Thus, by choosing the z axis of the local reference frame that we attached to each particle to coincide with that axis, $\beta=\gamma=0$, and the average involves the Euler angle α only. This kind of orientational distribution has already been considered in Sect. 4.5 as Case 4 in Table 4.1. Accordingly, the total scattered intensity is

$$\bar{I}_{\eta\eta'} = N\langle I_{\eta\eta'}\rangle\ ,$$

where the average $\langle I_{\eta\eta'}\rangle$ is given by (4.51c) provided k' is substituted in place of k and $W_{\mathrm{E}\eta}$ in place of $W_{\mathrm{I}\eta}$. Let us also recall that $\bar{\mathrm{S}}$ is not the transition matrix of the actual scatterer but must be that of the effective scatterer.

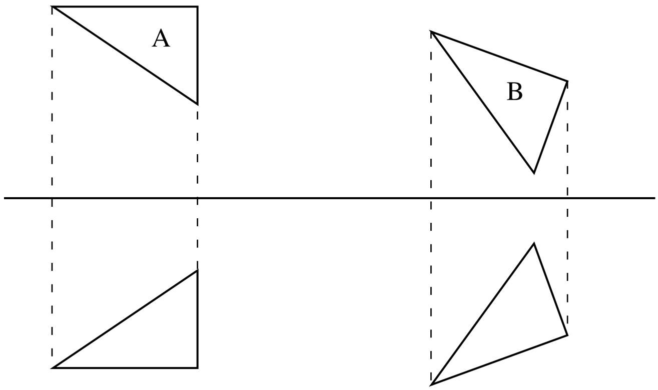

Fig. 6.2. Particles A and B are identical, but the respective effective scatterers they form are not because of the different distance and tilt of A and B with respect to the interface

The average over the orientations is, of course, not necessary and is not performed in actual calculations, in two important cases: when all the effective scatterers are oriented alike or when they have cylindrical symmetry around an axis perpendicular to the surface. However, even in these two special cases our orientational averaging procedure yields the correct results as we already remarked at the end of Sect. 4.5.

6.3 Dielectric Half-Space

When the half-space $z > 0$ is filled by a homogeneous dielectric material, the interface is not perfectly reflecting, and the field can propagate also within this half-space. When this occurs, the reflection condition for the vector spherical multipole fields must be reformulated. Obviously no problem exists for the reflection of the plane waves and thus neither for the $\boldsymbol{J}$-multipole fields that enter their expansion. This has already been shown in Sect. 6.1. On the contrary, the problem arises when we have to reflect the field scattered by a particle located within the accessible half-space. This field is indeed a superposition of $\boldsymbol{H}$-multipole fields whose reflection rule we are able to establish in general terms [14].

6.3.1 Reflection Rule for $\boldsymbol{H}$-Multipole Fields

We start by extending to the vector case the formula

$$h_l(kr)Y_{lm}(\vartheta,\varphi) = \frac{(-\mathrm{i})^l}{2\pi}\int_0^{2\pi} \mathrm{d}\varphi_{\mathrm{k}} \int_0^{\pi/2-\mathrm{i}\infty} \mathrm{d}\vartheta_{\mathrm{k}} \sin\vartheta_{\mathrm{k}}\, Y_{lm}(\vartheta_{\mathrm{k}},\varphi_{\mathrm{k}})\, \mathrm{e}^{\mathrm{i}\boldsymbol{k}\cdot\boldsymbol{r}} \,, \tag{6.12}$$

which Bobbert and Vlieger [112] obtained by extending to $l > 0$ an integral expression originally devised by Weyl [113]. Equation (6.12) expresses in the half-space $z > 0$ the scalar multipole field $h_l(kr)Y_{lm}(\vartheta,\varphi)$ as a superposition of plane waves with complex propagation vectors (inhomogeneous plane waves); the limits of integration are such that the real part of $\boldsymbol{k}$ points towards the half-space $z > 0$, so that the multipole field results from the superposition of plane waves coming from a point source at the origin and propagating in the half-space $z > 0$. Should the need arise, it would be possible to write an analogous expansion valid in the half-space $z < 0$ by considering the superposition of plane waves the real part of whose propagation vector points towards this half-space.

The geometry that we adopt is depicted in Fig. 6.3. Accordingly, we define a Cartesian frame of reference whose origin O lies on the plane interface between two media. Without loss of generality, we can assume that the interface coincides with the plane $z = 0$ and that a homogeneous medium of refractive index n' fills the half-space $z < 0$, whereas a different homogeneous medium of refractive index n'' fills the half-space $z > 0$ (see Fig. 6.3). We assume that a source of $\boldsymbol{H}$-multipole fields lies entirely within the half-space $z < 0$ and define a further frame of reference that is translated with respect to O and whose origin, O', lies within the source at a distance d from the interface. For our purposes, it is also convenient to define a third frame of reference that is also translated with respect to O and whose origin, O'', is the mirror image of O' with respect to the interface. We will denote with $\boldsymbol{R}'$

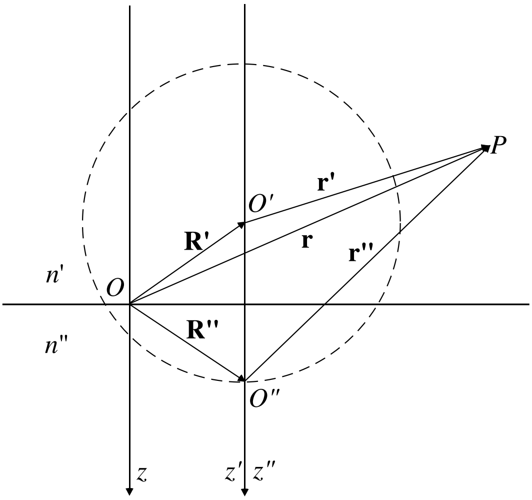

Fig. 6.3. Geometry for the reflection of multipole fields

and $\boldsymbol{R}''$ the vector position of the origins O' and O'' in the frame of reference with origin at O, respectively, whereas the vector position of the point of observation P in the three frames defined above will be denoted with $\boldsymbol{r}$, $\boldsymbol{r}'$, and $\boldsymbol{r}''$, respectively. Then, we recall the definitions of the $\boldsymbol{H}$-multipole fields in terms of irreducible spherical tensors [see (1.56) and (1.57)] and the definition of the spherical tensors themselves, (1.37), and apply (6.12) to each of the relevant scalar multipole fields. As a result, we obtain for the expansion of the vector multipole fields $\boldsymbol{H}^{(p)}_{lm}(\boldsymbol{r}', k')$ with origin at O'

$$\boldsymbol{H}^{(p)}_{lm}(\boldsymbol{r}', k') = \frac{(-\mathrm{i})^{p+l-1}}{2\pi} \int_{\mathcal{D}} \boldsymbol{Z}^{(p)}_{lm}(\hat{\boldsymbol{k}}) \exp(\mathrm{i}\boldsymbol{k} \cdot \boldsymbol{r}') \, \mathrm{d}\hat{\boldsymbol{k}} \, , \tag{6.13}$$

where the domain of integration $\mathcal{D}$ is the same as in (6.12). Equation (6.13) expresses the multipole field $\boldsymbol{H}$ as a superposition of vector plane waves with complex propagation vector (inhomogeneous plane waves) whose amplitudes are the transverse vector harmonics $\boldsymbol{Z}^{(p)}_{lm}$. The components parallel and orthogonal to the plane of incidence of the waves concerned can be reflected on the interface with the help the Fresnel coefficients (6.2). Before we do this, however, it is convenient to refer the waves in (6.13) to the origin O on the interface. Since $\boldsymbol{r}' = \boldsymbol{r} - \boldsymbol{R}'$, the result of this translation of origin is

$$\boldsymbol{H}^{(p)}_{lm}(\boldsymbol{r}', k') = \frac{(-\mathrm{i})^{p+l-1}}{2\pi} \int_{\mathcal{D}} \sum_{\eta} \left[\hat{\boldsymbol{u}}_\eta \cdot \boldsymbol{Z}^{(p)}_{lm}(\hat{\boldsymbol{k}})\right] \times \hat{\boldsymbol{u}}_\eta \exp(\mathrm{i}\boldsymbol{k} \cdot \boldsymbol{r}) \exp(-\mathrm{i}\boldsymbol{k} \cdot \boldsymbol{R}') \, \mathrm{d}\hat{\boldsymbol{k}} \, .$$

In fact, the term $\hat{\boldsymbol{u}}_\eta \exp(\mathrm{i}\boldsymbol{k} \cdot \boldsymbol{r})$ is a vector plane wave referred to the origin at O that can thus be reflected by the Fresnel reflection rule. In this respect we recall that the Fresnel coefficients hold true both for complex indices of refraction and for complex angle of incidence [6, 44]. As a result of the reflection we get the equation

$$\boldsymbol{H}^{(p)}_{\mathrm{R}lm} = \frac{(-\mathrm{i})^{p+l-1}}{2\pi} \int_{\mathcal{D}} \sum_{\eta} F_\eta(\vartheta_\mathrm{k}) \left[\hat{\boldsymbol{u}}_\eta \cdot \boldsymbol{Z}^{(p)}_{lm}(\hat{\boldsymbol{k}}\right] \times \hat{\boldsymbol{u}}_{\mathrm{R}\eta} \exp(\mathrm{i}\boldsymbol{k}_\mathrm{R} \cdot \boldsymbol{r}) \exp(-\mathrm{i}\boldsymbol{k} \cdot \boldsymbol{R}') \, \mathrm{d}\hat{\boldsymbol{k}} \, , \tag{6.14}$$

where $\boldsymbol{k}_\mathrm{R}$ and $\hat{\boldsymbol{u}}_{\mathrm{R}\eta}$ are, respectively, the wavevector and the polarization vector of the reflected plane wave. The integrand in (6.14) can be referred back to the origin at O' by the phase factor $\exp(\mathrm{i}\boldsymbol{k}_\mathrm{R} \cdot \boldsymbol{R}')$ with the result

$$\boldsymbol{H}^{(p)}_{\mathrm{R}lm} = \frac{(-\mathrm{i})^{p+l-1}}{2\pi} \int_{\mathcal{D}} \sum_{\eta} F_\eta(\vartheta_\mathrm{k}) \left[\hat{\boldsymbol{u}}_\eta \cdot \boldsymbol{Z}^{(p)}_{lm}(\hat{\boldsymbol{k}})\right] \times \hat{\boldsymbol{u}}_{\mathrm{R}\eta} \exp(\mathrm{i}\boldsymbol{k}_\mathrm{R} \cdot \boldsymbol{r}') \exp[\mathrm{i}(\boldsymbol{k}_\mathrm{R} - \boldsymbol{k}) \cdot \boldsymbol{R}'] \, \mathrm{d}\hat{\boldsymbol{k}} \, . \tag{6.15}$$

Let us now recall that according to Sect. 4.1.2 the multipole expansion of the plane wave in (6.15) is

$$\hat{\boldsymbol{u}}_{\mathrm{R}\eta} \exp(\mathrm{i}\boldsymbol{k}_\mathrm{R} \cdot \boldsymbol{r}') = 4\pi \sum_{plm} \mathrm{i}^{p+l+1}(-)^{m+1} \left[\boldsymbol{Z}^{(p)}_{l,-m}(\hat{\boldsymbol{k}}_\mathrm{R}) \cdot \hat{\boldsymbol{u}}_{\mathrm{R}\eta}\right] \boldsymbol{J}^{(p)}_{lm}(\boldsymbol{r}', k')$$

that, when substituted into (6.15), leads us to write the reflected field as

$$\boldsymbol{H}^{(p)}_{\mathrm{R}lm} = \sum_{p'l'm'} \boldsymbol{J}^{(p')}_{l'm'}(\boldsymbol{r}', k') \mathcal{F}^{(p'p)}_{l'm'lm} \, , \tag{6.16}$$

where we define

$$\mathcal{F}^{(p'p)}_{l'm'lm} = 2\mathrm{i}^{p'-p+l'-l}(-)^{m+1} \int_{\mathcal{D}} \sum_{\eta} F_\eta(\vartheta_\mathrm{k}) \left[\hat{\boldsymbol{u}}_\eta \cdot \boldsymbol{Z}^{(p)}_{lm}(\hat{\boldsymbol{k}})\right] \times \left[\hat{\boldsymbol{u}}_{\mathrm{R}\eta} \cdot \boldsymbol{Z}^{(p')}_{l',-m'}(\hat{\boldsymbol{k}}_\mathrm{R})\right] \exp(2\mathrm{i}k' a \cos\vartheta_k) \, \mathrm{d}\hat{\boldsymbol{k}} \, , \tag{6.17}$$

a being the distance of O' from the interface. The quantities $\mathcal{F}^{(p'p)}_{l'm'lm}$ can be understood as the elements of the matrix F that effects the reflection of the $\boldsymbol{H}$-multipole fields on the plane interface and thus gives a formal solution to the problem at hand. It may be surprising, however, that the reflected field is expressed in terms of $\boldsymbol{J}$-multipole fields that do not satisfy the radiation condition at infinity. It must be stressed, however, that this is a deceiving appearance because the region of validity of the series expansion in (6.16) is still to be determined. The best procedure to clarify this point is to rewrite (6.14) in terms of multipole fields with origin at O'', the mirror image of the source of the original $\boldsymbol{H}$ fields. The required expression is

$$\boldsymbol{H}^{(p)}_{\mathrm{R}lm} = \frac{(-\mathrm{i})^{p+l-1}}{2\pi} \int_{\mathcal{D}} \sum_{\eta} F_\eta(\vartheta_\mathrm{k}) \left[\hat{\boldsymbol{u}}_\eta \cdot \boldsymbol{Z}^{(p)}_{lm}(\hat{\boldsymbol{k}})\right] \hat{\boldsymbol{u}}_{\mathrm{R}\eta} \exp(\mathrm{i}\boldsymbol{k}_\mathrm{R} \cdot \boldsymbol{r}'')\, \mathrm{d}\hat{\boldsymbol{k}} \;, \tag{6.18}$$

whose integrand is expressed in terms of reflected plane waves referred to the origin at O'': the phase factor $\exp(-\mathrm{i}\boldsymbol{k} \cdot \boldsymbol{R}')$ in (6.14) effects, indeed, the translation of origin from O to O''. Now, as a consequence of (6.4) that relates the amplitudes of the incident and reflected field, we have

$$\hat{\boldsymbol{u}}_{\mathrm{R}\eta} \cdot \boldsymbol{Z}^{(p)}_{lm}(\hat{\boldsymbol{k}}_\mathrm{R}) = (-)^{\eta+p+l+m} \hat{\boldsymbol{u}}_\eta \cdot \boldsymbol{Z}^{(p)}_{lm}(\hat{\boldsymbol{k}}). \tag{6.19}$$

Therefore, (6.18) can be rewritten as

$$\begin{aligned} \boldsymbol{H}_{\mathrm{R}lm} =& \frac{(-)^{p+l+m-1}(-\mathrm{i})^{p+l-1}}{2\pi} \\ &\times \int_{\mathcal{D}} \sum_{\eta} (-)^{\eta+1} F_\eta(\vartheta_\mathrm{k}) \left[\hat{\boldsymbol{u}}_{\mathrm{R}\eta} \cdot \boldsymbol{Z}^{(p)}_{lm}(\hat{\boldsymbol{k}}_\mathrm{R})\right] \hat{\boldsymbol{u}}_{\mathrm{R}\eta} \exp(\mathrm{i}\boldsymbol{k}_\mathrm{R} \cdot \boldsymbol{r}'')\, \mathrm{d}\hat{\boldsymbol{k}} \;, \end{aligned} \tag{6.20}$$

whose interpretation is straightforward when the interface is perfectly reflecting. In fact, the Fresnel coefficients for a perfectly reflecting surface take on the limiting values

$$F_\eta = (-)^{\eta-1},$$

so that, in this case (6.20) represents, except for a sign, the multipole field $\boldsymbol{H}^{(p)}_{lm}(\boldsymbol{r}'', k')$ with origin at O''. This representation is valid in the half-space $z'' < 0$. This suggests that, in the general case, (6.20) represents in the half-space $z'' < 0$ a linear combination of $\boldsymbol{H}$-multipole fields with origin at O''. We write this combination as

$$\boldsymbol{H}^{(p)}_{\mathrm{R}lm} = \sum_{p''l''m''} \boldsymbol{H}^{(p'')}_{l''m''}(\boldsymbol{r}'', k') a^{(p''p)}_{l''m''lm} \;, \tag{6.21}$$

whose coefficients $a^{(p''p)}_{l''m''lm}$ can be determined by expressing each of the $\boldsymbol{H}$-multipole fields in (6.21) as a combination of multipoles centered at O' by means of the addition theorem of Sect. 1.8. Indeed, for the region inside the sphere of radius $|\boldsymbol{R}' - \boldsymbol{R}''|$ (see Fig. 6.3) we get

$$\boldsymbol{H}^{(p)}_{\mathrm{R}lm} = \sum_{p''l''m''} \sum_{p'l'm'} \boldsymbol{J}^{(p')}_{l'm'}(\boldsymbol{r}', k') \mathcal{H}^{(p'p'')}_{l'm'l''m''}(\boldsymbol{R}' - \boldsymbol{R}'', k') a^{(p''p)}_{l''m''lm} \;. \tag{6.22}$$

In turn, in the region outside this sphere, i.e., for $r' > |\boldsymbol{R}' - \boldsymbol{R}''|$,

$$\boldsymbol{H}^{(p)}_{\mathrm{R}lm} = \sum_{p''l''m''} \sum_{p'l'm'} \boldsymbol{H}^{(p')}_{l'm'}(\boldsymbol{r}', k') \mathcal{J}^{(p'p'')}_{l'm'l''m''}(\boldsymbol{R}' - \boldsymbol{R}'', k') a^{(p''p)}_{l''m''lm} \, . \quad (6.23)$$

Comparison of (6.22) with (6.16) leads to the following expression for the coefficients $a^{(p''p)}_{l''m''lm}$:

$$a^{(p''p)}_{l''m''lm} = \sum_{p'l'm'} \left[\mathrm{H}^{-1}\right]^{(p''p')}_{l''m''l'm'} \mathcal{F}^{(p'p)}_{l'm'lm} \, . \quad (6.24)$$

When (6.24) is substituted into (6.23) we get the reflected field in a form that is valid at a large distance from the source and satisfies the radiation condition at infinity as it contains $\boldsymbol{H}$-multipole fields only.

6.3.2 Calculation of the Reflected Field

Equation (6.17), which defines the elements of the multipole reflection matrix, may seem to give only a formal solution to the problem of reflection. Nevertheless, in this section we use the properties of the spherical multipole fields to put (6.17) into a form that is suitable for actual calculations. Indeed, in our opinion, showing the details of this kind of calculation may be a valuable tool to make the reader better acquainted with the usage of the machinery expounded so far.

First, by substituting (6.19) into (6.17) we eliminate the reflected direction $\hat{\boldsymbol{k}}_{\mathrm{R}}$ and the polarization vectors $\hat{\boldsymbol{u}}_{\mathrm{R}\eta}$ so that the only dot product within the integrand is $\hat{\boldsymbol{u}}_\eta \cdot \boldsymbol{Z}^{(p)}_{lm}(\hat{\boldsymbol{k}})$. The latter can be calculated by representing the polarization unit vectors on the spherical basis as

$$\hat{\boldsymbol{u}}_1 = \frac{\cos\vartheta_{\mathrm{k}} \exp(\mathrm{i}\varphi_{\mathrm{k}})}{\sqrt{2}} \boldsymbol{\xi}_{-1} - \sin\vartheta_{\mathrm{k}} \boldsymbol{\xi}_0 - \frac{\cos\vartheta_{\mathrm{k}} \exp(-\mathrm{i}\varphi_{\mathrm{k}})}{\sqrt{2}} \boldsymbol{\xi}_1 \, ,$$

$$\hat{\boldsymbol{u}}_2 = \frac{\mathrm{i}}{\sqrt{2}} \exp(\mathrm{i}\varphi_{\mathrm{k}}) \boldsymbol{\xi}_{-1} + \frac{\mathrm{i}}{\sqrt{2}} \exp(-\mathrm{i}\varphi_{\mathrm{k}}) \boldsymbol{\xi}_1 \, .$$

We get

$$\begin{aligned} \hat{\boldsymbol{u}}_1 \cdot \boldsymbol{Z}^{(1)}_{lm} = & \left[-\frac{1}{\sqrt{2}} c^{(1)}_{lm} \bar{P}_{l,m+1}(\cos\vartheta_{\mathrm{k}}) \cos\vartheta_{\mathrm{k}} + c^{(0)}_{lm} \bar{P}_{lm}(\cos\vartheta_{\mathrm{k}}) \sqrt{1 - \cos^2\vartheta_{\mathrm{k}}} \right. \\ & \left. + \frac{1}{\sqrt{2}} c^{(-1)}_{lm} \bar{P}_{l,m-1}(\cos\vartheta_{\mathrm{k}}) \cos\vartheta_{\mathrm{k}} \right] \frac{\exp(\mathrm{i}m\varphi_{\mathrm{k}})}{\sqrt{4\pi}} \, , \end{aligned}$$

$$\hat{\boldsymbol{u}}_2 \cdot \boldsymbol{Z}^{(1)}_{lm} = \left[\frac{\mathrm{i}}{\sqrt{2}} c^{(1)}_{lm} \bar{P}_{l,m+1}(\cos\vartheta_{\mathrm{k}}) + \frac{\mathrm{i}}{\sqrt{2}} c^{(-1)}_{lm} \bar{P}_{l,m-1}(\cos\vartheta_{\mathrm{k}}) \right] \frac{\exp(\mathrm{i}m\varphi_{\mathrm{k}})}{\sqrt{4\pi}} \, ,$$

where we define the functions

$$\bar{P}_{lm}(z) = \sqrt{(2l+1)\frac{(l-m)!}{(l+m)!}} P_{lm}(z) \ . \tag{6.25}$$

$P_{lm}(z)$ are the Legendre functions of complex argument that are defined by (1.16). The quantities $c_{lm}^{(0)}$ and $c_{lm}^{(\mp)}$ are the Clebsch–Gordan coefficients (see Table 1.1)

$$\begin{aligned} c_{lm}^{(0)} =& C(1,l,l;0,m) = -\frac{m}{\sqrt{l(l+1)}} \ , \\ c_{lm}^{(\mp 1)} =& C(1,l,l;\pm 1, m \mp 1) = \pm\sqrt{\frac{(l \pm m)(l \mp m + 1)}{2l(l+1)}} \ . \end{aligned}$$

Then, it can be easily verified that the relation $\hat{\boldsymbol{u}}_2 = \hat{\boldsymbol{k}} \times \hat{\boldsymbol{u}}_1$ yields the rules

$$\begin{aligned} \hat{\boldsymbol{u}}_2 \cdot \boldsymbol{Z}_{lm}^{(2)} &= -\hat{\boldsymbol{u}}_1 \cdot \boldsymbol{Z}_{lm}^{(1)} = -\hat{\boldsymbol{u}}_1 \cdot \boldsymbol{X}_{lm}, \\ \hat{\boldsymbol{u}}_1 \cdot \boldsymbol{Z}_{lm}^{(2)} &= \hat{\boldsymbol{u}}_2 \cdot \boldsymbol{Z}_{lm}^{(1)} = \hat{\boldsymbol{u}}_2 \cdot \boldsymbol{X}_{lm}, \end{aligned}$$

whereas the properties of the vector spherical harmonics yield the relation

$$\hat{\boldsymbol{u}}_\eta \cdot \boldsymbol{X}_{l,-m} = (-)^{\eta+m} \hat{\boldsymbol{u}}_\eta \cdot \boldsymbol{X}_{lm} \exp(-2\mathrm{i}m\varphi_\mathrm{k}) \ .$$

We are now able to perform at once the integration over the angle φ_k with the result

$$\int_0^{2\pi} \exp[\mathrm{i}(m - m')\varphi_\mathrm{k}] \, \mathrm{d}\varphi_\mathrm{k} = 2\pi\delta_{mm'} \ ,$$

so that the elements of the multipole reflection matrix $\mathcal{F}_{l'm'lm}^{(p'p)}$ with $m \neq m'$ do vanish. This property is conveniently expressed by the equation

$$\mathcal{F}_{l'm'lm}^{(p'p)} = \mathcal{F}_{l'l;m}^{(p'p)} \delta_{mm'} \ , \tag{6.26}$$

that, when introduced into (6.17) yield the useful relation

$$\mathcal{F}_{l'l;m}^{(p'p)} = \mathcal{F}_{ll';-m}^{(pp')} \ . \tag{6.27}$$

At this stage, each element of matrix F is given by an integral of the form

$$\int_0^{\frac{\pi}{2}-\mathrm{i}\infty} f(\cos\vartheta_\mathrm{k}) \exp(2\mathrm{i}k'a\cos\vartheta_\mathrm{k}) \sin\vartheta_\mathrm{k} \, \mathrm{d}\vartheta_\mathrm{k}$$

that, through the substitution $x = 2\mathrm{i}k'a(1 - \cos\vartheta_\mathrm{k})$ takes on the form

$$\frac{\exp(2\mathrm{i}k'a)}{2\mathrm{i}k'a} \int_0^{+\infty} f\left(1 - \frac{x}{2\mathrm{i}k'a}\right) \exp(-x) \, \mathrm{d}x \ ,$$

and is thus suitable for numerical integration through the Gauss–Laguerre method [114]. In practice, the integration formula is

$$\int_0^\infty f(x) \exp(-x)\, \mathrm{d}x \approx \sum_{i=1}^{N} w_i f(x_i) ,$$

where the weights w_i are

$$w_i = \frac{(N!)^2 x_i}{[(N+1)L_N(x_{i+1})]^2} ,$$

x_i being the ith zero of the Laguerre polynomial L_N. Thus, to get reliable values of the elements of F, the order N must be wisely chosen so as to ensure a fair convergence of the integrals.

Let us now recall that, according to (6.24), the calculation of the reflected field in the far zone requires the elements of the reflection matrix F as well as the quantities $\mathcal{H}^{(p'p)}_{l'm'lm}(\boldsymbol{R}' - \boldsymbol{R}'', k')$. Since in the present case the translation vector is parallel to the z axis, the involved quantities are $\mathcal{H}^{(p'p)}_{l'm'lm}(-2a\hat{\boldsymbol{e}}_z, k')$ that, as well as the quantities $[\mathrm{H}^{-1}]^{(p'p)}_{l'm'lm}(-2a\hat{\boldsymbol{e}}_z, k')$, have the property expressed by (1.74). On account of similar property of the elements of F [see (6.26)], also the amplitudes $a^{(p'p)}_{l'm'lm}$ do vanish unless $m' = m$, i.e.,

$$a^{(p'p)}_{l'm'lm} = a^{(p'p)}_{l'l;m} \delta_{mm'} . \tag{6.28}$$

6.4 Scattering from a Sphere on a Dielectric Substrate

The theory of the preceding section is the starting point for calculating the scattering pattern from a sphere in the vicinity of a dielectric substrate. In fact, the field scattered by any particle can always be expanded in a series of $\boldsymbol{H}$-multipole fields with origin within the particle itself. The reflection of these multipole fields on the plane interface can, of course, be dealt with through the theory of the preceding section.

We assume that a spherical scatterer lies entirely within the accessible half-space and is illuminated by a plane wave. We already pointed out that outside the scatterer the total field is

$$\boldsymbol{E}_{\mathrm{Ext}} = \boldsymbol{E}_{\mathrm{I}} + \boldsymbol{E}_{\mathrm{R}} + \boldsymbol{E}_{\mathrm{S}} + \boldsymbol{E}_{\mathrm{SR}} , \tag{6.29}$$

where $\boldsymbol{E}_{\mathrm{R}}$ and $\boldsymbol{E}_{\mathrm{I}}$ are the same as we would have if no particle were present. $\boldsymbol{E}_{\mathrm{SR}}$ and $\boldsymbol{E}_{\mathrm{S}}$ are related to each other by the reflection condition and $\boldsymbol{E}_{\mathrm{S}}$ is determined by imposing to $\boldsymbol{E}_{\mathrm{Ext}}$ the appropriate boundary conditions across the surface of the scattering particle. The formalism that we are going to expound is appropriate to a homogeneous sphere, but we will show later that its application to radially nonhomogeneous spheres implies minor changes only.

The geometry that we adopt for our study is sketched in Fig 6.4 and differs slightly from that depicted in Fig. 6.3. In fact, we found it convenient to take the center of the spherical scatterer O' and its image O'' on the z axis, a minor difference that allows us to make full use of the symmetry of the problem while preserving the generality of our approach.

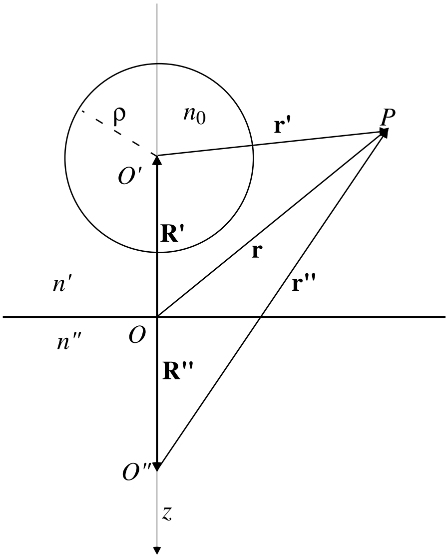

Fig. 6.4. Geometry for scattering from a sphere in the vicinity of a dielectric surface

6.4.1 Reflection of the Incident and Scattered Wave

The incident and the reflected fields have the same multipole expansion that has been established in Sect. 6.1 for the case of a perfectly reflecting surface. The respective multipole amplitudes are related to each other by (6.4) that holds true for general values of n' and n''. Nevertheless, since $\boldsymbol{E}_\mathrm{I}$ and $\boldsymbol{E}_\mathrm{R}$ must also satisfy the boundary conditions on the surface of the scattering sphere, it is convenient to expand both fields in terms of multipole fields with origin at the center of the sphere, O'. The simplest way to do this is by resorting to the appropriate phase factors with the results

$$\boldsymbol{E}_\mathrm{I} = \exp(\mathrm{i}\boldsymbol{k}_\mathrm{I} \cdot \boldsymbol{R}') \sum_\eta E_{0\eta} \sum_{plm} \boldsymbol{J}_{lm}^{(p)}(\boldsymbol{r}', k') W_{\mathrm{I}\eta lm}^{(p)} , \tag{6.30}$$

$$\boldsymbol{E}_\mathrm{R} = \exp(\mathrm{i}\boldsymbol{k}_\mathrm{R} \cdot \boldsymbol{R}') \sum_\eta E_{0\eta} F_\eta(\vartheta_\mathrm{I}) \sum_{plm} \boldsymbol{J}_{lm}^{(p)}(\boldsymbol{r}', k') W_{\mathrm{R}\eta lm}^{(p)} .$$

The field that is scattered by a sphere that lies entirely in the accessible half-space can be expanded in a series of vector multipole fields that satisfy the radiation condition at infinity. The component of the incident field that is polarized along $\hat{\boldsymbol{u}}_{\mathrm{I}\eta}$ yields, indeed, a scattered field that, with respect to an origin O' within the particle, can be written as

$$\boldsymbol{E}_{\mathrm{S}\eta} = E_{0\eta} \sum_{plm} \boldsymbol{H}_{lm}^{(p)}(\boldsymbol{r}', k') \mathcal{A}_{\eta lm}^{(p)} .$$

The amplitudes $\mathcal{A}$, which are as yet unknown, are determined by the boundary conditions at the surface of the particle. The scattered field impinges on the plane surface and, by reflection, yields a field that can be obtained through the technique that was described in Sect. 6.2. Accordingly, the reflected-scattered field in the vicinity of the surface of the particle can be written as the superposition of $\boldsymbol{J}$-multipole fields with origin at O'

$$\boldsymbol{E}_{\mathrm{SR}\eta} = E_{0\eta} \sum_{plm} \sum_{p'l'} \boldsymbol{J}_{lm}^{(p)}(\boldsymbol{r}', k') \mathcal{F}_{ll';m}^{(pp')} \mathcal{A}_{\eta l'm}^{(p')} , \tag{6.31}$$

where the quantities $\mathcal{F}_{ll';m}^{(pp')}$ are defined by (6.17), and we used the diagonality property (6.26).

6.4.2 Amplitudes of the Scattered Field

The results in Sect. 6.4.1 show that the fields that contribute to $\boldsymbol{E}_{\mathrm{Ext}}$ in the vicinity of the surface of the particle, according to (6.30)–(6.31), are all expressed in terms of vector multipole fields with origin at O'. $\boldsymbol{E}_{\mathrm{Ext}}$ is thus ready for the imposition of the boundary conditions.

We now explicitly assume that the scattering particle is a homogeneous sphere with (possibly complex) refractive index n_0 and radius ρ. Since the field within the sphere must be regular at O', its multipole expansion can be taken in the form

$$\boldsymbol{E}_{\mathrm{T}\eta} = E_{0\eta} \sum_{plm} \boldsymbol{J}_{lm}^{(p)}(\boldsymbol{r}', k_0) \mathcal{C}_{\eta lm}^{(p)} .$$

The multipole expansion of the magnetic field $\boldsymbol{B}$, that is also needed to impose the boundary conditions, is readily obtained through the Maxwell equation

$$\mathrm{i}\boldsymbol{B}_{\eta} = \frac{1}{k} \nabla \times \boldsymbol{E}_{\eta} .$$

In order to impose the boundary conditions across the surface of the scattering sphere, we apply to $\boldsymbol{E}$ and $\boldsymbol{B}$ the procedure that we described in Chap. 5. This procedure yields, for each p, l, and m, four equations among which the amplitudes of the internal field $\mathcal{C}_{\eta lm}^{(p)}$ can be easily eliminated. As a result, we get, for each m, a system of linear nonhomogeneous equations for the amplitudes $\mathcal{A}_{\eta lm}^{(p)}$, namely

$$\sum_{p'l'} \mathcal{M}_{ll';m}^{(pp')} \mathcal{A}_{\eta l'm}^{(p')} = -\mathcal{W}_{\eta lm}^{(p)} , \tag{6.32}$$

where

$$\mathcal{M}^{(pp')}_{ll';m} = \left(R^{(p)}_l\right)^{-1} \delta_{pp'} \delta_{ll'} + \mathcal{F}^{(pp')}_{ll';m} , \tag{6.33}$$

and

$$\mathcal{W}^{(p)}_{\eta lm} = \exp(\mathrm{i}\boldsymbol{k}_\mathrm{I} \cdot \boldsymbol{R}') W^{(p)}_{\mathrm{I}\eta lm} + \exp(\mathrm{i}\boldsymbol{k}_\mathrm{R} \cdot \boldsymbol{R}') F_\eta W^{(p)}_{\mathrm{R}\eta lm} . \tag{6.34}$$

The quantities $R^{(1)}_l$ and $R^{(2)}_l$, as usual, coincide with the Mie coefficients b_l and a_l, respectively, for a homogeneous sphere of refractive index n_0 embedded into a homogeneous medium of refractive index n'. We remark that our theory can easily deal also with sphere sustaining longitudinal waves or with radially nonhomogeneous spheres. Even in this case, in fact, one gets (6.33), but $R^{(2)}_l$ are given by (5.13) or $R^{(p)}_l$ by (5.19), respectively.

6.4.3 Scattering Amplitude and Transition Matrix

Once the amplitudes $\mathcal{A}^{(p)}_{\eta lm}$ of $\boldsymbol{E}_{\mathrm{S}\eta}$ have been calculated by solving (6.32), the reflected-scattered field $\boldsymbol{E}_{\mathrm{SR}\eta}$ is also determined by (6.31). The latter equation, however, gives an expression of $\boldsymbol{E}_{\mathrm{SR}\eta}$ that is valid only in the vicinity of the surface of the sphere as it includes multipole fields that do not satisfy the radiation condition at infinity. Nevertheless, the considerations in Sect. 6.2. led us to conclude that, at any point of the accessible half-space, $\boldsymbol{E}_{\mathrm{SR}\eta}$ is given by the equation

$$\boldsymbol{E}_{\mathrm{SR}\eta} = E_{0\eta} \sum_{plm} \boldsymbol{H}^{(p)}_{lm}(\boldsymbol{r}'', k') \mathcal{A}^{(p)}_{\mathrm{R}\eta lm}, \tag{6.35}$$

where

$$\mathcal{A}^{(p)}_{\mathrm{R}\eta lm} = \sum_{p'l'} a^{(pp')}_{ll';m} \mathcal{A}^{(p')}_{\eta l'm} , \tag{6.36}$$

and the coefficients $a^{(pp')}_{ll';m}$ are given by (6.20) and (6.24). The superposition of $\boldsymbol{E}_{\mathrm{SR}\eta}$, (6.35), and of $\boldsymbol{E}_{\mathrm{S}\eta}$ yields the field that would be observed by an optical instrument in the far zone. The reflected field $\boldsymbol{E}_{\mathrm{R}\eta}$ would be observed in the direction of reflection only. Since $\boldsymbol{E}_{\mathrm{S}\eta}$ and $\boldsymbol{E}_{\mathrm{SR}\eta}$ are given as expansions in terms of $\boldsymbol{H}$-multipole fields with origin at O' and O'', respectively, it is convenient to again use the addition theorem of Sect. 1.8 [16] to refer both fields to a common origin that, for symmetry reasons, we choose to be the point O that is defined in Fig. 6.4. The observed field then becomes

$$\boldsymbol{E}_{\mathrm{Obs}\,\eta} = E_{0\eta} \sum_{plm} \boldsymbol{H}^{(p)}_{lm}(\boldsymbol{r}, k') A^{(p)}_{\eta lm} ,$$

where

$$A^{(p)}_{\eta lm} = \sum_{p'l'} \left[\mathcal{J}^{(pp')}_{ll';m}(a\hat{\boldsymbol{e}}_z, k') \mathcal{A}^{(p')}_{\eta l'm} + \mathcal{J}^{(pp')}_{ll';m}(-a\hat{\boldsymbol{e}}_z, k') \mathcal{A}^{(p')}_{\mathrm{R}\eta l'm} \right] . \tag{6.37}$$

We notice that in (6.37) we used the property (1.74) of the J translation matrix elements that holds true when, as in the present case, the translation takes place along the z axis. As usual, we have

$$f_{\eta\eta'} = -\frac{\mathrm{i}}{4\pi k'} \sum_{plm} W^{(p)*}_{\mathrm{S}\eta lm} A^{(p)}_{\eta' lm} \,. \tag{6.38}$$

The efficiency of the preceding equations can be improved because, as we assumed throughout, the refractive index n' is real. In this case, indeed, with the help of (5.31) and (5.33), (6.38) can be rewritten as

$$\begin{aligned} f_{\eta\eta'} = &-\frac{\mathrm{i}}{4\pi k'} \sum_{plm} W^{(p)*}_{\mathrm{S}\eta lm} \\ &\times \left[\exp(\mathrm{i}\boldsymbol{k}_{\mathrm{S}} \cdot \hat{\boldsymbol{e}}_z a) \mathcal{A}^{(p)}_{\eta' lm} + \exp(-\mathrm{i}\boldsymbol{k}_{\mathrm{S}} \cdot \hat{\boldsymbol{e}}_z a) \mathcal{A}^{(p)}_{\mathrm{R}\eta' lm}\right] . \end{aligned} \tag{6.39}$$

Equation (6.39) is the one that we actually used for our calculations.

We proceed now to a further modification of (6.39) that leads to the definition of the *transition matrix for a particle in the presence of a plane interface*. To this end, let us recall that the formal solution to (6.32) is

$$\mathcal{A}^{(p)}_{\eta lm} = -\sum_{p'l'} \left[\mathrm{M}^{-1}\right]^{(pp')}_{ll';m} \mathcal{W}^{(p')}_{\eta l'm} \,, \tag{6.40}$$

where M^{-1} is the inverse to the matrix M in (6.33). In this respect we notice that, on account of (6.27), the inversion of matrix M needs to be performed for $m \geq 0$ only. With the help of (5.30) and (6.4) we transform the amplitudes $\mathcal{W}^{(p)}_{\eta lm}$, (6.34), into the form

$$\mathcal{W}^{(p)}_{\eta lm} = \sum_{p'l'} \mathcal{J}^{(pp')}_{ll';m}(-a\hat{\boldsymbol{e}}_z, k') W^{(p')}_{E\eta l'm} \,, \tag{6.41}$$

where the multipole amplitudes of the exciting field are given by (6.7). Substitution of (6.41) into (6.40) and of (6.40) into (6.37) allows us to write the scattering amplitude as

$$f_{\eta\eta'} = -\frac{\mathrm{i}}{4\pi k'} \sum_{pp'} \sum_{ll'} \sum_{m} W^{(p)*}_{\mathrm{S}\eta lm} \mathcal{S}^{(pp')}_{ll';m} W^{(p')}_{\mathrm{E}\eta' l'm} \,, \tag{6.42}$$

so that the quantities

$$\begin{aligned} \mathcal{S}^{(pp')}_{ll';m} = &-\sum_{qL} \sum_{q'L'} \Bigg[\mathcal{J}^{(pq)}_{lL;m}(a\hat{\boldsymbol{e}}_z, k') \left[\mathrm{M}^{-1}\right]^{(qq')}_{LL';m} \\ &+ \mathcal{J}^{(pq)}_{lL;m}(-a\hat{\boldsymbol{e}}_z, k') \sum_{q''L''} a^{(qq'')}_{LL'';m} \left[\mathrm{M}^{-1}\right]^{(q''q')}_{L''L';m} \Bigg] \mathcal{J}^{(q'p')}_{L'l';m}(-a\hat{\boldsymbol{e}}_z, k') \end{aligned} \tag{6.43}$$

can be interpreted as the elements of the transition matrix for the spherical scatterer in the presence of the plane surface [3]. We remark that the multiple scattering processes that occur between the sphere and the substrate are accounted for by the elements of the transfer matrix J.

Using the transition matrix to get the observed field does not yield any advantage in the case that we deal with in this section; in fact, as we stated above, (6.39) is computationally more effective. However, our purpose was to show that the transition matrix can be defined even when a plane interface is present. The advantages yielded by the use of the transition matrix will become evident later when we will deal with the problem of the orientational average over an assembly of nonspherical particles deposited on a plane substrate.

6.5 Aggregated Spheres on a Dielectric Substrate

We go now to consider the scattering pattern from an aggregate of spherical scatterers in the vicinity of or deposited on a dielectric substrate. More precisely, our aim is to calculate the scattering pattern from an aggregate as a function of its orientation with respect to an incident plane wave field. This information is, in fact, the basis for the calculation of the scattering pattern from an assembly of identical aggregates with a known or assumed distribution of their orientations. $\boldsymbol{E}_{\mathrm{Ext}}$ is still given by (6.29), provided $\boldsymbol{E}_{\mathrm{S}}$ is the field scattered by the whole aggregate. Even in this case the scattered field $\boldsymbol{E}_{\mathrm{S}}$ is determined by imposing to $\boldsymbol{E}_{\mathrm{Ext}}$ the appropriate boundary conditions across the surface of the particle, i.e., across the surface of each one of the spheres in the aggregate. It will become apparent later that $\boldsymbol{E}_{\mathrm{S}}$ and $\boldsymbol{E}_{\mathrm{SR}}$ include all the multiple scattering processes that occur both among the spheres of the aggregate and between the aggregate and the substrate.

The geometry that we adopt for our study of the scattering from an aggregate of spheres is depicted in Fig. 6.5.

6.5.1 Multipole Expansion of the Fields

The expansion of $\boldsymbol{E}_{\mathrm{I}\eta}$ and $\boldsymbol{E}_{\mathrm{R}\eta}$ in terms of vector multipole fields with origin at O are

$$\begin{aligned} \boldsymbol{E}_{\mathrm{I}\eta} &= E_{0\eta}\sum_{plm}\boldsymbol{J}_{lm}^{(p)}(\boldsymbol{r},k')W_{\mathrm{I}\eta lm}^{(p)} , \\ \boldsymbol{E}_{\mathrm{R}\eta} &= E_{0\eta}F_{\eta}(\vartheta_{\mathrm{I}})\sum_{plm}\boldsymbol{J}_{lm}^{(p)}(\boldsymbol{r},k')W_{\mathrm{R}\eta lm}^{(p)} . \end{aligned} \tag{6.44}$$

We recall that $\boldsymbol{E}_{\mathrm{I}}$ and $\boldsymbol{E}_{\mathrm{R}}$ must also satisfy the boundary conditions on the surface of each of the scattering spheres. Therefore we need to rewrite the expansions (6.44) in terms of spherical vector multipole fields with origin at the center of the αth sphere, O'_{α}. This can be done in the simplest way

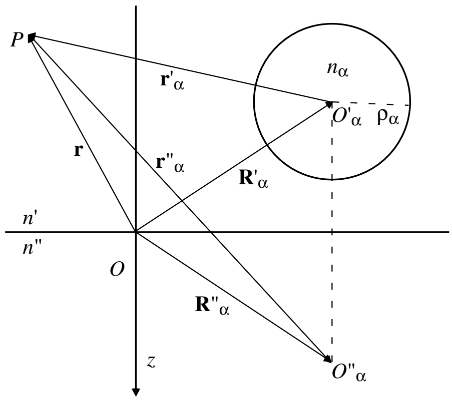

Fig. 6.5. Geometry for the calculation of the scattering pattern from aggregates on a dielectric surface. Only the αth *sphere* is shown for the sake of clarity

by resorting to the appropriate phase factors [108]. Actually, we used this technique in the case of a single sphere in the vicinity of the interface. We stress, however, that this procedure, though exact, yields expressions that are not suitable to effect averages over the orientation of the scatterers. Therefore we start from (6.44) and apply the addition theorem of Sect. 1.8 to express each of the $\boldsymbol{J}$-multipole fields with origin at O as a series of $\boldsymbol{J}$-multipole fields with origin at O'_α. The result is

$$\boldsymbol{E}_{\mathrm{I}\eta} = E_{0\eta} \sum_{plm} \sum_{p'l'm'} \boldsymbol{J}_{lm}^{(p)}(\boldsymbol{r}'_\alpha, k') \mathcal{J}_{lml'm'}^{(pp')}(\boldsymbol{R}'_\alpha, k') W_{\mathrm{I}\eta l'm'}^{(p')} ,$$

$$\boldsymbol{E}_{\mathrm{R}\eta} = E_{0\eta} F_\eta(\vartheta_\mathrm{I}) \sum_{plm} \sum_{p'l'm'} \boldsymbol{J}_{lm}^{(p)}(\boldsymbol{r}'_\alpha, k') \mathcal{J}_{lml'm'}^{(pp')}(\boldsymbol{R}'_\alpha, k') W_{\mathrm{R}\eta l'm'}^{(p')} .$$

The field that is scattered by an aggregate of spheres embedded within a homogeneous medium can be described as the superposition of the fields that are scattered by each one of the spheres. Since the latter fields must satisfy the radiation condition at infinity, we write

$$\boldsymbol{E}_{\mathrm{S}\eta} = E_{0\eta} \sum_\alpha \sum_{plm} \boldsymbol{H}_{lm}^{(p)}(\boldsymbol{r}'_\alpha, k') \mathcal{A}_{\eta\alpha lm}^{(p)} ,$$

where the amplitudes $\mathcal{A}_{\eta\alpha lm}^{(p)}$, which are as yet unknown, are determined by the boundary conditions at the surface of each of the component spheres.

We still need to consider the field $\boldsymbol{E}_{\mathrm{RS}}$ that after scattering by the aggregate is reflected by the surface. According to [108, 115] and in analogy to what we already did in the case of a single sphere, at any point of the accessible half-space, $\boldsymbol{E}_{\mathrm{SR}\eta}$ can be written as

$$\boldsymbol{E}_{\mathrm{SR}\eta} = E_{0\eta} \sum_\alpha \sum_{plm} \boldsymbol{H}_{lm}^{(p)}(\boldsymbol{r}''_\alpha, k') \mathcal{A}_{\mathrm{R}\eta\alpha lm}^{(p)} , \tag{6.45}$$

i.e., as a superposition of $\boldsymbol{H}$-multipole fields with origin at the image points O''_α. The amplitudes $\mathcal{A}^{(p)}_{\mathrm{R}\eta\alpha lm}$ in (6.45) are related to the amplitudes of the scattered field $\boldsymbol{E}_{\mathrm{S}}$ by the equation

$$\mathcal{A}^{(p)}_{\mathrm{R}\eta\alpha lm} = \sum_{p'l'} a^{(pp')}_{\alpha ll';m} \mathcal{A}^{(p')}_{\alpha\eta l'm} , \tag{6.46}$$

with the amplitudes $a^{(pp')}_{\alpha ll';m}$ explicitly given by

$$a^{(pp')}_{\alpha ll';m} = \sum_{p''l''} \left[\mathrm{H}^{-1}_\alpha\right]^{(pp'')}_{ll'';m} \mathcal{F}^{(p''p')}_{\alpha l''l';m} , \tag{6.47}$$

where H^{-1}_α is the inverse to the matrix $\mathrm{H}(\bar{\boldsymbol{R}}_{\alpha\alpha}, k')$ that effects the transfer of the origin of the $\boldsymbol{H}$-multipole fields from O''_α to O'_α and $\bar{\boldsymbol{R}}_{\alpha\alpha} = \boldsymbol{R}'_\alpha - \boldsymbol{R}''_\alpha$. In turn, F_α is the reflection matrix for $\boldsymbol{H}$-multipole fields with origin at O'_α. It is to be calculated as in Sect. 6.3.

The last expansion that we need to consider is that of the field within the αth sphere, namely

$$\boldsymbol{E}_{\mathrm{T}\eta\alpha} = E_{0\eta} \sum_{plm} \boldsymbol{J}^{(p)}_{lm}(\boldsymbol{r}'_\alpha, k_\alpha) \mathcal{C}^{(p)}_{\alpha\eta lm} .$$

Now, we reexpand $\boldsymbol{E}_{\mathrm{S}\eta}$ and $\boldsymbol{E}_{\mathrm{SR}\eta}$ in terms of multipole fields with origin at O'_α through the use of the addition theorem of Sect. 1.8 [16]. The result for the scattered field $\boldsymbol{E}_{\mathrm{S}\eta}$ is

$$\begin{aligned}\boldsymbol{E}_{\mathrm{S}\eta} = E_{0\eta} \sum_{plm} \Bigg[&\boldsymbol{H}^{(p)}_{lm}(\boldsymbol{r}'_\alpha, k') \mathcal{A}^{(p)}_{\eta\alpha lm} + \boldsymbol{J}^{(p)}_{lm}(\boldsymbol{r}'_\alpha, k') \\ &\times \sum_{p'l'm'} \sum_{\alpha'\neq\alpha} \mathcal{H}^{(pp')}_{lml'm'}(\boldsymbol{R}'_{\alpha'\alpha}, k') \mathcal{A}^{(p')}_{\eta\alpha' l'm'} \Bigg] ,\end{aligned} \tag{6.48}$$

where $\boldsymbol{R}'_{\alpha'\alpha} = \boldsymbol{R}'_\alpha - \boldsymbol{R}'_{\alpha'}$. For the reflected scattered field $\boldsymbol{E}_{\mathrm{SR}}$ we obtain

$$\begin{aligned}\boldsymbol{E}_{\mathrm{SR}\eta} = E_{0\eta} \sum_{plm} \boldsymbol{J}^{(p)}_{lm}(\boldsymbol{r}'_\alpha, k') \sum_{p'l'm'} \Bigg[&\mathcal{H}^{(pp')}_{lml'm'}(\bar{\boldsymbol{R}}_{\alpha\alpha}, k') \mathcal{A}^{(p')}_{\mathrm{R}\eta\alpha l'm'} \\ &+ \sum_{\alpha'\neq\alpha} \mathcal{H}^{(pp')}_{lml'm'}(\bar{\boldsymbol{R}}_{\alpha'\alpha}, k') \mathcal{A}^{(p')}_{\mathrm{R}\eta\alpha' l'm'} \Bigg],\end{aligned}$$

where $\bar{\boldsymbol{R}}_{\alpha'\alpha} = \boldsymbol{R}'_\alpha - \boldsymbol{R}''_{\alpha'}$. Then, with the help of (6.46) and (6.47), and taking into account that $\mathcal{H}^{(pp')}_{lml'm'}(\bar{\boldsymbol{R}}_{\alpha\alpha}, k') = \mathcal{H}^{(pp')}_{ll';m}(\bar{\boldsymbol{R}}_{\alpha\alpha}, k')\delta_{mm'}$, we get the required expression

$$\begin{aligned}\boldsymbol{E}_{\mathrm{SR}\eta} =&E_{0\eta} \sum_{plm} \boldsymbol{J}^{(p)}_{lm}(\boldsymbol{r}'_\alpha, k') \sum_{p'l'} \Bigg[\mathcal{F}^{(pp')}_{\alpha ll';m} \mathcal{A}^{(p')}_{\eta\alpha l'm} \\ &+ \sum_{\alpha'\neq\alpha} \sum_{p''l''m'} \mathcal{Q}^{(pp'')}_{lml''m'}(\bar{\boldsymbol{R}}_{\alpha'\alpha}, k') \mathcal{F}^{(p''p')}_{\alpha' l''l';m'} \mathcal{A}^{(p')}_{\eta\alpha' l'm'} \Bigg] ,\end{aligned} \tag{6.49}$$

where

$$\mathcal{Q}^{(pp'')}_{lml''m''}(\bar{\boldsymbol{R}}_{\alpha'\alpha},k') = \sum_{p'l'} \mathcal{H}^{(pp')}_{lml'm'}(\bar{\boldsymbol{R}}_{\alpha'\alpha},k')\big[\mathsf{H}^{-1}_{\alpha'}\big]^{(p'p'')}_{l'l'';m'} \,.$$

A few words of comment on the physical content of (6.48) and (6.49) are in order. Equation (6.48) shows that the field scattered by the whole aggregate includes the effect of all the multiple scattering processes that occur among the spheres of the aggregate. In turn, according to (6.49), $\boldsymbol{E}_{\mathrm{SR}}$ collects the contribution from all the multiple scattering processes occurring between each of the spheres of the aggregate and the substrate.

The boundary conditions across the surface of each of the scattering spheres can now be imposed and we get, for each α, p, l, and m, four equations among which the amplitudes of the internal field C can be easily eliminated. As a result, we get for the amplitudes $\mathcal{A}^{(p)}_{\eta\alpha lm}$ the system of linear nonhomogeneous equations

$$\sum_{\alpha'}\sum_{p'l'm'} \mathcal{M}^{(pp')}_{\alpha lm\alpha'l'm'}\mathcal{A}^{(p')}_{\eta\alpha'l'm'} = -\mathcal{W}^{(p)}_{\eta\alpha lm} \,, \tag{6.50}$$

where

$$\begin{aligned}\mathcal{M}^{(pp')}_{\alpha lm\alpha'l'm'} =& \big[R^{(p)}_{\alpha l}\big]^{-1}\delta_{\alpha\alpha'}\delta_{pp'}\delta_{ll'}\delta_{mm'} + \mathcal{H}^{(pp')}_{lml'm'}(\boldsymbol{R}'_{\alpha'\alpha},k') \\ &+ \mathcal{F}^{(pp')}_{\alpha ll';m}\delta_{\alpha\alpha'}\delta_{mm'} + \sum_{p''l''} \mathcal{Q}^{(pp'')}_{lml''m'}(\bar{\boldsymbol{R}}_{\alpha'\alpha},k')\mathcal{F}^{(p''p')}_{\alpha'l''l';m'} \,.\end{aligned}$$

Again, the quantities $R^{(1)}_{\alpha l}$ and $R^{(2)}_{\alpha l}$ coincide with the Mie coefficients b_l and a_l, respectively, for a homogeneous sphere of refractive index n_α embedded into a homogeneous medium of refractive index n'. Of course, where appropriate, $R^{(2)}_{\alpha l}$ can be substituted for by (5.13) or $R^{(p)}_{\alpha l}$ by (5.19). In turn,

$$\mathcal{W}^{(p)}_{\eta\alpha lm} = \sum_{p'l'm'} \mathcal{J}^{(pp')}_{lml'm'}(\boldsymbol{R}'_{\alpha},k')W^{(p')}_{\mathrm{E}\eta l'm'} \,,$$

where the multipole amplitudes of the exciting field $W^{(p)}_{\mathrm{E}\eta lm}$ are still defined by (6.7).

6.5.2 Transition Matrix for an Aggregate in the Presence of a Surface

Once the amplitudes $\mathcal{A}^{(p)}_{\eta\alpha lm}$ of $\boldsymbol{E}_{\mathrm{S}\eta}$ have been calculated by solving (6.50), the reflected-scattered field, $\boldsymbol{E}_{\mathrm{SR}\eta}$, is also determined by (6.45)–(6.47). Then, we resort again to the addition theorem of Sect. 1.8 to refer $\boldsymbol{E}_{\mathrm{S}\eta}$ and $\boldsymbol{E}_{\mathrm{SR}\eta}$ to a common origin that we choose to be the point O that is defined in Fig. 6.5. The observed field then becomes

$$\boldsymbol{E}_{\mathrm{Obs}\,\eta} = E_{0\eta} \sum_{plm} \boldsymbol{H}^{(p)}_{lm}(\boldsymbol{r}, k') A^{(p)}_{\eta lm} \ ,$$

where

$$A^{(p)}_{\eta lm} = \sum_{\alpha} \sum_{p'l'm'} \left[\mathcal{J}^{(pp')}_{lml'm'}(-\boldsymbol{R}'_\alpha, k') \mathcal{A}^{(p')}_{\eta\alpha l'm'} + \mathcal{J}^{(pp')}_{lml'm'}(-\boldsymbol{R}''_\alpha, k') \mathcal{A}^{(p')}_{\mathrm{R}\eta\alpha l'm'} \right] . \tag{6.51}$$

The amplitudes $A^{(p)}_{\eta lm}$ can be related to the amplitudes of the exciting field, $W^{(p)}_{\mathrm{E}\eta lm}$, through the equation

$$A^{(p)}_{\eta lm} = \sum_{p'l'm'} \mathcal{S}^{(pp')}_{lml'm'} W^{(p')}_{\mathrm{E}\eta' l'm'} \ ,$$

where the quantities $\mathcal{S}^{(pp')}_{lml'm'}$ can be interpreted as the elements of the transition matrix for the aggregate in the presence of the plane substrate. The transition matrix S can be defined by recalling that the formal solution to (6.50) is

$$\mathcal{A}^{(p)}_{\eta\alpha lm} = -\sum_{\alpha'} \sum_{p'l'm'} \left[\mathrm{M}^{-1} \right]^{(pp')}_{\alpha lm\alpha' l'm'} \mathcal{W}^{(p')}_{\eta\alpha' l'm'} \ .$$

When this formal solution is introduced into (6.51), we find

$$\begin{aligned} \mathcal{S}^{(pp')}_{lml'm'} = &-\sum_{\alpha\alpha'} \sum_{qLM} \sum_{q'L'M'} \left[\mathcal{J}^{(pq)}_{lmLM}(-\boldsymbol{R}'_\alpha, k') \left[\mathrm{M}^{-1} \right]^{(qq')}_{\alpha LM\alpha' L'M'} \right. \\ &\left. + \mathcal{J}^{(pq)}_{lmLM}(-\boldsymbol{R}''_\alpha, k') \sum_{q''L''} a^{(qq'')}_{\alpha LL'';M} \left[\mathrm{M}^{-1} \right]^{(q''q')}_{\alpha L''M\alpha' L'M'} \right] \\ &\times \mathcal{J}^{(q'p')}_{L'M'l'm'}(\boldsymbol{R}'_{\alpha'}, k') \ . \end{aligned} \tag{6.52}$$

Then, substituting (6.52) into (6.42) we get the components of the scattering amplitude of the aggregate in the presence of the interface.

At this stage, the orientational averages over an assembly of particles deposited on the interface can be performed along the lines of Sect. 6.2.1, as the procedure that we expounded there applies independently of the reflecting power of the interface. Here we stress that the considerations on the effective scatterers, i.e. actual particles plus images, hold true also in the present case. In fact, (6.52) that defines the elements of the transition matrix depends on the distance between the spheres and their respective images. Therefore, two identical clusters with a different canting angle with respect to the interface should be considered as different particles and the respective transition matrix elements need to be calculated anew.

A few words are still necessary on the determination of l_{I} both for the single sphere and for the aggregate. Of course, the considerations that we already made in Chap. 5 for the case of clusters in free space still hold. First, the presence of an interface may increase the value of l_I. For instance, in case of a perfectly reflecting surface we should deal with a cluster of $2N$ spheres. Second, the calculation either of H^{-1} or of H_α^{-1} becomes rather critical when l_I increases. As a result, the convergence and stability problems that are met in calculating the scattering properties of particles in the presence of a dielectric interface are the most complex among those considered so far.

6.6 Perfectly Reflecting vs. Dielectric Surface: Similarities and Differences

In this section we point out the similarities and the differences that one meets when calculating the scattering pattern from particles in the vicinity of a plane surface. We start by remarking that the expression of the scattering amplitude is given by (6.10) and holds true for both perfectly reflecting and dielectric surface. This is a formal result, however. In fact, the transition matrix to be used does depend on the dielectric properties of the surface. We already remarked that, when the surface is perfectly reflecting, the transition matrix is that of the effective scatterer that is a $2N$-spheres cluster when the actual scatterer is a N-spheres cluster. Nevertheless, once the transition matrix has been calculated, it would be possible to perform any kind of averages over orientations of the effective scatterer.

The transition matrix of a particle in the presence of a dielectric surface never coincides with that of the effective scatterer neither when we chose for the Fresnel coefficients the limiting value $F_\eta = (-)^{\eta-1}$ so that the surface becomes perfectly reflecting. Nevertheless, in this limiting case there is coincidence of the scattering amplitude $f_{\eta\eta'}$ and of the intensity of the scattered field as well as of the average of the intensity around an axis orthogonal to the surface. This can be explained by remarking that, for a perfectly reflecting surface, the transition matrix of the effective scatterer yields a description of the scattered field that holds true (in the far zone) in the whole space. On the contrary, for a dielectric surface the description yielded by the transition matrix is meaningful in the accessible half-space only.

Another related problem regards the validity of the optical theorem when a surface is present. Equation (4.23) has been obtained on the assumption that the scattering particles are in free space and that $\hat{\boldsymbol{k}}_\mathrm{S} = \hat{\boldsymbol{k}}_\mathrm{I}$. Then, considering an incident field which is polarized along $\hat{\boldsymbol{u}}_{\mathrm{I}\eta}$, we have

$$\sigma_{\mathrm{T}\eta} = \frac{4\pi}{k}\mathrm{Im}\big[f_{\eta\eta}(\hat{\boldsymbol{k}}_\mathrm{S} = \hat{\boldsymbol{k}}_\mathrm{I}, \hat{\boldsymbol{k}}_\mathrm{I})\big] \ .$$

When a perfectly reflecting surface is present, however, the forward-scattering direction coincides with the direction of reflection. In fact, an optical instrument aimed at the particle along $-\hat{\boldsymbol{k}}_\mathrm{R}$ detects, besides the scattered field, also the reflected wave

$$\boldsymbol{E}_{\mathrm{R}\eta} = E_0(-)^{\eta-1}\hat{\boldsymbol{u}}_{\mathrm{R}\eta}\exp(\mathrm{i}\boldsymbol{k}_{\mathrm{R}}\cdot\boldsymbol{r}) \ .$$

Therefore, by applying to $\boldsymbol{E}_{\mathrm{R}\eta}$ the same reasoning that in Sect. 2.3.1 started from the incident field (2.11), we can write the optical theorem in the modified form

$$\sigma_{\mathrm{T}\eta} = \frac{4\pi}{k}\mathrm{Im}\big[(-)^{\eta-1}f_{\eta\eta}(\hat{\boldsymbol{k}}_{\mathrm{S}} = \hat{\boldsymbol{k}}_{\mathrm{R}}, \hat{\boldsymbol{k}}_{\mathrm{I}})\big] \ . \qquad (6.53)$$

6.7 Total Internal Reflection and Evanescent Waves

The total internal reflection and the associated occurrence of evanescent waves is a well known feature of a dielectric half-space. The ability of the evanescent waves to excite scattering modes of small particles located in the accessible half-space in the vicinity of the interface is, in fact, the basis of the so-called *internal reflection spectroscopy* [116]. In particular this technique has been applied to biological spores in order to discriminate between their scattering response and their luminescence [117]. The evanescent waves are also the basis of the *near field microscopy* that permits to overcome the diffraction limit of the customary optical spectroscopy [118–120].

In this section we describe how evanescent waves can be generated by total internal reflection and study their interaction with a particle in the accessible half-space, where the resulting scattered wave is actually observed. To this end it is convenient to define the geometry of the problem according to Fig. 6.6. We assume that the plane wave

$$\boldsymbol{E}_{\mathrm{I}\eta} = E_0\hat{\boldsymbol{u}}_{\mathrm{I}\eta}\exp(\mathrm{i}\boldsymbol{k}_{\mathrm{I}}\cdot\boldsymbol{r})$$

polarized along $\hat{\boldsymbol{u}}_{\mathrm{I}\eta}$ with $\boldsymbol{k}_{\mathrm{I}} = n''k_{\mathrm{v}}\hat{\boldsymbol{k}}_{\mathrm{I}}$ propagates in the the half-space $z > 0$ which is filled by a homogeneous medium with real refractive index n'' and

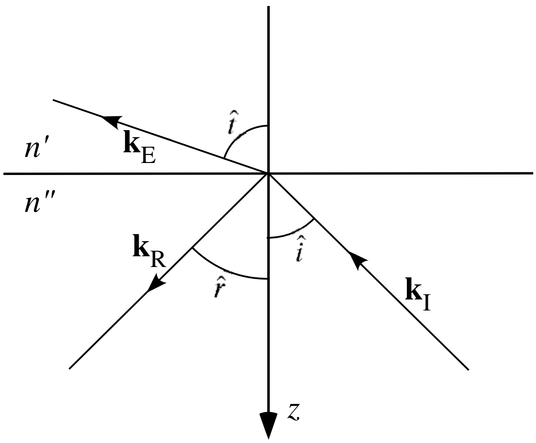

Fig. 6.6. Geometry for the description of evanescent waves

is reflected by the interface into the plane wave

$$\boldsymbol{E}_{\mathrm{R}\eta} = E_0''\hat{\boldsymbol{u}}_{\mathrm{R}\eta}\exp(\mathrm{i}\boldsymbol{k}_{\mathrm{R}}\cdot\boldsymbol{r})$$

with $\boldsymbol{k}_{\mathrm{R}} = n''k_{\mathrm{v}}\hat{\boldsymbol{k}}_{\mathrm{R}}$. In the preceding equations the subscript η indicates whether the polarization is parallel ($\eta = 1$) or perpendicular ($\eta = 2$) to the plane of incidence. As shown in Sect. 6.1, the polarized amplitudes of the fields are related through the appropriate reflection Fresnel coefficients, which are still given by (6.2), with the mutual exchange of n' and n'', however.

The refracted wave

$$\boldsymbol{E}_{\mathrm{E}\eta} = E_0'\hat{\boldsymbol{u}}_{\mathrm{E}\eta}\exp(\mathrm{i}\boldsymbol{k}_{\mathrm{E}}\cdot\boldsymbol{r}) \tag{6.54}$$

with $\boldsymbol{k}_{\mathrm{E}} = n'k_{\mathrm{v}}\hat{\boldsymbol{k}}_{\mathrm{E}}$ propagates in the half-space $z < 0$, which is filled by a different nonabsorptive homogeneous medium of refractive index n'; hereafter the refracted wave will be often referred to as the *transmitted wave*. The polarized amplitudes of the transmitted wave are determined by the Fresnel coefficients T_η that, using the notation that is customarily used in optics, are

$$T_1 = \frac{2n'n''\cos\hat{\imath}}{n'^2\cos\hat{\imath} + n''\sqrt{n'^2 - n''^2\sin^2\hat{\imath}}}\,, \tag{6.55a}$$

$$T_2 = \frac{2n''\cos\hat{\imath}}{n''\cos\hat{\imath} + \sqrt{n'^2 - n''^2\sin^2\hat{\imath}}}\,, \tag{6.55b}$$

where

$$\sqrt{n'^2 - n''^2\sin^2\hat{\imath}} = n'\cos\hat{t}\,. \tag{6.56}$$

According to Snell's law of refraction, when $n'' > n'$, we have $\hat{t} > \hat{\imath}$, so that $\hat{t} = \pi/2$ for $\hat{\imath} = \hat{\imath}_{\mathrm{c}}$ given by

$$\sin\hat{\imath}_{\mathrm{c}} = n'/n''\,.$$

Then, for $\hat{\imath} > \hat{\imath}_{\mathrm{c}}$ we have $\sin\hat{t} > 1$ and

$$\cos\hat{t} = \mathrm{i}\sqrt{\left(\frac{\sin\hat{\imath}}{\sin\hat{\imath}_{\mathrm{c}}}\right)^2 - 1}\,,$$

i.e. the incident wave is totally reflected at the interface. Nevertheless, the field in the half-space $z < 0$ does not vanish, but is a plane wave whose amplitude is damped along the negative z axis, and is therefore termed *evanescent wave*. To show this, let us establish on the interface a pair of orthogonal axes, say x and y, that form a right-handed triplet with z, and let the plane of incidence be the plane through the z axis that form an angle φ with the x axis. Then the polar angles of $\hat{\boldsymbol{k}}_{\mathrm{I}}$, $\hat{\boldsymbol{k}}_{\mathrm{R}}$, and $\hat{\boldsymbol{k}}_{\mathrm{E}}$ turn out to be

$$\vartheta_{\mathrm{I}} = \pi - \hat{\imath}, \quad \varphi_{\mathrm{I}} = \varphi,$$
$$\vartheta_{\mathrm{R}} = \hat{r}, \quad \varphi_{\mathrm{R}} = \varphi,$$
$$\vartheta_{\mathrm{E}} = \pi - \hat{t}, \quad \varphi_{\mathrm{E}} = \varphi \,.$$

Accordingly we can write the transmitted wave (6.54) in the form

$$\begin{aligned}\boldsymbol{E}_{\mathrm{E}\eta} =& E_0' \hat{\boldsymbol{u}}_{\mathrm{E}\eta} \exp\left\{\mathrm{i}k'[\sin\hat{t}(x\cos\varphi + y\sin\varphi) - z\cos\hat{t}]\right\} \\ =& T_\eta E_0 \hat{\boldsymbol{u}}_{\mathrm{E}\eta} \exp\left[\mathrm{i}k'(\sin\hat{\imath}/\sin\hat{\imath}_{\mathrm{c}})(x\cos\varphi + y\sin\varphi)\right] \\ & \times \exp\left\{k'[(\sin\hat{\imath}/\sin\hat{\imath}_{\mathrm{c}})^2 - 1]^{1/2} z\right\} ,\end{aligned} \tag{6.57}$$

where

$$k' = |\boldsymbol{k}_{\mathrm{E}}| = \sqrt{\boldsymbol{k}_{\mathrm{E}} \cdot \boldsymbol{k}_{\mathrm{E}}} \,.$$

Equation (6.57) shows that the field in the half-space $z < 0$ is an inhomogeneous plane wave with the planes of equal phase orthogonal to $\mathrm{Re}(\boldsymbol{k}_{\mathrm{E}})$ and the planes of equal amplitude perpendicular to $\mathrm{Im}(\boldsymbol{k}_{\mathrm{E}})$.

6.7.1 Scattering of Evanescent Waves by Single and Aggregated Spheres

In order to study the interaction of the evanescent waves either with a single sphere or with an aggregate of spheres, it is convenient to assume the same geometries that are depicted in Fig. 6.4 and 6.5, respectively. The field that is present in the region external to the particle can be written as

$$\boldsymbol{E}_{\mathrm{ext}} = \boldsymbol{E}_{\mathrm{E}} + \boldsymbol{E}_{\mathrm{S}} + \boldsymbol{E}_{\mathrm{SR}} \ ,$$

i.e. it is the superposition of the evanescent wave, the wave scattered by the particle, and the wave that after scattering by the particle is reflected on the interface. Since the scattered wave is only partially reflected by the interface, in the half-space $z > 0$ there is also the field $\boldsymbol{E}_{\mathrm{ST}}$ that after scattering by the particle is transmitted across the interface. The latter field has no influence on our further considerations and is mentioned for the sake of completeness. Unlike the cases we dealt with earlier in this chapter there is no incident and reflected wave in the accessible half-space: the primary field that excites the scattering modes of the particle is indeed that of the evanescent wave.

Let us expand all the fields in the accessible half-space into a series of spherical vector multipole fields. The multipole expansion of an evanescent wave presents no difficulty provided the techniques introduced in Sects. 4.1.2 and 6.3.2 are used. Thus, with respect to the origin at O, the evanescent wave has the expansion

$$\boldsymbol{E}_{\mathrm{E}\eta} = T_\eta E_0 \sum_{plm} \boldsymbol{J}_{lm}^{(p)}(\boldsymbol{r}, k') W_{\mathrm{E}\eta lm}^{(p)} \ , \tag{6.58}$$

where, according to (4.12),

$$W^{(p)}_{\mathrm{E}\eta lm} = W^{(p)}_{lm}(\hat{\boldsymbol{u}}_{\mathrm{E}\eta}, \hat{\boldsymbol{k}}_{\mathrm{E}}) = 4\pi \mathrm{i}^{p+l-1}(-)^{m+1}\hat{\boldsymbol{u}}_{\mathrm{E}\eta} \cdot \boldsymbol{Z}^{(p)}_{l,-m}(\hat{\boldsymbol{k}}_{\mathrm{E}}).$$

We notice that the preceding equation does not imply complex conjugation. In fact, we already stressed in Sect. 4.1.2 that complex conjugation, although required by (4.4), is inappropriate when the wavevector $\hat{\boldsymbol{k}}_{\mathrm{E}}$ is complex. Liu et al. [121], just for this reason, criticized the work of Chew et al. [122]. Of course, when $\hat{\imath} < \hat{\imath}_{\mathrm{c}}$, the exciting wave (6.58) is a refracted wave, and, as usual, $W^{(p)}_{\mathrm{E}\eta lm}$ can also be calculated through (4.4).

The next step requires redefining $\mathcal{W}^{(p)}_{\eta lm}$ and $\mathcal{W}^{(p)}_{\eta\alpha lm}$ to be introduced in (6.32) and (6.50), respectively. Since a change of origin of multipole fields is in order, e.g. we have for spherical scatterers in the E-scheme,

$$\mathcal{W}^{(p)}_{\eta lm} = T_\eta \exp(\mathrm{i}\boldsymbol{k}_{\mathrm{E}} \cdot \boldsymbol{R}')W^{(p)}_{\mathrm{E}\eta lm} \,,$$

where $\boldsymbol{R}'$ is defined in Fig. 6.4. At this point one can proceed as in Sects. 6.4 and 6.5.

Pursuing a simplified approach, there is a tradition of sort of crudely disregarding the effect of the interface that generates the evanescent waves onto the scattering, i.e. of disregarding $\boldsymbol{E}_{\mathrm{SR}}$. This amounts to substitute the presently considered $T_\eta W^{(p)}_{\mathrm{E}\eta lm}$ in place of $W^{(p)}_{\mathrm{I}\eta lm}$ considered in Chap. 5, and to proceed thereafter as expounded in that chapter.

As the last item, let us stress that, since the evanescent wave has amplitude and intensity varying with z, the normalization that enters the definitions of scattering quantities cannot be made to a constant intensity, but to a mean intensity over the surface of the particle or to the intensity at a chosen point [118].

7 Applications: Aggregated Spheres, Layered Spheres, and Spheres Containing Inclusions

The theory developed so far is suitable to investigate the optical properties both of single particles and of dispersions of particles that are of interest in several fields of physics. With the proviso that careful tests are necessary to verify the adequacy of the model in the sense explained in Sect. 1.1, aggregates of spheres may be suitable to model the nonspherical particles of atmospheric aerosols and the ice crystals that occur in the high atmosphere, as well as the cosmic dust grains that are of interest in astrophysics. In turn, spheres containing one or more spherical inclusions may be used to approximate the scattering properties of biological cells or of water droplets containing pollutants, but also to approximate the properties of the porous and fluffy particles that occur in the cosmic dust. Therefore we felt it convenient to devote the present and the next chapter to discussing applications of the theory developed so far with the purpose of highlighting the scattering features of the model particles, either in free space or in the presence of a plane surface. While the applications we present in this chapter can be easily specialized to atmospheric physics or to astrophysics, Chaps. 9 and 10 are specifically addressed to the study of the atmospheric ice crystals and of the cosmic dust, respectively.

Modeling actual particles as clusters of spherical scatterers or as spheres containing inclusions is made possible by the flexibility of the theory that does not imply any limitation of principle on the radii, refractive indices, and geometrical arrangement of the component spheres. This kind of modeling gives only an approximation to the actual shape of the particles, however, but the applications that we are going to describe support our opinion that in several cases the optical response of particles depends more on their general symmetry and on the quantity of refractive material than on the details of their shape.

Taking into account that the scatterers we will deal with either are spherical or are aggregates of spherical scatterers, it is convenient to consider the quantities

$$P'_\eta = \frac{4\pi}{kS}\,\mathrm{Re}\big[f_{\eta\eta}(\hat{\boldsymbol{k}}_\mathrm{S},\hat{\boldsymbol{k}}_\mathrm{I})\big]\,, \quad Q'_\eta = \frac{4\pi}{kS}\,\mathrm{Im}\big[f_{\eta\eta}(\hat{\boldsymbol{k}}_\mathrm{S},\hat{\boldsymbol{k}}_\mathrm{I})\big]\,, \tag{7.1}$$

where S is either the geometrical cross section of the spherical scatterer or the sum of the geometrical cross sections of the spheres that form the aggregate.

According to (2.10), $Q' = Q_{\mathrm{T}}$, i.e., Q' coincides with the extinction efficiency, when $\hat{\boldsymbol{k}}_{\mathrm{S}} = \hat{\boldsymbol{k}}_{\mathrm{I}}$ and $S = G$. Of course, the latter condition is automatically fulfilled for a scatterer with a spherical shape.

7.1 General Features of Scattering from Aggregated Spheres

We start by applying the theory in Chaps. 4 and 5 to a few simple clusters whose morphology is chosen so as to highlight the main features of scattering from these nonspherical model particles. All the results discussed in this section were obtained by assuming that the incident light is circularly polarized with $\eta = 1$. Almost all of them, however, are independent of η, either because of the orientation of clusters or because of the averaging over orientations. Anyway, index η is omitted throughout. Since a complex refractive index is not essential for our purpose, we assume that the component spheres have a real (nonabsorptive) index of refraction. As a consequence, according to Sect. 2.2, $\sigma_{\mathrm{S}} = \sigma_{\mathrm{T}}$. As a matter of fact, (5.28) and (5.29), which give the multipole amplitudes of the scattered field, show that the difference between an assembly of independent spheres and a true aggregate of spheres stems from the matrix elements $\mathcal{H}^{(pp')}_{\alpha lm\alpha' l' m'}$ that describe the multiple scattering processes among the components of the aggregate. This suggests that the effects due to clustering are well described by the quantity $\Gamma = \sigma_{\mathrm{S}}/\sigma_0$, where σ_{S} is the scattering cross section of the cluster and σ_0 is the sum of the scattering cross sections of the constituent spheres considered as independent scatterers. σ_0 is calculated through the Mie theory. As σ_{S} depends on the orientation of the cluster with respect to the incident field, whereas σ_0 does not, Γ gives full information on the effects due to the lack of sphericity and was, therefore preferred to the scattering efficiency Q_{S} (2.10).

As a first example [123], we consider a cluster composed of two identical spheres of radius ρ and (frequency-independent) refractive index $n_0 = 1.3$. The surrounding medium is assumed to be the vacuum ($n = 1$). The scattering features of the constituent spheres are known to depend on the size parameter $x = k\rho$, but, in view of the multiple scattering processes that occur between them, it is to be expected that the features of the cluster as a whole depend on the parameter kd, where d is the distance between the centers of the spheres. Accordingly, in Fig. 7.1 we report Γ as a function of ϑ_{I}, the angle between the incident wavevector and the axis of the cluster, for several values of kd. The incident wave is left-circularly polarized and the size parameter of the spheres is held fixed at $x = 0.1$. Since this choice of the size parameter coincides with that of Levine and Olaofe [124], who gave an analytic solution for the dependent scattering from two small spheres, the results that we are going to discuss are directly comparable with theirs. Actually, spheres with so small a size parameter can be dealt with in the RSA (see Sects. 4.6.1 and

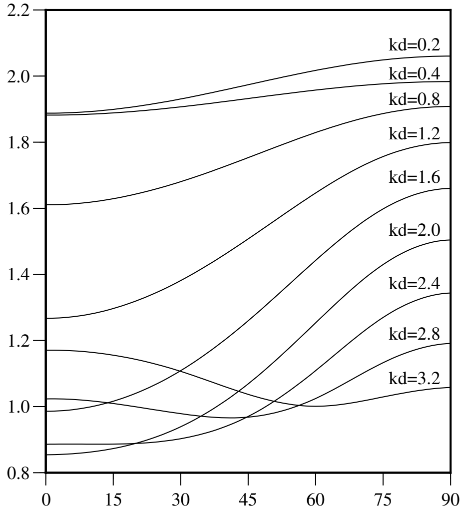

Fig. 7.1. Γ for the binary cluster as a function of $\vartheta_{\rm I}$ for several values of kd

5.1), and, because $kd = 0.2$ when the spheres are in mutual contact, one could argue that the whole cluster also can be dealt with $l_{\rm M} = 1$. The results that we present in Fig. 7.1 show that it is not so. Actually, comparison of our results with those of Levine and Olaofe [124] shows that Γ decreases with increasing kd. Nevertheless, the rate of diminution of Γ is noticeably smaller than that predicted by Levine and Olaofe. Indeed, the approximation that they use amounts just to truncating the multipole expansions to $l = 1$, whereas we had to use (5.33) and (5.35), and up to $l_{\rm I} = 3$ (see Sect. 5.4.1), to get fully convergent results. We are thus led to conclude that the RSA cannot be extended to the cluster as a whole, even though it would certainly apply to each of the constituent spheres if they were not in the presence of one another. This conclusion is in substantial agreement with the considerations of Barber and Wang [125].

A further consideration that highlights the role of the multiple scattering processes stems from the remark that, for the highest values of kd reported in Fig. 7.1, the ratio Γ may be smaller that unity. This somewhat surprising result is a manifestation of the so-called shadow effect. In fact, for $\vartheta_{\rm I} = 0°$ the incidence is head-on, so that the incident beam *sees* one sphere only. The spheres are seen as two distinct objects when the angle of incidence increases to a sufficient value. Ultimately, one should bear in mind that the details of the geometry of a scattering particle become well distinguishable only for sufficiently small wavelength.

As a second example [123], we present Γ for a cluster of three identical spheres at the vertices of an equilateral triangle. This cluster, that will be referred to as "ozone" because its geometry recalls the stick-and-ball model of

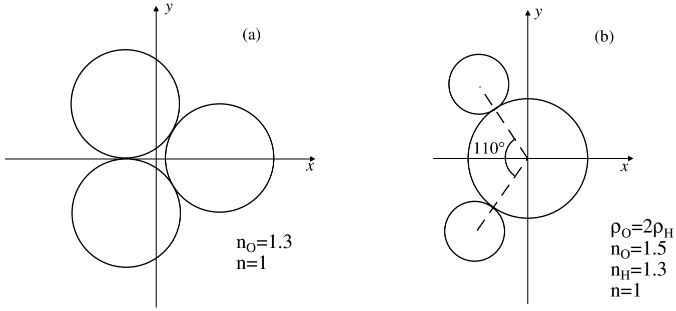

Fig. 7.2. Geometry for **(a)** "ozone" and **(b)** "water"

this molecule, is depicted in Fig. 7.2 (a). In this case the component spheres are held in mutual contact and the calculations are performed for several directions of incidence as a function of $x = k\rho$. Therefore, we had to use $l_M = 5$ to achieve full convergence. The results are presented in Fig. 7.3. We first notice that for all values of x there is an evident dependence of Γ on ϑ_I that becomes more striking with increasing value of x, whereas we found that the dependence on φ_I is rather weak because of the high symmetry around the z axis. For this reason, results are reported for $\varphi_I = 0°$ only. The most important feature of Fig. 7.3 is the intersection of all the curves at about the same value of x. The dotted line is the average of Γ for random distribution of the orientations and passes almost exactly through the crossing point. We will see below that this feature does not pertain to "ozone" only.

The third cluster that we consider has a geometry depicted in Fig. 7.2 (b)

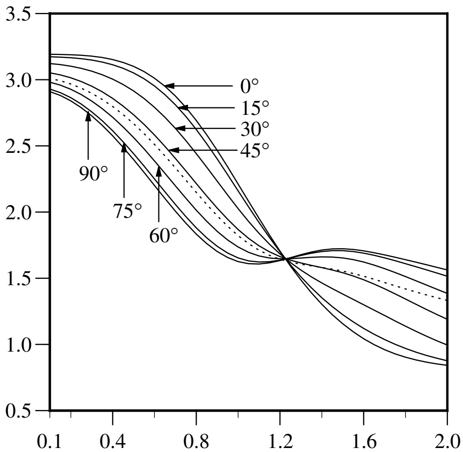

Fig. 7.3. Γ for "ozone" as a function of x for several values of ϑ_I and $\varphi_I = 0°$. The *dotted curve* is the average for random distribution of the orientations

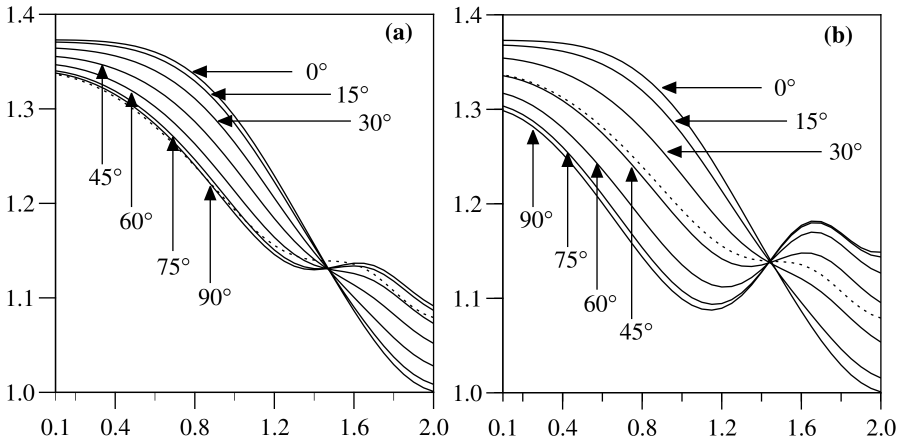

Fig. 7.4. Γ for "water" as a function of $x = k\rho_{\mathrm{O}}$ for several values of ϑ_{I}. In **(a)** $\varphi_{\mathrm{I}} = 0°$ and in **(b)** $\varphi_{\mathrm{I}} = 90°$. The *dotted curve* is the average for random distribution of the orientations

and will be referred to as "water" [45, 123]. Full convergence required us to use $l_{\mathrm{M}} = 5$. The curves of Γ as a function of $x = k\rho_{\mathrm{O}}$ for several values of ϑ_{I} are reported in Fig. 7.4 (a) for $\varphi_{\mathrm{I}} = 0°$ and in Fig. 7.4 (b) for $\varphi_{\mathrm{I}} = 90°$. The curves in Fig. 7.4 (b), with the obvious exceptions of the dotted curve and of the 0°-curve, depend on η. Such a dependence is very slight, however, so that we felt unnecessary to report also the results for $\eta = 2$. Beyond the evident dependence of Γ on φ_{I}, we see again that all the curves intersect at about the same value of $x \approx 1.45$. The dotted curve, that also passes through, or almost through, the crossing point is the average of Γ for a randomly-oriented dispersion of the clusters. This result, together with analogous result in Fig. 7.3, suggests that there exist wavelengths at which nonspherical particles behave as if they were spherical and explains the success of the Mie theory in some cases in which the scattering particles are nonspherical. Of course, actual extinction spectra may be complicated by the possible frequency dependence of the refractive index.

7.1.1 Comparison with Experimental Data

Before we discuss further applications, it is convenient to assess the reliability of our results by comparison with experimental data. In recent times this task has been successfully performed by Mishchenko and Mackowski [126] in the optical range in spite of the experimental difficulties connected with an accurate determination of the geometrical and physical parameters of the scatterers [127]. We prefer, instead, to compare our results with the experimental data of Wang and Schuerman who performed a large set of experiments aimed at the measurement of the forward-scattering amplitude of *macroscopic* clusters of up to 8 spherical scatterers in the microwave range [87]. The specific purpose of the authors was the assessment of the contribution of the multiple scattering processes that occur among the component spheres to the scattering amplitude of the clusters as a whole [86]. The interested reader may find in the original technical report all the experimental details on the determination of the refractive index of the spheres and of their exact diameter. These are, indeed, critical input factors for any calculation meant to compare experiments with theoretical predictions. Note that the principle of electromagnetic scaling [68] that we already mentioned in Sects. 5.1 and 5.4 makes the results in the microwave range applicable to small clusters of spheres of the kind that are often found in atmospheric or industrial aerosols. This fact was borne in mind by the authors of the measurements. They point out that the refractive indexes of the clusters considered are near to $n_0 = 1.365$ that is appropriate for water and ice crystals in the optical range. Moreover, all their results are reported in terms of the adimensional parameters x_α and $x_{\alpha\beta}$ that we defined in Sect. 5.4.

In order to prove the reliability of our predictions, we compare the results of our calculations [85] with the experimental measurements for clusters of two identical spheres that Wang, Greenberg, and Schuerman report in their paper [86]. More precisely, we report ${P'}_\eta$ vs. ${Q'}_\eta$ for $\hat{\boldsymbol{k}}_\mathrm{S} = \hat{\boldsymbol{k}}_\mathrm{I}$ as a function of ϑ_I, the angle between the incident wavevector and the axis of the aggregate. The plane of scattering is defined by $\boldsymbol{k}_\mathrm{I}$ and the axis of the aggregate and ${P'}_\eta$ and ${Q'}_\eta$ were calculated both for parallel and perpendicular polarization. In this respect we remark that Wang, Greenberg, and Schuerman do not report data for parallel polarization because of some technical problems that are fully explained in the original technical report [87]. We notice that the quantities ${P'}_\eta$ and ${Q'}_\eta$ were expressed in the original report in terms of the quantity $S_1(0)$ defined by van de Hulst, and the incident plane wave was assumed to depend on time through the factor $\exp(\mathrm{i}\omega t)$. This implies the mutual exchange of the real and imaginary parts of the scattering amplitude and a redefinition of the normalization factors. The sign of the imaginary part of the refractive index must also be changed [21,88]. Anyway, the vector drawn from the origin of the axes to any point on the curves gives the forward-scattering amplitude of the cluster. The length of the vector is the magnitude of the scattering amplitude whereas the angle that the vector forms with the Q'-axis gives the phase. In all the cases that we consider below the estimated experimental error, according to Wang and Schuerman, is 12° in phase and 10% in magnitude.

In Fig. 7.5 we compare our predictions for two binary clusters whose component spheres are mutually contacting. Figure 7.5 (a) refers to clusters of acrylic with complex refractive index. The clusters in Fig. 7.5 (b) are composed of expanded polystyrene and have a real refractive index. In both cases, full convergence required $l_\mathrm{M} = 12$. Note that although in both figures our curves were calculated anew for each direction of incidence, their behavior turns out to be consistent with the transformation properties of the transi-

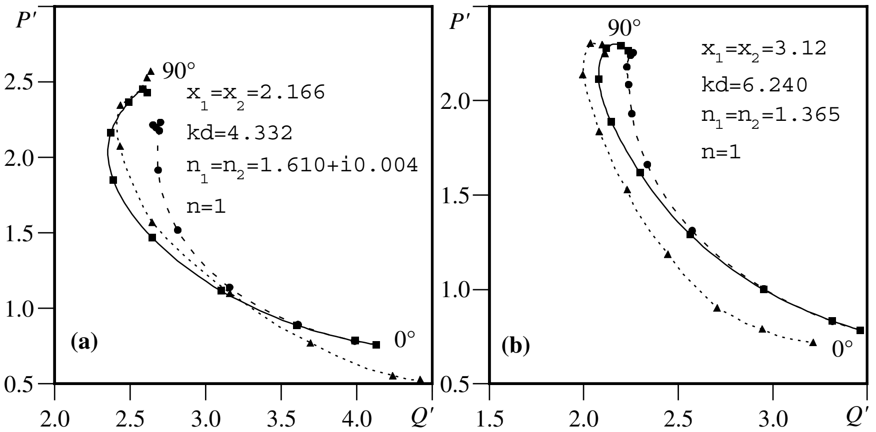

Fig. 7.5. Comparison of the calculated and experimental dependence on ϑ_{I} of the forward-scattering amplitude of a binary cluster of acrylic **(a)** and of expanded polystyrene **(b)**. The *dotted curve* shows the experimental results for polarization orthogonal to the plane of scattering. The *solid curve* is the corresponding result of our calculations. We also report for the sake of completeness our results for parallel polarization. The *symbols* on all the curves mark the value of ϑ_{I} at $10°$ intervals. For the component spheres $Q' = 2.7031,\ P' = 2.4154$ in (a) and $Q' = 2.2777,\ P' = 2.2956$ in (b)

tion matrix. The dots both on the theoretical and on the experimental curves mark the value of ϑ_{I} at $10°$ intervals. For completeness, we also report the curves for parallel polarization that, as expected, do not differ much from those for perpendicular polarization. In particular the calculated curves for parallel and perpendicular polarization stick together for $\vartheta_{\mathrm{I}} = 0°$, as they must for head-on incidence. The general agreement of the theoretical and experimental curves appears to be rather good, the differences being well within the experimental error.

A further comparison is effected in Fig. 7.6 with the measurements for head-on incidence on a binary cluster whose component spheres were allowed to increase their separation. In this respect, we recall that the rate of convergence depends on kd, i.e., on the overall size of the aggregate. According to Sect. 5.4.1, to get well convergent results at the highest values of kd, calculations would require a large l_{E}. However, performing the calculation by using the T-scheme would require an undue effort. Since this kind of calculation does not imply orientational averages, we had the opportunity to perform the calculations with the minimum effort by using the E-scheme and comparatively small values for l_{I}. In fact, l_{I} decreases from 13 for contacting spheres to 7 for well-separated spheres.

Actually, our curves show, in even greater detail, the wiggles that were observed in the experiment when the component spheres are well separated. In Fig. 7.6 the value of the scattering amplitude for infinite separation is marked

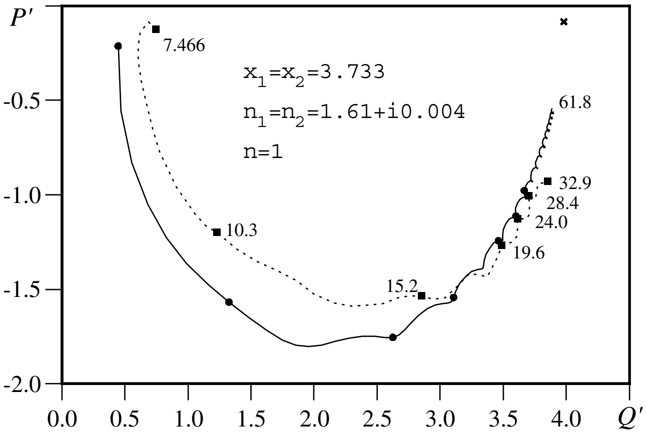

Fig. 7.6. Comparison of calculated and experimental dependence of the forward-scattering amplitude of a binary cluster of acrylic for head-on incidence on the mutual separation of the component spheres. The *dotted curve* reports the experimental data, whereas our predictions are reported by the *solid curve*. The *symbols* on all the curves report the value of kd. The *cross* at $Q' = 3.9807,\ P' = -8.4684 \cdot 10^{-2}$ gives the forward-scattering amplitude of the cluster for infinite separation of the component spheres

by a small cross. Of course, neither the experiment nor our calculations could be stretched to this limit, but we were able to extend our calculations to a larger value of kd than allowed by the experimental setup. On account of the experimental error, the comparison effected in Fig. 7.6 shows that even in this case the reliability of the theory and of our codes is rather good.

7.1.2 Effect of the Structural Changes

The results in Figs. 7.1, 7.3, and 7.4 show that the extinction cross section of a cluster has a noticeable dependence on the geometry. It is therefore to be expected that if the clusters of a dispersion are allowed to recombine to form clusters of different geometry, the process should produce detectable effects on the extinction. Of course, studying these effects is not of academic interest only because such recombination with consequent changes of morphology are known to occur among the aerosol particles.

Let us recall that the refractive index of a tenuous dispersion of particles is given by (2.31) and that, when more than one kind of particle is present, the refractive index of the whole dispersion is the linear combination of the indexes of the partial dispersions [128]. In particular, the absorption coefficient for a dispersion of N particles, turns out to be

$$\gamma_\eta = 2k\,\mathrm{Im}\big[\mathcal{N}_{\eta\eta}\big] = N\frac{4\pi}{k}\sum_s c_s\,\mathrm{Im}\left[\langle f_{s,\eta\eta}(0)\rangle\right] ,$$

where Nc_s is the number density of the particles of the sth species and the average of the forward-scattering amplitude is given by the formulas in Sect. 4.5. The extent to which the optical properties of a dispersion of clusters is influenced by the rearrangement will be studied by comparing γ_η before and after the rearrangement has taken place. To this end, let

$$\gamma_\eta^{(i)} = \sum_s c_s \gamma_{s,\eta}$$

be the initial absorption coefficient and

$$\gamma_\eta^{(f)} = \sum_{s'} c_{s'} \gamma_{s',\eta}$$

the absorption coefficient after the rearrangement, where s' denotes the species of the particles after the rearrangement. Note that the particles may be quite different both in structure and in concentration. From the preceding equations, one easily sees that a useful quantity for the detection of the changes is

$$\Gamma_\eta = \frac{p\gamma_\eta^{(f)} + (1-p)\gamma_\eta^{(i)}}{\gamma_\eta^{(i)}} ,$$

where $0 \leq p \leq 1$ is the completion index of the process. The effect of the clustering for the single species is given by

$$g_{s,\eta} = \gamma_{s,\eta}/\gamma_{0s} ,$$

where γ_{0s} is the sum of the extinction cross sections, calculated by the Mie theory, of the spheres that form the cluster of the sth species.

The remainder of this section is devoted to the discussion of the results that we obtained for a few processes that are listed in Table 7.1. In our calculations we assumed circular polarization of the incident wave with $\eta = 1$ and random distribution of the orientations for all the clusters. The surrounding medium is assumed to be the vacuum ($n = 1$). Note that, since the clusters recall the popular stick-and-ball model of molecules, we indicated for each process the actual chemical reaction by which both the clusters and their rearrangements were inspired. The reader is warned, however, that the spheres and the clusters we deal with are macroscopic objects and in no case they should be understood as actual atoms and molecules. The clusters are individuated by their "chemical formulas" in terms of the "elements" A, B, and C and their structures are built so as to match those of the actual chemical compounds listed under the heading Example in Table 7.1. The processes are partitioned into three groups: the group 1–4 implies the spheres A and B only; the group 5 and 6 also implies the spheres C; the group 7–10 includes processes that from the same "reagents" produce different structures.

In Table 7.2 we list the clusters as well as the processes in which they are involved according to Table 7.1. We also report the coordinates of the centers

Table 7.1. List of the processes. The refractive indexes and the radii of the elemental spheres A, B, and C are $n_A = 1.30$, $n_B = 1.50$, $n_C = 1.40$, and $\rho_A = 1.0\,u_l$, $\rho_B = 0.50\,u_l$, $\rho_C = 0.75\,u_l$, where u_l is an arbitrary unit of length

Process	Example
1 $3B_2 \to 2B_3$	$3O_2 \to 2O_3$
2 $2AB + B_2 \to 2AB_2$	$2CO + O_2 \to 2CO_2$
3 $2AB_2 + B_2 \to 2AB_3$	$2SO_2 + O_2 \to 2SO_3$
4 $A_2 + 3B_2 \to 2AB_3$	$N_2 + 3H_2 \to 2NH_3$
5 $AC + 3B_2 \to AB_4 + B_2C$	$CO + 3H_2 \to CH_4 + H_2O$
6 $2AB_3 + C_2 \to 2ACB_3$	$2PH_3 + O_2 \to 2POH_3$
7 $C_2 + AB_4 \to AB_3C + BC$	$Cl_2 + CH_4 \to CH_3Cl + HCl$
8 $2C_2 + AB_4 \to AB_2C_2 + 2BC$	$2Cl_2 + CH_4 \to CH_2Cl_2 + 2HCl$
9 $3C_2 + AB_4 \to ABC_3 + 3BC$	$3Cl_2 + CH_4 \to CHCl_3 + 3HCl$
10 $4C_2 + AB_4 \to AC_4 + 4BC$	$4Cl_2 + CH_4 \to CCl_4 + 4HCl$

of the spheres in each cluster. In this respect, we stress that neighboring spheres are always in mutual contact. The quantities Γ and g_s were calculated for k in the range from $0.002\,u_l^{-1}$ to $2.0\,u_l^{-1}$ but in the following figures k goes from $0.02\,u_l^{-1}$ to $2.0\,u_l^{-1}$ because in this range the results show the most striking k-dependence. We had to use at most $l_M = 10$ to get full convergence.

In Figs. 7.7, 7.9, and 7.11 we report Γ for the processes listed in Table 7.1. The values of g_s for the clusters concerned are reported in Figs. 7.8, 7.10, and 7.12. Note that, due to the different normalization, the corresponding curves of Γ and g_s are not directly comparable. Nevertheless the chosen normalization makes Γ independent of N and g_s independent of $N_s = Nc_s$. It should be borne in mind, however, that the results we are going to discuss hold true as long as we consider a tenuous dispersion. We start remarking that, from a general point of view, Figs. 7.8, 7.10, and 7.12 show that the multiple scattering processes that occur among the spheres in a cluster cannot be neglected without dramatically affecting the correctness of the results. Therefore it is an easy prediction that the rearrangement of the clusters should cause detectable changes in the absorption coefficient of the dispersion. This is actually shown by the curves in Figs. 7.7, 7.9, and 7.11, where Γ is significantly different from unity in the whole range of k concerned, although with increasing k the effect of the rearrangement becomes smaller and smaller.

Of course, the more the process changes the structure of the clusters the more Γ remains different from unity. A similar consideration also applies to the curves of g_s. Figures 7.8, 7.10, and 7.12, indeed, show that the curves differ from each other the more the structures of the clusters are different, so that similar structures have virtually the same behavior. This is confirmed, e.g., by the curves for CO_2 and SO_2 that are indistinguishable from each other. The

Table 7.2. Coordinates of the centers of the spheres constituting the clusters. The coordinates refer to each sphere in the same order in which they appear in the name of the cluster. The processes in which the clusters are involved are also listed

Cluster	Coordinates	Processes
B_2	(-0.5, 0, 0) (0.5, 0, 0)	1, 2, 3, 4, 5
A_2	(-1.0, 0, 0) (1.0, 0, 0)	4
C_2	(-0.75, 0, 0) (0.75, 0, 0)	6, 7, 8, 9, 10
AB	(-1.0, 0, 0) (0.5, 0, 0)	2
AC	(-1.0, 0, 0) (0.75, 0, 0)	5
BC	(-0.5, 0, 0) (0.75, 0, 0)	7, 8, 9, 10
B_3	(0, 0.577, 0) (0.5, -0.289, 0) (-0.5, -0.289, 0)	1
AB_2	(0, 0, 0) (-1.5, 0, 0) (1.5, 0, 0)	2
AB_2	(0, 0, 0) (1.229, -0.860, 0) (-1.229, -0.860, 0)	3
B_2C	(1.024, -0.717, 0) (-1.024, -0.717, 0) (0, 0, 0)	5
AB_3	(0, 0, 0) (0, 1.5, 0) (1.299, -0.75, 0) (-1.299, -0.75, 0)	3
AB_3	(0, 0, 1.384) (0.5, -0.289, 0) (-0.5, -0.288, 0) (0, 0.577, 0)	4, 6
AB_4	(0, 0, 0) (-0.866, -0.866, 0.866) (-0.866, 0.866, -0.866) (0.866, -0.866, -0.866) (0.866, 0.866, 0.866)	5, 7, 8, 9, 10
ACB_3	(0, 0, 1.384) (0, 0, 3.134) (0, 0.577, 0) (0.5, -0.289, 0) (-0.5, 0.289, 0)	6
AB_3C	(0, 0, 1.384) (0, 0.577, 0) (0.5, -0.289, 0) (-0.5, -0.289, 0) (0, 0, 3.134)	7
AB_2C_2	(0, -0.375, 1.452) (0, 0, 0) (0, -0.375, 2.952) (0.75, -1.0, 0) (-0.75, -1.0, 0)	8
ABC_3	(0, 0, 3.021) (0, 0, 1.521) (0, 0.866, 0) (0.75, -0.433, 0) (-0.75, -0.433, 0)	9
AC_4	(0, 0, 0) (-1.010, -1.010, 1.010) (-1.010, 1.010, -1.010) (1.010, -1.010, -1.010) (1.010, 1.010, 1.010)	10

spheres that compose the two clusters AB_2 are identical, and the differences of structure are too small to give appreciably different spectra, especially on account of the randomness of the orientations. We also notice the identity of the spectra of NH_3 in Fig. 7.8 and PH_3 in Fig. 7.10. According to Table 7.2, both clusters have AB_3 composition and the same pyramidal structure. The difference from the spectrum of SO_3 in Fig. 7.8 is easily explained on account that the latter cluster is also AB_3 but has a planar structure.

The considerations above led us to conclude that the change of structure of clusters, whatever their cause, have well detectable effectson the absorption

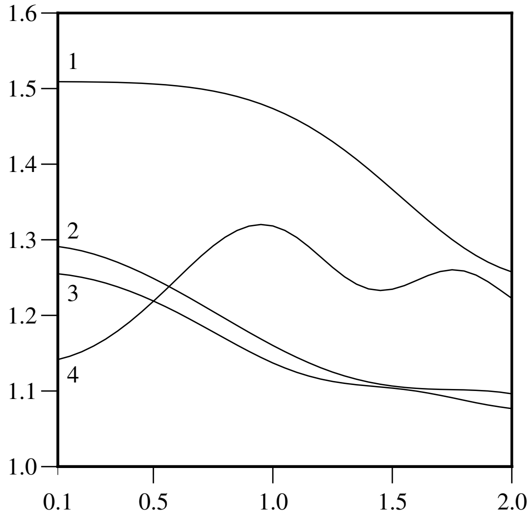

Fig. 7.7. Γ vs. k (in arbitrary units) for $p = 1$, for the first group of processes in Table 7.1

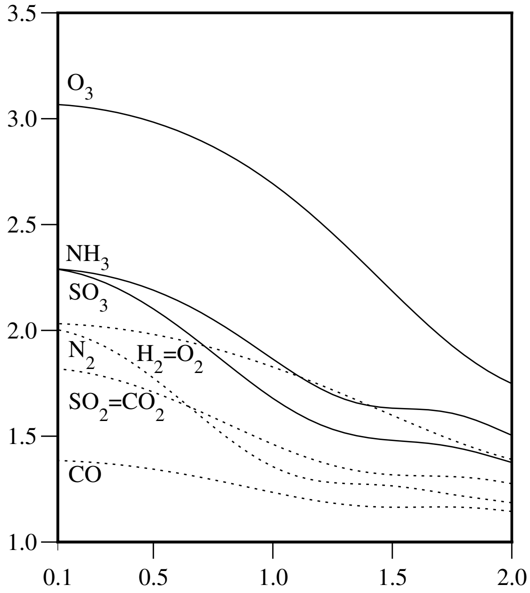

Fig. 7.8. g_s vs. k (in arbitrary units) for the first group of processes in Table 7.1. The *solid lines* refer to the "reaction products," whereas the *dotted lines* refer to the "reagents"

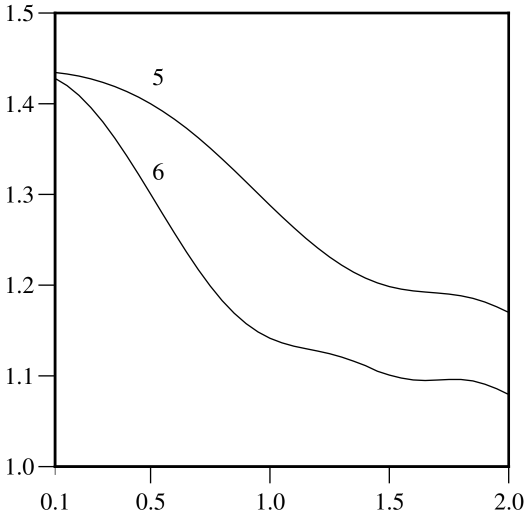

Fig. 7.9. Same as Fig. 7.7 but for the second group of processes in Table 7.1

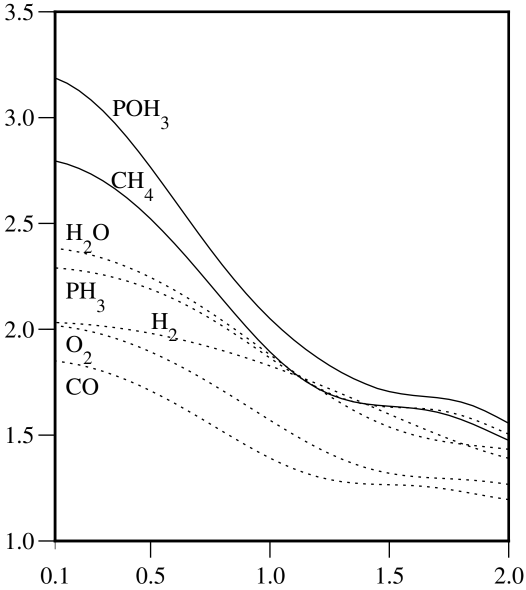

Fig. 7.10. Same as Fig. 7.8 but for the second group of processes in Table 7.1

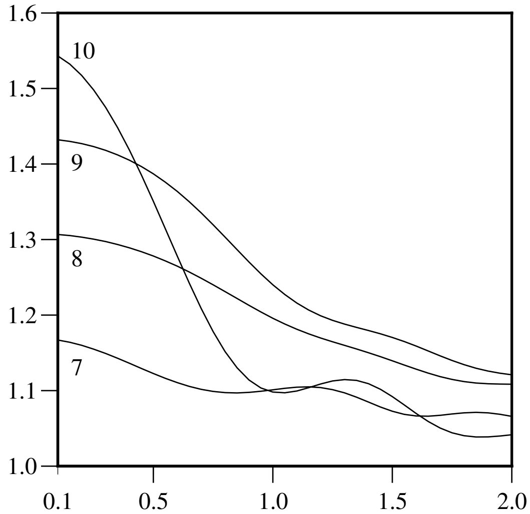

Fig. 7.11. Same as Fig. 7.7 but for the third group of processes in Table 7.1

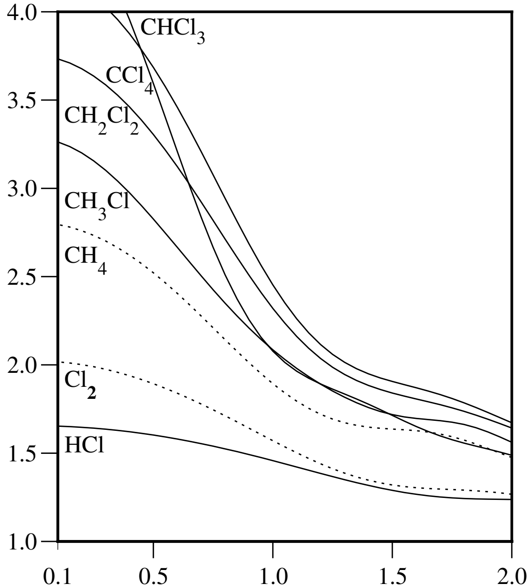

Fig. 7.12. Same as Fig. 7.8 but for the third group of processes in Table 7.1

coefficient of a dispersion even when the orientations of the particles are randomly distributed.

7.2 Clusters of Large Spheres

The convergence of the multipole expansions is the main problem in calculating the scattering properties of aggregated spheres. Dealing with large clusters requires an heavy computational effort that can be reduced to some extent by resorting to the E-scheme of Sect. 5.4.1. However, the E-scheme cannot be used to get the transition matrix so that it proves useful only when orientational averages of the scattering properties are not needed.

One has often to deal with the optical properties of clusters of large spheres that are relevant, e.g., for medical and meteorological applications. In these cases, the quest for fully convergent results prevents the real-time calculation that would possibly be required by the problem at hand. As a consequence, the characterization of the optical properties of the particles may be more useful than finding the *exact* solution to the problem of scattering, i.e., the solution with all the accuracy that is mathematically and computationally possible. In other words, in view of the unavoidable imprecision of the experimental measurements, it may be sufficient to require that the theoretical calculations are able to give the qualitative features of the scattering pattern. For this reason, this section is devoted to the assessment of the minimal *acceptable accuracy* in such kind of scattering calculations. This study is done with reference both to a cluster of 13 big spheres with a

Table 7.3. Coordinates of the centers of the component spheres in μm. The radius and refractive index of each sphere are 1.145 μm and 1.59, respectively

Sph. no.	x	y	z
1	0.00000	0.00000	0.00000
2	0.00000	1.92500	-1.18900
3	0.00000	-1.92500	-1.18900
4	0.00000	-1.92500	1.18900
5	0.00000	1.92500	1.18900
6	1.92500	-1.18900	0.00000
7	-1.92500	1.18900	0.00000
8	-1.92500	-1.18900	0.00000
9	1.92500	1.18900	0.00000
10	-1.18900	0.00000	1.92500
11	1.18900	0.00000	1.92500
12	1.18900	0.00000	-1.92500
13	-1.18900	0.00000	-1.92500

compact structure and to a linear chain of big spheres with the purpose to see the effect of the compactness of structure on the rate of convergence.

Since the calculation of the transition matrix is based on a series expansion, the most straightforward method to study the rate of convergence would be to start the calculation with a comparatively low value of l_{M} to be incresed as long as the scattering features of the particle do not change within numerical accuracy, i.e., the exact solution is achieved. Nevertheless, on account of the large matrices to be manipulated, the quest for the exact solution would require a big computational effort that may soon become unsustainable.

When we are searching for an acceptable solution, in the sense outlined above, the two-step calculation that we are going to describe proves a viable approach. In the first step, we reduce the geometrical dimensions of the scatterer leaving unchanged everything else; doing this, on one hand, reduces the difficulties connected with the computation and the time required to perform it, and, on the other hand, allows us to work out the conditions that ensure the stability of the results from a qualitative point of view. In other words, we want to determine the conditions under which the calculated scattering pattern qualitatively reproduce the exact one. In the second step, we consider the model scatterer with its full dimensions and we apply the already tested stability criteria so to get a scattering pattern whose validity, at least from a qualitative point of view, is reasonably ensured.

7.2.1 Compact Clusters

The cluster that we study in this section is the same 13-spheres clusters considered by Holler et al. [129] with the purpose of investigating, through a specific but significant case, how and to what extent the computational effort can be reduced still getting a reliable qualitative description of the scattering pattern. The cluster of interest is composed of 13 identical polystirene latex spheres, of radius $\rho_{\mathrm{s}} = 1.145$ µm and refractive index $n_{\mathrm{s}} = 1.59$ arranged in a closely packed structure with a roundish geometry. The coordinates of the centers of the spheres are listed in Table 7.3. Assuming that the surrounding medium is the vacuum ($n = 1$) and that the incident wavelength is $\lambda = 0.532\,\mu\mathrm{m}$, the size parameter of each sphere is $x_{\mathrm{s}} = nk_{\mathrm{v}}\rho_{\mathrm{s}} = 13.36$, and the overall size parameter of the whole aggregate results $x_{\mathrm{c}} = nk_{\mathrm{v}}\rho_{\mathrm{c}} \approx 40$, where ρ_{c} is the radius of the smallest mathematical sphere that contains the cluster. According to the considerations in Sect. 5.4.1, a conservative choice to get convergence of the scattered field to 3 decimal places would be $l_{\mathrm{M}} > 40$. In [129], the calculations were performed through the recursive algorithm by Chew [130] that shares in common with our approach the fact that the only approximation lies in the choice of the value of l_{M} at which the multipole expansions of the electromagnetic fields are stopped. Nevertheless, it appears that a generalized use of the perturbative-iterative approach of [129] would require some caution and artwork in its implementation. For instance, the actual achievement of convergence for a given choice of l_{M} should be carefully verified. On the contrary, the approach that we use, i.e., the E-scheme, appears to be straightforward and leaves to the researcher full control of the accuracy that can be achieved.

In the following discussion the incident plane wave is assumed to be linearly polarized along $\hat{\boldsymbol{\vartheta}}$ and the wavevector $\boldsymbol{k}_{\mathrm{I}}$ has $\vartheta_{\mathrm{I}} = 90°$, or $\vartheta_{\mathrm{I}} = 45°$, and $\varphi_{\mathrm{I}} = 0°$. The scattered intensity is reported in the forward zone, i.e. for $0° \le \vartheta_{\mathrm{S}} \le 180°$ and $-90° \le \varphi_{\mathrm{S}} \le 90°$ and is represented through contour plots. In a few cases are also reported sections of these contour plots for $\vartheta_{\mathrm{S}} = 30°$ and $\vartheta_{\mathrm{S}} = 90°$. Choosing $\vartheta_{\mathrm{I}} = 90°$ corresponds to incident field viewing the scatterer as a highly symmetric object.

With the aim of finding a qualitative stability criterion we consider a cluster of spheres with the same geometry as the one we chose but scale down the dimensions of the component spheres to the 20 %. Consequently, the size parameter will be reduced to $x_{\mathrm{s}} = 2.672$ for the single component sphere and to $x_{\mathrm{c}} = 8$ for the whole cluster. We make an angular analysis of the scattered intensity in the forward scattering zone.

In Figs.7.13 and 7.14 we report the contour plots, calculated using the E-scheme, of $\mathcal{I}_{\vartheta\vartheta} = |f_{\vartheta\vartheta}|^2 = r^2 I_{\mathrm{S}\vartheta\vartheta}/I_{\mathrm{I}}$ (see (4.46)), where ϑ is the symbolic value that η and η' assume when the incident plane wave is polarized along $\hat{\boldsymbol{\vartheta}}_{\mathrm{I}}$ and we consider the component of the scattered field polarized along $\hat{\boldsymbol{\vartheta}}_{\mathrm{S}}$, for $l_{\mathrm{M}} = 3$, 5, 8, respectively. The corresponding plots for $\mathcal{I}_{\varphi\varphi}$ show the same trend that we are going to discuss and are therefore not reported. Comparison

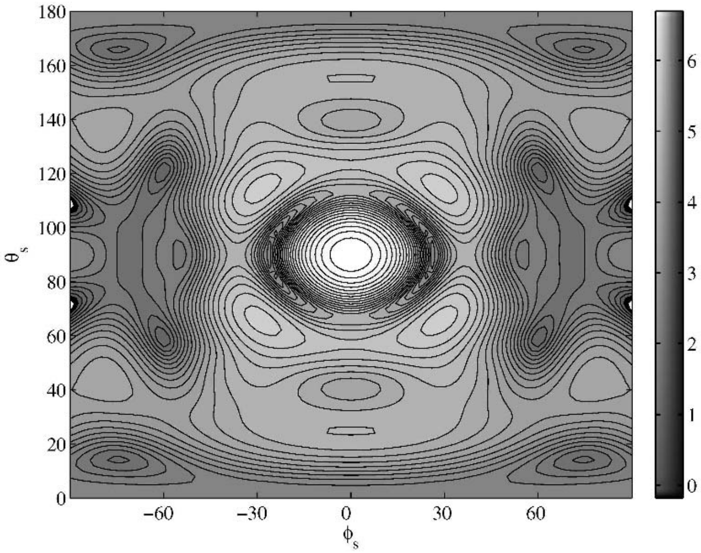

Fig. 7.13. Contour plot of $\mathcal{I}_{\vartheta\vartheta}$ (in μm^2, log scale) for the aggregate reduced to 20 % of its real size, calculated in the E-scheme with $l_{\mathrm{M}} = 3$. The incident field has $\vartheta_{\mathrm{I}} = 90°$ and $\varphi_{\mathrm{I}} = 0°$.

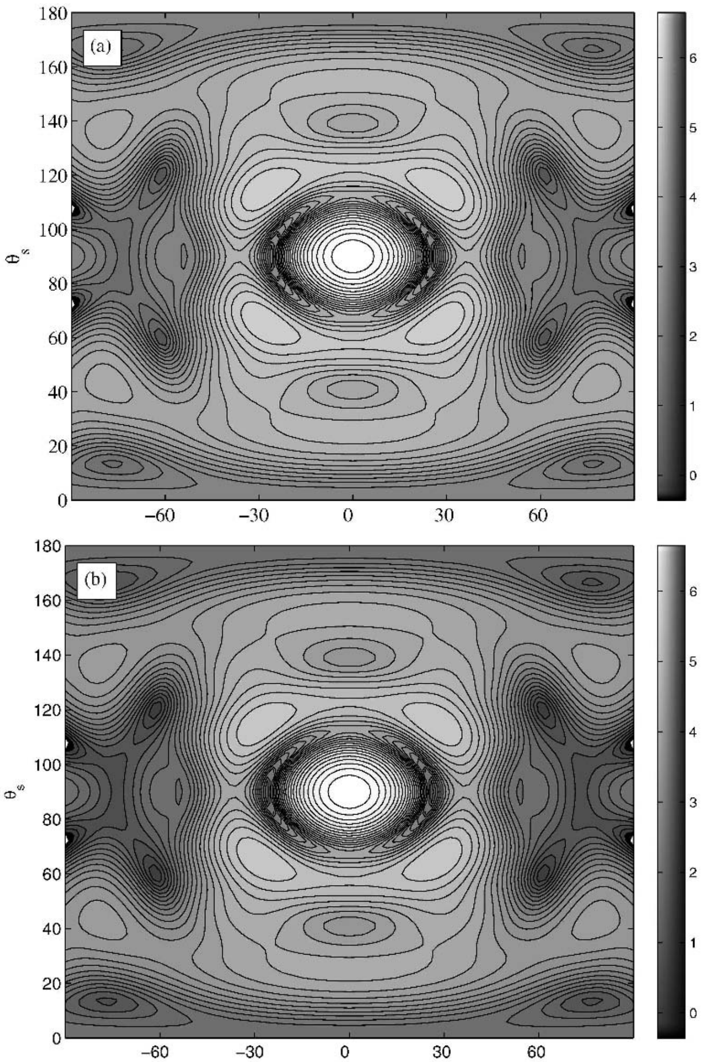

Fig. 7.14. Same as Fig. 7.13 but for $l_{\mathrm{M}} = 5$ in **(a)** and $l_{\mathrm{M}} = 8$ in **(b)**

of the plots shows that the stability is already reached for $l_{\mathrm{M}} = 5$; in fact, the plots for $l_{\mathrm{M}} = 5$ (Fig. 7.14 (a)) and $l_{\mathrm{M}} = 8$ (Fig. 7.14 (b)) do not show any important difference. Note that $l_{\mathrm{M}} = 5$ is, in principle, a little larger than the value barely sufficient to get the convergence for the component spheres.

This result has been further investigated by reporting in Fig. 7.15 (a) $\mathcal{I}_{\vartheta\vartheta}$ for $\vartheta_{\mathrm{I}} = 90°$ and $\varphi_{\mathrm{I}} = 0°$ for $l_{\mathrm{M}} = 2, 3, 4, 5$; in Fig. 7.15 (a) $\vartheta_{\mathrm{S}} = 90°$ and $-90° \leq \varphi_{\mathrm{S}} \leq 90°$; in Fig. 7.15 (b) $\vartheta_{\mathrm{S}} = 30°$ and $-90° \leq \varphi_{\mathrm{S}} \leq 90°$. The plots in both Fig. 7.15 (a) and (b) show that the changes undergone

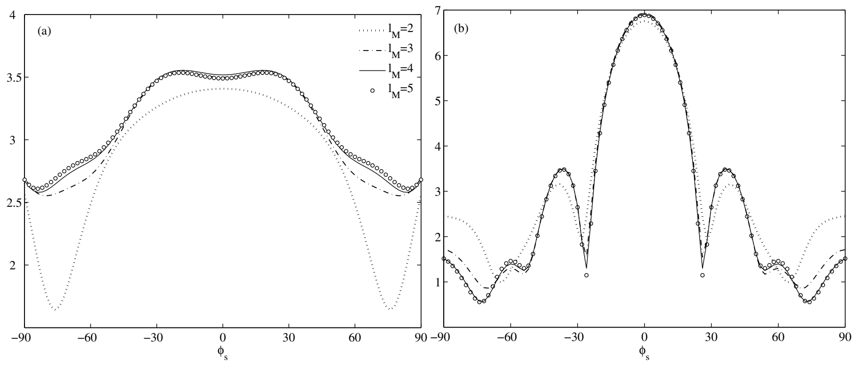

Fig. 7.15. $\mathcal{I}_{\vartheta\vartheta}$ (in μm^2, log scale) for the cluster reduced to 20 % of its real size, calculated in the E-scheme for $l_M = 2$–5, $\vartheta_I = 90°$, and $\varphi_I = 0°$. In **(a)** $\vartheta_S = 90°$; in **(b)** $\vartheta_S = 30°$

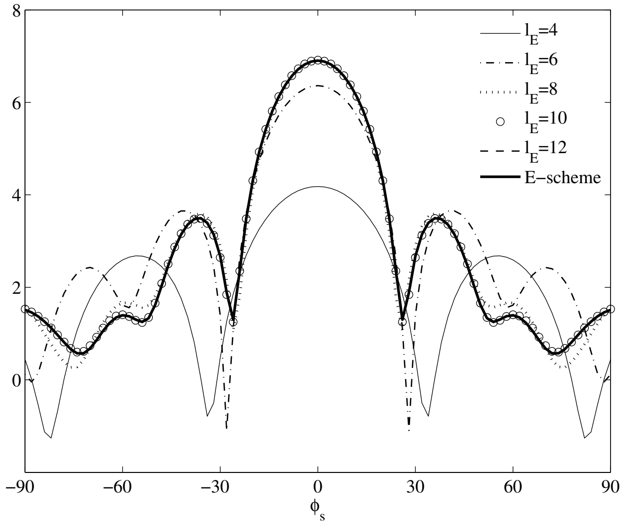

Fig. 7.16. Comparison of $\mathcal{I}_{\vartheta\vartheta}$ (in μm^2, log scale) for the cluster reduced to 20% of its real size calculated in the E-scheme for $l_M = 4$ (*heavy solid line*) with that yielded by the T-scheme for $l_I = 4$ and $l_E = 4$, 6, 8, 10, and 12. $\vartheta_I = 90°$, $\varphi_I = 0°$, and $\vartheta_S = 90°$. Note that the heavy *solid curve* and the *dashed curve* are perfectly superposed on the scale of the figure

by the intensity profiles for $l_M \geq 4$ are quite negligible. We do not report the profiles for $l_M > 5$ because, on the scale of the figure they are perfectly superposed to the profile for $l_M = 5$. We are thus led to conclude that the contour plot in Fig. 7.14 (a), i.e. for $l_M = 5$, gives a good description of the actual scattered intensity and that $l_M = 4$ is sufficient to get an acceptable qualitative description.

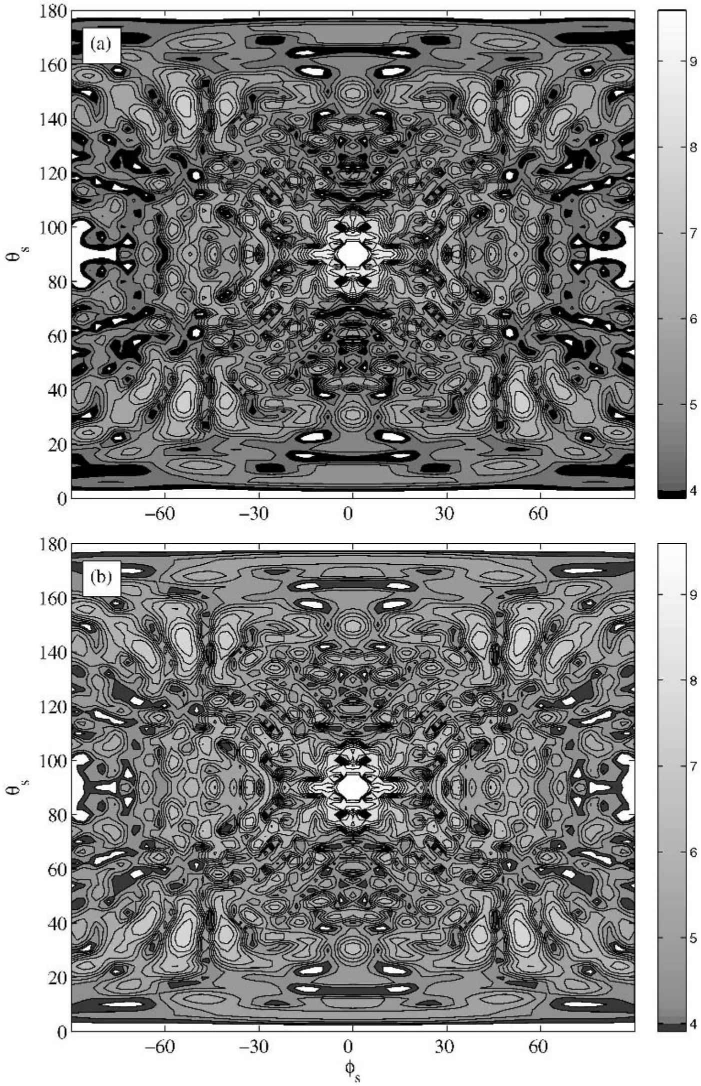

Fig. 7.17. Contour plot of $\mathcal{I}_{\vartheta\vartheta}$ (in μm^2, log scale) for the cluster considered with its real size calculated in the E-scheme for $\vartheta_{\mathrm{I}} = 90°$ and $\varphi_{\mathrm{I}} = 0°$ with $l_{\mathrm{M}} = 13$ in **(a)** and $l_{\mathrm{M}} = 15$ in **(b)**

As regards the behavior of the T-scheme, we found, as expected, that to get full convergence in the sums 5.33 and 5.35 l_{E} should be larger than the value of l_{M} so as to reproduce the results obtained in the E-scheme for $l_{\mathrm{M}} = l_{\mathrm{I}}$. In practice, we report in Fig. 7.16 the intensity profiles of Fig. 7.15 (a), calculated with $l_{\mathrm{M}} = l_{\mathrm{I}} = 4$ both in the E-scheme and in the T-scheme and,

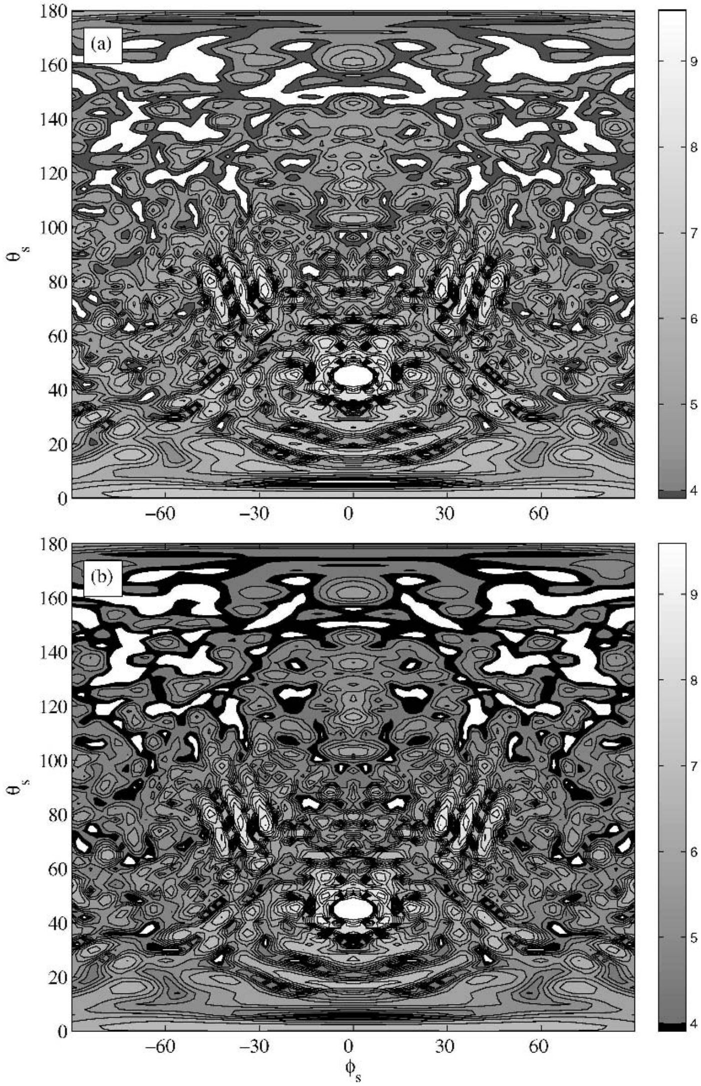

Fig. 7.18. Same as Fig. 7.17 but for $\vartheta_\mathrm{I} = 45°$ with $l_\mathrm{M} = 13$ in **(a)** and $l_\mathrm{M} = 15$ in **(b)**

in the latter case, for increasing values of l_E. The curves in Fig. 7.16 show at once that, although $l_\mathrm{E} = 8$ is quite acceptable and $l_\mathrm{E} = 10$ is even better, the results of the E-scheme and T-scheme become indistinguishable on the scale of the figure for $l_\mathrm{E} = 12$. Such a perfect convergence is unnecessary, however, as it would yield the perfect reproduction of the results of the E-scheme for $l_\mathrm{M} = 4$, that are in their nature qualitative results. Thus, one could choose for l_{E} the least value that would not disrupt the qualitative behavior of the scattering pattern: according to Fig. 7.16, $l_{\mathrm{E}} = 8$ is a fair choice. This is yet a large value so that there is a cost, in particular when averaging over the orientation of the scatterer is in order. Anyway, we can conclude that using the E-scheme, a good stability criterion requires using, in the present case, a value of l_{M} just a little bigger than necessary to get the convergency for the component spheres.

In order to test the stability criterion just found, we calculated, using the E-scheme, the scattering pattern of the cluster considered with its real dimensions: in this respect we recall that now $x_{\mathrm{s}} = 13.36$. The results are reported for $\vartheta_{\mathrm{I}} = 90°$ and $\varphi_{\mathrm{I}} = 0°$ in Fig. 7.17 for $l_{\mathrm{M}} = 13$ in (a) and for $l_{\mathrm{M}} = 15$ in (b); the pattern for $\vartheta_{\mathrm{I}} = 45°$ and $\varphi_{\mathrm{I}} = 0°$ is reported in Fig. 7.18 for $l_{\mathrm{M}} = 13$ in (a) and for $l_{\mathrm{M}} = 15$ in (b). Even a cursory examination of the patterns in Figs. 7.17 and 7.18 shows that the stability criterion is effective in yielding patterns that give an acceptable qualitative description of the scattering properties of the cluster at hand. In fact, when l_{M} is increased from 13 to 15 the changes undergone by the patterns are small on the scale of the figure.

7.2.2 Linear Chains

Although the results that we presented in Sect. 7.2.1 are satisfactory, the question arises whether they are due to the compactness of the cluster under study. In order to clarify this point we consider in this section a linear chain of 5 spheres of the same size and material that formed the cluster dealt within the preceding section [131]. We choose a frame of reference whose z axis passes through the center of the spheres that compose the linear chain; the origin is located at the geometrical center of the aggregate. The incident field is a linearly polarized plane wave that propagates along the y axis with polarization along the x axis; accordingly, the polar angles of the incident wavevector are $\vartheta_{\mathrm{I}} = 90°$ and $\varphi_{\mathrm{I}} = 90°$. Let us recall that the spheres that compose the aggregate have a refractive index $n = 1.59$ and a radius $\rho = 1.145\,\mu\mathrm{m}$; their size parameter is $x = 2\pi\rho/\lambda = 13.6$ at $\lambda = 531\,\mathrm{nm}$. The size parameter of the smallest mathematical sphere that includes the aggregate is $x_{\mathrm{c}} = 68$ at the same wavelength. Solving the electromagnetic scattering problem from such a big object through a brute force calculation would require to include into the multipole expansions terms up to $l_{\mathrm{M}} \geq 70$. As a result, the computational demand grows heavy, in spite of the applicable factorization of matrix M (see Sect. 5.4.1)

According to the procedure devised in [132] and reported in the preceding section, in the first step we scale the geometry of the whole cluster to 20% of its actual size leaving unchanged everything else. The size parameter of the spheres that compose the scaled scatterer is $x = 2.75$ whereas for circumscribed sphere $x_{\mathrm{c}} = 13.6$. The calculations of $\mathcal{I}_{\eta\eta'}$ for this scaled object were performed using the E-scheme. In Fig. 7.19 we report $\mathcal{I}_{\vartheta\vartheta}$ for the reduced object for several values of l_M. Comparison of the panels in Fig. 7.19 shows that the central panel ($l_\mathrm{M} = 5$) reproduces fairly well the lower panel ($l_\mathrm{M} = 7$): this is a clear indication that convergence has been achieved using $l_\mathrm{M} = 5$ which is a value that is barely sufficient to ensure the convergence of the field scattered by the component spheres considered as independent objects. In Fig. 7.20 we report $\mathcal{I}_{\vartheta\vartheta}$ from the scaled object calculated in the T-scheme, i.e. by full transition matrix approach, using $l_\mathrm{I} = 5$ and $l_\mathrm{E} = 5$, 12, 20. It is an easy matter to see that the lower panel of Fig. 7.20 reproduces quite well the central panel of Fig. 7.19. Since it may be difficult for the reader to appreciate the levels of a contour plot, especially on a logarithmic scale, we report in Fig. 7.21 a summary of the calculations performed so far as a function of the direction of observation ϑ_S in the meridional plane $\varphi_\mathrm{S} = 50°$; note that the choice of this plane has no particular meaning. Figure 7.21 shows that the information obtained from the T-scheme with $l_\mathrm{I} = 5$ and $l_\mathrm{E} = 20$ yields a quite acceptable convergence onto the results of the E-scheme for $l_\mathrm{M} = 5$.

At this stage we feel authorized to restore the cluster to its real size and to use the E-scheme to calculate $\mathcal{I}_{\vartheta\vartheta}$. The results are reported in Fig. 7.22 using $l_\mathrm{M} = 17$, 19. It is quite clear that the results of the upper panel are practically indistinguishable from those of the lower panel, i.e. an acceptable convergence has been achieved.

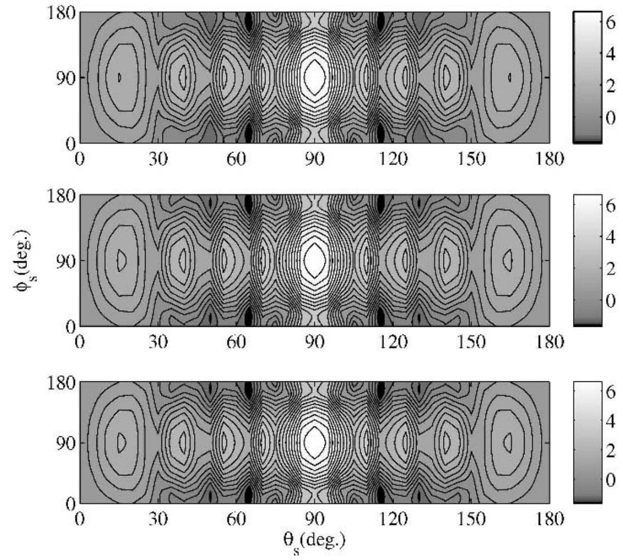

Fig. 7.19. Contour plot of $\mathcal{I}_{\vartheta\vartheta}$ (in μm^2, log scale) for the scaled cluster calculated in the E-scheme for (from *top* to *bottom*) $l_\mathrm{M} = 3$, 5, 7

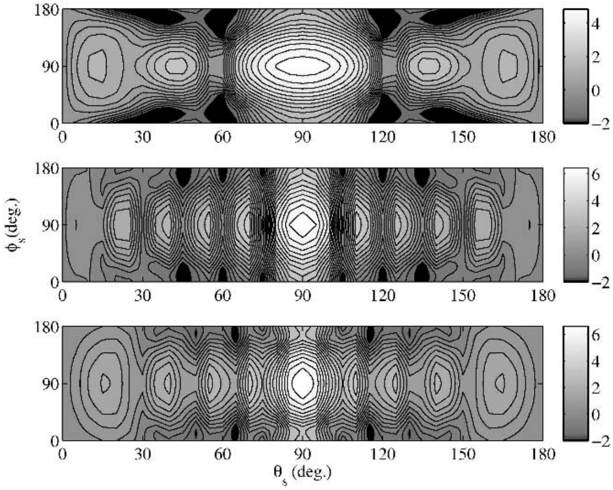

Fig. 7.20. Contour plot of $\mathcal{I}_{\vartheta\vartheta}$ (in μm^2, log scale) for the scaled cluster calculated in the T-scheme for $l_I = 5$ and (from *top* to *bottom*) $l_E = 5$, 12, 20

7.2.3 Acceptable Convergence

At first glance, the stability criterion that we found in the preceding sections may be rather surprising. In fact, the calculations in Sects. 7.2.1 and

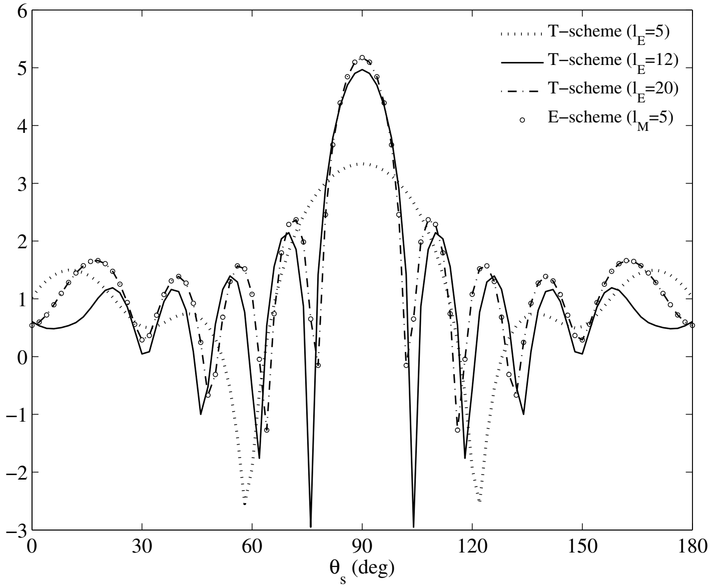

Fig. 7.21. Comparison of $\mathcal{I}_{\vartheta\vartheta}$ (in μm^2, log scale) for the scaled aggregate in the meridional plane $\varphi_S = 50°$ as a function of ϑ_S calculated in the E-scheme for $l_M = 5$ and in the T-scheme for $l_I = 5$

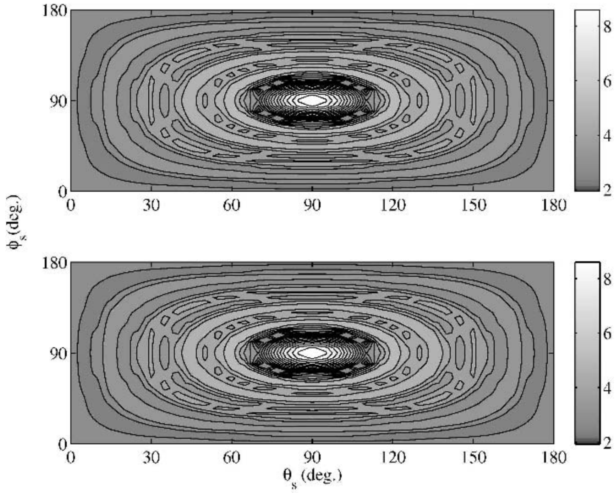

Fig. 7.22. Contour plot of $\mathcal{I}_{\vartheta\vartheta}$ (in μm^2, log scale) for the real size aggregate calculated in the E-scheme for $l_M = 17$ (*top panel*) and $l_M = 19$ (*bottom panel*)

7.2.2 support the conclusion that by chosing an l_M barely sufficient to ensure the convergence of the field scattered by the component spheres, one also achieves an acceptable stability of the scattering pattern from the whole cluster. Nevertheless, let us recall that the pattern from the cluster differs from that of the independent spheres because of the coupling effected by the multipole translation matrix elements $\mathcal{H}^{(pp')}_{\alpha lm\alpha' l' m'}$ in (5.28). These quantities, as appears from their explicit expression in Sect. 1.8.3 and in [89], depend on the distance between the centers of the spheres and are bound to be small, in general, in comparison to $\left(\mathrm{R}^{(p)}_{\alpha l}\right)^{-1}$, even for contacting spheres, when the radius of the latter is large. Of course, the translation matrix elements are even smaller for noncontacting spheres. As a result, in spite of the coupling, the scattering pattern from a cluster of big spheres is governed by the scattering power of the spherical components, that is given by the Mie coefficients $R^{(p)}_{\alpha l}$. Of course, the criterion that we found in Sects. 7.2.1 and 7.2.2, may not be strictly valid for a cluster whose spherical components have strongly different scattering power. In such a case a more detailed analysis is in order by chosing, as we suggested in Sect. 5.4.1, a different l_M for each sphere.

Anyway, the calculations that we presented in the preceding sections support our considerations on the accuracy that is reasonable to pursue when calculating the optical properties of model particles. In fact, the particles that are produced in actual experiments are often not well characterized, whereas the calculations may give results that are strongly dependent on the exact geometry, size, and orientation of the particles concerned. This is just the problem that has been faced by Mishchenko and Mackowski in comparing their theoretical predictions with the experimental data from bispheres. [133, 134] These authors state that they were forced to repeat their calculations several times changing the size of the particles in order to get results reasonably resembling the experimental findings. It is evident that the computational effort in the case of bispheres is much lighter than in the case of the 13-sphere cluster and of the linear chain we dealt with in the preceding sections [135]. Therefore, using the stability criterion we established in Sects. 7.2.1 and 7.2.2, possibly in the framework of the E-scheme, will save a lot of calculations, still reproducing the main features of the signature of the particle concerned. This, in turn, would make viable repeating the calculations in order to get the patterns that better resemble the experimental data.

7.3 Clusters in an Electrostatic Field

In Sect. 4.6 we stressed that a possible cause of nonrandom orientational distribution could be the presence of an external electrostatic field. The theory developed so far makes us able to investigate the extent to which the optical properties of a dispersion of clusters are influenced by the presence of an external electrostatic field [42]. As a representative example we chose aggregates of four identical spheres each of radius $\rho = 0.1\,\mu\mathrm{m}$. Using these building blocks two kinds of aggregates were formed: the first kind, which should simulate a prolate particle, was built by arranging the four spheres in a linear chain; the second kind, which was shaped by arranging the spheres at the vertices of a square, should model an oblate particle. In both kinds of cluster the neighboring spheres are in mutual contact. The wavevector of the incoming plane wave was chosen to be either parallel or orthogonal to the electrostatic field and, in the latter case, the polarization was chosen either parallel or perpendicular to the field itself.

The dielectric function of the spheres was assumed in the form [136]

$$\frac{\epsilon - \epsilon_\infty}{\epsilon_0 - \epsilon_\infty} = \frac{\omega_\mathrm{T}^2}{\omega_\mathrm{T}^2 - \omega(\omega + i\Gamma\omega_\mathrm{T})}$$

that is appropriate for a dielectric material, where ω_T is the (circular) frequency of the transverse phonons. In our calculations, the parameters of MgO were assumed according to [137], i.e., $\omega_\mathrm{T} = 7.5 \cdot 10^{13}\,\mathrm{s}^{-1}$, $\epsilon_0 = 9.8$, $\epsilon_\infty = 2.95$, and $\Gamma = 0.27$. As a result, using (4.66)–(4.68), we obtained $\alpha_\perp = 0.259 \cdot 10^{-14}\,\mathrm{cm}^3$, $\alpha_\parallel = 0.435 \cdot 10^{-14}\,\mathrm{cm}^3$ for the prolate particles and $\alpha_\perp = 0.336 \cdot 10^{-14}\,\mathrm{cm}^3$, $\alpha_\parallel = 0.245 \cdot 10^{-14}\,\mathrm{cm}^3$ for the oblate particles. In this respect, let us recall that, according to (4.67), the calculation of the polarizability tensor requires the elements of the transition matrix for $l = l' = 1$ only, whereas the calculation of the optical properties requires well converged values of the whole transition matrix. The results that we are going to discuss required at most $l_\mathrm{M} = 11$.

In view of the cylindrical symmetry of the linear chains, their transition matrix can be made diagonal in m by choosing the local reference frame with the z axis parallel to the cylindrical axis. For the square clusters we notice that, by choosing the local reference frame with the z axis along the quaternary axis, the elements with $l, l' = 1$ of their transition matrix, i.e., the elements that are relevant for the calculation of the polarizability, are nonzero for $m' = m$ only. This is not a numerical accident, but a necessary consequence of the symmetry of the square clusters [123, 138]. It is for this reason that (4.67) that we established in Sect. 4.6.1 for axially symmetric scatterers apply to both kinds of clusters and the orientational distribution function depends on the Eulerian angle β only for both kinds of clusters. The resulting function $v(\beta)$ is reported in Fig. 7.23 at $T = 300°\mathrm{K}$ for some values of the strength of the static field, that, as usual, is given in Volt/cm whereas electrostatic units were used in (4.57). Figure 7.23 shows that the difference $\alpha_{\|} - \alpha_{\perp}$ is paramount in determining the distribution of the orientations. It is easily seen that the prolate particles tend to orient their symmetry axis along

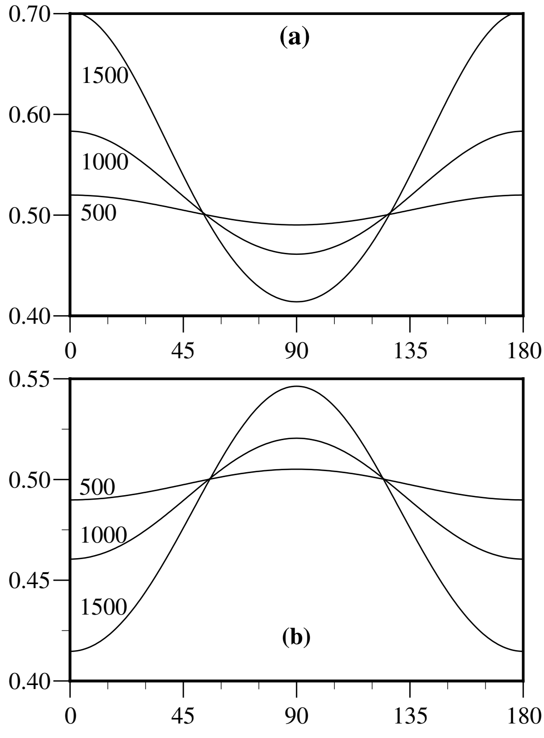

Fig. 7.23. Weight function $v(\beta)$ for the linear chains **(a)** and for the square clusters **(b)**. The curves are labelled by the strength of the external electrostatic field (in V/cm)

the electrostatic field whereas the quaternary axis of the oblate particles tends to become perpendicular to the field. Thus, in the limit of infinite strength of the field, all the prolate particles orient with their cylindrical axes parallel to the field itself, whereas all we can state on the orientation of the oblate particles is that their quaternary axes lie in a plane that is perpendicular to the field but that the particles are otherwise randomly oriented.

The results reported in Fig. 7.23, suggest to see preliminarily to what extent the orientational distribution influences the optical properties. For a dispersion with number density N_0 we define the quantity

$$\varDelta G_\eta = \frac{1}{N_0}\left[\mathrm{Im}(\mathcal{N}^\infty_{\eta\eta}) - \mathrm{Im}(\mathcal{N}^0)\right] ,$$

where the factor $1/N_0$ has been introduced to normalize $\varDelta G_\eta$ to unit number density. $\mathcal{N}^\infty_{\eta\eta}$ and $\mathcal{N}^0$ were calculated by using in (4.45) $N = N_0 P(\varTheta)$, where $P(\varTheta)$ is the weight function appropriate for infinite and for zero strength of the electrostatic field, respectively. Since for $E = \infty$ the linear chains are all likely oriented, one has $\langle f_{\eta\eta}\rangle = f_{\eta\eta}$. For $E = 0$ they are randomly oriented so that the relevant $\langle f_{\eta\eta}\rangle$ is given by (4.47a) or by (4.53a), as appropriate. We also notice that $\langle f_{\eta\eta}\rangle$ is actually independent of the polarization. Consequently, the index η has been dropped from $\mathcal{N}^0$. It is also convenient to define the quantity

$$g_\eta = \frac{1}{N_0}\mathrm{Im}(\mathcal{N}_{\eta\eta}) ,$$

where $\mathcal{N}_{\eta\eta}$ is calculated at the actual strength of the applied electrostatic field.

We define $\varDelta G_\eta$ even for the square clusters, but in this case the appropriate weight function is that reported in Table 4.1, Case 5. With the help of (4.49a) and (4.50) we get

$$\langle f_{\eta\eta'}\rangle_{\beta=90^\circ} = -\frac{\mathrm{i}}{4\pi k}\sum_L\sum_{pp'}\sum_{ll'}\sum_{m\mu}(-)^{m-\mu}C(l,l',L;m,-m)$$
$$\times C(l,l',L;\mu,-\mu)W^{(p)*}_{\mathrm{S}\eta lm}\,\bar{\mathcal{S}}^{(pp')}_{l\mu l'\mu}\,W^{(p')}_{\mathrm{I}\eta' l'm}P_L(0) .$$

The curves in Fig. 7.24, where $\varDelta G_\eta$ is plotted as a function of the size parameter of the component spheres, are very useful for the choice of the value of x at which the effect of the electrostatic field is more evident. Indeed, for both kinds of clusters, $\varDelta G_\eta$ vanishes for some value of x in agreement with the results in Sect. 6.1 [45] that there exist values of the size parameter at which the optical behavior of a dispersion of clusters is identical to that of a dispersion of spherical particles. Accordingly, in Fig. 7.26 we report g_η for a dispersion of linear chains of spheres as a function of the strength of the external field. Both figures show that the effect of the external field on the extinction coefficient of the dispersion is fairly visible even at relatively small values of E, i.e., when the number of the chains with their axis along the field is still relatively small. The corresponding results for the square clusters are reported in Fig. 7.27

Figures 7.26 and 7.27 show that the saturation of the effect for the linear chains is achieved for values of the field larger than the value that is needed for the dispersion of prolate particles. Anyway, the effect of the electrostatic field is quite noticeable even when its strength is so low that only a relatively small number of square clusters is oriented with the quaternary axis orthogonal to the field itself. Although all the curves in Fig. 7.26 and 7.27 go steadily towards the saturation, this should not be taken as a general rule. In fact, for the linear chains, we found that there are some ranges of x at which the curves of g_η as a function of the static field strength are nonmonotonic; for instance, this behavior occurs for $x > 1.2$, as is shown in Fig. 7.28 (a) for $x = 1.35$ and in Fig. 7.28 (b) for $x = 1.5$. In particular, Fig. 7.28 (a) shows that g_η for perpendicular incidence is almost independent of the polarization up to ≈ 200 V/cm. On the contrary, in Fig. 7.28 (b) the nonmonotonicity of g_l^r and g_r^r results in the crossing of the curves between 200 and 500 V/cm. This kind of behavior never occurs for the square clusters.

The examples and the results that were presented above show that our four-sphere clusters are suitable both to achieve an effective description of the optical phenomena that are produced by the electrostatic field and to

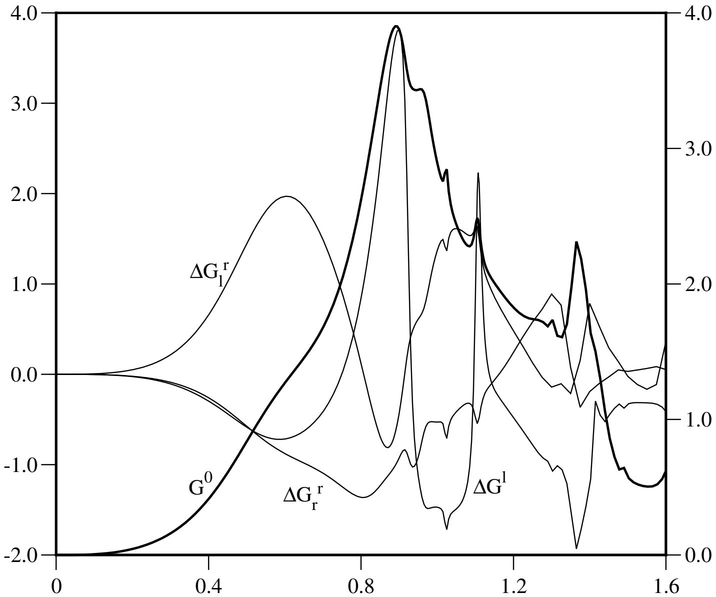

Fig. 7.24. $\Delta G_\eta \cdot 10^{14}$ for the linear chains as a function of the size parameter of the component spheres. The *upper* indices r and l refer to incidence perpendicular or parallel to the static field, respectively. The scale to the *right* refers to $G^0 = (1/N_0)\mathrm{Im}(\mathcal{N}^0) \cdot 10^{14}$ (*thick line*) that is reported for the sake of completeness

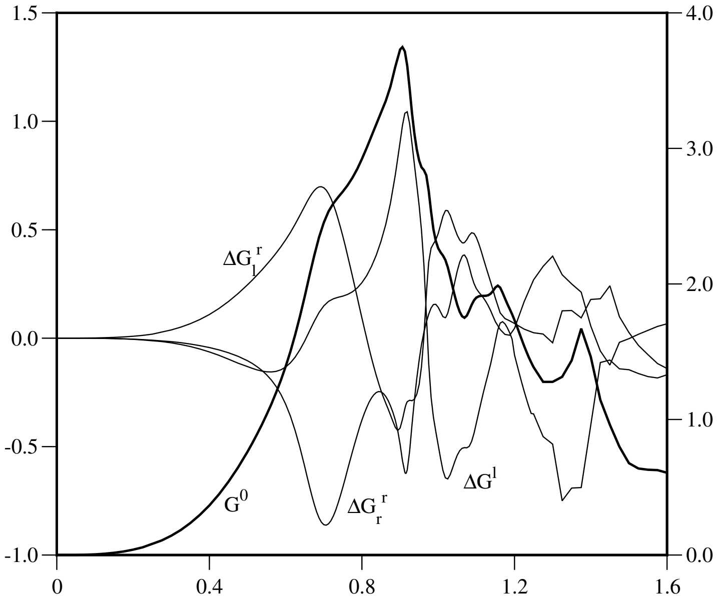

Fig. 7.25. $\Delta G_\eta \cdot 10^{14}$ for the square clusters as a function of the size parameter of the component spheres. The *upper* indices r and l refer to incidence perpendicular or parallel to the static field, respectively. The scale to the *right* refers to $G^0 = (1/N)\text{Im}(\mathcal{N}^0) \cdot 10^{14}$ (*thick line*) that is reported for the sake of completeness

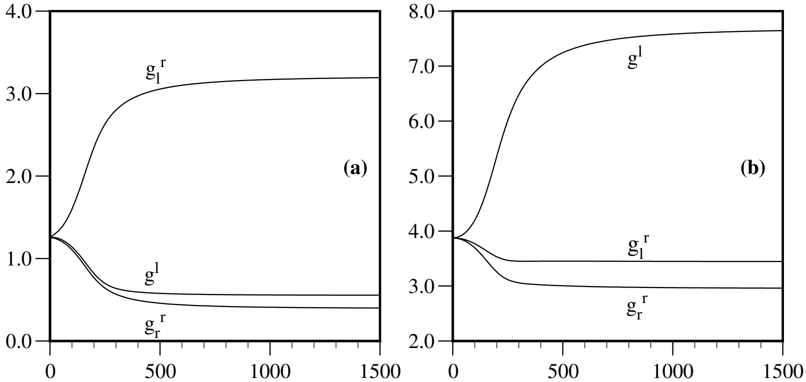

Fig. 7.26. g_η in $\text{cm}^3 \cdot 10^{-14}$ for the linear chains of spheres with size parameter $x = 0.6$ **(a)** and $x = 0.9$ **(b)** as a function of the electrostatic field strength (in V/cm)

contain the computational effort. We stated earlier in this section that the convergence of the calculations required at most $l_\text{M} = 11$. Therefore, the matrix to be inverted was of order 1144. The computational situation is rather

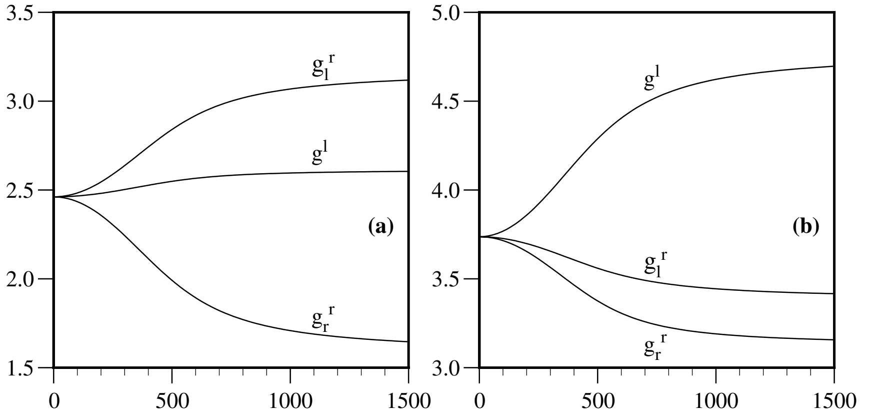

Fig. 7.27. g_η in $\mathrm{cm}^3 \cdot 10^{-14}$ for the square clusters with size parameter of the component spheres $x = 0.7$ **(a)** and $x = 0.91$ **(b)** as a function of the strength of the electrostatic field (in V/cm)

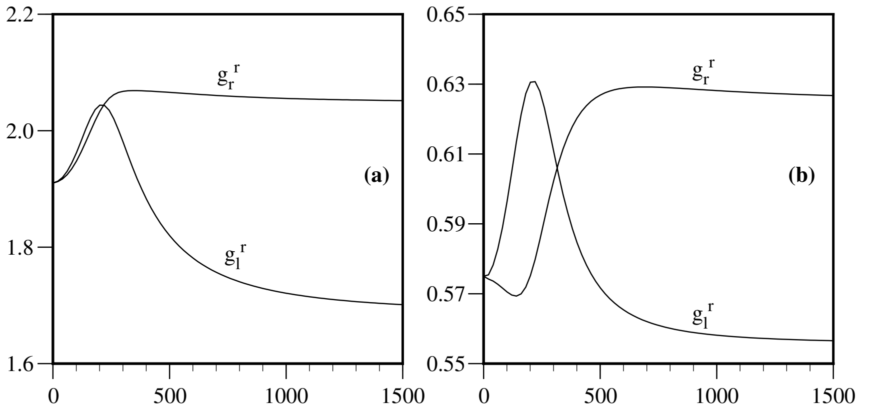

Fig. 7.28. g_η^r in $\mathrm{cm}^3 \cdot 10^{-14}$ for the linear chains of spheres with size parameter $x = 1.35$ **(a)** and $x = 1.5$ **(b)** as a function of the strength of the electrostatic field (in V/cm)

different if only the polarizability need to be calculated. As the polarizability is a static quantity, indeed, one must take the limit for $k \to 0$ of the calculated transition matrix, according to (4.65). In this limit only the elements with $l = l' = 1$ need to be included in (5.26). The matrix to be inverted to calculate the transition matrix is thus of order $d = 3N = 12$ on account of the vanishing of the magnetic terms. As a result, the calculation of the polarizability tensor can be performed even for clusters that include a large number of spheres without undue computational effort.

On account of the structure of the polarizability tensor, the modifications of the macroscopic optical properties that are induced by an electrostatic field cannot be used to gain information on the shape of the particles. In fact, it is not possible, on general grounds, to distinguish, e.g., a cone from a cylinder because the axial symmetry of both figures implies that only two components of their polarizability tensor are different. Moreover, one is neither able to distinguish a disk from a square because the polarizability tensor of both figures has an identical axially symmetric structure. The electrostatic field, however, may help in discriminating the optical properties of oblate particles from those of prolate particles. This is suggested by the crossing of the g_r^r and of the g_l^r curves for the linear chains when $x > 1.2$. As stressed above, such crossings never occur for the square clusters. Actually, it is to be borne in mind that, in general, the collective optical behavior of the prolate and of the oblate particles looks rather similar. This is due to the fact that the different orientational response of the two kinds of particles to the electrostatic field tend to compensate for the different orientational dependence of their forward-scattering amplitudes.

7.4 Extinction from Single and Aggregated Layered Spheres

This section is devoted to discussing the extinction properties of single and aggregated concentrically layered spheres composed of materials with a frequency-dependent dielectric function. We also consider single and aggregated spheres in which the change from the refractive index of the bulk material to that of the surrounding medium is not sharp but occurs with continuity through a transition layer of suitable thickness according to (5.20) in Sect. 5.2. We say that these spheres have a soft surface. A previous study of the properties of all these kinds of radially nonhomogeneous spheres and of their binary aggregates had the specific purpose of assessing the effect of the aggregation on the resonances in their extinction spectrum [76]. Here we also focus on the effect of the imaginary part of the refractive index on the convergence of the calculations. In this respect, we recall that both the real and the imaginary part of the refractive index of metal particles may be rather large.

Hereafter, we consider spheres of two different radii, i.e., $\rho_1 = 10$ nm and $\rho_2 = 50$ nm, inclusive of the thickness of the covering layer or of the soft surface when present [76]. The dielectric function of the metallic material was assumed to be of the free electron Drude form [139, 140]

$$\epsilon = 1 - \frac{\omega_{\mathrm{p}}^2}{\omega(\omega + \mathrm{i}\Gamma\omega_{\mathrm{p}})} , \tag{7.2}$$

where ω_{p} is the plasma frequency of the metal concerned. In turn, for the dielectric material we chose the damped-oscillator form [140] that we already used in Sect. 7.3. The relevant parameters were taken from Kittel [137] and

Table 7.4. Parameters used in the calculations in this section

Material	ω_{p} (s^{-1})	ω_{T} (s^{-1})	Γ	ϵ_0	ϵ_∞
K	6.500×10^{15}		0.02		
Mg	1.610×10^{16}		0.01		
Al	2.400×10^{16}		0.01		
Ag	5.743×10^{15}		0.01		
MgO		7.5×10^{13}	0.27	9.8	2.95

are listed in Table 7.4. The calculations for the layered spheres where performed through the technique that we expounded in Sect. 5.2, i.e., by interposing between each pair of layers a thin transition layer within which the dielectric function varies continuously as a function of r according to (5.20). In all cases, the thickness of the transition layer was chosen to be 0.1 nm. We report, for $\hat{\boldsymbol{k}}_{\mathrm{S}} = \hat{\boldsymbol{k}}_{\mathrm{I}}$, Q'_{sp} for the single spheres and Q' averaged over randomly oriented aggregates as a function of $\nu = \omega/\omega_{\mathrm{p}}$. When more than one metal is present, ω_{p} is the highest of the implied plasma frequencies. The polarization of the incident wave is assumed to be linear.

All the results that we are going to discuss were obtained using $l_{\mathrm{M}} = 12$ in the whole range $0.1 \leq \nu \leq 1.1$, the corresponding wavelength ranging, in all cases, from the far infrared to the ultraviolet. We stress, however, that although $l_{\mathrm{M}} = 12$ is sufficient to ensure full convergence for the single spheres, i.e. convergence to four decimal places, it is not sufficient, in general, to ensure full convergence for the aggregates. Therefore, the plots that we report are included with the purpose of showing the complexities that the aggregation induces into the spectra. Anyway, the lack of full convergence, that stems from the features of the dielectric function of metals, will be further discussed in Sects. 7.4.5, and 7.5. In the latter section, we will, indeed, deal with binary aggregates of metallic spheres that can sustain longitudinal waves and will show that, in this case, the problems of convergence can be overcome.

In the range of frequency we considered, all the scatterers present one or more resonance peaks. Since a resonance peak may be rather sharp, locating its maximum requires a fine scanning on the ν axis lest the peak be missed at all. Often, the preliminary location of the resonances is done by resorting to the so called Güttler formula [5] that estimates the polarizability of a small sphere coated by a thin concentric layer through effective medium considerations. For a coated sphere in vacuo Güttler formula reads

$$\alpha = \frac{(\epsilon_{\mathrm{s}} - 1)C_+ + (2\epsilon_{\mathrm{s}} + 1)C_-}{(\epsilon_{\mathrm{s}} + 2)C_+ + (2\epsilon_{\mathrm{s}} - 2)C_-}\rho^3,$$

with

$$C_+ = \epsilon_{\mathrm{N}} + 2\epsilon_{\mathrm{s}}, \quad C_- = (\epsilon_{\mathrm{N}} - \epsilon_{\mathrm{s}})(\rho_{\mathrm{N}}/\rho)^3 ,$$

where ϵ_{N} and ρ_{N} are the dielectric constant and the radius of the core, respectively, and ϵ_{s} is the dielectric constant of the coating. Then, with the help of the Lorentz–Lorenz formula [5]

$$\alpha = \frac{\epsilon - 1}{\epsilon + 2}\rho^3,$$

the effective dielectric constant of a coated sphere can be defined as

$$\epsilon_{\text{eff}} = \frac{C_+ + 2C_-}{C_+ - C_-}\epsilon_{\text{s}}$$

and the condition for the occurrence of a resonance reads

$$\epsilon_{\text{eff}} + 2 = 0 \; . \tag{7.3}$$

Of course, (7.3) can safely be applied to small spheres only. In fact, the Güttler formula, from which it stems, can be applied only to spheres that can be dealt with in the small particle approximation, viz., when only dipole terms need to be considered. Moreover, it should be borne in mind that, besides the latter approximation, (7.3) encompass an effective medium approximation also [141]. Therefore, if the particle is not sufficiently small and the coating layer is not sufficiently thin, neither can the resonance peaks be accurately located, nor can ϵ_{eff} be introduced into the Mie theory to calculate the extinction spectrum. Equation (7.3) was successfully used in [76] to estimate the frequency of the resonances of 5 nm spheres. Nevertheless, our calculations show that (7.3) becomes unreliable when applied to the 10 nm spheres.

7.4.1 Metal Spheres with a Soft Surface

Considering spheres with a soft surface may be a useful tool to describe scatterers whose radius is not perfectly known, for instance because of smooth irregularities of the surface. This kind of sphere is often invoked in astrophysics to explain the optical behavior of dust particles originated by accretion by interstellar gas atoms.

As far as we know, spheres with a soft surface were first dealt with by Ruppin [77] who calculated the extinction from 5 nm spheres with a soft surface of 0.4 nm thickness within which the transition from the bulk material to the surrounding medium occurs according to a linear law. On the contrary, we assume a law of transition given by (5.20) and in Fig. 7.29 report Q'_{sp} for spheres of potassium with a soft surface whose thickness is 1 nm for the 10 nm spheres and 5 nm for the 50 nm spheres, and Q' for their binary aggregates. We first remark that the results for the 10 nm spheres are practically identical to those for the 5 nm spheres with a soft surface of 0.4 nm thickness that are reported in [76] and that were in fair agreement with the results of Ruppin [77]. It is therefore not surprising that the curves in Fig. 7.29 (a) and (b) are also in good agreement with those of Ruppin, both in the position of the

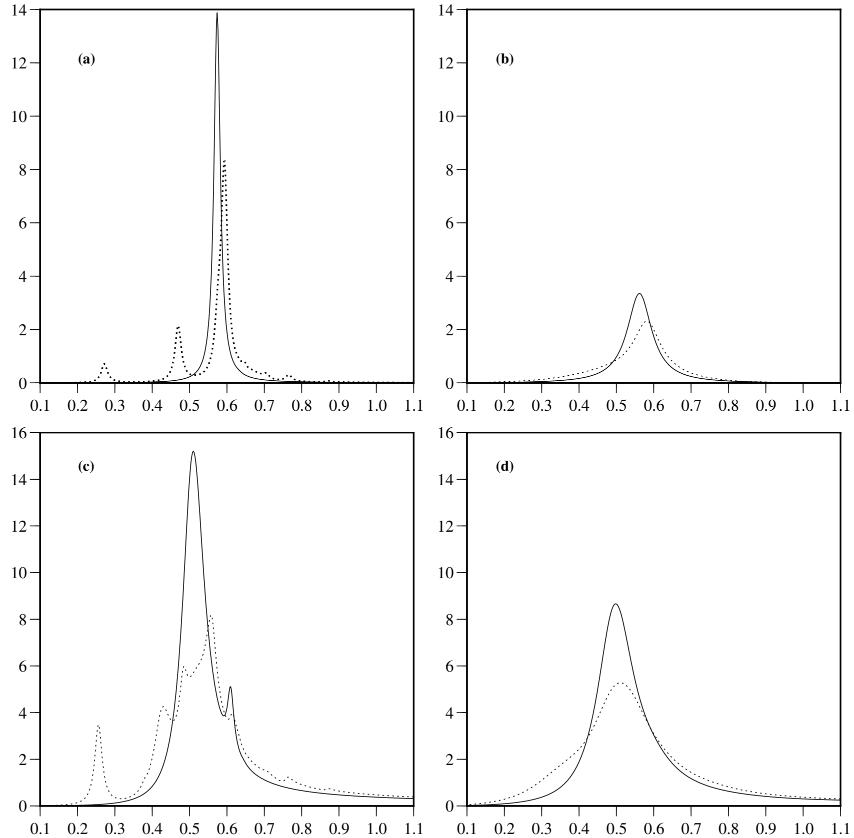

Fig. 7.29. Q'_{sp} (*solid curves*) and Q' (*dotted curves*) as a function of ν for spheres of potassium and for their binary aggregates in random orientation. **(a)** and **(c)** refer to 10 nm and to 50 nm spheres with a sharp surface. **(b)** and **(d)** refer to 10 nm and to 50 nm spheres with a soft surface whose thickness is 1 nm and 5 nm, respectively

peaks and in their width, in spite of our choice of a different law of variation of the refractive index within the transition layer. This suggests that the effect of the diffuseness is qualitatively almost independent of the details of the radial dependence of ϵ and, to a certain extent, also of the radius of the spheres. The interested reader can find in [75] a thorough analysis of the effects that are due to the shape of the radial dependence. The results in Fig. 7.29 show that, as a general rule, the presence of a diffuse surface attenuates the extinction peaks and makes noticeably smoother the spectra both of the single spheres and of their binary aggregates. We do not present here specific results but we can state that, according to our calculations, this behavior is accentuated by the increase of the thickness of the transition layer. In turn, the curves of g for the binary aggregates of spheres with a sharp surface show the duplication of the peaks that is expected as far as only dipole terms ($l_M = 1$) are considered. Nevertheless, we also see the appearance of further peaks whose maxima are rather small, however. When we go to consider the binary aggregates of spheres with a soft surface, we see that the duplication of the peaks occurs in the form of smooth shoulders, especially for the 50 nm spheres.

7.4.2 Metal Spheres with a Dielectric Coating

In Fig. 7.30 we report the extinction spectrum for spheres of Mg coated by MgO. The radius of the spheres is 10 nm and 50 nm inclusive of the respective thickness of a coating of 2 nm and 5 nm, when present.

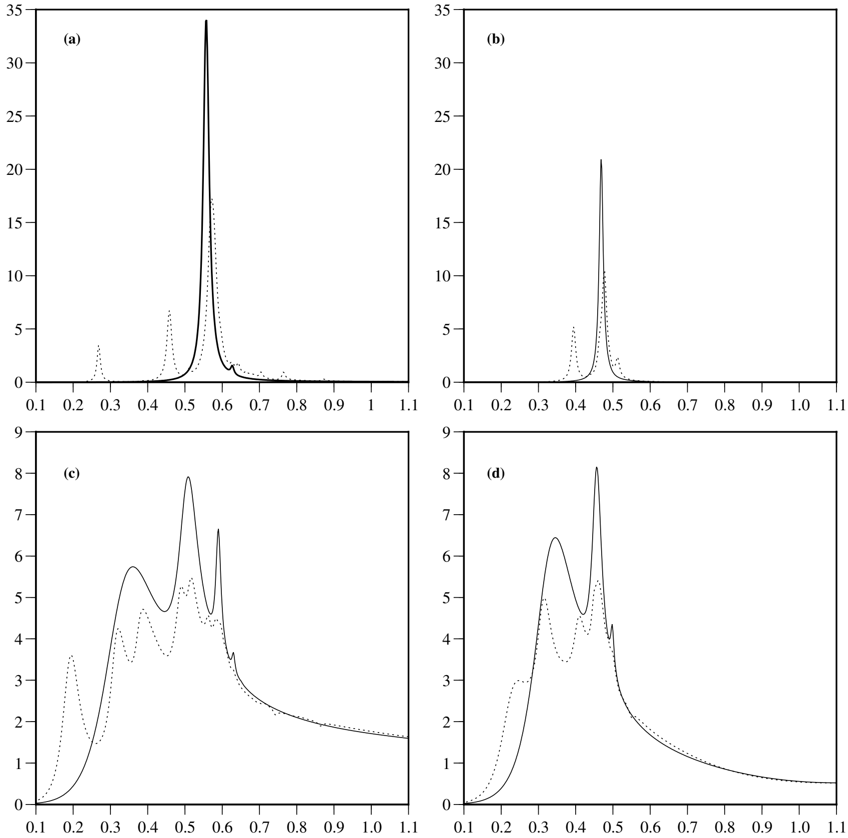

Fig. 7.30. Q'_{sp} (*solid curves*) and Q' (*dotted curves*) as a function of ν for spheres of radius 10 nm and 50 nm of solid Mg in **(a)** and **(c)** and of Mg coated by a layer of MgO in **(b)** and **(d)**. The radius of the spheres is inclusive of the thickness of the coating of 2 nm in (b) and 5 nm in (d)

For the 10 nm spheres, the presence of the coating produces two main effects on the resonance peaks: a shift toward lower frequencies and an attenuation that does not depend on the normalization. In fact, the attenuation remains even when σ_T is normalized to the geometrical cross section of the metal core rather than to S. The spectrum of the 50 nm spheres shows sharper peaks for the coated spheres, i.e., the coating affects more the width than the heigth of the resonances. However, the qualitative features are on the whole unaffected.

A look to Fig. 7.30 shows that the aggregation produces analogous effects both for the metal-only spheres and for the coated ones. The duplication of the peaks that is due to the aggregation occurs in complete analogy with the case of spheres with a soft surface. Note that, although we do not report the specific results, the change of the thickness of the coating does not produce any further effect.

For the sake of argument, it may be of interest to remark that (7.3) predicts for the 10 nm spheres with coating, the occurrence of three peaks, only one of them occurring in the range of interest. Unfortunately, the location of this peak is inaccurately estimated by (7.3).

7.4.3 Dielectric Spheres with a Metal Coating

The spectrum for 10 nm spheres of MgO with a coating of Al are reported in Fig. 7.31, together with the spectrum of solid Al spheres of the same radius. The thickness of the coating varies form 1.6 nm to 6.4 nm and, for each choice of the thickness there occur two resonance peaks whose frequency is lower

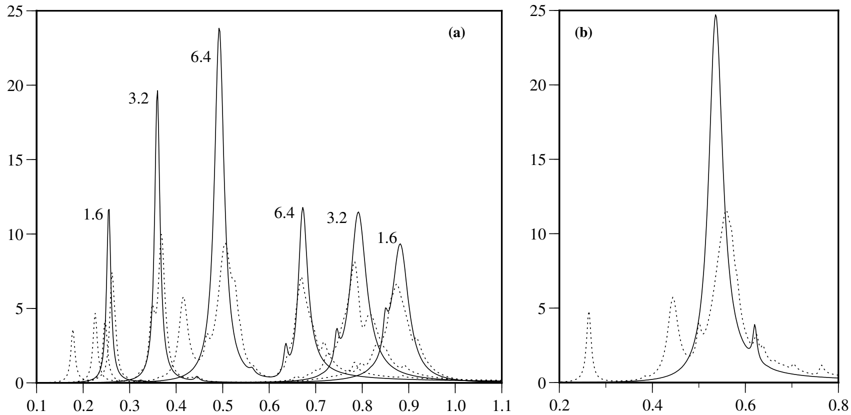

Fig. 7.31. **(a)** Q'_{sp} (*solid curves*) and Q' (*dotted curves*) as a function of ν for spheres of MgO of radius 10 nm inclusive of a coating of Al of thickness 1.6, 3.2, and 6.4 nm. In **(b)** we report Q'_{sp} (*solid curves*) and Q' (*dotted curves*) as a function of ν for spheres of solid Al with 10 nm radius

and higher than the resonance peak at $0.57\,\omega_\mathrm{p}$ that is characteristic of a sphere of solid Al. This pair of peaks, when the thickness increases, tends to converge towards the peak of the solid Al sphere. Of course, the overall radius of the spheres influences the behavior of the peaks. In fact, we also calculated the extinction spectrum of 50 nm spheres, but the features that we described above disappear, especially when the thickness of the coating is a nonnegligible fraction of the radius. This confirms that the presence of the resonance peaks depends critically on the radius of the spheres in analogy with the well known fact that resonances of homogeneous spheres depend on the size parameter and thus on the combination of radius and frequency, not to speak of the refractive index.

The results that we presented above suggest that, with a wise choice of the thickness of a coating layer, we may produce strong extinction in any chosen region of the spectrum. This conclusion is supported by the results of analogous calculations that we performed by substituting the Al coating with one of Ag. As a consequence, we can safely state that, as far as (7.2) is valid, the extinction spectrum is only slightly affected by the choice of ω_p and Γ.

7.4.4 Metal Spheres with a Metallic Coating

As a last example, we consider spheres of Al with a coating of Ag and spheres of Ag with a coating of Al. In both cases, the radius is 10 nm inclusive of a coating of 2 nm. The resulting extinction is shown in Fig. 7.32, where we also include the extinction for Ag-only spheres. The choice of these two metals has been suggested by the remark that $\omega_\mathrm{p}(\mathrm{Ag})/\omega_\mathrm{p}(\mathrm{Al}) = 0.239$, i.e., their plasma frequencies are rather different. Comparison of Figs. 7.32 (a) and (b) shows that the most striking effect of this difference is the different intensity of the peaks when the role of Al and Ag is exchanged. Actually, we made a detailed study of the position and intensity of the peaks as a function of the thickness of the coating. We do no report the specific results of our study that can, however, be summarized as follows. When the metal with the higher ω_p coats a core of the metal with the lower ω_p, the peak at $0.365\,\omega_\mathrm{p}$ in Fig. 7.32 (a), with increasing thickness, moves from $0.574\,\omega_\mathrm{p}(\mathrm{Ag}) = 0.137\,\omega_\mathrm{p}(\mathrm{Al})$ (characteristic of Ag-only spheres) to $0.536\,\omega_\mathrm{p}(\mathrm{Al})$ (Al-only spheres). This shift is quite significant, especially in units of $\omega_\mathrm{p}(\mathrm{Ag})$. At the same time, the less intense peak becomes smaller and smaller with increasing thickness of the coating up to complete disappearance, as expected, when the sphere becomes of Al only.

When the roles of two metals are exchanged and the higher-ω_p metal forms the core (coating of Ag), neither of the two peaks is the more important within a large range of the thickness of the coating. The mobility of the peak is smaller than in the preceding case, although in units of $\omega_\mathrm{p}(\mathrm{Ag})$ it is still considerable. We are thus lead to the conclusion that the optical behavior of spheres composed of two metals is governed by the ratio of the plasma

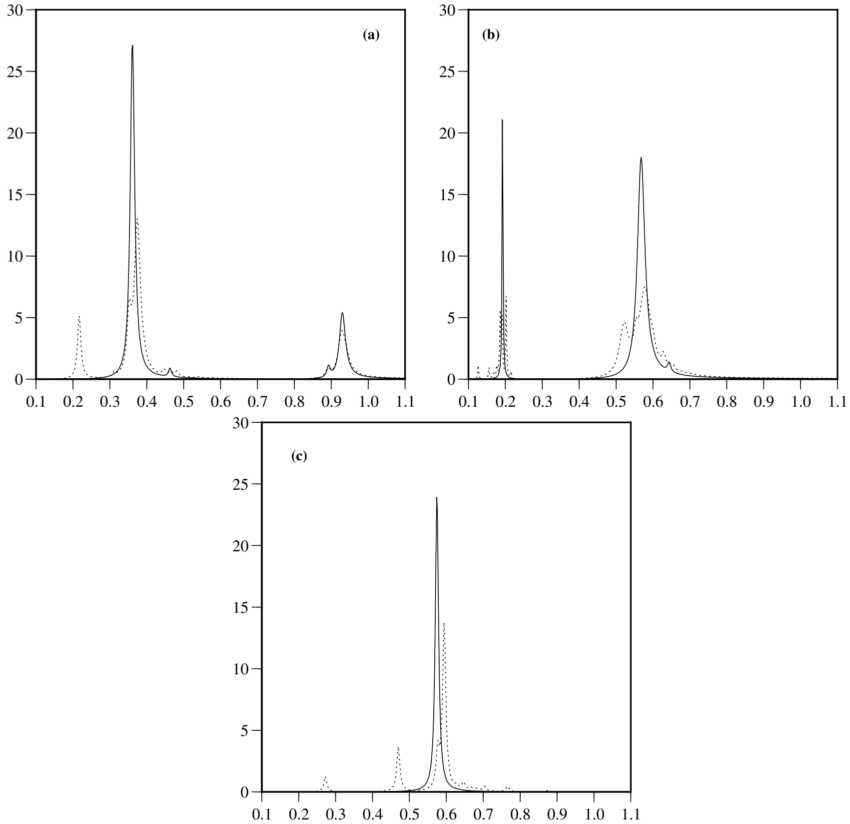

Fig. 7.32. Q'_{sp} (*solid curves*) and Q' (*dotted curves*) as a function of ν for spheres of radius 10 nm of Ag coated by a layer of Al **(a)** and of Al coated by a layer of Ag **(b)**. The radius of the spheres in (a) and (b) is inclusive of the thickness of the coating of 2 nm. In **(c)** we report Q'_{sp} and Q' as a function of ν for spheres of solid Ag with 10 nm radius

frequencies. As the mobility of the peaks as a function of the thickness of the coating can be enhanced by a convenient choice of the ratio of the respective ω_{p}, the considerations made for the case of dielectric spheres with a metal coating about designing particles intended to produce extinction in selected regions of the spectrum also apply.

7.4.5 Considerations on Convergence

In this section we make some specific remarks regarding the convergence of the calculations described in Sects. (7.4.1)–(7.4.4). The analogous calculations in [76] were performed at most with $l_{\mathrm{M}} = 4$, which was sufficient to ensure the convergence of the single spheres. However, the results that we presented above were obtained with $l_M = 12$ in order to increase the degree of convergence also for the aggregates in case they contain some metallic material. In fact, the features of the refractive index of metallic materials are known to affect the rate of convergence at resonance. We already remarked that in the case of the binary aggregates of metal spheres with a dielectric coating the increase of l_M yields further peaks of small intensity in the lower part of the spectrum. A similar situation occurs for the aggregates of metal spheres with a metallic coating. Since this is the worst case we dealt with for coated spheres, further investigation was felt to be in order. Accordingly, we report in Fig. 7.33 the results of our study for the aggregates of spheres of Ag with a coating of Al. First, we notice that the increase of l_M from 12 to 16 has no influence on the high-frequency part of the spectrum. Actually, Fig. 7.33 shows that the peak at $0.93\,\omega_p$ remains unaffected. On the contrary, at low frequency the increase of l_M yields small but still noticeable shifts of the peaks toward lower frequencies; no new peaks appear in the region of interest, however. Therefore, one may wonder what value of l_M would ensure the true convergence. In practice, since with increasing l_M the shift of the low-frequency peaks is comparatively small on a wavelength scale, we are led to conclude that the choice of l_M depends on the experimental capabilities. In other words, one must consider that the shifts may be smaller than the experimental error and that, when further small peaks are invoked by

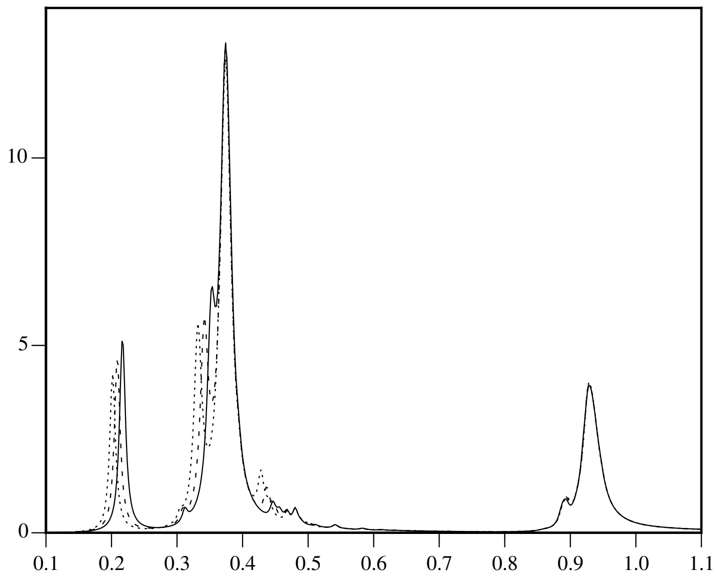

Fig. 7.33. Q' as a function of ν for spheres of Ag of radius 10 nm inclusive of a coating of Al of 2 nm thickness, for $l_M = 12$ (*solid curve*), $l_M = 14$ (*dashed curve*), and $l_M = 16$ (*dotted curve*)

the calculation, their intensity may be hard to be discriminated against the unavoidable background noise.

7.5 Spheres Sustaining the Propagation of Longitudinal Waves

The solution to the problem of convergence for aggregates of metal spheres may stem from the remark that many metals can sustain the propagation of longitudinal waves. The calculations that were discussed in the preceding sections are based on the assumption that the optical properties of a metal are sufficiently well described by a dielectric function of the Drude form. Actually, the results obtained by Ruppin [73] for single spheres of sodium with radius 15 and 30 Å suggest that considering also the propagation of longitudinal waves may be effective in improving the convergence. This section is just devoted to the examination of this possibility.

We consider homogeneous spheres of potassium with radius $\rho = 10\,\text{nm}$ and their binary aggregates. The dielectric properties of the metal were assumed to be well described by the simplified form reported by Pack [142] of the Lindhard [143] dielectric function. The transverse part of the dielectric function turns out to coincide with that of Drude, whereas the longitudinal part reads

$$\epsilon_{\mathrm{L}} = 1 - \frac{\omega_{\mathrm{p}}^2}{\omega(\omega + \mathrm{i}\Gamma\omega_{\mathrm{p}}) - \beta^2 k^2}$$

where, to first approximation, $\beta^2 = \frac{3}{5}v_{\mathrm{F}}^2$, where v_{F} is the Fermi velocity, whose value for potassium [137] is 0.86 cm/s. Nevertheless, since the quoted value of β is the one appropriate for bulk materials, we preferred to use the value corrected by Kleinman [144] for small particles, i.e. $\beta^2 = 0.53v_{\mathrm{F}}^2$, that is little different from the uncorrected value, however. The value of $\Gamma = 0.02$ throughout the whole range of interest has been taken from Table 7.4. We do not consider the case of layered spheres because it should be dealt with through a specific approach.

In order to allow for a direct comparison with the results of Sect. 7.4.5, the polarization of the incident wave has been assumed to be linear and the binary aggregates were assumed to be in random orientation. Our first step is to study the rate of convergence of the single spheres when the dielectric function allows for longitudinal waves. The results are reported in Fig. 7.34 where we compare Q'_{sp} calculated for $l_{\mathrm{M}} = 8$ using the dielectric function of Drude with the same quantity calculated with the dielectric function reported by Pack [142]. We notice that $l_{\mathrm{M}} = 8$ is quite sufficient to get fair convergence for the single spheres when the Drude dielectric function is used. Even a cursory glance at Fig. 7.34 shows that allowing for longitudinal waves has dramatic effects both on the shape of the resonance peaks and on the rate of convergence. In practice, the single resonance peak yielded by the Drude

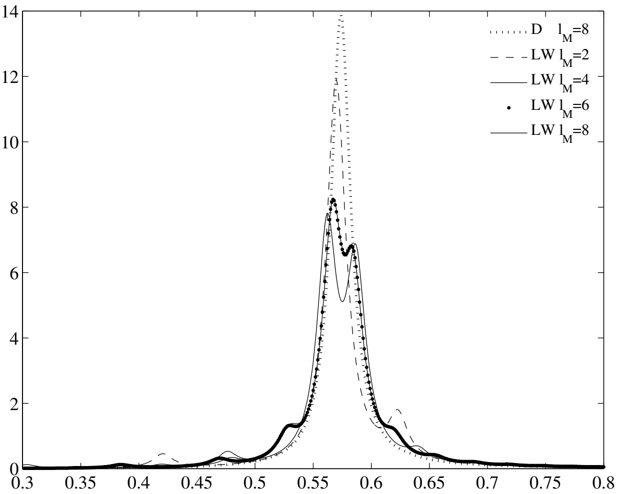

Fig. 7.34. Comparison of $Q'_{\rm sp}$ as a function of $\nu = \omega/\omega_{\rm p}$ for single spheres of potassium calculated with the Drude dielectric function and with the dielectric function of Lindhard as reported by Pack

function splits into two peaks when longitudinal waves can be sustained. In the latter case the rate of convergence is a little slower, as $l_{\rm M} = 12$ is necessary to get fair convergence. Moreover, in the presence of longitudinal waves, an increasing number of small peaks appear on the low-frequency part of the spectrum as $l_{\rm M}$ is increased. This result may seem to be rather discouraging as we get, for single spheres, the same result that in the preceding section we got for binary aggregates. Actually, Fig. 7.35 in which we report Q' for binary aggregates in random orientation, clearly shows that the appearance of new peaks with incresing $l_{\rm M}$ is a feature of the spectrum of binary aggregates when the Drude dielectric function is used. The analogy with our findings for aggregates of layered spheres (see Fig. 7.33) is evident, but the present result suggests that the occurrence of new peaks is not due to stratification of the aggregating spheres. Finally, in Fig. 7.36 we report the rate of convergence of Q' for binary aggregates that can sustain the propagation of longitudinal waves. It is quite evident that the low frequency peaks are strongly damped and that stability of the spectra has been achieved. Note finally, that the splitting of the main peak that occurs for single spheres remains as a shoulder on low-frequency side of the main peak in the spectrum of binary clusters.

In conclusion, although considering the propagation of longitudinal waves, slows down the rate of convergence and complicates the spectra of single spheres, in the case of binary aggregates it yields simpler spectra that are well convergent for quite acceptable values of $l_{\rm M}$. Of course, further investigation is granted in order to verify the generality of this result when the degree of aggregation increases and when the size of the spheres is changed.

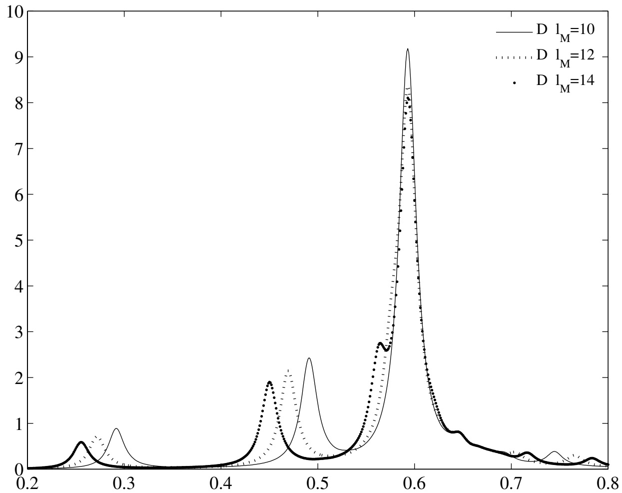

Fig. 7.35. Q' as a function of $\nu = \omega/\omega_{\mathrm{p}}$ for several values of l_{M} for binary aggregates of spheres of potassium in random orientation calculated with the Drude dielectric function

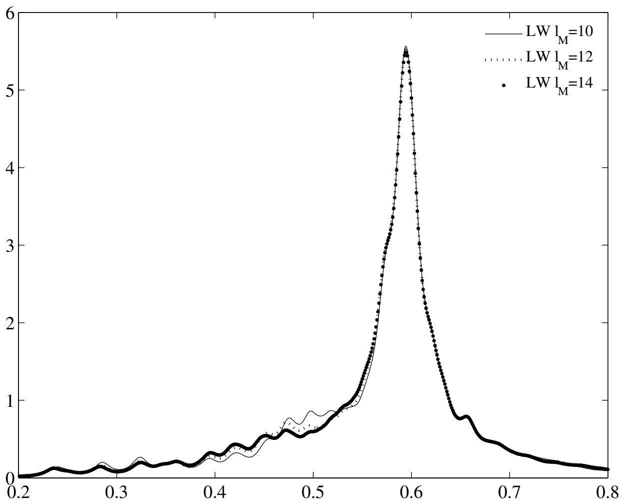

Fig. 7.36. Q' as a function of $\nu = \omega/\omega_{\mathrm{p}}$ for several values of l_{M} for binary aggregates of spheres of potassium in random orientation calculated with dielectric function of Lindhard as reported by Pack

Needless to say that the reliability of the spectra calculated by considering the propagation of longitudinal waves should be also verified through appropriate experiements.

7.6 Spheres Containing Inclusions

Spheres containing one or more spherical inclusions may be a good model for several interesting objects, such as biological cells, water droplets containing pollutants, and complex interstellar dust grains, e.g. fluffy grains.

The calculations we are going to discuss are based on the theory of Sect. 5.5 that is subject to no limitation of principle as regards the size of the host sphere and the number and chemical composition of the inclusions [88, 89]. Nevertheless, in the present section, we consider spheres containing at most two inclusions that may be either metallic, dielectric, or also empty. In fact, it would be an impossible task to extract from the results for spheres containing many inclusions the general features that depend on the configuration of the inclusions present. The case of many inclusions will be dealt with as a specific application in Chap. 10.

Our calculations are performed with reference to the following geometry. The host sphere is centered at the origin of a system of Cartesian axes and the center of one of the inclusions always lies on the z axis. The incident field is a plane wave whose wavevector is individuated by the polar angles ϑ_{I} and φ_{I}, whereas ϑ_{S} and φ_{S} are the polar angles of the direction of observation. Our calculations were performed with $\vartheta_{\mathrm{I}} = 0$, $\pi/4$, $\pi/2$, and $\varphi_{\mathrm{I}} = 0$, and, indicating by Φ $(0 \le \Phi \le \pi)$ the angle of scattering,

$$\begin{aligned} \vartheta_{\mathrm{S}} &= \vartheta_{\mathrm{I}} + \Phi \text{ and } \varphi_{\mathrm{S}} = 0 \qquad \text{for } \vartheta_{\mathrm{I}} + \Phi < \pi\,, \\ \vartheta_{\mathrm{S}} &= 2\pi - (\vartheta_{\mathrm{I}} + \Phi) \text{ and } \varphi_{\mathrm{S}} = \pi \quad \text{for } \vartheta_{\mathrm{I}} + \Phi > \pi\,. \end{aligned}$$

Therefore the plane of scattering coincides with the zx plane to which the polarization vector both of the incident and of the scattered field is always parallel ($\hat{\boldsymbol{e}} = \hat{\boldsymbol{u}}_1$) or orthogonal ($\hat{\boldsymbol{e}} = \hat{\boldsymbol{u}}_2$).

The scattering properties of a sphere containing spherical inclusions are described through its normalized scattering amplitude. More precisely, we report the quantities [86] P' and Q' that are defined in (7.1). We also report the averages $\bar{P}$ and $\bar{Q}$ for random orientational distribution. Of course, the latter are meaningful for forward scattering only ($\Phi = 0$) (see Sect. 4.5). The quantities $\bar{P}$ and $\bar{Q}$ give information on the macroscopic optical properties of a tenuous dispersion of the scatterers we deal with.

Since the objects we deal with have a size parameter $x = k\rho_0 > 1$, the value of l_{M} that is necessary to get fully converged results turns out to be rather large. As a criterion of full convergence, we required that, with respect to the any increase of l_{M}, our results be stable at least to 4 significant digits. This accuracy is by far higher than required for any graphical display. It may be interesting to notice that, in agreement with the remarks by other workers dealing with dependent scattering from aggregated spheres, we met the slowest convergence when the surfaces of one of the inclusions and of the host sphere touch each other [145].

In Sects. (7.6.1)–(7.6.3), we present the results of our calculations for a dielectric host sphere with refractive index $n_{\mathrm{D}} = 1.61 + \mathrm{i}0.004$, which describes satisfactorily the optical properties of spheres of acrylic in a large frequency range. In all cases, the external medium is assumed to be the vacuum ($n = 1$). For the sake of simplicity, the dielectric properties of the metallic inclusion are assumed to be well described by the free-electron Drude function with $\Gamma = 0.01$ and $\omega = 0.1\,\omega_{\mathrm{p}}$. The latter for most metals corresponds to a frequency in the visible or in the infrared range [137], and the resulting refractive index of the inclusion is $n_{\mathrm{M}} = \sqrt{\epsilon_{\mathrm{M}}} = 0.4994 + \mathrm{i}9.9126$. Note that no resonance occur for this value of the refractive index. The resonances of a dielectric sphere containing a metallic inclusion will be discussed in Sect. 7.6.4.

7.6.1 Metallic Inclusion in a Dielectric Sphere

The size parameter of the host dielectric sphere and of the inclusion are $x_{\mathrm{D}} = 3$ and $x_{\mathrm{M}} = 1$, respectively, so that the ratio of their radii is $\rho_{\mathrm{D}}/\rho_{\mathrm{M}} = 3$. The *eccentricity* of the inclusion is accounted for by the parameter $x_{\mathrm{E}} = k_{\mathrm{v}} z$, where z is the coordinate of the center of the inclusion. Therefore $|x_{\mathrm{E}}|$ can range from $|x_{\mathrm{E}}| = 0$, when the inclusion is concentric, to $|x_{\mathrm{E}}| = 2$, when it is tangent to the surface of the host sphere [88]. In our calculations for $\hat{\boldsymbol{k}}_{\mathrm{S}} = \hat{\boldsymbol{k}}_{\mathrm{I}}$, i.e., when forward scattering is considered, z is allowed to assume positive values only, on account of the symmetry properties of the scattering amplitude that are discussed, e.g., by van de Hulst [5]. The results we are going to illustrate required at most $l_{\mathrm{M}} = 10$ to reach full convergence.

The quantities P' and Q' as a function of x_{E} for the three directions of incidence referred to above and for polarization both parallel and orthogonal

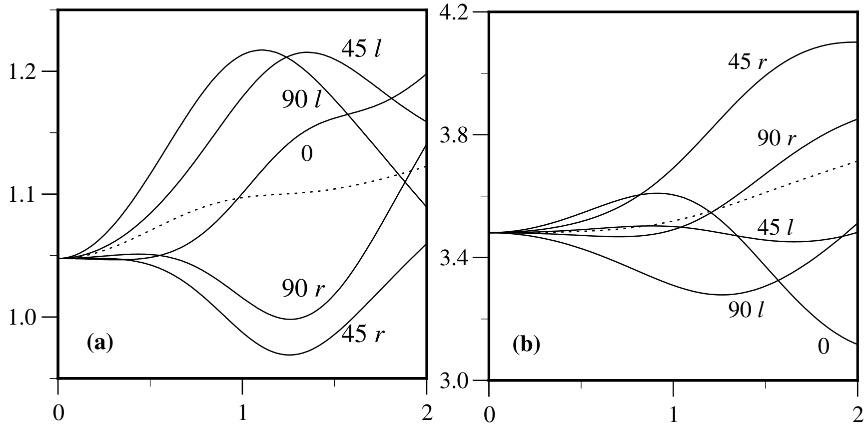

Fig. 7.37. P' **(a)** and Q' **(b)** for $\hat{\boldsymbol{k}}_{\mathrm{S}} = \hat{\boldsymbol{k}}_{\mathrm{I}}$ as a function of the eccentricity x_{E} for a dielectric sphere containing a metallic spherical inclusion (*solid curves*). These curves are labeled by the value of ϑ_{I} and by l or r to denote polarization parallel or perpendicular to the plane of scattering, respectively. The *dotted curves* report $\bar{P}$ in **(a)** and $\bar{Q}$ in **(b)**

to the plane of scattering are reported in Fig. 7.37. In the same figure we also report the averages $\bar{P}$ and $\bar{Q}$ that, for random orientational distribution, are independent both of the direction and of the polarization of the incident wave. Of course, P' and Q' are also independent of the polarization when the direction of incident wavevector lies along the symmetry axis ($\vartheta_{\mathrm{I}} = 0$), but, when $\vartheta_{\mathrm{I}} = \pi/4$ and $\vartheta_{\mathrm{I}} = \pi/2$, they become strongly dependent on the polarization. A further interesting remark is at hand in the results of Fig. 7.37. If we consider only one state of polarization, either parallel or orthogonal, the curves for $\bar{P}$ and $\bar{Q}$ do not always lie within the curves for the various incidences, contrary to what would be expected of averaged quantities. A similar effect that also occurred for clusters in free space (see Sect. 6.1) is due to the contributions to $\bar{P}$ and $\bar{Q}$ coming from scatterers so oriented that their symmetry axis do not lie in the plane of scattering. These contributions are never explicitly computed but are automatically accounted for by the averaging procedure. Indeed, the response of a scatterer with its symmetry axis not lying in the scattering plane is easily recognized as identical to the response of a scatterer with its axis in that plane when this latter object is excited by a wave with an appropriate state of polarization that, in general, is neither parallel nor orthogonal. Therefore, the above mentioned response must be a linear combination of the responses for parallel and orthogonal polarization and, since the scattering properties of the objects we are dealing with here show a noticeable sensitivity to the state of polarization, we get the seemingly anomalous behavior of $\bar{P}$ and $\bar{Q}$ described above.

As a reference we also calculated P' and Q' for a homogeneous dielectric sphere either with the same radius of the host sphere ($P'_{\mathrm{h}} = 1.3173$ and $Q'_{\mathrm{h}} = 3.9117$) or containing the same quantity of dielectric material as the sphere with the inclusion ($P'_{\mathrm{e}} = 1.3151$ and $Q'_{\mathrm{e}} = 3.9044$). Indeed, a comparison of these values with those of the curves in Fig. 7.37 will give a better insight into the effect of the very presence of the inclusion and of its eccentricity as well. Let us remark, first of all, that P'_{h} and P'_{e} as well as Q'_{h} and Q'_{e} differ very little from each other because the ratio of the volumes of the homogeneous spheres defined above is 27/26 on account of our choice $\rho_{\mathrm{D}}/\rho_{\mathrm{M}} = 3$. Moreover, the values of P' and Q' for a sphere with a centered inclusion ($x_{\mathrm{E}} = 0$) are remarkably different from the corresponding values for the homogeneous dielectric spheres of both sizes considered above. When x_{E} increases the difference of $\bar{P}$ and P'_{h} and, especially, that of $\bar{Q}$ and Q'_{h}, tend to decrease while the behavior of the difference of P' and P'_{h} as well as that of Q' and Q'_{h} depends on the direction of incidence and, in general, also on the polarization. In fact, the spread of the curves of P' and Q' is rather large and reaches its maximum in the range $x_{\mathrm{E}} \simeq 1.15$–$1.35$ (Fig. 7.37 (a)) and for $x_{\mathrm{E}} = 2$ (Fig. 7.37 (b)), respectively.

In Fig. 7.38 we show $P'(\Phi)$ vs. $Q'(\Phi)$ for parallel polarization and for $\vartheta_{\mathrm{I}} = 0$ (a), $\vartheta_{\mathrm{I}} = \pi/4$ (b), and $\vartheta_{\mathrm{I}} = \pi/2$ (c). In each figure, we report the curves for the extreme values of the eccentricity ($x_{\mathrm{E}} = 2$ and $x_{\mathrm{E}} = -2$) as well

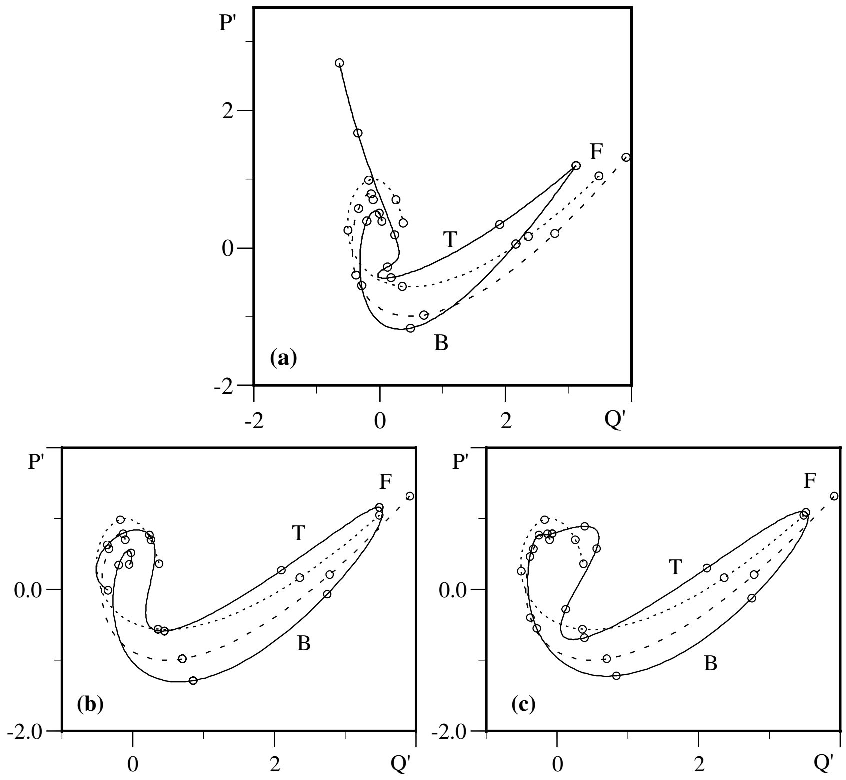

Fig. 7.38. $P'(\Phi)$ vs. $Q'(\Phi)$ for $\vartheta_{\mathrm{I}} = 0$ **(a)**, $\pi/4$ **(b)** and $\pi/2$ **(c)** for the dielectric sphere containing the metallic inclusion. The polarization is parallel to the plane of scattering. The *solid curves* labeled T and B refer to the inclusion at eccentricity $x_{\mathrm{E}} = 2$ and $x_{\mathrm{E}} = -2$, respectively. The *dotted curve* refers to a centered inclusion and the *dashed curve* to $P'_{\mathrm{h}}(\Phi)$ vs. $Q'_{\mathrm{h}}(\Phi)$. The *circles* on all the curves mark the value of the scattering angle Φ at 30° intervals. The forward direction $\Phi = 0°$ is labeled F

as the curve for the centered inclusion ($x_{\mathrm{E}} = 0$). As a reference, the curve of $P'_{\mathrm{h}}(\Phi)$ vs. $Q'_{\mathrm{h}}(\Phi)$ is also reported. Of course, both the curves for the centered inclusion and for the homogeneous sphere do not depend on the incidence and are thus the same in all these figures. It is easily seen that the curves for the spheres with an eccentric inclusion are rather different from each other and differ also from those both for the sphere with a centered inclusion and for the homogeneous sphere. For forward scattering ($\Phi = 0$), the curves for the two eccentric positions stick together as expected on account of the symmetry properties of the scattering amplitude. At all incidences, the position of the inclusion within the external sphere has an evident effect on the shape of the Q'-P' curves, although the general behavior remains unchanged. When the incidence is orthogonal to the symmetry axis ($\vartheta_{\mathrm{I}} = \pi/2$), the curves for $x_{\mathrm{E}} =$

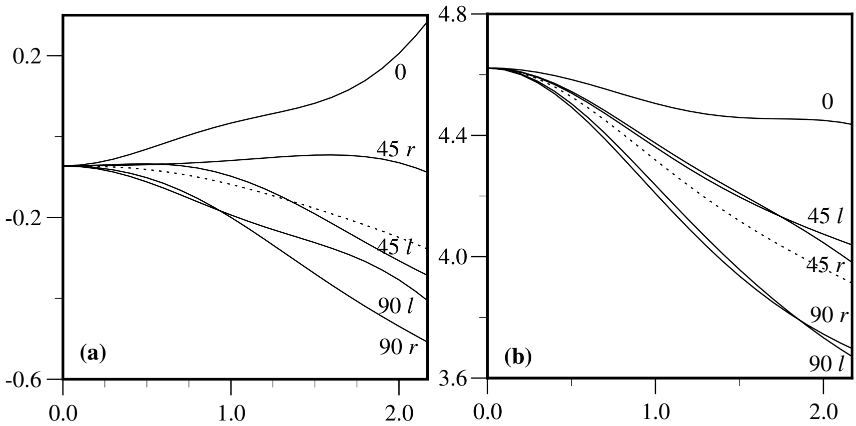

Fig. 7.39. P' **(a)** and Q' **(b)** as a function of x_{E} for dielectric spheres containing the empty spherical cavity. The curves are labelled by ϑ_{I} and by l or r to denote polarization parallel or perpendicular to the plane of scattering, respectively. The *dotted curve* refers to the averages for random orientational distribution

2 and for $x_{\mathrm{E}} = -2$ stick together, not only for forward scattering ($\Phi = 0$) but also at backscattering ($\Phi = \pi$) as required by an obvious symmetry property of the matrix of the scattering amplitude (Fig. 7.38 (c)).

We do not report the curves for orthogonal polarization because, although the numerical values are rather different from those for parallel polarization, the general shape and properties of the curves are identical to those reported in Fig. 7.39 and do not deserve, in our opinion, a separate comment.

7.6.2 Empty Cavity in a Dielectric Sphere

The size parameter of the dielectric external sphere and of the empty cavity ($n_{\mathrm{C}} = 1$) are $x_{\mathrm{D}} = 4.3410$ and $x_{\mathrm{C}} = 2.1705$, respectively, and the ratio of their radii is $\rho_{\mathrm{D}}/\rho_{\mathrm{C}} = 2$. As a consequence, the eccentricity can range from $x_{\mathrm{E}} = 0$ to $x_{\mathrm{E}} = 2.1705$ [88]. Our choice of $x_{\mathrm{D}} = 4.341$ is due to the fact that the experimental scattering properties of a solid dielectric sphere with these features are known [87], so that we often used such an object as a reference scatterer. In the present case the convergence of the results required at most $l_{\mathrm{M}} = 8$.

The main body of our results is displayed in Figs. 7.39 (a) and (b) that are analogous to Figs. 7.37 (a) and (b), respectively. As compared with the results for a metallic inclusion, the present results show a less strong dependence on the polarization and, in particular, this dependence is rather weak for Q' [Fig. 7.39 (b)]. As an immediate consequence, we notice that the curve of $\bar{Q}$ always lies within the curves of Q' for a single polarization although they refer only to orientations with the symmetry axis in the scattering plane.

The results both for the solid dielectric sphere with radius equal to that of the external sphere (the reference sphere mentioned above) and of the sphere containing the same quantity of dielectric material as the sphere with the inclusion are $P'_{\rm h} = -0.9238$, $Q'_{\rm h} = 3.8373$, and $P'_{\rm e} = -0.7796$, $Q'_{\rm e} = 4.1082$, respectively. In the present case these values are noticeably different from each other since the ratio of the radii $\rho_{\rm D}/\rho_{\rm C} = 2$ implies that the ratio of the volumes is $8/7$. Furthermore, the relative positions of these values show that P' and Q' for a homogeneous sphere are, in this range, decreasing functions of the size parameter. Figures 7.39 (a) and (b) show that even in the present case, $\bar{P}$ and especially $\bar{Q}$, as the eccentricity increases, tend to reduce their difference both from $P'_{\rm h}$ and $Q'_{\rm h}$ and from $P'_{\rm e}$ and $Q'_{\rm e}$. The spread of the values for the different incidences we considered reaches a rather large maximum at the highest value of the eccentricity. Although we also performed calculations analogous to those displayed in Fig. 7.38, we resolved not to report the results because they do not show any new significant feature worthy of a separate comment.

7.6.3 Spheres Containing Two Metallic Inclusions

We now go to consider a homogeneous sphere containing two identical spherical inclusions. In fact, the subdivision of the included material into two identical inclusions proved to be quite sufficient to appreciably change the scattering properties in comparison to the case of a single inclusion with the same volume. The size parameter of the host sphere is $x_{\rm D} = 3$. Both the inclusions have size parameter $x_{\rm I} = k_{\rm v}\rho_{\rm I} = 0.7937$, so that their total volume equals that of a single inclusion with unit size parameter [89]. The centers of the two inclusions lie either both on the z axis or one on the z axis and the other outside the z axis in the plane $\varphi = 0$. The latter choice prevents, of course, the existence of a cylindrical symmetry. In the following figures, we report, for each of the three directions of incidence mentioned above, the efficiencies Q'_η for $\hat{\boldsymbol{k}}_{\rm S} = \hat{\boldsymbol{k}}_{\rm I}$ and $\bar{Q}$ as a function of the position of the inclusions within the external sphere. The geometrical arrangements that we consider in this section are such that the position of the two inclusions can be defined by the parameters $x_{{\rm E}_1} = k_{\rm v}z_1$ and $x_{{\rm E}_2} = k_{\rm v}z_2$, where z_1 and z_2 are the z coordinates of their centers. As $x_{{\rm E}_1}$ and $x_{{\rm E}_2}$ turn out to be mutually dependent, Q'_η and $\bar{Q}$ are reported as a function of the eccentricity $x_{{\rm E}_2}$ only. Q'_η and $\bar{Q}$ are also reported for the sphere containing a single spherical inclusion, with its center on the z axis and volume equal to the sum of the volumes of the two inclusions above, as a function of its eccentricity $x_{\rm E} = k_{\rm v}z$. This kind of inclusion, that we dealt with in Sect. 7.6.1, hereafter will be referred to as the equivalent inclusion. It has unit size parameter so that its eccentricity always range between 0 and 2. The comparison of the curves for the case of two inclusions and the case of the equivalent inclusion will give a clear view of the effects of the subdivision of the included material.

In Figs. 7.40 (a), (b), and (c) we report, for $\vartheta_{\mathrm{I}} = 0$, $\pi/4$ and $\pi/2$, respectively, the results for spheres containing two inclusions with the centers on the z axis and lying symmetrically with respect to the center of the host sphere. Therefore $x_{E_1} = -x_{E_2}$ and the smallest value of $x_{\mathrm{E}_2} = 0.7937$ occurs when the inclusions contact each other at the center of the external sphere; the maximum value of $x_{\mathrm{E}_2} = 2.2063$ occurs when the inclusions touch the surface of the host sphere.

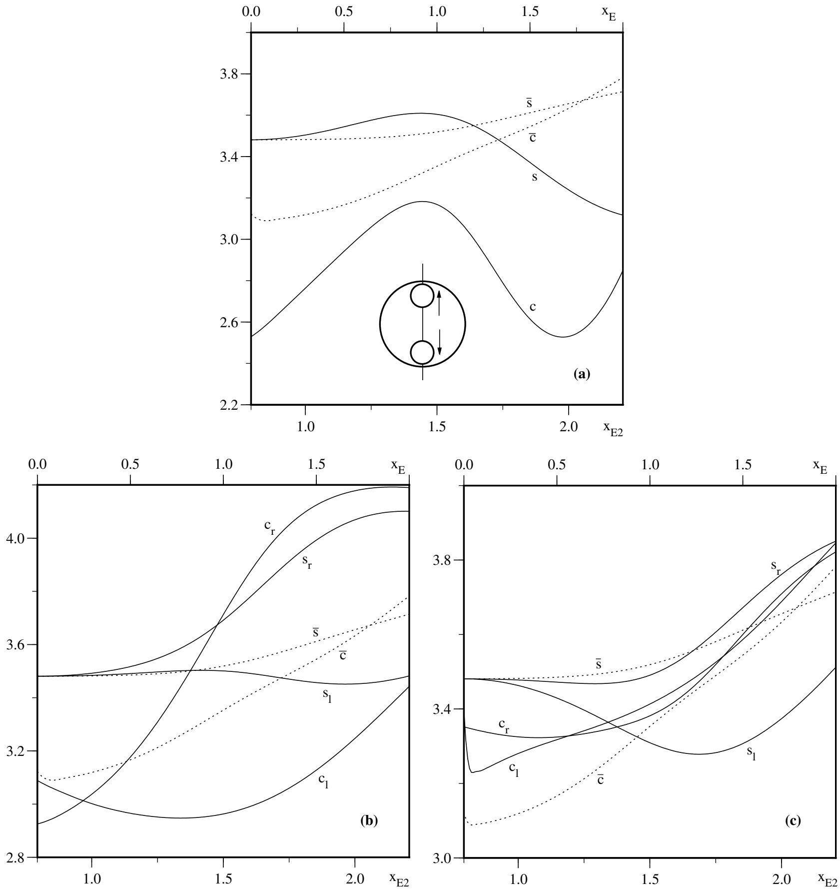

Fig. 7.40. Q'_η (*curves* c) and $\bar{Q}$ (*curves* $\bar{\mathrm{c}}$) for spheres containing two identical inclusions arranged as in the inset in **(a)**, plotted versus x_{E_2} in the range from 0.7937 to 2.2063. For the sake of comparison, Q'_η (*curves* s) and $\bar{Q}$ (*curves* $\bar{\mathrm{s}}$) for spheres containing the equivalent inclusion are also plotted versus x_{E}. The angles of incidence are $\varphi_{\mathrm{I}} = 0$ in all cases and $\vartheta_{\mathrm{I}} = 0$, $\pi/4$ and $\pi/2$ in **(a)**, **(b)**, and **(c)** respectively. The subscripts l and r refer to polarization parallel and perpendicular the plane of scattering, respectively

In Fig. 7.41 the centers are still on the z axis but the two inclusions are always in contact and are translated along the z axis. In this case, $x_{\mathrm{E}_1} = x_{\mathrm{E}_2} - 2x_{\mathrm{I}}$ and $x_{\mathrm{E}_2} = 0.7937$, when the point of contact coincides with the center of the external sphere, and $x_{\mathrm{E}_2} = 2.2063$, when inclusion 2 touches the surface of the external sphere. The true minimum of x_{E_2} actually occurs at the negative value $x_{\mathrm{E}_2} = 3x_{\mathrm{I}} - x_{\mathrm{D}} = -0.6189$, i.e., when inclusion 1 touches the surface of the external sphere. Nevertheless, this choice would add no new information on account of the symmetry properties of the scattering amplitude [5].

In Fig. 7.42 we consider a configuration in which, unlike the preceding cases, no cylindrical symmetry is present. In fact, we put the two inclusions

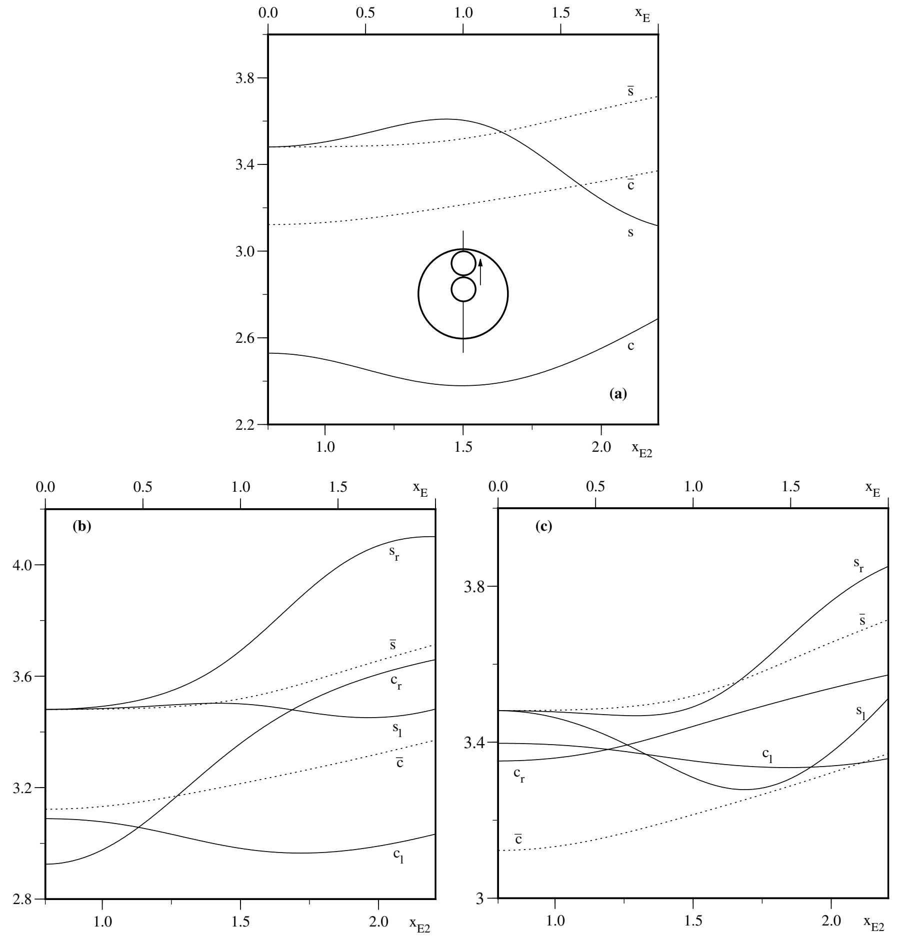

Fig. 7.41. Q'_η and $\bar{Q}$ same as in Fig. 7.40 but for the geometric arrangement of the inclusions illustrated in the inset in **(a)**

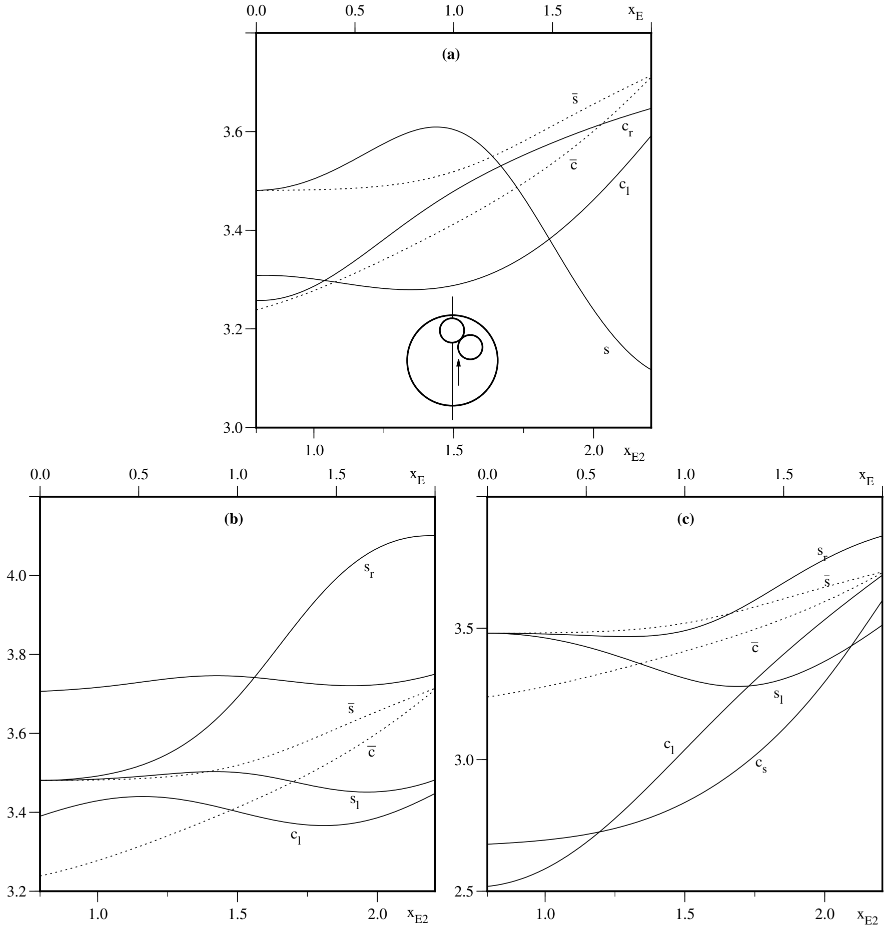

Fig. 7.42. Q'_η and $\bar{Q}$ same as in Fig. 7.40 but for the geometric arrangement of the inclusions illustrated in the inset in **(a)**

in contact and the center of inclusion 2 always lies on the z axis while the center of inclusion 1 is in the plane $\varphi = 0$ with $z_1 = z_2 - \rho_\mathrm{I}$ so that its distance from the z axis is $d = \rho_\mathrm{I}\sqrt{3}$; x_{E_2} ranges from $x_{\mathrm{E}_2} = 0.7937$ to $x_{\mathrm{E}_2} = 2.2063$. In this case, our choice of the minimum value of x_{E_2} privileges the uniformity of the presentation of our results even at the cost of excluding some new information that, in our opinion, is not particularly significant, however. Note that $\bar{\mathrm{s}}$ at $x_\mathrm{E} = 2$ and $\bar{\mathrm{c}}$ at $x_{\mathrm{E}_2} = 2.2063$ seem to coincide. This is a mere accident, however, that is due to the scale of the figure.

As regards the value of l_M that is necessary to get fairly convergent results, we found that $l_\mathrm{M} = 10$ is quite sufficient to get the required accuracy.

When considering the results reported in Figs. 7.40–7.42 it should be borne in mind that a rather complex mechanism displays its effects. In fact, when the inclusions become more and more distant, the effects of the multiple scattering processes occurring between them may become faint. When the inclusions are going to touch the surface of the host sphere it is easy to foresee a strong interaction. Both the decreasing symmetry of the scatterers we dealt with and the direction of $\hat{\boldsymbol{k}}_{\mathrm{I}}$ concur with the above mentioned multiple scattering processes in determining the calculated dependence on the polarization.

In Fig. 7.43 we summarize all the preceding results for $\bar{Q}$ as a function of x_{E_2} so as to give a general view of the optical properties of the model media composed of a tenuous dispersion of the scatterers considered so far. In particular, since Fig. 7.43 also includes the curve of $\bar{Q}$ as a function of x_{E} for a dispersion of spheres containing the equivalent inclusion (curve a), one can easily see the effect on the extinction of the subdivision of the included material. At least for the cases we considered in this section the subdivision slightly reduces the extinction efficiency; $\bar{Q}$, however, recovers the loss when the separation between the inclusions increases (curve b). Anyway, even a careful examination of the results does not reveal a trend that allows us to understand whether the included material is subdivided or not. Of course, the optical properties of the random dispersions do not show any dependence on the polarization as it is compensated for by the average over the orientations. On the contrary, the dependence on the polarization is present in the spectra of the single spheres and is, as expected, dominated by the symmetry of the distribution of the included material. We can summarize our findings by remarking that the optical properties of a tenuous dispersion are determined by the strength of the multiple scattering processes that occur within each sphere.

We do not compare our findings with specific experimental data that, as far as we know, are not available, but we are confident that our results have a high degree of reliability. In fact, our results were reproduced by Ioannidou and Chrissoulidis [92] as a test of their reformulation of the theory of scattering by spheres containing several inclusions. Moreover, even in the present case, all the tests that we described in our previous work [88] were successfully performed. In particular, by putting $n_0 = 1$, i.e., by assuming that the interstitial medium is the vacuum, we got the same results as for bare clusters.

The results that we presented above do not pretend to be exhaustive, as their purpose is to give relevant examples of the effects of the subdivision of the included material according to known geometries. In fact, even a cursory examination of the results shows that the subdivision has rather visible effects on the properties both of single objects and of their dispersions. It is also apparent that the optical behavior is so dependent on the geometry that

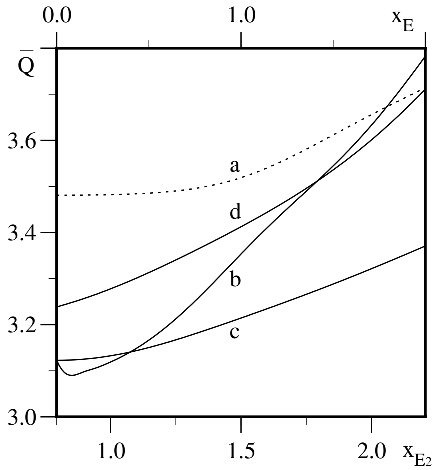

Fig. 7.43. Summary of the curves for $\bar{Q}$ versus x_{E_2}. For the sake of comparison we also include the curve for $\bar{Q}$ (*curve* a) versus x_E for the sphere containing the equivalent inclusion. The labels b, c, and d refer to the curves coming from Figs. 7.40, 7.41 and 7.42, respectively

understanding how the included material is subdivided seems to be excluded, at least by a simple examination of the extinction spectrum.

We considered spheres containing at most two inclusions, whereas, in actual cases, the included material is often more minutely subdivided. Such a choice is not dictated by any limitation of the formalism but rather by the consideration that a rigorous treatment of spheres containing a very large number of small inclusions may be a nonsense. In fact, when the number of the inclusions is very large, the spheres may present a spongy appearance and could be more efficiently described, for instance, by simulating their properties through an effective dielectric function and, possibly, by assuming the presence of a soft surface [76]. Nevertheless, some experimental results show that sometimes, when the number of the inclusions is large but not too large, there occur effects that cannot be explained in terms of an effective dielectric constant. We refer to the correlation-spectroscopy experiments of Bronk, Smith, and Arnold on 30 μm droplets containing more than 100 small inclusions [146] and on the suppression of the lasing effect from ethanol droplets by the presence of several submicrometer latex inclusions as reported by Armstrong et al. [147]. Furthermore a perturbation technique has been devised by Ng, Leung, and Lee [148] just to deal, with not too heavy computational effort, with the case of spheres containing many inclusions. In view of these experimental findings as well as on account of the results in this section, we are led to conclude that a lot of both experimental and theoretical work is still necessary in order to gain understanding of the effects of included material within an otherwise homogeneous particle.

7.6.4 Resonances of a Sphere Containing a Spherical Inclusion

In this section we resort to the potentialities of the transition matrix approach to study the resonances of spheres containing a spherical eccentric inclusion. This kind of scatterer, in spite of its seemingly spherical appearance, is intrinsically nonspherical so that it may be useful to highlight the differences of its resonance spectrum from that of truly spherical particles. According to (5.39) that gives, in compact form, the transition matrix of a homogeneous sphere containing a single spherical inclusion,

$$\left(\mathrm{R}_0^{-1} - \mathrm{R}_W \mathrm{J}_{0\leftarrow 1} \mathrm{R}_1 \mathrm{J}_{1\leftarrow 0}\right)^{-1} \tag{7.4}$$

is responsible for resonances, just as R_0 does in the case of homogeneous spheres. Nevertheless, (5.39) contains the translation matrices $\mathrm{J}_{0\leftarrow 1}$ and $\mathrm{J}_{1\leftarrow 0}$ that account for the eccentricity of the inclusion. As a result, we should expect an evolution of the resonance spectrum when a centered inclusion becomes more and more eccentric.

The particle that we choose for our study is of interest in astrophysics. In fact, we consider the extinction spectrum of spheres of MgO with a radius $\rho_0 = 25\,\mathrm{nm}$ containing a spherical inclusion of Mg with a radius of $\rho_1 = 16.6\,\mathrm{nm}$. In other words, we are considering a metal sphere coated by its oxide [149]. ρ_0 and ρ_1 were chosen so as to lie within the estimated ranges for the particles in the interstellar medium [150]. Furthermore, our choice of the radii implies that the particles, although small, can have resonances also for $l > 1$. As in Sect. 7.4.2, the dielectric function of Mg was assumed to be of the free-electron Drude form [137], that of MgO was assumed of the damped oscillator form [136], and the related parameters are reported in Table 7.4. The geometry that we assumed is identical to what we used in Sects. 7.6.1–2. Accordingly, the center of the inclusion always lies on the z axis and the plane of scattering was assumed to be the zx plane.

The results are presented by reporting the extinction efficiency Q'_η as a function of the ratio $\nu = \omega/\omega_\mathrm{p}$. Of course, Q'_η is independent of the polarization both when the incidence is along the z axis and when the inclusion takes a centered position so that the scatterer as a whole becomes spherically symmetric. In these cases, the polarization index η will be dropped. The results are better understood by recalling (4.29) for the elements of the scattering amplitude in terms of the transition matrix elements and of the amplitudes both of the incident and of the scattered field. It is an easy matter to show that, on account of the assumed geometry,

$$W^{(p)}_{\mathrm{I}\eta lm} = (-)^{\eta+p+m-1} W^{(p)}_{\mathrm{I}\eta l,-m}$$

and that the transition matrix elements have the property

$$\mathcal{S}^{(pp')}_{ll';m} = (-)^{p-p'} \mathcal{S}^{(pp')}_{ll';-m} \,.$$

An immediate consequence of the equations above is that the resonances for given η, p, and l that are associated to $\pm m$ are degenerate, i.e., they occur at the same frequency. These considerations are useful when we separate the contributions from each l to the scattering amplitude. To this end, we carry to convergence the calculation of the transition matrix and write the corresponding scattering amplitude as

$$f_{\eta\eta'} = \sum_l B_{\eta\eta' l} \ , \tag{7.5}$$

where

$$B_{\eta\eta' l} = -\frac{\mathrm{i}}{4\pi k} \sum_{pm} \sum_{p'l'} W^{(p)*}_{\mathrm{S}\eta lm} \mathcal{S}^{(pp')}_{ll';m} W^{(p')}_{\mathrm{I}\eta' l' m} \ .$$

We then define the partial efficiencies

$$q_{\eta l} = \frac{4}{k\rho_0^2} \mathrm{Im}\big(B_{\eta\eta l}\big) \ ,$$

which give the contribution to the extinction from multipoles of order l.

In Fig. 7.44 we report Q' for a sphere of solid Mg with radius ρ_1. The reader may find useful the comparison with Fig. 7.30 (a). In order to check the convergence of our calculations and to associate the computed resonances to the appropriate value of l, the extinction efficiency is reported for $l_{\mathrm{M}} = 1$ and $l_{\mathrm{M}} = 2$, l_{M} being the maximum value of l included into (7.5). We notice that taking $l_{\mathrm{M}} > 2$ neither yield any higher order resonance nor produces visible changes on the scale of the figure. Therefore, although all the calculations were performed with $l_{\mathrm{M}} = 10$, we can state that using $l_{\mathrm{M}} = 5$ is sufficient

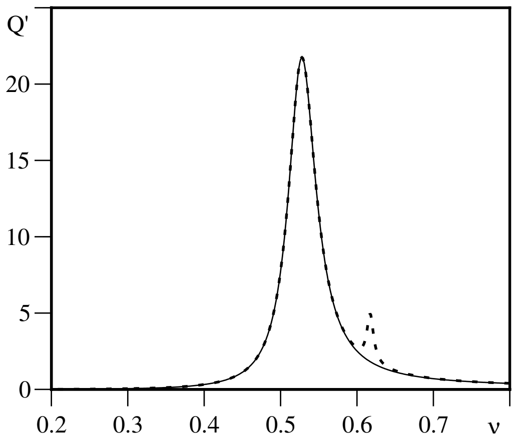

Fig. 7.44. Extinction efficiency for a sphere of solid Mg with radius $\rho_1 = 16.6\,\mathrm{nm}$. The *continuous curve* was obtained with $l_{\mathrm{M}} = 1$ and the *dashed curve* with $l_{\mathrm{M}} = 2$. The incidence is along the z axis

to achieve a numerical accuracy to four significant digits. The sphere of Mg presents two resonances: the lowest-frequency peak is associated with $l = 1$ whereas the second peak is associated with $l = 2$. An analysis of the elements of the transition matrix suggests that both peaks are electric resonances, and, due to the independence of m of the elements of the transition matrix for a sphere, the value of m need not be specified. We do not report Q' for the sphere of MgO of radius ρ_0 because this scatterer does not present any resonance in the range of interest.

As one should expect, we found that the effects that are due to the eccentricity achieve the maximum of evidence when the inclusion becomes tangent to the surface of the external sphere so that in the following figures only the results for this extreme case are reported. Accordingly, Fig. 7.45 shows, for incidence along the z axis, Q'_η for the scatterer with the inclusion at maximum eccentricity together with the partial efficiencies $q_{\eta l}$ with $l = 1, 2$. Of course, due to the cylindrical symmetry of the scatterer, both the total and the partial extinction efficiencies are independent of η. Figure 7.45 also reports Q' for the centered inclusion. In the latter case there occurs a single electric resonance that is associated to $l = 1$, whereas the resonance that for a sphere of solid Mg is associated to $l = 2$ turns out to be so damped as to reduce to a small shoulder. This behavior is easily understood in the framework of the theory of Johnson [78] that we summarized in Sect. 5.3. In fact, the presence of a coating may modify the radial shape of the refractive index $n_0(r)$, and thus of the effective potential (5.22), to such an extent that the potential well for the appropriate value of l (in the present case for $l = 2$) may not occur at all, thus preventing the occurrence of the corresponding resonance, or may become so shallow as to produce the damping that is observed in Fig. 7.45. Considerations of this kind do not apply when the inclusion is off center because of the lack of spherical symmetry. Indeed, Fig. 7.45 shows four resonances. The one at the lowest frequency is associated to $l = 1$ and is the evolution of the main peak that occurs when the inclusion is centered. The three further resonances can be attributed to the multiple scattering processes between the inclusion and the external sphere [88]. Due to the off-center position of the inclusion, these processes are asymmetric and thus yield the observed multiplication of peaks. The behavior of the quantities q_l clearly shows that all these peaks arise from the superposition of contributions for $l = 1$ and $l = 2$. The occurrence of this superposition calls for a word of caution about the classification of the resonances into electric and magnetic as well as about the order of the resonating multipoles. In [151] we noticed that this classification depends on the origin to which the multipole fields are referred. For a sphere with a centered inclusion there exists a natural origin, namely the center of the external sphere that coincides with the center of symmetry of the whole scatterer. Of course, when the inclusion is eccentric such a center of symmetry does not exist. Now, we remarked in Sect. 1.8.3 that a multipole field that is purely electric or magnetic when referred to a

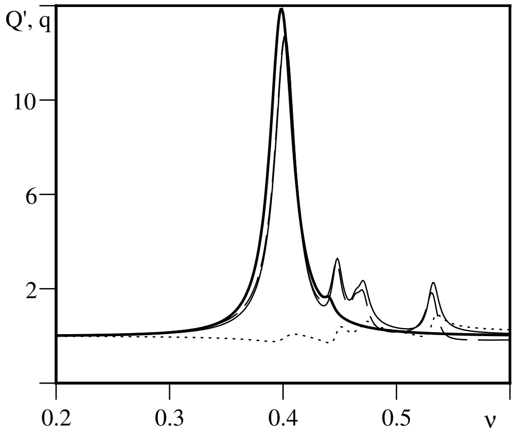

Fig. 7.45. Extinction efficiency for the scatterer with the inclusion centered (*thick solid line*) and with the inclusion at maximum eccentricity (*solid line*). The *dashed curve* and the *dotted curve* report the partial efficiencies for $l = 1$ and $l = 2$, respectively, for the case of maximum eccentricity. The incidence is along the z axis

given origin becomes a superposition of both electric and magnetic multipole fields, in general of all the multiplicities, when referred to a different origin. On the other hand, in the framework of our present approach, the addition theorem of Sect. 1.8, gives rise to the nondiagonal matrices $\mathsf{J}_{0\leftarrow 1}$ and $\mathsf{J}_{1\leftarrow 0}$ in the expression (5.39) of the transition matrix. As these matrices account for the multiple scattering processes between the components of the scatterer, we feel authorized to state that the high frequency peaks are due to multiple scattering processes and that their electric or magnetic nature cannot be stated in an absolute sense but only with reference to the chosen origin that, in the present case, coincides with the center of the host sphere. With this exception in mind, we can safely state, however, that all the resonances in Fig. 7.45 belong to $|m| = 1$ because, for any η, p, and l, the multipole amplitudes $W_{\eta lm}^{(p)}$ of a plane wave that propagates along the z axis do not vanish for $m = \pm 1$ only. Furthermore, the cylindrical symmetry of the scatterer implies that the resonances associated to m and to $-m$ must occur at the same frequency. We finally notice that the same spectrum is obtained by changing the direction of incidence from $\vartheta_{\mathrm{I}} = 0°$ to $\vartheta_{\mathrm{I}} = 180°$. This is an expected result that stems from the symmetry properties of $f_{\eta\eta}$ for forward scattering [5].

The results that we have presented so far show the expected independence of the polarization either because the scatterer is spherically symmetric, Fig. 7.44, or because the incidence is along the cylindrical axis, Fig. 7.45. In this respect let us recall that the dependence of the scattering amplitude on the polarization as well as on $\hat{\boldsymbol{k}}_{\mathrm{I}}$ and on $\hat{\boldsymbol{k}}_{\mathrm{S}}$ is entirely due to the amplitudes $W_{\mathrm{I}\eta lm}^{(p)}$ and $W_{\mathrm{S}\eta lm}^{(p)}$, which are independent of frequency, however. On

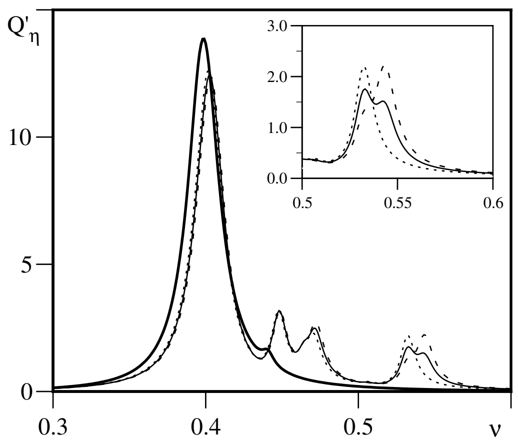

Fig. 7.46. Extinction efficiency for the actual scatterer with the inclusion at maximum eccentricity for polarization parallel (*dashed curve*) and perpendicular (*dotted curve*) to the plane of scattering. The incidence is individuated by the polar angles $\vartheta_{\mathrm{I}} = 52°$, $\varphi_{\mathrm{I}} = 0°$. The *thin continuous curve* reports the extinction efficiency of a dispersion of scatterers with random distribution of the orientations. A detail of the rightmost part of the spectrum is shown in the inset. For comparison, the efficiency for the case of the centered inclusion (*thick continuous curve*) is also reported

the contrary, the ability to produce resonances is contained in the frequency-dependence of the elements of the transition matrix, which do not depend either on η or on $\hat{\boldsymbol{k}}_{\mathrm{I}}$ or on $\hat{\boldsymbol{k}}_{\mathrm{S}}$. With this in mind, let us go on to discuss the results of Fig. 7.46 where the dependence of the spectrum on the choice of the polarization shows to its full extent. In Fig. 7.46, indeed, we superpose to the spectrum for a sphere with the centered inclusion (that we already reported in Fig. 7.45) the extinction efficiency for the case of the inclusion at maximum eccentricity for polarization both parallel and perpendicular to the plane of scattering. The direction of incidence is individuated by the polar angles $\vartheta_{\mathrm{I}} = 52°$, $\varphi_{\mathrm{I}} = 0°$. This choice of the incidence does not bear any particular significance thus ensuring the true generality of our results. In the same figure we also report the result of the average over the particles with the eccentric inclusion on the assumption that they are randomly distributed in orientation. Of course, the latter spectrum, which gives information on the extinction from a dispersion of identical scatterers, is independent of the polarization. We first notice that, except for the leftmost peak, all resonances for the case of an eccentric inclusion arise from a superposition of contributions from $l = 1$ and for $l = 2$. This is shown by the values of the partial efficiencies $q_{\eta 1}$ and $q_{\eta 2}$, which are not reported, however. Therefore our previous considerations both on the origin and on the classification of the resonances apply. Comparison of the spectra for the individual particles shows that the resonance at $\nu_1 = 0.535$ occurs only in perpendicular polarization, whereas the resonance at $\nu_2 = 0.545$ occurs only in parallel polarization. The separation $\nu_2 - \nu_1$, although small on the scale of the figure, is quite noticeable in wavelength. The peak at ν_1 is the same that appears in Fig. 7.45 for $\vartheta_{\rm I} = 0°$. In fact, this resonance mainly stems from the elements $\mathcal{S}^{(2\,2)}_{1\,1;\pm1}$ that, for $\vartheta_{\rm I} = 0°$, are excited for both polarizations as the relevant amplitudes $W^{(2)}_{\eta1,\pm1}$ are independent of the choice of η. On the contrary, for general direction of incidence $W^{(2)}_{\eta1,\pm1}$ are unchanged for $\eta = 2$, whereas they are smaller for $\eta = 1$. The peak at ν_2 originates instead from the leading element $\mathcal{S}^{(2\,2)}_{1\,1;0}$ that is excited for parallel polarization as the exciting amplitude $W^{(2)}_{\eta10}$, provided that the incidence is not along the z axis, does not vanish for $\eta = 1$ only.

When the particles are randomly oriented, the averaged spectrum shows that both peaks at ν_1 and ν_2 are present. This is an expected result in connection to what we already noticed in Sect. 7.6.1 about the averaging of the optical properties of spheres containing an eccentric inclusion [88]. Since the extinction efficiency of the individual scatterers displays a peak whose frequency changes with the polarization (ν_2 for $\eta = 1$, ν_1 for $\eta = 2$), we get the spectrum for random orientation in Fig. 7.46. Ultimately, a dependence on the polarization in the resonance spectrum from a dispersion of particles of the very kind we dealt with here may provide an indication that a noticeable fraction of them has a preferred orientation.

A careful analysis of the extinction spectrum from spheres containing a spherical inclusion may help in establishing whether the inclusion is concentric or eccentric, as the eccentricity yields a multiplicity of resonances. In case the inclusion is eccentric, measurements performed with polarized light may give an indication on the fraction of particles that are oriented alike. Getting this kind of information can be of importance, e.g. in astrophysics. Indeed, the galactic extinction shows an evident dependence on the polarization for certain lines of sight. This fact has been interpreted as being due to the presence of nonspherical particles of the kind we dealt with in this section, which are partially oriented by the general magnetic field of the galaxy. Except for the cause of the alignment, which does not concern us here, the results discussed above support the reliability of this interpretation.

7.7 Spheres with Cavities and Depolarization of the Internal Field

In Sect. 2.9 we stressed that for waves of general form the customary Stokes parameters are not appropriate to give a complete description of the state of polarization. Since the most general state of polarization is the elliptical one, we introduced, according to the suggestion of Carozzi et al. [30], the vector $\boldsymbol{V}$ (see (2.48)) which describes the polarization ellipse and the quantity $V_{\rm s}$ which gives the sense of rotation of the field with respect to the direction of propagation. In the present section we exploit the quantity V_s, which can vanish only for linear polarization, to show that when a sphere containing spherical cavities is illuminated by a linearly polarized plane wave, the field within the cavities undergo to depolarization and acquires the features of an elliptically polarized wave. Of course, this is not a mere exercise because the elliptical polarization of the field within the cavities may be the key tool to understand the origin of some photolisis reactions that are important to understand the origin of life. We will return to the subject in an astrophysical framework [37] in Chap. 10.

In [38] we already dealt with the problem of depolarization within a single cavity embedded into an otherwise homogeneous sphere. Nevertheless, since homogeneous spheres containing several cavities are a widely used model for some kind of the interstellar dust grains, we feel that an extension of our original work to the case of at least two cavities is in order. We will discuss the case of more than two cavities in Chap. 10 in an astrophisical framework.

Accordingly, in this section we consider a sphere of radius $\rho_0 = 100\,\mathrm{nm}$ containing two spherical cavities of radius $\rho_1 = \rho_2 = 20\,\mathrm{nm}$. The chosen radius of the host sphere lies in the accepted range of the size of the interstellar dust grains. The calculation of the field has been effected through the technique described in Sect. 5.5, by assuming that the interstitial region is filled by a mixture composed of 30% silicates, 30% amorphous carbon, and 40% ice; the dielectric function of the mixture has been simulated using the Bruggeman mixing rule. The choice of this material has been suggested by the result, reported in [38], that the depolarization of the field undergo no qualitative changes by using other materials of astrophysical interest.

Our calculation were performed in a frame of reference with origin at the center of the host sphere. The centers of the two cavities were assumed to lie symmetrically with respect to the origin on a diameter contained in the meridional plane with $\varphi = 45°$. The diameter forms with the z axis an angle $\vartheta = 30°,\ 60°,\ 90°$. In turn the incident field is a plane wave, with the propagation vector parallel to the z axis, linearly polarized along the x axis. Four values of the distance between the centers of the cavities were considered. In both cavities V_s was calculated at the points F and B that are indicated in Fig. 7.47.

Let us first stress that, no depolarization occurs, i.e. $V_s = 0$, when the centers of the cavities are located along the z axis. The results for the other cases are reported in Figs. 7.48, 7.49 and 7.50, in which we actually plot

$$\mathcal{V}_s = V_s / I_I$$

at point F of both cavities for four values of the distance between their centers when $\vartheta = 30°, 60°, 90°$, respectively, as a function of λ in the range 0.15–0.25 μm. In fact, this range of wavelengths is the most relevant for photochemical reactions [152]. Analogous results were obtained at point B, and are, therefore, not reported.

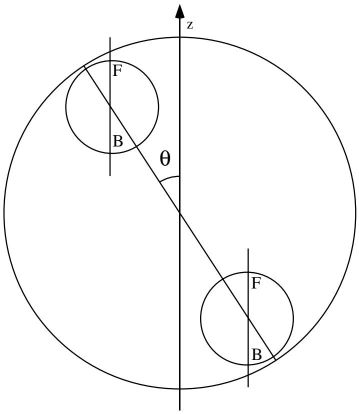

Fig. 7.47. Adopted geometry to study the depolarization within two cavities. The plane containing the diameter forms an angle $\varphi = 45^\circ$ with the zx plane. The cavity whose center has positive z will be referred to as n. 1

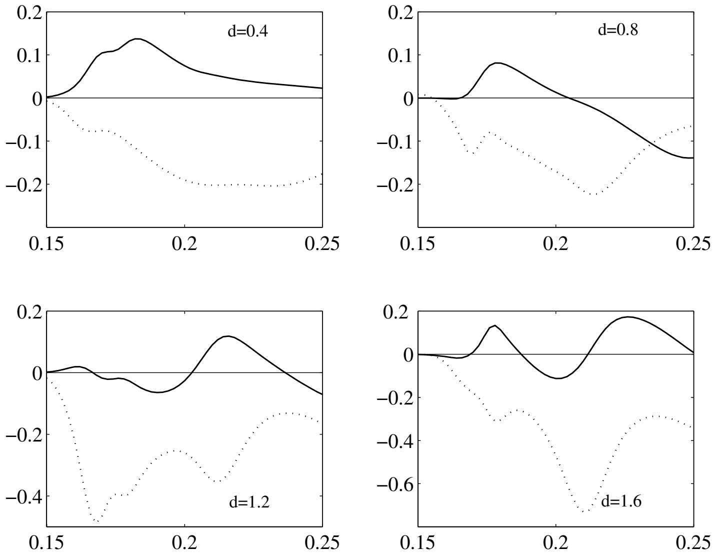

Fig. 7.48. $\mathcal{V}_s$ at point F for cavity 1 (*solid line*) and 2 (*dotted line*) for $\vartheta = 30^\circ$ as a function of the incident wavelength in the range $0.15 < \lambda < 0.25\,\mu$m. The distance (in μm) between the centers of the cavities is indicated in each panel

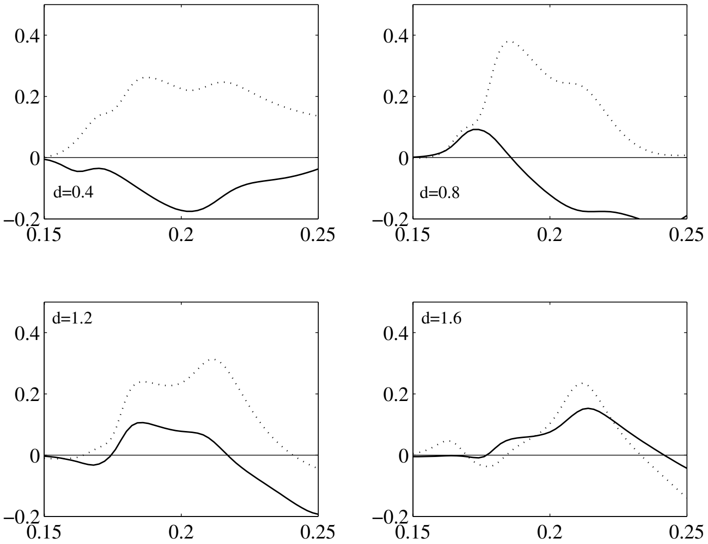

Fig. 7.49. Same as Fig. 7.48 but for $\vartheta = 60°$

The results in Fig. 7.48 show that the depolarization occurs in both cavities and that $\mathcal{V}_s$ changes its sign in at least one of them. What is more interesting, however, is the evolution of $\mathcal{V}_s$ as ϑ increases. Comparison of

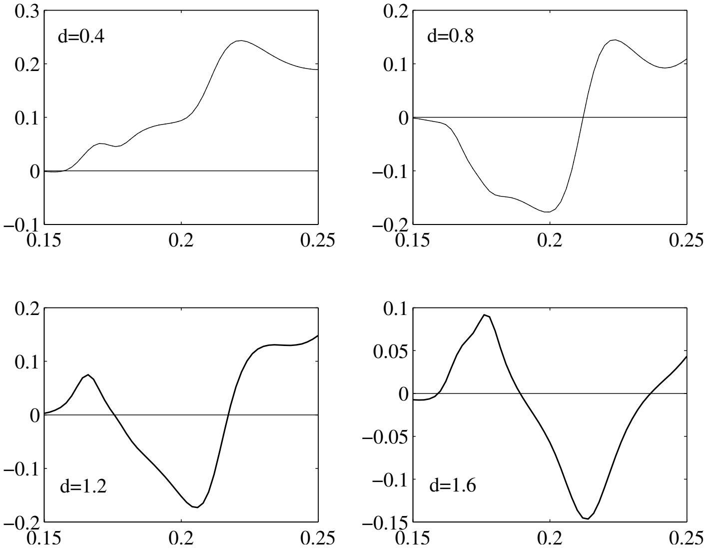

Fig. 7.50. Same as Fig. 7.48 but for $\vartheta = 90°$. Note the superposition, due to the symmetry, of the curves for cavity n. 1 and n. 2

Fig. 7.48 with Figs. 7.49 and 7.50 show, indeed, that for whatever distance of the cavities the depolarization tends to become identical in both of them, and achieves the identity when $\vartheta = 90°$. This confirms that the depolarization depends on the asymmetry of the configuration. In fact, even in the case of a single cavity we found that no depolarization occurs when the diameter on which the cavity has its center is parallel the z axis, whereas the maximum occurs when the diameter is orthogonal to the z axis. Of course, the distance between the centers of the civities plays a role in determining the details of the behavior of $\mathcal{V}_{\mathrm{s}}$.

This was expected because the general behavior of the field should be governed by the multiple scattering processes that occur between the surfaces of the cavities and between the cavities and the internal surface of the host sphere. In this respect, the considerations on the multiple scattering processes of Sect. 7.6.3 for the case of two metallic inclusions still apply.

7.8 Correlation Spectroscopy

Correlation spectroscopy is a useful tool for investigating the features of the diffusive motion, both translational and rotational, that may occur within a dispersion of particles whose individual optical properties are known. The observed time-domain spectra have in general an exponential-like behavior, as required by statistical mechanics. Nevertheless, it is a hard matter to deduce from the observations the number and the amplitudes of the exponentials that give an effective contribution. Actually, by modeling the scattering particles as clusters of spherical scatterers, we are able to give a better description of their optical properties and to recover, in the limit of a sufficiently long wavelength, the same results that can be obtained in the small particle approximation (SPA). According to the SPA, the elements $\mathcal{S}^{(2\,2)}_{1\mu 1\mu'}$ are sufficient for the description of the scattering properties of a particle. Since these elements and the polarizability are related, as we discussed in Sect. 4.6.1, the SPA is related to the RSA that assumes the particles to be so small that their properties can be described through their polarizability. Actually, several experiments are interpreted on the assumption that the particles concerned are so small that the RSA or, at least, the SPA applies [153], so that the optical properties of the particles can be described through their polarizability tensor. Now, it is well known that a second rank Cartesian tensor is equivalent to the sum of three irreducible spherical tensors [7] whose rank (angular momentum) is 0, 1, and 2. As a result, using the SPA at most three exponentials can enter the description of the time-domain spectral intensity. On the contrary, we have already shown in Sect. 4.7 that, when the optical properties of the individual particles are described exactly through their transition matrix, exponentials of all orders should occur. In this section, we show what kind of new information can be gained by modeling the scattering particles as clusters of spheres and comparing the results obtained by an exact description

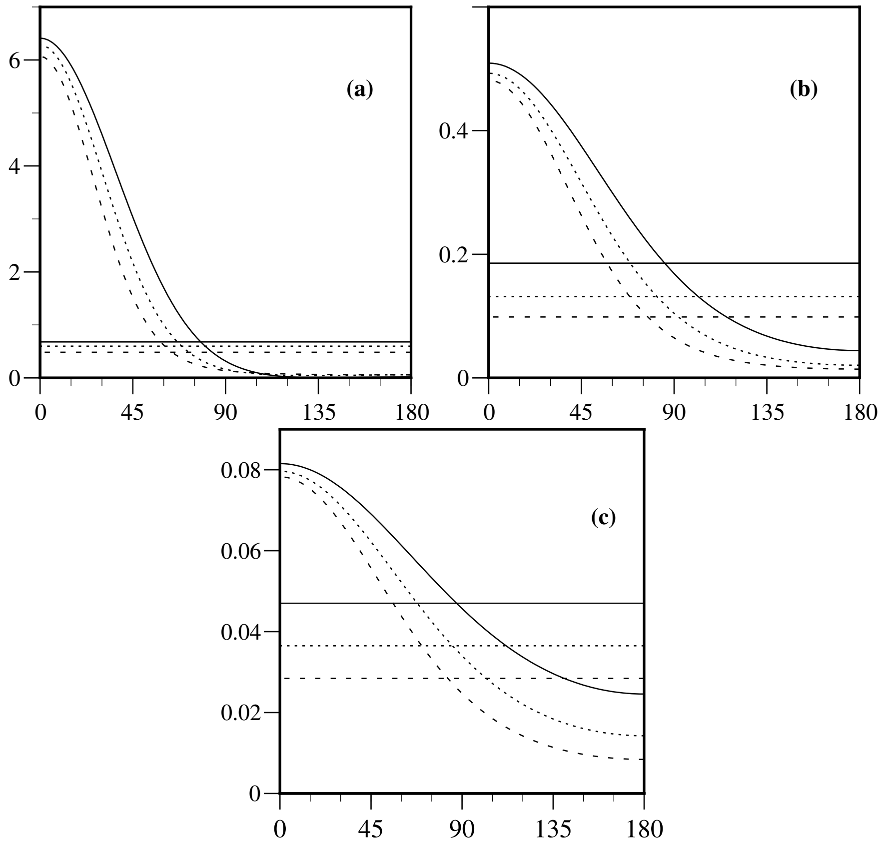

Fig. 7.51. $R_0/16\pi^2$ as a function of the angle of scattering Φ for polarization both of the incident and of the *scattered field* orthogonal to the plane of reference. The wavelength of the incident field is 400 nm in **(a)**, 600 nm in **(b)**, and 800 nm in **(c)**. The *solid*, *dotted*, and *dashed curves* refer to clusters of two, three, and four spheres, respectively. The *flat lines* are those obtained in the SPA

through the transition matrix method with those obtainable in the SPA. To this end, we consider axially symmetric particles built as linear chains of 2, 3, and 4 identical spheres whose radii are chosen so the total volume of each chain is independent of the number of its components [58]. We are thus able to follow the behavior of the amplitudes $R_{\eta'\eta L}$ defined in (4.71) with increasing elongation of the particles. Accordingly, the chosen radii are 90.2, 78.8, and 71.6 nm, respectively. All our calculations were performed for a wavelength range from 400 to 800 nm and the refractive index of the spheres was assumed to be $n = 1.61 + \mathrm{i}0.004$, which is appropriate for acrylic in the visible and near infrared. Note that our choice of the structure of the particles and of the wavelength range is such that our calculations are well beyond the range

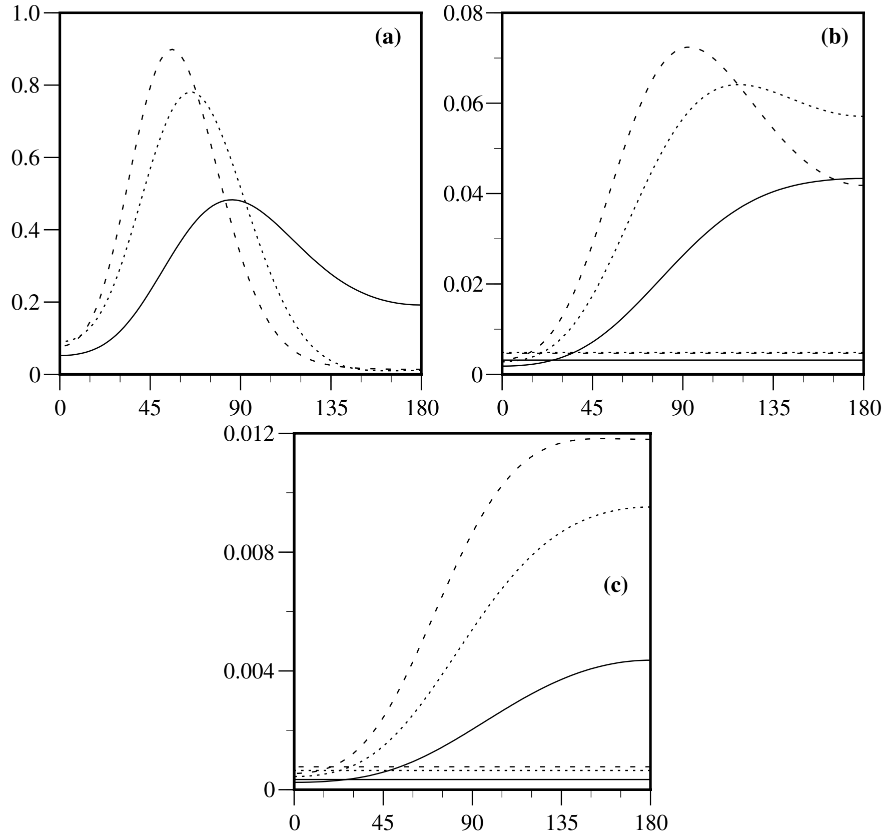

Fig. 7.52. $R_2/16\pi^2$ as a function of the angle of scattering Φ for polarization both of the incident and of the *scattered field* orthogonal to the plane of reference. The wavelength of the incident field is 400 nm in **(a)**, 600 nm in **(b)**, and 800 nm in **(c)**. The *solid*, *dotted*, and *dashed curves* refer to clusters of two, three, and four spheres, respectively. The *flat lines* are the results yielded by the SPA, and they do not appear in (a) because R_2 is vanishingly small at $\lambda = 400$ nm

of applicability of the RSA. Nevertheless, $l_{\mathrm{M}} = 10$ proved sufficient to ensure the convergence to four significant digits. Before we discuss our specific results we stress that, due to the axial symmetry of all the particles we deal with and to the presence of a reflection plane orthogonal to the main axis, the only terms that are nonvanishing are those with even L. A few sparse calculations on axially-symmetric particles which do not posses such reflection plane, e.g., linear chains formed of spheres with different radii or refractive indexes, show that the odd-L terms do not vanish.

In Fig. 7.51 we report R_0 calculated for the three clusters described above as a function of the angle of scattering, together with the results of the calculation in the SPA. The polarization both of the incident and of the scattered

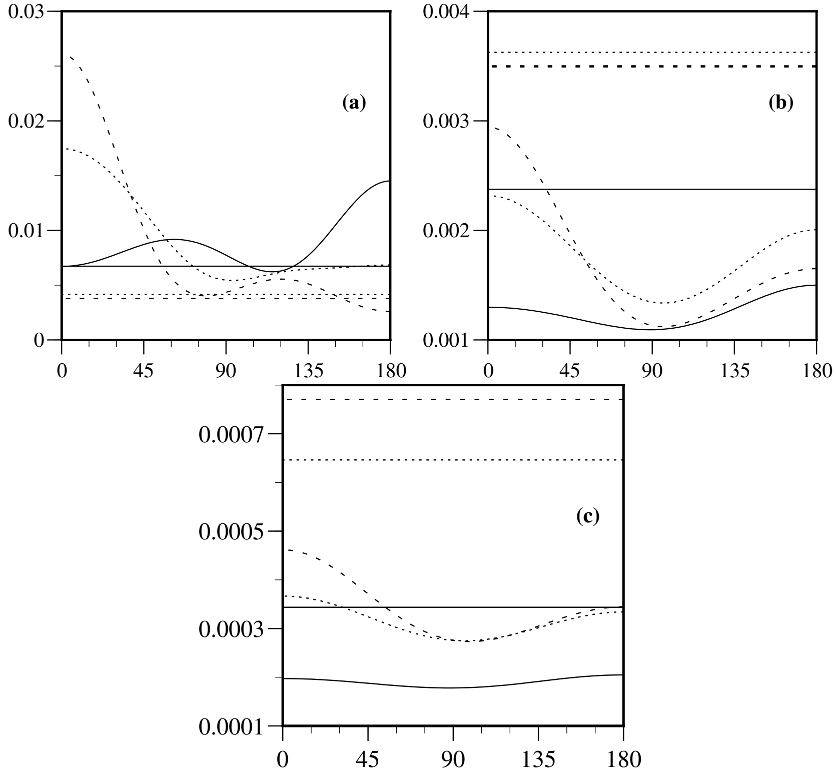

Fig. 7.53. $R_2/16\pi^2$ as a function of the angle of scattering Φ when the polarization of the incident field is orthogonal, whereas that of the scattered field is parallel to the plane of reference. The wavelength of the incident field is 400 nm in **(a)**, 600 nm in **(b)**, and 800 nm in **(c)**. The *solid*, *dotted*, and *dashed curves* refer to clusters of two, three, and four spheres, respectively. The *flat lines* are those obtained in the SPA

field is orthogonal to an arbitrarily chosen plane of reference (see Sect.4.7). As expected, the SPA gives R_0 independent of the angle of scattering in contrast with the result of the exact calculations, although the dependence on Φ flattens as the wavelength increases. In this respect, it is worth stressing that at 800 nm the SPA R_0 is more or less the average of the exact results. This may explain why, at certain angles of scattering, the observations may appear to be consistent with the assumption that the particles are small. According to calculations that are not reported here, R_0 becomes practically flat at $\lambda = 1200$ nm. The trend towards smaller wavelengths shows that the dependence on Φ becomes stronger and stronger thus making the SPA quite unacceptable. The curve for the two-sphere chain always lies above those for the three- and four sphere chains. This behavior is contrary to what one would expect when taking into account that the more elongated particles

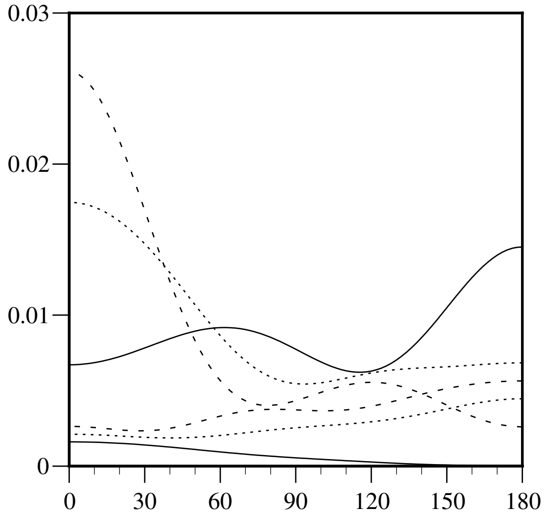

Fig. 7.54. $R_2/16\pi^2$ (*higher curves*) and $R_4/16\pi^2$ (*lower curves*) cross-polarization amplitudes yielded by the exact theory for λ = 400 nm. The *solid*, *dotted*, and *dashed curves* refer to clusters of two, three, and four spheres, respectively

should have a more striking dependence on the angle of scattering. Nevertheless, this apparent contradiction is easily disentangled when one thinks that the two-sphere chains are more akin to spherical particles and that, therefore, their scattering power is almost entirely contained in the $L = 0$ term, whereas it is to be expected that the higher-L terms contain a good part of the scattering power of the more elongated three- and four-sphere chains.

That this is, indeed, the case is confirmed by Fig. 7.52, where we report R_2. The curves for the four-spheres chains are, in fact, the highest ones, except for forward scattering when $\lambda = 400$ nm or $\lambda = 600$ nm. Note that at $\lambda = 400$ nm the SPA terms are so small that they do not appear on the scale of the figure. Of course, with increasing wavelength, i.e., when the SPA becomes more or less acceptable, the exact curves for R_2 assume a monotonic shape. Therefore, a first conclusion that can be drawn from the examination of Figs. 7.51 and 7.52 is that the SPA cannot, at least in principle, be applied to the nonspherical particles we deal with, neither to the less anisotropic such as the two-sphere chains. Nevertheless, the dependence of R_0 and R_2 on the angle of scattering turns out to be rather complicated, so that it is not always true that the most elongated particles yield the larger effects at a given Φ.

In Fig. 7.53 we present the cross-polarization results for R_2. We first notice that the Φ-dependence of the exact results is fully appreciable at the shortest wavelengths only. Nevertheless, as expected, the largest variation with the scattering angle occurs for the four-sphere chains, i.e., for the most elongated particles, although, in agreement with Figs. 7.51 and 7.52, it is in no way certain that these particles produce the strongest effect at a given Φ. Anyway, the behavior of our results is, in all circumstances, rather different from that one would expect in the SPA.

The results that we have presented so far refer to $L \leq 2$ and have their counterpart in the results that can be obtained by using the polarizability tensor of the particles. On the contrary, the results that we present in Fig. 7.54 cannot be obtained but with an exact calculation. In fact, we present the cross-polarization Φ-dependence of the R_4 terms together with the R_2 exact terms. Although on the scale of the figure the R_4 terms appear to be rather flat, specially in comparison with the R_2 terms, their range of variation is still considerable, and they appear to be in no way negligible. As the strongest Φ-dependence pertains to the four-sphere chains, we conclude that the R_4 terms should be considered when dealing with highly nonspherical particles.

7.9 Radiation Force on Aggregates of Spheres

In Chap. 3 we stressed that as a result of conservation theorems for any combined system of electromagnetic fields and particles, the latter experience mechanical effects. In particular, in Sect. 3.2.1 we established the basic concepts for the calculation of the radiation force on particles of any shape, whereas, in Sect. 4.8 we formalized the theory of the radiation force in terms of the transition matrix approach. In the present section we apply the theory to a few model particles built as aggregates of spherical scatterers. Although the radiation force, and in particular its transverse components, are of importance for the dynamics of cosmic dust grains [40], our present aim is not at calculating the radiation force on actual particles, but rather at assessing how the radiation force components depend on the structure and on the refractive index of the particles themselves [59]. Of course, the convergence of the multipole expansions have been carefully checked. For all the particles we deal with in this section, convergence to 4 significant digits was ensured by extending the multipole expansions to $l_{\mathrm{M}} = 8$.

The results that we are going to discuss show that not only the customary radiation pressure, but also the transverse components of the radiation force, have a noticeable dependence on the shape and orientation of the particles concerned and are in no case negligible. Moreover, the radiation pressure shows a noticable dependence on the absorptivity of the particles. Therefore, all these parameters may play an important role in the dynamics of particle systems. We will return on this subject in Chap. 10 in an astrophysical context.

Since in Sect. 4.8.1 we proved on general grounds that for random orientational distribution, the transverse components are rigorously zero for whatever shape of the particles, the only averages that we will consider are the axial ones. In this case, indeed, the orientational average is performed around an axis fixed in space, and the resulting transverse components are in general nonzero for whatever direction of propagation and polarization of the incident wave. Of course, the axial average plays an important role when the particles concerned are aligned. We do not discuss here the source of the alignment, but we recall that, for atmospheric aerosols and atmospheric ice crystals, alignment may occur under the influence of hydrometeors [154] or of electrostatic [42] or magnetostatic fields; in the physics of cosmic dust the alignement may be produced, e.g., by galactic magnetic fields or by collisions of the dust grains with molecules of the interstellar gas [155].

Our calculations assume that in the laboratory frame Σ the plane of reference is the meridional plane of $\boldsymbol{k}_{\mathrm{I}}$, whose polar angles are ϑ_{I} and φ_{I}. Therefore, the triplet $\hat{\boldsymbol{v}}_\zeta$ with respect to which, according to Sect. 3.2.1, the components of the radiation force are taken is $\hat{\boldsymbol{v}}_1 = \hat{\boldsymbol{\vartheta}}_{\mathrm{I}}$, $\hat{\boldsymbol{v}}_2 = \hat{\boldsymbol{\varphi}}_{\mathrm{I}}$, and $\hat{\boldsymbol{v}}_3 = \hat{\boldsymbol{k}}_{\mathrm{I}}$. In our calculations the polarization of the incident field has been chosen to be either along $\hat{\boldsymbol{\vartheta}}_{\mathrm{I}}$ or along $\hat{\boldsymbol{\varphi}}_{\mathrm{I}}$, so that $E_0 = E_{0\eta'}$, and, according to (3.15) and (4.25), $I_0 = (c/8\pi)I_{\mathrm{I}\eta'\eta'} = (c/8\pi)I_{\mathrm{I}}$, where the subscript η' take on the symbolic values ϑ and φ.

The quantities that we calculated are $\mathcal{F}_{\eta'\mathrm{T}} = c(F^2_{\eta'1} + F^2_{\eta'2})^{1/2}/I_0$ for the transverse component and $\mathcal{F}_{\eta'k} = cF_{\eta'3}/I_0$ for the radiation pressure, as well as their axial averages. Actually,

$$\langle \mathcal{F}_{\eta'\mathrm{T}} \rangle = c\big(\langle F_{\eta'1}\rangle^2 + \langle F_{\eta'2}\rangle^2\big)^{1/2}/I_0 \; .$$

All the particles that we are going to consider are composed of polystirene latex whose dielectric function, according to Ma et al. [156], has the value $\varepsilon = 2.490087 + \mathrm{i}\,0.001578$ at an incident wavelength $\lambda = 600\,\mathrm{nm}$. In all the following figures the quantities $\mathcal{F}_{\eta'\mathrm{T}}$ and $\mathcal{F}_{\eta'k}$ are reported, in $\mu\mathrm{m}^2$, as a function of ϑ_{I} in the range 0°–90°.

7.9.1 Binary Clusters

We consider as a reference a sphere of polystirene of radius 200 nm. For this sphere $\mathcal{F}_{\eta'k} = 0.125027\,\mu\mathrm{m}^2$. Since we want to consider particles of equal mass, the quantity of polystirene that is contained in the sphere mentioned above was subdivided into two mutually contacting identical spheres, of resulting radius 158.77 nm (cluster A). The size parameter of the smallest mathematical sphere that includes cluster A is $x = 3.1$. The centers of the spheres lie in the zx plane of Σ, whose origin coincides with the contacting point of the spheres. Our calculations were performed for four particular configurations of cluster A that differ for the angle between the line through the centers of the spheres and the z axis: (*i*) 90°, (*ii*) 60°, (*iii*) 30° and (*iv*) 0°. Nevertheless, we report here in Fig. 7.55 the results for configuration (*i*) only, whereas the results for the other configurations can be found in [59]. We stress that the results for configuration (*iv*), because of the geometry, are independent of φ_{I} so that a single curve would appear; of course, this curve coincides with that of the axial average (see below). Anyway, we notice that for the

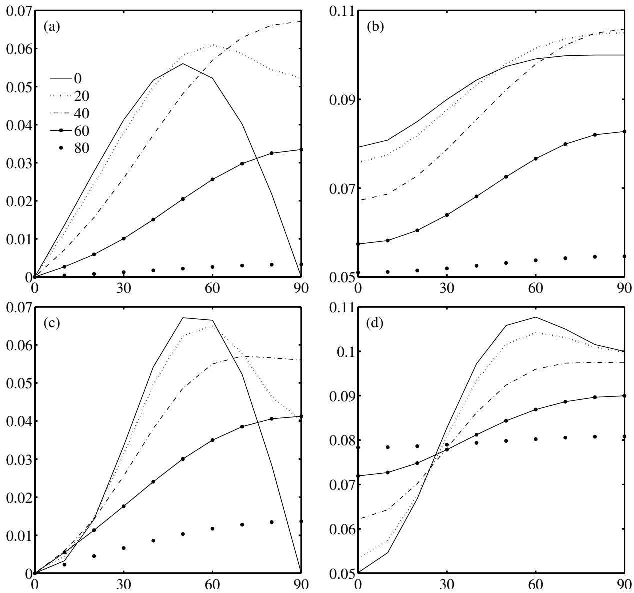

Fig. 7.55. $\mathcal{F}_{\eta'\mathrm{T}}$ ((**a**) and (**c**)), and $\mathcal{F}_{\eta' k}$ ((**b**) and (**d**)), in $\mu\mathrm{m}^2$ for the binary cluster in configuration (i), for polarization parallel ((a) and (b)), and perpendicular ((c) and (d)) to the plane of reference, as a function of ϑ_I for the values of φ_I indicated in the inset in (a)

other configurations both $\mathcal{F}_{\eta'\mathrm{T}}$ and $\mathcal{F}_{\eta' k}$ show a noticeable dependence on the direction of incidence. As expected, the transverse component is always smaller than the radiation pressure. In order to perform the axial average, the choice of the local frame attached to the particles is essential. In fact, the axial average is performed by constraining the $\bar{z}$ axis of the local frame to remain always parallel to the z axis of Σ. Therefore, we resolved to choose the local frame so that, for each of the configurations described above in turn , the coordinates of the sphere are identical in $\bar{\Sigma}$ and Σ. In this way, we get a different axial average for each of the configurations (i), (ii), (iii) and (iv). The results for all the configurations are reported in Fig. 7.56: note that, due to the particular average, the results depend on the polarization as well as on the configuration. As expected, the average for random distribution of the orientations vanish for the transverse component whereas the radiation pressure is $0.08543\,\mu\mathrm{m}^2$. Of course, this value does not depend either on the configuration or on the polarization.

Finally, we investigated to what extent the imaginary part of the dielectric constant influences the results. To this end, we repeated the calculations for the axial averages $\langle\mathcal{F}_{\eta'\mathrm{T}}\rangle$ and $\langle\mathcal{F}_{\eta' k}\rangle$ of cluster A in configuration (iii) by changing the imaginary part of ε. The results that are reported in Fig. 7.57 show that the value of $\mathrm{Im}(\varepsilon)$ has little effect on the transverse components

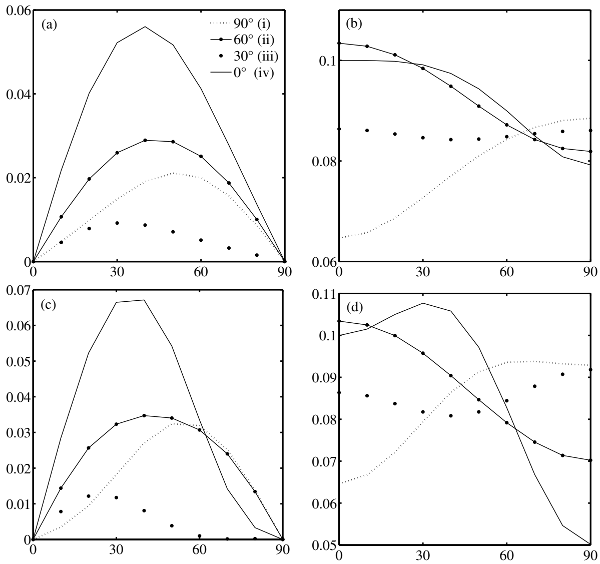

Fig. 7.56. Axial averages of $\mathcal{F}_{\eta'\mathrm{T}}$ ((**a**) and (**c**)), and of $\mathcal{F}_{\eta' k}$ ((**b**) and (**d**)) in $\mu\mathrm{m}^2$ for the binary cluster in configurations (*i*), (*ii*), (*iii*), and (*iv*), for polarization parallel ((a) and (b)), and perpendicular ((c) and (d)) to the plane of reference, as a function of ϑ_I. The random average of $\mathcal{F}_{\eta' k} = 0.08543\,\mu\mathrm{m}^2$

but may have a strong effect on the radiation pressure. This is not surprising because the radiation pressure, according to (3.16) and (3.17), implies both the extinction and the scattering cross sections, whereas the transverse component implies the scattering cross section only. In any case, this behaviour might be important for understanding the possible expulsion of cosmic dust grains from galaxies and protoplanetary disks [157].

7.9.2 Six-Spheres Clusters

In order to build the six-spheres clusters, the same quantity of material that was used for the binary cluster, i.e. the quantity contained in a sphere of 200 nm radius, was subdivided into six identical spheres, with resulting radius 110.06 nm. The six spheres were arranged either at the vertices of a regular hexagon (cluster B) or in a random structure (cluster C); the resulting structures are shown in Fig. 7.58. The size parameter of the smallest circumscribed sphere are $x_\mathrm{B} = x_\mathrm{C} = 3.3$ for both cluster B and cluster C. Even in this case we report, in Fig. 7.59 for cluster B and in Fig. 7.60 for cluster C, the quantities $\mathcal{F}_{\eta'\mathrm{T}}$ and $\mathcal{F}_{\eta' k}$, whereas the corresponding axial averages, that are to be understood in the same sense as for the binary clusters, are reported in Fig. 7.61. It is quite interesting to observe that the curves for cluster B in Fig. 7.59 show very little dependence on φ_I. Actually, only

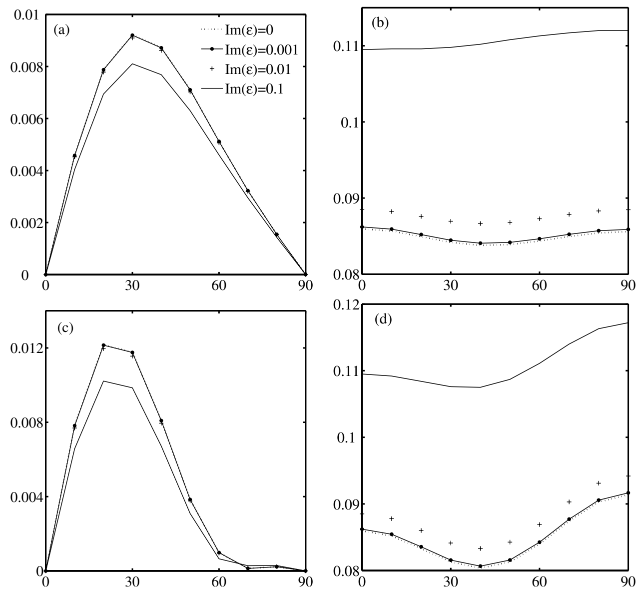

Fig. 7.57. Dependence on $\mathrm{Im}(\varepsilon)$ of the axial averages of $\mathcal{F}_{\eta'\mathrm{T}}$ ((**a**) and (**c**)), and of $\mathcal{F}_{\eta' k}$ ((**b**) and (**d**)) in $\mu\mathrm{m}^2$ for the binary cluster in configuration (iii) for polarization parallel ((a) and (b)), and perpendicular ((c) and (d)) to the plane of reference as a function of ϑ_I. The random averages of $\mathcal{F}_{\eta' k}$ (in $\mu\mathrm{m}^2$) are 0.08595, 0.08621, 0.08499, and 0.1095 for $\mathrm{Im}(\varepsilon) = 0$, 0.001, 0.01, and 0.1, respectively. Note that in (a) and (c) the curves for $\mathrm{Im}(\varepsilon) = 0.0$, 0.001, and 0.01 are almost coincident on the scale of the figure

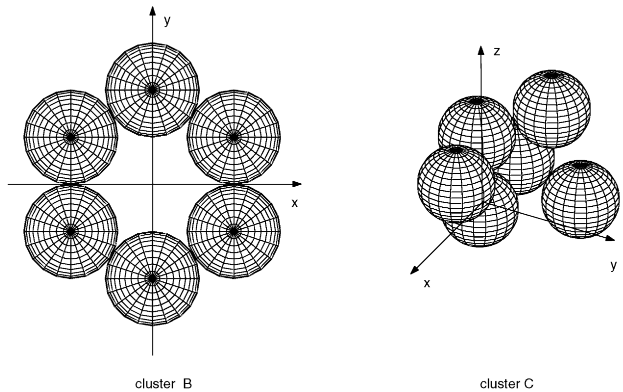

Fig. 7.58. Geometry of the six-spheres clusters

two curves appear because the curves for $\varphi_\mathrm{I} = 0°, 60°$, as well as the curves for $\varphi_\mathrm{I} = 20°, 40°, 80°$, superpose. This result is due to the high symmetry of cluster B around the local $\bar{z}$ axis. On the contrary, since cluster C was so built

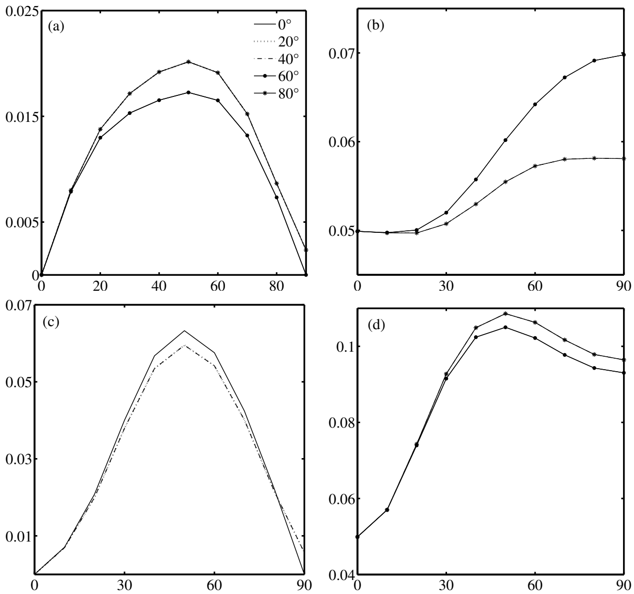

Fig. 7.59. $\mathcal{F}_{\eta' \mathrm{T}}$ ((**a**) and (**c**)), and $\mathcal{F}_{\eta' k}$ ((**b**) and (**d**)) in μm^2 for the six-spheres cluster B, for polarization parallel ((a) and (b)), and perpendicular ((c) and (d)) to the plane of reference, as a function of ϑ_{I} for several values of φ_{I}. Note that the curves for $\varphi_{\mathrm{I}} = 0°$, $60°$ superpose as well as the curves for $\varphi_{\mathrm{I}} = 20°$, $40°$, $80°$

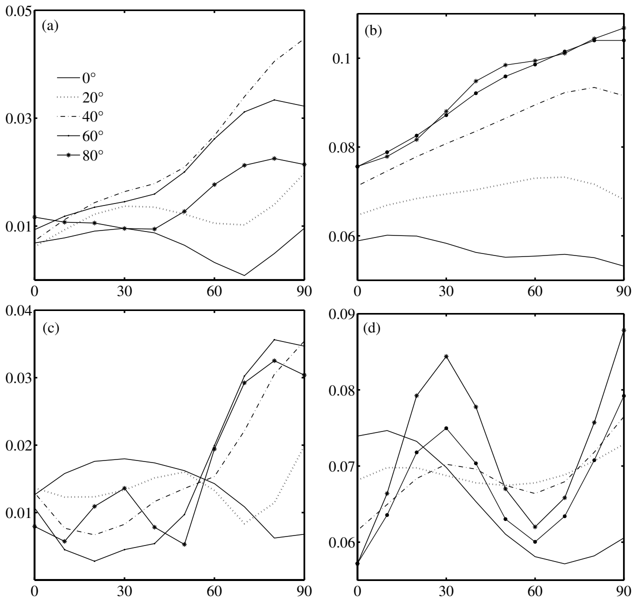

Fig. 7.60. $\mathcal{F}_{\eta' \mathrm{T}}$ ((**a**) and (**c**)), and $\mathcal{F}_{\eta' k}$ ((**b**) and (**d**)) in μm^2 for the six-spheres cluster C, for polarization parallel ((a) and (b)), and perpendicular ((c) and (d)) to the plane of reference, as a function of ϑ_{I} for several values of φ_{I}.

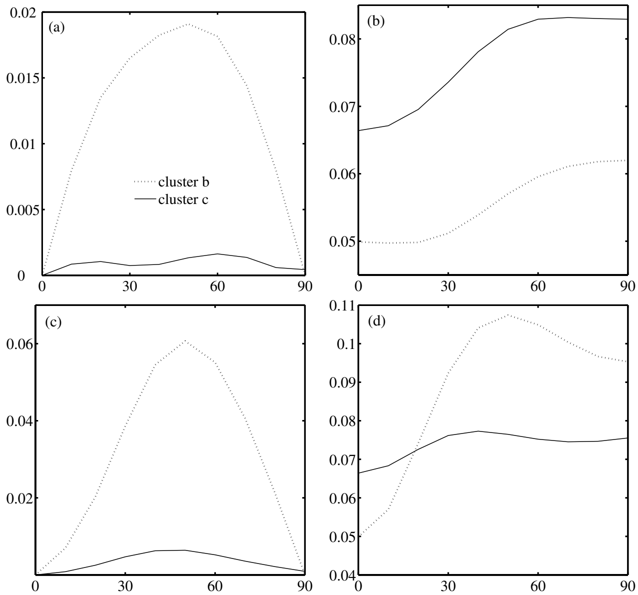

Fig. 7.61. Axial averages of $\mathcal{F}_{\eta' \mathrm{T}}$ ((**a**) and (**c**)), and of $\mathcal{F}_{\eta' k}$ ((**b**) and (**d**)) in $\mu\mathrm{m}^2$ for the six-spheres clusters, for polarization parallel ((a) and (b)), and perpendicular ((c) and (d)) to the plane of reference as a function of ϑ_{I}. The random averages of $\mathcal{F}_{\eta' k} = 0.07772\,\mu\mathrm{m}^2$ for cluster B and $0.07767\,\mu\mathrm{m}^2$ for cluster C

to have no symmetry, the curves in Fig. 7.60 show a noticeable dependence both on ϑ_{I} and on φ_{I}. The random averages of the radiation pressure turn out to be $0.07772\,\mu\mathrm{m}^2$ for cluster B and $0.07767\,\mu\mathrm{m}^2$ for cluster C.

7.10 Radiation Torque on Aggregated Spheres

The torque esperienced by a particle as a result of the interaction with electromagnetic radiation is at present believed to be the main agent of the (at least partial) alignment of the cosmic dust grains. In principle, the alignment should also occur for the particles that compose the atmospheric aerosols. Nevertheless, the frictional forces that oppose the alignment are comparatively stronger in the atmosphere than they are in the interstellar medium, where they are due to collision of the particles with the atoms and molecules of the interstellar gas [61]. In any case we are here interested in the electromagnetic aspects of the radiation torque, so that, for our purposes, we upright neglect the frictional forces. We stress, however, that the mechanical effects of the embedding medium should be taken into account when a realistic description of the dynamics of the particles is required. Several of the calculations that we are going to describe were performed on the assumption that the incident wave is circularly polarized. This assumption may seem contradictory because, with a single exception [158], no astronomical source of circularly polarized light has been detected up today. Nevertheless, let us insist that here we are interested mainly in clarifying the electromagnetic aspects of the effect of the radiation torque on nonspherical particles.

The quantity whose components we actually report in the following figures is the adimensional vector

$$\boldsymbol{T}_\eta = \frac{8\pi k}{I_{\mathrm{I}}\sigma_{\mathrm{T}\eta}} \boldsymbol{\Gamma}_{\mathrm{Rad}\,\eta} ,$$

where $\boldsymbol{\Gamma}_{\mathrm{Rad}\,\eta}$ is the radiation torque calculated for incident light with polarization η.

First, we consider a binary aggregate of identical spheres with radius 50 nm, composed of astronomical silicates [159]. According to Sect. 4.9, the torque depends on the absorptivity of the particles. Therefore, we report in Fig. 7.62, for circularly polarized incident light, the component of $\boldsymbol{T}_1$ along $\boldsymbol{k}_{\mathrm{I}}$ as a function of the wavelength for the cluster considered with its axis perpendicular to $\boldsymbol{k}_{\mathrm{I}}$ itself both in the case in which the imaginary part of the dielectric function is set to zero or assumes its actual value. We show the results for $\eta = 1$ only, because, on account of the symmetry of the scatterer, the results for $\eta = 2$ are identical, except for the sign. As expected, the transverse components of $\boldsymbol{\Gamma}_{\mathrm{Rad}\eta}$, i.e., those in the plane orthogonal to $\boldsymbol{k}_{\mathrm{I}}$, were found to be zero. We do not report the results for the case in which the axis of the cluster is parallel to $\boldsymbol{k}_{\mathrm{I}}$, because they are a direct consequence of (4.88), i.e., $\boldsymbol{\Gamma}_{\mathrm{Rad}\,\eta} \cdot \hat{\boldsymbol{k}}_{\mathrm{I}}$ is nonvanishing only for complex refractive index, and changes its sign with the change of polarization. Even in this case the transverse components are rigorously zero for symmetry reasons. Anyway, the results in Fig. 7.62 show the great importance of the absorptivity of the

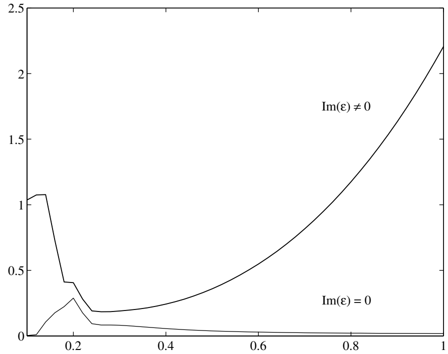

Fig. 7.62. Component of $\boldsymbol{T}_1$ along $\boldsymbol{k}_{\mathrm{I}}$ as a function of the wavelength in μm for a binary cluster composed of astronomical silicates both when the imaginary part of their dielectric function has its actual value and when it is arbitrarily set to zero. The axis of the cluster is orthogonal to $\boldsymbol{k}_{\mathrm{I}}$

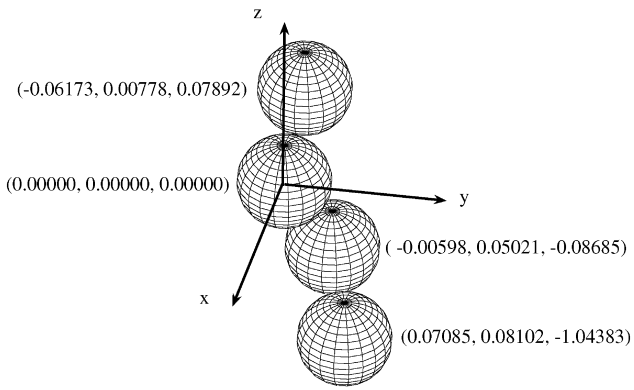

Fig. 7.63. Adopted geometry for the four spheres cluster. The coordinates of the center of the spheres, in μm, are indicated

particles on the value of the torque, and in our opinion do not deserve further comments.

In the second example we now consider a more complex cluster composed of four spheres identical to each other and to the spheres we used above to compose the binary cluster. The geometry, chosen so that no symmetry is present, is sketched in Fig. 7.63. The incident wavevector $\boldsymbol{k}_{\mathrm{I}}$ is parallel to the z axis ($\hat{\boldsymbol{k}}_{\mathrm{I}} \equiv \hat{\boldsymbol{e}}_z$) and circular polarization is assumed. In Fig. 7.64 we report the cartesian components of $\boldsymbol{T}_\eta$ both for $\eta = 1$ and for $\eta = 2$. Since the role of the absorptivity has been already clarified in discussing the binary cluster, we assume here that the imaginary part of the refractive index (astronomical silicates [159]) has its actual value. We first notice that the x and y components of $\boldsymbol{\Gamma}_{\mathrm{Rad}}$ do not change their sign with changing polarization, unlike the z component which does change sign. Of course, the lack of symmetry prevents the curves of each component to coincide with changing polarization. Nevertheless, the most striking result is the coincidence of the axial average around the z axis, $\langle \boldsymbol{\Gamma}_{\mathrm{Rad}\,\eta} \cdot \hat{\boldsymbol{k}}_{\mathrm{I}} \rangle$, with $\boldsymbol{\Gamma}_{\mathrm{Rad}\,\eta} \cdot \hat{\boldsymbol{k}}_{\mathrm{I}}$. This result would be quite evident for the axial average of the binary cluster with its axis along $\boldsymbol{k}_{\mathrm{I}}$. In the present case, because of the lack of symmetry, the occurrence of this coincidence deserves a few additional comments. In fact, we performed the same calculations still assuming incidence along z, but using a radiation both linearly polarized along the x axis and linearly polarized along the y axis. It is not easy to extract any conclusion from the results on the basis of the formulas of Sects. 4.9 and 4.9.1. Nevertheless, a few heuristic remarks can be drawn. Both when we assume circular and when we assume linear polarization, the components of $\boldsymbol{\Gamma}_{\mathrm{Rad}\,\eta}$ in a plane orthogonal to $\boldsymbol{k}_{\mathrm{I}}$ are, in general, nonzero and different from each other, whereas their axial averages around

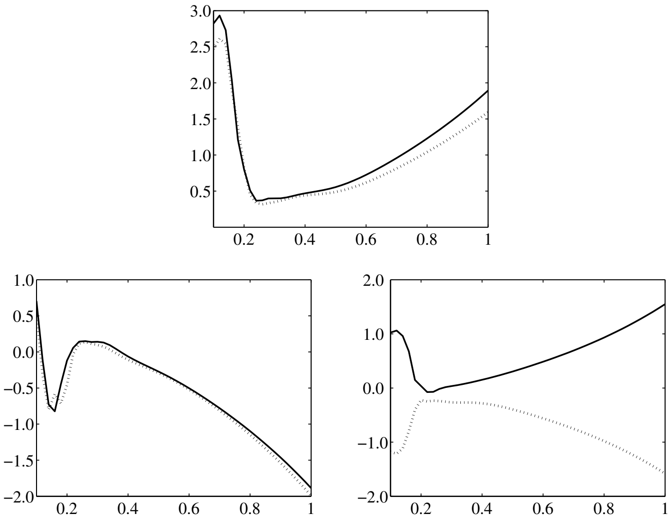

Fig. 7.64. Cartesian components of $\boldsymbol{T}_1$ (*solid line*) and $\boldsymbol{T}_2$ (*dotted line*) as a function of λ in µm for the four spheres cluster. The direction of the incident wavevector is along the z axis. The *top*, *bottom left*, and *bottom right panels* report the x, y and z components, respectively

$\boldsymbol{k}_{\mathrm{I}}$ do vanish. Actually, averaging around $\boldsymbol{k}_{\mathrm{I}}$ makes the average particle akin to an axially symmetric particle, for which the mentioned result is to be expected. Furthermore, assuming circular polarization, $\langle \boldsymbol{\Gamma}_{\mathrm{Rad}\,\eta} \cdot \hat{\boldsymbol{k}}_{\mathrm{I}} \rangle = \boldsymbol{\Gamma}_{\mathrm{Rad}\,\eta} \cdot \hat{\boldsymbol{k}}_{\mathrm{I}}$ follows at once, if one considers the behaviour of the field of a circularly polarized wave. On the other hand, in case linear polarization is assumed, the axial average of $\boldsymbol{\Gamma}_{\mathrm{Rad}\,\eta}$ around $\boldsymbol{k}_{\mathrm{I}}$ turns out to be independent of η. In fact, as regards the axial averaging, the different polarization is seen only as a different orientation of the particle around $\bar{z}$. Of course, in general, the axial average $\langle \boldsymbol{\Gamma}_{\mathrm{Rad}\,\eta} \cdot \hat{\boldsymbol{k}}_{\mathrm{I}} \rangle \neq \boldsymbol{\Gamma}_{\mathrm{Rad}\,\eta} \cdot \hat{\boldsymbol{k}}_{\mathrm{I}}$ for linear polarization.

Further results on this topic can be found in Ref. [65].

7.11 Thermal Emission Force on Aggregated Spheres

In Sect. 3.3 we stressed that the thermal emission is a feature pertaining to the particles independently of the fact that they are or are not in thermal equilibrium. Actually, in Sect. 4.10 the theory for the calculation of the force yielded by thermal emission has been set up in terms of the transition matrix of the particles of interest. In this section we presenta few examples of calculation of the thermal emission force on particles modelled as aggregates of spherical scatterers with complex refractive index. We recall, indeed, that the absorptivity of the particles is a condition for thermal emission and consequent occurrence of thermal emission forces.

Actually, we calculated the quantity $\tilde{\boldsymbol{K}} = \tilde{\boldsymbol{K}}^{(\text{ext})} - \tilde{\boldsymbol{K}}^{(\text{sca})}$ that enters (4.92). The model scattering particles we considered are aggregates of two mutually contacting spheres either composed of materials with different index of refraction or of the same material but different radii. The centers of the spheres lie on the z axis of a frame of reference whose origin coincides with the contacting point. In Fig. 7.65 we report the z component of $\tilde{\boldsymbol{K}}$, in μm^2, as a function of the wavelength, in µm, for an aggregate of two spheres of the same radius $\rho = 100\,\text{nm}$ (upper panel) and $\rho = 50\,\text{nm}$ (lower panel). The sphere with center on the positive z axis is composed of astronomical silicates [159], the other sphere is composed of polymeric carbons [160]. These silicates are, in fact, the most widely used to model cosmic dust grains. We first note that, since we assumed that the the axis of the cluster is along the z axis, the only nonvanishing component of $\tilde{\boldsymbol{K}}$ is the z component for evident symmetry reasons. Moreover, $\tilde{\boldsymbol{K}}$ is independent of temperature, which will enter the calculation (see (4.92)) only through the Planck blackbody energy distribution I_{b}. Thus, $\tilde{\boldsymbol{K}}$ characterizes the emission by a given particle. This can be easily guessed by comparing to each other the plots in Fig. 7.65 and to the plots in Fig. 7.66, where we report the z component of $\tilde{\boldsymbol{K}}$ for binary aggregates of spheres of the same material but different radii. We see that all the plots show a general exponential decay towards longer wavelengths,

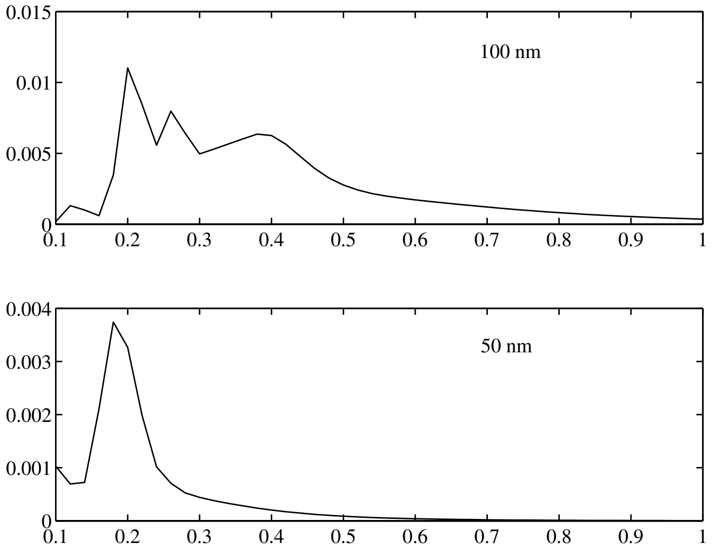

Fig. 7.65. Plot of the z component of $\tilde{\boldsymbol{K}}$, in μm^2, as a function of λ in µm for aggregates of two spheres of the same radius but composed of astronomical silicates [159] and of polymeric carbon [160]. The centers of the spheres lie on the z axis

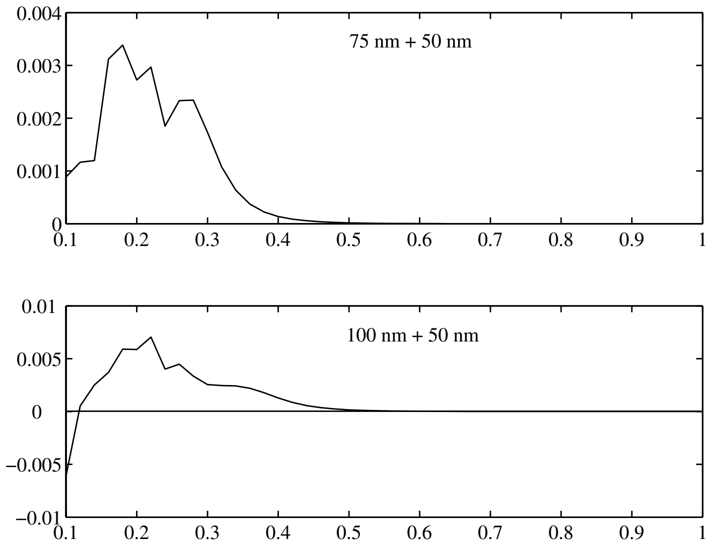

Fig. 7.66. Plot of the z component of $\tilde{\boldsymbol{K}}$, in μm^2, as a function of λ in µm for aggregates of two spheres of different radii both composed of astronomical silicates [159]. The centers of the spheres lie on the z axis. The largest sphere has its center on the positive z axis

but differ from each other for the details. In particular we call the attention of the reader to the negative value that the z component of $\tilde{\boldsymbol{K}}$ assumes at $\lambda = 0.1\,\mu m$ in Fig. 7.66. In any case, the fast decay of the curves in Figs. 7.65 and 7.66 with increasing wavelength ensure the convergence of the integral in (4.92) for whatever choice of the temperature.

8 Applications: Single and Aggregated Spheres and Hemispheres on a Plane Interface

The detection and characterization by nondestructive methods of particles deposited on a plane substrate is a problem that is frequently met in several fields of physics. For instance, particles are often studied after deposition on a suitable substrate. Of course, the effect of the substrate needs to be discriminated. This chapter is devoted to the study of the results that can be obtained from calculations of the scattering pattern of model particles deposited on or in the vicinity of a plane surface. Our purpose is not so much interpreting the spectra from actual particles but to point out for the interested reader the kind of information that can be gained by such calculations.

We recall that, according to Chap. 6, when an object is in the presence of a plane surface, two different approaches are in order to solve the scattering problem. The choice of the appropriate approach is dictated by the material of the surface. In the case of a metal surface it is convenient to resort to image theory (see Sect. 6.2). In the case of a dielectric surface we found it convenient to establish first the reflection rule for vector multipole fields (see Sect. 6.3). While discussing specific results yielded by the method described in Sect. 6.4, we also take the opportunity to highlight the effect of some approximations that were often used to solve the scattering problem.

The final section of this chapter deals with the scattering from particles excited by evanescent waves produced by total internal reflection (see Sects. 6.7 and 6.7.1). In fact, the so-called internal reflection spectroscopy proved to be the technique of choice for studying biological spores, that could be otherwise destroyed or modified by direct illumination techniques.

8.1 Aggregated Spheres and Hemispheres on a Metallic Surface

In this section we discuss the results for the pattern of the scattered intensity from particles on a metallic surface, that, due to the high conductivity, can be considered as perfectly reflecting. As a result, the calculations we are going to describe were performed by resorting to image theory as described in Sect. 6.2. We recall that image theory can deal with any choice of the incidence and polarization and does not imply any limitation of principle either on the size or on the refractive index of the particles of interest. By associating image theory and the transition matrix approach we are able to present the full pattern of the scattered intensity not only for a single sphere on the reflecting surface but also for some representative nonspherical model particles. In practice, we also present the scattering pattern for a cluster of two identical and mutually contacting spheres lying on the surface as well as for clusters of two identical mutually contacting hemispheres and for linear chains of four identical hemispheres, the neighboring hemispheres being in contact with each other, with their flat face lying on the reflecting surface.

As far as we know, the first exact calculation of this kind was performed by Johnson [161] who dealt with a single sphere in contact with the metallic surface. His calculations were restricted to the case of normal incidence, however. The computational technique devised by Johnson need not be described here because it turns out to be a particular case of the general theory of Sect. 6.2. The fact that Johnson's approach does not consider the phase factor $(-)^{\eta-1}$ that we found necessary in (6.53) to get the correct form of the scattered field and of the optical theorem is irrelevant at normal incidence.

With the exception of the case of a single sphere, almost all the patterns that we report refer to a dispersion of identical objects whose orientations are randomly distributed around an axis orthogonal to the reflecting surface. In this respect, the reader should bear in mind the remarks in Sect. 6.2.1 on the need that all the effective scatterers are identical particles. The results were obtained on the assumption that the medium that fills the accessible half-space is the vacuum ($n' = 1$) and that the wavelength of the incident radiation is $\lambda = 628.3\,\mathrm{nm}$. The refractive index of both the spheres and the hemispheres is $n_0 = 3$ while the radius both of the single sphere and of the hemispheres that form a binary cluster was chosen to be $\rho_{\mathrm{s}} = 126.0\,\mathrm{nm}$. In turn, the radius both of the spheres that form the binary cluster and of the hemispheres that form the four-hemisphere chain is $\rho_{\mathrm{h}} = 100.0\,\mathrm{nm}$. This choice of the radii makes the total volume of all the clusters, either of spheres or of hemispheres, equal to the volume of the single sphere. In fact, beyond studying the effect of the presence of the reflecting surface, we are also interested in the effects of the nonsphericity of the particles. Therefore, according to our previous experience [162], we found it convenient to investigate objects with a different geometry but containing the same quantity of refractive material.

The theory in Chap. 6 has been set up on the assumption that the z axis is orthogonal to the reflecting surface. This choice is hardly compulsory but, for cylindrically-symmetric particles, it yields the automatic factorization of the matrix M whose inversion is necessary to get the transition matrix. Accordingly, the polar angles of the direction of observation should be in the range $0 \leq \vartheta_{\mathrm{S}} \leq 90°$ and $0 \leq \varphi_{\mathrm{S}} \leq 360°$. We preferred, instead, to display our results with respect to the frame of reference that is sketched in Fig. 8.1. The reflecting surface coincides with the zx plane and the y axis is thus orthogonal to the surface and directed towards the accessible half-space [107]. Thus, the scattering pattern is reported for $0° \leq \vartheta_{\mathrm{S}} \leq 180°$ and $0 \leq \varphi_{\mathrm{S}} \leq 180°$.

As regards the direction of incidence, once the transition matrix of the effective scatterer S is known, the generation of the scattering pattern for several values of ϑ_{I} and φ_{I} is a fast and low-cost operation that produces a large amount of data, however. Therefore, we report all the scattering patterns for a single direction of incidence, that is indicated by the arrow in Fig. 8.1. It was chosen to form an angle of 45° with the normal to the surface and has thus $\vartheta_{\mathrm{I}} = 90°$ and $\varphi_{\mathrm{I}} = 225°$. We also chose to not refer the state of polarization to the pair of basis vectors that are parallel and orthogonal to the plane of scattering, i.e., to the plane of $\boldsymbol{k}_{\mathrm{I}}$ and $\boldsymbol{k}_{\mathrm{S}}$. In fact, we assumed that the polarization vector of the incident wave lies along either $\hat{\boldsymbol{\vartheta}}$ or $\hat{\boldsymbol{\varphi}}$, so that $E_0 = E_{0\eta'}$, and $I_{\mathrm{I}} = I_{\mathrm{I}\eta'\eta'}$. $\hat{\boldsymbol{\vartheta}}$ and $\hat{\boldsymbol{\varphi}}$, in turn, are tangent to the the meridians and to the parallels, respectively, of the large spherical surface in Fig. 8.1. In other words, we describe the scattering with reference to the meridional planes of $\hat{\boldsymbol{k}}_{\mathrm{I}}$ and $\hat{\boldsymbol{k}}_{\mathrm{S}}$. As a consequence, the appearance of cross-polarization effects is expected even when the scatterer is a single sphere.

The quantity that we report in Figs. 8.2–8.4 as a function of ϑ_{S} and φ_{S} is $\mathcal{I}_{\eta\eta'} = |f_{\eta\eta'}|^2$ for the single particles and $\langle \mathcal{I}_{\eta\eta'} \rangle$ for the dispersions. According to (6.9), $|f_{\eta\eta'}|^2 = r^2 I_{\eta\eta}/I_{\mathrm{I}}$. For the sake of clarity, the subscripts η and η' take on the symbolic values ϑ and φ to denote polarization along the meridians (ϑ-polarization) and along the parallels (φ-polarization), respectively.

We first notice that even when ϑ_{S} reaches its limiting values, $\vartheta_{\mathrm{S}} = 0°$ and $\vartheta_{\mathrm{S}} = 180°$, the angle φ_{S} is still well defined as this angle characterizes an observation with a well defined choice of the polarization, e.g. along the

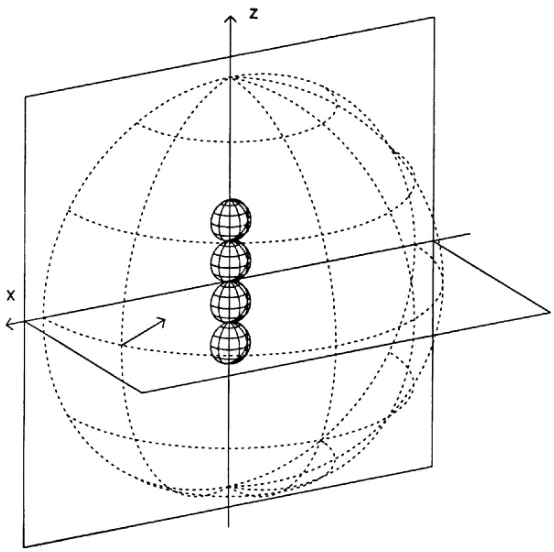

Fig. 8.1. Geometry that we adopted to display our results. The orientation of the four-hemisphere linear chain we will discuss in this section is also shown

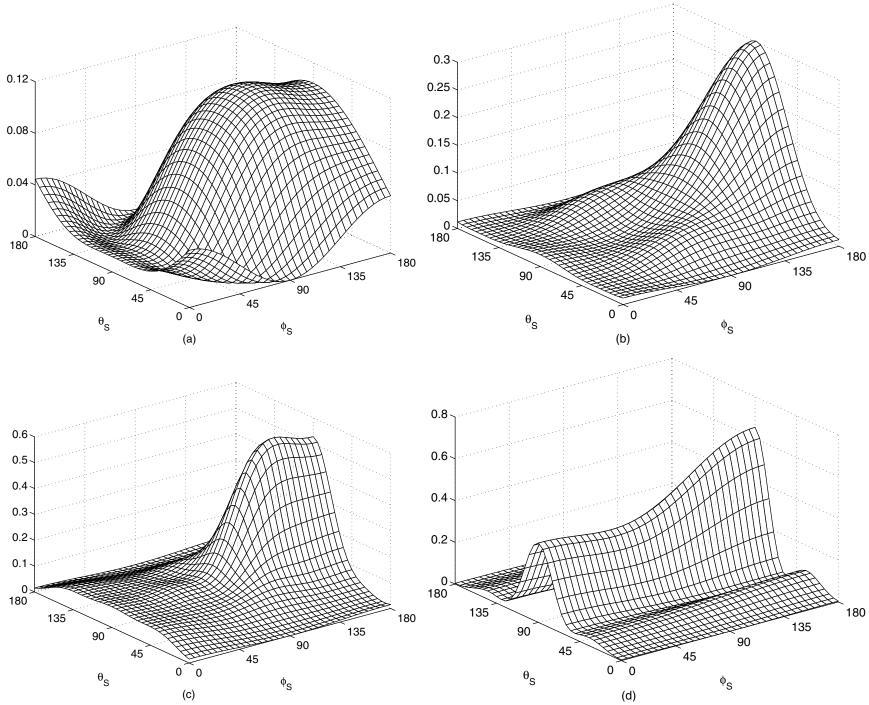

Fig. 8.2. Pattern of the scattered intensity from **(a)** the single sphere on the reflecting surface, **(b)** the dispersion of randomly oriented two-sphere clusters, **(c)** the dispersion of randomly oriented four-hemisphere linear chains, and **(d)** the four-hemisphere linear chain oriented as shown in Fig. 8.1. The wavelength of the incident field is $\lambda = 628.3\,\mathrm{nm}$ and the refractive index of the scatterers is $n_0 = 3$. The radius of the single sphere in (a) is $\rho_\mathrm{s} = 126\,\mathrm{nm}$, whereas the radius of the spheres in the two-sphere clusters in (b) and of the hemispheres of the four-hemisphere linear chain in (c), and (d) is $\rho_\mathrm{h} = 100\,\mathrm{nm}$. We actually report (in $\mu\mathrm{m}^2$) the quantity $\mathcal{I}_{\varphi\varphi}$ in (a) and (d) and $\langle\mathcal{I}_{\varphi\varphi}\rangle$ in (b) and (c) as a function of the angles of observation ϑ_S and φ_S

meridians. Thus, the limiting curves of our patterns ($\vartheta_\mathrm{S} = 0°$ and $\vartheta_\mathrm{S} = 180°$) describe the observation of the scattered beam that propagates along the reflecting surface at right angles to the plane of incidence with a polarization that depends on φ_S. So, for the ϑ-polarized component of the scattered wave, when $\varphi_\mathrm{S} = 90°$, $\boldsymbol{E}_\mathrm{S}$ is orthogonal to the surface, whereas when $\varphi_\mathrm{S} = 0°$ or $\varphi_\mathrm{S} = 180°$, $\boldsymbol{E}_\mathrm{S}$ is parallel to the reflecting surface, and thus, as a direct consequence of the boundary conditions, the scattered intensity must vanish. For the φ-polarized component of the scattered wave, when $\varphi_\mathrm{S} = 0°$ or $\varphi_\mathrm{S} = 180°$, $\boldsymbol{E}_\mathrm{S}$ is orthogonal to the surface whereas, when $\varphi_\mathrm{S} = 90°$, $\boldsymbol{E}_\mathrm{S}$ is parallel to the reflecting surface, and thus the scattered intensity must again vanish. Since, for any given polarization, the four extreme vertices of

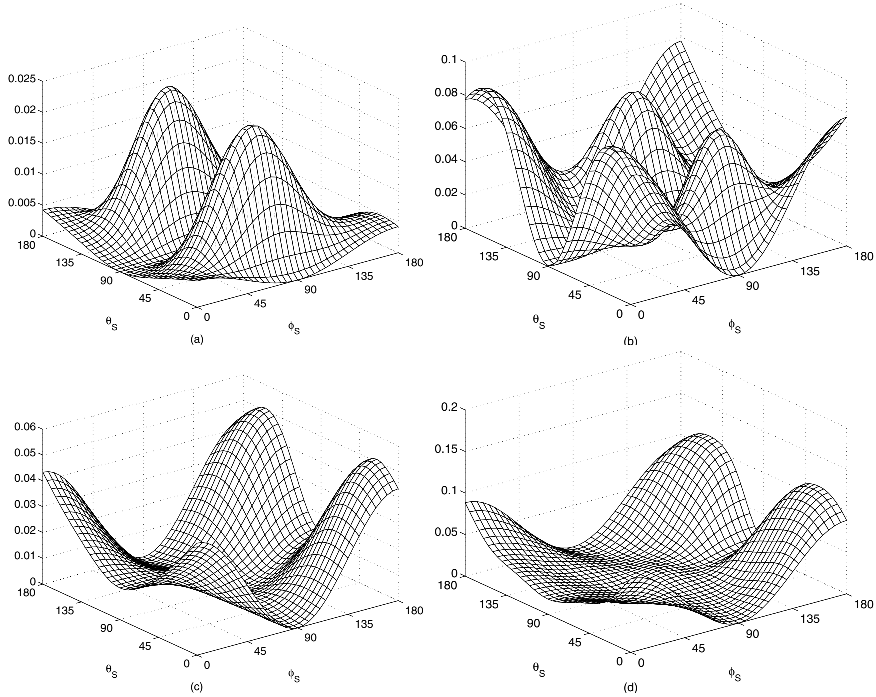

Fig. 8.3. Pattern of the scattered intensity from **(a)** the single sphere on the reflecting surface, **(b)** the dispersion of randomly oriented two-sphere clusters, **(c)** the dispersion of randomly oriented two-hemisphere clusters, and **(d)** the dispersion of randomly oriented four-hemisphere linear chains. The wavelength of the incident field is $\lambda = 628.3\,\text{nm}$ and the refractive index of the scatterers is $n_0 = 3$. The radius of the single sphere in (a) and of the hemispheres in (c) is $\rho_\text{s} = 126\,\text{nm}$, whereas the radius of the spheres in the two-sphere clusters in (b) and of the hemispheres of the four-hemisphere linear chain in (d) is $\rho_\text{h} = 100\,\text{nm}$. We actually report (in μm^2) the quantity $\mathcal{I}_{\varphi\vartheta}$ in (a) and $\langle \mathcal{I}_{\varphi\vartheta} \rangle$ in (b), (c), and (d) as a function of the angles of observation ϑ_S and φ_S

the pattern correspond to the same physical situation, the scattered intensity must have the same value at all these extreme points. A further consequence is that, e.g. $\mathcal{I}_{\varphi\varphi}(\vartheta_\text{S} = 0°, \varphi_\text{S} = 0°) = \mathcal{I}_{\vartheta\varphi}(\vartheta_\text{S} = 0°, \varphi_\text{S} = 90°)$.

All these features can be seen in Figs. 8.2–8.4 that report the results of calculations. In particular, Fig. 8.2 reports the scattering pattern (a) for a single sphere in contact with the surface, (b) for a dispersion of randomly oriented clusters of two mutually contacting spheres on the surface, (c) for a dispersion of randomly oriented linear chains of four hemispheres, and (d) for a linear chain of four hemispheres along the z axis. The incident field is φ-polarized and the φ-polarized component of the scattered wave is considered. The pattern for a single sphere in Fig. 8.2 (a) shows only a symmetry of

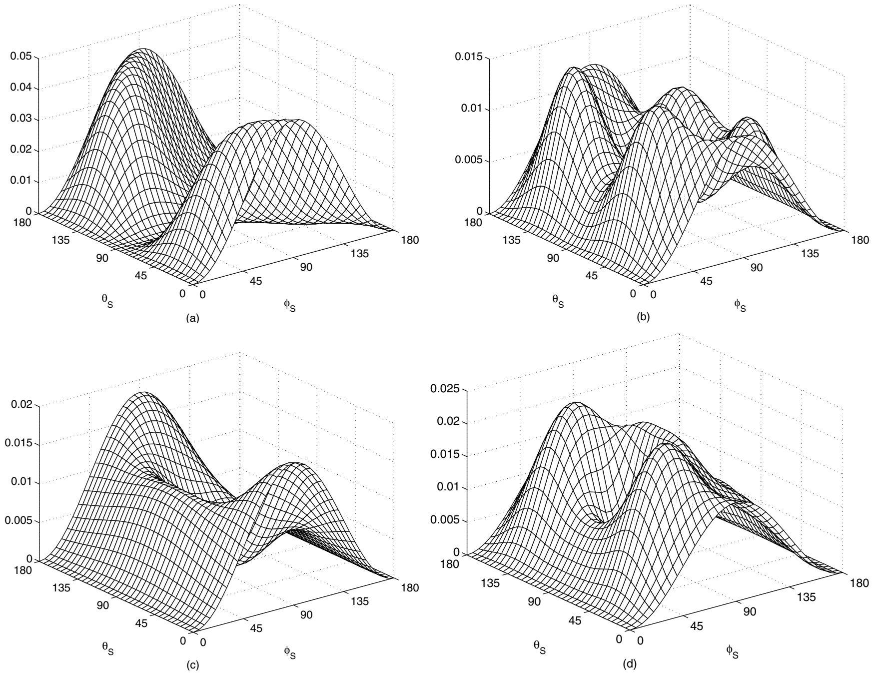

Fig. 8.4. Same as Fig. 8.3, except that $\mathcal{I}_{\vartheta\varphi}$ and $\langle\mathcal{I}_{\vartheta\varphi}\rangle$ are considered

reflection in the plane of incidence. Therefore, even for such a cylindrically symmetric object all the directions of scattering must be considered when the incidence is not normal to the reflecting plane. In all the four patterns in Fig. 8.2 we notice the presence of a strong scattered beam that propagates along the reflecting surface for $\vartheta_{\mathrm{S}} = 90°$ and $\varphi_{\mathrm{S}} = 180°$. We also notice the two wings in the pattern from the linear chain of four hemispheres in Fig. 8.2 (d). The comparison with the orientationally averaged pattern in Fig. 8.2 (c) suggests that the wings are a result of the particular orientation of the scatterer. The limiting curves at $\vartheta_{\mathrm{S}} = 0°$ and $\vartheta_{\mathrm{S}} = 180°$ turn out to be almost flat for all the clusters but are in no way flat for the single sphere. This suggests that the observation of the scattered light that propagates along the reflecting surface may yield useful information on the shape of the scattering particles.

This is confirmed by Fig. 8.3 that reports the patterns for a single sphere in (a) and for the assemblies of randomly-oriented two-sphere clusters in (b), two-hemisphere clusters in (c), and four-hemisphere linear chains in (d). The incident wave is ϑ-polarized and the φ-polarized component of the scattered wave is considered. Thus, all these patterns describe cross-polarization effects. The patterns in (a) and (b), present a couple of peaks for nonlimiting values of ϑ_{S} and φ_{S}. Such peaks are not present in the patterns in (c) and (d). Furthermore, the patterns for all the clusters, either of spheres and of hemispheres reach their maximum value at the four vertices ($\vartheta_{\mathrm{S}} = 0°$, $180°$ and $\varphi_{\mathrm{S}} = 0°$, $180°$). This is not the case for the single sphere in (a). The differences of the patterns of the single sphere and of the clusters can be attributed on one hand to the cylindrical symmetry of the single sphere and on the other hand to the lack of sphericity of the clusters in spite of their random orientation. In other words, the process of averaging does not cancel the effects that are due to the lack of sphericity of the scatterers. The patterns in Fig. 8.3 suggest that the effects of the nonsphericity are still visible provided that the observation is made with the appropriate polarization.

In Fig. 8.4 we report the patterns for the same objects that we considered in Fig. 8.3. The only difference is the choice of the polarization, i.e., the incident wave is φ-polarized and the ϑ-polarized component of the scattered wave is considered. The patterns in (a) and (c), that refer to the single sphere and to the two-hemispheres clusters, show some similarities. Such a similarity is also shown by the patterns in (b) and (d) that refer to the two-sphere and to the four-hemisphere clusters, respectively. Thus, the general structure of the patterns seems to be related to the number of the spheres that compose the effective scatterers. In this respect, we recall that all the scatterers that we consider in this section have the same volume.

We do not report any result for the case in which both the incident and the scattered wave are ϑ-polarized because these patterns do not add any information worthy of a separate comment.

In order to achieve convergence to four significant digits, we had to extend the multipole expansions up to $l_{\mathrm{M}} = 8$ for the single sphere, $l_{\mathrm{M}} = 9$ for the two-hemisphere clusters, and $l_{\mathrm{M}} = 10$ both for the two-sphere and the four-hemisphere clusters. The need to use so large a value of l_{M} even for the single sphere is due to the fact that, using image theory, we do not actually deal with a single sphere but rather with the two-sphere cluster that forms the effective scatterer. Now, the size parameter of the smallest sphere that contains the effective scatterer is $x = 2.52$ when the real scatterer is a single sphere, and we have even larger values for the other clusters that we considered here. If one also adds that the refractive index is $n_0 = 3$, the values of l_{M} that we quoted above can in no way be considered too large.

Ultimately, the results of calculations show that the scattering pattern of the model anisotropic scatterers are remarkably different from those of the spherical particles. Therefore, provided this behavior pertains also to more general anisotropic scatterers than those we considered here, a polarization analysis of the grazing scattered intensity could yield useful information on the possible nonsphericity of the particles on the surface.

8.2 Inclusion-Containing Hemispheres on a Metallic Surface

The discussion in Sect. 8.1 proves that image theory is a convenient method to calculate the optical properties of particles in the presence of a perfectly reflecting plane surface [107, 161, 163, 164]. When the particles themselves can be modeled as clusters of spheres or of hemispheres, the association of image theory with the transition matrix approach yields a safe ground for the calculations.

In this section we resort again to image theory to investigate the optical properties of a hemisphere with its flat face on a perfectly reflecting surface, and the investigation is extended to hemispheres containing either a hemispherical or a spherical inclusion. The case of an inclusion composed by a pair of mutually contacting identical spheres is also considered. The purpose is the assessment of how and to what extent the presence of inclusions of various morphologies affects the observed spectrum. Such a study, however, goes beyond the academic interest of solving a problem of electromagnetism through an exact procedure. In fact, the objects we are going to consider may be acceptable models for liquid droplets, possibly containing pollutants, deposited on a metal surface. Furthermore, independent hemispheres on a metallic surface are known to form at the early stages of the deposition of an electrolyte. The dielectric properties of such hemispheres are of interest to the electrochemists who, in general, face the problem through statistical methods [165,166]. Our study may thus make a useful contribution to the solution of this problem as well as to the problem of detecting whether, during their growth, the hemispheres include any impurity that may be present.

We discuss the scattered intensity from homogeneous hemispheres of radius $\rho_0 = 380\,\mathrm{nm}$ and refractive index $n_0 = 1.59$ on the assumption that the homogeneous medium that fills the accessible half-space is the vacuum ($n' = 1$) [167]. The geometry is depicted in Fig. 8.5. The incident wavevector is taken to lie in the first quadrant of the zx plane and the angle of incidence ϑ_{I}, as usual in optics, is measured between the negative z axis and the positive $\hat{\boldsymbol{k}}_{\mathrm{I}}$ direction. The angle of observation ϑ_{S} is always measured from the

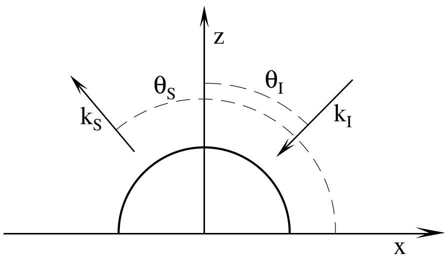

Fig. 8.5. Geometry for the hemisphere on a metallic surface

positive x axis. When inclusions are present, their refractive index is assumed to be $n_1 = 3.8$, whereas their geometrical parameters are so chosen that their total volume is 1/8 of the volume of the host hemisphere. In all instances, the wavelength of the incident field is taken to be $\lambda_I = 632.8\,\mathrm{nm}$ and is thus comparable to the size of the scattering objects. Therefore, even in view of our choice of the refractive indices n_0 and n_1, the convergence of all the multipole expansions that are involved in the calculations must be carefully checked. In this respect we found that, for any geometry that we considered for the inclusions, using $l_M = 9$ achieves convergence to three significant digits, whereas we had to use $l_M = 13$ to get a convergence to four significant digits. Of course, the correctness of our results was checked through the usual tests [88]. Thus, by letting the refractive index of the host hemisphere tend to that of the vacuum ($n_0 \to 1$), we followed the evolution of the scattered intensity towards that expected from the bare inclusions. Moreover, by letting $n_1 \to n_0$ the scattered intensity evolved to that of homogeneous hemispheres with no inclusion.

In all the following figures we report the quantity $\mathcal{I}_{\eta\eta}$, (see Sect. 8.1), in $\mu\mathrm{m}^2$ for a few selected values of ϑ_I. Accordingly, in Fig. 8.6 we report $\mathcal{I}_{\eta\eta}$ for a homogeneous hemisphere when $\vartheta_I = 0°$, 45° and 70°. The polarization of the incident light is parallel ($\eta = 1$) in Fig. 8.6 (a) and perpendicular ($\eta = 2$) in Fig. 8.6 (b). As we stated in Sect. 6.2, the effective scatterer is a homogeneous sphere so that these patterns were calculated by using the Mie theory. Nevertheless, they look quite different from the patterns from a isolated homogeneous sphere because the exciting field is, in the present case, the superposition of two plane waves whose phase relation, given by (6.4), is dictated by the boundary conditions on the reflecting plane. As a result we get a strong dependence of the pattern on the polarization and in particular the vanishing of the scattered field for $\eta = 2$ (perpendicular polarization) at $\vartheta_S = 0°$ and $\vartheta_S = 180°$. The latter result stems from the boundary conditions

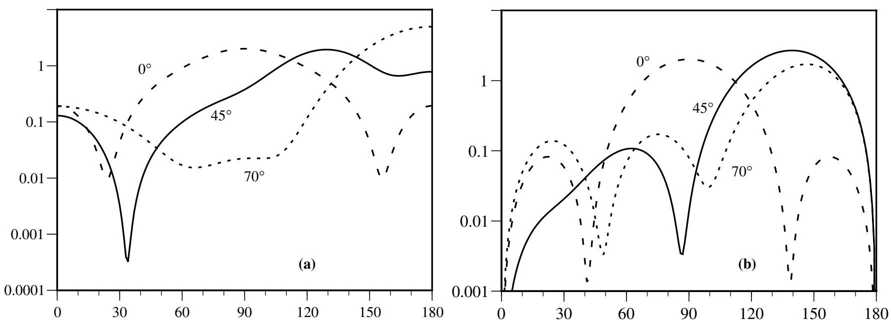

Fig. 8.6. $\mathcal{I}_{\eta\eta}$ for $\eta = 1$ **(a)** and $\eta = 2$ **(b)**, in $\mu\mathrm{m}^2$, for the homogeneous hemisphere as a function of the angle of observation ϑ_S. The curves are labeled by the angle of incidence ϑ_I

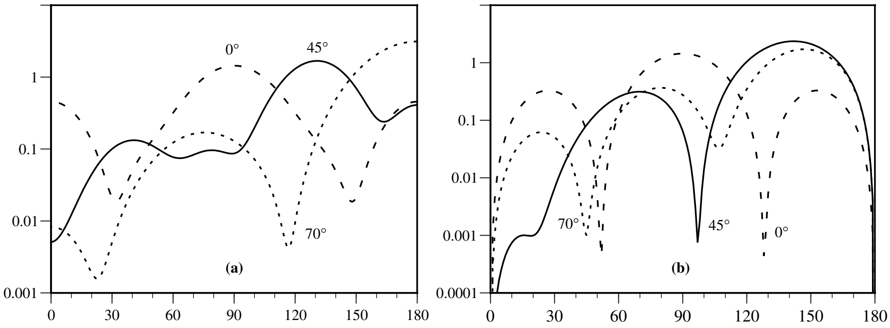

Fig. 8.7. $\mathcal{I}_{\eta\eta}$ for $\eta = 1$ **(a)** and $\eta = 2$ **(b)**, in μm^2, for the hemisphere containing the centered hemispherical inclusion as a function of the angle of observation ϑ_S. The curves are labeled by the angle of incidence ϑ_I

because for polarization perpendicular to the plane of incidence the field is parallel to the metallic surface.

Figure 8.7 refers to the hemisphere containing a centered hemispherical inclusion of radius 190 nm. The angles of incidence and the polarization are as in Fig. 8.6 so that the respective curves can be directly compared. Actual comparison shows that the effect of the presence of the hemispherical inclusion is quite evident. In particular, we notice that the most striking changes occur in the pattern for parallel polarization ($\eta = 1$). For this choice of the polarization, indeed, the patterns for $\vartheta_I = 70°$ and $\vartheta_I = 45°$ are qualitatively different from the corresponding patterns in Fig. 8.6 (a). Less evident changes, such as shifts of the minima, are also present in the patterns for $\eta = 2$ in Fig. 8.7 (b). It may be worth noticing that the patterns in Fig. 8.7 are determined both by the properties of the multipole amplitudes of the exciting field and by the multiple scattering processes that occur between the inclusion and the internal surface of the host hemisphere. Of course, it is to be expected that when the included hemisphere is off center the multiple scattering processes are effective in accounting also for the loss of spherical symmetry of the equivalent scatterer.

To pursue this point, we calculated $\mathcal{I}_{\eta\eta}$ for $\vartheta_I = 45°$ for several positions of the included hemisphere. The results are reported in Fig. 8.8 for the included hemisphere at maximum eccentricity along both the positive and the negative x axis as well as along the y axis. For the sake of comparison, we also report, from Fig. 8.7, $\mathcal{I}_{\eta\eta}$ for the case in which the included hemisphere is concentric. It is then an easy matter to see that for both choices of the polarization the eccentricity of the inclusion induces qualitative changes in the scattering pattern. In particular, for $\eta = 1$, we notice the occurrence of the deep minimum at $\vartheta_S = 37°$ when the included hemisphere is at maximum eccentricity in the $+x$ direction. Such a minimum is also present in the case of the homogeneous hemisphere, however (see Fig. 8.6 (a)). On the contrary, for

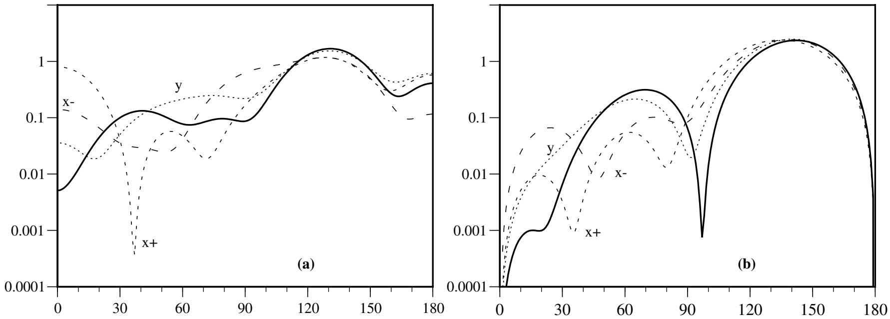

Fig. 8.8. $\mathcal{I}_{\eta\eta}$ for $\eta = 1$ **(a)** and $\eta = 2$ **(b)**, in μm^2, for the hemisphere containing an eccentric hemispherical inclusion as a function of the angle of observation ϑ_S. $\vartheta_I = 45°$. The curves labeled $x\pm$ refer to the inclusion at maximum eccentricity along the positive and negative x axis, respectively. The curve labeled y refer to the inclusion at maximum eccentricity along the y axis. The solid curve is reported for comparison with Fig. 8.7

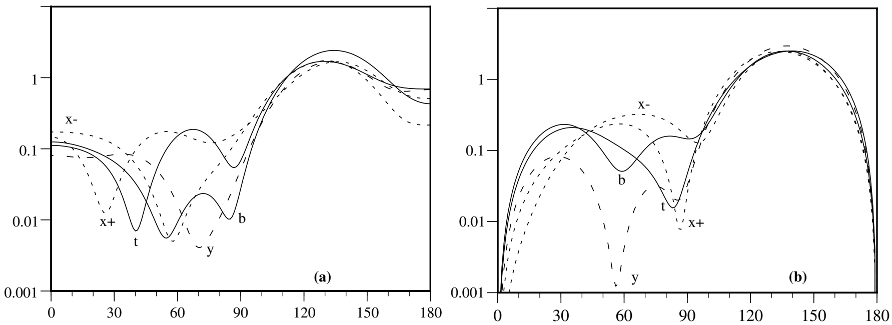

Fig. 8.9. $\mathcal{I}_{\eta\eta}$ for $\eta = 1$ **(a)** and $\eta = 2$ **(b)**, in μm^2, for the hemisphere containing a spherical inclusion as a function of the angle of observation ϑ_S. $\vartheta_I = 45°$. The curve labeled b refers to the sphere on the reflecting surface with its center on the z axis. The curve labeled t refers to the sphere tangent to the top of the host hemisphere and with its center on the z axis. The curves labeled $x\pm$ and y refer to the sphere at maximum eccentricity along the $\pm x$ axis and the y axis, respectively

$\eta = 2$, we should remark the disappearance of the deep minimum that occurs at $\vartheta_S = 96°$ when the inclusion is centered, and the onset of less deep minima when the inclusion moves both in the $\pm x$ as well as in the y direction. The occurrence and the disappearance of minima as a function of the position of the inclusion are expected, on general grounds, to be due to interference effects as the field propagates back and forth between the inclusion and the internal surface of the host hemisphere.

In Fig. 8.9 we report, for $\vartheta_I = 45°$, $\mathcal{I}_{\eta\eta}$ for the hemisphere containing a whole sphere of radius $\rho_1 = 150.8\,\text{nm}$. The included sphere was considered touching both the reflecting surface and the internal surface of the host hemisphere along the $\pm x$ and the y directions. We also considered the included sphere with its center on the z axis either touching the reflecting surface or touching the surface of the host hemisphere. Comparison of the patterns for the corresponding configurations and polarizations in Figs. 8.8 and 8.9 show that the change of the shape of the inclusion, even though with no change of its volume, produces visible qualitative changes of the scattered intensity. These changes are easily understood when one recalls that, in the framework of image theory, the equivalent scatterer of a hemisphere with a spherical inclusion is a whole sphere containing a cluster composed by two identical spheres. Accordingly, the scattering pattern of the whole object is determined not only by the multiple scattering processes that occur between the inclusion and the surface of the host sphere, but also by the processes that occur between the components of the inclusion (see also Sect. 7.6.3). For example, when the included sphere with its center on the z axis and tangent to the reflecting plane is lifted so as to become tangent to the top of the host hemisphere, the resulting configuration is equivalent to considering a pair of spheres that are somewhat separated. This nonzero separation implies a decrease of the intensity of the multiple scattering processes that occur between them.

Finally, in Figs. 8.10 and 8.11 we report, for $\vartheta_{\mathrm{I}} = 45°$, $\mathcal{I}_{\eta\eta}$ for the hemisphere containing two identical, mutually contacting spheres that lie on the reflecting surface. The radius of both spheres is $\rho_1 = 120\,\mathrm{nm}$. The axis of the included bisphere is considered both in the plane of incidence (the zx plane) and in the yz plane. In Fig. 8.10 the contacting point between the spheres lies on the z axis. In Fig. 8.11 one of the spheres touches the surface of the host hemisphere, so that the bisphere is as eccentric as possible. The dependence

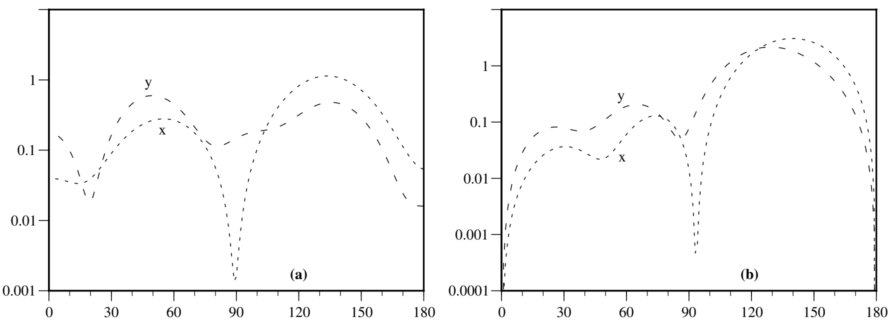

Fig. 8.10. $\mathcal{I}_{\eta\eta}$ for $\eta = 1$ **(a)** and $\eta = 2$ **(b)**, in $\mu\mathrm{m}^2$, for the hemisphere containing the inclusion composed by two mutually contacting identical spheres as a function of the angle of observation ϑ_{S}. $\vartheta_{\mathrm{I}} = 45°$. The point of contact between the included spheres always lies on the z axis. The curves labeled x and y refer to the bisphere with its axis in the plane of incidence (zx plane) and in the xy plane, respectively

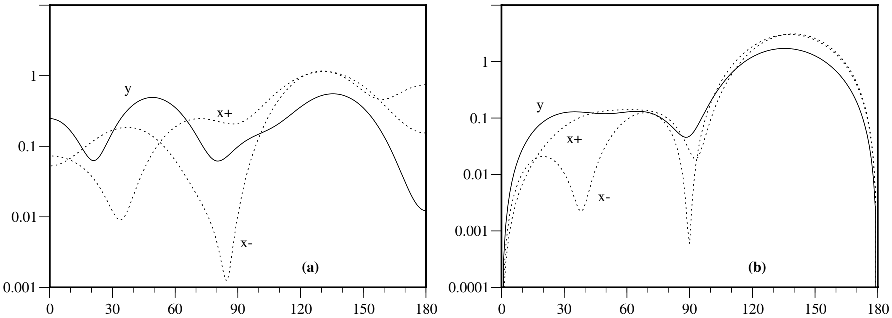

Fig. 8.11. $\mathcal{I}_{\eta\eta}$ for $\eta = 1$ **(a)** and $\eta = 2$ **(b)**, in μm^2, for the hemisphere containing the inclusion composed by two mutually contacting identical spheres as a function of the angle of observation ϑ_S. $\vartheta_I = 45°$. The curves labeled $x\pm$ refer to the bisphere with its axis in the zx plane and one of its components touching the surface of the host hemisphere along the $\pm x$ direction. The curve labeled y refers to the bisphere with its axis in the yz plane and one of its components touching the host hemisphere

of all the curves both on the position of the cluster and on the polarization of the incident field can be traced back to the fact that the multiple scattering processes now occur between the four spheres that form the equivalent scatterer and thus give rise to patterns that may be rather complicated. It is worth noticing, however, that $\mathcal{I}_{\eta\eta}$ has a weaker dependence on ϑ_S than one would expect, e.g. the number of the minima is not as large as one could expect from the calculations for bare clusters with a comparable complexity. This result is in agreement with our finding that the more minutely subdivided is the matter of the inclusions the smoother are the curves of the scattered intensity [89]. Nevertheless when we compare $\mathcal{I}_{\eta\eta}$ in Fig. 8.10 with $\mathcal{I}_{\eta\eta}$ for the eccentric cluster in Fig. 8.11, we see that the curves are quite distinguishable, in particular for $\eta = 2$, even though the maximum eccentricity is achieved with a small displacement of the contacting point between the spheres from the z axis.

The results that we reported above are aimed at informing the interested reader of the potentialities of the formalism of the transition matrix in association with image theory. Beyond the interest for the electrochemists, the formalism may also be of interest to people studying the effect of atmospheric pollution, for instance, for the interpretation of the optical observations aimed at the detection of the presence and of the nature of pollutants deposited on a metal surface. In this respect, the results that we reported above should be understood as a demonstrative sample of the patterns that can be found in actual experiments. Nevertheless, the reported results are sufficient to show that, beyond the expected dependence on the direction of incidence and on the polarization, one has also to expect a noticeable dependence on the geometry of the inclusions. Of course, these features are not sufficient to allow the experimentalists to discriminate among the possible geometries, in particular when several different inclusions are present. However, further information on the nature and on the configuration of the inclusions could stem from the comparison of patterns taken for different choices both of the angle of incidence and of the wavelength.

8.3 Resonance Suppression Mechanism

It is intuitive that the spectrum of a homogeneous hemisphere on a metallic surface can display optical resonances. According to image theory, the resonances are those of the effective scatterer, a homogeneous sphere, illuminated by the exciting field. It is not so intuitive that the hemisphere may not present some of the resonances that are present in the spectrum of the effective scatterer when illuminated by the actual incident field only. This resonance suppression mechanism can be understood when one thinks that the exciting field is the superposition of the actual incident field and of the field that comes from the image source and that the phase relation between these fields are dictated by the condition of perfect reflection on the metallic surface. As discussed in Sect. 6.2, the multipole amplitudes of the exciting field are given by (6.8). Then, it is an easy matter to see that, when in (6.8) $\left[1-(-)^{p+l+m}\right]=0$, i.e., when $p+l+m$ is even, the corresponding multipole is not present in the exciting field, even when the corresponding amplitude of the incident field is nonvanishing. This vanishing of some amplitudes of the exciting field may thus affect the scattered field up to the suppression of some of the characteristic resonance peaks. Although the considerations above refer to a homogeneous hemisphere, the resonance-suppressing mechanism has no evident dependence on the shape of the particle. Therefore, it would be tempting use this effect to interpret the spectra from particles of arbitrary shape, according to the suggestion of Li and Chýlek [168] and by Johnson [161, 169]. We will see below that this task is rather difficult [115]. Let us, in fact, recall that the scattering amplitude of a hemisphere on a perfectly reflecting surface is

$$f_{\eta\eta}(\hat{\boldsymbol{k}}_{\mathrm{R}},\hat{\boldsymbol{k}}_{\mathrm{I}})=\frac{\mathrm{i}}{4\pi k'}\sum_{plm}W^{(p)*}_{\mathrm{R}\eta lm}R^{(p)}_{l}W^{(p)}_{\mathrm{E}\eta lm}\,, \tag{8.1}$$

where the quantities $R^{(p)}_l$, except for the minus sign, are the elements of the transition matrix for the effective (spherical) scatterer, and are defined by (5.7). In turn, the amplitudes $W^{(p)}_{\mathrm{R}\eta lm}$ are defined by (6.4). Note that (8.1) is a particular case of (6.10) for observation in the plane of incidence. The amplitudes $W^{(p)}_{\mathrm{I}\eta lm}$ satisfy the sum rule (4.8) or (4.9) according to whether the field is linearly or circularly polarized [41, 42]. Here we assume linear polarization, so that (4.8) applies. Since the transition matrix of the effective scatterer is independent of m, it is meaningful to define the quantity

$$U_{\eta l}^{(p)} = \sum_m W_{\mathrm{R}\eta lm}^{(p)*} W_{\mathrm{E}\eta lm}^{(p)} = (-)^{\eta-1} 2\pi(2l+1) + \sum_m (-)^{\eta+p+l+m} W_{\mathrm{I}\eta lm}^{(p)*} W_{\mathrm{I}\eta lm}^{(p)} , \tag{8.2}$$

which has been obtained with the help of (4.8). We can then rewrite (8.1) in the form

$$f_{\eta\eta}(\hat{\boldsymbol{k}}_{\mathrm{R}}, \hat{\boldsymbol{k}}_{\mathrm{I}}) = \frac{\mathrm{i}}{4\pi k'} \sum_{pl} U_{\eta l}^{(p)} R_l^{(p)} ,$$

that shows at once that any resonance associated with a vanishing $U_{\eta l}^{(p)}$ is bound to disappear.

The situation is quite different when the effective scatterer is nonspherical. In this case, indeed, the scattering amplitude is given by (6.10) and the elements of the matrix S depend both on m and on m'. In this case, the resonance suppression it is just due to the vanishing of the amplitude $W_{\mathrm{E}\eta lm}^{(p)}$, which should excite the resonating element of S. In order to show how the resonance suppression mechanism works both for spherical and nonspherical effective scatterers, we will consider a homogeneous hemisphere whose flat face lies on a metal surface, and a binary aggregate of identical hemispheres with their flat faces on the perfectly reflecting surface. In the latter case, the radius of the component hemispheres is chosen to be small while the refractive index is assumed to be rather large. These choices result in a spectrum with a simple structure of the resonances.

8.3.1 Single Hemispheres

We report in Fig. 8.12 the plots of $U_{\eta l}^{(p)}$ for $l \leq 4$, $\eta = 1, 2$ and $p = 1, 2$ as a function of ϑ_{I}. We notice in Figs. 8.12 (a) and (b) that at $\vartheta_{\mathrm{I}} = 0°$ all the $U_{1l}^{(1)}$ vanish for even l, whereas all the $U_{1l}^{(2)}$ do vanish for odd l. This result was expected because when $\vartheta_{\mathrm{I}} = 0°$ the only nonvanishing amplitudes $W_{\mathrm{I}\eta lm}^{(p)}$ are those with $m = \pm 1$, so that

$$W_{\mathrm{E}\eta l,\pm 1}^{(p)} = \left[1 + (-)^{p+l}\right] W_{\mathrm{I}\eta l,\pm 1}^{(p)} .$$

Although the preceding argument is based on the vanishing of the individual amplitudes $W_{\mathrm{E}\eta lm}^{(p)}$ at $\vartheta_{\mathrm{I}} = 0°$, the usefulness of the quantity $U_{\eta l}^{(p)}$ remains unaffected. In fact, the vanishing of $U_{1l}^{(2)}$ for $l = 2$ at $\vartheta_{\mathrm{I}} = 45°$ (see Fig. 8.12 (b)) is due to the sum over m in (8.2). The plots in Figs. 8.12 (c) and (d) show that the behavior of $U_{2l}^{(p)}$ is similar to that of $U_{1l}^{(p)}$. We remark that again all the $U_{2l}^{(1)}$ vanish at $\vartheta_{\mathrm{I}} = 0°$ for even l, whereas all the $U_{2l}^{(2)}$ vanish at the same incidence for odd l and, in particular, $U_{21}^{(2)}$ turns out to be identically zero. These features were expected on the ground of the structure of (8.2).

We report in Fig. 8.13 the adimensional quantity

$$\tilde{\gamma}_{\mathrm{R}\eta} = 2k' \mathrm{Im}[(-)^{\eta-1} f_{\eta\eta}(\hat{\boldsymbol{k}}_{\mathrm{R}}, \hat{\boldsymbol{k}}_{\mathrm{I}})],$$

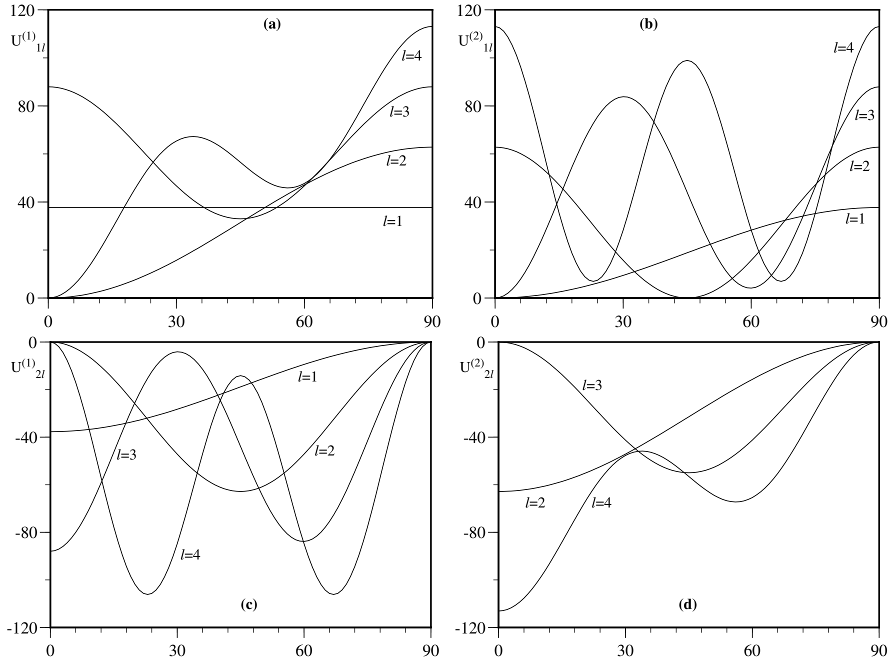

Fig. 8.12. Plot of $U_{\eta l}^{(p)}(\vartheta_{\mathrm{I}})$ for $l \leq 4$. Note that in (d) the curve for $l = 1$ does not appear as it is identically vanishing

for $\eta = 1$, for a hemisphere of refractive index $n_0 = 3$ on the reflecting surface. The homogeneous medium that fills the accessible half-space was assumed to be the vacuum ($n' = 1$). In fact, according to Sects. 2.6.3 and 6.6, we have

$$\tilde{\gamma}_{\mathrm{R}\eta} = \frac{k'^2}{2\pi}\sigma_{\mathrm{T}\eta} \ ,$$

a quantity that depends on ρ and k_{v} only through their product. $\tilde{\gamma}_{R\eta}$ is plotted as a function of the size parameter $x = k_{\mathrm{v}}\rho$ in the range from $x = 1$ to $x = 3$. The angle of incidence is $\vartheta_I = 0°$ in Fig. 8.13 (a), $45°$ in Fig. 8.13 (b), and $70°$ in Fig. 8.13 (c).

Now, it is quite natural to compare the spectrum from the hemisphere on the reflecting surface with the spectrum from the *equivalent sphere*, i.e., from the effective scatterer, illuminated by the actual incident field only. Therefore, in each of Figs. 8.13 (a), (b), and (c) we also report the plot of the quantity

$$\tilde{\gamma} = 2k'\mathrm{Im}[f_{\eta\eta}(\hat{\boldsymbol{k}}_{\mathrm{I}}, \hat{\boldsymbol{k}}_{\mathrm{I}})]$$

for the equivalent sphere. In this case, $f_{\eta\eta}$ does not actually depend on the polarization (see also (4.8)) so that the quantity $\tilde{\gamma}$ need not carry the subscript η.

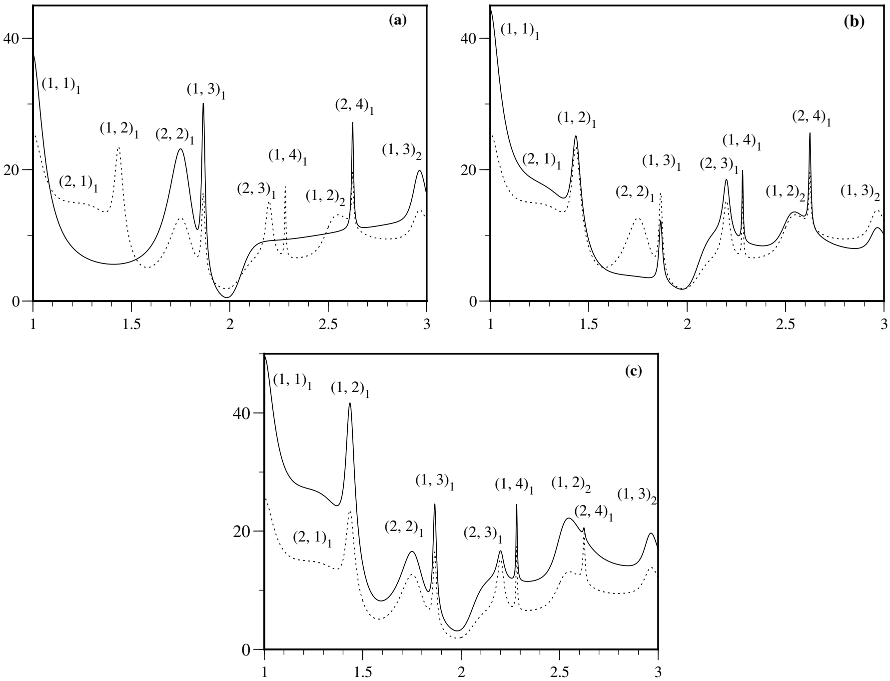

Fig. 8.13. $\tilde{\gamma}_{\mathrm{R}\eta}$ (*solid curves*) for a homogeneous hemisphere of radius ρ and refractive index $n_0 = 3$ on the reflecting surface as a function of $x = k_{\mathrm{v}}\rho$ for $\eta = 1$. The angle of incidence is $\vartheta_{\mathrm{I}} = 0°$ in **(a)**, $\vartheta_{\mathrm{I}} = 45°$ in **(b)**, and $\vartheta_{\mathrm{I}} = 70°$ in **(c)**. We also report for the sake of comparison $\tilde{\gamma}$ for the equivalent sphere (*dotted curves*). The resonances are labelled as $(p,\, l)_n$ where n distinguishes different resonances with the same value of p and l

The strict correspondence between the resonances that disappear and the vanishing of the respective $U_{1l}^{(p)}$ is so evident that, in our opinion, no further comment would be necessary. However, we call the attention of the reader to the simultaneous disappearance, in Fig. 8.13 (a), of the two resonances at $x = 1.3118$, that is associated to $p = 2$ and $l = 1$, and at $x = 1.437$, that is associated to $p = 1$ and $l = 2$. Both peaks belong, in fact, to an odd value of $p + l$. The same mechanism also explains the simultaneous disappearance of the peaks at $x = 2.2$ and at $x = 2.28$. The former peak is associated with $p = 2$ and $l = 3$ whereas for the latter peak $p = 1$ and $l = 4$. Again, both peaks belong to an odd value of $p + l$. Even the resonance spectrum for $\eta = 2$ strictly follows the behavior of the $U_{2l}^{(2)}$ so that we resolved not to report the specific plot that, in spite of its significance, does not add any further information worthy of a separate comment.

8.3.2 Binary Clusters

The lack of a general theory for the resonances of nonspherical particles makes an unambiguous classification of their resonances rather difficult. According to (6.10), the lack of diagonality of the transition matrix prevents a meaningful definition of a function analogous to the quantity $U^{(p)}_{\eta l}$ we defined above. Even in the case of aggregated spheres the transition matrix is not a diagonal matrix so that there is no one-to-one association of the multipole amplitudes of the exciting field to those of the scattered field. Nor there is a simple relation between the resonances of the component spheres and those of the aggregate as a whole. Nevertheless, (6.8) does not depend on the shape of the particles so that the vanishing of any of the amplitudes of the exciting field is expected to affect the resonances even of a nonspherical particle. To show that this is indeed the case, we calculate the resonance spectrum for two contacting spheres of radius ρ and refractive index n_0. We also calculate the spectrum for two contacting hemispheres of radius ρ and refractive index n_0 with their flat face on the reflecting surface. The surrounding medium is the vacuum ($n' = 1$), whereas $n_0 = 10\pi$ has an unusually high value. According to Newton [22] and to our experience [151], this choice makes the resonances of the aggregate as a whole, as well as of its components, occur at so small values of $x = k'\rho$ that fully convergent values of the scattered field are obtained for $l = l' = 1$ only. As a result, the resonances of the aggregate as a whole can surely be associated to the multipole amplitudes with $l = 1$.

In Fig. 8.14 (a) we report, for both values of η, the quantity

$$\tilde{\gamma}_\eta = 2k'\mathrm{Im}[f_{\eta,\eta}(\hat{\boldsymbol{k}}_\mathrm{I}, \hat{\boldsymbol{k}}_\mathrm{I})],$$

for the aggregate of spheres referred to above, whereas in Fig. 8.14 (b) we report $\tilde{\gamma}_{\mathrm{R}\eta}$ for the aggregate of hemispheres on the reflecting surface. All the plots are reported as a function of x and the angle of incidence is $\vartheta_\mathrm{I} = 70°$. Figures 8.15 (a) and (b) are the same as Figs. 8.14 (a) and (b), respectively, except that the angle of incidence is $\vartheta_\mathrm{I} = 0°$.

On the whole, Figs. 8.14 and 8.15 present three peaks at $x_1 = 0.09629$, $x_2 = 0.09813$, and $x_3 = 0.10183$. Since for $l = 1$ the component spheres have a single resonance at $x = 0.1$, Figs. 8.14 and 8.15 confirm that the multiple scattering processes within an aggregate produce resonances whose location cannot be related to the locations of the resonances of the component spheres [76, 151]. The dependence of the resonance spectrum of an aggregate on the polarization of the incident light can be understood only through a close examination of the features of the transition matrix and of the amplitudes of the exciting field.

Now, at x_1 the largest elements of S are $\mathcal{S}^{(1\,1)}_{1,\pm1,1,-1} \approx -\mathcal{S}^{(1\,1)}_{1,\pm1,11}$ so that a magnetic resonance ($p = 1$) is expected. At x_2 the leading elements are $\mathcal{S}^{(2\,2)}_{1010}$ and $\mathcal{S}^{(2\,2)}_{1,\pm1,1,-1} \approx \mathcal{S}^{(2\,2)}_{1,\pm1,11}$ so that an electric resonance ($p = 2$) is expected. Finally, at x_3 the leading elements of S are $\mathcal{S}^{(1\,1)}_{1010}$ and $\mathcal{S}^{(1\,1)}_{1,\pm1,1,-1} \approx$

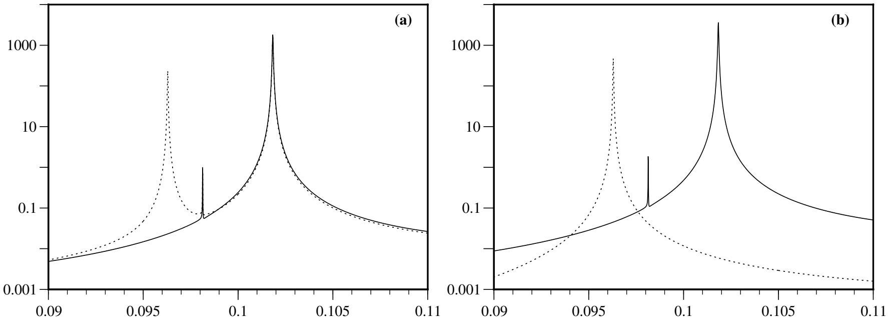

Fig. 8.14. $\tilde{\gamma}_\eta$ for the aggregate of two identical mutually contacting spheres of radius ρ and refractive index $n_0 = 31.4$ **(a)**, and $\tilde{\gamma}_{\mathrm{R}\eta}$ for the aggregate of two mutually contacting hemispheres with the same radius and refractive index on the reflecting surface as a function of x **(b)**. The axis of the aggregate lies in the zx plane and is parallel to the x axis. The plane of incidence coincides with the zx plane and the angle of incidence is $\vartheta_{\mathrm{I}} = 70°$. The *solid* and the *dotted curves* refer to polarization parallel and orthogonal to the plane of incidence, respectively. Note that the spike at $x = 0.09813$ in (a) is double as it appears for both choices of the polarization although this is not visible on the scale of the figure

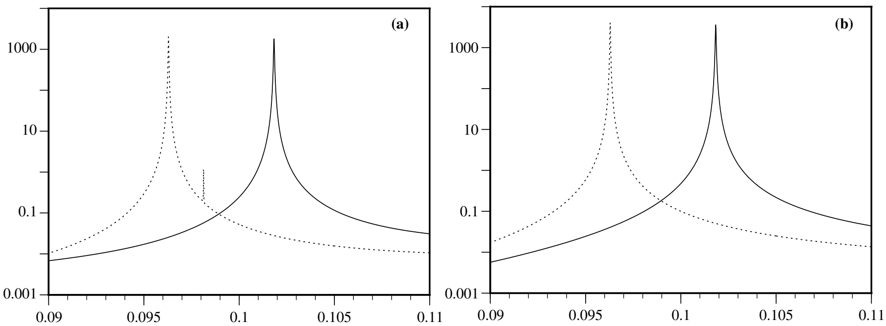

Fig. 8.15. Same as Fig. 8.14 except that the angle of incidence is $\vartheta_{\mathrm{I}} = 0°$

$\mathcal{S}^{(1\,1)}_{1,\pm 1,11}$ thus suggesting that this resonance is a magnetic one. Nevertheless, by comparing Figs. 8.14 and 8.15 one sees that not all the possible resonances actually occur. This is due to the dependence of the amplitudes $W^{(p)}_{\mathrm{I}\eta lm}$ both on the polarization and on the angle of incidence ϑ_I.

As an example, let us discuss the behavior of the resonance at x_2 that appears in Fig. 8.14 (a) for any choice of the polarization. According to (6.10), the implied amplitudes of the incident field are the $W^{(2)}_{\mathrm{I}\eta 1m}$, with $W^{(2)}_{\mathrm{I}210} = 0$ and $W^{(2)}_{\mathrm{I}\eta 11} = (-)^\eta W^{(2)}_{\mathrm{I}\eta 1,-1}$. Therefore, when $\eta = 1$, the peak at x_2 belongs to $m = 0$, whereas for $\eta = 2$ it belongs to $m = \pm 1$. When the reflecting surface is present, the implied amplitudes of the exciting field are the $W^{(2)}_{\mathrm{E}\eta 1m}$, but only $W^{(2)}_{\mathrm{E}110} \neq 0$. This is enough to explain why the peak at x_2 may appear in Fig. 8.14 (b) for $\eta = 1$ only.

When $\vartheta_{\mathrm{I}} = 0°$ the appropriate resonance spectra are those in Fig. 8.15. The behavior of the peak at x_2 is easily understood when one considers that at $\vartheta_I = 0°$ we have $W^{(2)}_{\mathrm{I}110} = W^{(2)}_{\mathrm{E}110} = 0$. Therefore this resonance can occur in Fig. 8.15 (a) for $\eta = 2$ only and cannot appear at all in Fig. 8.15 (b). The behavior of the resonances at x_1 and at x_3 that appear in Figs. 8.14 and 8.15 can be understood through a quite similar analysis.

In conclusion, the resonance suppressing mechanism should be taken into account when interpreting the spectra from a perfectly reflecting surface sparsely seeded by hemispherical particles such as liquid droplets. As regards the spectra of the single hemispheres, the discussion in Sect. 8.3.1 emphasizes the importance of the function $U^{(p)}_{\eta l}$ to getting insight into the behavior of the resonances as a function of the direction of propagation and of the polarization of the incident wave.

In turn, the discussion above can provide the guidelines for understanding the mechanism through which the combined effect of the boundary conditions on the reflecting surface and of the polarization of the incident field affect the behavior of the resonance spectrum of aggregated hemispheres. In fact, to understand the behavior of the spectrum from aggregated hemispheres, we were forced to examine the behavior of the single elements of the transition matrix as well as of the the multipole amplitudes of the exciting field as a function of ϑ_{I} and of the polarization. Of course, such an analysis is practicable only when the parameters of the aggregate are so chosen that the order of the transition matrix is small.

8.4 Particles on a Dielectric Substrate

In Chap. 6 we stressed that the techniques that can be used to deal with scattering from particles on a metallic surface are not applicable when the surface has a finite conductivity. For the case of particles on a dielectric substrate, the appropriate approach is described in Sects. 6.3–6.5. This approach, hereafter referred to as multipole reflection theory (MRT), will now be applied to the calculation of the pattern of the scattered intensity from model particles on a dielectric substrate.

8.4.1 Single Spheres

We remark that the approximations to which Bobbert and Vlieger [112, 170] and Johnson [171] resorted, as well as any analogous approximation, can be entirely described as specific approximations of MRT [108]. According to the approximation devised by Bobbert and Vlieger [112] (hereafter referred to as B0), the far zone expression of $\boldsymbol{E}_{\mathrm{SR}\eta}$ equals that of the scattered field, calculated for the direction $\pi - \vartheta_{\mathrm{S}}$, where ϑ_{S} denotes the direction of observation, with its amplitude scaled by the value of the Fresnel coefficient $F_\eta(\pi - \vartheta_{\rm S})$. Our variant to B0 (approximation B1) assumes that $\boldsymbol{E}_{{\rm SR}\eta}$ equals the field that is obtained by scaling by the factor $(-)^{\eta-1}F_\eta(\pi - \vartheta_{\rm S})$, the field that would come from the image sphere with center at O'' (see Fig. 6.4) if the surface were perfectly reflecting. In practice, this is achieved by calculating, for the direction $\vartheta_{\rm S}$, $\boldsymbol{E}_{{\rm SR}\eta}$ as given by (6.35) and (6.36), but scaling by the factor $(-)^{\eta-1}F_\eta(\pi - \vartheta_{\rm S})$ the amplitudes $a^{pp')}_{ll';m}$, defined by (6.24) and (6.28), evaluated for a perfectly reflecting surface.

Johnson [171], besides using B0 to get the far zone expression of $\boldsymbol{E}_{\rm SR}$, introduces a further approximation that affects the imposition of the boundary conditions that yield the equations for the amplitudes $\mathcal{A}^{(p)}_{\eta lm}$, defined by (6.32). Johnson's procedure (hereafter referred to as J0) stems from the equation

$$\begin{aligned}\sum_{p''l''}\sum_{p'l'm'} \boldsymbol{J}^{(p')}_{l'm'}(\boldsymbol{r}', k')\mathcal{H}^{(p'p'')}_{l'l'';m'}(-2a\hat{\boldsymbol{e}}_z, k')\mathcal{A}^{(p'')}_{{\rm R}\eta l''m'} \\ = \sum_{plm}\sum_{p'l'} \boldsymbol{J}^{(p')}_{l'm}(\boldsymbol{r}', k')\mathcal{F}^{(p'p)}_{l'l;m}\mathcal{A}^{(p)}_{\eta lm},\end{aligned} \tag{8.3}$$

that is a consequence of (6.22) and (6.31), and is valid on the surface of the scattering sphere. Equation (8.3) shows that the calculation of the elements of F can be overcome provided that the amplitudes $\mathcal{A}^{(p)}_{\eta lm}$ and $\mathcal{A}^{(p'')}_{{\rm R}\eta l''m'}$ can be related through some F-independent equation. Johnson, by invoking the so-called Yousif–Videen approximation [163,172], states such a relation in the form

$$\mathcal{A}^{(p)}_{{\rm R}\eta lm} = (-)^{\eta+p+l+m}\mathcal{A}^{(p)}_{\eta lm}F_\eta(\vartheta = 0^\circ),$$

which becomes exact in the limit of a perfectly reflecting interface. Approximation J0 has been tested together with a variant (approximation J1) that keeps in (6.17) the Fresnel coefficients to the value $F_\eta(\vartheta_{\rm k} = 0^\circ)$ to get approximate values for the elements of F.

All the approximations above, as well as MRT, were applied to the calculation of the scattered intensity from the systems that were considered by Johnson. Doing this has the further advantage that the results of MRT can also be compared both with experimental data [173] and with results of calculations [174]. Accordingly, the scattered intensity $\mathcal{I}_{\eta\eta}$ (see Sect. 7.1) from a sphere of radius $\rho = 0.27\,\mu$m lying on the dielectric surface, illuminated by a radiation of wavelength $\lambda = 632.8\,$nm, is reported as a function of the angle of observation for parallel polarization in Fig. 8.16 (a) and for perpendicular polarization in Fig. 8.16 (b). Analogous results for a sphere of radius $\rho = 0.38\,\mu$m are reported in Figs. 8.17 (a) and 8.17 (b). In all the figures $\vartheta_{\rm I} = 0^\circ$, $n_0 = 1.59$, $n' = 1$ and $n'' = 3.8$. The angle of observation is measured from the negative z axis. The result that we report in Figs. 8.16 and 8.17 required to extend the multipole expansions up to $l_{\rm M} = 10$ to achieve an accuracy to three significant digits.

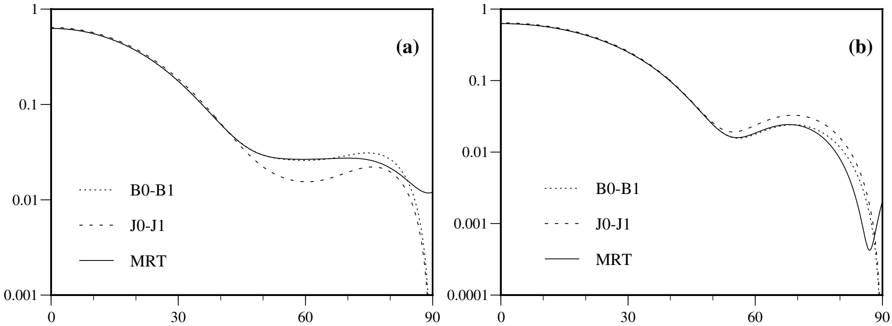

Fig. 8.16. Comparison of the results of the theory of Sect. 6.4 with those yielded by approximations B0, B1, J0 and J1 for a sphere of radius $\rho = 0.27\,\mu\text{m}$ and refractive index $n_0 = 1.59$ in contact with the surface and illuminated by light of wavelength $\lambda = 632.8\,\text{nm}$. The refractive index of the medium beyond the surface is $n'' = 3.8$. We report in μm^2 and for normal direction of incidence the quantities $\mathcal{I}_{11}$ in **(a)** and $\mathcal{I}_{22}$ in **(b)** as a function of the angle of observation

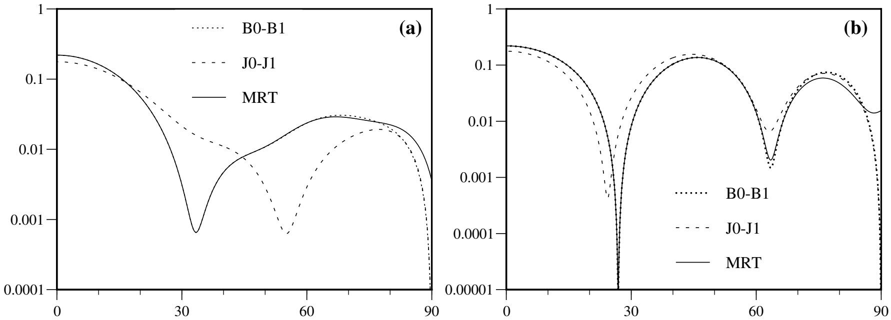

Fig. 8.17. Same as Fig. 8.16 but for a sphere of radius $\rho = 0.38\,\mu\text{m}$

Figures 8.16 (a) and 8.16 (b) seem to report three curves only. In fact, the pair B0-B1 and J0-J1 yield identical results to a high degree of precision. This is not surprising when one recalls how these approximations are defined. Anyway, the approximate results compare well with the results of our theory provided that the angle of observation is not near to 90° because MRT predicts the occurrence of a nonvanishing field that propagates along the interface. The situation is analogous in Figs. 8.17 (a) and 8.17 (b). Even in this case, MRT is the only one that gives a nonvanishing field that propagates along the interface. Moreover, the minima of the intensity occur at different angles of observation when different approximations are used. The best coincidence with the results of MRT is attained by B0-B1 for both choices of the polarization. The different result yielded by J0-J1 was to be expected because the latter, besides including approximation B0 to get the far zone expression of $\boldsymbol{E}_{\mathrm{SR}}$, also resort to a further approximation to simplify the imposition of the boundary conditions.

The results in Figs. 8.16 and 8.17 can be compared with the experimental data of Lee et al. [173] and the simulation of Wojcik, Vaughan, and Galbraith [174] that Johnson reports in Figs. 3 and 4 of [171]. A fair agreement is attained not only in the position of the minima but also in our prediction that the field along the surface does not vanish. Of course the calculations needed to complete simulations such as the one in [174] require a computational effort very large with respect to MRT.

In Fig. 8.18 we report the results of the application of MRT as well as of B0, B1, J0, and J1 to the case of a small particle in the vicinity of a plane interface that Muinonen et al. [175] deal with by means of a variant of image theory designed to take account of the actual refractive index of the substrate, that they call the exact-image theory. In practice, these authors consider a sphere so small that it can be dealt with through the RSA, with polarizability α, for several values of the distance from a plane surface that separates the vacuum from a homogeneous dielectric medium with $\varepsilon = 2.4$. The results in [175] are normalized so as to ensure their independence of the choice of α, the angle of incidence is held fixed at $\vartheta_{\mathrm{I}} = -45°$ and the incident light is assumed to be unpolarized. The results that we report in Fig. 8.18 refer to a distance such that $k'a = \pi/2$ and their convergence to four significant digits is ensured by including terms up to $l_{\mathrm{M}} = 6$ both in our exact theory and in the approximations B0, B1, J0, and J1. The need to use so high a value for l_{M} in spite of the smallness of the scattering particle stems from the fact that the particle itself is not in contact with the surface,

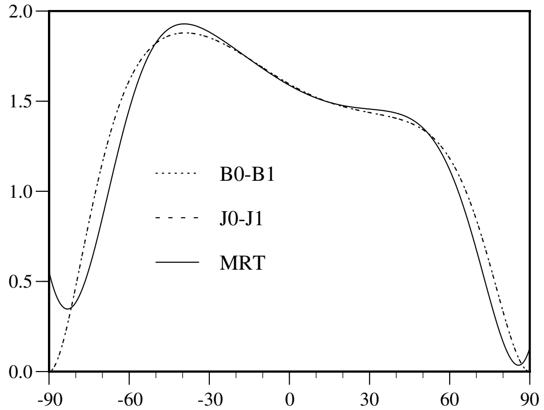

Fig. 8.18. Comparison of the results of the theory of Sect. 6.4 with those of approximations B0, B1, J0, and J1 for a small sphere with polarizability α, whose distance a from the surface is such that $k_{\mathrm{v}}a = \pi/2$. The quantity that is actually reported is $i = (I_1 + I_2)/(2I_0\alpha^2 k_{\mathrm{v}}^4)$ as a function of the angle of observation. The angle of incidence is held fixed at $\vartheta_{\mathrm{I}} = -45°$

as, according to (6.17) and (6.26), $\mathcal{F}^{(pp')}_{ll';m}$ depend on $k'a$ and are independent of the scattering particle.

Actually, Fig. 8.18 seems to report two curves only but this is due to the almost perfect coincidence of all the approximate results that, in turn, agree fairly well with the results that Muinonen et al. report in Fig. 2 of [175]. In particular this coincidence suggests that the further approximation that is included in J0 and J1 beyond the approximation implied in B0 and B1 has little effect on the results on account of the distance of the particle from the surface [171]. The results of our theory have the general shape of the results cited above but for the fact that the observed field does not vanish for grazing angle of observation.

Finally, we come to discuss MRT results for the full scattering pattern from a sphere of radius $\rho = 126\,\mathrm{nm}$ and refractive index $n_0 = 3$ in contact with the surface. We already discussed in Sect. 8.1 the scattering pattern from such a sphere on a perfectly reflecting surface [107] so that, for the sake of comparison, MRT results are plotted in the same frame of reference that is depicted in Fig. 8.1. Even in the present case, we chose $n' = 1$, $\lambda = 628.3\,\mathrm{nm}$ and $\varphi_\mathrm{I} = 225°$. In Fig. 8.19 (a) $n'' = \infty$, in Fig. 8.19 (b) $n'' = 9$, and in

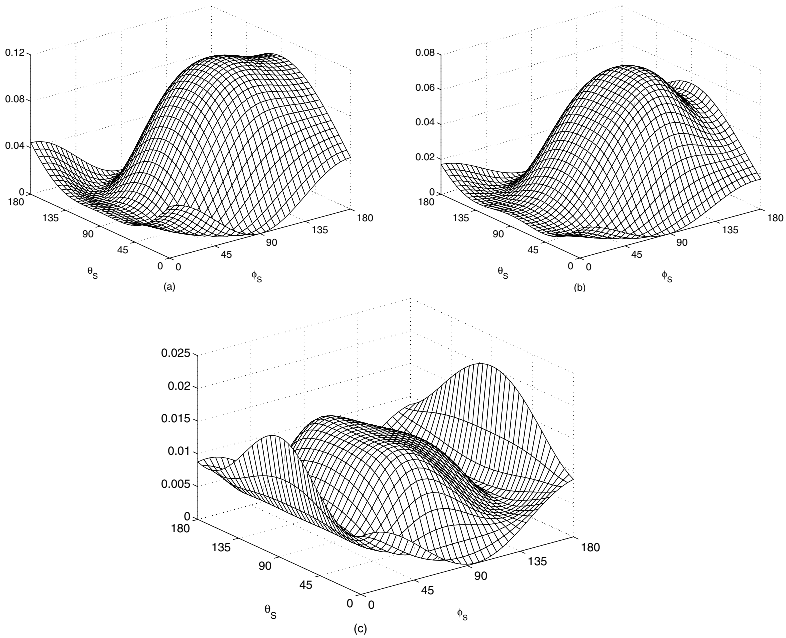

Fig. 8.19. Full scattering pattern for the sphere of radius $\rho = 126.0\,\mathrm{nm}$ and refractive index $n_0 = 3$ in contact with the surface. The quantity that is actually reported is $\mathcal{I}_{\varphi\varphi}$ in $\mu\mathrm{m}^2$. In **(a)** the surface is perfectly reflecting ($n'' = \infty$); the refractive index of the medium beyond the surface is $n'' = 9.0$ in **(b)** and $n'' = 1.3$ in **(c)**

Fig. 8.19 (c) $n'' = 1.3$. In all the figures we report $\mathcal{I}_{\varphi\varphi}$, i.e., both the incident and the observed field are polarized along $\hat{\boldsymbol{\varphi}}$. We first notice that the plot in Fig. 8.19 (a) is identical to the one in Fig. 8.2 (a). We stress, however, that in the present case we did not use image theory but calculated the scattered field by putting in (6.33) the elements of the multipole reflection matrix to the value that is obtained from (6.17) when the Fresnel coefficients take on the values $F_\eta = (-)^{\eta-1}$ that are appropriate to a perfectly reflecting surface. The plots in Figs. 8.19 (b) and 8.19 (c) show the evolution of the scattering pattern when the refractive index n'' of the medium that fills the half-space $z > 0$ becomes smaller and smaller.

The case of a nonperfectly reflecting surface shares in common with the case of a perfectly reflecting surface all the features that do not depend on the refractive index but are due to the geometry only. These feature were fully described in Sect. 8.1. We do not report the patterns for the other possible choices of the incident and observed polarization because, at least for a single sphere, they do not show any significant new feature worthy of a separate comment.

MRT proved to yield reliable predictions for the scattering pattern from a sphere on a dielectric surface. On the contrary, on account of the comparisons that we presented above, it can be stated that the approximations that were assumed by other authors may affect the predicted spectrum not only quantitatively but also qualitatively. In this respect, a careful examination of Figs. 8.19 (a), (b), and (c) shows that, when the refractive index of the medium beyond the surface is comparable with the refractive index of the sphere, the intensity of the field that propagates along the surface becomes so relevant that the pattern predicted by approximate approaches may be unacceptable.

MRT may appear to be complicated by the introduction of the multipole reflection matrix F and of H^{-1}. The calculation of these matrices proved, however, to add little to the computational effort. In this respect, calculation of H^{-1} may require some caution (see Appendix A.5). On the contrary, the integrals that are involved in the calculation of F can be computed with high precision through the Gauss–Laguerre method [10, 14]. On the other hand, according to our tests, B0 and J0 are computationally somewhat faster than MRT, but the reliability of the results that they yield need to be carefully checked. We are thus led to conclude that the approximations above do not present substantial computational advantages over MRT. On the other hand, the results of the simulation [174] agree fairly well with MRT predictions but require a heavy computational effort. In fact, what the authors of [174] call *simulation* is actually an ab initio calculation performed through the FDTD method, which we summarized in Sect. 5.6.2. Therefore, both on the side of the computations and on the side of the reliability of the results MRT appears to be more expedient than the other methods.

8.4.2 Aggregates of Spheres in Fixed Orientation

In this section, we apply MRT to the case of aggregates of spherical scatterers deposited on a dielectric plane substrate [108]. Such a move is easily understood when one thinks that aggregation phenomena often occur among the particles on a substrate. In particular, aggregated spheres give origin to particles whose scattering patterns are expected to be rather different from the patterns from single spheres and to depend on the orientation of the aggregate with respect to the incident field. In this respect, we recall that the pattern of the scattered intensity from a tenuous monolayer (in the sense of Sect. 2.4) of identical particles all oriented alike but randomly distributed on the surface is merely proportional to the pattern from a single particle [54]. The case of a monolayer of particles whose orientations are randomly distributed around an axis orthogonal to the surface instead requires considering the average over the orientational distribution. However, in this section we want to focus on the effects of the anisotropy so that we defer to the next section the discussion of the patterns from assemblies of aggregates with random distribution of their orientations.

We deal with binary aggregates of identical mutually contacting spheres embedded in vacuo ($n' = 1$) and deposited on a substrate of Si ($n'' = 3.85 + \mathrm{i}0.018$). We consider spheres of Si_3N_4 with refractive index $n_1 = 2.0$ and radius $\rho_1 = 225\,\mathrm{nm}$, illuminated by radiation of wavelength $\lambda = 632.8\,\mathrm{nm}$ [109]. The scattered intensity from single spheres of such a morphology deposited on the same substrate has already been calculated by Taubenblatt and Tran through the DDA method [176], which we summarized in Sect. 5.6.1, and by Johnson [171] with the help of the Yousif–Videen approximation [163, 172]. Thus MRT is used to investigate the effect of the aggregation on scatterers whose properties are already well known. We also dealt with the pattern from binary aggregates of contacting spheres of Si_3N_4 with radius $\rho_2 = 178.5\,\mathrm{nm}$ deposited on the surface because the total volume of such an aggregate equals that of a single sphere of radius ρ_1. This choice allows us to study also the effect of the subdivision of the material of a sphere. Hereafter, we will refer to the aggregate of spheres of radius ρ_1 as the case of aggregation and to the aggregate of spheres of radius ρ_2 as the case of subdivision.

The geometry that we adopted to display MRT results is the one depicted in Fig. 8.1. Thus, the surface of the substrate coincides with the zx plane and the normal to the surface coincides with the y axis. The plane of incidence coincides with the xy plane and the direction of incidence forms an angle of 45° with the normal to the surface. More precisely, the polar angles of the direction of incidence are $\vartheta_I = 90°$ and $\varphi_I = 225°$. The incident light is polarized either along the meridians (ϑ-polarization) or along the parallels (φ-polarization) and both the φ-polarized and the ϑ-polarized component of the scattered wave are considered. In practice, the quantity that we calculate is $\mathcal{I}_{\eta\eta'}$ and both co-polarized ($\mathcal{I}_{\varphi\varphi}$ and $\mathcal{I}_{\vartheta\vartheta}$) and cross-polarized ($\mathcal{I}_{\vartheta\varphi}$ and $\mathcal{I}_{\varphi\vartheta}$) patterns are reported. Binary aggregates have their axis perpendicular to the plane of incidence. The numerical results from which all the patterns were drawn achieve a convergence to three significant digits that required us to use $l_{\mathrm{M}} = 12$. Of course, the patterns have all the features that do not depend on the system under study but rather stem from the boundary conditions and from the geometry of the problem [107, 108] and were fully described in Sect. 8.1.

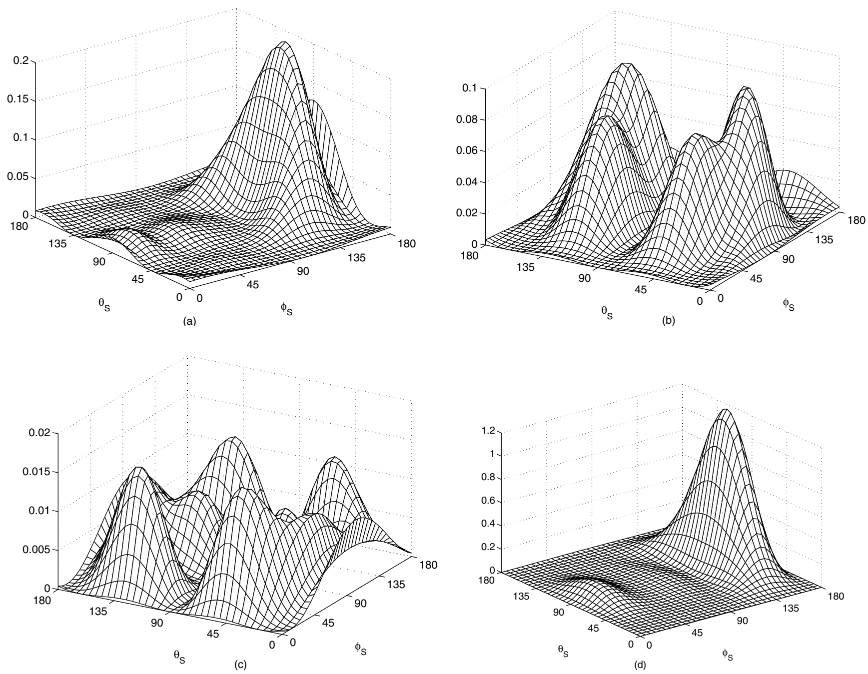

Fig. 8.20. Pattern of the scattered intensity from the single sphere of radius ρ_1. The quantity that is actually reported (in μm^2) is $\mathcal{I}_{\varphi\varphi}$ in **(a)**, $\mathcal{I}_{\vartheta\varphi}$ in **(b)**, $\mathcal{I}_{\varphi\vartheta}$ in **(c)**, and $\mathcal{I}_{\vartheta\vartheta}$ in **(d)**

In Fig. 8.20 we report the pattern from a single sphere of radius ρ_1 in contact with the substrate. The section of the $\mathcal{I}_{\varphi\varphi}$ and of the $\mathcal{I}_{\vartheta\vartheta}$ patterns along the plane $\vartheta_{\mathrm{I}} = 90°$ can be compared with the results of Taubenblatt and Tran [176] and of Johnson [171]. The differences that emerge from this comparison are easily explained along the lines of Sect. 8.4.1, where we stressed how the approximations used by these authors, possibly in conjunction with the approximation used by Bobbert and Vlieger [170] to get the far zone field, may substantially affect even the qualitative features of the scattering pattern [108]. The results in Fig. 8.21 refer to a binary aggregate of spheres

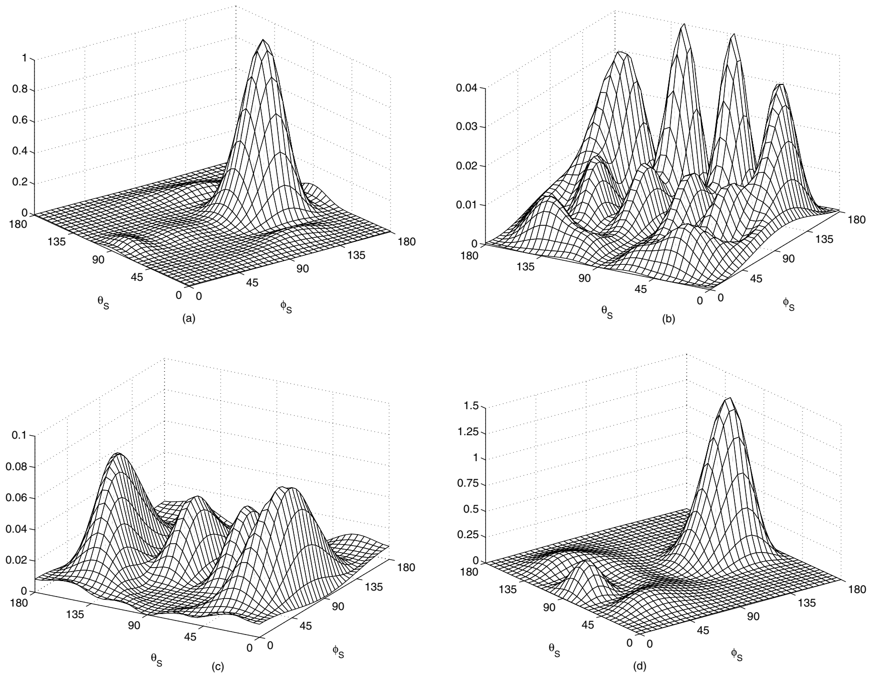

Fig. 8.21. Pattern of the scattered intensity from the binary aggregate of the spheres of radius ρ_1. The quantity that is actually reported (in μm^2) is $\mathcal{I}_{\varphi\varphi}$ in **(a)**, $\mathcal{I}_{\vartheta\varphi}$ in **(b)**, $\mathcal{I}_{\varphi\vartheta}$ in **(c)**, and $\mathcal{I}_{\vartheta\vartheta}$ in **(d)**

of radius ρ_1. The patterns from the aggregate of two spheres of radius ρ_2 are presented in Fig. 8.22.

We first notice that in agreement with MRT findings, the $\mathcal{I}_{\varphi\varphi}$ patterns show a nonvanishing field that propagates along the surface. Its intensity is smaller than the intensity reported in [108] but this is due to the fact that the refractive index of the substrate has a nonvanishing imaginary part.

To confirm this interpretation, we compared the pattern of $\mathcal{I}_{\varphi\varphi}$ from a single sphere in Fig. 8.20 (a) with the pattern from the same sphere on a perfectly reflecting surface. The latter pattern (not reported here) has a rounded shape in contrast to the rather peaked shape of the pattern in Fig. 8.20 (a). The patterns in Fig. 8.19 for spheres of different size and refractive index and for several choices of the (real) refractive index of the substrate also present a rounded shape. We are thus led to conclude that a nonvanishing imaginary part of n'' produces a strong damping of the scattering patterns. As a result, we are left with a noticeable peak around the direction of reflection. This effect is not restricted to the case of a single sphere because the same peaked shape of the $\mathcal{I}_{\varphi\varphi}$ and of $\mathcal{I}_{\vartheta\vartheta}$ patterns can be observed in the case of the aggregated spheres. In other words, this feature does not depend on the

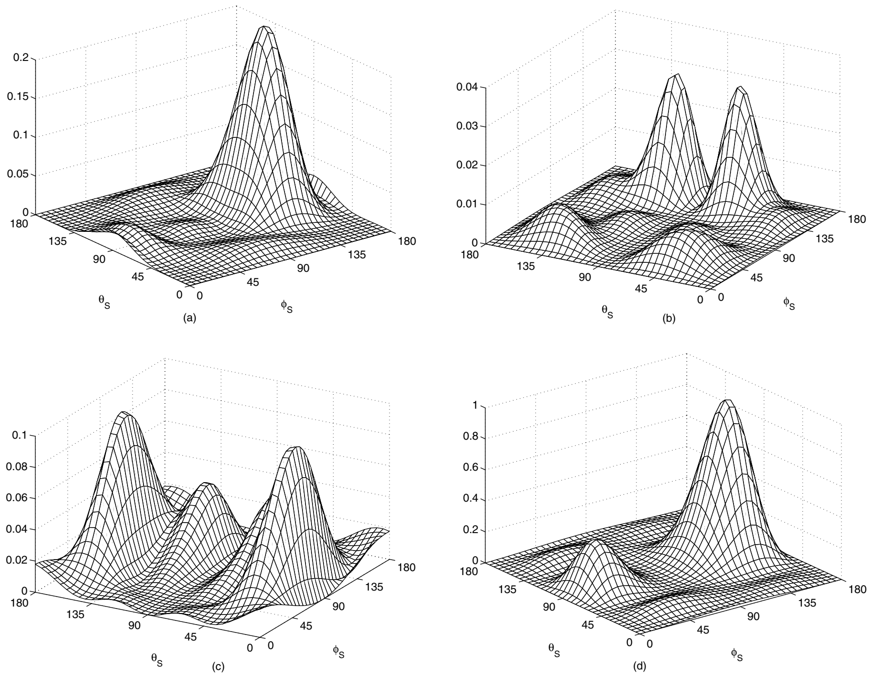

Fig. 8.22. Pattern of the scattered intensity from the binary aggregate of the spheres of radius ρ_2. The quantity that is actually reported (in μm^2) is $\mathcal{I}_{\varphi\varphi}$ in **(a)**, $\mathcal{I}_{\vartheta\varphi}$ in **(b)**, $\mathcal{I}_{\varphi\vartheta}$ in **(c)**, and $\mathcal{I}_{\vartheta\vartheta}$ in **(d)**

shape of the scatterers and should thus be due to the nonvanishing imaginary part of n''. The height of the main peaks, for φ-polarized incident field, depends more or less on the quantity of refractive material. For instance, the height of the $\mathcal{I}_{\varphi\varphi}$ peak is almost equal for the single sphere and for the case of subdivision, whereas the height for the case of aggregation is about four times larger. Furthermore, the $\mathcal{I}_{\varphi\varphi}$ pattern for the case of aggregation show a noticeable increase, with respect to the case of subdivision, in the direction $\vartheta_S = 90°$, $\varphi_S = 180°$.

Anyway, the largest value of the scattered intensity does not occur exactly in the direction of reflection ($\vartheta_S = 90°$, $\varphi_S = 135°$). This may be surprising because, according to our calculations for the same particles in free space, the largest scattered intensity occurs in the forward direction that, for particles on a surface, coincides with the direction of reflection [115]. Actually, for the single sphere the maximum both of $\mathcal{I}_{\varphi\varphi}$ and $\mathcal{I}_{\vartheta\vartheta}$ occurs at $\varphi_S = 155°$, so that the coupling with the surface is so large as to produce a significant shift of the main peak with respect to the direction of reflection. For the aggregates of spheres of radius ρ_1 and ρ_2 the maximum of $\mathcal{I}_{\varphi\varphi}$ occurs at $\varphi_S = 135°$ but it occurs at $\varphi_S = 150°$ for $\mathcal{I}_{\vartheta\vartheta}$. Even if specific patterns are not reported we can state that a similar behavior occurs even when the axis of the aggregates is parallel to the x axis. This seemingly erratic location of the maximum arises from the coupling of the scattering particles with the substrate and, for the case of aggregated spheres, also on the competing coupling of the component spheres among themselves. The strength of both these couplings is likely to differ for different polarization, whereas the coupling among the component spheres is expected to depend on their size. Hence, the dependence of the location of the maximum on the polarization as well as on the radius of the aggregated spheres can be explained in terms of the ratio between these couplings.

The $\mathcal{I}_{\varphi\varphi}$ and $\mathcal{I}_{\vartheta\vartheta}$ patterns from single spheres as well as from aggregated spheres both of radius ρ_1 and ρ_2 are of rather similar shape, even though the specific values of the scattered intensity may be noticeably different as we noted above with regard to the maximum. This means that an analysis of the scattered intensity restricted into the plane of incidence cannot yield enough information to discriminate the shape and size of the particles. In turn, even a cursory examination of the cross-polarized patterns $\mathcal{I}_{\vartheta\varphi}$ and $\mathcal{I}_{\varphi\vartheta}$ show that they depend both on the shape and on the size of the scattering particles. Thus, any attempt to gain information on the morphology of particles deposited on a dielectric substrate requires considering both the co-polarized and the cross-polarized aspects of their scattering pattern.

The patterns that we discussed above are only a sample of the changes of the scattered intensity yielded by the aggregation of spheres deposited on a dielectric substrate. However, these results prove that the feature of a nonvanishing field propagating along the interface is distinctive of MRT, which does not imply any approximation. In particular, no approximation is required to get the far zone expression of the scattered field. Strictly speaking, MRT requires the truncation of the multipole expansions on which the formalism is based. Nevertheless, this unavoidable truncation is of numerical and not of physical nature. Therefore, once the convergence has been checked, MRT results remain physically reliable.

8.4.3 Randomly Oriented Aggregates

In this section we report the patterns of the scattered intensity from a dispersion with random orientation of the same aggregates considered in Sect. 8.4.2 [110]. We first stress that the numerical results from which all the patterns were drawn achieved a convergence to three significant digits by using $l_{\mathrm{M}} = 12$, i.e., the same value of l_{M} that we had to use in [109] to deal with the same kind of aggregates in fixed orientation. In fact, according to Sect. 4.5, the averaging procedure does not introduce any quantity whose convergence needs to be investigated, its only effect being the disappearance from the final formulas of the rotation matrices. [7]

MRT results for radius ρ_1 are reported in Fig. 8.23, whereas those for radius ρ_2 are reported in Fig. 8.24. We note once again that all the patterns do have all the features that do not depend on the morphology of the particles on the surface but are due to the geometry of the problem. The patterns also show that a nonvanishing field propagates along the dielectric surface. Thus, this distinctive feature of MRT [108, 109] persists even after averaging, as expected, because it occurs for any chosen orientation of a single particle on the surface.

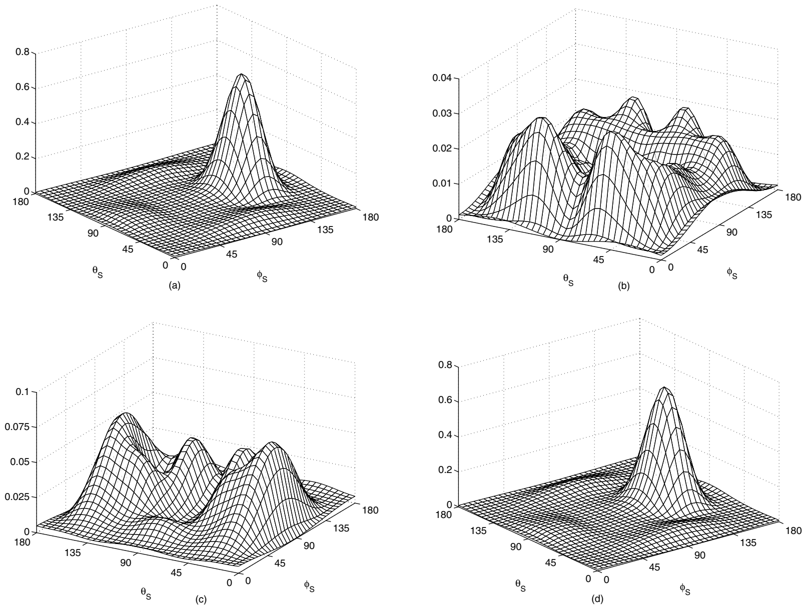

Fig. 8.23. Pattern of the scattered intensity from the assembly of randomly oriented binary aggregates of the spheres of radius ρ_1. The quantity that is actually reported (in $\mu\mathrm{m}^2$) is $\langle \mathcal{I}_{\varphi\varphi} \rangle$ in **(a)**, $\langle \mathcal{I}_{\vartheta\varphi} \rangle$ in **(b)**, $\langle \mathcal{I}_{\varphi\vartheta} \rangle$ in **(c)**, and $\langle \mathcal{I}_{\vartheta\vartheta} \rangle$ in **(d)**

The effect of the orientational average can be guessed by comparing Figs. 8.23 and 8.24 with Figs. 8.21 and 8.22 of Sect. 8.4.2, respectively, because the latter figures report the patterns from the same binary aggregates on the assumption that they are all oriented alike with their axes perpendicular to the plane of incidence. It is apparent that the averaging procedure has small qualitative effects on the patterns of the observed intensity. In particular, the orientational average does not shift appreciably the location of the main maxima of the co-polarized intensity $\langle \mathcal{I}_{\varphi\varphi} \rangle$ and $\langle \mathcal{I}_{\vartheta\vartheta} \rangle$ in Figs. 8.23 and 8.24 with respect to the location of the main maxima of $\mathcal{I}_{\varphi\varphi}$ and $\mathcal{I}_{\vartheta\vartheta}$ in Figs. 8.21 and 8.22. Thus, the constraint in the sums (see (4.51c)) has only a small influence on the general shape of the patterns. In other words, it does not alter appreciably the ratio between the interaction among the spheres of the aggregates and the interaction of each sphere with the surface. In [108]

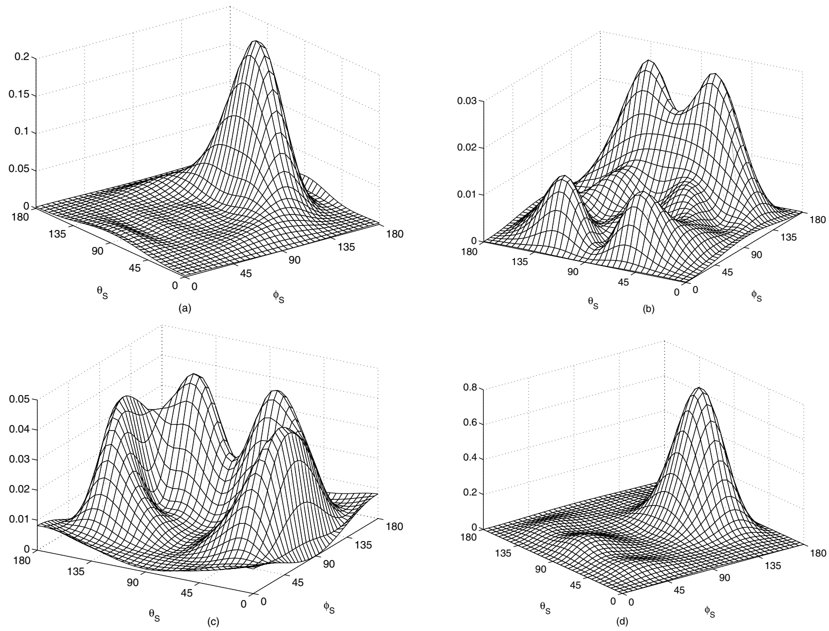

Fig. 8.24. Pattern of the scattered intensity from the assembly of randomly oriented binary aggregates of the spheres of radius ρ_2. The quantity that is actually reported (in μm^2) is $\langle \mathcal{I}_{\varphi\varphi} \rangle$ in **(a)**, $\langle \mathcal{I}_{\vartheta\varphi} \rangle$ in **(b)**, $\langle \mathcal{I}_{\varphi\vartheta} \rangle$ in **(c)**, and $\langle \mathcal{I}_{\vartheta\vartheta} \rangle$ in **(d)**

this ratio was held responsible for the location of the main maxima of the pattern from an aggregate.

In fact, the maxima of $\langle \mathcal{I}_{\varphi\varphi} \rangle$ and of $\langle \mathcal{I}_{\vartheta\vartheta} \rangle$ occur at $\varphi_S = 135°$ and at $\varphi_S = 150°$, respectively, for radius ρ_1 and at $\varphi_S = 135°$ and $\varphi_S = 145°$, respectively, for radius ρ_2. These values turn out to be more or less the same as those for the patterns in Figs. 8.21 and 8.22. Anyway, the location of the main maximum of the scattered intensity from aggregates is nearer to the direction of reflection than for the case of a single sphere. This point has been further investigated by calculating the pattern for single spheres of radius ρ_1 as well as for aggregated spheres of the same radius and with random orientation, on a perfectly reflecting surface. Of course, this can be done either according to Sect. 8.2, or by MRT with $n'' = \infty$, indifferently. The distinctive feature of the resulting patterns (not reported here) is that the maximum of $\mathcal{I}_{\varphi\varphi}$ occurs at $\varphi_S = 180°$ and that of $\mathcal{I}_{\vartheta\vartheta}$ occurs at $\varphi_S = 155°$ for the single sphere, whereas for the aggregates the main maximum occurs at $\varphi_S \approx 140°$ for both choices of the polarization. These results are analogous to those that, in [107], refer to a different choice both of the radius and of the refractive index of the spheres, however. Thus, even in the limit of a perfectly reflecting surface, i.e., when the strongest interaction between the sphere and the substrate seems to occur, the interaction among the spheres is the prevalent one.

The cross-polarized patterns in Figs. 8.23 and 8.24 show another feature that may be useful to gain information on the possible nonsphericity of the particles on the surface. Indeed, we note that in Fig. 8.20 the cross-polarized intensity from a single sphere do vanish in the plane of incidence ($\vartheta_S = 90°$). Thus, as expected, a spherical scatterer even in the presence of a substrate does not give rise to depolarization. Of course, we cannot exclude that nonspherical particles may produce no depolarization for particular choices of their orientation. This is suggested by the vanishing for $\vartheta_S = 90°$ of the cross-polarized intensities reported in Figs. 8.21 and 8.22 that refer to binary aggregates with their axis orthogonal to the plane of incidence. On the contrary, $\langle \mathcal{I}_{\vartheta\varphi} \rangle$ and $\langle \mathcal{I}_{\varphi\vartheta} \rangle$ for the aggregates of spheres both of radius ρ_1 (see Fig. 8.23) and of radius ρ_2 (see Fig. 8.24) do not vanish in the plane of incidence. We are thus led to conclude that a dispersion of randomly oriented nonspherical particles gives rise to depolarization.

8.5 Scattering of Evanescent Waves

The applications discussed in the preceding sections share in common the fact that the primary exciting field is a plane wave that propagates in the accessible half-space. In this section we consider a new kind of excitation, i.e., that yielded by an evanescent wave generated by total internal reflection. Thus, as stressed in Sect. 7.6.1 the field that propagates through the accessible half-space does not include either an incident plane wave nor a reflected wave. The lack of an incident wave may be useful when studying the optical properties of biological particles such as spores. In fact, the literature reports several cases in which the incident plane wave yields modifications of the biological material [177] so that the observed wave does not carry reliable information.

In the next two sections we will deal with the scattered intensity both of single spheres and of aggregates of spheres when excited by an evanescent wave. We will consider both the case in which the multiple scattering processes between the scatterer and the surface are neglected and the case in which these processes are fully taken into account. The convergence of all the calculations that we discuss below was ensured using $l_M = 12$, but further calculations were performed up to $l_M = 18$ in order to verify the extent to which the rate of convergence is slowed down by the presence of the interface. We stress that the intensities that we report in the following figures, except for the sphere in free space, are normalized assuming as unit intensity the one of the evanescent field at the interface, i.e.,

$$\mathcal{I}_{\eta\eta'} = |f_{\eta\eta'}|^2 = \frac{r^2}{|T_{\eta'}|^2 I_I} I_{\eta\eta'} \; .$$

The results that we are going to discuss show that neglecting the interaction of the scatterer with the surface may have noticeable effects on the resonance spectrum, not only from a quantitative but also from a qualitative point of view. Therefore, the interaction should be taken into account when the calculations are aimed at the comparison with the observations.

8.5.1 Single Spheres

In this section we consider a single sphere of radius $\rho_0 = 300$ nm and refractive index $n_0 = 2.47$. We first calculate, as a reference, the forward scattered intensity when the sphere is excited by a plane wave. We then calculate the scattered intensity from the same sphere when excited by an evanescent wave produced by total internal reflection, e.g., by a prism. Assuming the refractive index of the prism to be $n'' = 1.5$, and that the medium that fills the accessible half-space be the vacuum ($n' = 1$), total internal reflection occurs for $\hat{\imath} > 42°$, on the assumption that the refractive index of the prism does not depend on the wavelenght. In the top panel of Fig. 8.25 we report

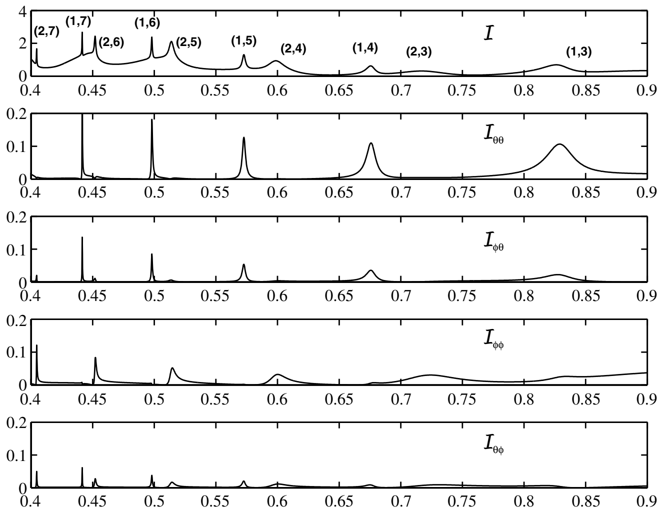

Fig. 8.25. $\mathcal{I}_{\eta\eta'}$ in μm^2 as a function of wavelength in μm from a sphere in free space (top panel) and from the same sphere excited by an evanescent wave generated by a prism (lower panels). The direction of observation forms an angle of 60° with the normal to the surface of the prism. The sphere has radius $\rho_0 = 300$ nm and refractive index $n_0 = 2.47$. The resonances in the top panel are labelled as in Sect. 8.3.1. The interaction with the surface of the prism is neglected

the forward scattered intensity from the sphere excited by a plane wave. In this case there are no cross-polarized intensities, and $\mathcal{I}_{11} = \mathcal{I}_{22}$ is denoted as $\mathcal{I}$. The wavelenght range is $0.4 \leq \lambda \leq 0.7\,\mu$m in which the main resonances occur, and the resonance peaks are labelled in the same notation we used in Sect. 8.3.2. The remaining panels report the scattered intensity in a direction forming an angle 60° with the normal to the surface, i.e. along the direction of incidence, for the same sfere, in contact with the surface, excited by the evanescent wave. It is important to notice that all the multiple scattering processes between the scattering sphere and the surface that generates the evanescent wave have been neglected. Therefore the role of the surface is only to generate the evanescent wave and to define the plane of incidence with respect to which the polarization is considered. We notice at once the different scales used in the top panel and in the lower ones in Fig. 8.25. We also notice the selection of the resonances according to the polarization. In other words, the resonances may be suppressed by the choice of the polarization, in analogy with our findings of Sect. 8.3.1. In any case, our results confirm that excitation of a sphere by an evanescent wave may select the resonances that, however, occur at an unshifted wavelength. These results are in substatial agreement with those reported by Pack [118] and are easily explained by recalling that, in the absence of interaction with the surface, the transition matrix of the sphere is still the one given by (5.7) and (5.8).

Considering the interaction of the sphere with the interface, i.e. taking into account the multiple scattering processes that occur between the sphere and the interface, has small effect on the position of the resonances. Moreover, we notice a general lowering and smoothing of the peaks. The lowering is easily explained by the fact that the interface is not perfectly reflecting, so that part of the light is transmitted to the non-accessible half-space and is thus lost to the observer. In this respect we recall our remark in Sect. 6.7.1 about the scattered transmitted field $\boldsymbol{E}_{\mathrm{ST}}$, that does not enter the calculations but subtracts light from the observable intensity. As regards the smoothing, one has to recall that, in the presence of interaction with the surface, the transition matrix of the sphere is no longer given by (5.8) but by (6.43). As the transition matrix is formally different from that of a free sphere, shifts of the resonances may occur. Nevertheless, in the present case, possible shifts are not evident on the scale of Fig. 8.26.

8.5.2 Binary Aggregates

We now go to consider the scattered intensity from a binary aggregate of spheres identical in radius and refractive index to the one discussed in the preceding section. The component spheres are in mutual contact and lie on the interface. The axis of the aggregate is in the plane of incidence, and the scattered intensity is again observed at 60° from the normal to the surface.

The results of our calculations are reported in Fig. 8.27 for the case in which the interaction with the surface is neglected, whereas the case of full

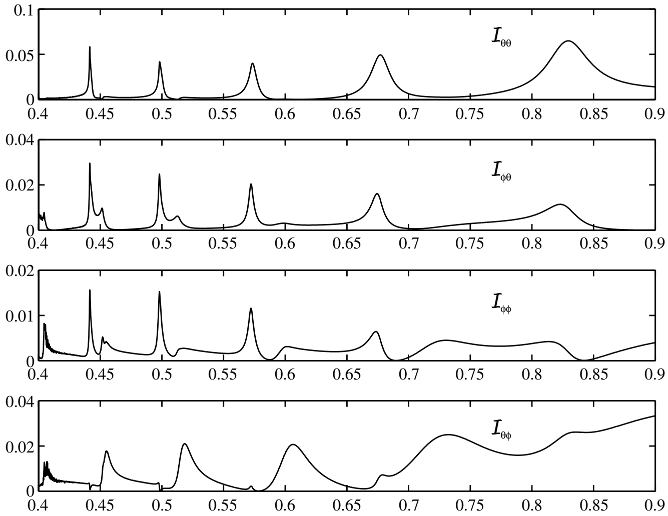

Fig. 8.26. Same as Fig. 8.25 but including the interaction with the surface of the prism

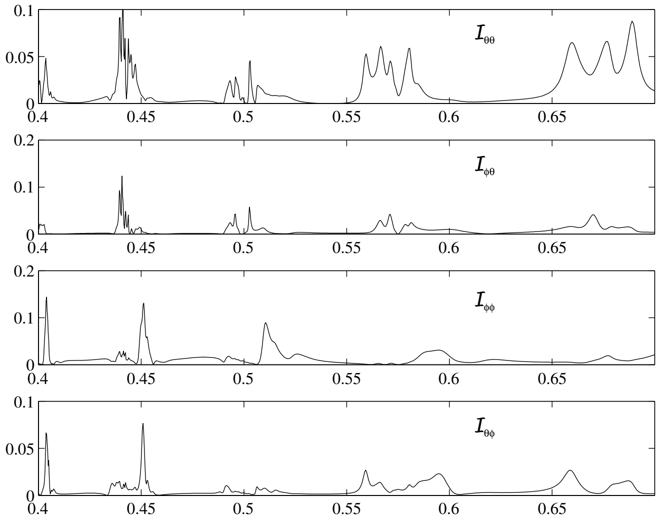

Fig. 8.27. Same as Fig. 8.25 but for a binary cluster with its axis in the plane of incidence. The interaction with the surface of the prism is neglected

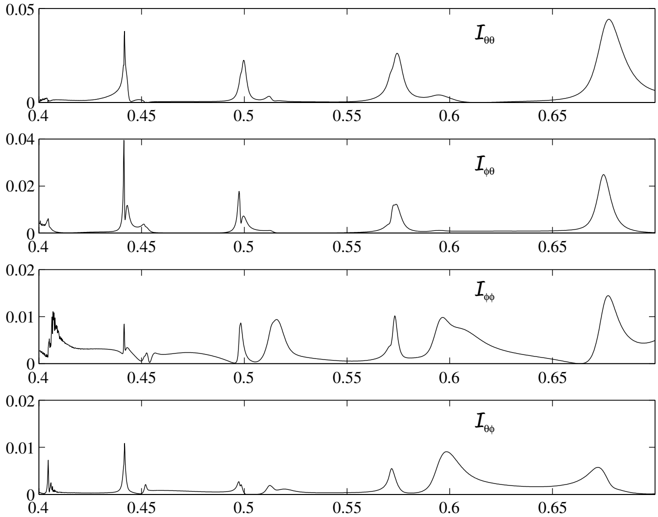

Fig. 8.28. Same as Fig. 8.27 but including the interaction with the surface of the prism

interaction is reported in Fig. 8.28. We first remark that the resonances that appear in Figs. 8.27 and 8.28 bear no classification label. In fact, as we remarked in Sects. 1.8.3 and 8.3.2, the lack of spherical symmetry of the whole aggregate makes impossible an unambiguous classification of the resonances into electric and magnetic. Moreover the quantum numbers of the scattered multipole fields cannot be of help because of the multiple scattering processes that occur between the aggregated spheres, not to mention, when appropriate, the multiple scattering processes between the aggregate as a whole and the interface.

We remark that the process of aggregation does not yield a mere duplication of the resonances as is easily seen by comparing Fig. 8.25 with Fig. 8.27. In fact, the multiple scattering processes between the component spheres, tend to complicate the spectrum yielding, in general, more that two peaks in place of the single resonances of the independent spheres. When the interaction with the interface is taken into account, the selection mechanism yielded by the polarization appears to be even more active. This is quite apparent in Fig. 8.28 which, for any choice of the polarization shows a simpler spectrum than the one in Fig. 8.27.

9 Applications: Atmospheric Ice Crystals

The aggregates (both external and internal) that were considered in Chap. 6 were not meant to simulate specific kinds of particles, but rather to illustrate the capabilities of the cluster model in association with the transition matrix approach in describing the optical properties of some system of interest. In the present chapter, on the contrary, we describe a specific application to the atmospheric ice crystals. The study of their scattering properties is an important topic in view of the role that they play in the meteorological phenomena and in the thermal budget of Earth. In particular, two problems are currently among the most studied ones: the contribution of the atmospheric ice crystals to the greenhouse effect, and the possibility of discriminating their shape by means of polarimetric radar devices.

In the following sections we use the cluster model to approximate the shape of the ice crystals, although this choice may appear restrictive. Nevertheless, the discussion of our results will make clear that the cluster model may be adequate to give a qualitative description of the scattering features. In fact, it will be inadequate as regards those effects that depend on the precise shape of the scatterers, such as the halos produced by some big atmospheric ice crystals.

9.1 Properties of Atmospheric Ice Crystals in the Infrared

According to recent studies, the atmospheric ice crystals may contribute to the greenhouse effect by scattering back a nonnegligible part of the infrared radiation that is emitted by Earth [178]. In this section a quantitative content is given to this statement by calculating the infrared optical properties of model particles built so as to fit the shape of the ice crystals that are most commonly met in atmospheric studies. In fact, according to Pruppacher and Klett [179], the atmospheric ice crystals occur in several different shapes among which the most common are sticks, crosses, and hexagonal platelets. In this Section we focus on the hexagonal platelets.

Each platelet is modeled as an aggregate of six identical spheres of radius $\rho = 2.5\,\mu\text{m}$, whose centers lie at the vertices of a regular hexagon. The neighboring spheres are in mutual contact, so that the resulting aggregate has the overall diameter $d = 15\,\mu\text{m}$ [46]. This choice locates these model particles within the range of size of the hexagonal platelets that are most often met in the atmosphere. They have, in fact, an overall diameter of 10–50 μm and a thickness of 5–15 μm. The refractive index of the component spheres is taken from the paper of Warren [180] whose tabulations cover the wavelength range of interest, i.e., from 8 to 100 μm. In all our calculations we put $n = 1$, but this choice can be changed to simulate, e.g., the water content of the environment.

The transition matrix of the model platelets has been calculated through the procedure of Sect. 5.4 and particular attention has been payed both to the rate of convergence and to the possible occurrence of resonances. Moreover, a few orientational distributions that are likely to occur are considered. According to Sect. 5.4.1, the rate of convergence of our procedure depends both on the size parameter $x_\rho = 2\pi\rho/\lambda$ of the component spheres and on the size parameter $x_{\mathrm{d}} = \pi d/\lambda$ of the aggregate as a whole. In the present case $1.96 \geq x_\rho \geq 0.157$ and $5.89 \geq x_{\mathrm{d}} \geq 0.471$, so that, in order to get fair convergence for the transition matrix elements, one has to use $l_{\mathrm{M}} = 15$ at the shortest wavelengths. We remark that the convergence of the calculations is not affected by the orientational averaging procedure that is necessary to deal with the dispersion of ice crystals. In order to perform the required averages according to Sect. 4.5 we want to assign to each platelet a local reference frame $\bar{\Sigma}$ chosen with regard to their symmetry. Actually, we chose the $\bar{x}\bar{y}$ plane to coincide with the plane of the hexagon on whose center we put the origin of the coordinates; a pair of opposite vertices were chosen to lie on the $\bar{y}$ axis. In turn, the laboratory frame Σ, to which the whole dispersion is referred, is chosen to have the z axis vertical. The orientational distribution assumes that the $\bar{z}$ axes of the platelets form an angle β with the z axis with probability $v(\beta) \propto \cos^4\beta$, whereas the α and γ angles are randomly distributed. This choice of $v(\beta)$ ensures that 50 % of the particles have their $\bar{z}$ axes forming an angle $\beta \leq 30°$ with the vertical. Hereafter, this kind of dispersion will be referred to as constrained dispersion. Two other dispersions are also considered: the dispersion of platelets with random distribution of the orientations and the dispersion of platelets all oriented alike with the axes of their local frame $\bar{\Sigma}$ parallel to the respective axes of Σ. Hereafter, these cases will be referred to as random dispersion and equioriented dispersion, respectively. Finally, in order to assess to what extent the peculiarities of the cluster model affect the results we also calculated the quantities of interest for the equivalent sphere, i.e., the homogenous sphere whose volume equals that of the six spheres that compose the aggregate. The radius of the equivalent sphere is thus $r_{\mathrm{e}} = 4.543\,\mu\text{m}$ and the size parameter range is $3.57 \geq x_{\mathrm{e}} \geq 0.285$.

For forward and backward scattering the definition of the plane of scattering is not unique as any plane through the common direction of $\hat{\boldsymbol{k}}_{\mathrm{I}}$ and $\hat{\boldsymbol{k}}_{\mathrm{S}}$

is suitable as a plane of reference. Therefore, since we are interested just in forward and backscattered intensities, the plane of scattering is at our choice and it is taken to coincide with the zx plane. Accordingly, both $\hat{\boldsymbol{u}}_{\mathrm{I}\,2}$ and $\hat{\boldsymbol{u}}_{\mathrm{S}\,2}$ turn out to be oriented along the y axis.

In Fig. 9.1 we report the quantity

$$\mathcal{I}_{\mathrm{f}} = (r^2/I_{\mathrm{I}})\langle I_{\mathrm{S}11}(\hat{\boldsymbol{k}}_{\mathrm{I}}, \hat{\boldsymbol{k}}_{\mathrm{I}})\rangle = \langle |f_{11}(\hat{\boldsymbol{k}}_{\mathrm{S}} = \hat{\boldsymbol{k}}_{\mathrm{I}}, \hat{\boldsymbol{k}}_{\mathrm{I}})|^2\rangle$$

as a function of λ for $\hat{\boldsymbol{k}}_{\mathrm{I}}$ parallel to the z axis. This quantity, that is proportional to the transmitted intensity through a dispersion of particles for polarization in the plane of scattering, is reported for the equioriented, for the randomly oriented and for the constrained dispersions. The curve for the equivalent sphere is also included. The calculations were actually performed for $8 \leq \lambda \leq 100\,\mu\mathrm{m}$ but Fig. 9.1, as well as all the other figures in this section, report the resulting curves only in the most significant part of the range of λ. We first notice that the choice of the orientational distribution function does not have much effect on the qualitative features of our results. Moreover, the curve for the equivalent sphere does not differ substantially from the other curves. In fact, the main peak that occurs at $\approx 14\,\mu\mathrm{m}$ for the dispersions of platelets appears to be slightly shifted towards longer wavelengths for the equivalent sphere and to be slightly lower. This suggests that fitting the optical behavior of highly symmetric particles by means of a sphere of suitable radius may lead to conclusions that are not too incorrect, in particular, when the particles are randomly oriented. As expected,

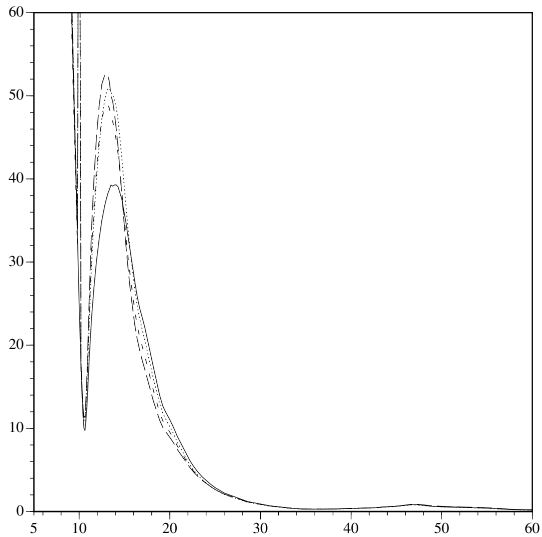

Fig. 9.1. $\mathcal{I}_{\mathrm{f}}$ in $\mu\mathrm{m}^2$ as a function of λ in $\mu\mathrm{m}$ for the equivalent sphere (*solid line*), for the equioriented dispersion (*long dashed line*), for the constrained dispersion (*dashed line*) and for the random dispersion (*dotted line*)

the approximate description yielded by the equivalent sphere slightly worsens when the orientational distribution of the actual anisotropic particles becomes more and more different from the random distribution. Nevertheless, a weak dependence of the transmitted intensity on the choice of the orientational distribution, as well as on the direction of incidence and on the polarization, appears to be an expected result. Therefore we performed calculations also for $\hat{\boldsymbol{k}}_{\mathrm{I}}$ forming an angle of 30°, 60°, and 90° with the z-axis and for polarization both parallel and perpendicular to the plane of reference. The results for the equivalent sphere and for the randomly oriented dispersion are, of course, rigorously independent both of the direction of incidence and of the polarization. On the contrary, this is not the case either for the equioriented or for the constrained dispersions. A dependence both on the direction of $\hat{\boldsymbol{k}}_{\mathrm{I}}$ and on the polarization was actually found, but the differences with respect to the case of 0°-incidence were rather small. For this reason the resulting curves do not deserve a separate comment and are consequently not reported. It may be useful to notice, however, that, due to the high symmetry of the platelets around their $\bar{z}$ axis, this weak dependence on the polarization can be easily understood for the equioriented dispersion. The similarity of behavior of the constrained dispersion may, in turn, be attributed to our choice of the orientational distribution function. In fact, the weighting function is strongly peaked for $\beta = 0°$ and β itself is likely to be smaller than 30°. As a result, this kind of orientational distribution may differ little from an equioriented distribution. As a further result, the transmitted intensity should show almost no depolarization. This expectation is confirmed as the ratio $\langle I_{\mathrm{S21}}(\hat{\boldsymbol{k}}_{\mathrm{I}}, \hat{\boldsymbol{k}}_{\mathrm{I}})\rangle / \langle I_{\mathrm{S11}}(\hat{\boldsymbol{k}}_{\mathrm{I}}, \hat{\boldsymbol{k}}_{\mathrm{I}})\rangle$ for any choice of $\hat{\boldsymbol{k}}_{\mathrm{I}}$ and of the wavelength never exceeds $7 \cdot 10^{-3}$.

All the curves, including the curve from the equivalent sphere, present for $\lambda \approx 10\,\mu\mathrm{m}$ a narrow sharp peak which, on an expanded scale, appears to be superposed on a quite regular curve. Therefore, this is a striking example of a wavelength at which the value of the refractive index plays a dominant role for the forward scattering, whereas the actual structure and orientational distribution of the ice crystals have on the whole little importance.

We define the quantity $\mathcal{I}_{\mathrm{b}\eta} = \langle |f_{\eta\eta}(\hat{\boldsymbol{k}}_{\mathrm{S}} = -\hat{\boldsymbol{k}}_{\mathrm{I}}, \hat{\boldsymbol{k}}_{\mathrm{I}})|^2 \rangle$, that is proportional to the backscattered intensity, and in Fig. 9.2 we report the quantity $\mathcal{I}_{\mathrm{b}1}$ for the equioriented, for the randomly oriented, and for the constrained dispersions. Even in this case the curve for the equivalent sphere is included. The direction of incidence is parallel to the z axis. Even a cursory examination shows that the backscattered intensity is rather sensitive to the choice of the orientational distribution function. In this case the maximum occurs at $15\,\mu\mathrm{m}$ both for the equioriented and for the constrained dispersions, but the value at the maximum is four times larger for the equioriented dispersion than it is for the constrained dispersion. The curve for the random dispersion, in turn, reaches its maximum at $\approx 16\,\mu\mathrm{m}$, whereas the equivalent sphere has the least backscattering power with its maximum at $14\,\mu\mathrm{m}$.

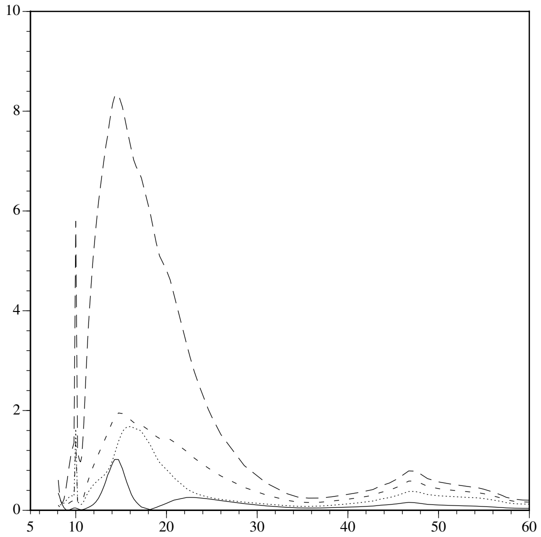

Fig. 9.2. $\mathcal{I}_{\mathrm{b}\,1}$ in µm^2 as a function of λ in µm for the equivalent sphere (*solid line*), for the equioriented dispersion (*long dashed line*), for the constrained dispersion (*dashed line*) and for the random dispersion (*dotted line*)

The sensitivity of the backscattering to the choice of the orientational distribution suggests also the occurrence of a noticeable dependence on the polarization and on the direction of incidence. To assess this point, we report in Fig. 9.3 (a) the quantity $\mathcal{I}_{\mathrm{b}\,1}$ and in Fig. 9.3 (b) the quantity $\mathcal{I}_{\mathrm{b}\,2}$ for the constrained dispersion and for $\hat{\boldsymbol{k}}_{\mathrm{I}}$ forming an angle of 0°, 30°, 60°, and 90° with the z axis. The dependence of the backscattered intensity on the choice of $\hat{\boldsymbol{k}}_{\mathrm{I}}$ and on the polarization is evident and deserves no further comment.

Another quantity of interest that shows a clear dependence on the direction of incidence, is the depolarization ratio of the constrained dispersion, $D_{\mathrm{b}} = \langle I_{\mathrm{S}21}(-\hat{\boldsymbol{k}}_{\mathrm{I}}, \hat{\boldsymbol{k}}_{\mathrm{I}})\rangle / \langle I_{\mathrm{S}11}(-\hat{\boldsymbol{k}}_{\mathrm{I}}, \hat{\boldsymbol{k}}_{\mathrm{I}})\rangle$, that we report in Fig. 9.4 for $\hat{\boldsymbol{k}}_{\mathrm{I}}$ forming an angle of 0°, 30°, 60°, and 90° with the z axis. For any choice of the direction of incidence the depolarization of the backscattered radiation can be found to be noticeably larger than that of the transmitted radiation D_{f} that is not reported, however.

The choice of the orientational distribution, has little influence also on the albedo, as is apparent from the curves in Fig 9.5 where we report $\varpi = \langle\sigma_{\mathrm{S}}\rangle/\langle\sigma_{\mathrm{T}}\rangle$. In fact, the similarity of the curves should be noticed. Taking into account that $\sigma_{\mathrm{T}} = \sigma_{\mathrm{S}} + \sigma_{\mathrm{A}}$, one can guess that, with changing distribution, $\langle\sigma_{\mathrm{A}}\rangle$ behaves just as $\langle\sigma_{\mathrm{S}}\rangle$ does. As regards $\langle\sigma_{\mathrm{S}}\rangle$, it may well turn out to be almost insensitive to the choice of any of the distributions considered. In fact, the definition of σ_{S} implies integration of the flux across a sphere that surrounds the particle of interest. Now, the results that we discussed above show that the forward-scattered intensity, that gives the largest

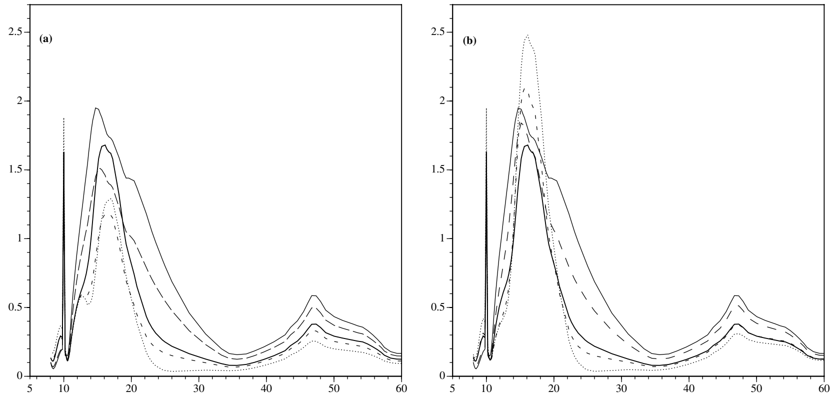

Fig. 9.3. $\mathcal{I}_{\mathrm{b}\,1}$ **(a)** and $\mathcal{I}_{\mathrm{b}\,2}$ **(b)** in $\mu\mathrm{m}^2$ for the constrained dispersion as a function of λ in μm, for several choices of the direction of incidence. $\vartheta_{\mathrm{I}} = 0°$ (*solid line*), 30° (*long dashed line*), 60° (*dashed line*), and 90° (*dotted line*). For comparison the results for the random dispersion is also reported (*heavy solid line*)

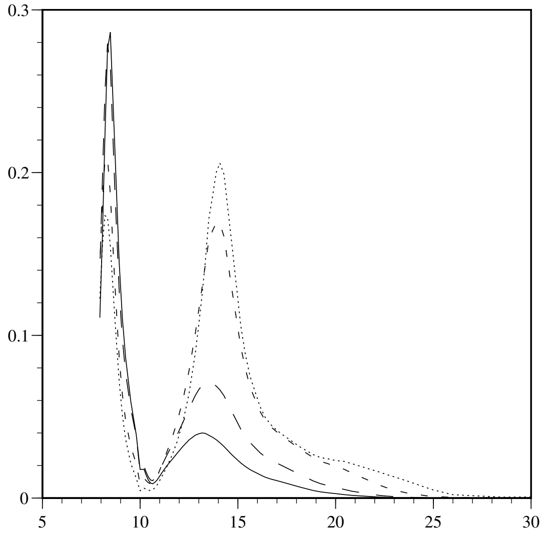

Fig. 9.4. Depolarization ratio D_{b} for the constrained dispersion as a function of λ in μm, for several choices of the direction of incidence. $\vartheta_{\mathrm{I}} = 0°$ (*solid line*), 30° (*long dashed line*), 60° (*dashed line*), and 90° (*dotted line*)

contribution to the integration, is almost independent of the choice of the distribution, whereas the distribution-sensitive backscattered intensity gives a comparatively smaller contribution.

At this stage a few comments are in order. In fact, a reader acquainted with the aerodynamics of atmospheric ice crystals may argue that some of the distribution functions are unrealistic for 15 μm crystals. Actually, we are

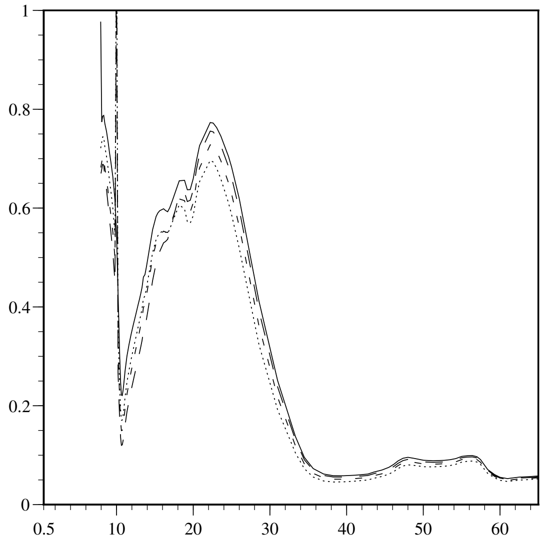

Fig. 9.5. Albedo ϖ as a function of λ in μm for the equivalent sphere (*solid line*), the equioriented dispersion (*long dashed line*), the constrained dispersion (*dashed line*), and the random dispersion (*dotted line*)

aware that ice crystals of this size are likely to be randomly distributed in orientation [181]. Nevertheless, once the transition matrix of a single crystal has been calculated, considering a further distribution function does not add much to the computational effort, whereas considering several instances of orientational distributions may help to interpret the experimental data [182]. Moreover, the results that we discussed above can, to a certain extent, be scaled [68] to get information on the behavior of particles of larger size to which equioriented or constrained distribution is more likely to apply. Of course, the principle of the electromagnetic scaling applies when the refractive index is independent of the wavelength. Now, in the infrared, the refractive index of ice depends weakly on the wavelength, at least on the long wavelength side [180]. Therefore, the results that we discussed above may be considered to apply, e.g., to clusters of six spheres of radius 25 μm and thus with an overall diameter of 150 μm in the wavelength range $100 \leq \lambda \leq 1000$ μm. A few sample calculations for the latter cluster confirm this expectation.

9.2 Ice Crystals in the mm Wave Range

In spite of the results mentioned at the end of Sect. 8.1, a complete and reliable extension of our investigation to the millimeter wave range cannot be made by resorting to the principle of optical scalability because of the noticeable difference of the refractive index of ice in the infrared and in the millimeter wave range. Therefore, in this section the investigation of the effectiveness of the cluster model to simulate the scattering properties of atmospheric ice crystals is extended to the millimeter wave range [183]. The results will be compared with those of the analogous calculations performed by Lemke et al. [184]. These authors used the DDA method (see Sect. 5.6.1) that, unlike the cluster model, allows for a better fitting of the actual shape of the crystals. In fact, the question arises as to whether a less coarse model than the one we considered in Sect. 8.1 may give more reliable results. However, experience suggests that the scattering properties of model particles depend more on the quantity of refractive material and on the general symmetry properties than on the detailed fitting of the shape of the actual particles [162].

We calculate the backscattered intensity from aggregates of a few different shapes. The incident radiation is chosen to be a 94 GHz plane polarized wave ($\lambda = 3.2 \cdot 10^{-3}\,\mathrm{m}$, $k_{\mathrm{v}} = \omega/c = 1.96 \cdot 10^{3}\,\mathrm{m}^{-1}$), that is a working frequency of polarimetric radar devices [184]. The refractive index of ice has been taken from the tabulation of Warren [180], i.e., $n = 1.782 + \mathrm{i}0.002701$. In all our calculations we assume that the medium surrounding the ice crystals is the vacuum.

The study of scattering properties proceeds in two steps. First, we study the backscattered intensity from single ice crystals of a few selected shapes when they change their orientation; both polarizations are considered. All the crystals are assumed to contain the same quantity of refractive material, namely, the quantity contained into a sphere of radius $\rho_{\mathrm{e}} = 1.0\,\mathrm{mm}$. The size parameter of this equivalent sphere is $x_{\mathrm{e}} = k_{\mathrm{v}}\rho_{\mathrm{e}} = 1.96$. Second, taking into account that radar returns are determined by simultaneous scattering by particles that may be of different size, we calculate the backscattered intensity and the depolarization ratio from dispersions of model ice crystals, for the same distributions which we considered in Sect. 8.1, as a function of the size parameter x_{e} of the equivalent sphere.

The shapes of the crystals that we consider are those that are usual in atmospheric studies, namely needles, columns, hexagonal platelets, and compact hexagonal columns [179]. These structures are customarily characterized by their aspect ratio $a = l/d$, where l and d denote the length and the diameter of the crystal, respectively. Each of these crystals is modeled as an aggregate of spheres of appropriate radius and the axes of their local frame $\bar{\Sigma}$ have origin in the center of mass of the aggregate. The orientation of the axes is sketched in Fig. 9.6. Accordingly, the needles are approximated as linear chains of six spheres of radius $\rho = 0.550 \cdot 10^{-3}\,\mathrm{m}$ and thus with an aspect ratio $a = l/d = 6$. Even the columns were approximated as linear chains of three identical spheres with radius $\rho = 0.693 \cdot 10^{-3}\,\mathrm{m}$ and aspect ratio $a = 3$. Of course, using this approximation results in the loss of the details that are due to the hexagonal cross section of the actual column crystals. It will become apparent, however, that these details are rather small

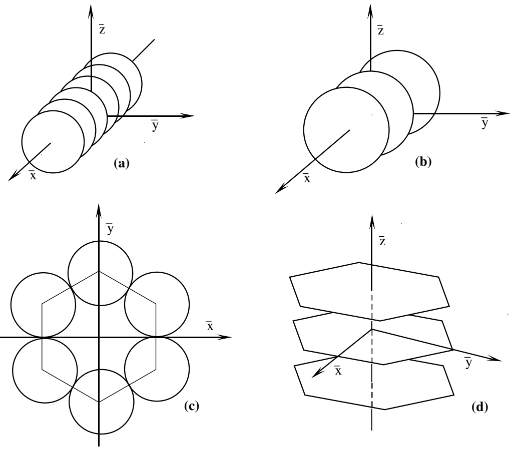

Fig. 9.6. Geometry of the clusters that model the needles **(a)**, the columns **(b)**, the hexagonal platelets **(c)**, and the compact hexagonal columns **(d)**. The local axes are also shown and, in the case of the compact hexagonal columns only the supporting hexagons are shown for the sake of clarity

and would anyway be smoothed out by the averaging procedure. For both the needles and the columns the centers of the component spheres lie on the $\bar{x}$ axis (see Figs. 9.6 (a) and (b)). This choice is the most convenient for averaging purposes, although for calculating the transition matrix the choice of the axis of the chains as $\bar{z}$ axis would be highly convenient in order to exploit the cylindrical symmetry of the cluster. As a matter of fact, one calculates the transition matrix putting the centers of the spheres just on the local $\bar{z}$ axis, then transforms the matrix elements to the reference frame $\bar{\Sigma}$ in which the centers lie on the $\bar{x}$ axis [107]. The hexagonal platelets are modeled as clusters of six spheres of radius $\rho = 0.550 \cdot 10^{-3}$ m and, as their centers are at the vertices of a regular hexagon, the resulting aspect ratio is $a = 0.3$. The hexagon lies on the $\bar{x}\bar{y}$ plane with two opposite vertices on the $\bar{y}$ axis (see Fig. 9.6 (c)). Finally the compact hexagonal columns are approximated as clusters of 18 spheres of radius $\rho = 0.382 \cdot 10^{-3}$ m whose centers lie at the vertices of a stack of three regular hexagons. These hexagons, in turn, have their centers on the $\bar{z}$ axis, lie on planes orthogonal to the $\bar{z}$ axis and have a pair of opposite vertices on the $\bar{y}\bar{z}$ plane. The aspect ratio of this structure is $a = 1$ (see Fig. 9.6 (d)).

In the first step of this study, namely, in assessing the dependence of the backscattered intensity on the orientation of single ice crystals, we consider the approximating clusters with their $\bar{z}$ axis vertical. This choice is not an undue restriction because aerodynamical considerations led to the conclusion that, in calm air, the ice crystals tend to present their largest area perpendicular to the direction of fall [181]. The incident wavevector is assumed to form an angle of $\vartheta_{\mathrm{I}} = 30°$ with the z axis of Σ. As expected, the backscattered

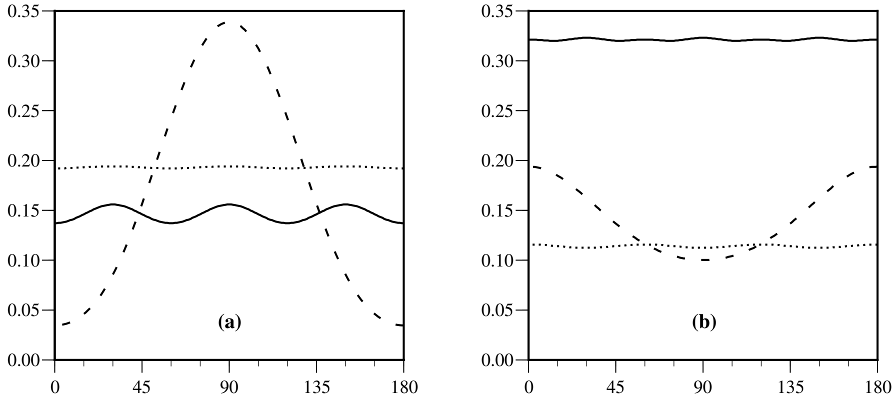

Fig. 9.7. Backscattered intensity $i_{\eta\eta}$, for $\eta = 1$ in **(a)** and for $\eta = 2$ in **(b)**, as a function of the Eulerian angle α from the hexagonal platelets (*solid line*) and from the compact hexagonal columns with their $\bar{z}$ axis vertical (*dotted line*) and horizontal (*dashed line*)

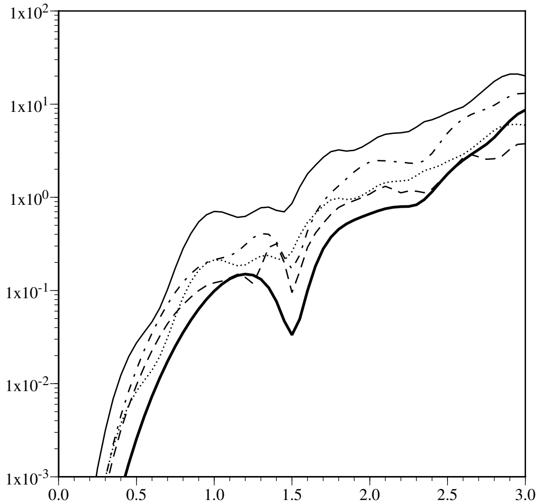

Fig. 9.8. Backscattered intensity i_{11} as a function of the size parameter of the equivalent sphere x_{e} from randomly oriented dispersions of needles (*dashed line*), columns (*dot-dashed line*), hexagonal platelets (*dotted line*), and compact hexagonal columns (*thin solid line*). The intensity from the equivalent sphere (*heavy solid line*) is also reported

intensity shows all the angular periodicities that are due to the symmetry of the model crystals. In fact, due to the transformation properties of the elements of the transition matrix, any periodicity that is due to the symmetry of the scattering particle is automatically included in the scattered intensity. For this reason we do not report the intensities from all the model particles in

Fig. 9.6. We prefer instead to compare the backscattered intensity from the hexagonal platelets and from the compact hexagonal columns, because these structures, in spite of their common hexagonal symmetry have a quite different aspect ratio. As we stated above, the hexagonal platelets were oriented with their local $\bar{z}$ axis vertical and the dependence of the backscattering on the Eulerian angle α was considered. Since the compact hexagonal columns have $a = 1$, we considered these model particles with their $\bar{z}$ axis both parallel

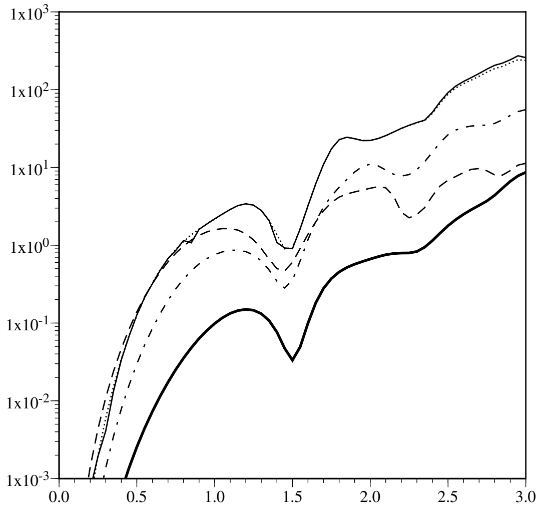

Fig. 9.9. Same as Fig.9.8 but for the equioriented dispersions

to the z axis and lying in the xy plane of Σ, i.e., the backscattered intensity as a function of α was considered not only for $\beta = 0°$ but also for $\beta = 90°$ and $\gamma = 0°$. In Fig. 9.7 we report the adimensional backscattered intensity $i_{\eta\eta} = k_{\mathrm{V}}^2 |f_{\eta\eta}(\hat{\boldsymbol{k}}_{\mathrm{S}} = -\hat{\boldsymbol{k}}_{\mathrm{I}}, \hat{\boldsymbol{k}}_{\mathrm{I}})|^2$. Therefore, the quantities i_{11} and i_{22} coincide with van de Hulst's $|S_2|^2$ and $|S_1|^2$, respectively [5]. Both the platelets and the hexagonal columns with the $\bar{z}$ axis vertical show little dependence on the angle α. This confirms our previous statement that the details due to the hexagonal cross section are negligibly small. On the contrary, when we consider the compact hexagonal columns with their $\bar{z}$ axis horizontal, the dependence on α of the backscattered intensity becomes quite evident. In spite of the fact that this structure has $a = 1$, the α-dependence looks, indeed, rather similar to that of the needles and of the columns. These results suggest that the aspect ratio is not always a good parameter for the classification of the different shapes of the ice crystals, at least in the millimeter wave range.

In the second step of this study, we deal with tenuous dispersions of identical particles whose orientational distribution is assumed to be known. We

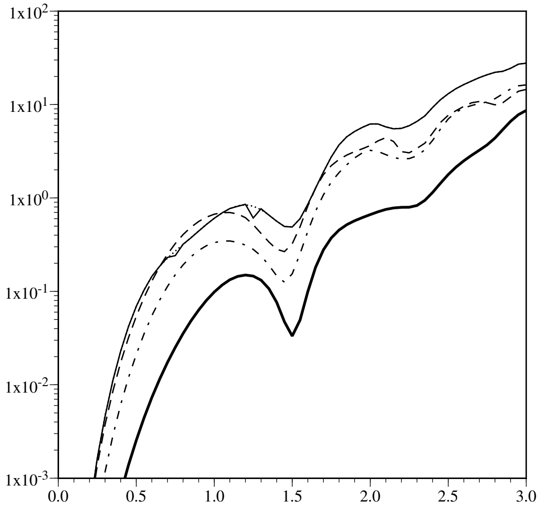

Fig. 9.10. Same as Fig. 9.8 but for the constrained dispersions

calculate the backscattered intensity $i_{\eta\eta}$ as a function of the size parameter of the equivalent sphere in the range $0.25 \leq x_{\mathrm{e}} \leq 3.0$ by choosing the direction of incidence parallel to the z axis. In order to grant direct comparison with the DDA results of Lemke et al. [184], in the following figures we report i_{11} again for $\lambda_0 = 3.2\,\mathrm{mm}$. The results thus apply for the radius of the equivalent sphere that goes from 0.127 mm to 1.53 mm. Nevertheless, since the refractive index of ice does not significantly depend on the wavelength within the millimeter wave range, the principle of electromagnetic scaling applies [68]. As a consequence the same results, when multiplied by the factor $(\lambda_0/\lambda)^2$, can be interpreted as the backscattering from particles of fixed size for varying wavelength. In this case, by assuming an equivalent sphere of 1 mm radius, the wavelength goes from $\lambda = 25\,\mathrm{mm}$ for $x_{\mathrm{e}} = 0.25$ to $\lambda = 2.1\,\mathrm{mm}$ for $x_{\mathrm{e}} = 3$. The usefulness of this twofold possibility of interpretation stems from the fact that the orientational distribution of the atmospheric ice crystal may depend on their size [181]. We report in Fig. 9.8 the results for the case of random distributions, in Fig. 9.9 those for equioriented distributions, and in Fig. 9.10 the results for constrained distributions. The latter distribution has been included to consider the case in which canting of the ice crystals occurs, e.g. as an effect of air turbulence.

Even a cursory comparison of the results in Figs. 9.8–9.10 shows that the backscattering intensity is about one order of magnitude larger for the equioriented dispersions than it is for the random and for the constrained distributions. This result stems from the fact that, in the equioriented distribution, the ice crystals present their largest geometrical cross section orthogonal to the vertical axis that we chose to coincide with the direction of incidence. For all the distributions considered, all the crystal structures display a relatively sharp feature more or less at $x_\mathrm{e} \approx 1.5$. A further feature of the random distribution is the separation of all the curves. This result can be understood by considering that the backscattered intensity comes from the collection of contributions, all with the same weight, from particles that are seen under all possible orientations. Thus, in the case of a random distribution, the aspect ratio may play a role for discriminating among the various structures. This conclusion may not hold in the case of other distributions. In fact, the curves for the compact hexagonal columns and for the hexagonal platelets are practically indistinguishable from each other both in the equioriented distribution and in the constrained distribution. For the equioriented distribution, this behavior agrees with the results for i_{11} in Fig. 9.7. On the other hand, the constrained distribution differs little from the equioriented one as we already stressed in Sect. 8.1.

Further insight into the behavior of the ice crystals as a function of their orientational distribution comes from the backscattering depolarization ratio D_b. This quantity is reported in Fig. 9.11 for the needles, the columns, the hexagonal platelets, and the compact hexagonal columns. In all these figures, the most striking features are the two large peaks that occur at $x_\mathrm{e} \approx 1.5$ and $x_\mathrm{e} \approx 2.3$ for the case of random distribution. The first peak corresponds to the minimum that all the clusters present in Figs. 9.8–9.10, whereas the second peak corresponds to a value of x_e at which dips or shoulders occur. The depolarization for random distribution presents a satellite peak that occurs at $x_\mathrm{e} \approx 1.3$ where the backscattering displays clear features in the form of dips or of shoulders. Note that this satellite peak of the depolarization does not appear for the constrained and for the equioriented distribution, with the exception of a small peak in the constrained distribution of the compact hexagonal columns.

To all these features one could add the vanishing of the depolarization ratio from the hexagonal platelets and from the compact hexagonal columns in the equioriented distribution (see Figs. 9.11 (c) and (d)). This result was expected on account of the high (hexagonal) symmetry of the crystals around their $\bar{z}$ axis, which yields a weak dependence on α of the co-polarized backscattered intensity and rather small values of the cross-polarization elements of the scattering amplitude. The average over α smooths out any angular dependence to a virtual cylindrical symmetry and yields, as a result, the vanishing of the depolarization referred to above.

Figure 9.7 suggests that, as far as single particles are concerned, the aspect ratio is not always a good parameter for discriminating the scattering properties of ice crystals of different shape. In fact, we have already remarked that, when the compact hexagonal columns are considered with their $\bar{z}$ axis horizontal, the angular dependence of the backscattered intensity looks rather similar to that from more elongated particles such as the needles and the columns. On the contrary, when the $\bar{z}$ axis is vertical, the backscattered intensity is more akin to that from the hexagonal platelets. Figures 9.8–9.10

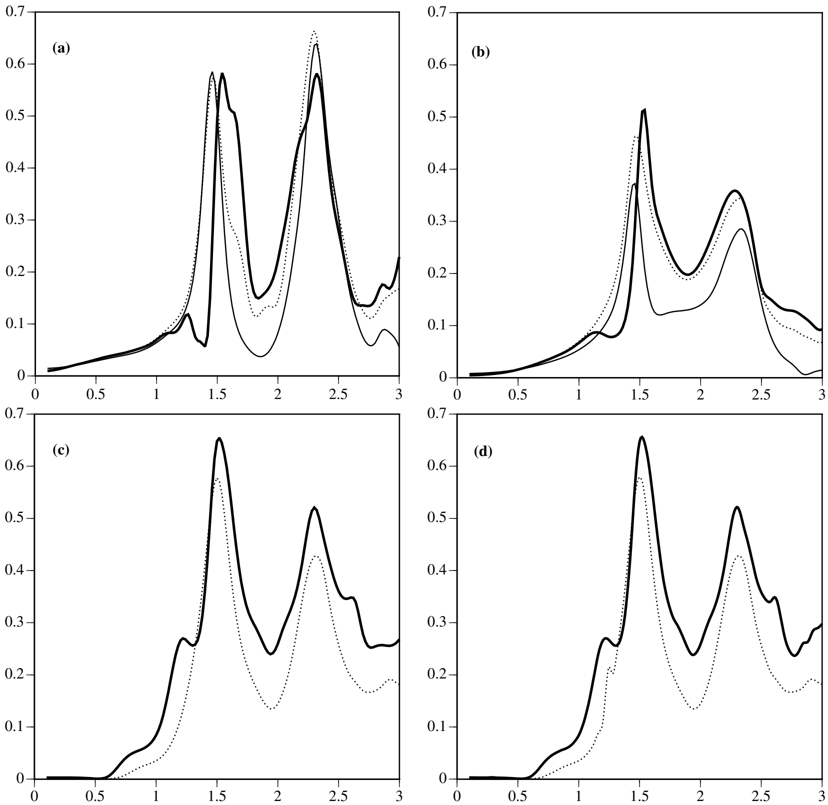

Fig. 9.11. Backscattering depolarization ratio D_b for dispersions of needles **(a)**, columns **(b)**, hexagonal platelets **(c)**, and compact hexagonal columns **(d)** as a function of the size parameter of the equivalent sphere x_e, in cases of random (*heavy solid line*), equioriented (*thin solid line*), and constrained (*dotted line*) orientational distributions

show that, when dispersions of compact hexagonal columns and of hexagonal platelets are considered, the curves of the backscattered intensity as a function of x_e coincide, except when the orientational distribution is random, at least as far as i_{11} only is considered. In practice, Figs. 9.8–9.10 show that particles with a different aspect ratio yield well-distinguishable curves only for random distribution. In any case, the curves for a given shape have a spread, with changing orientational distribution, no greater than one order of magnitude, just as large as the spread, for a chosen distribution, of the curves from various shapes. The general trend of all these curves follows the curve for the equal volume sphere that lies generally lower, however. This suggests that a better fitting of the results from model ice crystals could be attained by considering, instead of the equal-volume sphere, the equal-projected-area sphere [185]. In this respect, the conclusions of West on the optical behavior of aggregations of small spheres [186] and the considerations of Zakharova and Mishchenko on the optical properties of ice ellipsoids [187] may be a valuable guide. The analysis of the polarization may be important. For instance, the depolarization ratio in Fig. 9.11 seems to give more information for discriminating the shape of the ice crystals, e.g. because of its vanishing for the equioriented distribution both of the compact hexagonal columns and of the hexagonal platelets. Unfortunately, such a distribution is rather unlikely to occur because of air turbulence. Even when a modest amount of canting occurs the depolarization ratio becomes akin to that from the constrained and from the random distribution. The latter distribution, however, could yet be discriminated provided that the satellite peak at $x_{\mathrm{e}} = 1.3$ could actually be observed.

Even bearing in mind that the aspect ratio is not always a good discriminating parameter, the results presented so far suggest that modeling an actual ice crystal as a cluster of spheres of appropriate geometry yields the correct features of the scattering process that stem from the symmetry of the particles. This, as we already remarked, is a consequence of the transformation properties of the transition matrix under rotation. The regularity of the curves in Fig. 9.7 shows that using the cluster model does not introduce any spurious feature of importance, especially because at 94 GHz the wavelength is noticeably larger that the size of the component spheres so that, for instance, no resonance of the single spheres occurs. Nevertheless, the small dips that occur in the curves for the compact hexagonal columns are certainly specific features of the 18 sphere cluster. Of course, an approach such as the DDA attains a better fitting of the actual shape of the particles of interest. The price to be paid, however, is a noticeable increase of the computational effort because, unlike the transition matrix method, the DDA requires a separate calculation for each direction of incidence and for each direction of observation. Anyway, the results of the transition matrix approach are in substantial agreement with the DDA results of Lemke et al. [184]. Therefore, when a distribution of ice crystals needs to be considered, the conditions outlined in Sect. 1.1 may occur and modeling the single crystals as clusters of spheres is certainly convenient. Ultimately, what computational method is preferable could be established only by comparison of the theoretical predictions with the results of laboratory experiments under controlled conditions.

10 Applications: Cosmic Dust Grains

The importance of the cosmic dust forming the interstellar medium (ISM) has long been recognized in astronomy. The interaction of the cosmic dust grains with the radiation field of the stars, beyond yielding extinction and polarization of the starlight by linear dichroism, also yields mechanical interactions such as the radiation pressure and the radiation torque that, together with the gravitational interactions, determine the dynamics of the grains themselves. According to Chaps. 4 and 7, all these phenomena, both optical and mechanical, can be traced back to the transition matrix of the dust grains. Moreover, the technique of Sect. 5.5 is appropriate to investigate also the state of polarization of the electromagnetic radiation that penetrates into the cavities contained in the interstellar dust grains. Therefore, a great deal of information could be gained by applying to the ISM the methods and procedures that have been expounded in the preceding chapters. Accordingly, this chapter is devoted to the discussion of some astrophysical problems which we deal with through the theory of electromagnetic scattering.

10.1 Interstellar Dust

Most of the information on the interstellar matter comes from spectroscopical analysis and from the study of the extinction of the starlight that propagates through the ISM. We can summarize the available information as follows:

- In the range from the visible to the near infrared, the average galactic extinction curve depends more or less linearly on λ^{-1}, with the noticeable exception of the 2175 Å bump. This kind of dependence, which is easily discerned in the curve reported, e.g., by Aiello et al. [188], is consistent with an interstellar medium which includes solid grains whose overall size is of the order of the wavelength [189].
- Since the extinction of the starlight by the ISM yields linearly polarized light, the dust grains should be intrinsically nonspherical. Moreover, the detail of the polarization dependence sets to 0.1–0.2 μm the upper limit for the size of the grains [189].
- The spectroscopic analysis is consistent with a chemical composition of the grains that includes carbon, both in its amorphous and graphitic form, silicates, and (possibly organic) ices [190].

Now, the wealth of new data yielded by the observations of the past few years made clear that practically all dust models proposed before 1995 face a serious crisis in explaining interstellar dust phenomenology. All the old models for the cosmic dust were, indeed, based on the assumption that the elemental abundances, i.e., the number of the available elemental atoms per 10^6 H atoms, were more or less constant throughout the Galaxy. Therefore, the relative abundances of the elements that form the ISM were assumed to be more or less the same that were observed within the solar system. On the contrary, a number of authors who discussed the elemental abundances [191–194] had to conclude that the solar system is not representative of the cosmic abundances, but is instead enriched in those elements which are supposed prominent in the composition of interstellar dust. As a result, the available quantity of carbon, oxygen, and silicates that is tied up into the cosmic dust grains must be noticeably smaller than assumed before. This conclusion is commonly referred to as *elemental shortage*.

A few authors addressed the problem of the construction of models able to reproduce the observed extinction while complying with the new observed abundances. For instance, Mathis [195] and Li [196] proposed models for the interstellar dust in which the bulk of the infrared, visual, and ultraviolet extinction arises from composite, core-mantle and multilayered grains with varying degree of porosity. These fluffy, or porous, aggregates can produce more extinction per unit mass than their combined individual components. Such models could thus be consistent with tighter abundance constraints. However, scattering and absorption of light by such complex model particles were not dealt rigorously, a noticeable exception being the analysis of the interstellar extinction produced by porous grains performed by Vaidya and Gupta [197] in the framework of DDA [94, 96, 97].

We have good indications of the chemical nature of interstellar dust [198]. What is still unclear is how the dust material is assembled to form an interstellar grain. Therefore, in this chapter we explore the potentialities of the cluster model in describing the optical properties of the cosmic dust grains [199]. Among the modeling problems that we deal with, there are:

- Investigating how and to what extent the extinction of a given mass of astronomical material changes when it is subdivided into several clustering spheres, and whether the change of the geometry of the clusters may produce detectable effects on their extinction spectrum.
- Investigating the change of the extinction due to modifications of the chemical composition of the clusters.
- Studying the effect of the morphology and refractive index of the clusters on the radiation pressure.

The other important topic that we consider in this chapter is:

- Studying the state of polarization of the electromagnetic radiation that penetrates into cavities embedded in fluffy and porous grains.

Of course, we do not propose a specific model for the dust grains, especially on account of the revised standards for the abundances in interstellar dust published in recent years by Sofia and Mayer [200, 201]. These revised standards, in fact, suggest that the elemental shortage is actually not so constraining as assumed before. Nevertheless, we are confident that the techniques that we presented throughout this book will be of help in the definition of new strategies in cosmic dust modeling.

10.2 Modeling Cosmic Dust Grains as Aggregates

In this section, we present a few samples of the relevant information that can be obtained through the theory of Sect. 5.4. Since the problem of the extinction by the available mass in the cosmic dust is a critical one, we consider the extinction produced by the mass of astronomical silicates [96,159] that would be contained in a homogeneous sphere of radius $\rho = 100\,\mathrm{nm}$ [199]. Hereafter, this sphere will be referred to as the equivalent sphere. We consider also the subdivision of the mass of the equivalent sphere into an increasing number of spherical subunits clustering in a roundish geometry. All the spherical subunits have the same radius that, when N subunits are considered, is given by $\rho_{\mathrm{s}} = \rho/N^{1/3}$, where ρ is the radius of the equivalent sphere. Accordingly, we study the behavior of the extinction cross sections in the following cases:

1. Subdivision of a given mass of astronomical silicates into clustering subunits.
2. Substitution of the material of some subunits in a cluster with amorphous carbon. Of course, in this case the mass is not conserved.
3. Change of the geometry of the clusters.

We use the amorphous carbon dielectric functions derived by Rouleau and Martin (sample Be1) [202]. Clusters of up to 12 spherical subunits are considered and the orientational average is performed, through the formulas of Sect. 4.5, on the assumption of random orientational distribution. In other words, at this stage the possibility of a preferential orientation induced by some external agent is not considered. All the calculations required $l_{\mathrm{M}} = 14$ to get an accuracy of four significant digits.

In Fig. 10.1 is shown the extinction cross section of the equivalent sphere and of the clusters containing the same mass of astronomical silicates as a function of λ^{-1} in $\mu\mathrm{m}^{-1}$ in the range $1 \leq \lambda^{-1} \leq 10$. Roundish geometries are assumed (see Fig. 10.3 (a)). The curves show that the effect of the subdivision and clustering of astronomical silicates may be quite different in the different regions of the spectrum. In fact, the binary clusters produce a larger extinction than that of the equivalent sphere in the visible range, whereas clustering up to 12 subunits produces less extinction in the same spectral region. The effect is reversed in the ultraviolet, where subdivision and clustering yield more extinction than the equivalent sphere, the extent of the effect increasing with

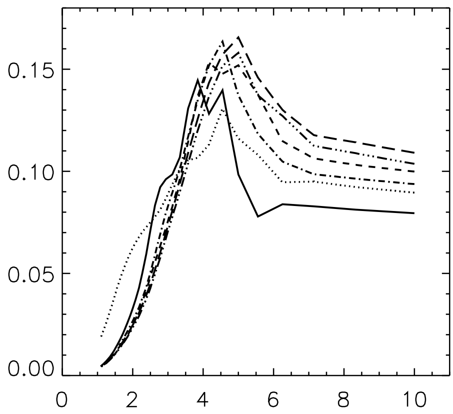

Fig. 10.1. Effects of subdivision on the extinction cross sections. The quantity that is actually reported is σ_{T} in $\mu\mathrm{m}^2$ as a function of λ^{-1} in $\mu\mathrm{m}^{-1}$ for the equivalent sphere (*solid line*), for a random dispersion of 2-sphere clusters (*dotted line*), of 4-sphere clusters (*short dashed line*), 6-sphere clusters (*dot-dashed line*), 10-sphere clusters (*triple dot-dashed line*), and 12-sphere clusters (*long dashed line*)

increasing degree of subdivision. The origin of this behavior can be tracked back to the multiple scattering processes that occur among the components of a cluster. These processes appear to give a more effective contribution when the wavelength is of the same order of magnitude of the mutual distance of the centers of two subunits. Accordingly, when this distance is comparatively large, as in the case of binary clusters, the largest effect is bound to occur in the visible. The reverse situation occurs, as expected, at shorter wavelengths, i.e., in the ultraviolet. Of course, no such effect can be present in the case of a single homogeneous sphere.

In Fig. 10.2 we show the effect of changes in chemical composition of dust grains through the partial substitution of silicate subunits by amorphous carbon spheres of the same radii. In this case, the total mass is not conserved. Starting from the same 10-sphere cluster whose extinction is already reported in Fig. 10.1, with the help of a random number generator, first 2 and then 4 spheres are selected and their material is substituted with amorphous carbon, leaving everything else unchanged. Again, the curves in Fig. 10.2 show that the effect of the substitution is different in the different regions of the spectrum. Substitution of carbon to silicon increases the extinction in the visible. Finally, let us consider the effect of the geometry on the extinction from a dispersion of clusters. In fact, so far we have considered the roundish geometry of Fig. 10.3 (a) for the 10-sphere clusters. By means of a random number generator, we built three further 10-spheres clusters whose geometry is shown in Figs. 10.3 (b)–(d). Note that, in Fig. 10.3 the dots that represent the subunits are well separated to emphasize geometry, but in actual calculations the neighboring subunits were kept in mutual contact. The results

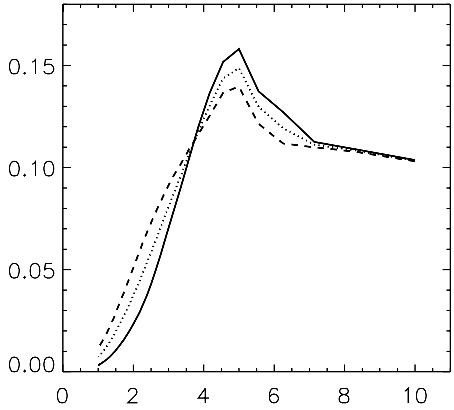

Fig. 10.2. Effects of chemical composition on the extinction cross sections. The quantity that is actually reported is σ_T in μm^2 as a function of λ^{-1} in μm^{-1} for a random dispersion of 10 silicate sphere clusters (*solid line*), of 8 silicate sphere and 2 amorphous carbon spheres clusters (*dotted line*), and 6 silicate spheres and 4 amorphous carbon spheres clusters (*dashed line*)

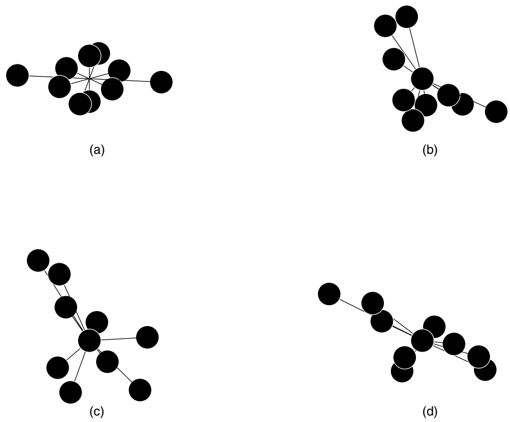

Fig. 10.3. Adopted cluster shapes. **(a)** roundish morphology, **(b)** compact random structure, **(c)** and **(d)** elongated random structures

are summarized in Fig. 10.4 where the orientational averages of the extinction cross section for the clusters of Figs. 10.3 (b), (c), and (d) are compared with that for the original 10-sphere cluster in Fig. 10.3 (a). The curves in Fig. 10.4 seemingly show that, as a general rule, the randomization of the geometry produces less extinction in the visible but a noticeably larger extinction in the ultraviolet. Close examination of the curves and comparison with the morphologies of Fig. 10.3 suggests that this behavior is mainly due to the fact that the randomization procedure produces somewhat elongated

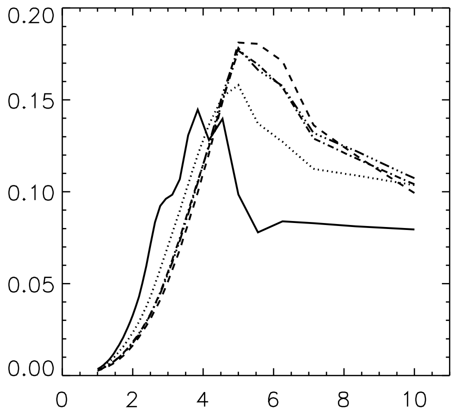

Fig. 10.4. Effects of geometry changes on the extinction cross sections. The quantity that is actually reported is σ_T in μm^2 as a function of λ^{-1} in μm^{-1} for the equivalent sphere (*solid line*) and for random dispersions of the 10-sphere clusters: namely, for the roundish morphology (a) (*dotted line*) and for the random structures (b) (*dashed line*), (c) (*dot-dashed line*), and (d) (*triple dot-dashed line*) in Fig. 10.3

structures. Actually, the results show that the more elongated structures in Figs. 10.3 (c) and (d) produce less extinction in the ultraviolet than the less elongated structure in Fig. 10.3 (b), whereas the latter structure produces more extinction than the roundish structure in Fig. 10.3 (a). Of course, this behavior depends on the strength of the multiple scattering processes that occur among the subunits and contribute to the strength of the scattered field. It is, in fact, expected that these processes are less intense in the more elongated structures in Figs. 10.3 (c) and (d). In general, multiple scattering processes increase the extinction. Nevertheless, the details depend on the relative position of the subunits, so that a roundish structure, such as the one in Fig. 10.3 (a), might originate processes that, on the whole, are weaker than those occurring within the structure of Fig. 10.3 (b). In any case, these results give a clear indication that, in spite of the random orientational average, the details of the morphology play a relevant role in determining the extinction.

Voshchinnikov and Mathis [203] determined the optical cross sections of composite grains [195] by assuming an approximate description, in which a composite grain consists of many concentric spherical layers of various materials, each with a specified volume fraction. The model calculations show that the ordering of materials in the layering makes some difference to the derived cross sections, but the effect converges rapidly with an increasing number of shells. The net result is a *stiffness* in the extinction cross sections, i.e., a very weak dependence on the assumed geometry. However, real interstellar grains are rough surfaced, irregular, and have their materials arranged in pieces that may occupy appreciable fractions of their size. As a consequence, it is interesting to compare the extinction cross sections for composite grains with relatively large component spheres to those for composite grains for which,

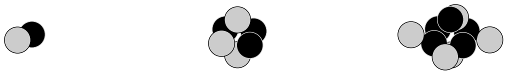

Fig. 10.5. Adopted cluster shapes. Silicates are represented in *grey*, while amorphous carbon materials in *black*

according to the method of Voshchinnikov and Mathis, the components can be much smaller than the wavelength. As these authors did, we consider three materials, silicates, amorphous carbon, and vacuum, occupying an equal volume in the grain. Vacuum is not included in the component spheres but rather in the dispersed geometry of the cluster, deriving by the process of aggregation in which subparticles of different types stuck together. As a consequence, the equivalent spheres are two thirds in volume with respect to the ones considered in [203] and contain an equal fraction of silicates and amorphous carbon. We consider clusters of two, six, and ten spheres assembled with the geometries shown in Fig. 10.5 and calculate their extinction cross section at $\lambda = 0.55\,\mu\text{m}$. In Fig. 10.6, for the sake of comparison, we display the results of various cross sections following the nonstandard way of [203], so that the quantity that we actually report is $k_{\text{v}}^2\sigma_{\text{T}}/\pi x^{2.5}$ for a dispersion of randomly oriented clusters as a function of the size parameter $x = 2\pi R/\lambda$, where R is the radius of the spheres considered by Voshchinnikov and Mathis. This choice for R accounts, in an average sense, for the presence of the vacuum, and one has $\rho = (3/2N)^{1/3}R$, where ρ is the radius of each component of the N-sphere clusters in Fig. 10.5. There are several differences in the behavior of the cluster cross sections with respect to the approximate results of multilayered spheres. First of all, the cross sections loose the stiffness shown in the results in [203], and the position and the intensity of the peak of the extinction efficiency depend significantly on the number of components spheres. For instance, the intensity grows steadily with the number of subunits, while the dependence on the size parameter of the position of the peak does not. Secondly, relevant size parameters are shifted to values much larger ($\approx 5-6$) than those derived in [203] ($\approx 2-3$).

The results in Fig. 10.1 show that the extinction from a dispersion of clusters may be strikingly different from that yielded by a dispersion of equal-volume spheres even when the clusters are assumed to be randomly oriented. In any case, the optical behavior of a dispersion of clusters turns out to be quite different in the different regions of the spectrum, depending on the number of individual component spheres. This behavior is due to the multiple scattering processes occurring among the subunits. As a consequence, modeling a complex particle as a homogeneous sphere whose refractive index is determined by an effective medium approximation, can lead to somewhat misleading results. Furthermore, the results in this section suggest that it is unlikely that the whole extent of the galactic extinction curve can be de-

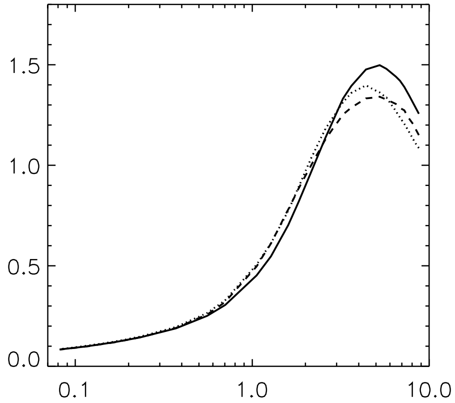

Fig. 10.6. Quantity $k_{\mathrm{v}}^2 \sigma_{\mathrm{T}} / x^{2.5}$ as a function of $x = 2\pi R/\lambda$, where R is the radius of the sphere considered by Voshchinnikov and Mathis, for dispersions of randomly oriented clusters whose geometry is depicted in Fig. 10.5. The *dashed line*, *dotted line*, and *solid line* refer to clusters of 2, 6, and 10 spheres, respectively

scribed by using grains of a single morphology. Doubtless, cosmic dust consists of several components. They are typical of the special environments in which they are formed and/or decisively modified. Models of interstellar dust must take into account a variety of observational data that provide constraints on the composition. The results of Fig. 10.2 show that the change in chemical composition may significantly affect the grain cross sections. The results in Fig. 10.4 show that the choice of the geometry is important for the extinction in the ultraviolet. This is not surprising because the scale of details of the structure of composite particles is comparable to the wavelength.

10.3 Fluffy Particles

We mentioned in Sect. 10.1 that the existence of solid grains containing empty inclusions has been proposed to overcome the difficulties connected with the elemental abundances constraints of the ISM. Since the existence of porous dust grains is an important and still open question, it is instructive to study the effect of adding vacuum to spherical and irregularly shaped particles [204]. We first consider the presence of one or more spherical inclusions in a population of spherical grains. Jones [205] has discussed this problem by describing a porous grain as a hollow sphere, whose optical properties were computed by means of the Mie theory for coated spherical particles. We prefer, instead, to resort to the theory in Sects. 5.2, 5.4, 5.5 and 4.5 to calculate the optical properties of dispersions of spheres containing one or more spherical inclusions, of dispersions of multilayered spheres, and of dispersions of clusters.

10.3.1 Optical Properties of Porous Bare Grains

It is interesting to explore how the presence of inclusions of vacuum in the grains affects the interstellar extinction curve [188]. The extinction cross sections are computed by modeling the grains as spheres containing a central hole. In the assumed wavelength range (100–1000 nm) the radii of the spheres are of the order of the wavelength and the thickness of the solid mantle around the central void can be a significant fraction of the total particle size. This fact, as we stressed in Sect. 7.4, rules out some common approximations used in the literature such as the Rayleigh approximation and the Güttler formula for coated particles [5], so that we use the theory of Sect. 5.2. We assume a polydispersion of grains of graphite and *astronomical* silicate whose dielectric functions were constructed by Draine and Lee [159], and whose size distribution is governed by the widely accepted Mathis, Rumpl and Nordsiek model (MRN) [206]. According to this model the number of grains with radius between a and $a + \mathrm{d}a$ is

$$dn_\mathrm{d} = K n_\mathrm{H} a^{-q} \mathrm{d}a, \text{ with } 5\,\mathrm{nm} \leq a \leq 250\,\mathrm{nm}\,. \tag{10.1}$$

In (10.1) n_H is the number density of hydrogen atoms, and K is a scaling factor related to the number of grains along the line of sight. In the MRN model only two parameters are used to constrain the size distribution: the power-law index q, customarily assumed as $q = 3.5$, and the maximum size allowed a_M. Note that the minimum size a_m is not well constrained because the mass mainly resides in large grains. However, the limiting values of a quoted in (10.1) are the most commonly used. The scaling factors K are related, through the mass of the material, to the number abundance of atoms $\mathcal{A}$ (ppM) of the particular material tied up in grains. The K factors derived by Draine and Lee [159] are $K_\mathrm{C} = 10^{-25.16}\mathrm{cm}^{2.5}/\mathrm{H}$ and $K_\mathrm{Si} = 10^{-25.11}\mathrm{cm}^{2.5}/\mathrm{H}$, which correspond to $\mathcal{A}_\mathrm{C} = 300$ ppM and to $\mathcal{A}_\mathrm{Si} = 32$ ppM. The values used previously would require about twice as much carbon and silicon being available.

At this stage, let us follow the suggestion of Mathis by carrying out a calculation in which the standard MRN model has been modified to allow for the presence of central voids with a volume fraction f_v. The purpose is just to study the effect of such voids on the extinction curve. In Fig. 10.7 is shown the trend of the size average of the extinction cross section

$$\langle \sigma_\mathrm{T} \rangle = \frac{\int_{a_\mathrm{m}}^{a_\mathrm{M}} \sigma_\mathrm{T} \mathrm{d}n_\mathrm{d}}{\int_{a_\mathrm{m}}^{a_\mathrm{M}} \mathrm{d}n_\mathrm{d}} \tag{10.2}$$

for the graphite grain population. As the degree of vacuum increases, the peaks of the curves move towards longer wavelengths. This behavior is in striking contrast with the well-known stability of the bump at 217.5 nm along all the lines of sight. Therefore, the results in Fig. 10.7 rule out the possibility

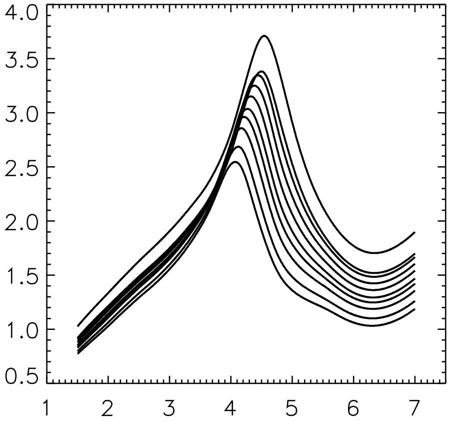

Fig. 10.7. $\langle\sigma_\mathrm{T}\rangle \cdot 10^{-4}$ in $\mu\mathrm{m}^2$ as a function of λ^{-1} in $\mu\mathrm{m}^{-1}$ calculated according to (10.2) for a population of porous graphite grains characterized by a different degree of vacuum. The curves refer, in steps of 0.05, to a degree of vacuum from $f_\mathrm{v} = 0.05$ (*topmost curve*) to $f_\mathrm{v} = 0.5$ (*bottom curve*). The size distribution is given by (10.1)

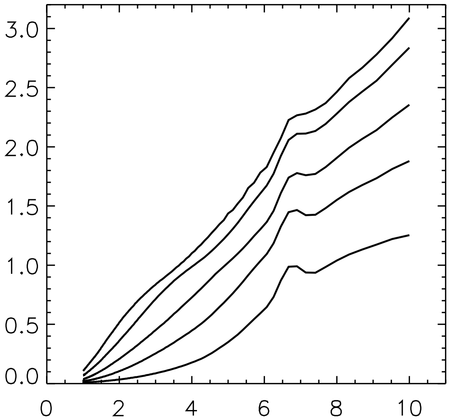

Fig. 10.8. η in $(\mathrm{cm}^{0.5}/\mathrm{H})^{-1} \cdot 10^4$ as a function of λ^{-1} in $\mu\mathrm{m}^{-1}$, calculated according to (10.3) for a population of porous silicate grains characterized by a different degree of vacuum. The curves refer, in steps of 0.2, to a degree of vacuum from $f_\mathrm{v} = 0$ (*topmost curve*) to $f_\mathrm{v} = 0.8$ (*bottom curve*)

of constructing models containing porous graphite grains. Accordingly, we explore the effect of introducing porosity in the silicate population only.

In Fig. 10.8 we plot the quantity

$$\eta = \int_{a_\mathrm{m}}^{a_\mathrm{M}} \sigma_\mathrm{T}\, a^{-q} \mathrm{d}a \,. \tag{10.3}$$

η is a measure of the average cross section per H atom and per unit mass of silicon and depends on the cavity fraction. The presence of a central cavity in

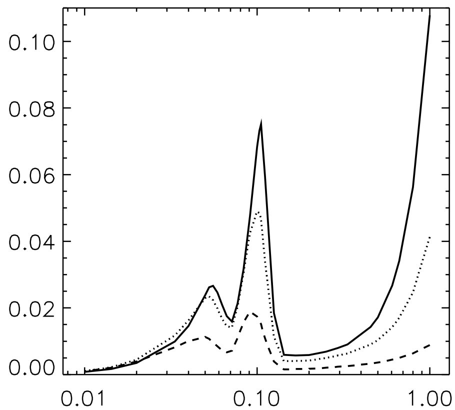

Fig. 10.9. η in $(\mathrm{cm}^{0.5}/\mathrm{H})^{-1} \cdot 10^4$ as a function of λ^{-1} in $\mu\mathrm{m}^{-1}$ in the infrared, calculated according to (10.3), for a population of porous silicate grains characterized by a different degree of vacuum. The curves refer to homogeneous particles (*solid curve*), to a population with a degree of vacuum $f_\mathrm{v} = 0.4$ (*dotted curve*), and to a population with a degree of vacuum $f_\mathrm{v} = 0.8$ (*dashed curve*)

the silicate particles does not change the general trend of the extinction curve. The global effect is a lowering of the extinction curve in response to a decrease of the material inside the grains. However, the extinction curve is affected in a selective way. In particular, the curve experiences a larger shift in the visible portion of the spectrum than in the ultraviolet part. In Fig. 10.9 we show the effects of introducing porosity by a centered void with $f_\mathrm{v} = 0.4$ and $f_\mathrm{v} = 0.8$, compared to homogeneous spheres, on the infrared extinction properties of bare silicate grains. The optical properties of grains can change when more than one vacuum inclusion is considered. In Fig. 10.10 (a) a sequence of extinction curves is plotted relative to a silicate grain with a radius $a = 100\,\mathrm{nm}$ and $f_\mathrm{v} = 0.2$, which refer to different numbers of spherical inclusions. The extinction cross sections are obtained from the average over orientations of the inclusions. When the vacuum is more distributed inside the particles the visual extinction is more depressed. In Fig. 10.10 (b) we compare the effects due to different geometrical configurations. The long-dashed curve refers to the case in which the four inclusions are symmetrically located, namely, two inclusions on the z axis and the other two along the x axis. The solid curve refers to the case in which the symmetry in the configuration of the inclusions is broken, as we moved one of the inclusions from the x axis to the y axis. Large differences in the cross sections are evident, since multiple scattering processes among the inclusions have a strong dependence on the mutual geometrical disposition of voids.

The results shown in this section suggest that silicate grains with added vacuum yield a somewhat higher extinction than solid particles in the ultraviolet and the infrared. Unfortunately, the visual extinction follows a different

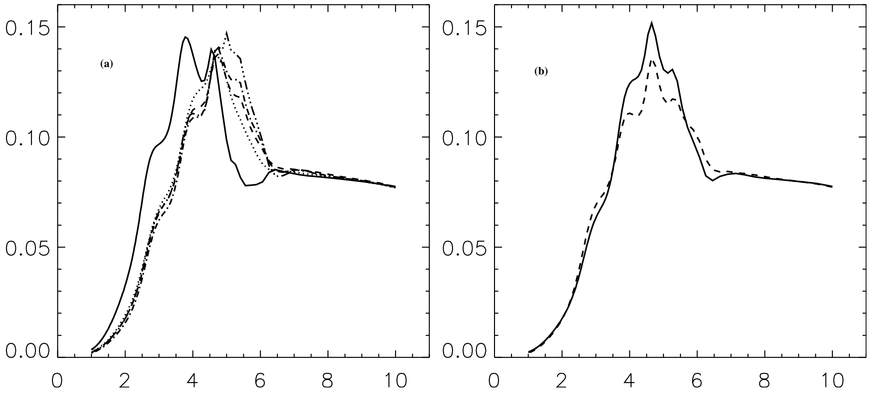

Fig. 10.10. σ_T in μm^2 as a function of λ^{-1} in μm^{-1} for a dispersion of spherical silicate grains with radius $a = 100\,nm$ and $f_v = 0.2$ with a single central void (*solid line*), two (*dotted line*), three (*dashed line*), four (*dot-dashed line*), and six (*triple dot dashed line*) vacuum inclusions **(a)** and for the same dispersion of grains with two different geometrical configurations of four vacuum inclusions **(b)**. The averages are performed on the assumption of random orientational distribution

trend that prevents the matching of the extinction curve through a model of bare porous particles.

10.3.2 Coated Grains and Clustering

Some dust models postulate the presence of coated grains [207, 208], e.g., silicate cores with an icy mantle including hydrocarbons or a cover of hydrogenated amorphous carbon. Early core-mantle models were constructed without any limitation about the elemental depletions. Incorporation of oxygen into models cannot help, since oxygen abundance is facing the same shortage experienced by carbon [191]. There are indications that core-mantle grains including voids might be able to reproduce the observed extinction within the revised interstellar elemental budget [209].

In fact, when more than two layers are present in a composite particle, the optical properties are often studied by means of the effective medium theory [210]. This kind of mean description could disguise important physical processes, such as resonance effects due to the interaction of the layers. On the contrary, we want to use the technique in Sect. 5.2, which allows a realistic description of a multilayered sphere. We apply just that technique to calculate the optical properties of a grain of olivine $(Mg,Fe)_2SiO_4$ with radius $a = 100\,nm$ with a centered void ($f_v = 0.2$), coated with an external layer of amorphous carbon with optical constants taken from Duley [211].

In Fig. 10.11 we compare the cross sections obtained for the bare silicate grain and for the same grain coated with mantles of different widths. The extinction peak shifts towards longer wavelengths and the shape of the curve

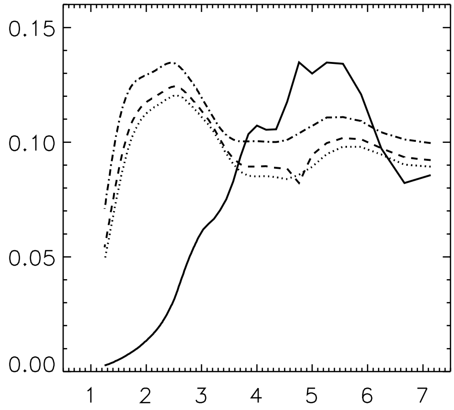

Fig. 10.11. $\sigma_{\rm T}$ in μm^2 as a function of λ^{-1} in μm^{-1} for a bare silicate grain of radius $a = 100$ nm, containing a centered vacuum inclusion ($f_{\rm v} = 0.2$) (*solid line*) and for the same grain coated with a carbonaceous mantle of width $\Delta a = 3$ nm (*dotted line*), $\Delta a = 5$ nm (*dashed line*), and $\Delta a = 10$ nm (*dot-dashed line*)

is noticeably altered. It is very well known that the presence of a mantle produces drastic changes in the optical properties of the particles regarding not only a frequency shift of the extinction peaks but even the possibility of their disappearance [78]. The important point is that the change in the extinction shape is present even for a mantle width of 3 nm, which corresponds roughly to 12 atomic monolayers. Any increase in the mantle thickness produces a smooth enhancement in the extinction but no further change in the overall shape of the curves.

The mantle width is given by

$$\Delta a = \frac{m_{\rm C} A_{\rm C}}{\epsilon \rho_{\rm C}} \left(1 - f_{\rm C}\right) ,$$

where $m_{\rm C}$ is the mass of carbon atom, $A_{\rm C} = 2.25 \times 10^{-4}$ the carbon cosmic abundance [192], $\rho_{\rm C} = 2.25$ g cm^{-3} the carbon density, $\epsilon = 2.1 \times 10^{-21}$ cm^2 (H atom cm^{-3})$^{-1}$ [212], and $f_{\rm C}$ is the fraction of the total carbon abundance that is in the gas-phase. Thus, the maximum possible mantle width ($f_{\rm C} = 0$) is approximately 10 nm. Therefore, one third of the total carbon abundance is enough to cause a sharp increase in the visual extinction, which is exactly what is required, i.e., larger extinction per unit mass.

The mass contained in the mantle corresponds to an equivalent porous sphere composed of the mantle material with an external radius

$$a_{\rm eq} \approx a \left(\frac{3\Delta a/a}{1 - f_{\rm v}}\right)^{1/3} , \text{ with } \Delta a \ll a ,$$

which for $a = 100$ nm, $\Delta a = 3$ nm, and $f_{\rm v} = 0.5$ leads to $a_{\rm eq} = 5.6$ nm.

We compute also the extinction cross section for two isolated bare porous particles, and its orientational average for the same two spheres clustered together. The silicate grain has a radius of 100 nm and a vacuum fraction $f_\mathrm{v} = 0.2$ (the core of coated grain), while the amorphous carbon grain has a radius of 70 nm and $f_\mathrm{v} = 0.5$ (therefore it holds a mass larger than the one inside the mantle). The above choices for particle morphology and composition are made in order to have three extremely different configurations for the available mass, and the size of carbon grain is enlarged to increase the extinction efficiency in the visible. The results of calculations are shown in Fig. 10.12. Clustered spheres produce significantly more extinction in the visible than isolated particles, but the largest contribution (a factor of two) is produced by the layered sphere.

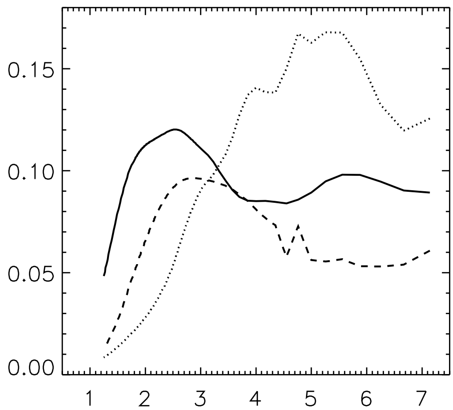

Fig. 10.12. σ_T in $\mu\mathrm{m}^2$ as a function of λ^{-1} in $\mu\mathrm{m}^{-1}$ for a core-mantle grain with a silicate nucleus of radius $a = 100$ nm and vacuum fraction $f_\mathrm{v} = 0.2$ covered by an amorphous carbon mantle of width $\Delta a = 3$ nm (*solid line*); for a pair of independent grains, one of silicate with radius $a = 100$ nm with a fraction of vacuum $f_\mathrm{v} = 0.5$, and another of amorphous carbon with radius $a = 70$ nm with the same fraction of vacuum (*dotted line*); σ_T for the preceding two grains clustered together (*dashed line*) averaged on the assumption of random orientational distribution

Drastic changes, similar to those occurring in the extinction in the visible, are also found in the infrared range. In Fig. 10.13 we show the extinction cross sections in this range for the same particles considered in Fig. 10.11. Even in this case, coated grains produce more extinction than bare grains. This result strengthens the need to perform a further analysis to get a wider view of the possible impact on the interstellar extinction curve of porous core-mantle structures. The problem is, however, far from being solved. Even an exact calculation for a particular grain morphology necessarily involves rather arbitrary assumptions about the geometry of each grain constituent, including voids. Furthermore, the use of laboratory optical constants of pure material is

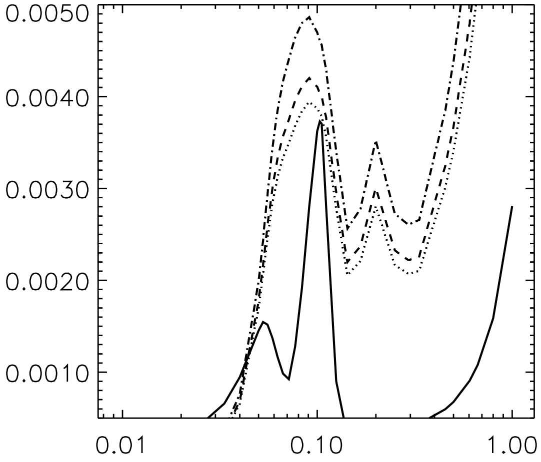

Fig. 10.13. σ_T in μm^2 as a function of λ^{-1} in μm^{-1} in the infrared range for a bare silicate grain of radius $a = 100\,\mathrm{nm}$, containing a centered vacuum inclusion ($f_v = 0.2$) (*solid line*) and for the same grain coated with a mantle of width $\Delta a = 3\,\mathrm{nm}$ (*dotted line*), $\Delta a = 5\,\mathrm{nm}$ (*dashed line*), and $\Delta a = 10\,\mathrm{nm}$ (*dot-dashed line*)

not completely appropriate, because the strong environmental processing of grains in the interstellar medium produces large variations in the frequency and the strength of IR absorption and emission bands. Nevertheless, it appears that stratified scatterers show enhanced extinction properties with respect to bare grains or clusters. In this context, dust models based on coated grains could assume a renewed importance.

10.4 Radiation Pressure on Fluffy Cosmic Dust Grains

In Sect. 10.1 we stressed that the interaction of the radiation field with particles also yields mechanical effects, the most widely known of which is the radiation pressure [39]. Actually, radiation pressure on dust particles affects the dynamical behaviour of grains in interplanetary space, cometary atmospheres and stellar winds. Radiation forces in galactic disks lead to the possibility of confining a significant amount of dust in stable regions where gravitational and radiation forces balance well high above the galactic plane [157]. The possibility that galaxies may eject dusty metal-rich gas into their haloes and potentially into the intracluster medium may play an important role in galactic chemical evolution, providing a sink for heavy elements [213].

The existence of extraplanar dust is well established observationally. COBE meaurements of the FIR emission from Galaxy indicate an extended distribution of dust with scalelenghts larger than those of the stars [214]. The inferred dust temperature is lower than the one derived by IRAS observations of dust co-mixed with stars in the galactic plane. ISO observations [215] and SCUBA sub-millimeter imaging [216] clearly show extended emission from cold dust, which is very likely associated with dust expulsion. Dust outflows have been detected in B-1 colour images (SCUBA) of a few nearby starburst galaxies [217] and by means of an optical imaging polarimetry technique [218].

A number of papers have been devoted to assessing the forces acting on dust grains resulting from radiation, gravity, gas-drag, galactic magnetic fields [157, 219–221] and their motion through and out a galaxy [222]. Radiation pressure efficiency strongly depends on the morphology of grains. It is likely that interstellar grains have cavities and voids, as result of formation processes and evolution, with the extent of fluffiness depending on the particular host astronomical region. Because of the complexity in morphology and composition, the optical properties of these porous irregularly-shaped particles will be quite different from those of solid homogeneous spheres. The use of approximations, in which the effective dielectric constant for mixtures of materials is estimated in terms of the known dielectric constants of the various constituents, has been widely exploited in the literature. However, the validity of a mixing technique requires the size of the whole particle to be comparable to the wavelength, while the inhomogeneities should be much smaller than the latter [210]. When the sizes of voids and/or material inclusions become comparable to the wavelength of the incident light, the description of a composite particle as an homogenous one is questionable [141]. Mukai et al. [223] examined the radiation force on porous aggregates using Mie theory and Maxwell-Garnett effective medium approximation, giving useful and interesting recipes for handling radiation pressure cross-sections of large irregular fluffy grains. These authors compared their results [223] with those computed by the discrete dipole approximation (DDA) finding a reasonable agreement, except for highly porous/fluffy silicate aggregates. In this section we analyze how the degree of fluffiness affects the radiation pressure cross sections. To this end, we model cosmic dust grains as aggregates (clusters) of spheres of appropriate geometry, whose optical properties we calculate through the transition matrix method [3]. A more complete analysis of the dependence of the radiation pressure on the morphology of the aggregates is reported in [224].

Kozasa et al. [225, 226] described a Montecarlo simulation to generate aggregates of small spheres by ballistic aggregation. Using this procedure Mukai et al. [223] built clusters of up to 1024 with a radius of 10 nm and calculated the ratio β of radiation pressure force and gravitational force for these kind of aggregates. The optical properties were calculated through a Maxwell-Garnett approximation with the vacuum as matrix material and the constituent particles as inclusions, following an approach already tested by Hage and Greenberg [227]. The results of Mukai et al. [223] show that highly porous structures exhibit values of the ratio β that is independent of the overall size. The conclusion of the authors is, therefore, that the radiation

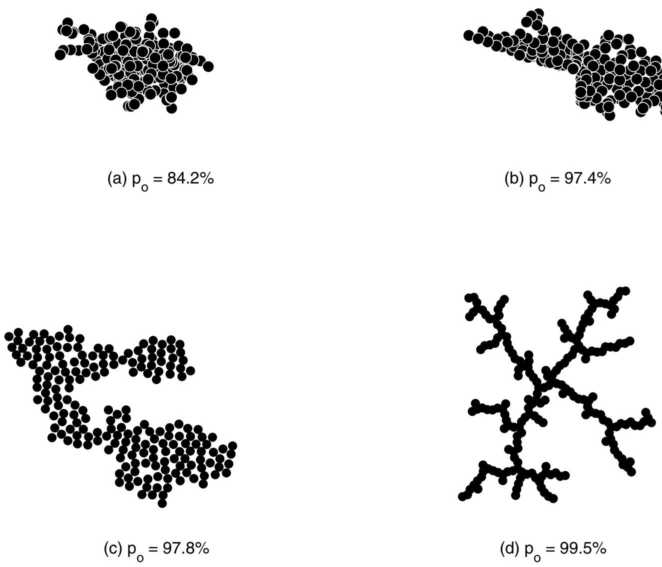

Fig. 10.14. Adopted cluster shapes. **(a)** roundish morphology, **(b)** compact random structure, **(c)** elongated random structure, **(d)** sparse structure

pressure cross-section of an aggregate differs very little from the sum of the radiation pressure cross sections of the component spheres. The results of Mukai et al. [223] are sufficiently accurate, when tested against DDA simulations, except for highly porous/fluffy silicate aggregates. To give a physical explanation and verify the results for a general morphology, we applied the theory of Sect. 4.8 to the calculation of the radiation pressure cross sections of fluffy particles, modelled as aggregates of 200 spheres of astronomical silicates with radius 5 nm. The geometrical structure of the aggregates was constructed through a random number generator with the only restriction that each sphere should be in contact with at least one other sphere of the aggregate. We show results for four morphological types (Fig. 10.14) representative of different degrees of porosity

$$p_0 = 1 - (r_\mathrm{c}/r_0)^3,$$

where r_0 is the radius of the spheres composing the cluster, and $r_\mathrm{c} = \sqrt{5/3}\, r_\mathrm{g}$ is the radius of the sphere whose radius of gyration r_g equals that of the whole cluster, i.e.

$$r_\mathrm{g} = \left[\frac{1}{2N^2} \sum_{ij} (\mathbf{r}_i - \mathbf{r}_j)^2 \right]^{1/2} .$$

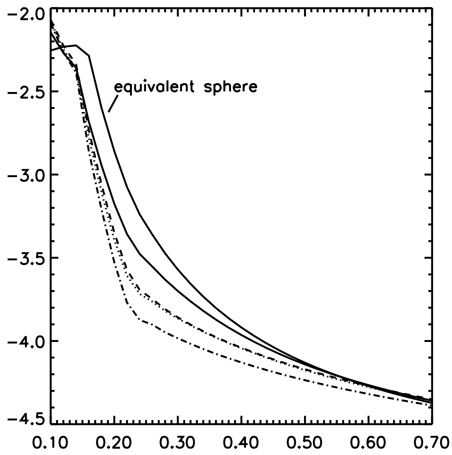

Fig. 10.15. Random averaged σ_{pr} in $\mu\mathrm{m}^2$ (on a log scale) as a function of the wavelength in μm. *Solid line*: cluster (a) in Fig. 10.14; *dashed line*: cluster (b); *dotted line*: cluster (c); *dot-dashed line*: cluster (d)

We also present the results for the roundish cluster configuration (see Fig. 10.14 (a)) using the optical constants for amorphous carbon (AC1 sample) given in [228].

The results of our calculations are reported in Fig. 10.15 for the wavelength range $0.1 - 0.7\,\mu\mathrm{m}$, together with those for the equal mass sphere, i.e. the sphere which contains the same mass of silicates as a whole aggregate. The radiation pressure cross sections of the structures have been analitically averaged for random orientation [46]. The curves for the various structures differ little from each other at shorter wavelenghts, while differences increase with the wavelength. However, beyond $0.7\,\mu\mathrm{m}$ cross-sections are asymptotically coincident. The equivalent sphere has a radiation pressure cross-section that is quite different from those relative to the four clusters. In general, the larger the porosity the lower the σ_{pr} profile. This behaviour strongly suggests that, when the porosity increases, the multiple scattering processes that couple the aggregated spheres to each other, become more and more negligible. In fact, since all the aggregates are formed of the same number of identical spheres, the description of the various structures may differ only for the values of the elements of matrix H in (5.26) and (5.28) which depend on the mutual positions of the component spheres. For very sparse structures, the results of the present calculation support the conclusions of Mukai et al. [223], although these authors, because of their choice of describing complex systems through an effective medium approximation, smear out the details of the structure into an homogeneous unstructured medium.

Although astronomical silicates possess a larger cross-section in the far-UV, fluffy amorphous carbon grains exhibit a much slower decrease of the radiation pressure cross-sections with wavelength (Fig. 10.16).

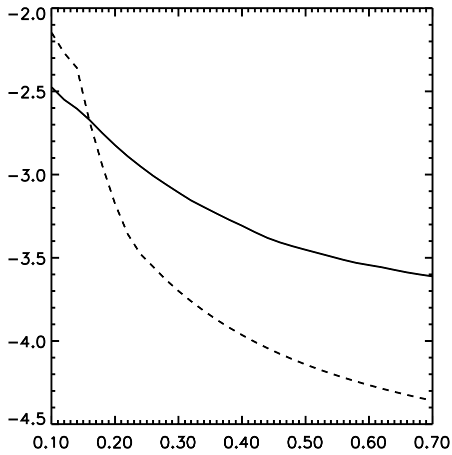

Fig. 10.16. Random averaged σ_{pr} in μm^2 (on a log scale) of aggregates with different chemical composition as a function of the wavelength in μm. *Solid line*: amorhous carbon; *dashed line*: astronomical silicate. The cluster configuration is the one shown in Fig. 10.14 (a)

The role of morphology is well described by the ratio

$$R(\lambda) = \frac{\sigma_{\mathrm{pr}}}{\sum_i \sigma_{\mathrm{pr}}^{(i)}}, \tag{10.4}$$

shown in Fig. 10.17, where σ_{pr} is the random average of radiation pressure cross section of the aggregates or the cross section of the equal mass sphere, and $\sigma_{\mathrm{pr}}^{(i)}$ is the cross section of the i-th sphere forming the cluster. The general trend is a decrease of the ratio R with increasing morphological complexity. All the considered clusters have the same mass and thus are subject to the same gravitational force. The important parameter is thus the colour of the radiation source. In the case of radiation fields at low blackbody temperatures, differences in radiation forces induced in clusters of different morphological types are negligibly small, because the main contribution to the radiation pressure comes from wavelengths longer than 0.7 μm. In that spectral range the shape effect on the cross sections plays a marginal role. To quantify the effects induced by differences in chemical composition and morphology of clusters, we compute the ratio β in the case of a stellar radiation source [223]

$$\beta = \frac{K}{m} \int_o^{\infty} \lambda^{-5} \sigma_{\mathrm{pr}}(\lambda) \left\{ \exp\left(\frac{hc}{\lambda k T_{\mathrm{eff}}} \right) - 1 \right\}^{-1} \mathrm{d}\lambda \tag{10.5}$$

with

$$K = \frac{2\pi h c R_\star^2}{G M_\star}$$

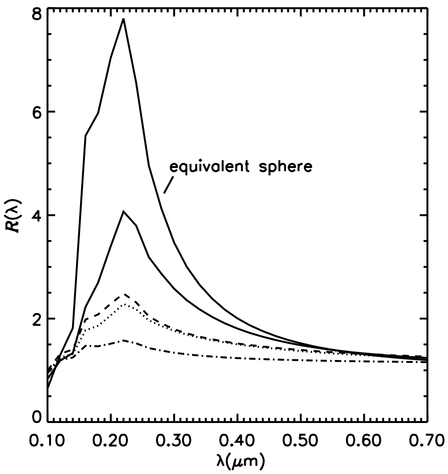

Fig. 10.17. The ratio of the radiation pressure cross-section of an aggregate to the sum of the individual radiation pressure cross-section of the spheres forming the cluster. *Solid line*: cluster (a) in Fig. 10.14, *dashed line*: cluster (b), *dotted line*: cluster (c), *dot-dashed line*:cluster (d)

where $R_\star$ and $M_\star$ are the radius and the mass of the star. The stellar spectrum is approssimated by the spectrum of a black body at an effective temperature T_{eff}. G is the gravitational constant and m the grain mass. Computed β values for the adopted four cluster configurations are shown in Table 10.1, for some circumstellar radiation field. Morphological effects are significant only for the solar-type star, because of the coincidence of the peak blackbody temperature with the largest differences in the cross-sections (cf. Fig. 10.15). Amorphous carbon grains exhibit larger β values than silicates, in agreement with the results of [223].

Table 10.1. The ratio β of the radiation pressure forces to the gravity on fluffy aggregates in circumstellar environments

	T_{eff} (K)		
cluster	2700 [1]	5800 [2]	10000 [3]
sil[4] (a)[5]	0.00101	0.1358	10.238
sil (b)	0.00103	0.1176	8.2045
sil (c)	0.00105	0.1198	8.6717
sil (d)	0.00098	0.1022	6.9619
ac[6] (a)	0.01028	1.1354	43.275

[1] $M_\star = 0.2M_\odot$, $R_\star = 0.3R_\odot$, [2] solar-type, [3] $M_\star = 3.2M_\odot$, $R_\star = 2.5R_\odot$, [4] astronomical silicates, [5] letters indicate the morphological types described in Fig. 10.14, [6] amorphous carbon

Ultimately, using an exact method to compute the radiation pressure cross-sections enabled us to confirm results of previous approximate calculations [223] only for very sparse cluster configurations. In the case of compact structures, cross-sections of grain aggregates show considerable departure from those of the constituent particles. The origin of this behaviour can be traced back to the multiple scattering processes that occur among the components of a cluster. In fact, neglecting multiple scattering processes, the scattered field is just the superposition of the fields scattered independently by the single subunits.

10.5 Ultraviolet Radiation Within Grain Cavities

According to Williams and Herbst [229], the surface of the cosmic dust grains may be the habitat for chemical reactions driven by ultraviolet radiation. Photochemical reactions leading to the formation of complex organic molecules could, however, occur also in the cavities of fluffy grains, provided enough UV light can penetrate their material [230]. There is a wide interest in this kind of reactions, especially because recent laboratory experiments demonstrated the synthesis of amino acids, basic ingredients in all vital processes, when ice mixtures representative of cold interstellar grain mantles were subjected to ultraviolet (UV) irradiation [233, 234]. Fifty years before, Stanley L. Miller [235] reported in *Science* the remarkable results he had achieved by the action of electric discharge on a mixture of the reducing gases CH_4, NH_3, H_2O and H_2 that simulated what was viewed at the time as possible primitive Earth conditions. Although the chemical compositions of the target mixtures appear very similar (see, e.g. Gibb et al. [236]), reaction pathways leading to the formation of complex organics are deeply different, because under interstellar conditions low temperatures preclude most chemical reactions that are efficient in the Miller apparatus.

However, in the complex process leading to the formation of circumstellar disks around young stars from pre-stellar dense molecular clouds, physical conditions similar to those of terrestrial laboratories might be present. In a gas containing dust grains, aggregation occurs naturally as the result of ballistic collisions, producing loosely packed structures with much of their internal volume being vacuum (cavities). It is this internal volume that leads to a completely different chemical scenario with respect to that on the surface of grains [230]. In the interior of dust aggregates UV radiation, X-rays, cosmic rays, thermal shocks, etc., induce a secondary chemistry where the reaction products cannot escape the cavity. This gives rise to a peculiar situation as chemistry is offered high-temperature, high-density and reducing conditions in a transient gas phase with rapid quenching of the reaction products.

The effective production of complex molecules depends critically on the dose of UV radiation impinging on the molecular material trapped in a grain [237]. Within the complex interplay of the molecular formation and destruction processes, the radiation field carries out a dual role. If, on the one hand, it might be one of the most important destruction mechanisms, on the other hand it drives the production of new molecular species. Since even a small amount of UV radiation has profound chemical consequences on the molecular content of the cavity, a knowledge of the radiation density distribution inside an interstellar aggregate is essential in order to understand the plausibility and the efficiency of the proposed mechanism. Grain aggregates are assumed to be fluffily substructured collections of dust particles covered by ice mantles, loosely attached to one another. Each particle consists of a single material, such as silicates or carbon, as formed in the various separate sources of cosmic dust. Voids are naturally generated by random accretion of particles leading to cavities of sizes comparable to those of the coagulating grains. Basic constituents of the aggregate might also be porous. Two kinds of cavities will then be considered: (*i*) interstitial cavities that form because of the aggregation process and (*ii*) central cavities aimed at simulating porous aggregating particles.

10.5.1 The Field Inside Central Cavities

In this section we present the results of our calculations of the UV radiation density inside both central and interstitial cavities [231, 232]. We first derive the time averaged distribution of the electromagnetic energy density

$$w(\mathbf{r}) = \frac{\epsilon|\boldsymbol{E}_\mathrm{T}|^2 + (1/\mu)|\boldsymbol{B}_\mathrm{T}|^2}{16\pi} \tag{10.6}$$

inside homogeneous spheres made of astronomical silicates [238] and amorphous carbon [239], with and without a central cavity. Both materials have $\mu = 1$ but complex dielectric function ϵ, so that the energy density is complex. The imaginary part when multiplied by 2ω gives the rate of dissipation [17]. In the whole set of related contour plot (see Figs. 10.18–10.20), we show the logarithm of both the real and imaginary parts of the energy density per unit intensity of the incident field, i.e. the adimensional quantity w/I_I, in the interior of spheres with radius $r_0 = 50\,\mathrm{nm}$. In the figures the energy density is reported in a grey-scale increasing from black to white. Fig. 10.18 displays results for homogeneous spheres of astronomical silicates and amorphous carbon in a plane through the centers of the spheres. We report only the case of polarization orthogonal to the plane of the plot because the distribution of the energy density in a plane e.g. parallel to the polarization vector differs little. Contour plots for spheres of the same radius but containing centered voids of different sizes, are shown in Fig. 10.19 for grains made of carbonaceous materials and in Fig. 10.20 for the silicate particles. The incident wave has $\lambda = 0.1\,\mu\mathrm{m}$ and unit amplitude. Carbonaceous materials present large changes in the energy density distribution because of the large imaginary part of their refractive index. The presence of intense dissipation

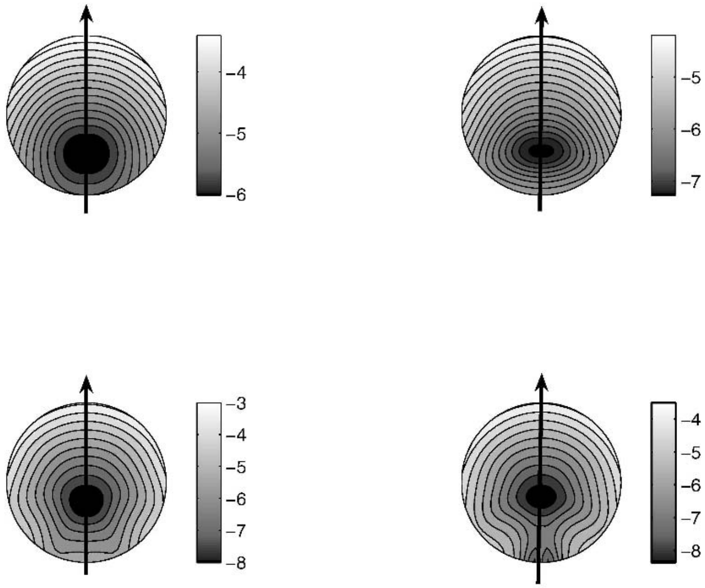

Fig. 10.18. Contour plots (log scale) of the the real (left panels) and imaginary parts (right panels) of w/I_I inside homogeneous spheres of amorphous carbon (top row) and astronomical silicates (bottom row). The radius of the spheres is $r_0 = 50\,\mathrm{nm}$. The wavelength of the incident wave is $\lambda = 0.1\,\mu\mathrm{m}$ and the polarization of the incident field is orthogonal to the plane of the figure

spots inside the interstitial material suggests the possibility of an highly non-uniform distribution of temperature in spite of their smallness. Anisotropic radiation energy deposition combined with dishomogeneities in the chemical composition of interstitial materials might favour excess infrared emission from large interstellar carbon grains, as originally suggested by Duley and Williams [240]. In Fig. 10.21 we show the logarithm of the distribution of the real part of the energy density on the internal surface of the cavities as a function of the polar angle θ measured from the direction of the incident wavevector. In Fig. 10.22 we report the profile of the logarithm of the real part of the energy density as a function of $q = z/r_0$ along a line through the centers of the spheres parallel to the incident wavevector (aligned to the z axis). As in the contour plots (Fig. 10.19 and 10.20), there is an evident difference in the behaviour of silicates and carbonaceous materials.

10.5.2 The Field Inside Interstitial Cavities

We now consider a plane wave impinging on a grain aggregate. We adopt as reference model a grain aggregate composed by $\mathcal{N} = 13$ spherical sub-units clustered in the roughly spherical shape shown in Fig. 10.23 (a). Grains have

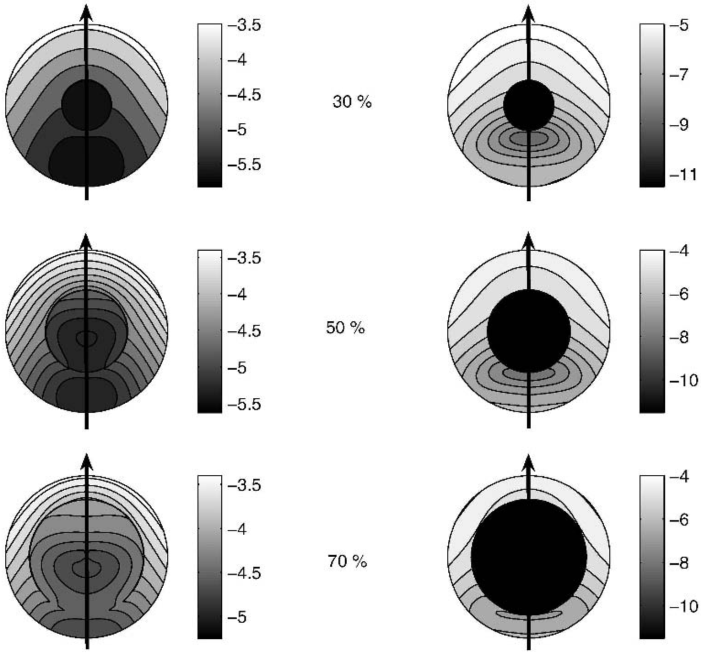

Fig. 10.19. Contour plots (log scale) of the real (left panels) and imaginary parts (right panels) of w/I_{I} inside amorphous carbon spheres containing central spherical voids of different radii. The radius of the spheres is $r_0 = 50\,\mathrm{nm}$. The radius of the internal cavity is reported for each couple of panels as a percentage of the radius of the host sphere. The wavelength of the incident wave is $\lambda = 0.1\,\mu\mathrm{m}$ and the polarization of the incident field is orthogonal to the plane of the figure

similar volume fractions of silicates and carbonaceous materials, $f_{\mathrm{C}} = 6/7 f_{\mathrm{sil}}$. Therefore, we assume that 7 spheres have the refractive index of silicates and the remaining 6 have that of the carbonaceous material.

This choice gives to the grain as a whole optical properties akin to those of silicates mixed with carbonaceous materials, e.g., GEMS [158]. The radius for the spherical basic constituents of the aggregate is chosen to be $r_{\mathrm{m}} =$ 20 nm, consistent with a recent evaluation of the IR/visible extinction and polarization of composite interstellar grains [241]. The diameter of aggregates results $D_{\mathrm{g}} = 120$ nm. The coordinates of the centres of the aggregate units (in nm) are reported in Table 10.2. Monomers are not homogeneous because coagulation is likely to occur when dust grains have already accreted an ice mantle. Therefore, we assume that the single spherical units are covered with a layer of condensed gas (mainly water), whose width is taken $\Delta r =$ 5 nm, which corresponds roughly to 20 monolayers. The thickness of the ice mantle is included in the radius of the monomers. Thus, the ice volume filling factor results $f_{\mathrm{ice}} \sim 0.5$. Dielectric constants of water ice are given

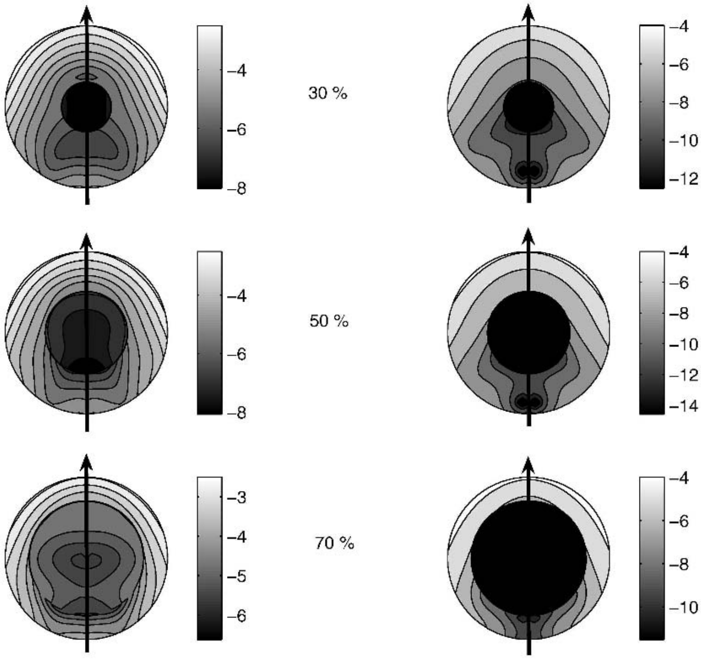

Fig. 10.20. Same as in Fig. 10.19 for silicate grains

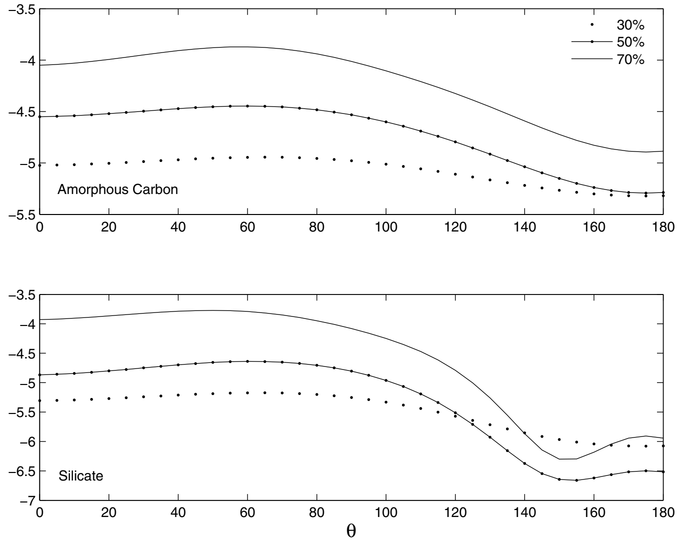

Fig. 10.21. Plot (log scale) of the real part of w/I_{I} for the same grains of Figs. 10.19 and 10.20 on the internal surface of the cavity, in a plane orthogonal to the polarization vector, as a function of the polar angle θ measured starting from the direction of the incident wavevector

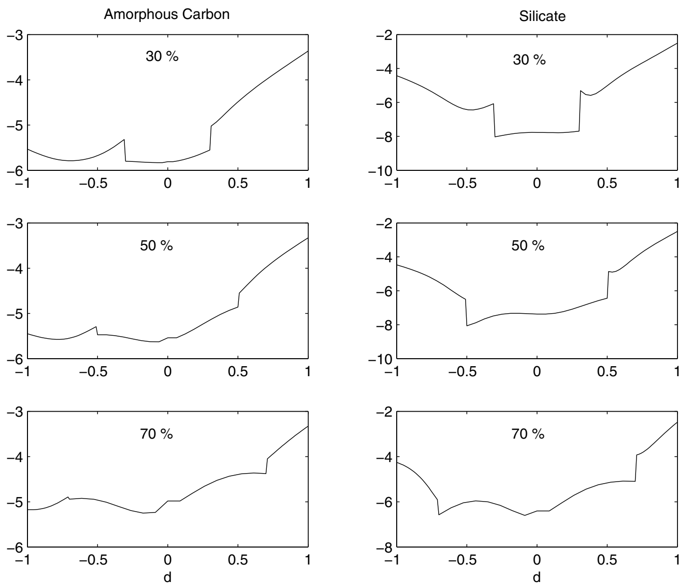

Fig. 10.22. Real part (log scale) of w/I_{I} for the same grains of Figs. 10.19 and 10.20 along the z axis (taken parallel to the incident wavevector) as a function of $d = z/r_0$

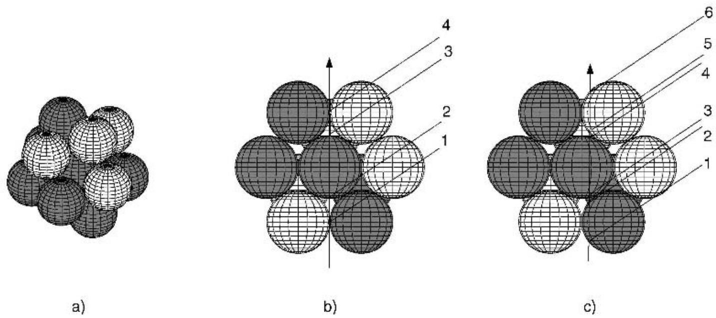

Fig. 10.23. (a) Adopted shape of the aggregate reference model, **(b)** a line parallel to the incident wavevector crossing xy plane at $x = 0,\ y = 0$ intercepts 4 points over the aggregate surface, **(c)** a line parallel to the incident wavevector crossing xy plane at $x = 0,\ y = 30\,\mathrm{nm}$ intercepts 6 points over the aggregate surface. Darker spheres in (b) and (c) represent carbon units while lighter ones represent silicate units

Table 10.2. Coordinates of the centers of the spheres (nm). The rows marked with an asterisk refer to spheres of silicates; the other spheres are of carbonaceous material

	x	y	z
1*	0.000000	0.000000	0.000000
2*	0.000000	40.000000	0.000000
3*	0.000000	20.000000	34.641016
4*	0.000000	-20.000000	-34.641016
5*	32.659863	-20.000000	-11.547005
6*	-32.659863	20.000000	-11.547005
7*	-32.659863	-20.000000	-11.547005
8	0.000000	-40.000000	0.000000
9	0.000000	-20.000000	34.641016
10	0.000000	20.000000	-34.641016
11	32.659863	20.000000	-11.547005
12	-32.659863	0.000000	23.094011
13	32.659863	0.000000	23.094011

by [180]. Physico-chemical properties of the aggregate reference model are summarized in Table 10.3. The (unit) incident wave is linearly polarized normally to the plane of the figure (cf. Fig. 10.23 (b), (c)). The energy density is computed just outside the surface of the spheres at the points of intersection of two straight lines parallel to the incident wavevector. As shown in Figs. 10.23 (b) and (c), these lines cross the surface of the clustered spheres at 4 and 6 points, respectively. The energy density, that in this case is real, cannot be represented as in the single sphere calculations (cf. Figs. 10.18-10.20). Therefore, we resort to bar diagrams with each bar proportional to the energy density at a particular point of intersection. The intersection points are labelled as in Figs. 10.23 (b), (c). Note that points 1 and 4 in Fig. 10.23 (b) are the points of contact between a carbonaceous and a silicate sphere. Results are presented in Fig. 10.24 and in Fig. 10.25 for some representative wavelengths. The density of radiation is larger at shorter wavelengths and tends to decrease with increasing wavelength. Our results show that the largest values of the energy density occur at points located on the internal surface of interstitial cavities.

Ultimately, for a given incident illumination, the internal illumination, i.e. the energy density within the cavities, may be noticeably different depending on the size and the material of the grains. Nevertheless, for the cases we considered so far the internal illumination is clearly not negligible.

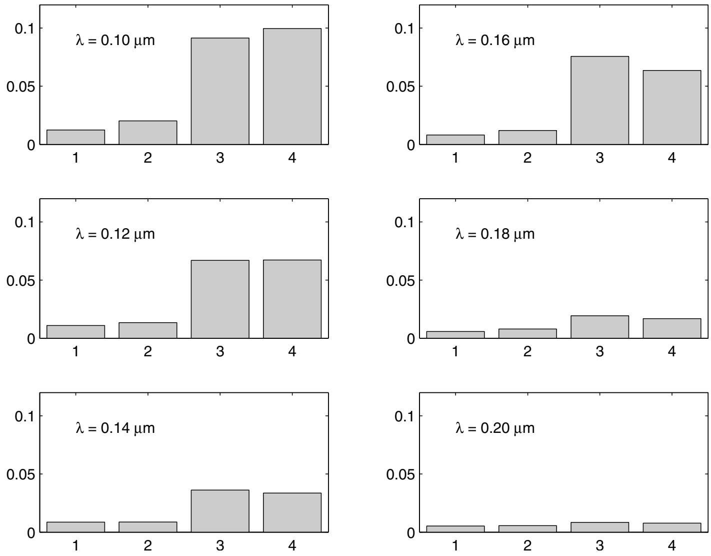

Fig. 10.24. w/I_{I} at the 4 intersection points depicted in Fig. 10.23 (b). The wavelengths of the incident radiation are reported in each panel

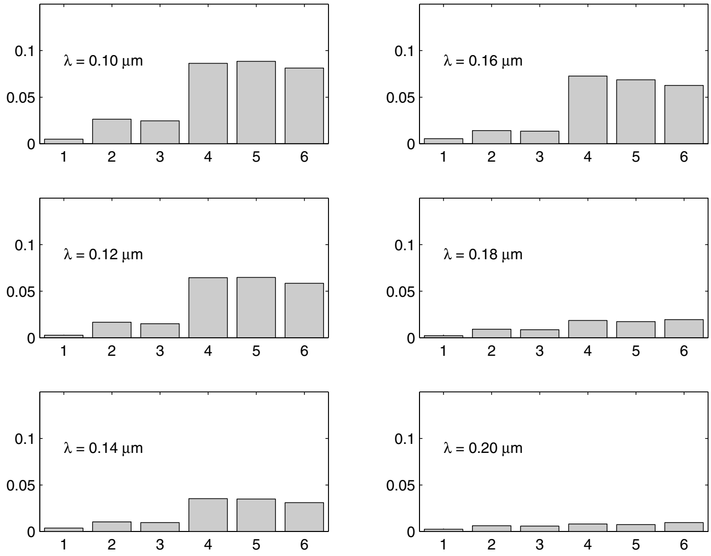

Fig. 10.25. w/I_{I} at the 6 intersection points depicted in Fig. 10.23 (c). The wavelengths of the incident radiation are reported in each panel

Table 10.3. Physico-chemical properties of the aggregate reference model

number of units	$\mathcal{N}$	13
aggregate size	$D_{\rm g}$ (nm)	120
monomer size	$2r_{\rm m}$ (nm)	40
mantle width	Δr (nm)	5
ice fraction	$f_{\rm ice}$	~ 0.5
carbon to silicate ratio	$f_{\rm C} : f_{\rm sil}$	6 : 7

10.5.3 Field Depolarization

The study of meteorites allowed close examination of extraterrestrial organic material delivered to the Earth. In the organic material extracted from the Murchison and Murray meteorites were found more than 70 amino acids, eigth of them occurring in proteins [242], as well as a variety of sugars, in amounts comparable to amino acids [243]. The small enantiomeric excess of L-aminoacids and of D-sugars detected in the materials of both meteorites seems to push the origin of biological homochirality, i.e. one-handedness of aminoacids and sugars, out into the cosmos.

Among the many scenarios put forward to explain the origin of this homochirality one involves the asymmetric photolysis of amino acids present in space, triggered by ultraviolet circularly polarized radiation [152]. This

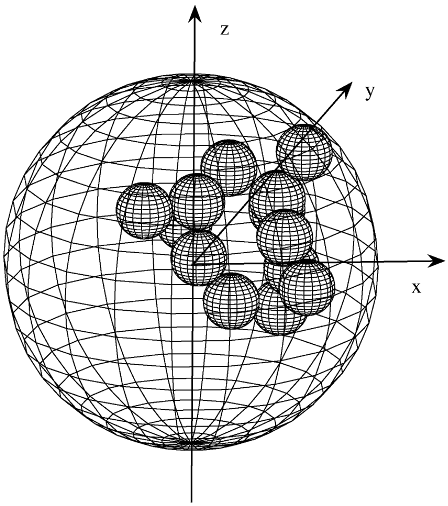

Fig. 10.26. Sketch of the configuration of a homogeneous sphere filled by the Bruggeman mixture of Sect. 7.7 containing 13 identical cavities. The radius of the host sphere is 100 nm and the radius of each of the cavities is 15 nm. The incident wave propagates along the z axis and is linearly polarized along the x axis

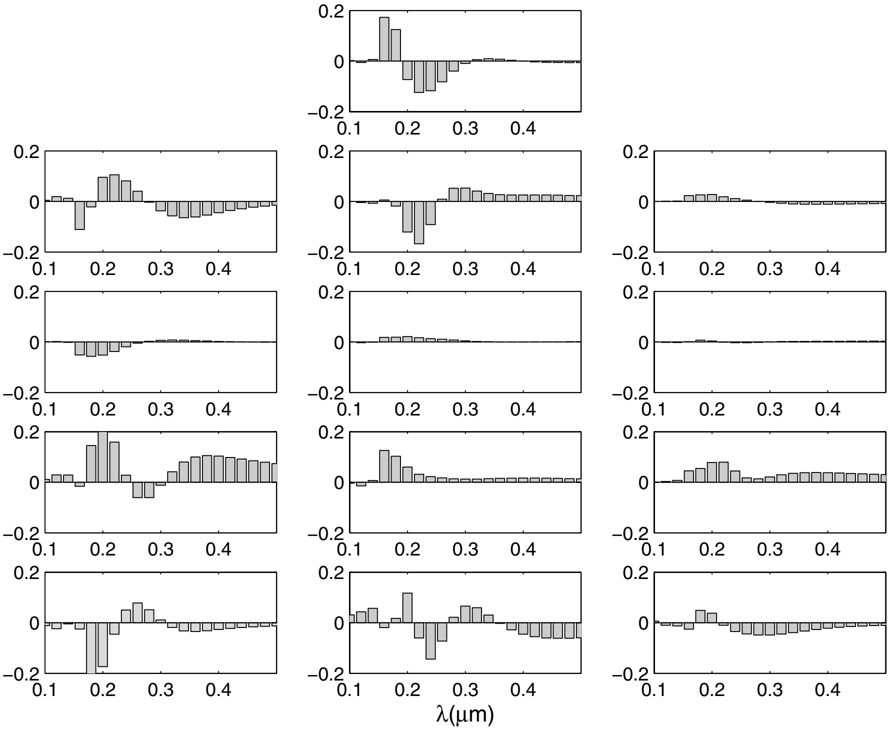

Fig. 10.27. $\mathcal{V}_{\mathrm{s}}$ at point F of the cavities sketched in Fig. 10.26 as a function of the wavelength in μm

scenario implies the existence of sources of UV circularly polarized light that, up today, has not been detected. Nevertheless, the existence of such external sources may be not necessary.

In Sect. 7.7 we proved that inside the cavities of porous grains UV linearly polarized radiation depolarizes, i.e. becomes elliptically polarized. As a consequence, the aminoacids contained in the cavities of interstellar grains might be exposed to asymmetric photolysis induced by an effective UV circularly polarized light generated *in situ*.

In spite of the results presented in Sect. 7.7, it may be argued that the configuration of cavities we dealt with is rather *ad hoc*. Actually, we performed a series of calculations for homogeneous spheres containing 13 cavities in random configuration [37]. More precisely we considered the same 100 nm radius sphere filled by the Bruggeman mixture we considered in Sect. 7.7. Through a random number generator we produced within the sphere a cluster of 13 cavities of radius $\rho_\alpha = 15\,\mathrm{nm}$ with the constraint that neighbouring cavities do not intersect and at least one of the cavities be tangent to the surface of the host sphere. One of the resulting configurations, that turns out to lack any symmetry, is shown in Fig. 10.26. A linearly polarized plane wave is assumed to incide along the z axis with the polarization vector along the x axis. The resulting values of $\mathcal{V}_{\mathrm{s}}$ (see Sect. 7.7) at point F in each of the cavities are reported in Fig. 10.27 as a function of the wavelength in μm. These results show that the depolarization occurs to a more or less large extent in all the cavities. Nevertheless, this is not the most important result. As regards the photolisys, indeed, it is more significant the change of sign of $\mathcal{V}_{\mathrm{s}}$ at several values of the wavelength. The exact values are fine-tuned by the details of the configuration as well as on the size of the host sphere [37, 38], but as a general rule, they occur in the range in which the dichroic bands of proteins and sugars were detected. Thus the mechanism of *in situ* depolarization allows for the Condon-Kuhn rule, that requires the vanishing of the sum of all the dichroic bands [244]. In order to satisfy this rule in the presence of an external source of circularly polarized UV light, somewhat *ad hoc* cut-off mechanisms are invoked [245]. On the contrary, the results described above stem from a correct and general treatment of the polarization of electromagnetic radiation.

A Appendix

This appendix is devoted to a brief description of the computational mathematics that is implied by the theory in Chaps. 1–6. In what follows, we will often refer to the quantities l_I and l_E that are defined in Sect. 5.4.1, and in the present context determine the size of the storage vectors of the codes that were used to perform the calculations presented in Chaps. 7–10.

A.1 Bessel and Hankel Functions

The spherical Bessel and Hankel functions, together with their derivatives, appear in several places of the theory. For instance, they enter the formulas for the Mie coefficients $R_l^{(p)}$, the translation matrix elements for the multipole fields $\mathcal{H}^{(pp')}_{\alpha lm\alpha' l' m'}$ and $\mathcal{J}^{(pp')}_{\alpha lm\alpha' l' m'}$, etc. Let us recall that by definition

$$h_l(z) = j_l(z) + \mathrm{i} n_l(z) ,$$

where $n_l(z)$ is a spherical Neumann function. The argument $z = kr$ is, in general, a complex variable. We recall that Bessel and Neuman functions, and thus also the Hankel functions, obey the recursion relation (1.42a) and that their derivatives can be calculated through (1.42b). Forward recursion can be used to calculate the Neumann functions $n_l(z)$ starting from the initial values

$$n_0(z) = -\frac{\cos z}{z} , \quad n_1(z) = -\frac{\cos z}{z^2} - \frac{\sin z}{z} .$$

On the contrary, because of numerical instability, backward recursion must be used to calculate $j_l(z)$. To this end, let us assume that the Bessel functions are needed for at most $l = l_\mathrm{M}$; then we start the backward recursion by choosing $l_\mathrm{s} > l_\mathrm{M}$ and assigning small arbitrary values to j_{l_s} and $j_{l_\mathrm{s}-1}$. The values resulting from the recursion are then so normalized that

$$j_0(z) = \frac{\sin z}{z} , \quad j_1(z) = \frac{\sin z}{z^2} - \frac{\cos z}{z} .$$

The choice of l_s is, in general, effected through some empirical rule. For instance, we used

$$l_\mathrm{s} \approx l_\mathrm{M} + 32\sqrt{l_\mathrm{M}}$$

everywhere, which proved adequate for all the cases we dealt with.

According to the theory of Chaps. 5 and 6, both j_l and n_l may have a complex argument and the maximum values of l are $l_{\mathrm{M}}+1 = l_{\mathrm{I}}+1$ for calculating the Mie coefficients (see Sects. 5 and 5.1.1), $2l_{\mathrm{I}}$ for calculating matrix H, and $2l_{\mathrm{IE}}$ for calculating J, where l_{IE} is the largest of l_{I} and l_{E}.

A.1.1 Mie Coefficients for Radially Nonhomogeneous Spheres

In Sect. 5.2 we discussed the case of radially nonhomogeneous spheres, i.e., spheres whose refractive index $n_0 = n_0(r)$ is a continuous function, with continuous first derivative, of the distance from the center. The appropriate Mie coefficients are then given by (5.19) and involve the radial functions that are the solution of (5.18). These functions must be calculated by numerical integration. Although more sophisticated methods are available, we found the Runge–Kutta method [114] to be adequate in all the cases we dealt with in this book (see e.g. Sect. 7.4). $l_{\mathrm{M}} = l_{\mathrm{I}}$ is the maximum value for calculating both radial functions and their derivatives.

A.2 Spherical Harmonics

According to definitions (1.15) and to (6.25), the spherical harmonics are given by

$$Y_{lm} = \frac{1}{\sqrt{4\pi}} \bar{P}_{lm}(z) \exp(\mathrm{i}m\varphi) ,$$

where $z = \cos\vartheta$ may be complex. The functions $\bar{P}_{lm}(z)$ for $m \geq 0$ are calculated through the recursion relation

$$\begin{aligned} \bar{P}_{lm} =& z\left[\frac{(2l-1)(2l+1)}{(l-m)(l+m)}\right]^{1/2} \bar{P}_{l-1,m} \\ &- \left[\frac{(2l+1)(l-1-m)(l-1+m)}{(2l-3)(l-m)(l+m)}\right]^{1/2} \bar{P}_{l-2,m} , \end{aligned}$$

which is obtained by the corresponding recursion for the associated Legendre functions. The starting values are

$$\bar{P}_{00} = 1 , \quad \bar{P}_{10} = z\sqrt{3} , \quad \bar{P}_{11} = (1-z^2)^{1/2}\sqrt{3/2} .$$

Of course, in case $z = \cos\vartheta = \pm 1$, it is sufficient to use (1.18).

The spherical harmonics with real argument are used in calculating the amplitudes $W^{(p)}_{\eta lm}$ with $l \leq l_{\mathrm{E}}$, the elements of H with $l \leq 2l_{\mathrm{I}}$ and the elements of J with $l \leq 2l_{\mathrm{IE}}$. Spherical harmonics with complex $z = \cos\vartheta$ and $l \leq l_{\mathrm{I}}$ are needed for calculating the elements of the multipole reflection matrix F (see Sects. 6.3 and 6.5), and the amplitudes $W^{(p)}_{\mathrm{E}\eta lm}$ of the evanescent waves of Sect. 6.7.1.

A.3 Clebsch–Gordan Coefficients

The Clebsch–Gordan coefficients $C(1, l, \bar{l}; \mu, \bar{m} - \mu)$ appear in many formulas, but they do not imply any computational problem as they are given in Table 1.1.

The Clebsch–Gordan coefficients $C(j_1, j_2, j; m_1, m_2)$ are required in the calculation of the elements of the transfer matrices H and J and in many calculations of orientational averages. Actually, to get these Clebsch–Gordan coefficients we resorted to the relation

$$
\begin{aligned}
&C(j_1, j_2, j; m_1, m_2) \\
&\qquad = (-)^{j_1 - j_2 + m_1 + m_2} (2j + 1)^{1/2} \begin{pmatrix} j_1 & j_2 & j \\ m_1 & m_2 & -(m_1 + m_2) \end{pmatrix} ,
\end{aligned}
$$

where the array on the right-hand side denotes a $3j$-symbol [7], and to some useful recursion relation for the latter. It is well known that, when the set of the $3j$-symbols generated by recursion spans a large interval of allowed values for the recursion index, calculation may undergo serious numerical errors. Thus one starts the forward recursion from the least admissible value of the recursion index and proceeds up to half-way. Then one starts a backward recursion from the largest value of the recursion index down to halfway and, after matching the halfway values, at last renormalizes the whole set [246]. As a matter of fact, the choice of the recursion rule stems from the internal structure of the specific routine in which the Clebsch–Gordan coefficients are required.

A.3.1 Translation of Origin

The coefficients $C(L, l, l'; M, m' - M)$ and $C(L, l, l'; 0, 0)$ enter the calculation of elements of H and J (1.73) through the Gaunt integrals (1.36) (see (1.65)). We recall that $l, l' \leq l_{\mathrm{I}}$ and $L \leq 2l_{\mathrm{I}}$ when calculating H, and that $l, l' \leq l_{\mathrm{IE}}$ and $L \leq 2l_{\mathrm{IE}}$ when calculating J. We calculate $C(L, l, l'; M, m' - M)$, $C(L, l, l'; 0, 0)$, and $C(L, l, l'; 0, m)$ through separate routines, but we used, in any case, the recursion over j_1 for the $3j$-symbols. In particular, when the translation is along the z axis, $C(L, l, l'; 0, m)$ was used in place of $C(L, l, l'; M, m' - M)$ in view of (1.74).

A.3.2 Orientational Averages

According to (4.47c), (4.48), (4.49), (4.53c), (4.54), (4.55), and (4.72), the Clebsch–Gordan coefficients are needed for $l, l', l'' \leq l_{\mathrm{E}}$, $L, L' \leq 2l_{\mathrm{E}}$, and $\lambda \leq 4l_{\mathrm{E}}$. The largest value of λ used in (4.49c) and in (4.54c) stems from (1.31). The recursion we resorted to calculate these Clebsch–Gordan coefficients is that involving m_2 for the $3j$-symbols [9], with the exception of (4.72). In fact, in (4.72) we used the recursion over j_1 both for $C(L, l, l'; M, m' - M)$ and for $C(L, l, l'; 0, m)$.

A.4 Rotation Matrices $\mathbf{D}^{(l)}$

In order to effect the calculation of the orientational averages, the actual calculation of the rotation matrices is not necessary, provided that the required integral that involves $\mathrm{D}^{(l)}$ matrices and the weight function can be performed analytically. Nevertheless, there is a case in which the burden of the calculation can be greatly reduced by calculating the rotation matrices, i.e., the case in which the particle of interest has cylindrical symmetry but the orientational average is required around an axis orthogonal to the cylindrical axis. In this case, it is convenient to calculate the transition matrix $\bar{\mathrm{S}}$ by assuming the $\bar{z}$ axis along the cylindrical-symmetry axis: in fact, this choice produces the automatic factorization of the matrix M that greatly reduces the computational effort required by its inversion (see Sects. 5.4 and 5.5). Then, with the help of (4.42), the transition matrix is transformed to a new frame of reference chosen so that the cylindrical axis coincides, e.g., with the x axis. The transformed S can be considered as a new $\bar{\mathrm{S}}$ to which all the considerations of Sect. 4.5 apply. In practice, we need

$$\mathcal{D}^{(l)}_{mm'}(\alpha = 0, \beta = \pi/2, \gamma = 0) = \mathrm{d}^{(l)}_{mm'}(\pi/2) \ ,$$

which can be calculated by using the recursion relations over m' and the specific formulas for $m = l$ and $m = l - 1$. This procedure is particularly convenient because $\beta = \pi/2$. The symmetry properties of $\mathrm{d}^{(l)}$ can be used to further reduce the computational effort, that is rather light, however. Note that $l \leq l_{\mathrm{E}}$.

A.5 Calculating $\mathbf{M}^{-1}$, $\mathbf{H}^{-1}$, and $\mathbf{H}_{\alpha}^{-1}$

To perform these calculations, we use the classical LU factorization [114]. Of course, complex algebra is necessary and all the calculations require double precision. In particular, calculating H^{-1} and H_{α}^{-1}, which is necessary when a particle is in the presence of a dielectric surface (see Sects. 6.3 and 6.5), may require an even higher precision within a specific approach to be used besides the main bulk of the calculations.

A.6 General Approach to the Computational Problem

According to our experience, a code designed to perform the calculations implied by the problem of scattering should be a reasonable compromise to contain both the storage required for the intermediate products of the calculations and the time required to perform the calculations themselves. The preferred procedure to achieve this task consists in calculating once and for all and storing into appropriate vectors all the quantities that are shared with the main stream of the calculations. Among these quantities, which will be picked up according to the need, there are just the Bessel and Hankel functions, the spherical harmonics, and the Clebsch–Gordan coefficients.

References

1. D. W. Mackowski, M. I. Mishchenko: J. Opt. Soc. Am. A **13**, 2266 (1996)
2. E. M. Rose: *Multipole fields* (Wiley, New York 1956)
3. P. C. Waterman: Phys. Rev. D **3**, 825 (1971)
4. J. D. Jackson: *Classical electrodynamics*, 2nd edition (Wiley, New York 1975)
5. H. C. van de Hulst: *Light scattering by small particles* (Wiley, New York 1957)
6. J. A. Stratton: *Electromagnetic theory* (McGraw-Hill, New York 1941)
7. E. M. Rose: *Elementary theory of angular momentum* (Wiley, New York 1957)
8. J. L. Powell, B. Crasemann: *Quantum mechanics* (Addison-Wesley, Reading, Mass. 1961)
9. D. A. Varshalovich, A. N. Moskalev, V. K. Khersonskii: *Quantum theory of angular momentum* (World Scientific, Singapore 1988)
10. M. Abramowitz, I. A. Stegun: *Handbook of mathematical functions* (Dover, New York 1965)
11. A. R. Edmonds: *Angular momentum in quantum mechanics* (Princeton University Press, Princeton, NJ 1957)
12. P. M. Morse, H. Feshbach: *Methods of theoretical physics* (McGraw-Hill, New York 1953)
13. W. W. Hansen: Phys. Rev. **47**, 139 (1935)
14. E. Fucile, F. Borghese, P. Denti, R. Saija, O. I. Sindoni: IEEE Trans. Antennas Propag. **AP 45**, 868 (1997)
15. R. Nozawa: J. Math. Phys. **7**, 1841 (1966)
16. F. Borghese, P. Denti, G. Toscano, O. I. Sindoni: J. Math. Phys. **21**, 2754 (1980)
17. A. Ishimaru: *Wave propagation and scattering in random media* (Academic press, New York 1978)
18. C. F. Bohren, D. P. Gilra: J. Colloid Interf. Sci. **72**, 215 (1979)
19. G. Videen, W. Sun: Appl. Opt. **42**, 6724 (2003)
20. M. I. Mishchenko, D. W. Mackowski, L. D. Travis: Appl. Opt. **34**, 4589 (1995)
21. M. I. Mishchenko, J. H. Hovenier, L. D. Travis: 'Concepts, terms, notations.' In: *Light scattering by nonspherical particles*, ed. by M. I. Mishchenko, J. W. Hovenier, L. D. Travis (Academic Press, New York 2000), pp. 3–25
22. R. Newton: *Scattering theory of waves and particles* (McGraw-Hill, New York 1966)
23. D. S. Saxon: Phys. Rev. **100**, 1771 (1955)
24. J. W. Hovenier, C. V. M. van der Mee: 'Basic relationships for matrices describing scattering by small particles.' In: *Light scattering by nonspherical particles*, ed. by M. I. Mishchenko, J. W. Hovenier, L. D. Travis (Academic Press, New York 2000), pp. 61–85

25. J. W. Hovenier, C. V. M. van der Mee: Astron. Astrophys. **128**, 1 (1983)
26. J. W. Hovenier, C. V. M. van der Mee: Astron. Astrophys. **196**, 287 (1988)
27. J. R. Bottiger: *Notes on 3-D Müller matrices.* Final Technical Report CRDEC-TR-1L162662, August 1989
28. M. Born, E. Wolf: *Principles of optics*, 7th edition (Cambridge University Press, Cambridge, UK 2002)
29. I. V. Lindell: Int. J. Electr. Eng. Educ. **20**, 33 (1983)
30. T. Carozzi, R. Calsson, J. Bergman: Phys. Rev. E **61**, 2024 (2000)
31. M. I. Mishchenko, J. W. Hovenier, D. W. Mackoski: Appl. Opt. **21**, 71 (2004)
32. M. Gell-Mann, Y. Ne'eman: *The eight-fold way* (Benjamin, New York 1964)
33. J. C. Samson: J. Geophys. **48**, 195 (1980)
34. R. Barakat: Opt. Comm. **23**, 147 (1977)
35. R. Barakat: Opt. Acta **39** 1171 (1983)
36. T. Setälä, M. Kaivola, A. T. Friberg: Phys. Rev. Lett. **88**, (2002)
37. R. Saija, C. Cecchi-Pestellini, M. A. Iatì, A. Giusto, F. Borghese, P. Denti, S. Aiello: Astrophys. J. **633**, 953 (2005)
38. F. Borghese, P. Denti, R. Saija, C. Cecchi-Pestellini: J. Phys. Conference Series. **6**, 59 (2005)
39. M. I. Mishchenko: J. Quant. Spectros. Radiative Transfer **70**, 811 (2001)
40. J. Klačka, M. Kocifaj: J. Quant. Spectros. Radiative Transfer **70**, 595 (2001)
41. L. Tsang, J. A. Kong, T. T. Shing: *Theory of microwave remote sensing* (Wiley, New York 1985)
42. E. Fucile, F. Borghese, P. Denti, R. Saija: Appl. Opt. **34**, 4552 (1995)
43. P. C. Clemmow: *The plane wave spectrum representation of electromagnetic fields* (Oxford Univ. Press, Oxford 1996)
44. A. Ishimaru: *Electromagnetic wave propagation, radiation and scattering* (Prentice-Hall, Englewood Cliffs, NJ 1991)
45. F. Borghese, P. Denti, R. Saija, G. Toscano, O. I. Sindoni: Nuovo Cim. B **81**, 29 (1984)
46. F. Borghese, P. Denti, R. Saija, M. A. Iatì, O. I. Sindoni: J. Quant. Spectr. Radiat. Transfer **70**, 237 (2001)
47. V. K. Varadan: 'Multiple scattering of acoustic, electromagnetic and elestic waves.' In: *Acoustic electromagnetic and elastic wave scattering–Focus on the T-matrix approach*, ed. by V. K. Varadan, V.V. Varadan (Pergamon, New York 1980), pp. 103–134
48. V. V. Varadan, V. K. Varadan: Phys. Rev. D **21**, 388 (1980)
49. N. G. Khlebtzov: Appl. Opt. **38**, 5359 (1992)
50. M. I. Mishchenko: Astrophys. Space Sci. **164**, 1 (1990)
51. M. I. Mishchenko: Kinem. Phys. Celest. Bodies **7**(5), 83 (1991)
52. M. I. Mishchenko: Astrophys. J. **367**, 561 (1991)
53. M. I. Mishchenko: J. Opt. Soc. Am. A **8**, 871 (1991); errata ibid. **9**, 497 (1992)
54. R. Balescu: *Equilibrium and nonequilibrium statistical mechanics* (Wiley, New York 1975)
55. R. Clark Jones: Phys. Rev. B **15**, 93 (1945); errata ibid. 213
56. L. E. Reichl: *A modern course in statistical physics* (University of Texas Press, Austin 1980)
57. L. D. Favro: Phys. Rev. **119**, 53 (1960)
58. E. Fucile, F. Borghese, P. Denti, R. Saija: J. Opt. Soc. Am. A **10**, 2611 (1993)

59. R. Saija, M. A. Iatì, A. Giusto, P. Denti, F. Borghese: J. Quant. Spectros. Radiative Transfer **94**, 163 (2005)
60. E. M. Purcell: Astrophys. J. **231**, 404 (1979)
61. B. T. Draine, J. C. Weingartner: Astrophys. J. **470**, 551 (1996)
62. P. L. Marston, J. H. Crichton: Phys. Rev. A **30**, 2508 (1984)
63. F. J. García de Abajo: Phys. Rev. B **70**, 115422 (2004)
64. F. J. García de Abajo: J. Quant. Spectros. Radiative Transfer **89**, 3 (2004)
65. F. Borghese, P. Denti, R. Saija, M. A. Iatì: Optics Express (2006, in press)
66. T. Levi Civita, U. Amaldi: *Lezioni di meccanica razionale* (Zanichelli, Bologna, 1930)
67. G. Mie: Ann. Phys. **25**, 377 (1908)
68. Bo Å. S. Gustafson: 'Microwave analog to light scattering measurements.' In: *Light scattering by nonspherical particles*, ed. by M. I. Mishchenko, J. W. Hovenier, L. D. Travis (Academic Press, New York 2000), pp. 367–390
69. R. A. Ferrell: Phys. Rev. **111**, 1214 (1958)
70. R. A. Ferrell, E. Stern: Am. J. Phys. **30**, 810 (1962)
71. F. Sauter: Z. Physik **203**, 488 (1967)
72. A. R. Melnyk, M. J. Harrison: Phys. Rev. B **2**, 835 (1970)
73. R. Ruppin: Phys. Rev. B **11**, 2871 (1975)
74. P. J. Wyatt: Phys. Rev. B **127**, 1837 (1962)
75. M. Kerker: *The scattering of light* (Academic Press, New York 1969)
76. F. Borghese, P. Denti, R. Saija, G. Toscano, O. I. Sindoni: J. Opt. Soc. Am. A **4**, 1984 (1987)
77. R. Ruppin: J. Opt. Soc. Am. **66**, 449 (1976)
78. B. R. Johnson: J. Opt. Soc. Am. A **10**, 343 (1993)
79. J. H. Bruning, Y. T. Lo: IEEEE Trans. Antennas Propag. **19**, 378 (1971)
80. B. Peterson, S. Ström: Phys. Rev. D **8**, 3661 (1973)
81. J. M. Gérardy, M. Ausloos: Phys. Rev. B **22**, 4950 (1980)
82. F. Borghese, P. Denti, R. Saija, G. Toscano, O. I. Sindoni: Aerosol Sci. Technol. **3**, 227 (1984)
83. Y.-L. Xu: Appl. Opt. **36**, 9496 (1997)
84. B. Stout, J.-C. Auger, J. Lafait: J. Modern Opt. **48**, 2105 (2001)
85. F. Borghese, P. Denti, R. Saija, O. I. Sindoni: J. Aerosol Sci. **20**, 1079 (1989)
86. R. T. Wang, J. M. Greenberg, D. W. Schuerman: Opt. Lett. **11**, 543 (1981)
87. D. W. Schuerman, R. T. Wang: *Experimental results of multiple scattering.* Chemical Systems Laboratory Contractor Report ARCSL-CR-81003, November 1981
88. F. Borghese, P. Denti, R. Saija, O. I. Sindoni: J. Opt. Soc. Am. A **9**, 1327 (1992)
89. F. Borghese, P. Denti, R. Saija: Appl. Opt. **33**, 484 (1994); errata ibid. **34**, 5556 (1995)
90. J. G. Fikioris, N. K. Uzunoglu: J. Opt. Soc. Am. **69**, 1359 (1979)
91. N. C. Skaropoulos, M. P. Ioannidou, D. P. Chrissoulidis: J. Opt. Soc. Am. A **11**, 1859 (1994)
92. M. P. Ioannidou, D. P. Chrissoulidis: J. Opt. Soc. Am. A **19**, 505 (2002)
93. M. I. Mishchenko, L. D. Travis: 'Electromagnetic scattering by nonspherical particles.' In: *Exploring the atmosphere by remote sensing*, ed. by R. Guzzi, K. Pfeilsticker (Springer, Heidelberg 2002)
94. E. M. Purcell, C. R. Pennypacker: Astrophys. J. **186**, 705 (1973)

95. B. T. Draine, P. J. Flatau: J. Opt. Soc. Am. A **11**, 1491 (1994)
96. B. T. Draine: Astrophys. J. **333**, 848 (1988)
97. B. T. Draine, J. J. Goodman: Astrophys. J. **405**, 685 (1993)
98. D. W. Mackowski: J. Opt. Soc. Am. A **19**, 881 (2002)
99. S. K. Yee: IEEE Trans. Antennas Propag. **14**, 302 (1966)
100. T. Levi Civita: *Caratteristiche dei sistemi differenziali e propagazione ondosa* (Zanichelli, Bologna 1992)
101. A. Taflove, M. E. Brodwin: IEEE Trans. Microwave Theor. Technol. **23**, 623 (1975)
102. G. Mur: IEEE Trans. Electromagn. Compat. **23**, 377 (1981)
103. Z. Liao, H. L. Wong, B. Yang, Y. Yuan: Scientia Sinica **27**, 1063 (1984)
104. K. Umashankar, A. Taflove: IEEE Trans. Electromagn. Compat. **24**, 397 (1982)
105. P. Yang, K. N. Liou: J. Opt. Soc. Am. A **13**, 2072 (1996)
106. P. Yang, K. N. Liou: 'Finite difference time domain method for light scattering by nonspherical and inhomogeneous particles.' In: *Light scattering by nonspherical particles*, ed. by M. I. Mishchenko, J. W. Hovenier, L. D. Travis (Academic Press, New York 2000), pp. 174–221
107. F. Borghese, P. Denti, R. Saija, E. Fucile, O. I. Sindoni: J. Opt. Soc. Am. A **12**, 530 (1995)
108. E. Fucile, P. Denti, F. Borghese, R. Saija, O. I. Sindoni: J. Opt. Soc. Am. A **14**, 1505 (1997)
109. P. Denti, F. Borghese, R. Saija, E. Fucile, O. I. Sindoni: J. Opt. Soc. Am. A **16**, 167 (1999)
110. P. Denti, F. Borghese, R. Saija, M. A. Iatì, O. I. Sindoni: Appl. Opt. **38**, 6421 (1999)
111. G. A. Korn, T. M. Korn: *Mathematical handbook for scientists and engineers* (Dover Publications, Mineola NY, 2000)
112. P. A. Bobbert, J. Vlieger: Physica **137A**, 209 (1986)
113. H. Weyl: Ann. Phys. **60**, 481 (1919)
114. W. H. Press, S. A. Teukolsky, W. T. Vetterling, B. P. Flannery: *Numerical recipes in fortran* (Cambridge University Press, New York 1992)
115. F. Borghese, P. Denti, R. Saija, E. Fucile, O. I. Sindoni: Appl. Opt. **36**, 4226 (1997)
116. N. J. Jarrick: *Internal reflection spectroscopy* (Interscience-Wiley, New York 1967)
117. T. Hirschfeld, M. J. Block, W. Mueller: J. Histochem. Cytochem. **25**, 719 (1977)
118. A. Pack, W. Grill, R. Wannemacher: Ultramicroscopy **94**, 109 (2003)
119. J.-J. Greffet, R. Carminati: Prog. Surf. Sci. **56**, 133 (1997)
120. P. C. Chaumet, A. Rahmani, F. de Fornel, J.-P. Dufour: Phys. Rev. B **58**, 2310 (1998)
121. C. Liu, T. Kaiser, S. Lange, G. Schweiger: Opt. Comm. **117**, 521 (1995)
122. H. Chew, D.-S. Wang, M. Kerker: Appl. Opt. **18**, 2679 (1979)
123. F. Borghese, P. Denti, R. Saija, G. Toscano, O. I. Sindoni: J. Opt. Soc. Am. A **1**, 183 (1984)
124. S. Levine, G. O. Olaofe: J. Colloid Interf. Sci. **27**, 442 (1968)
125. P. W. Barber, D.-S. Wang: Appl. Opt. **17**, 797 (1978)
126. M. I. Mishchenko, D. W. Mackowski: J. Quant. Spectr. Radiat. Transfer **55**, 683 (1996)

127. D. H. Woodward: J. Opt. Soc. Am. **54**, 1325 (1964)
128. R. Saija, G. Toscano, O. I. Sindoni, F. Borghese, P. Denti: Nuovo Cim. B **85**, 79 (1985)
129. S. Holler, B. Stout, Y. Pan, J. R. Bottiger, R. K. Chang, G. Videen: Appl. Opt. **39**, 6873 (2000)
130. W. C. Chew, *Waves and fields in inhomogeneous media*, IEEE Press Series on Electromagnetic Waves (Institute of Electrical and Electronic Engineers, Piscataway, N. J., 1990)
131. O. I. Sindoni: J. Phys. Conference Series **6**, 109 (2005)
132. R. Saija, M. A. Iatì, P. Denti, F. Borghese, A. Giusto, O. I. Sindoni: Appl. Opt. **42**, 2785 (2003)
133. M. I. Mishchenko, D. W. Mackowski: J. Quant. Spectros. Radiat. Transfer **55**, 683 (1996)
134. J. R. Bottiger, E. S. Fry, R. C. Tompson: 'Phase matrix measurements for electromagnetic scattering by sphere aggregates.' In: *Light scattering by irregularly shaped particles*, ed. by D. W. Schuerman (Plenum press, New York 1980), p. 283
135. M. I. Mishchenko, D. W. Mackowski, L. D. Travis: Appl. Opt. **34**, 4589 (1995)
136. J. I. Gittelman, B. Abeles: Phys. Rev. B **15**, 3297 (1977)
137. C. Kittel: *Introduction to solid state physics* (Wiley, New York 1976)
138. M. Hammermesh: *Group theory* (Addison-Wesley, Reading, Mass. 1962)
139. F. Wooten: *Optical properties of solids* (Academic Press, New York 1972)
140. F. Abeles: *Optical properties of solids* (North-Holland, Amsterdam 1972)
141. P. Chŷlek, G. Videen, D. J. Wally Geldart, J. S. Dobbie, H. C. W. Tso: 'Effective medium approximations for heterogeneous particles.' In: *Light scattering by nonspherical particles*, ed. by M. I. Mishchenko, J. W. Hovenier, L. D. Travis (Academic Press, New York 2000), pp. 274–307
142. A. Pack: *Current problems in nano-optics.* Ph.D. Thesis submitted to the University of Chemnitz (unpublished, 2001)
143. J. Lindhard: Kgl. Danske Videnskab. Selskab, Mat.-Fys. Medd. **28**, No. 8 (1954)
144. L. Kleinman: Phys. Rev. B**7**, 2288 (1973)
145. K. A. Fuller, G. W. Kattawar: Opt. Lett. **13**, 90 (1988)
146. B. V. Bronk, M. J. Smith, S. Arnold: Opt. Lett. **18**, 93 (1993)
147. R. L. Armstrong, J.-G. Xie, T. E. Ruekgauer, J. Gu, R. G. Pinnick: Opt. Lett. **18**, 119 (1993)
148. S. W. Ng, P. T. Leung, K. M. Lee: J. Opt. Soc. Am. B **19**, 154 (2001)
149. F. Borghese, P. Denti, R. Saija, M. A. Iatì, O. I. Sindoni: J. Opt. (France) **29**, 28 (1998)
150. B. T. Draine: *Planets and protostars* Vol. II, Ed. by D. C. Black, M. Shapley Mattews (University of Arizona Press, Phoenix 1985)
151. F. Borghese, P. Denti, R. Saija, G. Toscano, O. I. Sindoni: Nuovo Cim. D **6**, 545 (1985)
152. J. Bailey: Origins of Life and Evolution of Biosphere **31**, 167 (2001)
153. R. Pecora, B. Berne: *Dynamic light scattering* (Wiley, New York 1980)
154. M. I. Mishchenko: J. Electromagn. Waves Applic. **6**, 1341 (1992)
155. R. Nakamura, Y. Hidaka: Astron. Astrophys. **340**, 329 (1998)
156. X. Ma, J. Q. Lu, R. S. Brock, K. M. Jacobs, P. Yang, X.-H. Hu: Phys. Med. Biol. **48**, 4165 (2003)

157. M. J. Greenberg, F. Ferrini, B. Barsella, S. Aiello: Nature **327**, 214 (1987)
158. J. P. Bradley, L. P. Keller, T. P. Snow et al.: Science **285**, 1716 (1999)
159. B. T. Draine, H. M. Lee: Astrophys. J. **285**, 89 (1984)
160. J. Ashok, P. L. H. Varaprasad, J. R. Birch: in *Handbook of Optical Constants of Solids II*, ed. by E. D. Palik (Academic Press, New York 1991), p. 957
161. B. R. Johnson: J. Opt. Soc. Am. A **9**, 1341 (1992)
162. F. Borghese, P. Denti, R. Saija, G. Toscano, O. I. Sindoni: Aerosol Sci. Technol. **6**, 173 (1987)
163. G. Videen: J. Opt. Soc. Am. A **8**, 483 (1991); errata ibid. **9**, 844 (1992)
164. I. V. Lindell, A. H. Sihvola, K. O. Muinonen, P. Barber: J. Opt. Soc. Am. A **8**, 472 (1991)
165. M. M. Wind, J. Vlieger, D. Bedeaux: Physica **141A**, 33 (1987)
166. P. A. Bobbert, M. M. Wind, J. Vlieger: Physica **146A**, 69 (1987)
167. P. Denti, F. Borghese, R. Saija, M. A. Iatì, O. I. Sindoni: J. Opt. (France) **29**, 78 (1998)
168. J. Li, P. Chýlek: J. Opt. Soc. Am. A **10**, 687 (1993)
169. B. R. Johnson: J. Opt. Soc. Am. A **11**, 2055 (1994)
170. P. A. Bobbert, J. Vlieger, R. Greef: Physica **137A**, 243 (1986)
171. B. R. Johnson: J. Opt. Soc. Am. A **13**, 326 (1996)
172. H. Yousif: *Light scattering from parallel tilted fibers.* Ph.D. dissertation, Department of Physics, University of Arizona, Tucson, Ariz. (1987)
173. H. S. Lee, S. Chac, Y. Ye, D. Y. H. Pui, G. L. Wojcik: Aerosol Sci. Technol. **14**, 177 (1991)
174. G. L. Wojcik, D. K. Vaughan, L. K. Galbraith: 'Calculation of light scatter from structures on silicon surfaces.' In: *Lasers in microlithography*, ed. by J. S. Batchelder, D. J. Ehrlich, J. Y. Tsao, Proc. Soc. Photo-Opt. Instrum. Eng. **774**, 21 (1987)
175. K. O. Muinonen, A. H. Sihvola, I. V. Lindell, K. A. Lumme: J. Opt. Soc. Am. A **8**, 477 (1991)
176. M. A. Taubenblatt, T. K. Tran: J. Opt. Soc. Am. A **10**, 912 (1993)
177. A. Katz, A. Alimova, M. Xu, E. Rudolph, J. C. Steiner, R. R. Alfano: Optics Lett. **30**, 589 (2005)
178. B. Saltzmann: 'Climatic system analysis.' In Advances in geophysics, vol. 25, ed. by B. Saltzmann (Academic Press, New York 1983)
179. H. R. Pruppacher, J. D. Klett: *Microphysics of clouds and precipitation* (Kluwer, Dordrecht 1997)
180. S. G. Warren: Appl. Opt. **23**, 1206 (1984)
181. K. Sassen: J. Opt. Soc. Am. A **4**, 570 (1988)
182. K. Sassen: 'Lidar backscatter depolarization technique for cloud and aerosol research.' In *Light scattering by nonspherical particles*, ed. by M. I. Mishchenko, J. W. Hovenier, L. D. Travis (Academic Press, New York 2000), pp. 393–416
183. R. Saija, M. A. Iatì, P. Denti, F. Borghese, O. I. Sindoni: Appl. Opt. **40**, 5337 (2001)
184. H. Lemke, M. Quante, O. Danne, E. Raschke: 'Backscattering of radar waves by non-spherical atmospheric ice crystals: An application of the discrete dipole approximation.' In *Proc. 3rd workshop on electromagnetic and light scattering: Theory and applications* (University of Bremen, Bremen 1998), pp. 183–192
185. V. Vouk: Nature (London) **162**, 330 (1948)
186. R. A. West: Appl. Opt. **30**, 5316 (1991)

187. N. T. Zakharova, M. I. Mishchenko: Appl. Opt. **39**, 5052 (2000)
188. S. Aiello, B. Barsella, C. Chlewicki, J. M. Greenberg, P. Patriarchi, M. Perinotto: Astron. Astrophys. Suppl. **73**, 195 (1988)
189. D. C. B. Whittet: *Dust in the galactic environment* (Institute of Physics Publishing, Bristol, UK 1992)
190. L. Spitzer: *Physical processes in the interstellar medium* (Wiley, New York 1985)
191. T. P. Snow, A. N. Witt: Science **270**, 1455 (1995)
192. T. P. Snow, A. N. Witt: Astrophys. J. **468**, L65 (1996)
193. U. J. Sofia, E. Fitzpatrick, D. M. Meyer: Astrophys. J. **499**, 951 (1998)
194. D. M. Meyer, M. Jura, J. A. Cardelli: Astrophys. J. **493**, 222 (1998)
195. J. S. Mathis: Astrophys. J. **472**, 643 (1996)
196. A. Li, J. M. Greenberg: Astron. Astrophys. **323**, 566 (1997)
197. D. B. Vaidya, R. Gupta: Astron. Astrophys. **348**, 594 (1999)
198. D. A. Williams: Astr. Geophys. **41**, 3.8 (2000)
199. R. Saija, M. A. Iatì, F. Borghese, P. Denti, S. Aiello, C. Cecchi-Pestellini: Astrophys. J. **559**, 993 (2001)
200. U. J. Sofia, D. M. Meyer: Astrophys. J. **554**, L221 (2001)
201. U. J. Sofia, D. M. Meyer: Astrophys. J. **558**, L147 (2001)
202. F. Rouleau, P. G. Martin: Astrophys. J. **377**, 526 (1991)
203. N. V. Voshchinnikov, J. S. Mathis: Astrophys. J. **526**, 257 (1999)
204. M. A. Iatì, C. Cecchi-Pestellini, D. A. Williams, F. Borghese, P. Denti, R. Saija, S. Aiello: Mon. Not. R. Astron. Soc. **322**, 749 (2001)
205. A. P. Jones: Mon. Not. R. Astron. Soc. **234**, 209 (1988)
206. J. S. Mathis, W. Rumpl, K. M. Nordsiek: Astrophys. J. **217**, 425 (1977)
207. S. S. Hong, J. M. Greenberg: Astron. Astrophys. **88**, 194 (1980)
208. A. P. Jones, W. W. Duley, D. A. Williams: Q. J. R. Astron. Soc. **31**, 567 (1990)
209. C. Cecchi-Pestellini, D. A. Williams: Mon. Not. R. Astron. Soc. **296**, 414 (1998)
210. C. F. Bohren, D. R. Huffman: *Absorption and scattering of light by small particles* (Wiley, New York 1983)
211. W. W. Duley: Astrophys. J. **287**, 694 (1984)
212. W. W. Duley, D. A. Williams: *Interstellar chemistry* (Academic Press, London 1984)
213. S. Eales, M. Edmunds: Mon. Not. R. Astron. Soc. **280**, 1167 (1996)
214. J. I. Davies, M. Trewhella, H. Joners, C. Lisk, A. Madden, J. Moss: Mon. Not. R. Astron. Soc. **288**, 679 (1997)
215. J. I. Davies, P. B. Alton, M. Trewhella, R. Evans, S. Bianchi: Mon. Not. R. Astron. Soc. **304**, 495 (1999)
216. P. B. Alton, E. M. Xilouris, S. Bianchi, J. I. Davies, N. Kylafis: Astron. Astrophys. **356**, 795 (2000)
217. P. B. Alton, J. I. Davies, S. Bianchi: Astron. Astrophys. **343**, 51 (1999)
218. P. B. Alton, P. Draper, T. Gledhill et al.: Mon. Not. R. Astron. Soc. **238** (1994)
219. R. Chiao, N. Wickramasinghe: Mon. Not. R. Astron. Soc. **159**, 361 (1972)
220. B. Barsella, F. Ferrini, J. M. Greenberg, S. Aiello: Astron. Astrophys. **209**, 349 (1989)
221. J. Franco, F. Ferrini, A. Ferrara, B. Barsella: Astrophys. J. **366**, 433 (1991)

222. J. I. Davies, P. B. Alton, S. Bianchi, M. Trewhella: Mon. Not. R. Astron. Soc. **300**, 1006 (1998)
223. T. Mukai, H. Ishimoto, T. Kozasa, J. Blum, J. M. Greenberg: Astron. Astrophys. **262**, 315 (1992)
224. M. A. Iatì, A. Giusto, R. Saija, F. Borghese, P. Denti, C. Cecchi-Pestellini. S. Aiello: Astrophys. J. **615**, 286 (2004)
225. T. Kozasa, J. Blum, T. Mukai: Astron. Astrophys. **263**, 423 (1992)
226. T. Kozasa, J. Blum, H. Okamoto, T. Mukai: Astron. Astrophys. **276**, 278 (1992)
227. J. I. Hage, J. M. Greenberg: Astrophys. J. **361**, 260 (1990)
228. F. Rouleau, P. G. Martin: Astrophys. J. **377**, 526 (1993)
229. D. A. Williams, E. Herbst: Surface Sci. **500**, 823 (2002)
230. W. W. Duley: Mon. Not. R. Astron. Soc. **319**, 791 (2000)
231. C. Cecchi-Pestellini, R. Saija, M. A. Iatí, A. Giusto, F. Borghese, P. Denti, S. Aiello: Astrophys. J. **624**, 223 (2005)
232. C. Cecchi-Pestellini, R. Saija, M. A. Iatí, A. Giusto, F. Borghese, P. Denti, S. Aiello: Astrophys. J. **632**, 1204 (2005)
233. M. P. Bernstein, J. P. Dworkin, S. A. Sandford, G. W. Cooper, L. J. Allamandola: Nature **416**, 401 (2002)
234. G. M. Muñoz Caro, U. J. Meierhenrich, W. A. Schutte et al.: Nature **416**, 403 (2002)
235. S. L. Miller: Science, **117**, 528 (1953)
236. E. L. Gibb, D. C. B. Whittet, A. C. A. Boogert, A. G. G. M. Tielens: Astrophys. J. Supp. **151**, 35 (2004)
237. C. Cecchi-Pestellini, F. Scappini, R. Saija, M. A. Iatí, A. Giusto, S. Aiello, F. Borghese, P. Denti: Int. J. Astrobiol. **3**, 287 (2004)
238. K.-W. Suh: Mon. Not. R. Astron. Soc. **304**, 389 (1999)
239. K.-W. Suh: Mon. Not. R. Astron. Soc. **315**, 740 (2000)
240. W. W. Duley, D. A. Williams: 1988, Mon. Not. R. Astron. Soc. **231**, 969 (1988)
241. G. Wurm, M. Schnaiter: Astrophys. J. **567**, 370 (2002)
242. J. R. Cronin, S. Pizzarello, D. P. Crikshank: 'Organic matter in carbonaceous chondrites, planetary satellites, asteroids and comets.' In *Meteorites and the Early Solar System*, ed. by J. F. Kerridge and M. S. Matthews (University of Arizona Press, Tucson 1988)
243. G. Cooper: Nature **414**, 879 (2001)
244. A. Jorissen, C. Cerf: Origins off Life Evol. Biosphere **32**, 129 (2002)
245. S. F. Mason: Nature **389**, 804 (1997)
246. K. Schulten, R. G. Gordon: J. Math. Phys. **16**, 1961 (1975)

Index